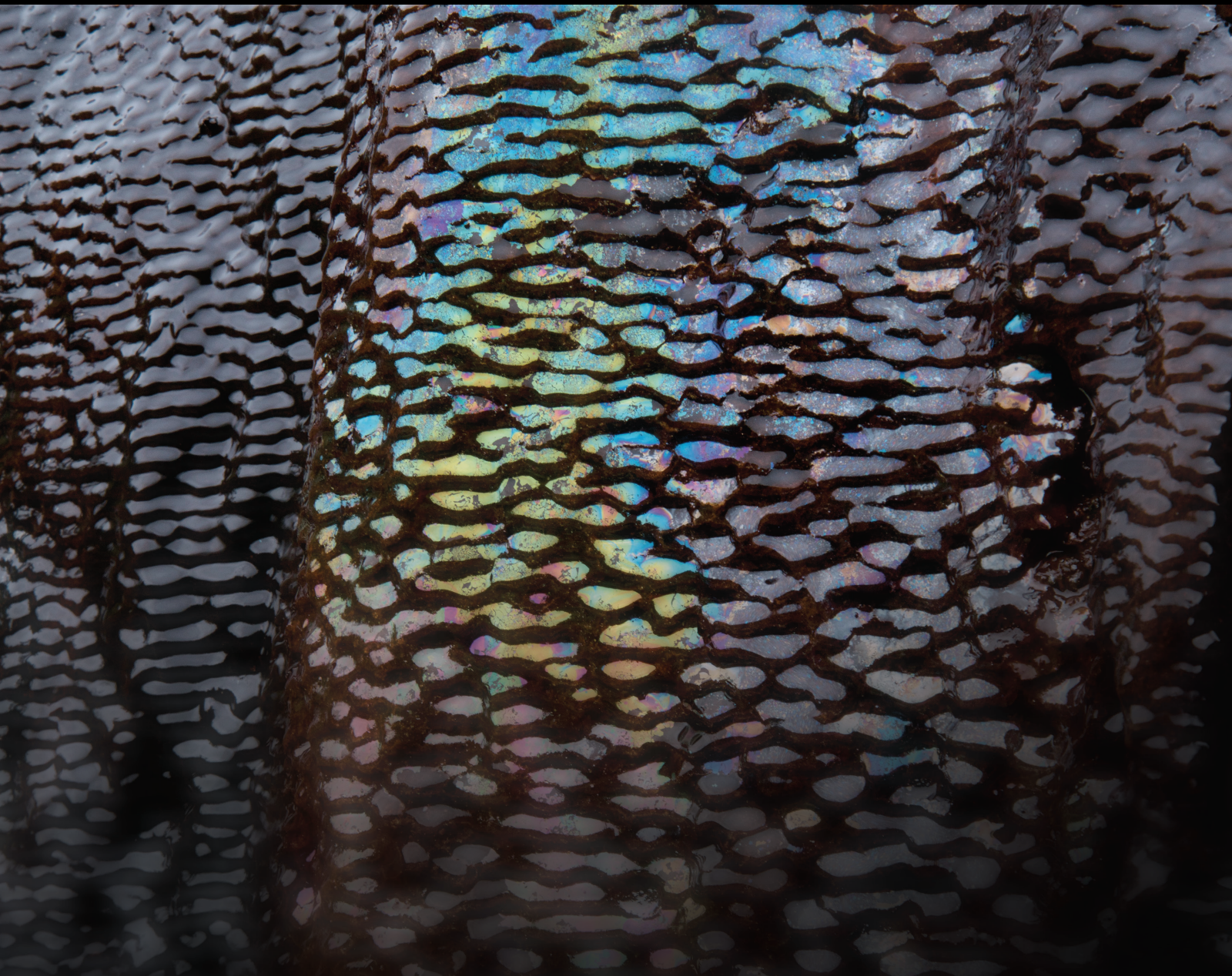


# Modeling and Simulation of Micro/ Nano-Scale Oil and Gas Migration in Tight Rocks and Shales

Lead Guest Editor: Jinze Xu

Guest Editors: Desheng Zhou, Keliu Wu, and Zhangxin Chen





---

**Modeling and Simulation of Micro/Nano-Scale Oil and Gas Migration in Tight Rocks and Shales**



Geofluids

---

**Modeling and Simulation of Micro/  
Nano-Scale Oil and Gas Migration in  
Tight Rocks and Shales**

Lead Guest Editor: Jinze Xu

Guest Editors: Desheng Zhou, Keliu Wu, and  
Zhangxin Chen



---

Copyright © 2021 Hindawi Limited. All rights reserved.





This is a special issue published in "Geofluids." All articles are open access articles distributed under the Creative Commons Attribution License, which permits unrestricted use, distribution, and reproduction in any medium, provided the original work is properly cited.





























# Chief Editor

































Umberta Tinivella, Italy

## Associate Editors

Paolo Fulignati , Italy  
Huazhou Li , Canada  
Stefano Lo Russo , Italy  
Julie K. Pearce , Australia

## Academic Editors

Basim Abu-Jdayil , United Arab Emirates  
Hasan Alsaedi , USA  
Carmine Apollaro , Italy  
Baojun Bai, USA  
Marino Domenico Barberio , Italy  
Andrea Brogi , Italy  
Shengnan Nancy Chen , Canada  
Tao Chen , Germany  
Jianwei Cheng , China  
Paola Cianfarra , Italy  
Daniele Cinti , Italy  
Timothy S. Collett , USA  
Nicoló Colombani , Italy  
Mercè Corbella , Spain  
David Cruset, Spain  
Jun Dong , China  
Henrik Drake , Sweden  
Farhad Ehya , Iran  
Lionel Esteban , Australia  
Zhiqiang Fan , China  
Francesco Frondini, Italy  
Ilaria Fuoco, Italy  
Paola Gattinoni , Italy  
Amin Gholami , Iran  
Michela Giustiniani, Italy  
Naser Golsanami, China  
Fausto Grassa , Italy  
Jianyong Han , China  
Chris Harris , South Africa  
Liang He , China  
Sampath Hewage , Sri Lanka  
Jian Hou, China  
Guozhong Hu , China  
Lanxiao Hu , China  
Francesco Italiano , Italy  
Azizollah Khormali , Iran  
Hailing Kong, China






Karsten Kroeger, New Zealand  
Cornelius Langenbruch, USA  
Peter Leary , USA  
Guangquan Li , China  
Qingchao Li , China  
Qibin Lin , China  
Marcello Liotta , Italy  
Shuyang Liu , China  
Yong Liu, China  
Yueliang Liu , China  
Constantinos Loupasakis , Greece  
Shouqing Lu, China  
Tian-Shou Ma, China  
Judit Mádl-Szonyi, Hungary  
Paolo Madonia , Italy  
Fabien Magri , Germany  
Micòl Mastroicco , Italy  
Agnes Mazot , New Zealand  
Yuan Mei , Australia  
Evgeniy M. Myshakin , USA  
Muhammad Tayyab Naseer, Pakistan  
Michele Paternoster , Italy  
Mandadige S. A. Perera, Australia  
Marco Petitta , Italy  
Chao-Zhong Qin, China  
Qingdong Qu, Australia  
Reza Rezaee , Australia  
Eliahu Rosenthal , Israel  
Gernot Rother, USA  
Edgar Santoyo , Mexico  
Mohammad Sarmadivaleh, Australia  
Venkatramanan Senapathi , India  
Amin Shokrollahi, Australia  
Rosa Sinisi , Italy  
Zhao-Jie Song , China  
Ondra Sracek , Czech Republic  
Andri Stefansson , Iceland  
Bailu Teng , China  
Tivadar M. Tóth , Hungary  
Orlando Vaselli , Italy  
Benfeng Wang , China  
Hetang Wang , China  
Wensong Wang , China  
Zhiyuan Wang , China  
Ruud Weijermars , Saudi Arabia

Bisheng Wu , China  
Da-yang Xuan , China  
Yi Xue , China  
HE YONGLIANG, China  
Fan Yang , China  
Zhenyuan Yin , China  
Sohrab Zendehboudi, Canada  
Zhixiong Zeng , Hong Kong  
Yuanyuan Zha , China  
Keni Zhang, China  
Mingjie Zhang , China  
Rongqing Zhang, China  
Xianwei Zhang , China  
Ye Zhang , USA  
Zetian Zhang , China  
Ling-Li Zhou , Ireland  
Yingfang Zhou , United Kingdom  
Daoyi Zhu , China  
Quanle Zou, China  
Martina Zucchi, Italy





# Contents

## **On the Imbibition Model for Oil-Water Replacement of Tight Sandstone Oil Reservoirs**

Xiong Liu , Desheng Zhou , Le Yan , Shun Liu , and Yafei Liu 






Research Article (7 pages), Article ID 8846132, Volume 2021 (2021)

## **Effect of Seepage Force on the Wellbore Breakdown of a Vertical Wellbore**

Desheng Zhou , Haiyang Wang, Yafei Liu , Shun Liu, Xianlin Ma, Wenbin Cai, and Hai Huang

Research Article (12 pages), Article ID 8871535, Volume 2021 (2021)

## **Study on the Effect of High-Temperature Heat Treatment on the Microscopic Pore Structure and Mechanical Properties of Tight Sandstone**

Liangbin Dou , Guanli Shu , Hui Gao , Jinqing Bao , and Rui Wang 


Research Article (13 pages), Article ID 8886186, Volume 2021 (2021)

## **Characterization of the Dynamic Imbibition Displacement Mechanism in Tight Sandstone Reservoirs Using the NMR Technique**

Liangbin Dou , Min Yang, Hui Gao, Dongxing Jiang, and Chenglu Liu

Research Article (12 pages), Article ID 8880545, Volume 2020 (2020)

## **Performance Optimization of CO<sub>2</sub> Huff-n-Puff for Multifractured Horizontal Wells in Tight Oil Reservoirs**

Mingqiang Hao, Songlin Liao, Guangming Yu, Xinhui Lei, and Yong Tang 






Research Article (13 pages), Article ID 8840384, Volume 2020 (2020)

## **Review on Phase Behavior in Tight Porous Media and Microscopic Flow Mechanism of CO<sub>2</sub> Huff-n-Puff in Tight Oil Reservoirs**

Yong Tang, Jiehong Tang, Qi Liu, Yong Wang , Zigang Zheng, Yingjie Yuan, and Youwei He

Review Article (15 pages), Article ID 8824743, Volume 2020 (2020)

## **Sand Production Prediction Model for Tight Sandstone Oil Reservoirs**

Zhan-dong Li , Hong Pang , Zhong Li , Hai-xiang Zhang , Dian-ju Wang , and Ji Li 


Research Article (7 pages), Article ID 8832703, Volume 2020 (2020)

## **Pore-Scale Investigation on the Plugging Behavior of Submicron-Sized Microspheres for Heterogeneous Porous Media with Higher Permeability**

Yafei Liu , Jingwen Yang, Tianjiang Wu, Yanhong Zhao, Desheng Zhou, and Shun Liu


Research Article (9 pages), Article ID 8869760, Volume 2020 (2020)

## **A Unified Multiple Transport Mechanism Model for Gas through Shale Pores**

Fanhui Zeng , Yu Zhang, Jianchun Guo, Wenxi Ren, Tao Zhang, Qifeng Jiang, and Jianhua Xiang



Research Article (17 pages), Article ID 1894149, Volume 2020 (2020)

## **Numerical Simulation of the Non-Darcy Flow Based on Random Fractal Micronetwork Model for Low Permeability Sandstone Gas Reservoirs**


Juhua Li  and Chen Chen

Research Article (9 pages), Article ID 8884885, Volume 2020 (2020)



**Study on Propagation Behaviors of Hydraulic Fracture Network in Tight Sandstone Formation with Closed Cemented Natural Fractures**

Jun Zhang , Yu-Wei Li , Wei Li, Zi-Jie Chen, Yuan Zhao, Fa-Hao Yu, and Yan Zheng  
Research Article (22 pages), Article ID 8833324, Volume 2020 (2020)

**A Comprehensive Model for Estimating Stimulated Reservoir Volume Based on Flowback Data in Shale Gas Reservoirs**

Qi Chen, Shaojun Wang, Dan Zhu, Guoxuan Ren, Yuan Zhang, and Jinghong Hu   
Research Article (14 pages), Article ID 8886988, Volume 2020 (2020)

**The Role of Microfabric and Laminae on Pore Structure and Gas Transport Pathways of Marine Shales from Sichuan Basin, China**

Yi Shu, Shang Xu , Feng Yang , Zhiguo Shu, Pan Peng, Senxin Huang, and He Zhen  
Research Article (19 pages), Article ID 8844229, Volume 2020 (2020)



## Research Article

# On the Imbibition Model for Oil-Water Replacement of Tight Sandstone Oil Reservoirs

Xiong Liu , Desheng Zhou , Le Yan , Shun Liu , and Yafei Liu 

*School of Petroleum Engineering, Xi'an Shiyou University, Xi'an, China*

Correspondence should be addressed to Shun Liu; 53337220@qq.com

Received 13 May 2020; Accepted 28 April 2021; Published 24 May 2021

Academic Editor: Umberta Tinivella

Copyright © 2021 Xiong Liu et al. This is an open access article distributed under the Creative Commons Attribution License, which permits unrestricted use, distribution, and reproduction in any medium, provided the original work is properly cited.

A model suitable for evaluating a tight sandstone reservoir is established. The model includes two oil-water replacement modes: capillary force mode and osmotic pressure mode. The relationship between oil-water displacement rate and dimensionless time under different parameters is drawn considering the influence of capillary force, osmotic pressure, production pressure difference, and starting pressure gradient. Results indicate that the higher the relative permeability of the water phase, the lower the relative permeability of the oil phase, the smaller the oil-water viscosity ratio, and the higher the oil-water replacement rate. The relative permeability of the water phase also affects the infiltration stabilization time. Low salinity fracturing fluid infiltration helps to improve the oil-water replacement rate.

## 1. Introduction

“Fracture network fracturing and oil-water infiltration and replacement” is a new attempt for effective development of tight sandstone reservoirs. The tight reservoir and physical properties provide great conditions for fluid imbibition and replacement. Fracturing fluid is not only the carrier of carrying sand to make fracture but also the tool of displacement. The widely recognized oil/water displacement modes of tight reservoirs include three main models: reverse imbibition replacement, replacement of infiltration, and absorption in the same direction and osmotic pressure replacement. The first two models are fluid imbibition displacement under capillary force, and the latter is based on the displacement caused by osmotic pressure difference caused by ionic concentration difference. Many scholars have done a lot of research in this area. In terms of imbibition and replacement, most laboratory experiments show that the imbibition process is the infiltration of the injected water into the pore channel under capillary force, driving the oil and gas resources away from the adjacent macropores, so as to realize imbibition replacement [1–4]. The scholars Oen et al. [5], Babadagli and Ershaghi [6], Shabir et al. [7], and the ET (Tayfun) (2015) have studied the imbibition and displacement between cracks

and matrix in fractured reservoirs and studied the imbibition characteristics of shale formations. Bertonecello et al. [8] based on imbibition to study the self-priming of single-well fracturing during the early stage of unconventional reservoirs. In terms of osmotic pressure replacement, Mitchell et al. [9], Kurtoglu [10], van Oort et al. [11], Xu et al. [12], [13], and ET (2016) et al. have mainly studied the characteristics of osmotic pressure and oil and water displacement in shale reservoirs and have studied in detail. Mirzaei et al. [14], Kathel and Mohanty [15], and Chahardowli et al. [16] studied that low salinity brine is an effective way to improve the recovery of fractured tight sandstone reservoirs.

Research on factors affecting oil-water imbibition and displacement in tight reservoirs: scholars Mirzaei et al. [14] based on CT scanning experimental methods, the factors affecting the permeability of fractured cores of oil wetting fracture are analyzed and studied. It is considered that wetting and viscosity are the main factors affecting the imbibition effect of oil wetting fractured cores. The research shows that the methods of increasing oil recovery in fractured oil reservoirs include steam injection, low salinity brine, and surfactant. Kathel and Mohanty [15] consider that the main controlling factors affecting the recovery of tight reservoirs are as follows: wettability > salt concentration > residual oil saturation; and

Liang et al. [17] for Buchan tight reservoirs, the influence parameters of single-well productivity are analyzed by means of information analysis, grey correlation, and orthogonal experimental design. Besides fracture parameters, reservoir permeability, formation pressure, and viscosity of crude oil have great influence on the output of a single well. Lan et al. [18] explore the relationship between the imbibition and water loss of a tight sandstone reservoir and the soaking time. The results show that the change of clay content has no effect on imbibition. The larger the TOC content is, the lower the permeation capacity is. Habibi et al.'s [19] study shows that the imbibition position in the same rock core is random. Saline immersion can help to increase the close relationship between fluid and rock and affect the contact angle size. Chahardowli et al.'s [16] study shows that the application of brine to weak water wetting and mixed wetting core improves EOR, and the first oil recovery can reach 38-46% OIIP. Valluri et al.'s [20] study shows that the interaction between sodium and calcium saline water and ultralow density rocks helps to enhance the recovery of tight reservoirs. Qing et al. [21] study the Chang 8 reservoir in the Wu Qi area by means of geothermal nitrogen adsorption, high-pressure mercury injection, Amott method, and imbibition NMR. The influencing factors are reservoir quality, maximum pore throat radius, specific surface area, and relative wetting index.

In summary, the mechanism of oil-water displacement in tight sandstone reservoirs is not clear enough. Most of them are based on laboratory experiments and analysis. Few literatures consider two models of displacement and replacement under the action of capillary force.

## 2. Displacement Mechanism

Tight sandstone reservoirs cannot form natural industrial productivity and need horizontal-well fracturing for reservoir reconstruction. Fracturing fluid can not only break the rock to communicate with fractures and form a complex fracture network but also replace the oil phase with a matrix to increase the output of a single well. The widely recognized mechanism of oil and water displacement in tight reservoirs includes capillary imbibition and displacement under osmotic pressure. As shown in Figure 1, assuming that reservoirs are hydrophilic, the water phase enters the throat under capillary force, the displacement of oil phase from the other end of the pore throat, the smaller the throat, the greater the capillary force, the more oil and water displacement. The pore throat of a tight sandstone reservoir is mostly concentrated in 0.1-1  $\mu\text{m}$ , so capillary force is more significant. Figure 2 shows the osmotic pressure mechanism. The low permeability solution on the left side of the semipermeable membrane and the high salinity solution on the right side, because of the osmotic pressure generated by the ion concentration difference on both sides, the water molecules in the low salinity solution of the left pipeline are under osmotic pressure. Through the semipermeable membrane into the right pipe, until the force is balanced again, the clay minerals in the tight sandstone reservoir contain 5%-10% oil. Two sides of the clay will produce double ionosphere, which has the function of semipermeable membrane. When the fractur-

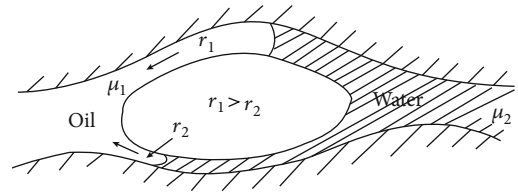


FIGURE 1: Oil and water displacement under capillary force.

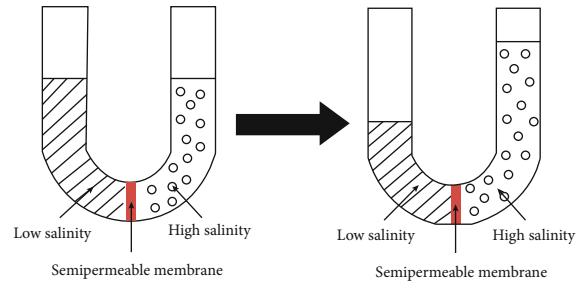


FIGURE 2: Oil-water displacement under osmotic pressure.

ing fluid and the formation water have poor mineralization, they will form osmotic pressure on both sides of the clay mineral, if the fracturing fluid salinity is relatively low. Then, the water molecules in the fracturing fluid penetrate the clay minerals into the reservoir, and the displacement of the oil phase is expelled from the other port. This is also the reason for the low salinity water drive to enhance the oil recovery.

Figures 3 and 4 show the core gravity imbibition experimental device and the experimental data of tight sandstone cores with capillary force and osmotic pressure, respectively. The experimental cores are taken from the Chang 7 group of tight sandstone reservoirs in Changqing Oilfield (China). The permeability of the core is  $0.084 \times 10^{-3} \mu\text{m}^2$ , the porosity is 7.39%, and the clay mineral content is 6.69%. The experimental process is as follows: (1) using core cutting machine, core drilling machine, and core grinding machine, the cores obtained from the field are made into standard rock samples with diameters of 2.5 cm and 4-5 cm in length. (2) The standard rock samples are washed and dried to constant weight, core weight is recorded, porosity and permeability are measured, and so on. (3) Saturate distilled water, then displace the saturated simulated oil, and leave it in the simulated oil for a period of time. (4) Wipe off the surface oil slick, and carry out the experiment by using the weighing method core imbibition experiment device shown in Figure 3; (5) record and process the experimental data; (6) after the experiment is finished, remove the core, reprocess steps (2) and (3), and proceed to the next group of experiments to make the experimental results have higher credibility.

A total of 3 sets of comparative experiments were carried out. As shown in Figure 4, the percolating solution was distilled water, 15000 mg/L mineralized solution (according to the formation water ion configuration), and 45000 mg/L mineralized solution, because the degree of osmotic fluid mineralization is larger than that of the core water phase, resulting in the opposite direction of the osmotic pressure



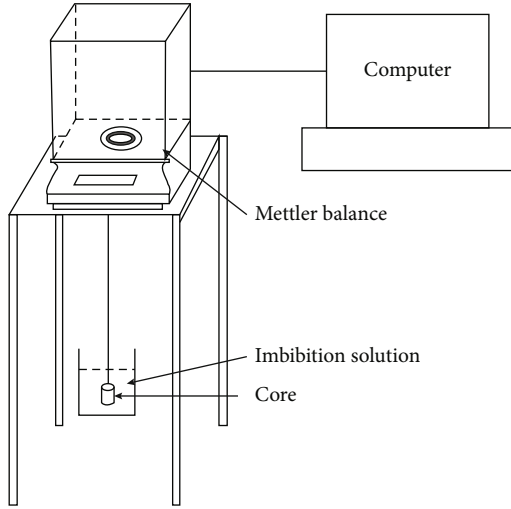


FIGURE 3: Weighting core imbibition experimental device.

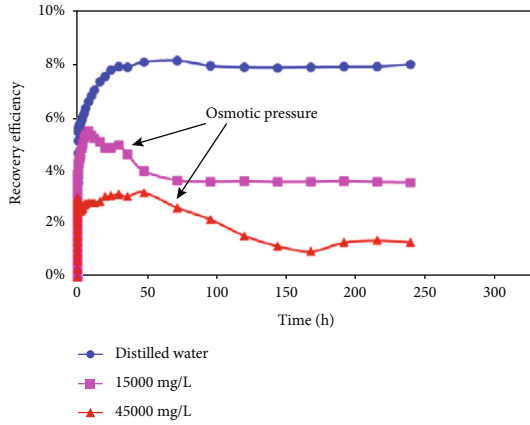


FIGURE 4: Imbibition test data of tight sandstone core considering capillary force and osmotic pressure.

direction and capillary force, which is convenient for experimental observation. From the comparison of the 3 curves, we can see that osmotic pressure is more obvious, and the downward section of the imbibition curve with downward osmotic pressure will have a downward trend. The greater the osmotic pressure, the greater the downward trend. This is because the capillary force in the early stage of osmosis is much larger than that of osmotic pressure, and the overall performance of the curve is rising rapidly. The overall force of the fluid tends to be balanced, the capillary force displacement reaches the limit, and the osmotic pressure displacement characteristics are revealed. The experimental results show that there are two modes of oil-water replacement in tight sandstone reservoirs: oil-water infiltration and replacement under capillary pressure and displacement under osmotic pressure.

### 3. Model Establishment

After fracturing, the tight sandstone oil reservoir is fractured by horizontal wells. The oil phase flows from the matrix to

the fracture network and then converges to the bottom of the well. The oil and water displacement occurs mainly in the flow network of the fracture network under the capillary force and osmotic pressure. The displacement of fluid can be regarded as a one-dimensional seepage process perpendicular to the fracture surface. As shown in Figure 5, a one-dimensional oil and water imbibition displacement model is constructed. The assumptions of the model include the following: (1) homogeneous and isotropic reservoir, rock and fluid slightly compressible; (2) oil-water two-phase isothermal percolation; (3) considering the effects of production pressure difference, capillary force, osmotic pressure, gravity, and starting pressure gradient; (4) salts only dissolve in the water; and (5) no physical and chemical reaction.

As shown in Figure 5, the left side is the fracture surface, the position for fluid replacement, and the right side is the fluid displacement limit distance, and the approximate closed end. Take the gravity effect into account, the equation of motion of the water phase and oil phase can be expressed as

$$v_w = -\frac{kk_{rw}}{\mu_w} \left( \frac{\partial p_w}{\partial z} + \rho_w g \sin \theta \right), \quad (1)$$

$$v_o = -\frac{kk_{ro}}{\mu_o} \left( \frac{\partial p_o}{\partial z} + \rho_o g \sin \theta \right). \quad (2)$$

Considering the microcompressibility of rock and fluid, the seepage velocity of water-phase and oil-phase fluid is satisfied:

$$v_o + v_w = 0. \quad (3)$$

The saturation equation is as follows:

$$\varphi \frac{\partial S_w}{\partial t} + \frac{\partial v_w}{\partial z} = 0. \quad (4)$$

The relative permeability curve is characterized by the Corey equation:

$$\begin{cases} k_{rw} = k_{rw}^* S^a, \\ k_{ro} = k_{ro}^* (1 - S)^b, \\ S = \frac{S_w - S_{wi}}{1 - S_{or} - S_{wi}}. \end{cases} \quad (5)$$

Capillary pressure is expressed by the  $J$  function:

$$P_c = J(S) \sigma \sqrt{\frac{\varphi}{k}}. \quad (6)$$

Formula:  $J(S) = eS^d$ .

Scholars Marine and Fritz [22] describe the osmotic pressure formula:

$$\Pi = \frac{RT_c}{V} \ln \left( \frac{a_I}{a_{II}} \right). \quad (7)$$

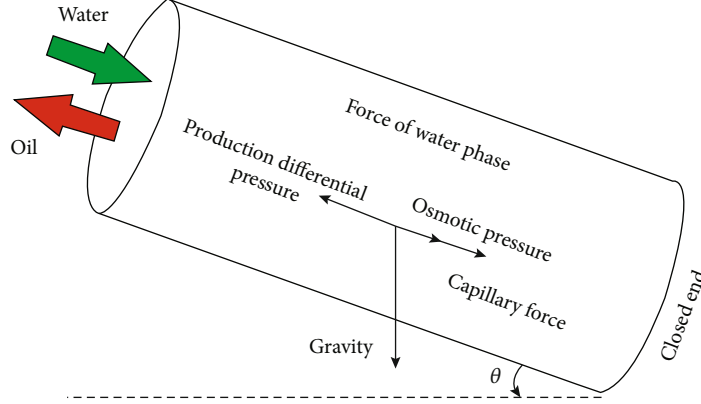


FIGURE 5: Oil-water percolation displacement model.

The reservoir is dense, and the flow of fluid in the reservoir follows the low-velocity non-Darcy law. Considering the effects of osmotic pressure, production pressure difference, and starting pressure gradient, comprehensive formula (1)–formula (7) can be rewritten as

$$\varphi \frac{\partial S_w}{\partial t} + \frac{\partial}{\partial z} \left[ \frac{kk_{rw}k_{ro}}{k_{ro}\mu_w + k_{rw}\mu_o} \left( \frac{\partial p_c}{\partial z} - \Delta\rho g \sin \theta - \frac{\partial \Pi}{\partial z} + \Delta P + G \right) \right] = 0. \quad (8)$$

Formula:  $\Delta\rho = \rho_w - \rho_o$ .

Dimensionless transformation:

$$\begin{cases} Z = \frac{z}{L}, \\ T = \frac{\sigma}{\mu_w L^2} \sqrt{\frac{k}{\varphi}} t. \end{cases} \quad (9)$$

Dimensionless processing, formula (8) transforms the expression:

$$\frac{\partial S}{\partial T} + A \frac{1}{\partial Z} \left[ f(S) \left( \frac{\partial J(S)}{\partial S} \frac{\partial S}{\partial Z} - \frac{L}{\sigma} \sqrt{\frac{k}{\varphi}} \Delta\rho g \sin \theta \right) - \frac{1}{\sigma} \sqrt{\frac{k}{\varphi}} \left( \frac{\partial \Pi}{\partial Z} - L\Delta P - LG \right) \right] = 0. \quad (10)$$

Formula:

$$A = \frac{\mu_w}{1 - S_{or} - S_{wi}}, \quad (11)$$

$$f(S) = \frac{k_{rw}^a S^a k_{ro}^* (1-S)^b}{k_{rw}^* S^a \mu_o + k_{ro}^* (1-S)^b \mu_w}.$$

The discretization equations are as follows:

$$\begin{aligned} & -A \frac{\nabla T}{\nabla Z^2} f(S_{i-1/2}^{m+1}) \frac{\partial J(S)}{\partial S} S_{i-1}^{m+1} \left[ 1 + A \frac{\nabla T}{\nabla Z^2} \left( f(S_{i+1/2}^{m+1}) \frac{\partial J(S)}{\partial S} \right. \right. \\ & \quad \left. \left. + f(S_{i-1/2}^{m+1}) \frac{\partial J(S)}{\partial S} \right) \right] S_i^{m+1} - A \frac{\nabla T}{\nabla Z^2} f(S_{i+1/2}^{m+1}) \frac{\partial J(S)}{\partial S} S_{i+1}^{m+1} \\ & = S_i^m + A \frac{\nabla T}{\nabla Z} [f(S_{i+1/2}^{m+1}) - f(S_{i-1/2}^{m+1})] \frac{L}{\sigma} \sqrt{\frac{K}{\varphi}} \Delta\rho g \sin \theta \\ & \quad + \frac{A}{\sigma} \sqrt{\frac{k}{\varphi}} \left\{ \frac{\Delta T}{\Delta Z} [(\Pi_{i+1}^m - \Pi_i^m) f(S_{i+1/2}^m) \right. \\ & \quad \left. - (\Pi_i^m - \Pi_{i-1}^m) f(S_{i-1/2}^m)] - L\Delta P - LG \right\}. \end{aligned} \quad (12)$$

It is assumed that the mineralization degree of fracturing fluid (water phase) is constant. Every time step needs to update the mineralization of each grid in the reservoir. If the grid size is uniform, the calculation formula of the corresponding mineralization degree of each grid is as follows:

$$c_i^{m+1} = \frac{c_{i-1}^m (S_i^{m+1} - S_i^m + \sum_{i+1}^N (S_j^{m+1} - S_j^m)) + c_i^m (S_i^m + S_c - \sum_{i+1}^N (S_j^{m+1} - S_j^m))}{S_i^{m+1} + S_c}. \quad (13)$$

By means of formula (12), the dimensionless saturation distribution along the path can be obtained, and the formula of oil-water displacement rate can be obtained by integrating the dimensionless saturation:

$$\eta(T) = \frac{\int_0^L S(Z, T) dZ}{L}. \quad (14)$$

#### 4. Sensitivity Analysis

The basic model parameters of sensitivity analysis are  $k = 0.02 \times 10^{-3} \mu\text{m}^2$ ,  $\varphi = 0.06$ ,  $k_{rw}^* = 0.2$ ,  $k_{ro}^* = 1.0$ ,  $u_o/u_w = 0.5$ ,  $u_w = 1.0$ ,  $a = 2.65$ ,  $b = 3.54$ ,  $d = 4.8088$ ,  $e = 0.0062$ ,  $\theta = 0^\circ$ ,  $S_{wi} = 39.61\%$ ,  $S_{or} = 30.83\%$ ,  $N = 41$ , compressive fracture fluid mineralization of 0 mg/L and remain unchanged, and water-phase initial mineralization of 25000 mg/L in a

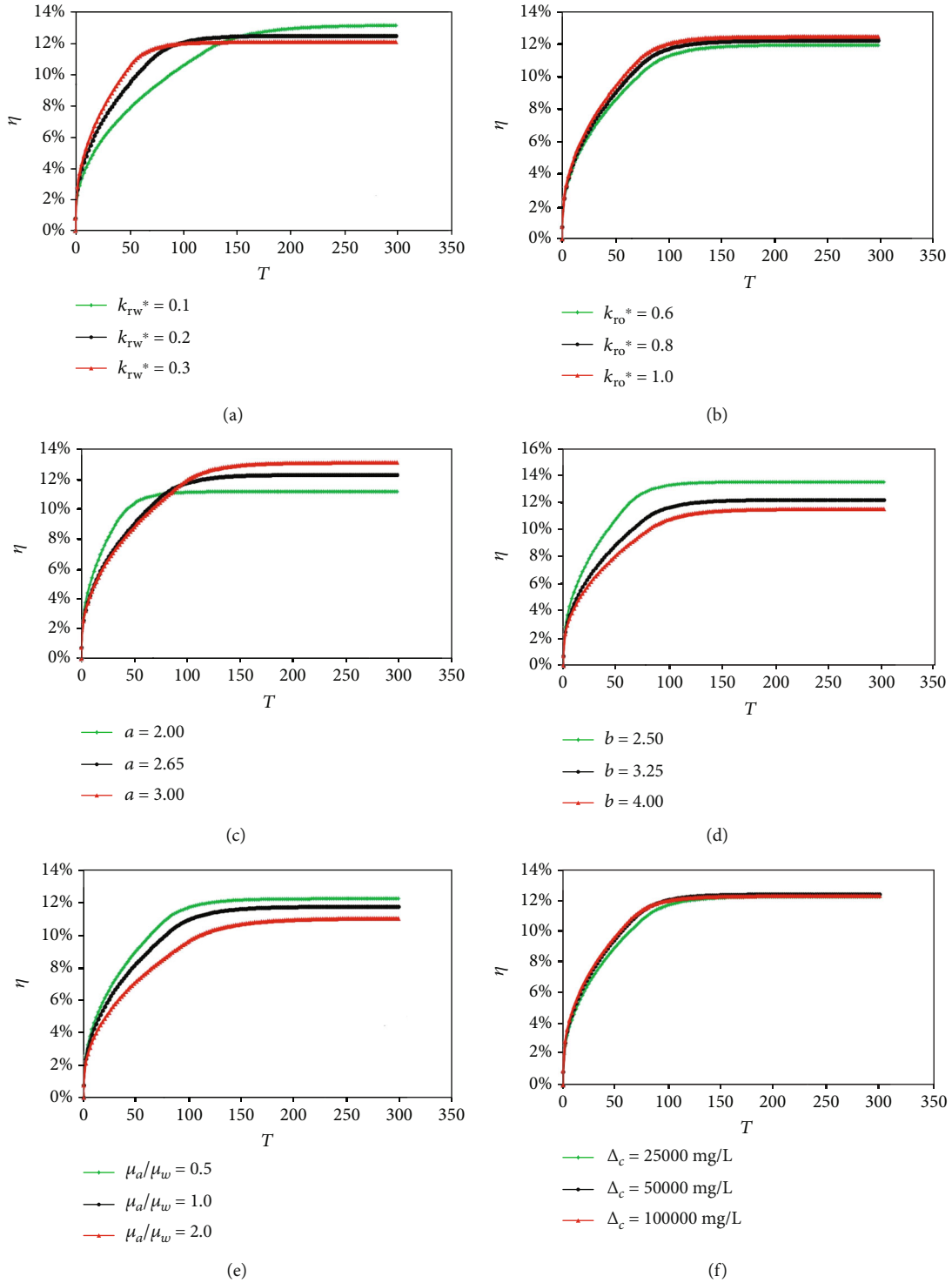


FIGURE 6: (a) When  $k_{rw}^* = 0.1, 0.2,$  and  $0.3,$  the relationship between oil-water displacement rate and dimensionless time; (b) when  $k_{ro}^* = 0.6, 0.8,$  and  $1.0,$  the relationship between oil-water displacement rate and dimensionless time; (c) when  $a = 2.00, 2.65,$  and  $3.00,$  the relationship between oil-water displacement rate and dimensionless time; (d) when  $b = 2.50, 3.25,$  and  $4.00,$  the relationship between oil-water displacement rate and dimensionless time; (e) when  $\mu_o/\mu_w = 0.5, 1.0,$  and  $2.0,$  the relationship between oil-water displacement rate and dimensionless time; (f) when  $\Delta_c = 25000 \text{ mg/L}, 50000 \text{ mg/L},$  and  $100000 \text{ mg/L},$  the relationship between oil-water displacement rate and dimensionless time.

reservoir. The relation curve between oil-water displacement rate and dimensionless time is drawn (Figure 6).

Figure 6(a) shows the relationship between oil-water replacement rate and dimensionless time when the maximum water-phase relative permeability value is 0.1, 0.2, and 0.3. From the curve comparison, it can be seen that the larger the maximum water-phase relative permeability value, the shorter the oil-water replacement time reaches the stable state, the lower the oil-water replacement rate; Figure 6(b) shows the maximum oil-phase relative permeability value is 0.6, 0.8, and 1. The relationship between oil-water displacement rate and nondimensional time is shown. It can be seen from the figure that the maximum relative permeability of oil phase has little influence on the oil-water replacement process. The larger the maximum relative permeability of oil phase is, the higher the oil-water replacement rate is. Figure 6(c) shows the relationship between oil-water displacement rate and dimensionless time when the water phase coefficient is 2.00, 2.65, and 3.00. From the diagram, it can be seen that the larger the water-phase coefficient is, the larger the oil-water displacement rate is, and the longer the time to reach the stable imbibition is. Figure 6(d) shows the relationship between oil-water displacement rate and dimensionless time when the oil-phase coefficient is 2.50, 3.25, and 4.00. It can be seen from the figure that the oil-phase coefficient has a little effect on the seepage and absorption stability time but has an obvious effect on the oil-water displacement rate. The smaller the oil-phase coefficient is, the greater the oil-water displacement rate is; Figure 6(e) shows the relationship between oil-water displacement rate and dimensionless time when the oil-water viscosity ratio is 0.5, 1.0, and 2.0. It can be seen from the curve that the smaller the oil-water viscosity ratio is, the higher the oil-water displacement rate is; Figure 6(f) shows the relationship between oil-water displacement rate and dimensionless time when the salinity difference is 25000 mg/L, 50000 mg/L, and 100000 mg/L. It is not difficult to see that the salinity difference has a certain impact on the infiltration and absorption process, but the impact is small.

## 5. Conclusions

A model for evaluating the permeability of tight sandstone reservoirs with capillary force and osmotic pressure is established. The model takes into account the influence of capillary force, osmotic pressure, production pressure difference, and starting pressure gradient on the process of oil-water permeation and displacement.

- (1) The main control factors affecting the process include the relative permeability of water phase, the relative permeability of oil phase, the oil-water viscosity ratio, the higher the relative permeability of water phase, the lower the relative permeability of oil phase, the smaller the oil-water viscosity ratio, and the higher the oil-water displacement ratio

- (2) The relative permeability of the water phase affects the infiltration stabilization time, and the larger the relative permeability of the water phase, the longer the infiltration stabilization time
- (3) Low salinity fracturing fluid infiltration can improve the oil-water displacement rate, but the effect is small

## Nomenclature

$a$ :	The water-phase coefficient is dimensionless
$a_I$ :	Low salinity water molar fraction (%)
$a_{II}$ :	High salinity water molar fraction (%)
$b$ :	The oil-phase coefficient is dimensionless
$B$ :	Coefficient, dimensionless
$c$ :	Mineralization (mg/L)
$\Delta c$ :	Salinity difference (mg/L)
$d$ :	$J$ function exponential coefficient, dimensionless
$e$ :	$J$ function coefficients, dimensionless
$g$ :	Acceleration of gravity ( $m/s^2$ )
$G$ :	Starts the pressure gradient (MPa/m)
$i$ :	Grid $i$
$j$ :	Grid $j$
$J(S)$ :	$J$ function
$k$ :	Absolute permeability of reservoir ( $1 \times 10^{-3} \mu m^2$ )
$k_{rw}$ :	The relative permeability of water phase is dimensionless
$k_{ro}$ :	The relative permeability of oil phase is dimensionless
$k_{rw}^*$ :	The maximum relative permeability of water phase is dimensionless
$k_{ro}^*$ :	The maximum relative permeability of oil phase is dimensionless
$L$ :	Model length (m)
$m$ :	Time step (m)
$N$ :	Discrete grid number, dimensionless
$p_w$ :	Water pressure (MPa)
$p_o$ :	Oil-phase pressure (MPa)
$p_c$ :	Capillary force (MPa)
$R$ :	The $R$ constant is equal to $0.00831 \text{ MPa}\cdot\text{L}/(\text{K}\cdot\text{Mol})$
$S$ :	Standardized water saturation is dimensionless
$S_c$ :	Standardized bound water saturation, dimensionless
$S_{wi}$ :	Irreducible water saturation is dimensionless
$S_{or}$ :	Residual oil saturation is dimensionless
$S_w$ :	The water saturation is dimensionless
$T$ :	Dimensionless time and dimensionless
$t$ :	Time (s)
$\mu_w$ :	Water viscosity (mPa-s)
$\mu_o$ :	Viscosity of oil phase (mPa-s)
$v_w$ :	Velocity of seepage in water phase (m/d)
$v_o$ :	Velocity of oil-phase seepage (m/d)
$V$ :	Water molar volume (0.018 L/mol)
$z$ :	Coordinate position (m)
$Z$ :	Dimensionless coordinate position, dimensionless
$\rho_w$ :	Water density ( $kg/m^3$ )
$\rho_o$ :	Oil-phase density ( $kg/m^3$ )
$\sigma$ :	Interfacial tension (mN/m)
$\varphi$ :	Porosity, decimal fraction
$\theta$ :	Horizontal angle
$\eta$ :	Oil water replacement rate, decimal fraction

$\Pi$ : Osmotic pressure (MPa)  
 $T_c$ : Temperature (Kelvin)  
 $\Delta P$ : Production pressure difference (MPa).

## Data Availability

Raw data and derived data supporting the findings of this study are available from the corresponding author Xiong Liu (Email: lx06106232@163.com) on request.

## Conflicts of Interest

The authors declare that they have no conflicts of interest.

## Acknowledgments

Xiong Liu would like to acknowledge the Chinese National Natural Science Foundation (No. 51804257) for providing research funding. Desheng Zhou would like to acknowledge the Chinese National Natural Science Foundation (No. 51934005 and No. 51874242) for providing research funding. Shun Liu would like to acknowledge the Natural Science Basic Research Program of Shaanxi (Program No. 2019JQ-403) for providing research funding.

## References

- [1] B. Roychoudhuri, J. Xu, T. T. Tsotsis, and K. Jessen, "Forced and spontaneous imbibition experiments for quantifying surfactant efficiency in tight shales," in *SPE 169500, SPE Western north American and Rocky Mountain and Rocky Mountain joint regional meeting held in*, pp. 16–18, Denver, Colorado, USA, 2014.
- [2] K. Makhanov, H. Dehghanpour, and E. Kuru, "An experimental study of spontaneous imbibition in Horn River Shales," in *SPE 162650, SPE Canadian unconventional resources conference held in*, Calgary, Alberta, Canada, 2012.
- [3] L. Shuai, D. Yunhong, M. Di et al., "Volume transformation experiment and multi-scale simulation of," *Oil drilling technology considering imbibition and displacement*, vol. 38, no. 5, pp. 678–683, 2016.
- [4] P. Yu, X. Wang, and P. Ling, "Static reservoir imbibition experiment," *Daqing petroleum geology and development*, vol. 35, no. 6, pp. 159–163, 2016.
- [5] P. M. Oen, M. Engell-Jensen, and A. A. Barendregt, "Skjold field, Danish north sea: early evaluations of oil recovery through water imbibition in a fractured reservoir," *SPE Reservoir Engineering*, vol. 3, no. 1, pp. 17–22, 1988.
- [6] T. Babadagli and I. Ershaghi, "Imbibition assisted two-phase flow in natural fractures," in *SPE 24044, Western regional meeting*, Bakersfield, CA, 1992.
- [7] S. Al-Lawati and S. Saleh, "Oil recovery in fractured oil reservoirs by low IFT imbibition process," in *SPE 36688, SPE annual technical conference and exhibition held in*, pp. 6–9, Denver, Colorado, USA, October 1996.
- [8] A. Bertonecello, J. Wallace, H. Corp, C. Blyton, M. Honarpour, C. S. Kabir et al., "Imbibition and water blockage in unconventional reservoirs: well management implications during flow-back and early production," in *SPE 167698, SPE/EAGE European unconventional conference and exhibition held in*, pp. 25–27, Vienna, Austria, 2014.
- [9] J. K. Mitchell and K. Soga, *Fundamentals of Soil Behavior*, John Wiley & Sons, Hoboken, N.J., 3rd edition, 2005.
- [10] B. Kurtoglu, *Integrated Reservoir Characterization and Modeling in Support of Enhanced Oil Recovery for Bakken*, Colorado School of Mines, USA, 2013.
- [11] E. van Oort, M. Ahmad, R. Spencer, and N. Legacy, "ROP enhancement in shales through osmotic processes," in *SPE 173138, SPE/IADC Drilling conference and exhibition held in*, London, U.K., 2015.
- [12] J. Xu, K. Wu, S. Yang et al., "Real gas transport in tapered non-circular nanopores of shale rocks," *AICHE Journal*, vol. 63, no. 7, pp. 3224–3242, 2017.
- [13] J. Xu, K. Wu, R. Li et al., "Real gas transport in shale matrix with fractal structures," *Fuel*, vol. 219, pp. 353–363, 2018.
- [14] M. Mirzaei, D. A. Dicarolo, and G. A. Pope, "Visualization and analysis of surfactant imbibition into oil-wet fractured core," in *SPE 166129, SPE Annual Technical Conference and Exhibition*, New Orleans, 2013.
- [15] P. Kathel and K. K. Mohanty, "EOR in tight oil reservoirs through wettability alteration," in *SPE 166281, SPE Annual Technical Conference and Exhibition*, New Orleans, 2013.
- [16] M. Chahardowli, R. Farajzadeh, S. K. Masalmeh, H. Mahani, and H. Bruining, "A novel enhanced oil recovery technology using dimethyl ether/brine: spontaneous imbibition in sandstone and carbonate rocks," in *SPE 181340, SPE annual technical conference and exhibition held in*, pp. 26–28, Dubai, UAE, September 2016.
- [17] L. Tao, C. Y. Wen, G. Xiaofei et al., "The order of influence degree of single well productivity parameter in tight oil reservoir," *Petroleum exploration and development*, vol. 40, no. 3, pp. 357–362, 2013.
- [18] Q. Lan, E. Ghanbari, H. Dehghanpour, and R. Hawkes, "Water loss versus soaking time: spontaneous imbibition in tight rocks," in *SPE 167713, SPE/EAGE European unconventional conference and exhibition held in*, Vienna, Austria, 2014.
- [19] A. Habibi, M. Binazadeh, H. Dehghanpour, D. Bryan, and G. Uswak, "Advances in understanding wettability of tight oil formations," in *SPE 175157, SPE Annual Technical Conference and Exhibition Held in Houston*, Texas, USA, 2015.
- [20] M. K. Valluri, J. O. Alvarez, and D. S. Schechter, "Study of the rock/fluid interactions of sodium and calcium brines with ultra-tight rock surfaces and their impact on improving oil recovery by spontaneous imbibition," in *SPE 180274, SPE Low Perm Symposium Held in*, Denver, Colorado, USA, 2016.
- [21] W. Qing, L. Zhiping, X. Wang et al., "Osmotic mechanism and influencing factors of fractured tight sandstone reservoirs: taking Chang 8 reservoir in Wuqi area of Ordos Basin as an example," *Oil and gas geology and recovery*, vol. 23, no. 4, pp. 102–107, 2016.
- [22] I. W. Marine and S. J. Fritz, "Osmotic model to explain anomalous hydraulic heads," *Water Resources Research*, vol. 17, no. 1, pp. 73–82, 1981.



## Research Article

# Effect of Seepage Force on the Wellbore Breakdown of a Vertical Wellbore

Desheng Zhou <sup>1,2</sup>, Haiyang Wang,<sup>1</sup> Yafei Liu <sup>1,2</sup>, Shun Liu,<sup>2</sup> Xianlin Ma,<sup>1</sup> Wenbin Cai,<sup>1</sup> and Hai Huang<sup>1,2</sup>

<sup>1</sup>School of Petroleum Engineering, Xi'an Shiyou University, Xi'an 710065, China

<sup>2</sup>Engineering Research Center of Development and Management for Low to Extra-Low Permeability Oil & Gas Reservoirs in West China, Ministry of Education, Xi'an Shiyou University, Xi'an, 710065 Shaanxi, China

Correspondence should be addressed to Desheng Zhou; [deshengzhou@126.com](mailto:deshengzhou@126.com)

Received 16 May 2020; Revised 20 September 2020; Accepted 20 March 2021; Published 8 April 2021

Academic Editor: Mauro Giudici

Copyright © 2021 Desheng Zhou et al. This is an open access article distributed under the Creative Commons Attribution License, which permits unrestricted use, distribution, and reproduction in any medium, provided the original work is properly cited.

As a fluid flows through a porous media, a drag force, called seepage force in the paper, will be formed on the matrix of the media in the fluid flowing direction. However, the seepage force is normally ignored in the analysis of wellbore fracturing during hydraulic fracturing operation. In this paper, an analytical model for seepage force around a vertical wellbore is presented based on linear elasticity theory, and the effect of the seepage force on wellbore breakdown has been analyzed. Also studied are the effects of the two horizontal principal stresses and the reservoir permeability on the action of seepage force. The paper proves that seepage force lowers formation breakdown pressure of a vertical wellbores; the deeper a formation is, the greater action of the seepage force; seepage force contributes more to breakdown formation with small difference of the two horizontal stresses such as unconventional reservoirs; seepage force increases as rock permeability decreases, and it should not be ignored in hydraulic fracturing analysis, especially for low-permeability formation.

## 1. Introduction

The evaluation of the stress fields around wellbores in porous media attracts plenty of interests due to its relevance in oil and gas production, with special emphasis on hydraulic fracturing. The distributions of the stress and pore pressure fields in wellbore rock are essential to studying the initiation of hydraulic fractures.

Haimson and Fairhurst [1–4] systematically studied the stress field around a wellbore during the initiation of fractures and proposed that when fluid was injected into a wellbore, three stress fields acted together to induce the breakdown of permeable reservoirs. These three stress fields include in situ stress, wellbore pressure, and poroelastic stress caused by pore pressure variations in wellbore rock after wellbore fluid flows into a reservoir.

Hubbert and Willis [5] and Medlin and Masse [6] investigated the mechanics of hydraulic fracture initiation by comparing laboratory experiments with theoretical predictions

based on poroelasticity. In the recent 20 years, quite a few scholars [7–11] have analyzed the influencing factors of formation breakdown pressure based on Haimson's theory combined with experimental results.

Based on the model of Hubbert and Hamison, Ito [12, 13] proposed a newly constructed fracture criterion that can explain the effects of wellbore diameter and pressurization rate on the breakdown pressure. Jin et al. [14] presented a weight function method to predict the breakdown pressure of two general symmetrical radial fractures emanating from a wellbore. Fatahi et al. [15] presented a simulation model based on a distinct element method to study the breakdown pressure during hydraulic fracturing tests. Xiao et al. [16] proposed a fracture initiation model for carbon dioxide fracturing under various bottom hole pressure and temperature conditions.

However, flowing into reservoir rock of wellbore fluid not only increases in situ pore pressure and thus creates poroelastic stress but also results in a pore pressure gradient along the fluid flowing direction in wellbore rock. Under the action of

fluid dragging, the flowing fluid exerts a force, called seepage force, on rock skeleton affecting stress fields around the wellbore. Mourgues et al. [17], Cobbold et al. [18], and Zanella and Cobbold [19] verified the existence of the seepage force during fluid flowing in a porous media based on sandbox experiments and evaluated the influence of seepage force on media structure. Rozhko et al. [20, 21] investigated the influence of seepage force on the failure of a porous elastic media and calculated the stress field created by the seepage force. Zhou et al. [22] analyzed the behavior of stabilizing piles for landslides in the Three Gorges Reservoir under the effect of seepage force. Zou et al. [23] derived theoretical solutions for a circular opening in an elastic-brittle-plastic rock mass incorporating the out-of-plane stress and seepage force. AlKhafaji et al. [24] studied the bearing capacity problem of shallow rigid foundations on rock matrix subjected to horizontal seepage force.

Although the seepage force has been proved and discussed in soil engineering, and applied in dam stability analysis for decades, it has been ignored in oil and gas production. Few literatures in hydraulic fracturing analysis discuss the effect of the seepage force on hydraulic fracturing process.

In this work, seepage force will be introduced into the analysis of a vertical well during hydraulic fracturing operation. A model analyzing the stress field around the wellbore by seepage force will be presented. To study the effect of seepage force, traditional stress field analyses around the wellbore during hydraulic fracturing process will be discussed firstly. Seepage force contribution to the wellbore breakdown will be compared by the results from cases with and without considering the seepage force. Also explored are the effects of formation confining pressure and permeability on wellbore fracture pressure in the case of considering the seepage force.

## 2. Stresses around a Vertical Wellbore

*2.1. Tradition Model.* Conventionally, the stress analysis of a vertical wellbore at an interested depth during hydraulic fracturing is simplified as a plane problem [25, 26]. As shown in Figure 1, a well with a radius of  $r_a$  is drilled in a formation with in situ horizontal principal stresses  $S_{11}$  and  $S_{22}$  ( $S_{11} > S_{22}$ ). In a cylindrical coordinate system  $(r, \theta)$ , the stresses at any point are the radial stress  $\sigma_r$  and circumferential stress  $\sigma_\theta$ , and tensile stresses were assumed to be negative in this paper. The circumferential stress  $S_\theta^1$  of the hollow square can be expressed as follows (all symbols in this paper are shown in Table 1):

$$S_\theta^1 = \frac{S_{11} + S_{22}}{2} \left(1 + \frac{r_a^2}{r^2}\right) - \frac{S_{11} - S_{22}}{2} \left(1 + \frac{3r_a^4}{r^4}\right) \cos 2\theta. \quad (1)$$

When the wellbore is pressurized by the injected fracturing fluid during hydraulic fracturing, two circumferential stresses  $S_\theta^2$  and  $S_\theta^3$  will be yielded at any point. The  $S_\theta^2$  is caused by the fluid pressure  $p_a$  at the borehole wall, which can be viewed as an internal pressure acting on a hollow thick cylinder.

$$S_\theta^2 = \frac{-p_a r_a^2}{r_e^2 - r_a^2} + \frac{-p_a r_a^2 r_e^2}{r^2 (r_e^2 - r_a^2)}. \quad (2)$$

The third stress  $S_\theta^3$  is introduced by the pore pressure variation in the formation when the fracturing fluid penetrates into the formation and flows through its pores. When the formation pore pressure changes, the rock skeleton undergoes an uneven elastic deformation, causing so-called  $S_\theta^3$  stress under the mutual constraint of the skeleton elements [27–30]:

$$S_\theta^3 = A \left[ \frac{1}{r^2} \frac{r^2 + r_a^2}{r_e^2 - r_a^2} \int_{r_a}^{r_e} (p(r) - p_o) r dr + \frac{1}{r^2} \int_{r_a}^r (p(r) - p_o) r dr - (p(r) - p_o) \right], \quad (3)$$

$$A = \frac{1 - 2\nu}{1 - \nu} \left(1 - \frac{K_B}{K_M}\right), \quad (4)$$

where  $p(r)$  is the pore pressure distribution around the wellbore (Pa);  $p_o$  is the initial pore pressure (Pa);  $\nu$  is Poisson's ratio, dimensionless; and  $K_B$  and  $K_M$  are the frame and matrix bulk moduli of the rock (Pa).

If the wellbore pressurization rate is relatively small and the fluid is noncompressible, the pore pressure distribution around the wellbore can be regarded as steady-state. This quasistatic pressure field in a domain with constant permeability is governed by the Laplace equation:

$$\frac{\partial^2 p}{\partial r^2} + \frac{1}{r} \frac{\partial p}{\partial r} = 0. \quad (5)$$

Once wellbore pressure  $p_a$  and pore pressure  $p_b$  at outer boundary  $r_e$  were determined, Equation (5) was solved by polar coordinates, and pore pressure distribution  $p(r)$  around the wellbore during steady-state flow was obtained as follows [2, 31, 32]:

$$p(r) = p_a - (p_a - p_b) \frac{\ln r - \ln r_a}{\ln r_e - \ln r_a}. \quad (6)$$

By taking the pore pressure distribution  $p(r)$  around the wellbore in Equation (6) into Equation (4), circumferential stress  $S_\theta^3$  due to pore pressure variation at any point under steady-state flow was obtained as ( $r_e^2 \geq r_a^2$ )

$$S_\theta^3 = \frac{A}{r^2} \left[ \frac{r^2 - r_a^2}{2} (p_a - p_o) + \frac{p_a - p_b}{\ln(r_e/r_a)} \frac{r^2}{2} \ln\left(\frac{r_a}{r}\right) + \frac{r^2 - r_a^2}{4} \frac{p_a - p_b}{\ln(r_e/r_a)} \right] - A \left[ p_a - p_o - (p_a - p_b) \frac{\ln(r/r_a)}{\ln(r_e/r_a)} \right]. \quad (7)$$

### 2.2. Introduction of Seepage Force

*2.2.1. Mechanism of Seepage Force.* As a viscous fluid flows through the pores of a porous media, the fluid imparts a friction force and normal thrust to the solid element of the matrix. The force is normally called seepage force in soil mechanics. Seepage force has long been considered in

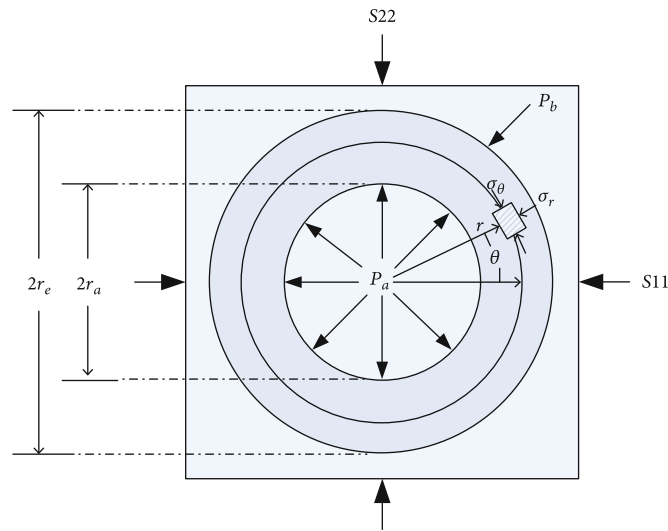


FIGURE 1: The cross-sectional graph of a vertical wellbore.

TABLE 1: Common symbols and units.

Symbol	The meaning of symbol	Unit
$\sigma_r$	Radial stress	Pa
$\sigma_\theta$	Circumferential stress	Pa
$\tau_{r\theta}$	Shear stress	Pa
$\nu$	Poisson's ratio	/
$K_B$	Frame bulk moduli of rock	Pa
$K_M$	Mineral matrix bulk moduli of rock	Pa
$\theta$	Radian	rad
$r$	Radial distance	m
S11	Maximum horizontal principal stress	Pa
S22	Minimum horizontal principal stress	Pa
$p_o$	Initial pore pressure	Pa
$p_a$	Wellbore pressure	Pa
$p_b$	Pore pressure at the outer boundary	Pa
$p(r)$	Pore pressure distribution around wellbore	Pa
$r_a$	Wellbore inner diameter	m
$F_{sp}$	Seepage force	Pa
$r_e$	Outer diameter of wellbore	m
$\Delta p$	Differential pressure	Pa
$\sigma_f$	Tensile strength of a rock	Pa
$\sigma_\theta'$	The effective circumferential stress	Pa
$S_\theta^1$	Circumferential total stress formed by formation principal stress	Pa
$S_\theta^2$	Circumferential stress formed by wellbore pressure	Pa
$S_\theta^3$	Circumferential stress formed by changes in pore pressure	Pa
$S_\theta^4$	Circumferential stress formed by seepage force	Pa
$K$	Permeability	$m^2$
$Q$	Flow rate of fluid	$m^3/s$
$\mu$	Fluid viscosity	Pa/s

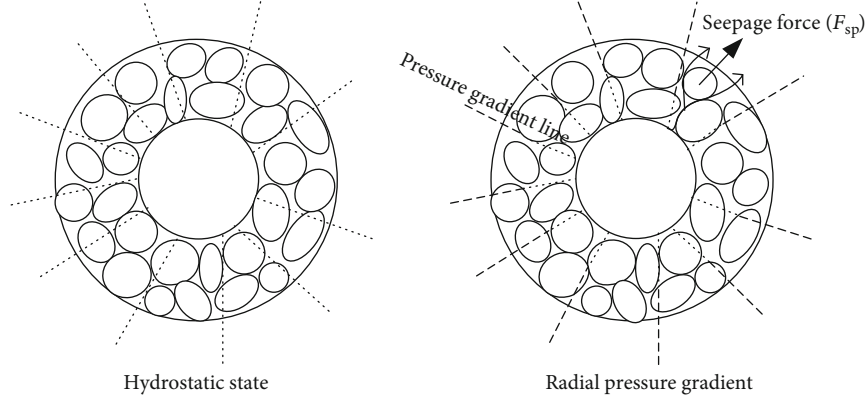


FIGURE 2: Schematic graph of a seepage force around a wellbore.

geotechnical engineering to assess the stability of a slope or the risk of sand liquefaction of dams [22, 33, 34] although its definition is still arguing in the engineering. In the paper, seepage force is defined as follows:

$$\vec{F}_{sp} = -\gamma_w i, \quad (8)$$

where  $i$  denotes pressure head gradient, dimensionless, and  $\gamma_w$  is the unit weight of fluid ( $\text{N/m}^3$ ).

For the radial flow in Figure 1, the seepage force is simplified as follows:

$$F_{sp} = -\frac{\partial p(r)}{\partial r}. \quad (9)$$

The direction of the seepage force is in the opposite direction of the pressure gradient.

During hydraulic fracturing, high pressure wellbore fluid flows into rock and the in situ pore pressure changes. Pore fluid flowing zone around the wellbore with certain pore pressure gradient will be formed. As shown in Figure 2, rock matrix around a vertical wellbore satisfies the total stress equilibrium equation under stable state.

$$\begin{cases} \frac{\partial \sigma_r}{\partial r} + \frac{1}{r} \frac{\partial \tau_{r\theta}}{\partial \theta} + \frac{\sigma_r - \sigma_\theta}{r} - R = 0, \\ \frac{1}{r} \frac{\partial \sigma_\theta}{\partial \theta} + \frac{\partial \tau_{r\theta}}{\partial r} + \frac{2\tau_{r\theta}}{r} - S = 0, \end{cases} \quad (10)$$

where  $R$  is the radial volume force per unit volume and  $S$  is the circumferential volume force per unit volume. When the fluid flows radially,  $R = F_{sp}$ ,  $S = 0$ . Under axisymmetric conditions, both the circumferential stress  $\sigma_\theta$  and the radial stress  $\sigma_r$  are only functions of  $r$ , and the shear stress  $\tau_{r\theta}$  is 0. Therefore, Equation (10) is reduced to

$$\frac{d\sigma_r}{dr} + \frac{\sigma_r - \sigma_\theta}{r} = F_{sp}. \quad (11)$$

As shown in Figure 2, when the fluid was under hydrostatic pressure state, pore pressure gradients in radius direction  $\partial p/\partial r$  is equal to 0, and there is no seepage force.

However, when fracturing fluid flows in the radial direction during hydraulic fracturing, there are pore pressure gradients  $\partial p/\partial r$ , and there is a seepage force  $F_{sp}$ . The direction of  $F_{sp}$  is consistent with the direction of fluid flowing.

**2.2.2. Calculation of Seepage Force Stress Field.** To study the effect of seepage force, solve the seepage force equation (Equation (11)). The internal and external boundary stresses are zero as the effects of wellbore pressure  $p_a$  and pore pressure  $p_b$  at outer boundary are already taken into account in Equation (11).

$$\begin{cases} \sigma_r = 0, & r = r_a, \\ \sigma_r = 0, & r = r_e. \end{cases} \quad (12)$$

Combining Equations (6), (11), and (12), the circumferential stress  $S_\theta^4$  formed by the seepage force under the plane strain condition during the steady-state flowing of wellbore fluid into a vertical wellbore:

$$S_\theta^4 = \frac{p_a - p_b}{2(1 - \nu)} \left[ \frac{\ln r - \ln r_a + 2\nu - 1}{\ln r_e - \ln r_a} - \frac{r_e^2 (r^2 + r_a^2)}{r^2 (r_e^2 - r_a^2)} \right]. \quad (13)$$

It is well known that rock failure is controlled by the Terzaghi's effective stress [35]. The theory assumes when the effective circumferential stress  $\sigma_\theta'$  reaches the tensile strength of a rock ( $\sigma_f$ ), at borehole wall, tensile fracture at the wellbore occurs [2, 5, 12].

$$\sigma_\theta' \geq \sigma_f. \quad (14)$$

To compare with traditional methods, three cases are considered: rock is impermeable, pressured wellbore fluid flows into rock without considering seepage force effect, and pressured wellbore fluid flows into rock with seepage force effect.

When considering the rock is impermeable, the total effective circumferential stress is expressed as follows:

$$\sigma_\theta' = S_\theta^1 + S_\theta^2 - p_o. \quad (15)$$

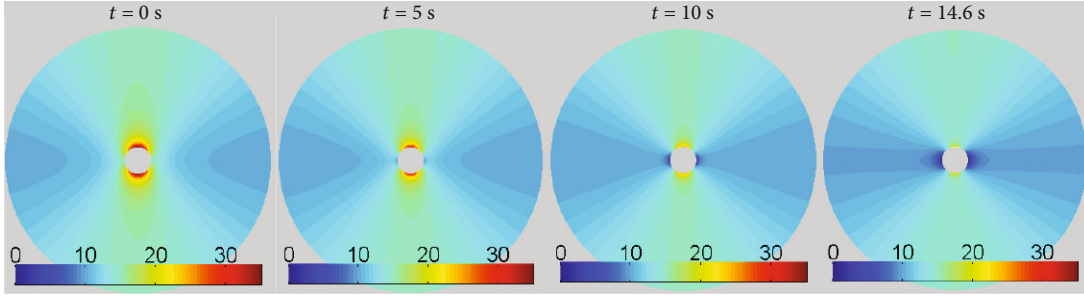


FIGURE 3: Wellbore breakdown process for impermeable rock case.

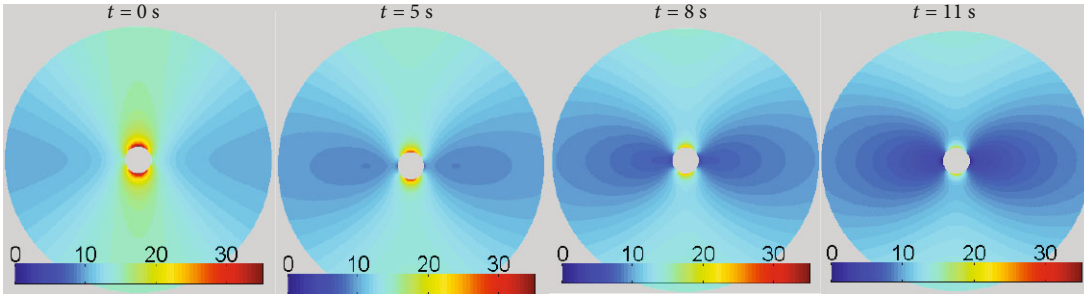


FIGURE 4: Wellbore breakdown process for the case of wellbore fluid flowing into rock but no seepage force.

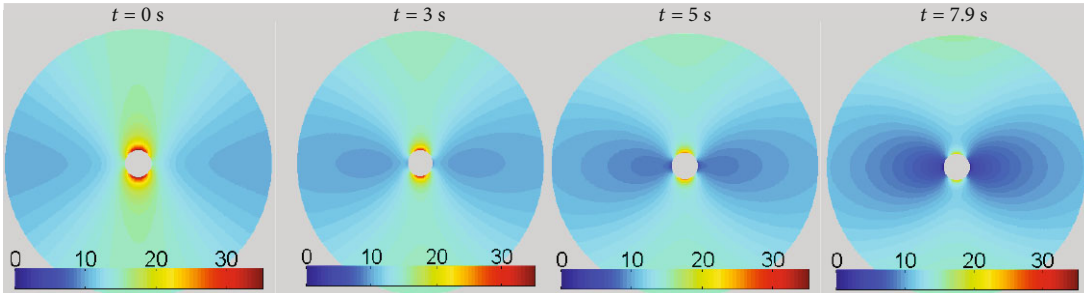


FIGURE 5: Wellbore breakdown process for the case of wellbore fluid flowing into rock and accounting seepage force.

When considering the fact that pressured wellbore fluid flows into the rock without considering seepage force effect,

$$\sigma'_\theta = S_\theta^1 + S_\theta^2 + S_\theta^3 - p(r). \quad (16)$$

When considering the effect of seepage force ( $S_\theta^4$ ), the total effective circumferential stress is

$$\sigma'_\theta = S_\theta^1 + S_\theta^3 + S_\theta^4 - p(r). \quad (17)$$

Note, in Equation (17),  $S_\theta^2$  is not included as the effect of wellbore pressure ( $p_a$ ) is already considered in  $S_\theta^4$ .

### 3. Analyses of Fracture Initiation under Seepage Force

3.1. Comparison of Wellbore Breakdown Process for Three Cases. In Section 2, circumferential stress fields around a well-

bore wall and corresponding formation breakdown conditions are derived for steady-state fluid flow condition. During hydraulic fracturing operation, wellbore pressurization rates are relatively slow. The operation can be modeled using quasi-static conditions [2].

The calculation conditions are given as follows. Considering a vertical circular wellbore borehole drilled in an isotropic geologic medium, a 2D isotropic plane is used in the analysis (Figure 1). The maximum and minimum horizontal stresses are  $S_{11} = 20$  MPa and  $S_{22} = 15$  MPa. The initial wellbore pressure  $p_a$  and pore pressure  $p_o$  is assumed as 5 MPa. The tensile strength of the rock  $\sigma_f$  is taken as 0 MPa. The Poisson's ratio in the isotropic plane is 0.25. The inner and outer diameters of the wellbore are supposed as 1 dm and 10 dm, respectively. It is assumed that starting from  $t = 0$  s, the wellbore pressure starts to increase at a rate of 1 MPa/s until the wellbore wall is broken. That is, the effective circumferential stress  $\sigma'_\theta$  reaches the tensile strength of the rock  $\sigma_f$ .

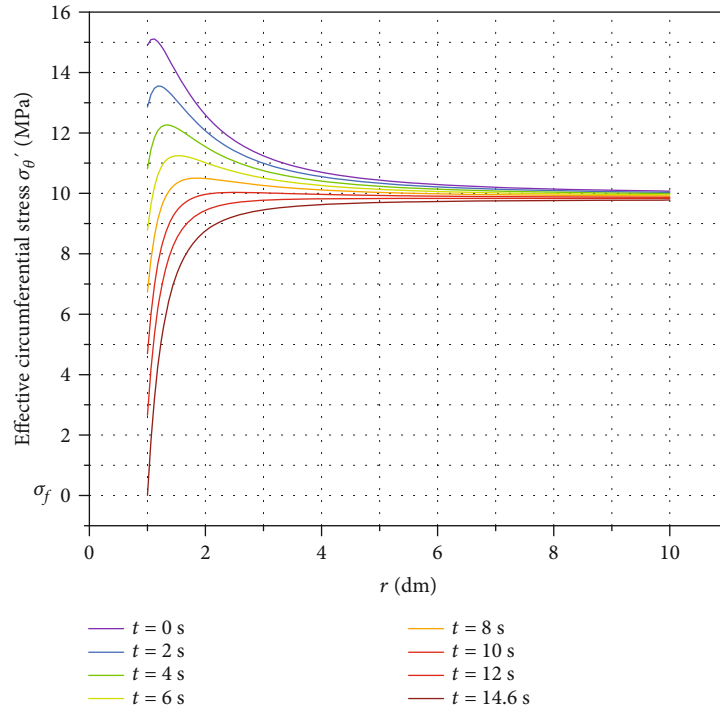


FIGURE 6: The variation of  $\sigma_{\theta}'$  with radial distance for impermeable rock.

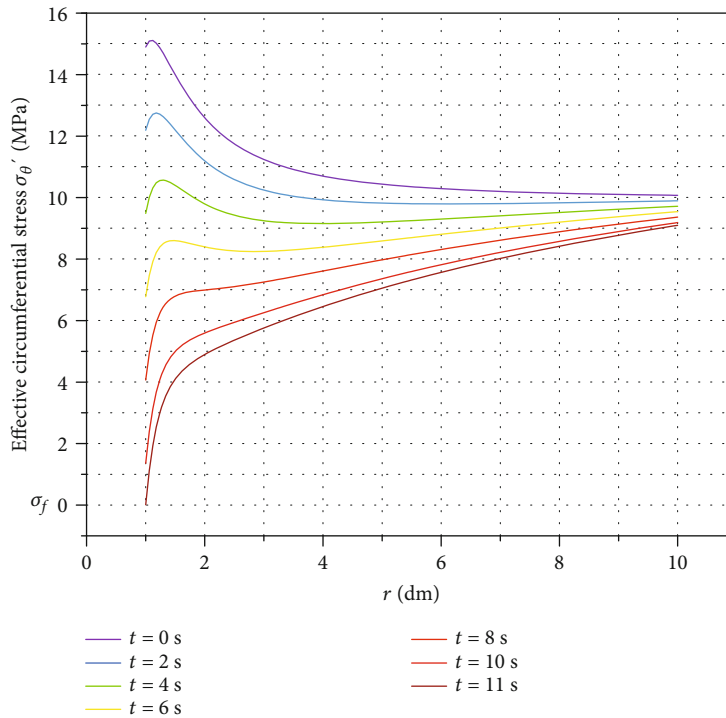


FIGURE 7: The variation of  $\sigma_{\theta}'$  with radial distance for the case of wellbore fluid flowing into rock but no seepage force.

The pore pressure at the outer boundary of wellbore during the entire pressurization process is maintained at  $p_o$  ( $p_b = p_o$ ).

Equations (15)–(17) represent the three cases: rock is impermeable, pressured wellbore fluid flows into rock with-

out considering seepage force effect, and pressured wellbore fluid flows into rock with seepage force effect. Using the given conditions, the wellbore breakdown processes for the three cases are calculated under quasistatic conditions.



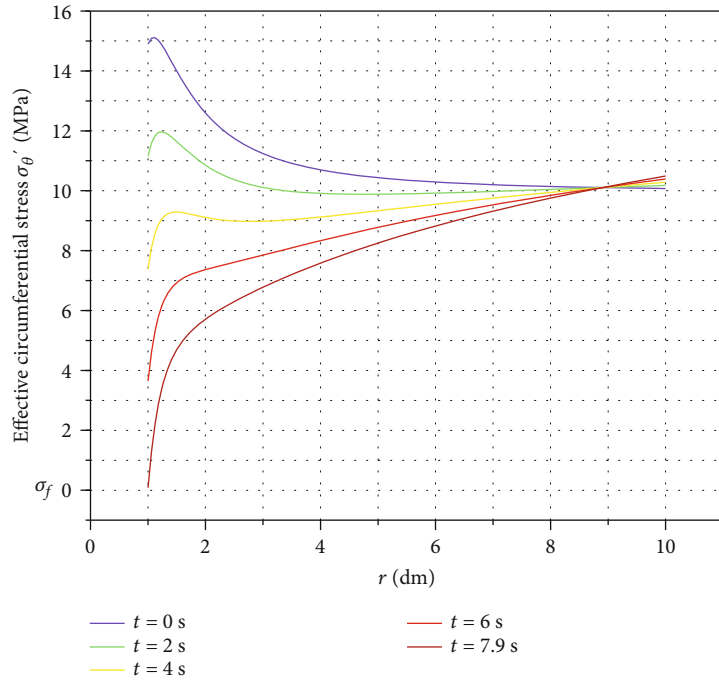


FIGURE 8: The variation of  $\sigma_{\theta}'$  with radial distance for the case of wellbore fluid flowing into rock and accounting seepage force.

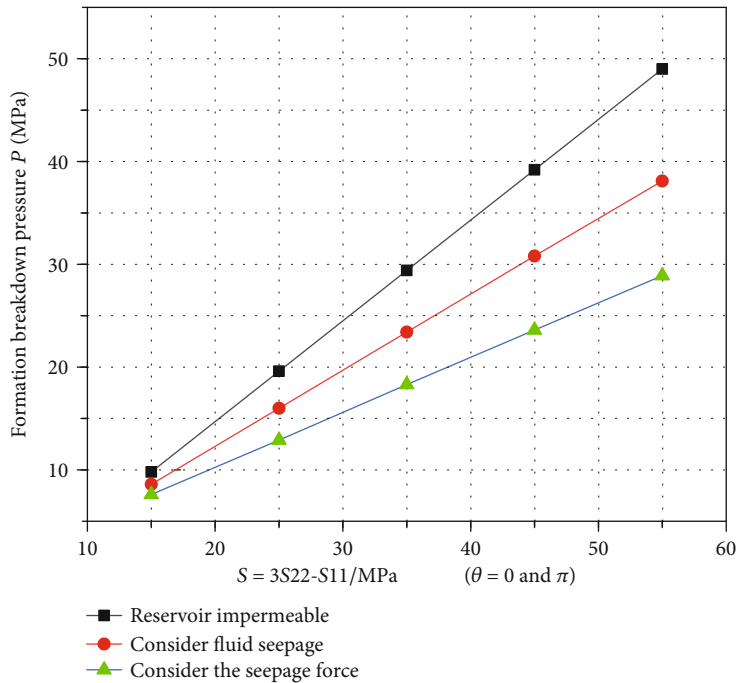


FIGURE 9: Formation breakdown pressures from the three cases when S11 and S22 increase uniformly.

The calculated results for the three cases are shown in Figures 3–5 (color ruler scale corresponds to the effective circumferential stress value  $\sigma_{\theta}'$ ).

From Figures 3–5, at time  $t = 0$  s, the wellbore has not been pressurized, and there is apparent stress concentration at the wellbore wall. As the wellbore is pressurized, the effective

circumferential compressive stress  $\sigma_{\theta}'$  around the wellbore gradually decreases and the stress concentration gradually disappears. The breakdown points at the wellbore wall for the three cases are in the directions of maximum horizontal principal stress S11 ( $\theta = 0$  and  $\pi$ ). When fluid flows into the formation (Figure 4), the stress field varies



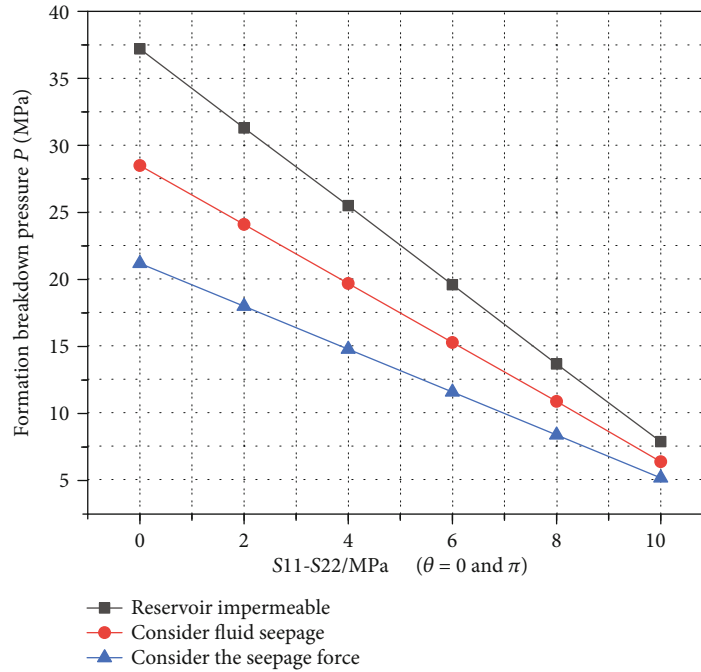


FIGURE 10: Formation breakdown pressures from the three cases when the difference between S11 and S22 varies.

more intensely comparing to Case 1 (Figure 3). This proves that fluid flowing into wellbore process should be considered during the analysis of hydraulic fracturing. Under the action of seepage force, as shown in Figure 5, the wellbore wall will be broken very quick, taking only 7.9 s. The effect of seepage force is markedly conducive to wellbore breakdown.

Figures 6–8 show the variations of the effective circumferential stresses  $\sigma_{\theta}'$  along the direction of the maximum horizontal principal stress S11 for the three cases. From Figures 6–8, the effective circumferential stress  $\sigma_{\theta}'$  from the wellbore wall  $r_a$  decreases the fastest, and the decreasing speed becomes slower gradually as  $r$  increases. For impermeable rock (Case 1),  $\sigma_{\theta}'$  trends to no variation anymore from the distance of  $r = 6.5r_a$  (Figure 6). When fluid flows in the wellbore, due to the variation of the pore pressure  $p(r)$ ,  $\sigma_{\theta}'$  varies in the whole modeling area. For the effect of seepage force (Case 3), the effective circumferential compressive stress  $\sigma_{\theta}'$  around the outer boundary even exceeds the initial stress state, indicating that the seepage force gives a compression effect at the outer boundary at the case condition (Figure 8).

**3.2. Wellbore Breakdown Pressure under Different Outer Boundary Conditions.** To study the effect of formation in situ stresses on wellbore breakdown for the three cases, two situations of varying formation maximum and minimum horizontal principal stresses are given. One situation is S11 and S22 increasing uniformly while keeping the difference between S11 and S22 unchanged. The other situation is that the difference between S11 and S22 is different.

From Equation (1), the circumferential compressive stress generated by S11 and S22 at the well wall in the direc-

tion of maximum stress S22 ( $\theta = 0$  or  $\pi$ ) is  $S(S = 3S22 - S11)$ . When S11 and S22 increase uniformly,  $S$  indicates the change in the stress concentration of the well wall and the magnitude of the compressive stress value that needs to be overcome to breakdown the wellbore wall by the fluid pressure in the wellbore. Figure 9 shows the calculated breakdown pressure versus the  $S$  values as S11 and S22 increase uniformly. From Figure 9, when S11 and S22 increase uniformly, the formation breakdown pressure increases linearly for the three cases. With  $S$  increasing, the gap of the formation breakdown pressure values for the seepage force case (Case 3) is getting greater for other two cases. The effect of seepage force becomes more and more significant as the principal stresses of the formation increase uniformly.

Figure 10 gives the variation of formation breakdown pressure with the difference of the two in situ stresses (S11 - S22). From Figure 10, for the three cases, with the increasing of S11 - S22, formation breakdown pressure decreases linearly and the gap of the formation breakdown pressure values for seepage force case and the other cases is getting smaller. The higher the difference between S11 and S22, the smaller the effect of the seepage force.

#### 4. Effect of Seepage Force for Different Permeability Rock

Steady-state fluid flow in porous media is controlled by Darcy's law. For given fluid pressure in a wellbore and pore pressure, the smaller the rock permeability, the greater the pressure difference  $\Delta p$  in wellbore radial direction. Therefore, the effect of seepage force on formation breakdown pressure will be affected by the rock permeability.

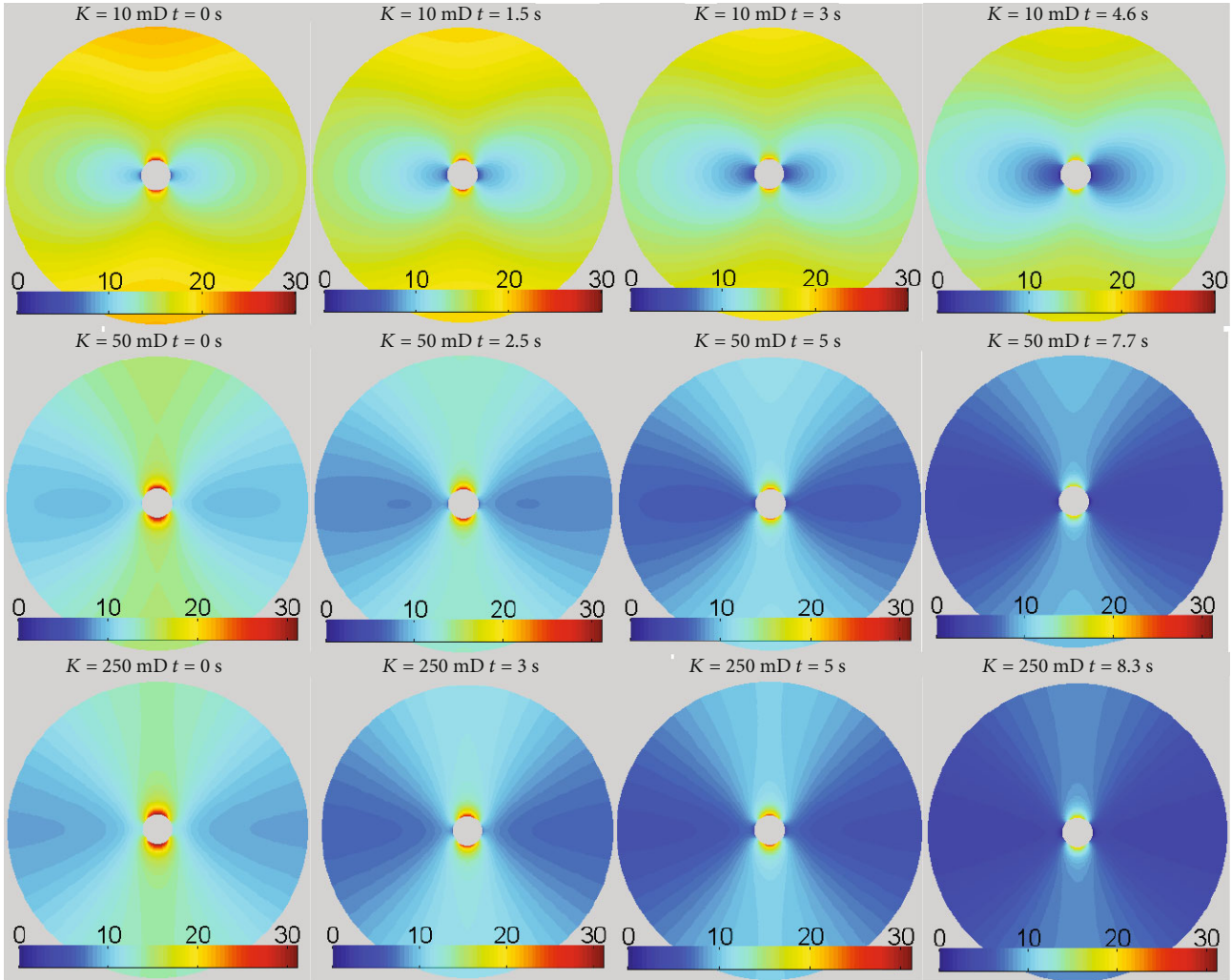


FIGURE 11: Formation breakdown process for three permeability rocks accounting seepage force.

Using the same condition in Section 3.1, the formation breakdown pressures are analysed with various permeabilities for the three cases. Noting that in this section the pore pressure  $p_b$  at the outer boundary  $r_e$  is determined by the rock permeability  $K$  ( $Q = 0.1 \text{ cm}^3/\text{s}$ ;  $L = 10 \text{ dm}$ ;  $\mu = 1 \text{ mPa}\cdot\text{s}$ ). During wellbore pressurization, different stable differential pressures  $\Delta p$  are formed around the wellbore with different permeability ( $K = 10 \text{ mD}$ ,  $\Delta p = 10 \text{ MPa}$ ;  $K = 50 \text{ mD}$ ,  $\Delta p = 2 \text{ MPa}$ ;  $K = 250 \text{ mD}$ ,  $\Delta p = 0.4 \text{ MPa}$ ).

The formation breakdown process of the three different permeability rocks under the acting of seepage force is shown in Figure 11.

As shown in Figure 11, low-permeability rock ( $K = 10 \text{ mD}$ ) is the first to initiate fracture under the action of seepage forces due to higher pressure differences and pore pressure gradients. As the pore pressure gradient is small and the effect of seepage force is not significant, the fracture initiation of high permeability rock ( $K = 250 \text{ mD}$ ) is slowest to get breakdown pressure. Although the pressure difference between the inner and outer boundaries of the high-permeability reservoir is small, the pore pressure at each point  $p(r)$  is relatively great.

Therefore, the area where the effective circumferential stress field around the wellbore of the high-permeability reservoir is disturbed during which wellbore pressurization is more significant than that of the low-permeability rock.

In addition, the relationships between formation breakdown pressure and permeability for the three cases are shown in Figure 12. Figure 13 gives the ratio between the formation breakdown pressure of the case with seepage force and those from other two cases.

It can be seen from Figures 12 and 13 that the formation breakdown pressure for the case of fluid flowing into rock is smaller than that for impermeable rock. As the permeability increases, the effect of seepage force becomes less important, and the formation breakdown pressure is gradually approaching that without considering the effect of seepage force.

The effect of seepage force is more significant in low-permeability rock, where the formation breakdown pressure is only 20.65% of the breakdown pressure of ignoring seepage force. Therefore, the effect of seepage force should be applied during the analysis of hydraulic fracturing.

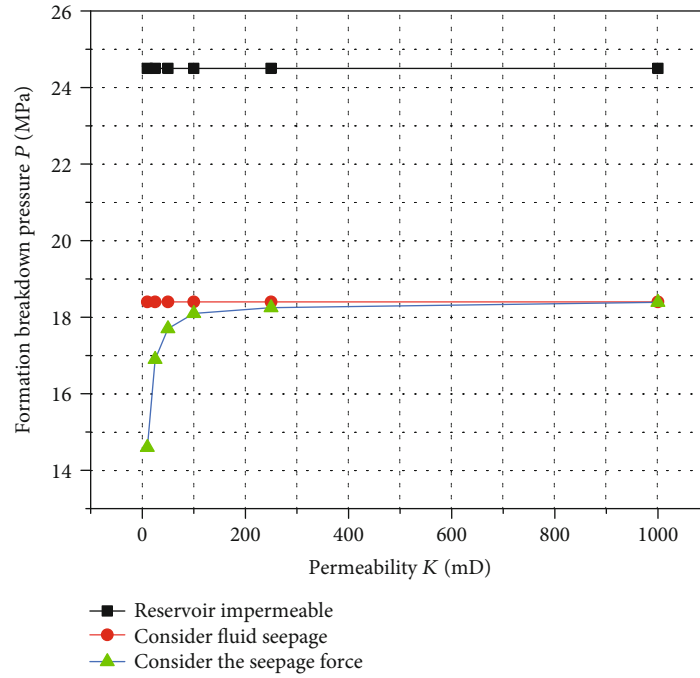


FIGURE 12: Relationship between formation breakdown pressure and permeability for three cases.

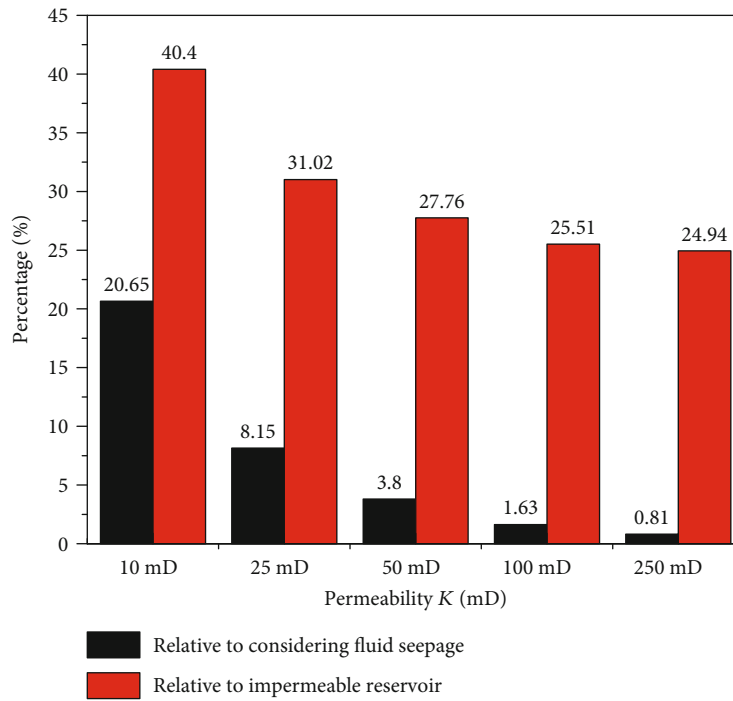


FIGURE 13: Reduction percentage of formation breakdown pressure from the case of considering seepage force to those from other cases.

## 5. Conclusions

- (1) During hydraulic fracturing, wellbore fluid flows into wellbore and will yield a seepage force due to fluid drag forces. The seepage force acts on the rock matrix in the fluid flowing direction and could be measured by pore pressure gradient
- (2) For a vertical well, the seepage force is beneficial to breakdown the formation and thus lowers the wellbore breakdown pressure
- (3) The effect of seepage force on formation breakdown increases as the two horizontal principal stresses increase uniformly. Therefore, the deeper a formation, the greater action of the seepage force
- (4) The greater the difference of the two horizontal principal stresses, the lower effect of seepage force on formation breakdown. Therefore, seepage force gives more contribution to breakdown formation for isotropy formation or formations with small difference of the two horizontal stresses such as unconventional reservoirs
- (5) The greater the pore pressure gradient, the greater the seepage force. Seepage force increases as rock permeability decreases, and it should not be ignored in hydraulic fracturing analysis, especially for low-permeability formation

## Data Availability

The [DATA TYPE] data used to support the findings of this study are available from the corresponding author upon request at deshengzhou@126.com.

## Conflicts of Interest

The authors declare no conflict of interest.

## Acknowledgments

This work was supported by the National Natural Science Foundation of China (Grant Nos. 51934005, 51874242, and 51904244); the National Science and Technology Major Project of China (Grant No. 2016ZX05050-009); the Natural Science Basic Research Plan in Shaanxi Province of China (Program No. 2019JQ-364); and the Scientific Research Program Funded by Shaanxi Provincial Education Department (Program No. 19JK0663).

## References

- [1] B. Haimson and C. Fairhurst, "Initiation and extension of hydraulic fractures in rocks," *Society of Petroleum Engineers Journal*, vol. 7, no. 3, pp. 310–318, 1967.
- [2] B. Haimson, *Hydraulic Fracturing in Porous and Nonporous Rock and its Potential for Determining In-Situ Stresses at Great Depth*, 1968.
- [3] B. Haimson and C. Fairhurst, "Hydraulic fracturing in porous-permeable materials," *Journal of Petroleum Technology*, vol. 21, no. 7, pp. 811–817, 1969.
- [4] B. Haimson and C. Fairhurst, "In-situ stress determination at great depth by means of hydraulic fracturing," in *The 11th US Symposium on Rock Mechanics (USRMS)*. American Rock Mechanics Association, Berkeley, CA, USA, June 1969.
- [5] M. K. Hubbert and D. G. Willis, *Mechanics of Hydraulic Fracturing*, 1972.
- [6] W. L. Medlin and L. Masse, "Laboratory investigation of fracture initiation pressure and orientation," *Society of Petroleum Engineers Journal*, vol. 19, no. 2, pp. 129–144, 1979.
- [7] F. Guo, N. R. Morgenstern, and J. D. Scott, "Interpretation of hydraulic fracturing breakdown pressure," *International Journal of Rock Mechanics and Mining Sciences & Geomechanics Abstracts. Pergamon*, vol. 30, no. 6, pp. 617–626, 1993.
- [8] I. Song, M. Suh, K. S. Won, and B. Haimson, "A laboratory study of hydraulic fracturing breakdown pressure in tablerock sandstone," *Geosciences Journal*, vol. 5, no. 3, pp. 263–271, 2001.
- [9] A. P. Bungler, A. Lakirouhani, and E. Detournay, "Modelling the effect of injection system compressibility and viscous fluid flow on hydraulic fracture breakdown pressure," in *Rock stress and earthquakes-proceedings of the 5th international symposium on in-situ rock stress*, pp. 59–67, Beijing, China, August 2010.
- [10] S. J. Ha, J. Choo, T. S. Yun, and C. O. Liquid, "Liquid CO<sub>2</sub> fracturing: effect of fluid permeation on the breakdown pressure and cracking behavior," *Rock Mechanics and Rock Engineering*, vol. 51, no. 11, pp. 3407–3420, 2018.
- [11] Z. Tariq, M. Mahmoud, A. Abdulraheem, A. al-Nakhli, and M. BaTaweel, "An experimental study to reduce the breakdown pressure of the unconventional carbonate rock by cyclic injection of thermochemical fluids," *Journal of Petroleum Science and Engineering*, vol. 187, p. 106859, 2020.
- [12] T. Ito and K. Hayashi, "Physical background to the breakdown pressure in hydraulic fracturing tectonic stress measurements," *International Journal of Rock Mechanics and Mining Sciences & Geomechanics Abstracts. Pergamon*, vol. 28, no. 4, pp. 285–293, 1991.
- [13] T. Ito, "Effect of pore pressure gradient on fracture initiation in fluid saturated porous media: Rock," *Engineering Fracture Mechanics*, vol. 75, no. 7, pp. 1753–1762, 2008.
- [14] X. Jin, S. N. Shah, J. C. Roegiers et al., "Breakdown pressure determination-a fracture mechanics approach," in *SPE Annual Technical Conference and Exhibition*. Society of Petroleum Engineers, New Orleans, LA, USA, September 2013.
- [15] H. Fatahi, M. M. Hossain, S. H. Fallahzadeh, and M. Mostofi, "Numerical simulation for the determination of hydraulic fracture initiation and breakdown pressure using distinct element method," *Journal of Natural Gas Science and Engineering*, vol. 33, pp. 1219–1232, 2016.
- [16] C. Xiao, H. Ni, X. Shi, and R. Wang, "A fracture initiation model for carbon dioxide fracturing considering the bottom hole pressure and temperature condition," *Journal of Petroleum Science and Engineering*, vol. 184, p. 106541, 2020.
- [17] R. Mourgues and P. R. Cobbold, "Some tectonic consequences of fluid overpressures and seepage forces as demonstrated by sandbox modelling," *Tectonophysics*, vol. 376, no. 1–2, pp. 75–97, 2003.
- [18] P. R. Cobbold, B. J. Clarke, and H. Løseth, "Structural consequences of fluid overpressure and seepage forces in the outer

- thrust belt of the Niger Delta,” *Petroleum Geoscience*, vol. 15, no. 1, pp. 3–15, 2009.
- [19] A. Zanella and P. R. Cobbold, *Beef: Evidence for Fluid Overpressure and Hydraulic Fracturing in Source Rocks during Hydrocarbon Generation and Tectonic Events: Field Studies and Physical Modelling*, 2012.
- [20] A. Rozhko, *Role of Seepage Forces on Hydraulic Fracturing and Failure Patterns*, 2007.
- [21] A. Y. Rozhko, Y. Y. Podladchikov, and F. Renard, “Failure patterns caused by localized rise in pore-fluid overpressure and effective strength of rocks,” *Geophysical Research Letters*, vol. 34, no. 22, 2007.
- [22] C. Zhou, W. Shao, and C. J. van Westen, “Comparing two methods to estimate lateral force acting on stabilizing piles for a landslide in the Three Gorges Reservoir, China,” *Engineering Geology*, vol. 173, pp. 41–53, 2014.
- [23] J. Zou, S. Li, Y. Xu, H. C. Dan, and L. H. Zhao, “Theoretical solutions for a circular opening in an elastic–brittle–plastic rock mass incorporating the out-of-plane stress and seepage force,” *KSCE Journal of Civil Engineering*, vol. 20, no. 2, pp. 687–701, 2016.
- [24] H. AlKhafaji, M. Imani, and A. Fahimifar, “Ultimate bearing capacity of rock mass foundations subjected to seepage forces using modified Hoek–Brown criterion,” *Rock Mechanics and Rock Engineering*, vol. 53, no. 1, pp. 251–268, 2020.
- [25] M. D. Zoback, D. Moos, L. Mastin, and R. N. Anderson, “Well bore breakouts and in situ stress,” *Journal of Geophysical Research: Solid Earth*, vol. 90, no. B7, pp. 5523–5530, 1985.
- [26] A. J. Miles and A. D. Topping, “Stresses around a deep well,” *Transactions of the AIIME*, vol. 179, no. 1, pp. 186–191, 1949.
- [27] W. Nowacki, *Thermoelasticity*, Elsevier, 2013.
- [28] S. P. Timošenko and J. N. Goodier, *Theory of elasticity*, McGraw-Hill, 1951.
- [29] J. R. Rice and M. P. Cleary, “Some basic stress diffusion solutions for fluid-saturated elastic porous media with compressible constituents,” *Reviews of Geophysics*, vol. 14, no. 2, pp. 227–241, 1976.
- [30] M. A. Biot, “General theory of three-dimensional consolidation,” *Journal of Applied Physics*, vol. 12, no. 2, pp. 155–164, 1941.
- [31] A. Y. Rozhko, “Benchmark for poroelastic and thermoelastic numerical codes,” *Physics of the Earth and Planetary Interiors*, vol. 171, no. 1–4, pp. 170–176, 2008.
- [32] J. Geertsma, “Problems of rock mechanics in petroleum production engineering,” in *1st ISRM Congress. International Society for Rock Mechanics and Rock Engineering*, Lisbon, Portugal, September 1966.
- [33] B. D. Collins and D. Znidarcic, “Stability analyses of rainfall induced landslides,” *Journal of Geotechnical and Geoenvironmental Engineering*, vol. 130, no. 4, pp. 362–372, 2004.
- [34] R. F. Craig, *Soil Mechanics*, ELBS Edition, Great Britain, 4th edition, 1987.
- [35] K. Terzaghi, *Theoretical Soil Mechanics*, John Wiley and Sons, 1965.



## Research Article

# Study on the Effect of High-Temperature Heat Treatment on the Microscopic Pore Structure and Mechanical Properties of Tight Sandstone

Liangbin Dou <sup>1,2,3</sup>, Guanli Shu <sup>4,5</sup>, Hui Gao <sup>1,2</sup>, Jinqing Bao <sup>1,2</sup> and Rui Wang <sup>1,2</sup>

<sup>1</sup>School of Petroleum Engineering, Xi'an Shiyou University, Xi'an 710065, China

<sup>2</sup>Key Laboratory of Unconventional Oil & Gas Development (China University of Petroleum (East China)), Ministry of Education, Qingdao 266580, China

<sup>3</sup>Engineering Research Center of Development and Management for Low to Ultra-Low Permeability Oil & Gas Reservoirs in West China, Ministry of Education, Xi'an 710065, China

<sup>4</sup>Department of Polymer Science and Engineering and State Key Laboratory of Metal Matrix Composites, Shanghai Jiao Tong University, 800 Dongchuan Road, Shanghai 200240, China

<sup>5</sup>Xinjiang Keli New Technology Development Co., Ltd., 138 Youyi Road, Karamay, 834000 Xinjiang, China

Correspondence should be addressed to Liangbin Dou; 77129dou@163.com and Guanli Shu; shugl824@gmail.com

Received 14 August 2020; Revised 13 October 2020; Accepted 15 March 2021; Published 5 April 2021

Academic Editor: Paolo Madonia

Copyright © 2021 Liangbin Dou et al. This is an open access article distributed under the Creative Commons Attribution License, which permits unrestricted use, distribution, and reproduction in any medium, provided the original work is properly cited.

The investigation of changes in physical properties, mechanical properties, and microscopic pore structure characteristics of tight sandstone after high-temperature heat treatment provides a theoretical basis for plugging removal and stimulation techniques, such as high energy gas fracturing and explosive fracturing. In this study, core samples, taken from tight sandstone reservoirs of the Yanchang Formation in the Ordos Basin, were first heated to different temperatures (25–800°C) and then cooled separately by two distinct cooling methods—synthetic formation water cooling and natural cooling. The variations of wave velocity, permeability, tensile strength, uniaxial compressive strength, and microscopic pore structure of the core samples were analyzed. Experimental results demonstrate that, with the rise of heat treatment temperature, the wave velocity and tensile strength of tight sandstone decrease nonlinearly, yet its permeability increases nonlinearly. The tight sandstone's peak strength and elastic modulus exhibit a trend of the first climbing and then declining sharply with increasing temperature. After being treated by heat at different temperatures, the number of small pores varies little, but the number of large pores increases obviously. Compared to natural cooling, the values of physical and mechanical properties of core samples treated by synthetic formation water cooling are apparently smaller, whereas the size and number of pores are greater. It can be explained that water cooling brings about a dramatic reduction of tight sandstone's surface temperature, generating additional thermal stress and intensifying internal damage to the core. For different cooling methods, the higher the core temperature before cooling, the greater the thermal stress and the degree of damage caused during the cooling process. By taking into consideration of changes in physical properties, mechanical properties, and microscopic pore structure characteristics, the threshold temperature of tight sandstone is estimated in the range of 400–600°C.

## 1. Introduction

With the further exploitation of oilfields, coal mines, and geothermal energy and the increasing operations under the deep geological conditions, the research on change in rock properties after high-temperature heat treatment attracts

great attention [1]. While drilling in deep and high-temperature reservoirs, the surrounding rock of the wellbore is subject to a rapid temperature decrease after contacting with drilling fluid and mechanical properties of the rock alter, resulting in a favorable condition for breaking the rock but undermining the stability of surrounding rock. In the course

of hydraulic fracturing in high-temperature reservoirs, there is a significant temperature difference between reservoir rock and fracturing fluid. In this case, the mechanism of fracturing involves both thermal fracturing and hydraulic pressure. During the long-term extraction of geothermal energy, the rock temperature gradually declines with the injection of circulation water. Under the combined actions of in situ stress, thermal stress, and hydraulic pressure, the reservoir rock may rupture twice or more times, further enhancing reservoir permeability and heat exchange efficiency. Moreover, as the development techniques advance, the phenomenon that the formation is first heated up and then cooled down in a quick manner takes place in the processes of the combined perforation and hydraulic fracturing and the high energy gas fracturing and plugging removal followed by water injection. For this reason, it is of great importance to study the changes in pores and permeability of high-temperature rock after water cooling [2].

Sandstone is one of the most common types of sedimentary rock and has been widely used in geological engineering research, such as the evolution of the earth's crust, oil and gas migration and accumulation, geological CO<sub>2</sub> storage, geothermal exploitation, and nuclear waste storage [3]. Many scholars [4–21] studied the physical and mechanical properties of sandstone under high temperatures. Of those studies, experiments for the investigation of mechanical properties of the rock under thermal treatment included the compression test under and after high temperature, the tensile test under and after high temperature, creep test under high temperature, and wave velocity measurements of the rock before and after high temperature; constitutive models were established for investigating the transient mechanical properties of the rock under and after high temperature; numerical simulations were performed for the understanding of the rock's thermodynamic properties under high temperature [22]. Specifically, those studies evaluated the changes in elastic modulus, uniaxial and triaxial compressive strength, tensile strength, deformation characteristics, wave velocity, and permeability of the sandstone after thermal treatment.

However, it is noted that the research on tight sandstone is lacking as compared with that on conventional sandstone. Tight sandstone reservoir is the key area of unconventional resource development in the world [23, 24]. Due to the complex mineral components and diverse depositional environments, tight sandstones have various pore types and intricate fractures, joints, and bedding planes. In the course of high-temperature heat treatment or cooling of tight sandstone, physicochemical changes occur to some extent, giving rise to a dramatic change in the internal structure of the sandstone and sophisticating its physical and mechanical properties [25]. Another point that lacks discussion is the effect of high-temperature heat treatment on the microscopic pore structure characteristics of tight sandstone. The influencing mechanism of thermal treatment on the microscopic pore structure and the corresponding mechanisms of plugging removal and stimulation are vital for the selection and optimization of techniques, such as high energy gas fracturing, explosive fracturing, and unconventional air oxidation thermal cracking.

In this work, the authors adopt tight sandstones taken from tight sandstone reservoirs of the Yanchang Formation in the Ordos Basin and investigate the variations of physical and mechanical properties of tight sandstone after heat treatment, especially the change in the microscopic pore structure characteristics. Additionally, the changes and evolution characteristics of microscopic structures at different scales are identified with different cooling methods and at various temperatures, aiming at providing a theoretical basis for the high energy gas or explosive fracturing and the combined perforation and hydraulic fracturing technique in tight sandstone reservoirs.

## 2. Experimental Section

*2.1. Core Samples.* The core samples used in the experiments were taken from tight sandstone reservoirs of the Yanchang Formation in the Ordos Basin, which is located in northwest China. The location and distribution of the studied tight sandstone are displayed in Figure 1. During the early Paleozoic, the Ordos Basin evolved from the continental margin ocean basin to the coastal shallow ocean basin, the inland basin, and the foreland basin and finally formed a basin pattern with complete stratigraphic structure and simple structure. In the Late Triassic, the Ordos Basin stretched and subsided, forming a large freshwater lake inside the basin and depositing a set of terrigenous clastic rock series dominated by fluvial-lacustrine facies, which is the Yanchang Formation. The Yanchang Formation is characterized by a fluvial-lacustrine facies sedimentary system formed during the continuous depression and stable sedimentation in the Ordos Basin, which experienced the whole process of generation, expansion, evolution, and subduction. According to the characteristics of the reservoirs, the Yanchang Formation can be divided into 10 sections. Chang 8 and Chang 6 are the main oil-bearing layers with relatively stable distribution and good oil-bearing properties. The buried depth of the Yanchang Formation in the study area is between 1650 and 2150 m with multiple overlapped oil layers. The distribution of oil layers is scattered, and the argillaceous and calcareous interlayer is relatively developed with different thicknesses and shielding conditions.

According to the general requirements of the rock mechanical test, cylindrical core samples were prepared with a diameter of 25 mm and a height of 50 mm. The porosity and permeability of the cores are low. Due to the limitations of coring costs and core quality, only three core samples were selected for testing for each well depth. The porosity and permeability were determined by the Core Measurement System (CM300, USA). The measurement ranges of porosity and permeability are 0.01–40% and 0.00005–15D, respectively. The device is composed of an ISCO pump, vacuum pump, confining pressure pump, core holder, transfer containers, flow meters, nitrogen bottle, and thermostat. The specific experiment method porosity and permeability are measured according to the industrial standard SY/T 5336-2006—Practices for Core Analysis. The contents of minerals in the core were measured with the X-ray diffractometer (XRD-6000, Japan). The measurement method followed



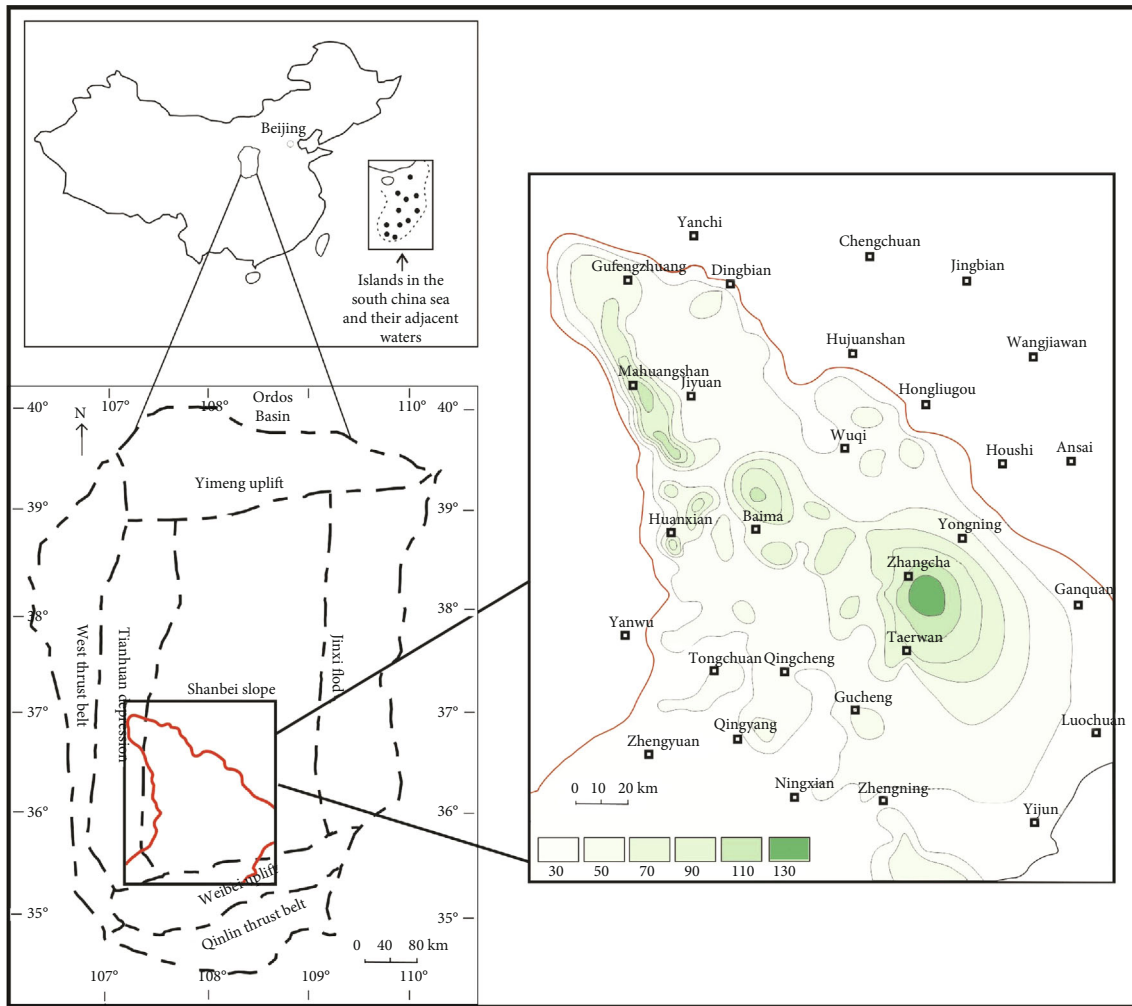


FIGURE 1: Location of the Ordos Basin and isopach map of the Yanchang Formation (contour intervals in meters).

the industrial standard SY/T 5163-2010–Analysis Method for Clay Minerals and Ordinary Non-Clay Minerals in Sedimentary Rocks by the X-Ray Diffraction. Table 1 summarizes the physical properties and mineral compositions of the studied tight sandstones.

The cores used in this study were taken from the Chang 7 Member of the Yanchang Formation. The green contour line in Figure 1 shows the thickness contour and sedimentary facies of the Chang 7 tight sandstone, which has the characteristics of large-scale distribution, good lateral continuity, and large thickness variation. The maximum thickness is 130 m, and the average thickness is above 10 m.

The X-ray diffraction analysis indicates that types of clay minerals in the studied area are mainly kaolinite, chlorite, illite, and mixed illite/smectite, and their contents are 17.0%, 41.3%, 21.3%, and 20.4%, respectively. The occurrence characteristics of clay minerals are analyzed and verified by SEM, and results are shown in Figure 2.

To avoid the impact of laboratory water on the microscopic pore throat structure of tight sandstone during water cooling and core flooding (for NMR measurement), the synthetic formation water from the target reservoir was used

in the experiments (the water type is  $\text{CaCl}_2$ , and salinity is approximately 18000 mg/L; the viscosity and density at  $50^\circ\text{C}$  are 0.521 mPa·s and  $1.02\text{ g/cm}^3$ , respectively [26]).

**2.2. Experimental Setups.** In the experiments, a servo control rock mechanics triaxial experimental system (Model TAW-1000) was applied for the uniaxial compression test. This system was equipped with the Germany DOLI company’s EDC full-digital servo control. The wave velocity test was performed using the Panameric Model 5058PR high voltage pulse-receiver; the longitudinal wave velocity was measured by the Vaseline coupling test. The SXW-1200 high-temperature box-type resistance furnace (manufactured by the Shanghai Shiyuan Electric Furnace Co., Ltd., China, with the highest stability of up to  $1200^\circ\text{C}$ ) was adopted for the high-temperature heat treatment of tight sandstones.

The nuclear magnetic resonance (NMR) setup (manufactured by the Niumag Corporation, China) was used to measure the  $T_2$  spectrum of synthetic formation water under various experimental conditions. The NMR instrument is comprised of a magnetic body, a radio frequency emitter, and a data collection system. The basic parameters for

TABLE 1: Properties and mineral compositions of the studied tight sandstone core samples.

Sample no.	Porosity (%)	Permeability (mD)	Density (g/cm <sup>3</sup> )	Type and content (%) of mineral			
				Quartz	Feldspar	Carbonate	Total content of clay minerals
H27-1	6.52	0.10	2.43	64.9	15.6	3.1	16.4
H27-2	6.76	0.12	2.42	59.7	18.4	4.4	17.5
H27-3	6.61	0.11	2.43	61.7	17.5	4.2	16.6
H28-1	6.98	0.15	2.58	60.2	16.8	10.7	12.3
H28-2	7.10	0.16	2.58	62.1	16.2	9.8	11.9
H28-3	7.08	0.16	2.57	61.4	16.4	9.5	12.7
H29-1	5.90	0.06	2.52	60.4	20.3	4.0	15.3
H29-2	6.31	0.07	2.53	61.5	21.5	3.5	13.5
H29-3	6.42	0.08	2.51	60.3	22.1	3.1	14.5
H30-1	9.11	0.21	2.50	52.7	20.9	12.0	14.4
H30-2	8.41	0.18	2.49	50.4	22.3	13.3	14.0
H30-3	9.03	0.19	2.50	50.5	22.3	12.4	14.8

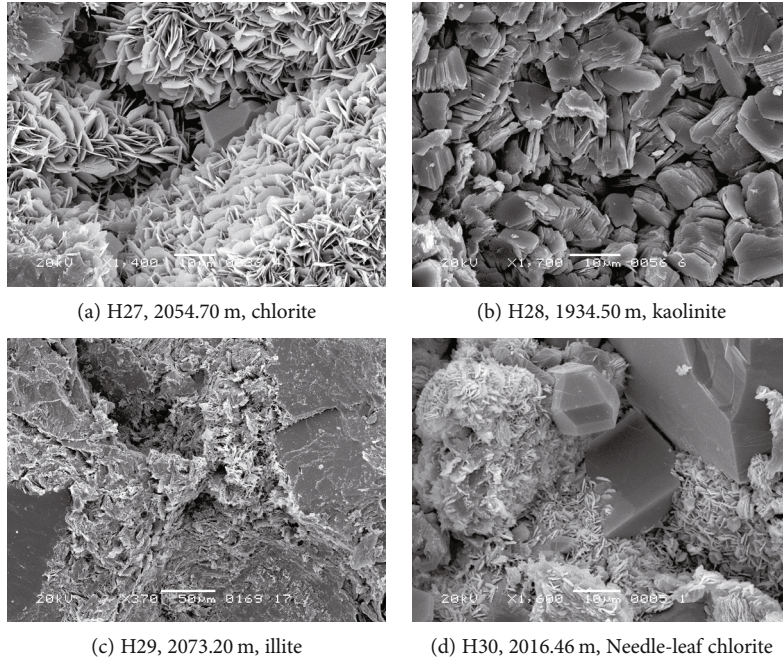


FIGURE 2: The occurrence characteristics of clay minerals of the Yanchang Formation in the Ordos Basin.

NMR measurements are configured with the waiting time of 5 s, the echo time of 0.25 ms, the scanning number of 16, and the echo number of 1024.

The NMR technique is a nondestructive detection method. The  $T_2$  spectrum of the core sample saturated with single-phase fluid can reflect the internal pore structure of the core. In a uniform magnetic field, the transverse relaxation time  $T_2$  is expressed as

$$\frac{1}{T_2} = \frac{1}{T_{2B}} + \frac{1}{T_{2S}} = \frac{1}{T_{2B}} + \rho \frac{S}{V}, \quad (1)$$

where  $\rho$  is the relaxation rate ( $\mu\text{m}/\text{ms}$ ) and  $S/V$  is the specific surface area ( $1/\mu\text{m}$ ).

Since  $T_{2B}$  is far greater than  $T_2$ ,  $1/T_{2B}$  can be neglected (i.e., the  $T_2$  relaxation contribution is mainly from surface relaxation). The following is given:

$$\frac{S}{V} = \frac{F_S}{r_c}, \quad (2)$$

where  $F_S$  is the shaper factor of the single pore ( $F_S = 3$  for spherical pore and  $F_S = 2$  for cylindrical pore) and  $r_c$  is the pore radius ( $\mu\text{m}$ ).

By replacing Equation (2), Equation (1) can be rewritten as

$$T_2 = \frac{r_c}{\rho F_S}. \quad (3)$$

Assuming  $C = \rho F_S$ , Equation (3) can be transformed to

$$T_2 = \frac{1}{C} \cdot r_c. \quad (4)$$

As seen from Equation (4), the transverse relaxation time  $T_2$  is in a positive linear relationship with the pore radius  $r_c$ . Thus, the measurement of hydrogen signals can be used to calculate the fluid distribution in different pores.

**2.3. Experimental Procedures.** Four groups of cores (H27, H28, H29, and H30) taken from the same well depth were selected for experiments. The physical properties of each core were measured at 25°C (i.e., the normal temperature). Each group had three core samples: two of them were treated separately at 200, 400, 600, and 800°C, and another sample was chosen as the blank case for comparison. The experimental objective was to simulate the stimulation process of a tight sandstone reservoir using high-energy gas or explosive fracturing followed by hydraulic fracturing and analyze the microscopic pore structure and mechanical properties of tight sandstone after water cooling and natural cooling. The experimental procedures were summarized as follows:

- (1) Core sample was put in an extraction container and flushed with benzene and alcohol with a volume ratio of 1:3 to remove residual oil. After that, the core was placed in a thermostat and heated to a formation temperature of 50°C; the temperature was remained unchanged for 48 h. Then the core was taken out to measure the weight, dimensions, and gas permeability
- (2) Given that the pore throat radius of tight sandstone was small and the conventional vacuum saturation was unable to fully saturate the pores of the core with water, the core sample was placed in a core holder and flushed with synthetic formation water using a high-pressure displacement device. When the produced liquid was about 5 PV, the core was considered fully saturated and the  $T_2$  spectrum was measured for the first time. After that, the synthetic formation water-saturated core was centrifuged by a PC-12B centrifuge (the rotational speed was set at 11000 r/min), and the  $T_2$  spectrum was measured again, as well as the permeability and longitudinal wave velocity of the core
- (3) After centrifugation, two cores chosen from the same group were heated at a rate of 5°C/min. After reaching the set temperature, it was kept for 2 h. Then the cores were taken out and cooled by two methods, i.e., natural cooling and synthetic formation water cooling. After cooling, step (2) was repeated, and the  $T_2$  spectrum and longitudinal wave velocity of the core were measured
- (4) At last, the uniaxial compression experiment was performed for the core sample with a loading speed of 0.02 mm/min to obtain the stress-strain curve

### 3. Results and Discussion

#### 3.1. Effect of High-Temperature Heat Treatment on Physical Properties of Tight Sandstone

**3.1.1. Variation of Acoustic Wave Velocity.** When an acoustic wave passes through different media, wave velocity varies. If there are cracks, cavities, or other defects inside the media, the acoustic wave velocity decreases. The wave velocity reflects the matrix integrity and fracture development of the rock. Due to the limited core samples, the normalization method has been applied to exclude the influences of physical properties and mineral compositions of different core samples on acoustic wave velocity:

$$a = \frac{S_i}{S_o} \times 100\%, \quad (5)$$

where  $a$  is the variation of acoustic wave velocity, dimensionless, and  $S_o$  and  $S_i$  are the acoustic wave velocities of the core before and after heat treatment, respectively (m/s).

Figure 3 displays variations of relative wave velocity of core samples with temperature under different cooling methods. It is observed that the declining amplitude of wave velocity increases with temperature in the range of 25-800°C. This is because core samples undergo heating and cooling processes in the experiments. On the one hand, the degree of damage in the core caused by heat treatment exacerbates with the increment of temperature. On the other hand, the temperature increase consequentially brings about a temperature difference between the core and cooling fluid, intensifying the effect of cold shock and aggravating the cooling-induced damage [27]. These two factors contribute to the decrease of wave velocity. At 600°C, the wave velocity falls off markedly. In addition to thermal damage, it is also attributed to the enlarged pores and newly formed microcracks that are caused by the physicochemical changes of some minerals due to heat adsorption during the high-temperature heat treatment. For instance, as indicated in Table 1, the tight sandstone contains a high content of quartz (the minimum content is greater than 50%). At 573°C, the transition from  $\alpha$ -type to  $\beta$ -type quartz takes place. When the temperature exceeds 400°C, the magnesium-illite and kaolinite begin decomposition; when the temperature is beyond 500°C, the dolomite, magnesium carbonate, and calcium montmorillonite decompose [19, 28, 29]. The physicochemical changes of these minerals significantly alter the microscopic pore structure of the core, increase the core volume, and further give rise to a certain degree of spalling and fragmentation.

In the range of 25-800°C, comparing wave velocity changes under two different cooling methods indicates that the declining amplitude of wave velocity of the core under synthetic formation cooling is 1.31%-10.12% higher than that of the natural cooling. The possible reason for this phenomenon can be explained that the surface temperature of the core has a sharp decline during the water cooling; hence, a higher temperature gradient is formed inside the core, which brings about the secondary thermal stress, causes

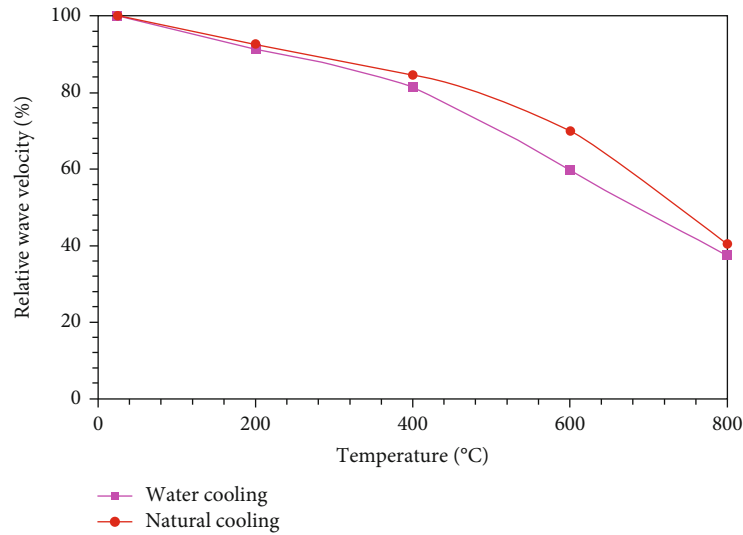


FIGURE 3: The variations of relative wave velocity of core samples with temperature under two different cooling methods.

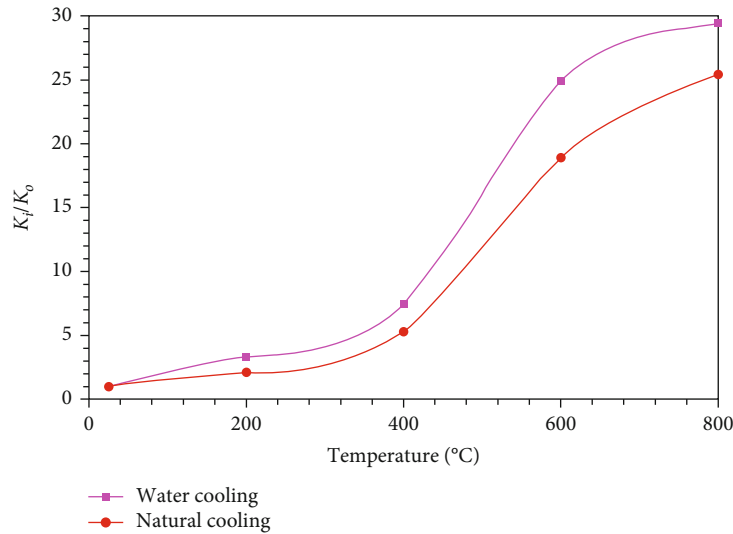


FIGURE 4: The variations of permeability of core samples with temperature under two different cooling methods.

greater thermal damage, and accelerates the deterioration of tight sandstone.

**3.1.2. Variation of Permeability.** Permeability change can be used as an indicator to evaluate the degree of damage to the core and the improvement of its physical properties under the high-temperature heat treatment intuitively and quantitatively. Figure 4 compares the permeability change of core samples under synthetic formation water cooling and natural cooling at 25–800°C (where  $K_0$  and  $K_i$  are the permeabilities of the core before and after heat treatment, respectively). It is noted that, under both cooling methods, the increasing amplitude of permeability of the core goes up with temperature and there is a sudden change in permeability, implying the existence of threshold temperature (i.e., the temperature at which the physical properties of the core alter drastically). Around the threshold temperature, the core's permeability undergoes a sudden change; below it, the permeability

increases slightly with temperature; above it, the permeability increases rapidly with temperature. Accordingly, the results from this figure imply that the threshold temperature of the studied tight sandstone is between 400°C and 600°C. In this range, the permeability of tight sandstone alters by orders of magnitude, signifying that the internal structure of tight sandstone has changed significantly. This change is consistent with the variation of acoustic wave velocity, which can be attributed to the chemical decomposition of some minerals (e.g., magnesium illite, kaolinite, dolomite, magnesium carbonate, and calcium montmorillonite), the phase transition of some minerals (e.g., quartz), or the oxidation of some rocks (such as siderite and pyrite).

Based on the permeability variations of core samples under two different cooling methods, it is found that the permeability of the synthetic formation water-cooled core is increased by 3.34–29.45 times and that of the naturally cooled core is risen by 2.08–25.45 times at 25–800°C. Considering



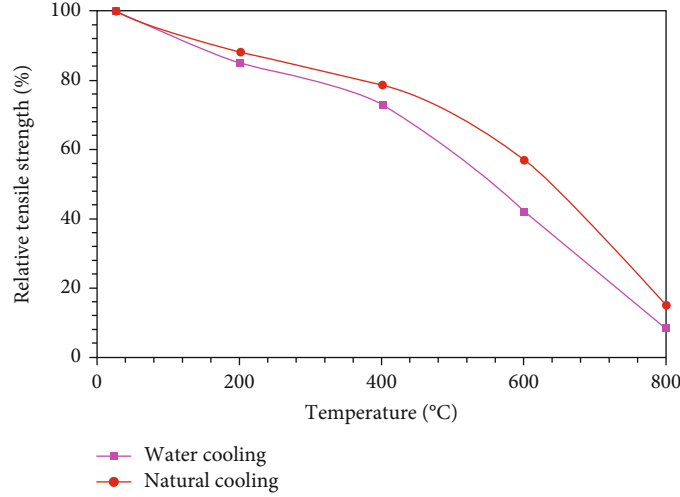


FIGURE 5: The variations of the tensile strength of core samples with temperature under two different cooling modes.

thermal damages are almost the same at the identical temperature under these two cooling methods, the effect of heating is negligible. For the cores at the same temperature, the effect of water cooling on the enhancement of permeability is more significant than that of natural cooling. This is because, compared to natural cooling, the temperature difference between synthetic formation water and high-temperature core is greater, leading to a stronger cold shock and the propagation of original cracks in the core. This, in turn, results in a higher increasing amplitude of permeability under the water cooling.

As plotted in Figures 3 and 4, the biggest differences in acoustic wave velocity and permeability emerge at 600°C, but the differences become smaller at 800°C. The reason is that the synthetic formation water cooling causes a more dramatic surface temperature drop of the core at 600°C, resulting in a larger temperature gradient and greater thermal damage which aggravates the degradation of the core. However, at 800°C, the minerals in tight sandstone are fully expanded after high-temperature heat treatment. A large number of micropores are formed, and the preexisting pores are further enlarged and connected, which weaken the mechanical properties of the core. Although the water cooling could further degrade mechanical properties, the effect is not significant and thus the differences between these two cooling methods are not obvious at 800°C.

### 3.2. Effect of High-Temperature Treatment on Rock Mechanical Properties of Tight Sandstone

**3.2.1. Variation of Tensile Strength.** Authors [30] have carried out a series of the Brazilian splitting tests and longitudinal wave velocity tests in tight sandstones of the Yanchang Formation in the Ordos Basin and established a tensile strength prediction model for tight sandstone in terms of the longitudinal wave velocity and density. The correlation coefficient of the model is greater than 0.93, and the maximum error is within 5% as compared to the measured field data.

$$\sigma_t = a \ln(V_p) + b \cdot \rho - c, \quad (6)$$

where  $\sigma_t$  is the uniaxial tensile strength (MPa);  $V_p$  is the longitudinal wave velocity (m/s);  $\rho$  is the rock density ( $\text{g/cm}^3$ ); and  $a$ ,  $b$ , and  $c$  are dimensionless coefficients. Considering the effect of heat-induced microcracks on wave velocity, the recommended values for coefficients  $a$ ,  $b$ , and  $c$  are 16.69, 9.36, and 136.12, respectively.

After the high-temperature heat treatment, the dimensions of the core at each temperature were measured. Experimental results show that the diameter of the core is slightly reduced, its length is enlarged somewhat, and its total volume is increased. Accordingly, the density of the core is slightly increased with temperature.

Due to the limited number of core samples in this study, the tensile strengths of tight sandstone samples after high-temperature heat treatment were analyzed by adopting the above model (Equation (6)). Likewise, the normalization method was applied to eliminate the effects of physical properties and densities of different rocks on tensile strength.

Figure 5 presents the comparison of the tensile strength of core samples under two different cooling methods. With the rise of temperature, the tensile strength of the core after being cooled exhibits a decreasing trend, indicating that the damage caused by heating and cooling the core reduces the tensile strength. The declining amplitude of tensile strength enlarges with the increase of heating temperature. Comparing Figures 3 and 5 indicates that the declining amplitude of tensile strength is greater than that of the acoustic wave velocity, signifying that the propagation of cracks in the tight sandstone after the heating and cooling treatments reduces wave velocity and density of the core concurrently.

The tensile strengths of the core treated by synthetic formation water cooling are 2.97% and 5.61% lower than that of the core under the natural cooling at 200°C and 400°C, respectively. It indicates that the effect of different cooling methods on the tensile strength is not significant in this temperature range. At 600°C, compared to the natural cooling, the tensile strength of the core under the water cooling is 14.21% lower. In addition, the density change is taken into account. The densities of the cores after the water cooling and natural cooling are  $2.45 \text{ g/cm}^3$  and  $2.47 \text{ g/cm}^3$ , respectively, which

are slightly decreased as compared to the densities of the cores before heat treatment ( $2.53 \text{ g/cm}^3$  and  $2.51 \text{ g/cm}^3$ , respectively). By combining these findings, it can be concluded that water cooling has a greater impact on the tensile strength of tight sandstone than natural cooling. This is because the water cooling can promote the propagation of original cracks in the core and aggravate the degree of thermal damage to the core. The higher the chance of water cooling-induced crack propagation and connectivity, the more severe the thermal damage.

**3.2.2. Stress-Strain Characteristics.** The stress-strain curves of tight sandstones after synthetic formation water cooling and natural cooling are plotted in Figures 6 and 7. After high-temperature heat treatment and under the uniaxial compression test, it is found that the stress-strain curve of the core samples generally includes four stages, i.e., densification, elasticity, yielding, and failure. With increasing temperature, the peak stress of the water-cooled tight sandstone shows a trend of first rising and then declining, same as the change in axial strain. In comparison with natural cooling, the peak stress of the core after water cooling is lower at each temperature and the stress drops rapidly after reaching the peak of the stress-strain curve, presenting certain brittle failure characteristics.

As indicated in these two figures, when the heating temperature is below  $600^\circ\text{C}$ , the densification stage is not noticeable in the stress-strain curve of tight sandstone after water cooling and natural cooling. As the temperature continues to rise, the densification stage emerges. The reason for this phenomenon is that when the temperature is not high, the thermal expansion coefficients of different minerals lead to a small extent of uneven thermal expansion and deformation between mineral particles. The consequent result is to cause thermal deformation of some fine sandstone particles, promote the gradual closure of some original microcracks, and improve the compactness of the core. As the temperature goes up, the uneven expansion between mineral particles becomes more pronounced. When the resulting thermal stress exceeds the tensile strength of the core, new cracks are induced and the number of microcracks climbs. Besides, the effusion of crystal water from the mineral destroys the crystal lattice structure of the mineral, resulting in increased internal cracks and enhanced connectivity and thus exhibiting a more obvious densification stage.

**3.2.3. Variations of Peak Strength and Elastic Modulus.** The peak strength of the core can directly reflect its ability to resist compression failure. Figure 8 compares the peak strengths of core samples under two cooling methods. The peak strengths of tight sandstones treated by synthetic formation water cooling and natural cooling increase first and then decrease sharply. For water cooling, the peak strength reaches the maximum at  $200^\circ\text{C}$  and decreases significantly when the temperature drops down to  $600^\circ\text{C}$ ; however, for natural cooling, the peak strength attains the maximum value at  $400^\circ\text{C}$  and falls thereafter. When the temperature is not high (i.e., below  $400^\circ\text{C}$  for water cooling and less than  $600^\circ\text{C}$  for natural cooling), the heat may cause the thermal deformation of some fine sandstone particles, but the

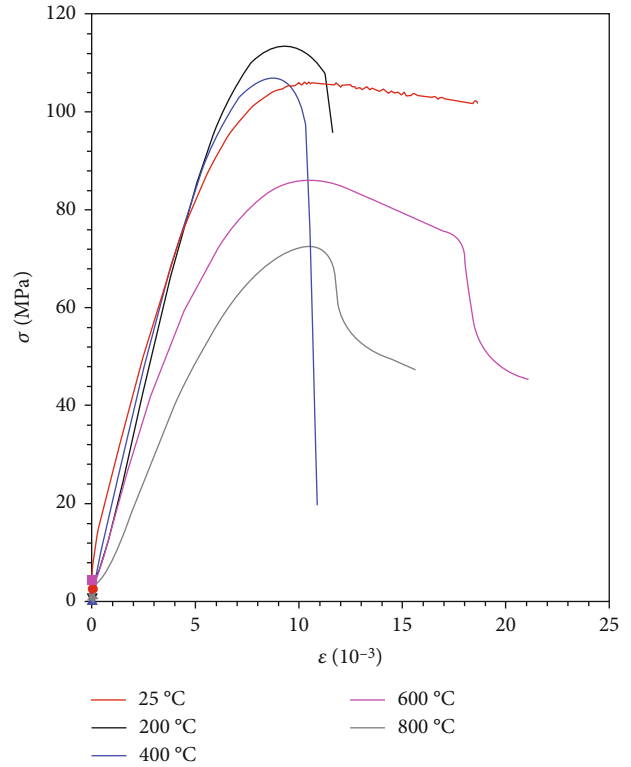


FIGURE 6: Stress-strain curves of tight sandstones after synthetic formation water cooling.

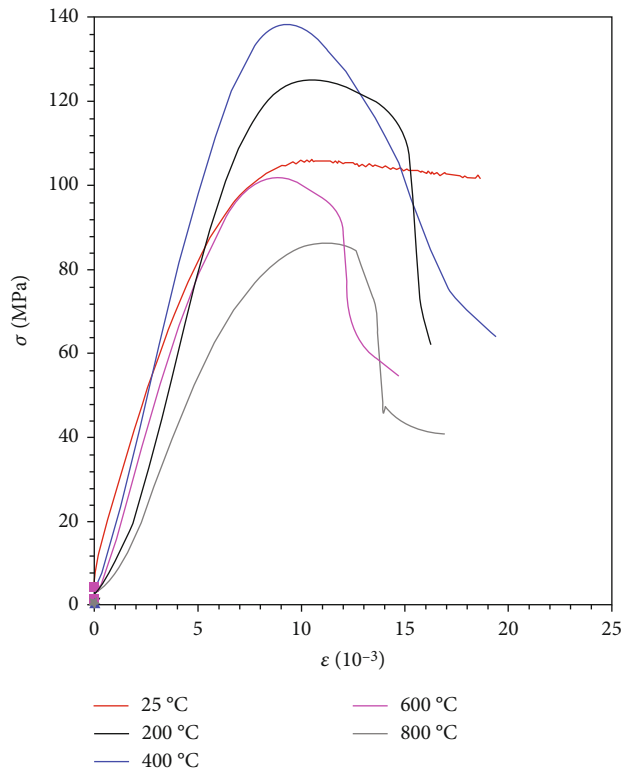


FIGURE 7: Stress-strain curves of tight sandstones after natural cooling.



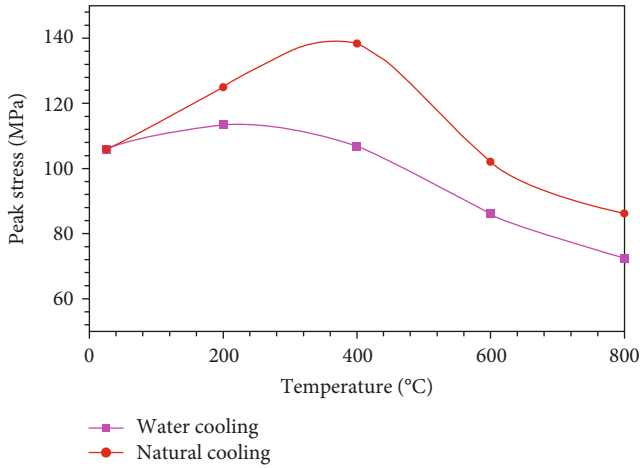


FIGURE 8: The variations of peak stress of core samples with temperature under two different cooling methods.

expansion and deformation of the minerals are small, which promotes the gradual closure of some original microcracks and enhances the compactness and strength of the core. Moreover, the damage caused by cooling after the high-temperature heat treatment is less than the strengthening effect of thermal action on the strength of the core. With the further increment of temperature, the peak strengths of the cores under two cooling methods drop significantly. The peak strength of the water-cooled core is still lower than that of the naturally cooled core, indicating that water cooling has a greater impact on the peak strength of tight sandstone after high-temperature heat treatment than natural cooling.

Figure 9 shows the comparison of elastic modulus of core samples under two different cooling methods, and a resemble trend is observed like the peak strength. At 25-400°C, the elastic moduli of core samples exhibit an overall increase with temperature. When the cores are heated to 600°C, the elastic moduli decline. The declining amplitude of elastic modulus of the water-cooled core sample is larger than that of the naturally cooled core, signifying that the significant deterioration has occurred to the mechanical properties of the core. Compared to water cooling, the elastic moduli of the cores under natural cooling are 8.41%, 15.32%, 34.93%, and 16.59% higher at four different temperatures (i.e., 25°C, 200°C, 400°C, and 600°C), respectively, which demonstrates that the impact of water cooling on the elastic modulus of the core is more obvious than that natural cooling.

### 3.3. Effect of High-Temperature Heat Treatment on Pore Structure Characteristics of Tight Sandstone

**3.3.1. Characteristics of NMR  $T_2$  Spectrum.** The  $T_2$  spectrum and pore size distributions of the tight sandstone samples before and after natural cooling and water cooling at four different temperatures are plotted in Figures 10–13. Before heat treatment,  $T_2$  values range from 0.1 to 1000.0 ms and  $T_2$  spectrums present bimodal distribution. Most of the pore diameters are less than 100.0 ms, indicating that the original core sample mainly contains micropore and mesopores and

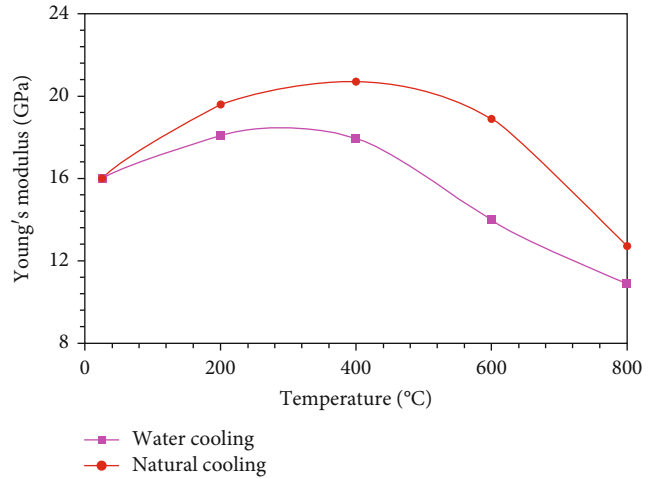


FIGURE 9: The variations of elastic modulus of core samples with temperature under two different cooling methods.

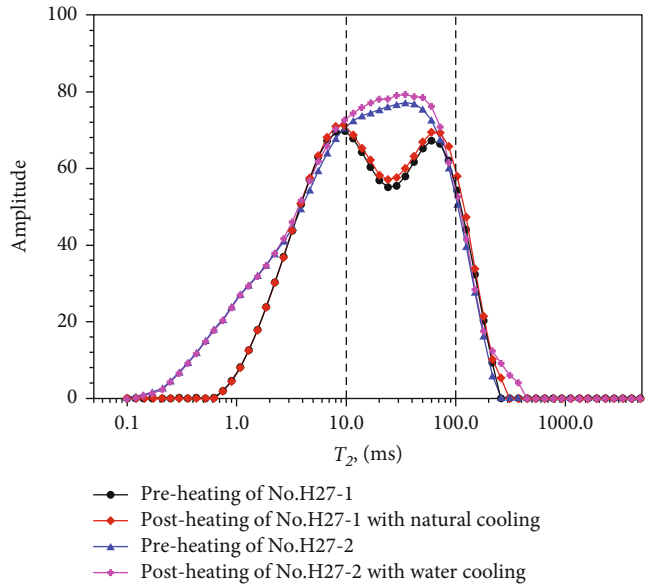


FIGURE 10:  $T_2$  spectrums and pore size distributions of the core samples (No. H27-1 and No. H27-2) at 200°C under two different cooling methods.

has a small number of macropores. After cooling,  $T_2$  spectrums change significantly with temperature and exhibit bimodal distribution generally. It is noticeable that, under the water cooling,  $T_2$  spectrums display triple-modal distribution at 600°C and 800°C.

In general, after heat treatment, the area enclosed by the  $T_2$  spectrum of the tight sandstone enlarges with the increment of temperature. The synthetic formation water cooling has a larger area of  $T_2$  spectrum than natural cooling. The number of pores in the core sample before and after cooling follows the sequence: original core sample < natural cooling < water cooling.

**3.3.2. Variation of Pore Structure.** According to previous studies on tight sandstone [26, 31], the pore sizes can be

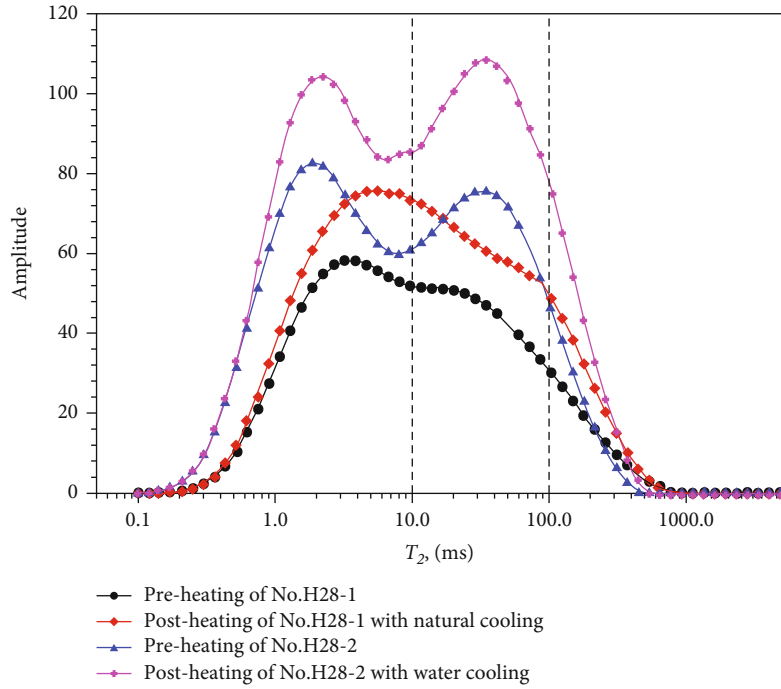


FIGURE 11:  $T_2$  spectrums and pore size distribution of the core samples (No. H28-1 and No. H28-2) at 400°C under two different cooling methods.

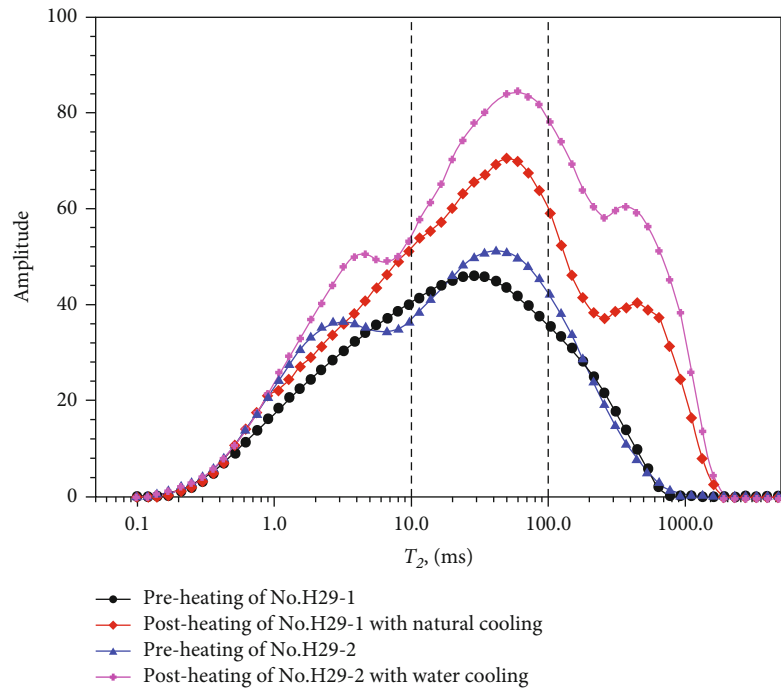


FIGURE 12:  $T_2$  spectrums and pore size distribution of the core samples (No. H29-1 and No. H29-2) at 600°C under two different cooling methods.

categorized into micropores (<10.0 ms), mesopores (10.0~100.0 ms), and macropores (>100 ms) in terms of the NMR  $T_2$  value. As the temperature changes, pores with different sizes exhibit different characteristics. As shown in Figure 14, the number of micropores has little change at different temperatures under two different cooling methods. Yet

the number of mesopores goes up with temperature. When the temperature reaches 800°C, the number of mesopores is risen by 1.92 times under natural cooling and 2.14 times under water cooling. It is worth noting that the number of macropores varies most obviously; especially at 600°C, there is a sudden increment of the number. At 800°C, the number

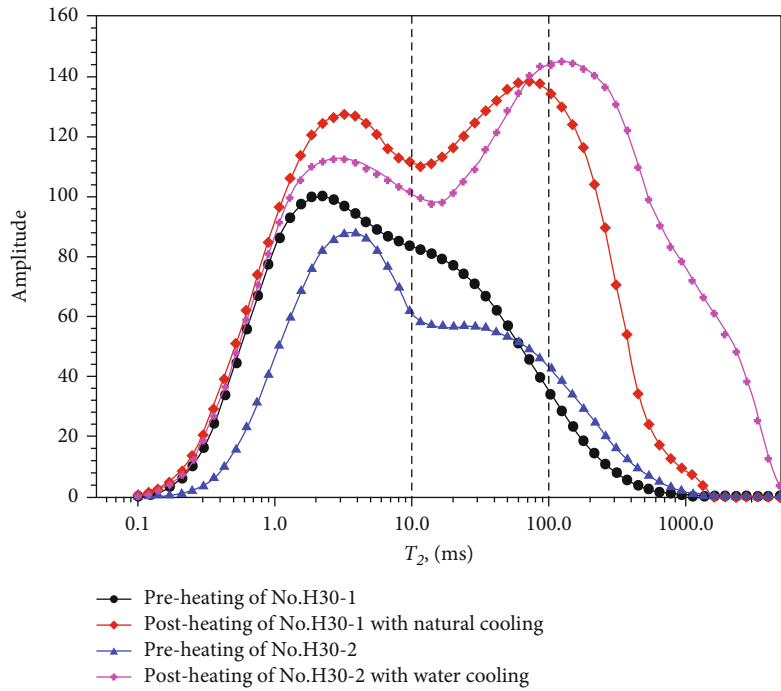


FIGURE 13:  $T_2$  spectrums and pore size distribution of the core samples (No. H30-1 and No. H30-2) at 800°C under two different cooling methods.

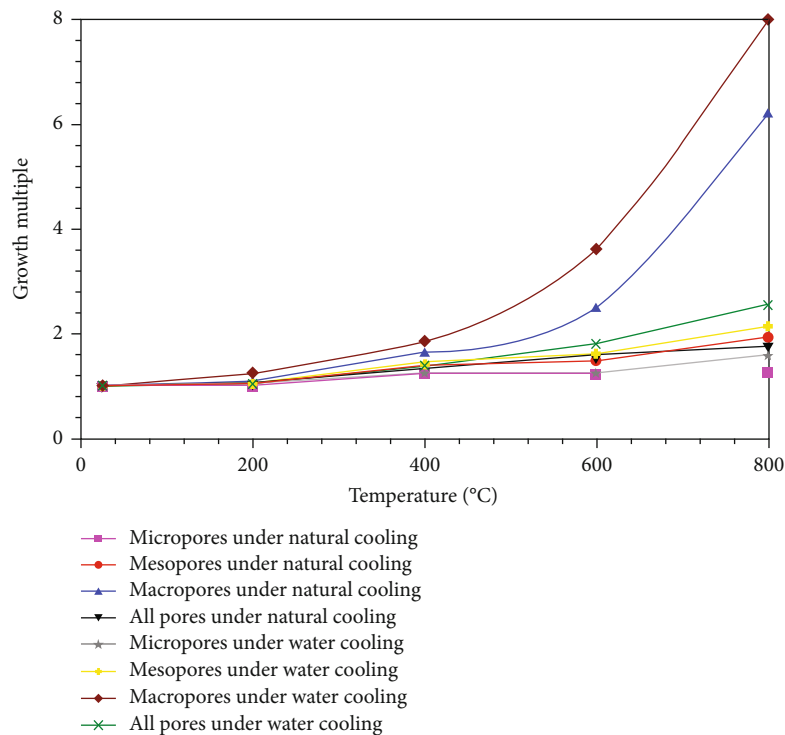


FIGURE 14: Variation of pores in tight sandstone with temperature under two different cooling modes.

of macropores is increased by 6.19 times under natural cooling and 8.00 times under water cooling. The increment amplitude of the overall pore volume is similar to that of the number of mesopores.

At 200°C, there is no evident change in the number of pores; at 400°C, the change is still not obvious, except that the number of macropores under water cooling increases. However, at 600°C, the number of micropores and

mesopores has a dramatic increase and this trend continues up to 800°C. When the temperature is at a relatively high value (e.g., 600°C or 800°C), the uneven thermal expansion between minerals in the core becomes significant and the ensuing temperature stress can exceed the strength limit of the core, forming more pores than the original core sample. Especially at 800°C, the pores in the core continue to grow and connect to form large pores and more microcracks, which leads to more severe damage to the core.

For the studied tight sandstone core samples, the variation of pore number measured by the NMR technique resembles the change in mechanical characteristics. This similarity explains to some extent the reason why the mechanical characteristics of tight sandstone alter with temperature. The permeability of the core primarily depends on the mesopores and macropores.

Based on the variations of physical properties, mechanical properties, and microscopic pore structure, the threshold temperature of the tight sandstone is estimated between 400°C and 600°C. Above the threshold temperature, the main characteristics of tight sandstone will change significantly. Another finding from this study is that the cooling method has no obvious impact on the threshold temperature.

In comparison with natural cooling, water cooling can cause greater damage and more dramatic change in the physical properties of the core at a relatively lower temperature. That explains why the threshold temperature under water cooling is slightly lower than that under natural cooling.

#### 4. Conclusions

In this paper, a series of tests have been carried out to study the effect of high-temperature heat treatment on the physical properties, mechanical properties, and microscopic pore structure of tight sandstone under synthetic formation water cooling and natural cooling. Based on the experimental results, the following conclusions are obtained:

- (1) Compared to natural cooling, the wave velocity of tight sandstone cooled by synthetic formation water is lower, but the permeability of the core is higher. The maximum differences in wave velocity and permeability appear at 600°C
- (2) With the increase of heating temperature, the tensile strength of tight sandstone decreases, and the declining amplitude of tensile strength enlarges. The peak strengths and elastic moduli of the tight sandstone after water cooling or natural cooling show the trend of first rising and then decreasing sharply. Under water cooling, the peak strength and elastic modulus reach the maximum values at 200°C; under natural cooling, the maximum values are attained at 400°C. When the core is heated up to 600°C, both peak strength and elastic modulus fall dramatically
- (3) The  $T_2$  spectrums of tight sandstone change significantly with temperature and generally exhibit bimodal distribution. At 600°C and 800°C under water cooling,  $T_2$  spectrums present triple-modal

distribution. As the temperature goes up, the number of micropores does not change evidently but the number of mesopores increases. When the temperature reaches 800°C, the number of mesopores rises 1.92 times under natural cooling and 2.14 times under water cooling. The number of macropores varies most obviously; especially at 600°C, there is a sudden increment of the number. The pore size and number of pores of the tight sandstone sample after water-cooling are higher than those after natural cooling

- (4) Based on the variations of physical properties, mechanical properties, and microscopic pore structure of tight sandstone, the threshold temperature is estimated in the range of 400-600°C. Above the threshold temperature, the main characteristics of tight sandstone will change dramatically

In this paper, the impact of heat treatment time on the physical and mechanical properties of tight sandstone is not addressed (based on previous studies, the treatment time of 2 h was selected for the experiments). Besides, due to the distinct mineral components of different tight sandstones, the relationship between mineral components of tight sandstone and changes in the microscopic pore structure and mechanical properties of the core during high-temperature heat treatment is not identified. Hence, these problems will be discussed in the next step.

#### Data Availability

All data, models, and code generated or used during the study appear in the article, and the authors are not restricted from sharing their data and materials.

#### Conflicts of Interest

The authors declare that they have no conflicts of interest.

#### Acknowledgments

This research was financially supported by the National Natural Science Foundation of China (Nos. 52074221, 52020105001, and 51974249) and the Foundation of Key Laboratory of Unconventional Oil & Gas Development (China University of Petroleum (East China)) (No. 19CX05005A-203).

#### References

- [1] C. Gu, J. Y. Xu, B. X. Meng, M. Wen, and C. X. Lou, "Dynamic mechanical behavior and mesoscopic analysis of two layered sandstone after high temperature," *Journal of China Coal Society*, vol. 44, no. 9, pp. 2710–2720, 2019.
- [2] P. H. Jin, Y. Q. Hu, J. X. Shao, Z. H. Liu, and Y. F. Hu, "Study on pore structure and permeability of granite subjected to heating and water quenching," *Journal of Taiyuan University of Technology*, vol. 50, no. 4, pp. 478–484, 2019.
- [3] J. J. Hu, X. H. Pan, and W. Q. Zhang, "Thermal effect on wave velocity of sandstone after high-temperature treatment: a review," *Arabian Journal of Geosciences*, vol. 12, no. 22, p. 689, 2019.

- [4] M. Hajpál, “Changes in sandstone of historical monuments exposed to fire or high temperature,” *Fire Technology*, vol. 38, no. 4, pp. 373–382, 2002.
- [5] M. Hajpál and A. Török, “Mineralogical and colour changes of quartz sandstones by heat,” *Environmental Geology*, vol. 46, pp. 311–322, 2004.
- [6] A. Török and M. Hajpál, “Effect of temperature changes on the mineralogy and physical properties of sandstone. A laboratory study,” *International Journal for Restoration of Buildings and Monuments*, vol. 11, no. 4, pp. 1–8, 2005.
- [7] H. Tian, T. Kempka, N. X. Xu, and M. Ziegler, “Physical properties of sandstones after high temperature treatment,” *Rock Mechanics and Rock Engineering*, vol. 45, no. 6, pp. 1113–1117, 2012.
- [8] G. Wu, Y. Wang, G. Swift, and J. Chen, “Laboratory investigation of the effects of temperature on the mechanical properties of sandstone,” *Geotechnical and Geological Engineering*, vol. 31, no. 2, pp. 809–816, 2013.
- [9] Z. Kompaníková, M. Gomez-Heras, J. Michňová, T. Durmeková, and J. Vlčko, “Sandstone alterations triggered by fire-related temperatures,” *Environmental Earth Sciences*, vol. 72, no. 7, pp. 2569–2581, 2014.
- [10] Q. Sun, W. Q. Zhang, T. M. Su, and S. Y. Zhu, “Variation of wave velocity and porosity of sandstone after high temperature heating,” *Acta Geophysica*, vol. 64, no. 3, pp. 633–648, 2016.
- [11] X. Liu, S. Yuan, Y. Sieffert, S. Fityus, and O. Buzzi, “Changes in mineralogy, microstructure, compressive strength and intrinsic permeability of two sedimentary rocks subjected to high-temperature heating,” *Rock Mechanics and Rock Engineering*, vol. 49, no. 8, pp. 2985–2998, 2016.
- [12] X. Liu, C. Zhang, S. Yuan, S. Fityus, S. W. Sloan, and O. Buzzi, “Effect of high temperature on mineralogy, microstructure, shear stiffness and tensile strength of two Australian mudstones,” *Rock Mechanics and Rock Engineering*, vol. 49, no. 9, pp. 3513–3524, 2016.
- [13] N. N. Sirdesai, T. N. Singh, P. G. Ranjith, and R. Singh, “Effect of varied durations of thermal treatment on the tensile strength of red sandstone,” *Rock Mechanics and Rock Engineering*, vol. 50, no. 1, pp. 205–213, 2017.
- [14] N. N. Sirdesai, T. N. Singh, and R. P. Gamage, “Thermal alterations in the poro-mechanical characteristic of an Indian sandstone - a comparative study,” *Engineering Geology*, vol. 226, pp. 208–220, 2017.
- [15] N. N. Sirdesai, T. Gupta, T. N. Singh, and P. G. Ranjith, “Studying the acoustic emission response of an Indian monumental sandstone under varying temperatures and strains,” *Construction and Building Materials*, vol. 168, pp. 346–361, 2018.
- [16] N. N. Sirdesai, A. Singh, L. K. Sharma, R. Singh, and T. N. Singh, “Determination of thermal damage in rock specimen using intelligent techniques,” *Engineering Geology*, vol. 239, pp. 179–194, 2018.
- [17] N. N. Sirdesai, B. Mahanta, P. G. Ranjith, and T. N. Singh, “Effects of thermal treatment on physico-morphological properties of Indian fine-grained sandstone,” *Bulletin of Engineering Geology and the Environment*, vol. 78, no. 2, pp. 883–897, 2019.
- [18] N. N. Sirdesai, A. Singh, L. K. Sharma, R. Singh, and T. N. Singh, “Development of novel methods to predict the strength properties of thermally treated sandstone using statistical and soft-computing approach,” *Neural Computing and Applications*, vol. 31, no. 7, pp. 2841–2867, 2019.
- [19] R. Lei, Y. Wang, L. Zhang et al., “The evolution of sandstone microstructure and mechanical properties with thermal damage,” *Energy Science & Engineering*, vol. 7, no. 6, pp. 3058–3075, 2019.
- [20] X. Shi, H. Jing, Q. Yin, Z. Zhao, G. Han, and Y. Gao, “Investigation on physical and mechanical properties of bedded sandstone after high-temperature exposure,” *Bulletin of Engineering Geology and the Environment*, vol. 79, no. 5, pp. 2591–2606, 2020.
- [21] M. Li, D. Wang, and Z. Shao, “Experimental study on changes of pore structure and mechanical properties of sandstone after high-temperature treatment using nuclear magnetic resonance,” *Engineering Geology*, vol. 275, p. 105739, 2020.
- [22] L. X. Xiong and L. J. Yu, “Advances of mechanical properties of rock under high temperature and after high temperature,” *Journal of Geological Hazards and Environment Preservation*, vol. 29, no. 1, pp. 76–82, 2018.
- [23] T. Jacobs, “Unconventional resources will require unconventional EOR,” *Journal of Petroleum Technology*, vol. 67, no. 9, pp. 68–70, 2015.
- [24] L. Dou, M. Zhang, G. Bi, and T. Li, “Transient flow in wellbores and phase transition of CO<sub>2</sub> during formation supercritical CO<sub>2</sub> invasion,” *Energy Science & Engineering*, vol. 7, no. 2, pp. 323–337, 2019.
- [25] M. J. Chen, Y. L. Kang, and L. J. You, “Advantages in formation heat treatment to enhance permeability in tight reservoir,” *Natural Gas Geoscience*, vol. 24, no. 6, pp. 1226–1231, 2013.
- [26] L. Dou, Y. Xiao, H. Gao, R. Wang, C. Liu, and H. Sun, “The study of enhanced displacement efficiency in tight sandstone from the combination of spontaneous and dynamic imbibition,” *Journal of Petroleum Science and Engineering*, vol. 199, p. 108327, 2021.
- [27] Z. W. Huang, H. T. Wen, X. G. Wu et al., “Experimental study on cracking of high temperature granite using liquid nitrogen,” *Journal of China University of Petroleum (Edition of Natural Science)*, vol. 43, no. 2, pp. 68–76, 2019.
- [28] P. W. J. Glover, P. Baud, M. Darot et al., “ $\alpha/\beta$  phase transition in quartz monitored using acoustic emissions,” *Geophysical Journal International*, vol. 120, no. 3, pp. 775–782, 1995.
- [29] W. Zhang and C. Lv, “Effects of mineral content on limestone properties with exposure to different temperatures,” *Journal of Petroleum Science and Engineering*, vol. 188, p. 106941, 2020.
- [30] K. S. Zhang, M. R. Tang, C. W. Wang, G. T. Wang, L. B. Dou, and H. B. Sun, “Study on prediction method of tensile strength for tight sandstone formation,” *Progress in Geophysics*, vol. 35, no. 4, pp. 1–10, 2020.
- [31] H. Gao, C. Wang, J. Cao, M. He, and L. Dou, “Quantitative study on the stress sensitivity of pores in tight sandstone reservoirs of Ordos basin using NMR technique,” *Journal of Petroleum Science and Engineering*, vol. 172, pp. 401–410, 2019.



## Research Article

# Characterization of the Dynamic Imbibition Displacement Mechanism in Tight Sandstone Reservoirs Using the NMR Technique

Liangbin Dou <sup>1,2,3</sup>, Min Yang,<sup>4</sup> Hui Gao,<sup>1,2</sup> Dongxing Jiang,<sup>5</sup> and Chenglu Liu<sup>1,2</sup>

<sup>1</sup>School of Petroleum Engineering, Xi'an Shiyou University, Xi'an 710065, China

<sup>2</sup>Engineering Research Center of Development and Management for Low to Ultra-Low Permeability Oil & Gas Reservoirs in West China, Ministry of Education, Xi'an 710065, China

<sup>3</sup>State Key Laboratory of Petroleum Resources and Prospecting, China University of Petroleum, Beijing 102249, China

<sup>4</sup>Department of Chemical and Petroleum Engineering, University of Calgary, Calgary, AB, Canada T2N 1N4

<sup>5</sup>CNPC Greatwall Drilling Company, Chaoyang, Beijing 100101, China

Correspondence should be addressed to Liangbin Dou; 77129dou@163.com

Received 11 May 2020; Revised 16 June 2020; Accepted 27 November 2020; Published 16 December 2020

Academic Editor: Reza Rezaee

Copyright © 2020 Liangbin Dou et al. This is an open access article distributed under the Creative Commons Attribution License, which permits unrestricted use, distribution, and reproduction in any medium, provided the original work is properly cited.

An experimental technique is developed to investigate the dynamic imbibition displacement mechanism in tight sandstone formations of the Yanchang group of the Ordos basin. By combining the dynamic imbibition core flooding experiments and NMR technique, the effects of the injection volume and rate on displacement efficiency are investigated. Moreover, the displacement efficiency of dynamic imbibition is compared with that of static imbibition. This study gains insights into the micromechanisms of dynamic imbibition in tight sandstone formations. It is found that the relative displacement efficiency of dynamic imbibition increases with the increase of injection volume. But the increment amplitude decreases with the increase of injection volume. With the same injection volume, the core displacement efficiency of dynamic imbibition with high permeability is obviously improved. However, the core displacement efficiency decreases rapidly with the increase of injection volume. Optimal injection volumes are recommended for tight sandstone formations with different permeabilities. With the increase of the displacement rate, the core displacement efficiency of dynamic imbibition shows a trend of first rising and then declining. There exists an optimal displacement rate in dynamic imbibition displacement, and the optimal displacement rate almost linearly increases with the increase of core permeability. The static imbibition displacement efficiency increases with the increase of soaking time, but the increment amplitude slows down obviously. The displacement efficiency of static imbibition in small pores is higher than that of dynamic imbibition. The displacement efficiency of dynamic imbibition in large pores or microcracks is significantly higher than that of static imbibition. This study provides theoretical support for the optimization and improvement of the waterflooding recovery process in tight sandstone reservoirs.

## 1. Introduction

Tight oil is a key area of global unconventional oil development [1]. Unconventional tight oil and gas resources in China are widely distributed and have great development potential [2, 3]. Tight oil and gas resources are found in the Triassic strata of the Ordos basin, Permian strata of the Junggar basin, Cretaceous strata of the Songliao basin, Paleogene strata of the Bohai-Bay basin, and other strata, which have

broad prospects of exploration and development [4]. The tight oil in the Ordos basin is a typical representative of the tight oil resources of continental sedimentation in China. However, compared with the marine tight oil in North America [5–7], there are various types of pores and throats in the tight sandstone reservoir of the Ordos basin. Moreover, the pores and throats are small and widely distributed, with developed microcracks and strong heterogeneity [8]. This results in difficulties in water injection, serious water



breakthrough and out, and low oil recovery in tight oil development. It is of great importance to take advantage of imbibition to improve waterflooding performance.

Imbibition, as an important displacement mechanism in ultralow-permeability reservoirs, has been widely investigated by a large number of scholars [9–23]. Extensive experimental and theoretical studies were carried out to investigate the effect of imbibition on oil recovery and establish classical imbibition models. Spontaneous imbibition experiments were conducted to investigate the ultimate oil recovery, pore structure, and relative permeability curve related to imbibition, further confirming the dominant parameters of imbibition. In addition, some scholars [24–28] have studied the effects of surfactants and other additives on imbibition displacement. With the development of shale oil, the study of imbibition displacement has been shifted from tight sandstone/carbonate reservoirs to shale oil reservoirs. Kuila et al. [29] found that water could be imbibed into almost all nanopores of shale. Later, some scholars [30–34] carried out experiments to study the imbibition displacement mechanism in shale oil reservoirs and analyzed its feasibility. They examined the effects of surfactant and pH value of suction liquid on spontaneous imbibition recovery.

Compared with static imbibition, dynamic imbibition considers the effect of fluid flow in the matrix and fracture on imbibition displacement in the tight reservoir development. Experimental studies on dynamic imbibition [35, 36] have been carried out. They proved the existence of a critical flow rate in the process of imbibition displacement. When the flow rate is higher than the critical flow rate, water breakthrough tends to occur. A corresponding numerical model was developed to capture this phenomenon. Pooladi-Darvish and Firoozabadi [37] analyzed the difference of counter-current imbibition and cocurrent imbibition after water breakthrough in the cores with different permeabilities. Some scholars [28, 38–42] have studied the effects of core wettability, initial water saturation, interfacial tension (IFT), fluid viscosity ratio, soaking time, and permeability on dynamic imbibition. Hammond and Unsal [43] simulated and developed the correlation between the displacement pressure and the imbibition rate during the dynamic imbibition process. Sharma et al. [44] quantitatively evaluated the effects of the flow rate and viscosity ratio on dynamic imbibition displacement. They established a scaling model of dynamic imbibition with the consideration of both the capillary and viscous forces. Qiao et al. [45] and Andersen et al. [46] studied the effect of viscous coupling on the efficiency of dynamic imbibition displacement.

Previous studies mainly applied the conventional core flooding setup to investigate the effect of dynamic imbibition on oil recovery and displacement efficiency. However, the real-time oil-water distribution in different pore-throat-fracture systems cannot be characterized quantitatively during the dynamic imbibition with conventional experiments. Although some scholars have studied the effect of the injection rate on dynamic imbibition, few studies have been done to investigate the relationship between the critical (optimal) injection rate and the core permeability. The total injection volume is very important for cost control and optimization

of water injection. Previous studies on the effect of injection volume on the efficiency of dynamic imbibition displacement are also lacking. Moreover, the comparison of oil and water distribution in pore-throat-fracture systems between static and dynamic imbibition has not been reported. The field application conditions of imbibition recovery in tight reservoirs are still not clear.

In this work, an experimental technique is developed to investigate the real-time distribution of oil and water in pore-throat-fracture systems using tight sandstone cores with various permeabilities in the Ordos basin. The effect of the displacement rate and volume on oil-water distribution in the core microstructure is well clarified. A correlation is developed to represent the relationship between the displacement rate, displacement volume, and core permeability. In addition, the differences between static and dynamic imbibition on imbibition displacement are quantitatively evaluated. This study provides a theoretical foundation for enhancing oil recovery in tight sandstone reservoirs.

## 2. Experimental Section

**2.1. Core Samples and Fluids.** The cores used in the experiments are from tight sandstone formations of the Yanchang group in the Ordos basin. The porosity and permeability are low, but microcracks are well developed. Based on the FE-SEM (FEI Quanta200F) and thin section petrography (TSP) technique tests for four samples shown in Figure 1, it is found that types of pores of tight sandstone in the Yanchang group are mainly intergranular pores, followed by feldspar dissolved pores and debris dissolved pores. The core properties are shown in Table 1. The porosity ranges from 8.29% to 12.36%, and the permeability ranges from 0.138 to 2.451 mD. Synthetic formation water in the target reservoir is used in the experiments. The water used in the experiments is the synthetic formation water in the target reservoir block (water type is CaCl<sub>2</sub>, salinity is about 18000 mg/l, and viscosity and density at 50°C are 0.523 mPa·s and 1.02 g/cm<sup>3</sup>, respectively). The fluorocarbon oil is used in the experiments (viscosity and density at 50°C are 3.67 mPa·s and 0.82 g/cm<sup>3</sup>, respectively). The viscosity and density are almost equivalent to the formation crude oil. Fluorocarbon oil is able to shield the signal of crude oil in NMR because it does not contain hydrogen. The measured IFT between synthetic formation water and fluorocarbon oil is 12.15 mN/m using an interface tensiometer. In addition, the contact angles of different cores in oil/water/core systems were measured.

**2.2. Experimental Setups.** In this experiment, a constant rate and constant pressure pump (ISCO-500D, USA) is used to control the displacement rate and pressure. The confining pressure can be controlled by injecting fluorocarbon oil with a manual pump, and the maximum confining pressure can reach 20 MPa. The test temperature is controlled by the incubator to maintain the formation temperature. The NMR setup (Niumag Corporation, China) is used to measure the  $T_2$  spectrum of synthetic formation water at various experimental conditions. In addition, the experimental setups also include transfer cylinders in which the brine is injected into

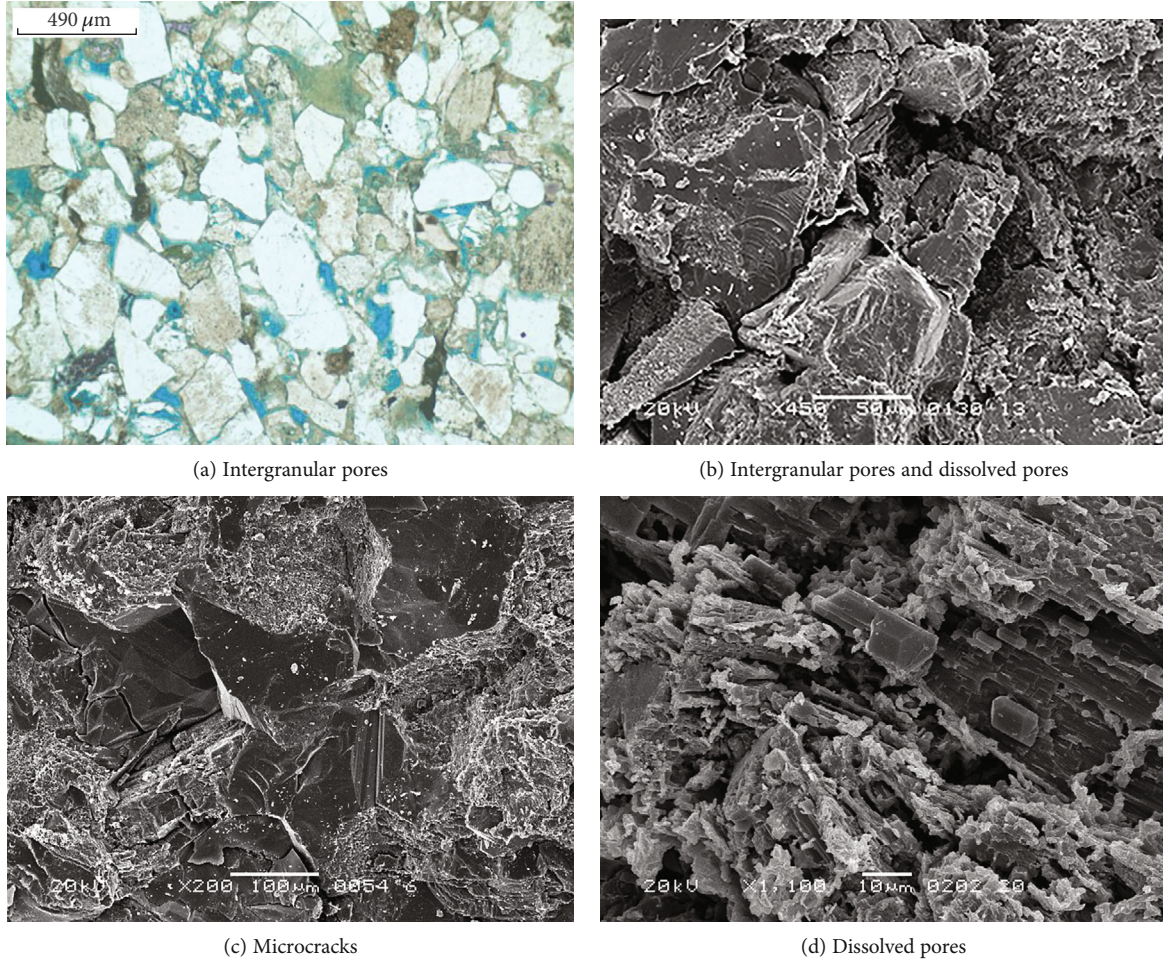


FIGURE 1: The pore types of the Yanchang group tight sandstone samples.

TABLE 1: Properties of experimental cores.

Sample no.	Diameter (mm)	Length (mm)	Porosity (%)	Permeability (mD)	Contact angle (°)
H-3	25.0	43.6	12.36	2.451	46.5
H-7	25.1	42.1	8.29	0.138	43.8
H-15	25.1	42.8	9.36	0.281	37.8
H-21	25.0	44.2	11.32	1.213	51.6

core samples and a core holder which is made of PEEK materials with no hydrogen.

The NMR instrument includes a magnetic body, radiofrequency emitter, and data collection system. The basic parameters of NMR measurements are set. The waiting time and echo time are 5 s and 0.25 ms, respectively. The scanning number and echo number are 16 and 1024, respectively. It was noted that fluorocarbon oil without hydrogen signals does not affect the NMR response. As a result, there is no effect on the measurement of the NMR  $T_2$  spectrum for brine.

2.3. *Experimental Procedures.* Figure 2 presents the schematic diagram of the dynamic imbibition displacement experiment

using the low-field NMR technique. The test temperature is 50°C. The experimental procedures are summarized as follows:

- (1) Place the core in an extraction vessel with a volume ratio of benzene to alcohol of 1:3 to wash the oil. Heat the core to 105°C in an incubator after washing oil and maintain the temperature for 48 h. Then, take out the core and measure the dry weight and dimensions of the core
- (2) Due to the small pore radius of the tight reservoir, conventional vacuum saturation cannot make the core pore completely saturated with water. So, the core is placed into the core holder, and a high-pressure displacement device is used to inject synthetic formation water into the core. When the produced liquid is about 5 PV, the NMR spectrum is measured for the first time. The injection is continued until the production reaches 10 PV. The NMR spectrum is measured again. When there is no significant difference between the two NMR spectra, it can be concluded that the core pore is completely saturated with formation water

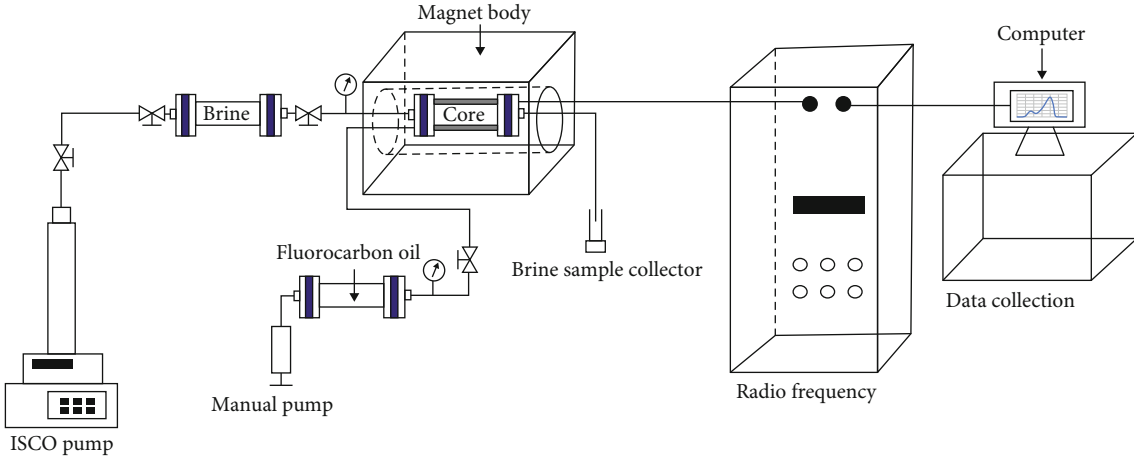


FIGURE 2: Schematic diagram of the dynamic imbibition displacement experiment.

- (3) Displace fluorocarbon oil at a low rate using the high-pressure displacement system. The core is considered to be saturated with fluorocarbon oil when the liquid production is 5 PV, and measure the  $T_2$  spectrum of the core
- (4) Displace the synthetic formation water at a constant rate using the high-pressure displacement system, and measure its  $T_2$  relaxation time spectrum
- (5) Change the experimental conditions (displacement rate, displacement volume, etc.) and repeat the experimental procedures (1)-(4). It should be noted that injection pressure can be adjusted timely to maintain the constant displacement rate

**2.4. Low-Field Nuclear Magnetic Resonance (NMR).** The decay rate of the NMR signal can be described by the longitudinal relaxation time  $T_1$  and transverse relaxation time  $T_2$ . Because the measurement speed of  $T_2$  is fast, the  $T_2$  measurement method is often used in NMR measurement. The collision between the hydrogen nucleus and the pore wall occurs when the hydrogen nucleus is in transverse relaxation motion, which results in the energy loss of the hydrogen nucleus. The more frequent the collisions, the faster the energy loss of the hydrogen nucleus, thus accelerating the transverse relaxation process of the hydrogen nucleus. The frequency of collision between the hydrogen nucleus and the pore wall is determined by pore size. The larger the pore, the smaller probability the hydrogen nucleus collides with the pore wall, and vice versa. The pore size is inversely proportional to the relaxation rate of hydrogen nuclei, which is the theoretical foundation to investigate pore structure using the NMR spectrum (or  $T_2$  spectrum) [47].  $T_2$  is calculated using the following formula:

$$\frac{1}{T_2} = \frac{1}{T_{2B}} + \frac{1}{T_{2D}} + \frac{1}{T_{2S}}, \quad (1)$$

where  $T_{2B}$  is the relaxation contribution from the fluid itself (i.e., bulk relaxation) with the unit of ms;  $T_{2D}$  is the relaxation contribution from the magnetic gradient diffusion (i.e.,

diffusion relaxation) with the unit of ms; and  $T_{2S}$  is the relaxation contribution from the rock surface (i.e., surface relaxation) with the unit of ms.

When NMR technology is applied to the analysis of tight sandstone cores, the diffusion relaxation can be ignored because it is too small. Therefore, the  $T_2$  relaxation time mainly comes from surface relaxation, followed by bulk relaxation. Surface relaxation is closely related to the specific surface area of tight sandstone cores. The specific surface area of rock refers to the ratio of the pore surface area to the pore volume in rock. The larger the specific surface area, the larger the surface relaxation, the smaller the  $T_2$  relaxation time, and vice versa. Therefore, the  $T_2$  relaxation time of the core can be expressed as

$$\frac{1}{T_2} = \frac{1}{T_{2B}} + \frac{1}{T_{2S}} = \frac{1}{T_{2B}} + \rho \frac{S}{V}, \quad (2)$$

where  $\rho$  is the relaxation rate in  $\mu\text{m}/\text{ms}$  and  $S/V$  is the specific surface area in  $1/\mu\text{m}$ .

Because  $T_{2B}$  is much larger than  $T_2$ ,  $1/T_{2B}$  can be neglected. The relaxation time is mainly from surface relaxation.

$$\frac{S}{V} = \frac{F_S}{r_c}, \quad (3)$$

where  $F_S$  is the shape factor of the single pore (dimensionless) and  $r_c$  is the pore radius in  $\mu\text{m}$ .

By combining Equation (3), Equation (2) can be simplified as

$$T_2 = \frac{r_c}{\rho F_S}. \quad (4)$$

Using  $C = \rho F_S$ , Equation (3) can be transferred as

$$T_2 = C \cdot r_c. \quad (5)$$

It is obvious that the relaxation time  $T_2$  is theoretically a linear function of pore radius  $r_c$ . Therefore, the distribution



of fluids in various pores can be calculated by measuring the signal of the hydrogen nucleus.

### 3. Results and Discussion

*3.1. Effect of Injection Volume on Dynamic Imbibition.* In order to quantitatively evaluate the effect of the injection volume and rate on the dynamic displacement efficiency in tight sandstone, the coefficient  $a$  is given to characterize the increment amplitude of displacement by dynamic imbibition at different injection volumes and rates of formation water, which is the relative displacement efficiency of dynamic imbibition under different injection volumes.

$$a = \frac{V_i}{V_0} \times 100\%, \quad (6)$$

where  $V_0$  is the area of the  $T_2$  spectrum peak of irreducible water in the core and  $V_i$  is the area of the  $T_2$  spectrum peak of formation water under different injection volumes and rates.

The displacement experiments are carried out using synthetic formation water with a 0.1 ml/min displacement rate at different injection volumes. The effects of different injection volumes on the dynamic imbibition displacement of the reservoir core in the target block are evaluated, respectively, as shown in Figures 3–6 and Table 2.

As shown in Figures 3–6 and Table 2, the relative displacement efficiency of core dynamic imbibition increases gradually with the increase of injection volume of synthetic formation water. But the increased amplitude decreases obviously. With the same injection volume, the relative displacement efficiency of core dynamic imbibition increases with the increase of core permeability, especially for core samples No. H-3 and No. H-21, as seen in Figures 3 and 6, respectively.  $T_2$  spectrums present bimodal distribution. For the cores with high permeability, it contains more large pores (including microcracks), and the displacement of dynamic imbibition exhibits the best results at the same injection volume.

For ultralow-permeability reservoirs (permeability lower than 1.0 mD), as shown in Figures 4 and 5 for core samples No. H-7 and No. H-15, when the injection volume is 1.0 PV, the increment amplitudes of relative displacement efficiency of dynamic imbibition reach the maximum values of 30.6% and 49.6%, respectively. When the injection volume increases from 1.0 PV to 1.5 PV, the increment amplitudes of relative displacement efficiency are 18.1% and 21.7%, respectively, with small reductions. When the injection volume increases from 1.5 PV to 2.0 PV, the increased amplitudes of relative displacement efficiency are only 10.5% and 11.3%, respectively, with obvious reductions. When the injection volume increases from 2.0 PV to 2.5 PV, the increment amplitudes of relative displacement efficiency reach the minimum values of only 5.0% and 4.9%, respectively. Therefore, for ultralow-permeability reservoirs with permeability less than 1.0 mD, it is recommended to select an injection volume of 1.5–2.0 PV in the field design of imbibition oil recovery to achieve a high oil recovery.

For conventional low-permeability reservoirs (permeability in the range of 1.0 to 10.0 mD), as shown in Figures 3 and 6, respectively, for core samples No. H-3 and No. H-21, when the injection volume is 1.0 PV, the increased amplitudes of relative displacement efficiency reach high values of 91.7% and 80.3%, respectively. When the injection volume increases from 1.0 PV to 1.5 PV, the increased amplitudes of relative displacement efficiency are only 9.6% and 18.0%, respectively, with obvious reductions. When the injection volume increases from 1.5 PV to 2.0 PV, the increased amplitudes of relative displacement efficiency are as low as only 3.0% and 8.6%, respectively. When the injection volume increases from 2.0 PV to 2.5 PV, the increased amplitudes of relative displacement efficiency are as low as only 1.9% and 3.6%, respectively. Therefore, for tight reservoirs with relatively high permeability, it is recommended to select an injection volume of 1.0–1.5 PV to appropriately reduce the injection volume, so as to minimize the construction cost to the most extent on the basis of ensuring the displacement efficiency of dynamic imbibition.

*3.2. Effect of the Displacement Rate on Dynamic Imbibition.* The dynamic imbibition displacement experiments are carried out with 1.0 PV injection volume at different displacement rates. The effects of different displacement rates on the displacement efficiency of dynamic imbibition in the reservoir core of the target area are evaluated (Figures 7–10). The displacement efficiency under different displacement rates is plotted based on Equation (6), as shown in Figure 11. It can be seen from the experimental results that the relative displacement efficiency of core dynamic imbibition increases and then decreases with the increase of the displacement rate. There exists an optimal displacement rate that achieves the highest relative displacement efficiency of dynamic imbibition. The synergistic effect of capillary pressure and viscous force can achieve the highest displacement efficiency at an optimal displacement rate. When the displacement rate is lower than the optimal displacement rate, capillary pressure plays a dominant role, and crude oil in small pores is easier to be produced. Therefore, it can be seen from Figures 7–10 that the relative displacement efficiency of small pores (left part of the  $T_2$  spectrum) at a low displacement rate is higher than that at a high displacement rate. When the displacement rate is higher than the optimal displacement rate, the differential pressure drive plays a dominant role, and the crude oil in large pores is easier to be produced. Therefore, there exists an optimal displacement rate to displace crude oil in the pores to the most extent. In addition, when the displacement rate is high, the time of the oil-water exchange in the pores is shortened, so that the water in the pores is displaced prematurely, resulting in the decrease of imbibition displacement efficiency. Therefore, it is necessary to select the appropriate injection rate to achieve the best displacement efficiency in the field construction design.

It can be seen from Figure 11 that core samples with high permeability (such as No. H-3 and No. H-21) have higher relative oil displacement efficiency of dynamic imbibition than core samples with low permeability (such as No. H-7

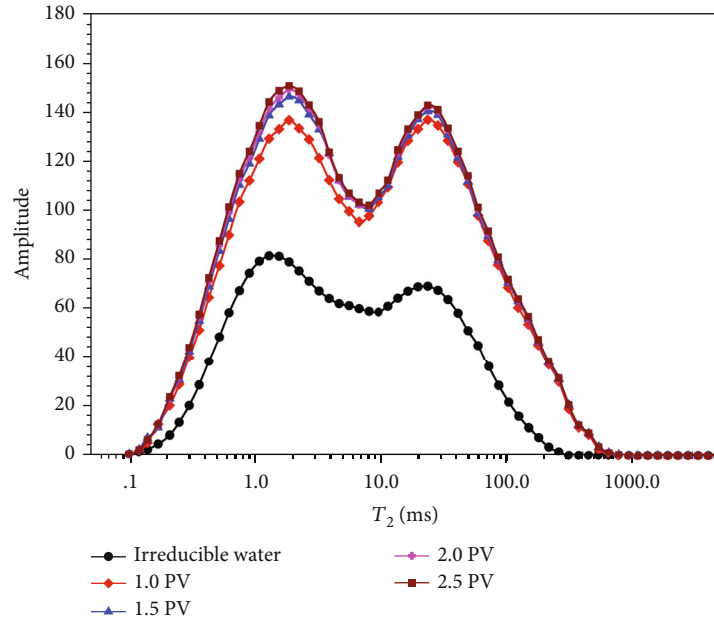


FIGURE 3:  $T_2$  spectrum of the core sample No. H-3 under different injection volumes.

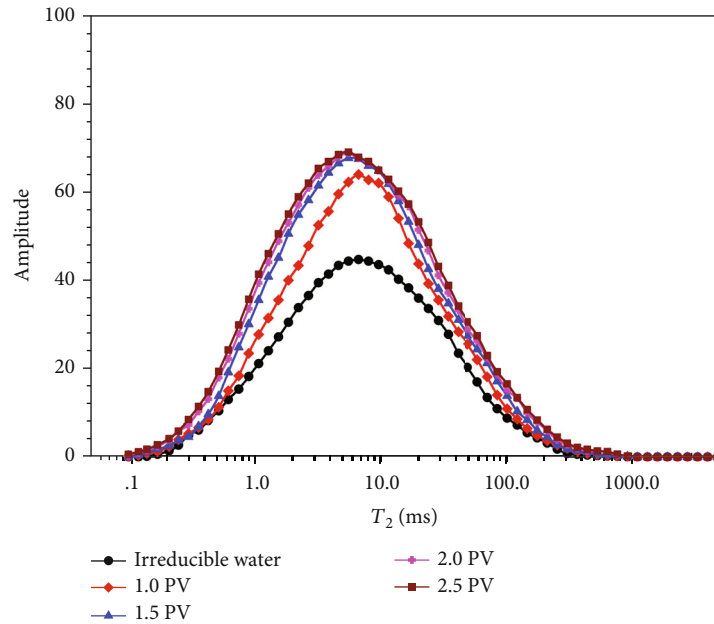


FIGURE 4:  $T_2$  spectrum of the core sample No. H-7 under different injection volumes.

And No. H-15). The high permeability of tight sandstone means that not only there are more large pores but also there might be more microcracks. These microcracks in the tight core can increase the surface area of the core for imbibition and provide more channels for the imbibition, effectively promoting the imbibition. Under the experimental condition of dynamic imbibition, the flowing formation water can timely displace the oil replaced by imbibition from the large pore, improving the imbibition to a certain extent.

It can be seen from Figure 12 that the optimal displacement rate almost linearly increases with the increase of core

permeability. When the reservoir permeabilities are 0.138, 0.281, 1.213, and 2.451 mD, the optimal displacement rates are 0.05, 0.1, 0.2, and 0.4 ml/s, respectively, and the corresponding maximum displacement efficiency of imbibition is 142.2%, 149.6%, 210.2%, and 211.6%, respectively.

The linear correlation between optimal displacement velocity and permeability is regressed as follows:

$$v_{\text{optimal}} = 0.1444K + 0.0401, \quad (7)$$

$$R^2 = 0.9897.$$

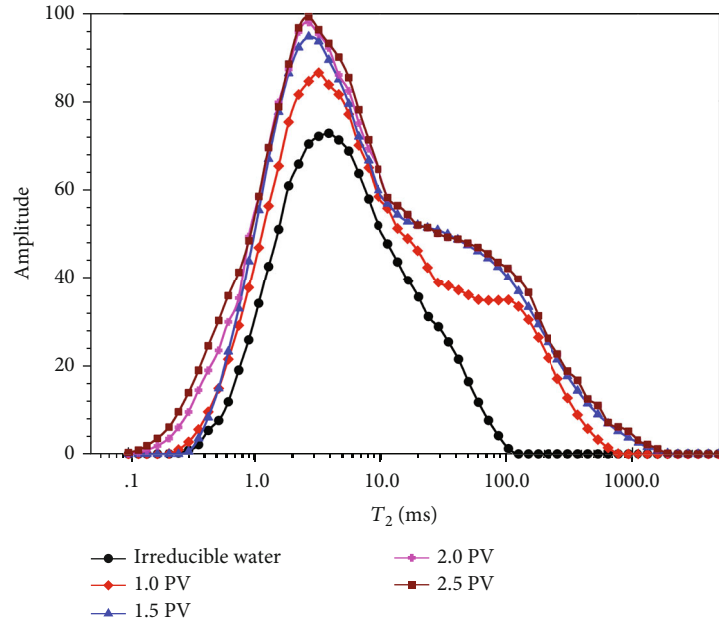


FIGURE 5:  $T_2$  spectrum of the core sample No. H-15 under different injection volumes.

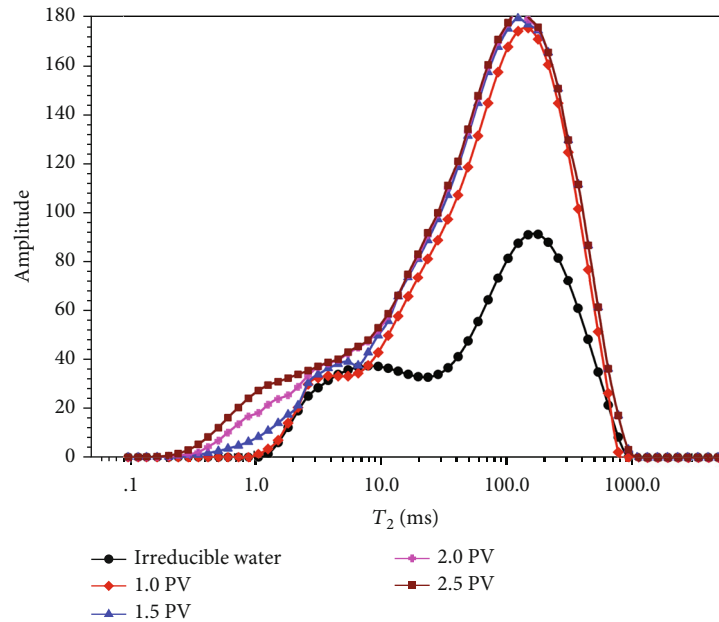


FIGURE 6:  $T_2$  spectrum of the core sample No. H-21 under different injection volumes.

TABLE 2: Dynamic imbibition displacement experiment results under different injection volumes.

Sample no.	Permeability (mD)	1.0 PV (%)	1.5 PV (%)	2.0 PV (%)	2.5 PV (%)
H-3	2.451	191.7	201.3	204.3	206.2
H-7	0.138	130.6	148.7	159.2	164.2
H-15	0.281	149.6	171.3	182.6	187.5
H-21	1.213	180.3	198.3	206.9	210.5

3.3. *Comparison of Static Imbibition and Dynamic Displacement.* From the results in Section 3.2, the relative displacement efficiency of imbibition in small pores is higher at the low displacement rate. Based on this conclusion, the core sample No. H-2 is used to compare and analyze the effects of static imbibition and dynamic imbibition on displacement efficiency in this section. Static imbibition is also referred to as spontaneous imbibition. A nonwetting phase is displaced by a wetting phase in the porous medium only by capillary pressure, without other pressure differences.

The static imbibition experiment is performed with the same experimental equipment in Figure 2. After the synthetic



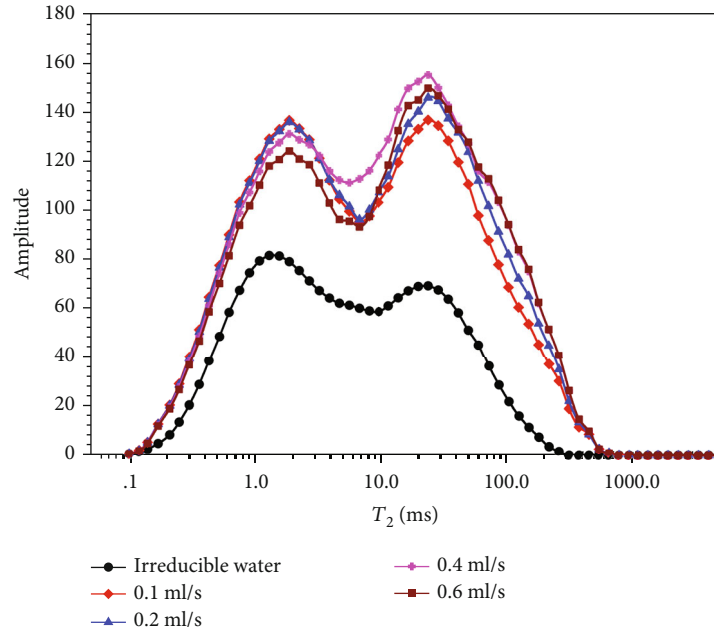


FIGURE 7:  $T_2$  spectrum of the core sample No. H-3 under different displacement rates.

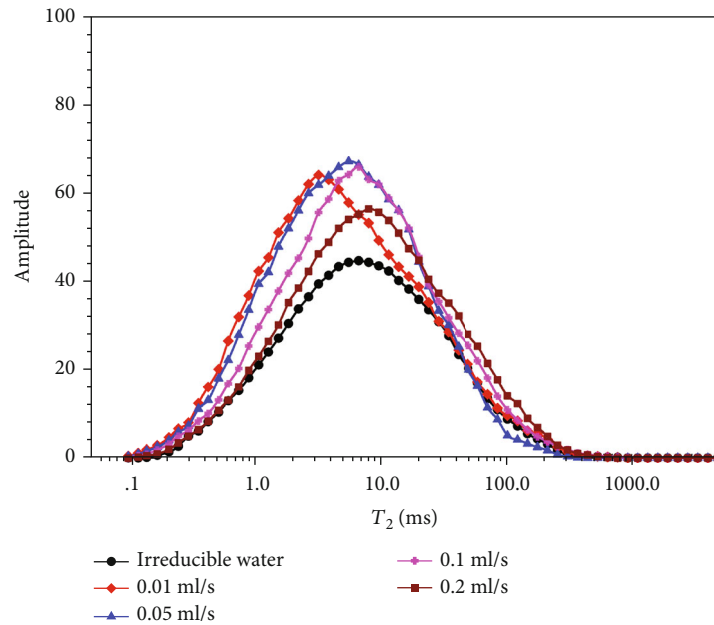


FIGURE 8:  $T_2$  spectrum of the core sample No. H-7 under different displacement rates.

formation water is injected, the valves at the inlet and outlet ends of the core are closed. The core is soaked for a period of time, then the  $T_2$  spectrum is measured. When the soaking time of static imbibition is 24 h, 48 h, and 96 h, the increments of the recovery factor are 172.1%, 206.2%, and 219.1%. The experimental results are shown in Figure 13, in which the experimental conditions of the dynamic imbibition  $T_2$  spectrum are measured at the injection volume of 1 PV and injection rate of 0.2 ml/s.

It can be seen from Figure 13 that the displacement efficiency of static imbibition in small pores is higher than that

of dynamic imbibition. The displacement efficiency of static imbibition increases with the increase of soaking time, but the increased amplitude slows down obviously after reaching a certain time, so the static imbibition also has the optimal imbibition time. However, the displacement efficiency of dynamic imbibition in large pores or microcracks is significantly higher than that of static imbibition. In the process of imbibition, the small pores can provide more forces for imbibition because of the small capillary radius, while the large pores or microcracks can provide an effective channel for the oil replaced by dynamic displacement. It is possible

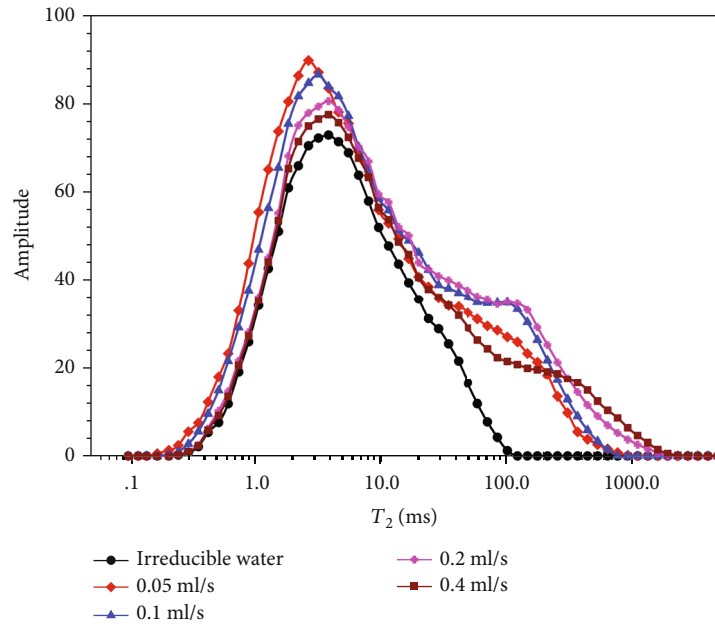


FIGURE 9:  $T_2$  spectrum of the core sample No. H-15 under different displacement rates.

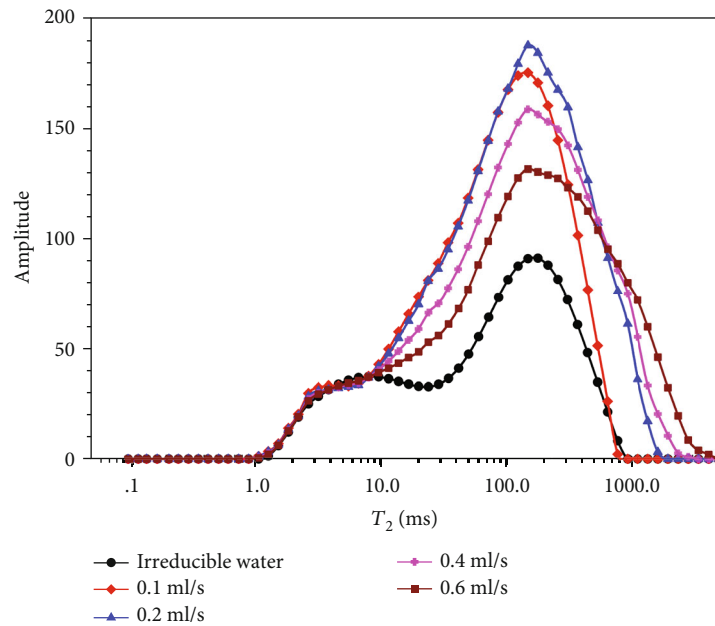


FIGURE 10:  $T_2$  spectrum of the core sample No. H-21 under different displacement rates.

to obtain the highest efficiency of imbibition recovery only when these two aspects are combined effectively.

Therefore, in the actual field process of waterflooding imbibition recovery, the static imbibition and the dynamic imbibition can be combined to achieve a higher recovery efficiency of tight sandstone reservoirs. In field application, a relatively small injection rate is applied to avoid water channeling. The well is then shut in for a while. The shut-in period is determined by laboratory spontaneous imbibition core experiments. An optimal injection rate is carried out based on the conclusions in Section 3.2 to perform dynamic imbibition to improve the final recovery factor.

#### 4. Conclusion

The microdisplacement mechanisms of dynamic imbibition are investigated based on the NMR technique. A set of experiments, including dynamic displacement, spontaneous imbibition, permeability measurements, and scanning electron microscopy, are performed to analyze the effect of displacement volume and displacement velocity on displacement efficiency. Furthermore, the comparison between static imbibition and dynamic imbibition on displacement efficiency is performed. The conclusion can be summarized based on experimental results:

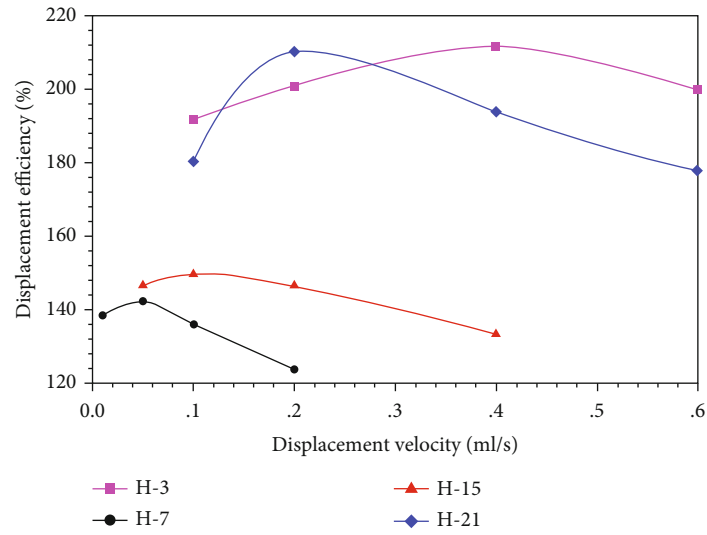


FIGURE 11: Dynamic imbibition displacement efficiency under different displacement rates.

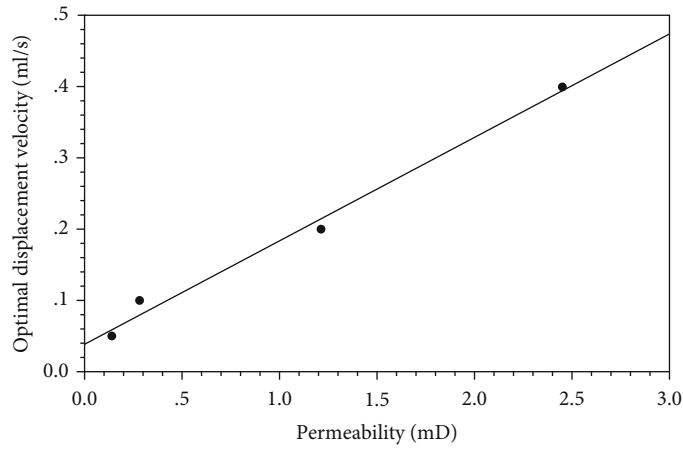


FIGURE 12: Relationship between optimal displacement velocity and permeability.

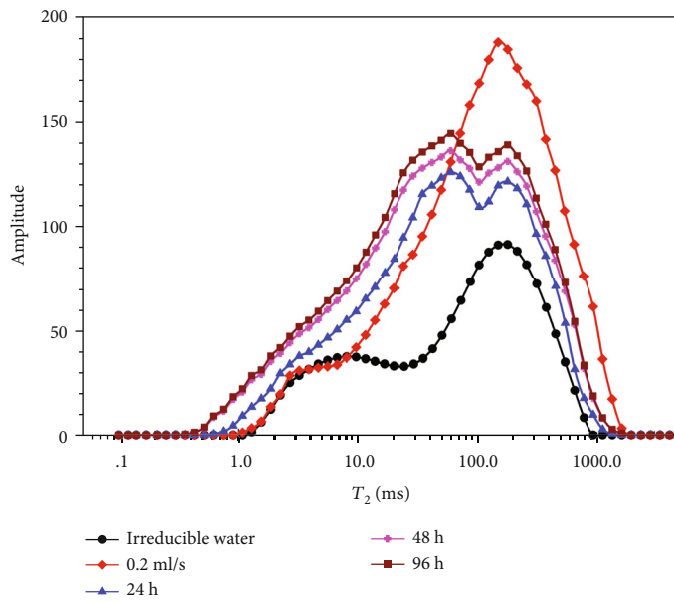


FIGURE 13: Comparison of static imbibition and dynamic displacement.

- (1) The relative displacement efficiency of core dynamic imbibition increases with the increase of injection volume, but the increased amplitude decreases with the increase of injection volume. Under the same injection volume, the relative displacement efficiency of core dynamic imbibition increases significantly with the increase of core permeability. For ultralow-permeability reservoirs with permeability less than 1.0 mD, it is recommended to select an injection volume of 1.5-2.0 PV. For low-permeability reservoirs with permeability greater than 1.0 mD, it is recommended to select an injection volume of 1.0-1.5 PV
- (2) The displacement efficiency of core dynamic imbibition shows a trend of first rising and then declining with the gradual increase of the displacement rate. There exists an optimal displacement rate, under which the synergistic effect of capillary pressure and viscous force can achieve the highest displacement efficiency of dynamic imbibition. The optimal displacement rate almost linearly increases with the increase of core permeability. At a low displacement rate, the relative displacement efficiency in small pores is higher
- (3) The displacement efficiency of static imbibition increases with the increase of soaking time, but the increased amplitude slows down obviously after reaching a certain time. The displacement efficiency of static imbibition in small pores is higher than that of dynamic imbibition. However, the displacement efficiency of dynamic imbibition in large pores or microcracks is significantly higher than that of static imbibition

## Data Availability

All data, models, and code generated or used during the study appear in the article, and the authors are not restricted from sharing their data and materials.

## Conflicts of Interest

The authors declare that they have no conflicts of interest.

## Acknowledgments

This research was financially supported by the National Natural Science Foundation of China (Nos. 52074221 and 51774236), the Foundation of State Key Laboratory of Petroleum Resources and Prospecting, China University of Petroleum, Beijing (No. PRP/open-1703), and the Natural Science Foundation of Shaanxi Province (2019JQ-403).

## References

- [1] T. Jacobs, "Unconventional resources will require unconventional EOR," *Journal of Petroleum Technology*, vol. 67, no. 9, pp. 68-70, 2016.
- [2] Z. Yang, L. H. Hou, S. Z. Tao et al., "Formation conditions and 'sweet spot' evaluation of tight oil and shale oil," *Petroleum Exploration and Development*, vol. 42, pp. 555-565, 2015.
- [3] L. B. Dou, M. Zhang, G. Bi, and T. T. Li, "Transient flow in wellbores and phase transition of CO<sub>2</sub> during formation supercritical CO<sub>2</sub> invasion," *Energy Science & Engineering*, vol. 7, no. 2, pp. 323-337, 2019.
- [4] W. ZHAO, S. HU, L. HOU et al., "Types and resource potential of continental shale oil in China and its boundary with tight oil," *Petroleum Exploration and Development*, vol. 47, no. 1, pp. 1-11, 2020.
- [5] R. G. Loucks, R. M. Reed, S. C. Ruppel, and D. M. Jarvie, "Morphology, genesis, and distribution of nanometer-scale pores in siliceous mudstones of the Mississippian Barnett Shale," *Journal of Sedimentary Research*, vol. 79, no. 12, pp. 848-861, 2009.
- [6] H. N. Philip, "Pore-throat sizes in sandstones, tight sandstones, and shales," *AAPG Bulletin*, vol. 93, pp. 329-340, 2009.
- [7] W. K. Camp, "Pore-throat sizes in sandstones, tight sandstones, and shales: discussion," *AAPG Bulletin*, vol. 95, no. 8, pp. 1443-1447, 2011.
- [8] H. YANG, X. LIANG, X. NIU, S. FENG, and Y. YOU, "Geological conditions for continental tight oil formation and the main controlling factors for the enrichment: a case of Chang 7 Member, Triassic Yanchang Formation, Ordos Basin, NW China," *Petroleum Exploration and Development*, vol. 44, no. 1, pp. 11-19, 2017.
- [9] E. W. Washburn, "The dynamics of capillary flow," *Physical Review*, vol. 17, no. 3, pp. 273-283, 1921.
- [10] L. Handy, "Determination of effective capillary pressures for porous media from imbibition data," *Transactions of the AIME*, vol. 219, no. 1, pp. 75-80, 2013.
- [11] G. Hamon and J. Vidal, "Scaling-up the capillary imbibition process from laboratory experiments on homogeneous and heterogeneous samples," in *European Petroleum Conference*, London, United Kingdom, October 1986.
- [12] G. Mason and N. R. Morrow, "Capillary behavior of a perfectly wetting liquid in irregular triangular tubes," *Journal of Colloid and Interface Science*, vol. 141, no. 1, pp. 262-274, 1991.
- [13] L. Cuiec, B. Bourbiaux, and F. Kalaydjian, "Oil recovery by imbibition in low-permeability chalk," *SPE Formation Evaluation*, vol. 9, pp. 34-52, 1994.
- [14] X. Zhang, N. R. Morrow, and S. Ma, "Experimental verification of a modified scaling group for spontaneous imbibition," *SPE Reservoir Engineering*, vol. 11, no. 4, pp. 280-285, 2013.
- [15] S. X. Ma, X. Y. Zhang, and N. R. Morrow, "Influence of fluid viscosity on mass transfer between fractures and matrix," *Journal of Canadian Petroleum Technology*, vol. 38, pp. 25-30, 1999.
- [16] D. Zhou, L. Jia, J. Kamath, and A. R. Kavscek, "Scaling of counter-current imbibition processes in low-permeability porous media," *Journal of Petroleum Science and Engineering*, vol. 33, no. 1-3, pp. 61-74, 2002.
- [17] M. Ding and M. Kantzas, "Investigation of liquid imbibition mechanisms using NMR," in *Proceedings of the International Symposium of the Society of Core Analysts*, Pau, France, 2003.
- [18] K. Li and R. Horne, "An analytical scaling method for spontaneous imbibition in gas/water/rock systems," *SPE Journal*, vol. 9, pp. 322-329, 2013.
- [19] D. Quere, "Wetting and roughness," *Annual Review of Materials Research*, vol. 38, no. 1, pp. 71-99, 2008.

- [20] N. Fries and M. Dreyer, "An analytic solution of capillary rise restrained by gravity," *Journal of Colloid and Interface Science*, vol. 320, no. 1, pp. 259–263, 2008.
- [21] D. C. Standnes, "Calculation of viscosity scaling groups for spontaneous imbibition of water using average diffusivity coefficients," *Energy & Fuels*, vol. 23, no. 4, pp. 2149–2156, 2009.
- [22] G. Mason, H. Fischer, N. R. Morrow, and D. W. Ruth, "Correlation for the effect of fluid viscosities on counter-current spontaneous imbibition," *Journal of Petroleum Science and Engineering*, vol. 72, no. 1-2, pp. 195–205, 2010.
- [23] K. Schmid and S. Geiger, "Universal scaling of spontaneous imbibition for arbitrary petrophysical properties: water-wet and mixed-wet states and Handy's conjecture," *Journal of Petroleum Science and Engineering*, vol. 101, pp. 44–61, 2013.
- [24] S. Strand, D. Standnes, and T. Austad, "Spontaneous imbibition of aqueous surfactant solutions into neutral to oil-wet carbonate cores: effects of brine salinity and composition," *Energy & Fuels*, vol. 17, no. 5, pp. 1133–1144, 2003.
- [25] L. Sun, W. F. Pu, J. Xin, and Y. L. Wu, "Influence of surfactant on high temperature imbibition of low permeability cores," *Journal of China University of Petroleum*, vol. 36, pp. 103–107, 2012.
- [26] Z. Y. Qi, M. Han, A. Fuseni et al., "Laboratory study on surfactant induced spontaneous imbibition for carbonate reservoir," in *SPE Asia Pacific Oil & Gas Conference and Exhibition*, Perth, Australia, October 2016.
- [27] J. O. Alvarez and D. S. Schechter, "Wettability alteration and spontaneous imbibition in unconventional liquid reservoirs by surfactant additives," *SPE Reservoir Evaluation & Engineering*, vol. 20, no. 1, pp. 107–117, 2017.
- [28] C. L. Dai, R. Cheng, X. Sun et al., "Oil migration in nanometer to micrometer sized pores of tight oil sandstone during dynamic surfactant imbibition with online NMR," *Fuel*, vol. 245, pp. 544–553, 2019.
- [29] U. Kuila, D. K. McCarty, A. Derkowski, T. B. Fischer, T. Topór, and M. Prasad, "Nano-scale texture and porosity of organic matter and clay minerals in organic-rich mudrocks," *Fuel*, vol. 135, pp. 359–373, 2014.
- [30] S. Takahashi and A. R. Kovscek, "Spontaneous countercurrent imbibition and forced displacement characteristics of low-permeability, siliceous shale rocks," *Journal of Petroleum Science and Engineering*, vol. 71, no. 1-2, pp. 47–55, 2010.
- [31] D. M. Wang, R. Butler, J. Zhang, and R. Seright, "Wettability survey in Bakken shale with surfactant formulation imbibition," *SPE Reservoir Evaluation & Engineering*, vol. 15, pp. 695–705, 2013.
- [32] Z. Zhou, H. Abass, X. Li, D. Beringer, and W. Frank, "Mechanisms of imbibition during hydraulic fracturing in shale formations," *Journal of Petroleum Science and Engineering*, vol. 141, pp. 125–132, 2016.
- [33] J. R. Liu, J. Sheng, X. K. Wang, H. K. Ge, and E. Yao, "Experimental study of wettability alteration and spontaneous imbibition in Chinese shale oil reservoirs using anionic and nonionic surfactants," *Journal of Petroleum Science and Engineering*, vol. 175, pp. 624–633, 2019.
- [34] A. M. Neves, V. C. Santanna, J. L. M. Barillas, T. N. Castro Dantas, and A. G. B. Góis, "Ionic surfactants applied in enhanced oil recovery: adsorption, imbibition, and zeta potential approaches," *Brazilian Journal of Chemical Engineering*, vol. 37, no. 1, pp. 263–269, 2020.
- [35] C. C. Mattax and J. R. Kyte, "Imbibition oil recovery from fractured, water-drive reservoir," *Society of Petroleum Engineers Journal*, vol. 2, pp. 177–184, 2013.
- [36] J. Kleppe and R. A. Morse, "Oil production from fractured reservoirs by water displacement," in *Fall Meeting of the Society of Petroleum Engineers of AIME*, Houston, Texas, 1974.
- [37] M. Pooladi-Darvish and A. Firoozabadi, "Experiments and modelling of water injection in water-wet fractured porous media," in *Annual Technical Meeting*, Calgary, Alberta, 1998.
- [38] G. C. Tzimas, T. Matsuura, D. G. Avraam, W. van der Bruggen, G. N. Constantinides, and A. C. Payatakes, "The combined effect of the viscosity ratio and the wettability during forced imbibition through nonplanar porous media," *Journal of Colloid and Interface Science*, vol. 189, no. 1, pp. 27–36, 1997.
- [39] A. Graue, T. Bognø, B. A. Baldwin, and E. A. Spinler, "Wettability effects on oil-recovery mechanisms in fractured reservoirs," *SPE Reservoir Evaluation & Engineering*, vol. 4, pp. 455–466, 2013.
- [40] G. Q. Tang and A. Firoozabadi, "Effect of pressure gradient and initial water saturation on water injection in water-wet and mixed-wet fractured porous media," *SPE Reservoir Evaluation & Engineering*, vol. 4, pp. 516–524, 2013.
- [41] A. A. Al-Quraishi, "Oil recovery by dynamic imbibition in low tension aqueous systems," *Oil & Gas Science and Technology*, vol. 59, no. 3, pp. 267–273, 2004.
- [42] E. Hamidpour, A. Mirzaei-Paiaman, M. Masihi, and B. Harimi, "Experimental study of some important factors on nonwetting phase recovery by cocurrent spontaneous imbibition," *Journal of Natural Gas Science and Engineering*, vol. 27, pp. 1213–1228, 2015.
- [43] P. S. Hammond and E. Unsal, "Spontaneous and forced imbibition of aqueous wettability altering surfactant solution into an initially oil-wet capillary," *Langmuir*, vol. 25, no. 21, pp. 12591–12603, 2009.
- [44] J. Sharma, S. B. Inwood, and A. R. Kovscek, "Experiments and analysis of multiscale viscous fingering during forced imbibition," *SPE Journal*, vol. 17, pp. 1142–1159, 2013.
- [45] Y. Qiao, P. Ø. Andersen, S. Evje, and D. C. Standnes, "A mixture theory approach to model co- and counter-current two-phase flow in porous media accounting for viscous coupling," *Advances in Water Resources*, vol. 112, pp. 170–188, 2018.
- [46] P. Ø. Andersen, Y. Qiao, D. C. Standnes, and S. Evje, "Cocurrent spontaneous imbibition in porous media with the dynamics of viscous coupling and capillary backpressure," *SPE Journal*, vol. 24, no. 1, pp. 158–177, 2019.
- [47] H. Gao, C. Wang, J. Cao, M. Q. He, and L. B. Dou, "Quantitative study on the stress sensitivity of pores in tight sandstone reservoirs of Ordos basin using NMR technique," *Journal of Petroleum Science and Engineering*, vol. 172, pp. 401–410, 2019.

## Research Article

# Performance Optimization of CO<sub>2</sub> Huff-n-Puff for Multifractured Horizontal Wells in Tight Oil Reservoirs

Mingqiang Hao,<sup>1</sup> Songlin Liao,<sup>2</sup> Guangming Yu,<sup>3</sup> Xinhui Lei,<sup>3</sup> and Yong Tang<sup>1,4</sup> 

<sup>1</sup>Research Institute of Petroleum Exploration & Development, PetroChina, Beijing 100083, China

<sup>2</sup>SINOPEC East China Company, Taizhou, Jiangsu 225300, China

<sup>3</sup>Research Institute of Petroleum Exploration & Development, Changqing Oilfield Company, PetroChina, Xi'an, Shaanxi 710018, China

<sup>4</sup>State Key Laboratory of Oil and Gas Reservoir Geology and Exploitation, Southwest Petroleum University, Chengdu, Sichuan 610500, China

Correspondence should be addressed to Yong Tang; tangyong2004@126.com

Received 14 August 2020; Revised 30 September 2020; Accepted 2 November 2020; Published 16 November 2020

Academic Editor: Jinze Xu

Copyright © 2020 Mingqiang Hao et al. This is an open access article distributed under the Creative Commons Attribution License, which permits unrestricted use, distribution, and reproduction in any medium, provided the original work is properly cited.

In this paper, the sensitivity factors of CO<sub>2</sub> huff-n-puff for multifractured horizontal wells (MFHWs) in tight oil reservoirs were investigated through an experimental test and numerical simulation. The pressure-volume-temperature (PVT) experiment and the slim tube experiment are used to understand the interaction mechanism between CO<sub>2</sub> and crude oil, and the minimum miscibility pressure (MMP) of the CO<sub>2</sub>-crude oil system is 17 MPa. The single-well model was firstly established to analyze the sensitivity factors on production performance of MFHWs by using CO<sub>2</sub> huff-n-puff. The controlling factors of CO<sub>2</sub> huff-n-puff for MFHWs in tight oil reservoirs were divided into three categories (i.e., reservoir parameters, well parameters, and injection-production parameters), and the impact of individual parameter on well performance was discussed in detail. The range of reservoir parameters suitable for CO<sub>2</sub> huff-n-puff of MFHWs is obtained. The reservoir permeability is from 0.1 mD to 1 mD, the reservoir thickness changes from 10 m to 30 m, and the reservoir porosity is from 7% to 12%. Based on the reservoir parameters of the target reservoir, the reasonable well and fracture parameters are obtained. The sensitivity intensity was followed by the horizontal well length, fracture conductivity, fracture spacing, and fracture half-length. CO<sub>2</sub> injection-production parameters are further optimized, and the sensitivity intensity was followed by the single-cycle cumulative CO<sub>2</sub> injection rate, the soaking time, the injection rates, and the production rates. It provides a reference for parameter optimization of CO<sub>2</sub> huff-n-puff for MFHWs in tight oil reservoirs.

## 1. Introduction

The tight reservoir has gradually become a hot spot of oil and gas exploration and development in recent years. However, due to the poor reservoir properties, the oil recovery factor by the primary depletion is usually less than 10% [1–4]. Advanced horizontal drilling and hydraulic fracturing technologies have obtained economic production of tight formations, but rapid production decline of tight reservoirs is still a major issue [5–7]. Gas injection through horizontal wells has become one of the most promising enhanced oil recovery

(EOR) methods for tight reservoirs [8–10]. Meanwhile, CO<sub>2</sub> injection is one of the most common EOR methods because of its excellent displacing capacity, sweep efficiency, and pressure propagation [11, 12]. CO<sub>2</sub> flooding can greatly improve the shortage of water flooding, and it is an effective way to improve oil recovery [13, 14]. Song and Yang [15] collected core samples from a tight formation with a permeability range of 0.27–0.83 mD to conduct a series of core flooding experiments, and both the near-miscible and miscible CO<sub>2</sub> huff-n-puff processes result in higher development efficiency compared to that of water flooding. Several field applications



of immiscible CO<sub>2</sub> flooding in this reservoir showed poor performance due to the early breakthrough of CO<sub>2</sub> resulting from the existing natural fractures [11, 16].

CO<sub>2</sub> puff-n-huff seems to be a feasible method for improving oil recovery in tight reservoirs. On the one hand, CO<sub>2</sub> huff-n-puff technology has relatively low cost and less gas consumption. On the other hand, the gas channeling risk caused by the reservoir heterogeneity can be greatly reduced, and the injected CO<sub>2</sub> can improve the oil displacement efficiency by expanding crude oil volume, extracting the light component, dissolving into crude oil, and reducing the viscosity of crude oil during its interaction with the reservoir oil [17–20]. Li et al. [21] proposed that CO<sub>2</sub> huff-n-puff is an important method for extra-ultra-low-permeability reservoirs or reservoirs with high water cut. And CO<sub>2</sub> huff-n-puff operations were more commonly applied in North America than in China [22].

Hydraulic fractures can provide a large contact area for the injected fluid, allowing CO<sub>2</sub> to be effectively diffused through the fractures [23]. In combination with the advantages of horizontal well technology and CO<sub>2</sub> stimulation, the Jilin oil field [21, 22], the Parshall Oil Field, and the Elm Coulee Oil Field in the Bakken Formation in the North Dakota part [11, 24] have explored the development of CO<sub>2</sub> huff-n-puff after fracturing in tight oil reservoirs and achieved good development performance. However, current studies on CO<sub>2</sub> huff-n-puff through MFHWs mostly focused on heavy oil reservoirs [25, 26] and complex faulted reservoirs, and there are few studies on parameter optimization of CO<sub>2</sub> huff-n-puff in tight oil reservoirs.

Optimization of the dominated factors of CO<sub>2</sub> huff-n-puff in tight reservoirs is significant for enhancing oil production. Sun et al. [26] measured five sensitivity factors to quantify their effects on CO<sub>2</sub> huff-n-puff effectiveness using the embedded discrete fracture model (EDFM) method. The most important factor is CO<sub>2</sub> diffusivity, followed by the number of cycles, CO<sub>2</sub> injection time, CO<sub>2</sub> injection rate, and CO<sub>2</sub> soaking time. Wang et al. [6] only optimized the operation parameters (i.e., CO<sub>2</sub> injection time, soaking time, and the injected CO<sub>2</sub> amount) by numerical simulation. Yu et al. [27] investigated the individual effects of reservoir permeability, fracture half-length, number of cycles, reservoir heterogeneity, and CO<sub>2</sub> diffusion coefficient for CO<sub>2</sub> injection into the Bakken Formation. The sensitivity study revealed that lower permeability, longer fracture half-lengths, larger number of cycles, and higher molecular diffusivity are favorable for the successful CO<sub>2</sub> huff-n-puff. Zuloaga et al. [28] performed cases studies with four uncertain parameters including matrix permeability, well spacing, well pattern, and fracture half-length with a reasonable range based on the middle Bakken Formation; however, the production parameters are not involved. Alharthy et al. [29] also performed simulation to evaluate the CO<sub>2</sub> huff-n-puff process in the Bakken Formation. However, the effect of uncertainties in matrix permeability and fracture half-length on well performance during CO<sub>2</sub> injection was not investigated. Alfarge et al. [17] applied the data analysis for the reported experimental results obtained from 95 cases of naturally preserved core samples to investigate the effect of 10 parameters which could

enhance or downgrade the CO<sub>2</sub>-EOR performance in shale-oil reservoirs. And the design of experiments reported that total organic carbon content (TOC) and exposure time are the two main parameters which control CO<sub>2</sub>-EOR success in shale reservoirs. Kerr et al. [30] conducted the sensitivity studies on well communication behavior/impacts, injection gas compositions, injection rates, injection/production cycling, and reservoir fluid types and informed the development strategies about the Eagle Ford Formation.

Therefore, parameter optimization of CO<sub>2</sub> huff-n-puff in tight oil reservoirs is chaotic and incomplete. The aim of this paper is to systematically investigate the influence of the significant parameters on production performance of MFHWs by using CO<sub>2</sub> huff-n-puff in tight oil reservoirs. In this paper, laboratory experiments including the pressure-volume-temperature (PVT) experiment and the slim tube experiment were conducted to evaluate the performance of CO<sub>2</sub> huff-n-puff processes in tight oil reservoirs and further clarify the mechanism of CO<sub>2</sub> injection into crude oil. In addition, we performed numerical simulation to optimize parameters by establishing mechanism models of CO<sub>2</sub> huff-n-puff for MFHWs in the tight oil reservoirs located in the Ordos Basin, China. The main factors of CO<sub>2</sub> huff-n-puff for MFHWs in tight oil reservoirs were divided into three categories: reservoir parameters, horizontal well parameters, and injection-production parameters. The influence of each parameter for CO<sub>2</sub> huff-n-puff was analyzed.

## 2. Laboratory Experiment

**2.1. Materials.** The light oil samples were collected from the Ordos Basin, northwestern China, and applied to analyze the phase behavior of the CO<sub>2</sub>-crude oil systems. The target reservoir belongs to Chang 8 layers, with an average thickness of 25 m, the average permeability of the reservoir is 0.39 mD, and the average porosity is 7.1%. The basic physical properties of the reservoir are shown in Table 1, and the components of the oil sample is presented in Table 2. Furthermore, the purity of CO<sub>2</sub> used in the experiments is 99.999%.

**2.2. Experimental Apparatus.** First, the phase behavior of the CO<sub>2</sub>-crude oil system was conducted using a PVT cell. Second, the MMP of the CO<sub>2</sub>-crude oil system was measured using a traditional slim tube.

A mercury-free DBR PVT system (produced by Canadian BDR Company) was applied to measure the crude oil properties and evaluate the CO<sub>2</sub>-crude oil interactions with injected CO<sub>2</sub>. The schematic diagram of the DBR instrument is shown in Figure 1. The main part of the PVT cell is a visible, high-pressure, high-temperature glass tube with a volume of 150 ml. The experimental temperature tolerance range of the instrument is 30–200°C, and the test accuracy is 0.1°C. The experimental pressure tolerance is between 0.1 and 70 MPa, and the test accuracy is 0.01 MPa.

The traditional slim tube system is a highly simplified one-dimensional model. Figure 2 shows the schematic of the slim tube experiment device. Through the slim tube model, the MMP of the injected gas and the actual reservoir fluid can be simulated. The value of MMP obtained by the

TABLE 1: The physical properties of the tight oil reservoir.

Parameter	Value
Original formation pressure (MPa)	20.9
Reservoir temperature (°C)	84
Saturation pressure (MPa)	10.18
Crude oil viscosity (mPa·s) (20.9 MPa, 84°C)	1.41
Solution gas-oil ratio (GOR) (Sm <sup>3</sup> /m <sup>3</sup> ) (0.1 MPa, 20°C)	88.9
Crude oil density (kg/m <sup>3</sup> ) (0.1 MPa, 20°C)	840

TABLE 2: Components of the oil sample under the reservoir conditions (20.8 MPa, 84°C).

Carbon no.	mol.%	Carbon no.	mol.%	Carbon no.	mol.%
CO <sub>2</sub>	0.05	C <sub>9</sub>	2.24	C <sub>21</sub>	1.37
N <sub>2</sub>	1.11	C <sub>10</sub>	2.93	C <sub>22</sub>	0.91
C <sub>1</sub>	24.53	C <sub>11</sub>	2.61	C <sub>23</sub>	0.91
C <sub>2</sub>	8.15	C <sub>12</sub>	1.69	C <sub>24</sub>	1.01
C <sub>3</sub>	11.04	C <sub>13</sub>	1.01	C <sub>25</sub>	0.96
iC <sub>4</sub>	1.59	C <sub>14</sub>	5.12	C <sub>26</sub>	0.82
nC <sub>4</sub>	4.06	C <sub>15</sub>	2.01	C <sub>27</sub>	0.87
iC <sub>5</sub>	2.43	C <sub>16</sub>	1.78	C <sub>28</sub>	0.82
nC <sub>5</sub>	2.7	C <sub>17</sub>	1.78	C <sub>29</sub>	0.87
C <sub>6</sub>	1.55	C <sub>18</sub>	1.05	C <sub>30</sub>	0.73
C <sub>7</sub>	0.8	C <sub>19</sub>	0.46	C <sub>31+</sub>	5.95
C <sub>8</sub>	2.73	C <sub>20</sub>	1.33	Total	100

slim tube experimental test method is closest to the actual reservoir gas injection. The length of the slim tube is 2000 cm, and the diameter is 3.8 mm. The total pore volume (PV) of the slim tube is 98.92 cm<sup>3</sup>, the average permeability of the tube is 17.54 D, and the average porosity is 42.73%.

**2.3. Experimental Procedures.** The preparation processes (including cleaning, leakage testing, and live oil preparation) were carried out before each test.

**2.3.1. Phase Behavior Test in CO<sub>2</sub>-Crude Oil Systems.** When the preparation was completed, the prepared crude oil was injected into the PVT cell under the reservoir conditions (20.9 MPa, 84°C). The properties of the crude oil were measured by changing the pressure and the CO<sub>2</sub> concentrations. The procedures are summarized as follows:

**(1) Single Flash Test.** The crude oil under the current formation temperature and pressure is simulated, and the oil and gas reach equilibrium instantly. The purpose of the single flash experiment is to obtain basic fluid parameters, such as the gas-oil ratio, volume coefficient, and formation oil density.

**(2) Constant Composition Expansion (CCE) Test.** The formation temperature is kept constant, and the expansion capacity of the formation fluid is analyzed when the pressure changes.

**(3) Swelling Test.** Under the current formation pressure and temperature, a certain proportion of CO<sub>2</sub> is injected into the crude oil. According to the designed gas injection times, the injected CO<sub>2</sub> is gradually dissolved completely into the oil. After injection of CO<sub>2</sub>, the properties of the crude oil will change, and the system saturation pressure, fluid density, and viscosity will be tested. The effect of injected CO<sub>2</sub> on the current formation fluid system will be studied.

**2.3.2. Slim Tube Experiment Test.** Experimental test temperature is 84°C. According to the conventional slim tube experimental test method, the MMP should be selected from 4 to 6 points, and there should be two points above the miscible pressure (satisfying the recovery factor above 90%) and two points below the miscible pressure. In this experiment, six injection pressures (11 MPa, 13 MPa, 14 MPa, 16 MPa, 18 MPa, and 20 MPa) will be chosen. During the displacement process, when the volume of injected CO<sub>2</sub> reaches 1.2 times PV of the slim tube at a certain rate (6.2 ml/h), the displacement experiment will be stopped. The recovery rate of the slim tube under different pressures will be measured.

### 3. Numerical Simulation

**3.1. Numerical Model.** Based on experimental test analysis, numerical simulation was used to better analyze the mechanism of the CO<sub>2</sub> huff-n-puff process and the sensitivity factors. Based on the laboratory oil analysis results of the single flash tests, constant composition expansion test, and swelling test, a PVT model of the oil sample was built by using the WinProp® module (version 2015), which was developed by Computer Modelling Group Ltd. (CMG).

Then, the slim tube model was developed using the GEM® module (CMG, version 2015) to match the MMP value. A reservoir model with MFHWs was further established in the GEM® module (CMG, version 2015) to analyze the effect of parameters and optimize the parameters of CO<sub>2</sub> huff-n-puff for MFHWs in tight oil reservoirs.

To better describe the properties of the oil sample and improve the calculation efficiency, the original components of the oil sample were divided into seven pseudocomponents using the WinProp® module, including CO<sub>2</sub>, N<sub>2</sub>, C<sub>1</sub>, C<sub>2</sub>-C<sub>3</sub>, C<sub>4</sub>-C<sub>6</sub>, C<sub>7</sub>-C<sub>15</sub>, and C<sub>16</sub>-C<sub>31+</sub>. More detailed data for the Peng-Robinson (PR) Equation Of State (EOS) are shown in Table 3. The relative permeability curves were taken from the experimental statistics of the core flood tests, shown in Figure 3. The relative permeability curves are assumed to be the same in the slim tube model and single-well model.

**3.1.1. Slim Tube Model.** The parameters of the slim tube model are consistent with the experiment. The dimension (length, width, and height) of the model is 20 m × 0.0038 m × 0.0038 m. The grid block is 0.25 m × 0.0038 m × 0.0038 m in *x*, *y*, and *z* directions, respectively. There is one production well at the beginning (*x* = 1) and one injection well at the end (*x* = 80). The one-dimensional model is shown in Figure 4. The model properties (reservoir temperature, permeability, and porosity), injection pressures (11 MPa,

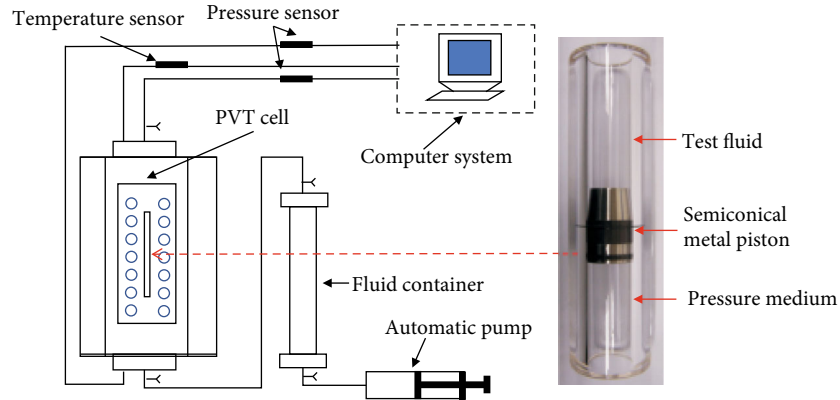


FIGURE 1: Schematic of the experimental setup for the property tests of the CO<sub>2</sub>-crude oil system.

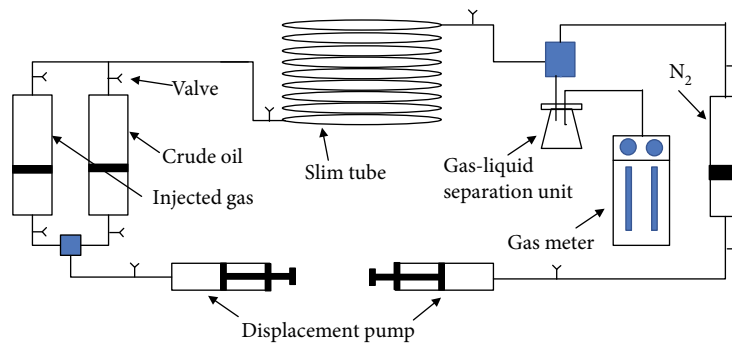


FIGURE 2: Schematic diagram of the slim tube experiment device.

TABLE 3: Properties of pseudocomponents of the oil sample.

Components	Molar fraction	Critical pressure (atm)	Critical temperature (K)	Acentric factor	Molar weight (g/mol)
CO <sub>2</sub>	0.0005	72.80	304.20	0.23	44.01
N <sub>2</sub>	0.0111	33.50	126.20	0.04	28.01
CH <sub>4</sub>	0.2454	45.40	190.60	0.01	16.04
C <sub>2</sub> -C <sub>3</sub>	0.1920	44.53	344.16	0.13	38.14
C <sub>4</sub> -C <sub>6</sub>	0.1233	34.92	451.05	0.22	67.46
C <sub>7</sub> -C <sub>15</sub>	0.2115	22.81	651.59	0.38	165.70
C <sub>16</sub> -C <sub>31+</sub>	0.2163	11.91	826.44	0.73	394.18

13 MPa, 14 MPa, 16 MPa, 18 MPa, and 20 MPa), and injection rate were the same as those of the experiment test.

**3.1.2. Single-Well Model.** The mechanism model of CO<sub>2</sub> huff-n-puff for MFHWs in tight oil reservoirs was established to study the sensitivity factors combined with the physical properties and fluid characteristics of the tight reservoir.

In order to consider the actual production situation and avoid the impact of the reservoir boundary on the CO<sub>2</sub> huff-n-puff, compositional models incorporated with Local Grid Refinement (LGR) of MFHWs for the tight reservoir were established. The dimension of the model (length, width, and height) is 2440 m × 1640 m × 26 m. The grid block is 40 m × 40 m × 2 m in *x*, *y*, and *z* directions. The single horizontal well is in the central area of the model with planar hydraulic fractures along the well, as shown in Figure 5.

The basic reservoir parameters for the simulation are summarized in Table 4. The horizontal well parameters and injection-production parameters are listed in Table 5. During the production stage, the minimum bottom-hole pressure (BHP) was set to 11 MPa (greater than saturation pressure 10.18 MPa).

**3.2. Design of Schemes.** Accordingly, the optimal values of these parameters were obtained to quantify the effects of several operation parameters [31]. There are 12 parameters which are divided into three categories, including reservoir parameters, horizontal well parameters, and injection-production parameters. Design of schemes are shown in Table 5. Each parameter includes 3 to 5 groups of scenarios, and each scenario is compared with depletion production.

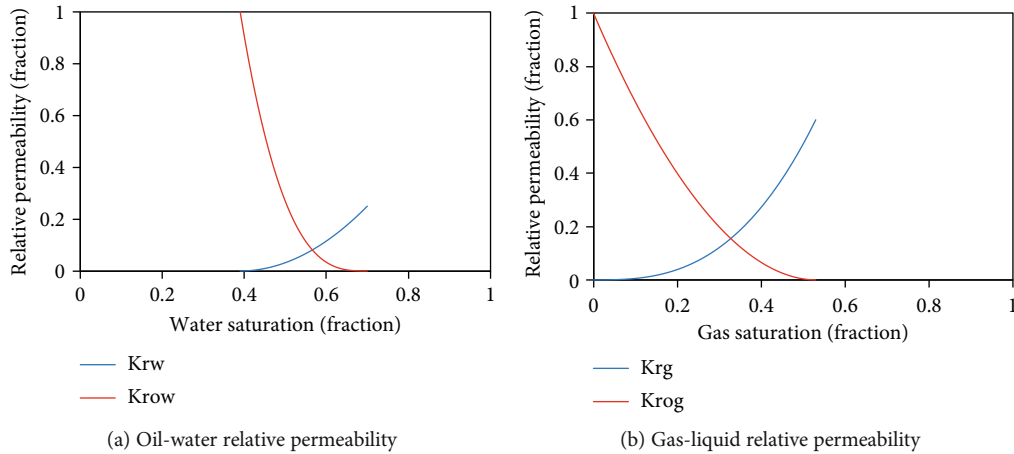


FIGURE 3: The relative permeability curves in the single horizontal well model.

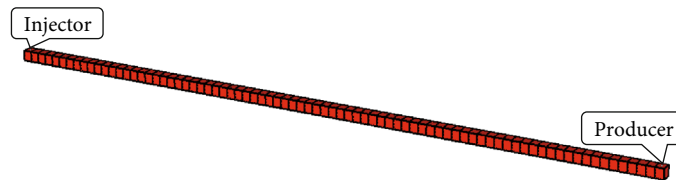


FIGURE 4: Schematic of the slim tube model.

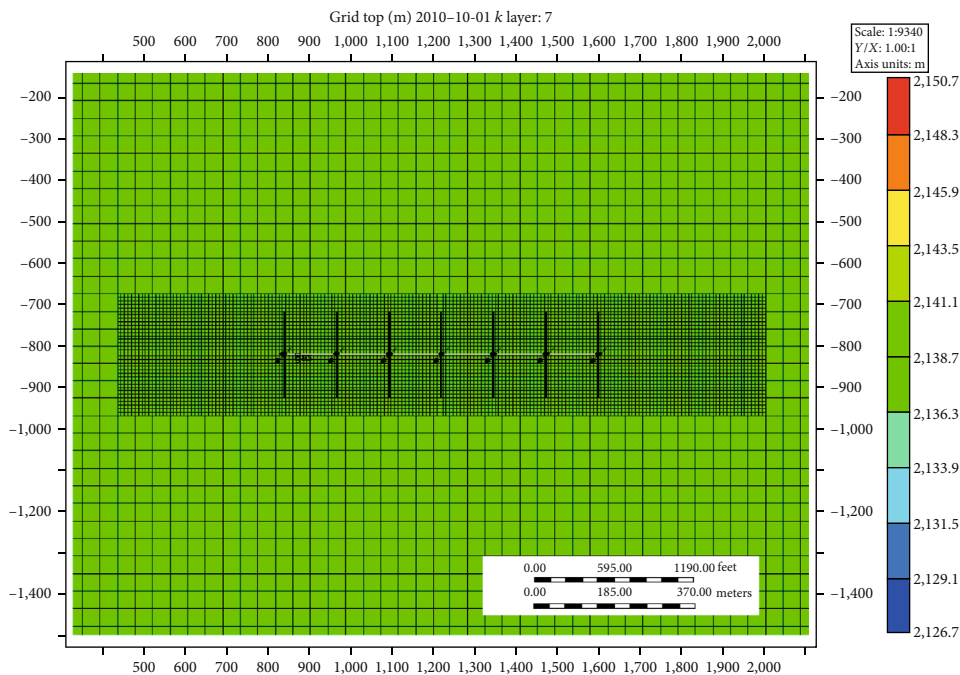


FIGURE 5: Planar grid distribution of the single horizontal well model.

The CO<sub>2</sub> injection timing is optimized based on the daily oil rate of depleted production. It is concluded that the appropriate delay of gas injection timing will help increase the production of CO<sub>2</sub> huff-n-puff [32–34].

Three indexes of the oil exchange rate, incremental oil production [31], and incremental oil recovery factor [28] were used to evaluate the effect of CO<sub>2</sub> huff-n-puff. The oil

exchange rate is defined as the ratio of injected quality of CO<sub>2</sub> and the produced oil quality. The incremental oil production is defined as the difference of cumulative oil production between the depletion production and the CO<sub>2</sub> huff-n-puff production. The incremental oil recovery factor is defined as the difference of the oil recovery factor between the depletion production and the CO<sub>2</sub> huff-n-puff production.



TABLE 4: Reservoir properties used for the simulation.

Properties	Value
Initial reservoir pressure (MPa)	20.9
Reservoir temperature (°C)	84
Matrix porosity	7.1%
Matrix permeability (mD)	0.39
Saturation pressure (MPa)	10.18

## 4. Results and Discussion

### 4.1. Phase Behaviors of the CO<sub>2</sub>-Crude Oil System

**4.1.1. Single Flash Test.** The single flash test results of crude oil are obtained by using the PVT test combined with numerical simulation obtained, shown in Table 6. The testing results agree with the field situation, and the relative error of the numerical simulation is less than 5%.

**4.1.2. CO<sub>2</sub>-Crude Oil Interaction Behaviors.** When the proportion of injected CO<sub>2</sub> reaches 50% compared with the original reservoir fluid, the saturation pressure of the crude oil can increase by 7.6 MPa. The crude oil expands by 1.35 times. The viscosity reduction is close to 30%, and the crude oil system becomes lighter. The experimental test results are shown in Table 7. Therefore, it can be concluded that injecting CO<sub>2</sub> into the target reservoir can effectively increase formation energy and reduce viscosity of crude oil.

### 4.2. CO<sub>2</sub> Miscibility Characteristics

**4.2.1. MMP Test.** Through the slim tube experiment test and numerical simulation, the MMP of the CO<sub>2</sub>-crude oil system is determined to be 17 MPa, and the corresponding recovery factor is above 90%. The test results are shown in Table 8 and Figure 6.

**4.2.2. Interphase Mass Transfer Mechanism of the CO<sub>2</sub>-Crude Oil System.** At the formation temperature, three pressure points were selected in the slim tube model, 11 MPa (less than the miscible pressure), 16 MPa (close to the miscible pressure), and 20 MPa (greater than the miscible pressure). The CO<sub>2</sub> injection volume was 0.6 PV.

More CO<sub>2</sub> will dissolve in the oil with a faster dissolution rate under greater injection pressure, shown in Figure 7(a). The amount of light components (C1) extracted by CO<sub>2</sub> also becomes greater (Figure 7(b)). The effect of viscosity reduction is more obvious (Figure 7(c)), and the interfacial tension of oil and gas phases (2 phases) is significantly reduced (Figure 7(d)). When the injection pressure is 20 MPa (greater than the miscible pressure), the viscosity can be reduced from 1.41 mPa·s to an average of 0.3 mPa·s, and the viscosity reduction can reach 78.7%. The interfacial tension of the displacement front is reduced to 0 dyne/cm.

### 4.3. Effect of Reservoir Parameters

**4.3.1. Reservoir Permeability.** The timing of CO<sub>2</sub> huff-n-puff is determined as the daily oil rate of depletion production is 1.5 m<sup>3</sup>/d. As shown in Figure 8, the permeability is enhanced

by 10 times and the cumulative oil production is increased by 3 to 4 times in the tight reservoir.

When the permeability varies from 0.1 mD to 1 mD, the oil exchange rate changes significantly. If the permeability is small enough, the diffusion of injected CO<sub>2</sub> is very difficult at the bottom of the hole, resulting in a rapid increase in the pressure around the well, pushing the formation crude oil farther. When the formation permeability exceeds 1 mD, CO<sub>2</sub> diffuses rapidly at the bottom of the wellbore, and the BHP decreases rapidly, leading to a decrease in relative incremental oil production. When the reservoir permeability is between 0.1 mD and 1 mD, it is more suitable for CO<sub>2</sub> huff-n-puff through MFHWs.

**4.3.2. Reservoir Thickness.** To evaluate the influence degree of CO<sub>2</sub> huff-n-puff on the reservoir, the influence of reservoir thickness will be evaluated based on the variation of the oil exchange rate and incremental oil recovery factor. Figure 9 shows that the oil exchange rate firstly increases and then decreases with the increase in the reservoir thickness. When the formation thickness is 26 m, the oil exchange rate gets the maximum value and the incremental oil recovery factor has a decreasing tendency. It can be obtained that the reservoir thickness continues to increase, and the effect of CO<sub>2</sub> huff-n-puff is less obvious. For the target tight reservoir, when the reservoir thickness is between 10 m and 30 m, it is better to use the CO<sub>2</sub> huff-n-puff technology to enhance oil recovery.

**4.3.3. Reservoir Porosity.** Similar to the evaluation of reservoir thickness, the influence of reservoir porosity on the CO<sub>2</sub> huff and puff effect will be evaluated based on the variation of the oil exchange rate and incremental oil recovery factor.

The timing of CO<sub>2</sub> huff-n-puff is determined as the daily oil rate of depletion production is 1.5 m<sup>3</sup>/d. With the increase in reservoir porosity, the oil exchange rate gradually increases, but the increasing trend gradually slows down, and the incremental oil recovery factor gradually decreases, as shown in Figure 10.

For the target tight reservoir, when the porosity of the reservoir is between 7% and 12%, it is better to use the CO<sub>2</sub> huff-n-puff technology of MFHWs to improve oil recovery.

### 4.4. Effect of Horizontal Well Parameters

**4.4.1. Length of the Horizontal Well.** The timing of CO<sub>2</sub> huff-n-puff is determined as the daily oil rate of depletion production is 1 m<sup>3</sup>/d. As the horizontal well length increases, the oil exchange rate and incremental oil production show an increasing trend, but the increasing trend is gradually slowing down as shown in Figure 11.

When the horizontal well is short, the BHP rises quickly after CO<sub>2</sub> injection, and the CO<sub>2</sub> diffusion rate is very slow. Therefore, the oil exchange rate and incremental oil production are relatively low. If the length of the horizontal well is long, the contact area between CO<sub>2</sub> and crude oil is increased, but the supplemental formation energy is weakened, and the friction of fluid in the wellbore will be increased, thus reducing the increase in productivity. When the length of the



TABLE 5: Twelve parameters used in the simulation cases.

Parameter types	Parameter	Design of schemes	Basic parameter value
Reservoir parameters	Permeability (mD)	0.039, 0.1, 0.39, 1, 3.9	0.39
	Thickness (m)	6, 14, 26, 34	26
	Porosity (%)	3, 7.1, 12, 15	7.1
	Length (m)	240, 480, 720, 960, 1200	720
Horizontal well parameters	Fracture half-length (m)	60, 100, 124, 140	100
	Fracture spacing (m)	80, 120, 180, 240	120
	Fracture conductivity (mD·m)	10, 20, 30, 50	30
	Total CO <sub>2</sub> injection (t)	500, 750, 1000, 1500, 2500, 4000	1500
Injection-production parameters	CO <sub>2</sub> injection rate (t/d)	30, 50, 75, 100, 150	50
	Soaking time (d)	5, 10, 20, 30, 50	20
	Production rate (m <sup>3</sup> /d)	5, 10, 20, 30, 50	50
	Cycles	1, 2, 3, 4, 5	1

TABLE 6: Single flash test results of crude oil.

Test items	Experimental value	Simulation value	Relative error (%)
Gas-oil ratio (GOR) (Sm <sup>3</sup> /m <sup>3</sup> )	85.2	82.4	3.24
Crude oil density (kg/m <sup>3</sup> ) (20.9 MPa, 84°C)	724.8	730.5	0.79
Crude oil density (kg/m <sup>3</sup> ) (0.1 MPa, 20°C)	840	845	0.68
Crude oil viscosity (mPa·s) (20.9 MPa, 84°C)	1.41	1.407	0.19
Saturation pressure (MPa)	10.18	10.41	2.30

TABLE 7: The CO<sub>2</sub>-crude oil interactions at formation temperature.

CO <sub>2</sub> mol percentage (%)	Saturated pressure (MPa)	Coefficient of expansion	Viscosity (mPa·s)
0	10.18	1	1.41
12.3	11.45	1.033	1.36
25.4	13.21	1.142	1.28
35.6	14.85	1.195	1.17
46.5	16.65	1.311	1.05
60.4	20.21	1.489	0.90
71.2	24.62	1.794	0.72

TABLE 8: Test results of MMP.

Displacement pressure (MPa)	Slim tube experimental recovery (%)	Numerical simulation recovery (%)	Relative error (%)
11	72.56	71.90	-0.66
13	79.70	77.80	-1.90
14	82.20	79.64	-2.56
16	89.10	85.53	-3.57
18	92.16	90.49	-1.67
20	93.12	95.04	1.92

horizontal well is between 700 m and 1200 m, the oil exchange rate is above 0.5.

4.4.2. *Fracture Half-Length.* The result of the influence is shown in Figure 12: the oil exchange rate and incremental

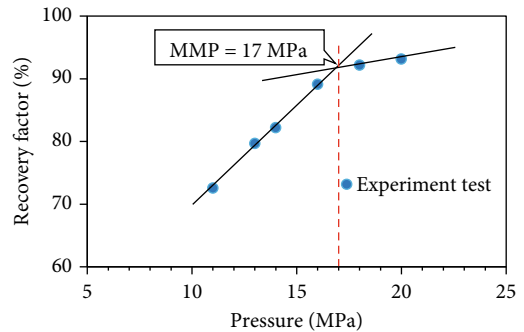


FIGURE 6: Experiment test results of MMP.

oil production are gradually increasing with the fracture half-length increased, but the trend is gradually slowing down. The half-length of the fracture increases from 100 m to 140 m, and the oil increase rate only increases by 12.4 t, which has little impact on CO<sub>2</sub> huff-n-puff. Meanwhile, the longer the half-length of the fracture, the more difficult it is to operate. It is concluded that the fracture half-length is about 100 m and the oil increase effect is better.

4.4.3. *Fracture Spacing.* Three groups of scenarios were defined (fracture spacing, 80 m (10 fractures), 120 m (7 fractures), 180 m (5 fractures), and 240 m (4 fractures)), and the results are shown in Figure 13. When the fracture spacing was reduced, the oil exchange rate and incremental oil production are gradually increasing. Overall, the fracture spacing changes from 240 m to 80 m, and the oil increase is about 50 t, which has little impact on CO<sub>2</sub> huff-n-puff. The

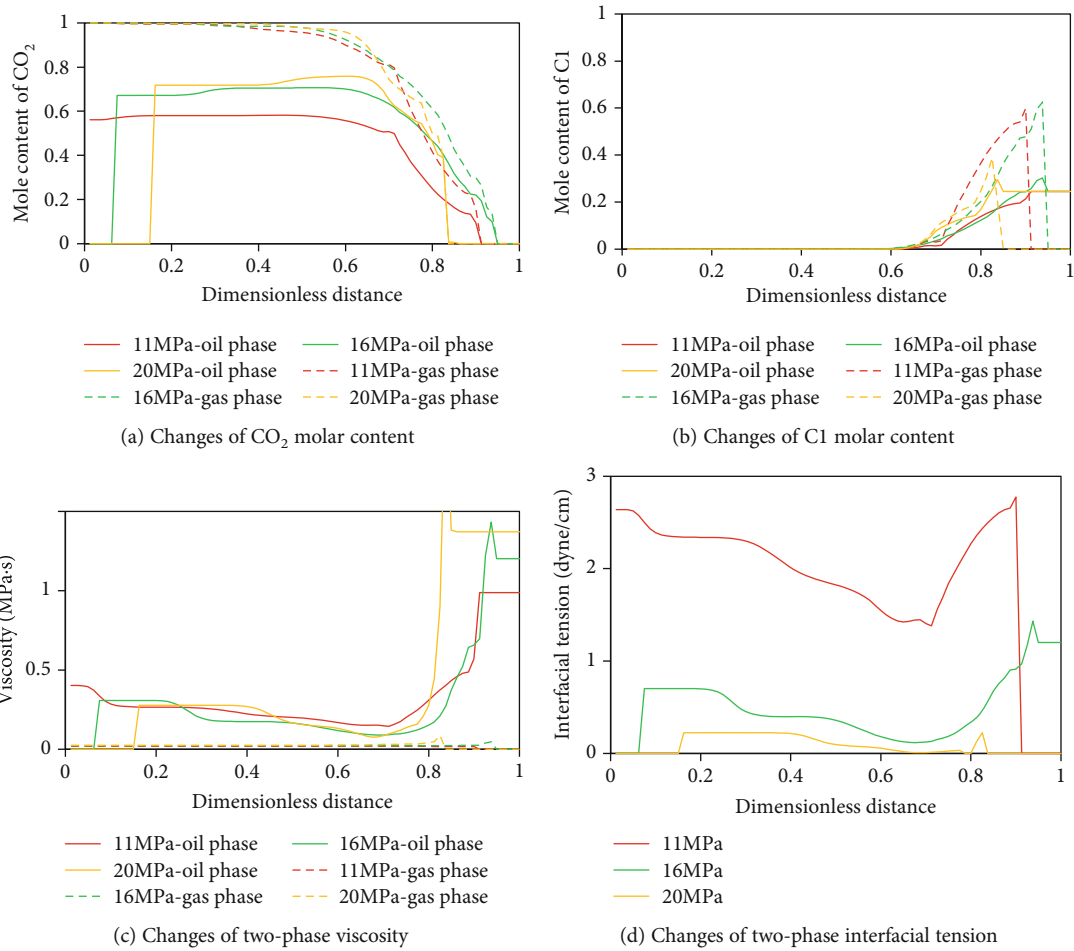


FIGURE 7: Changes of two-phase fluid properties at different pressures.

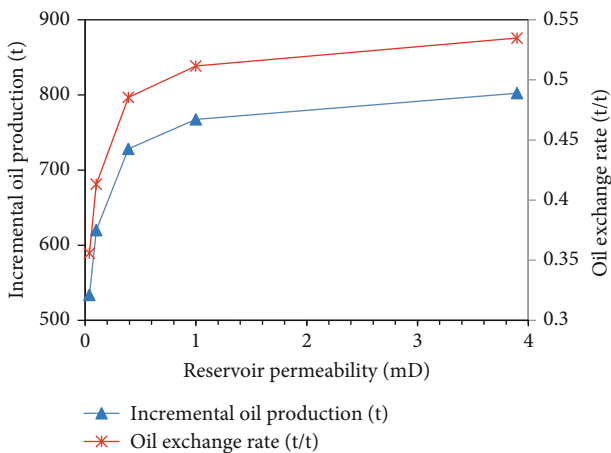


FIGURE 8: Variations of the incremental oil production and oil exchange rate at different reservoir permeability.

fracture spacing is about 120 m, the oil exchange rate reaches 0.51, and the EOR effect is better.

**4.4.4. Fracture Conductivity.** As shown in Figure 14, the cumulative oil production will be increased with larger fracture conductivity. However, the oil exchange rate and the

incremental oil production show a trend of increasing first and then decreasing, and an inflection point appeared around 30 mD·m. It is concluded that the fracture conductivity is 20 mD·m-30 mD·m, the oil exchange rate reaches 0.51, and the oil increase effect is better.

#### 4.5. Effect of Injection-Production Parameters

**4.5.1. Cumulative CO<sub>2</sub> Injection Rates.** The length of the horizontal well is 720 m, and the timing of CO<sub>2</sub> huff-n-puff is determined as the daily oil rate of depletion production is 1 m<sup>3</sup>/d. The CO<sub>2</sub> injection rate is 50 t/d ( $2.7 \times 10^4$  m<sup>3</sup>/d), and other conditions are consistent. Figure 15 shows that a large amount of CO<sub>2</sub> injection rates will increase more oil production. And the incremental oil production shows an increasing trend, but the trend gradually slows down. The oil exchange rate increases firstly and then decreases. When the cumulative CO<sub>2</sub> injection rates are between 750 t and 1000 t, the oil exchange rate reaches the maximum value. When the oil exchange rate is combined with the incremental oil production and economic benefits, the optimal injection amount should be selected after the maximum of the exchange rate. Therefore, the injection volume from 1000 t to 2500 t is preferred, and the economic benefit is better.

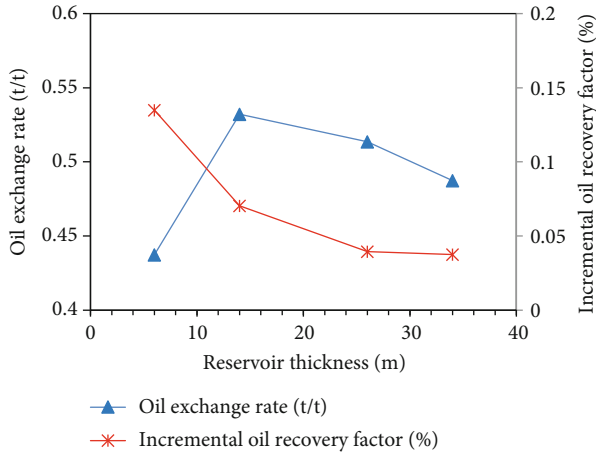


FIGURE 9: Oil exchange rate and incremental oil recovery through CO<sub>2</sub> huff-n-puff under different reservoir thickness.

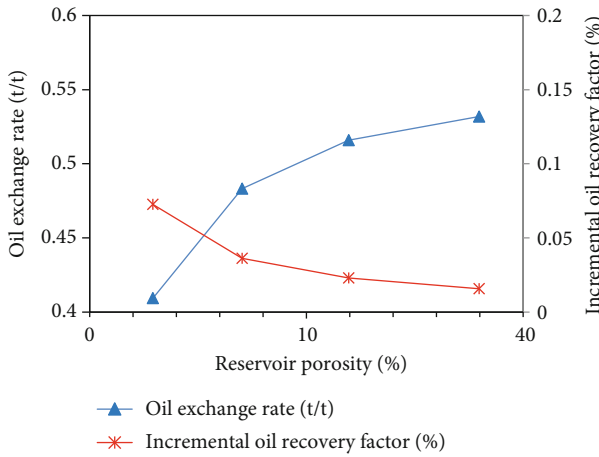


FIGURE 10: Oil exchange rate and incremental oil recovery through CO<sub>2</sub> huff-n-puff under different reservoir porosity.

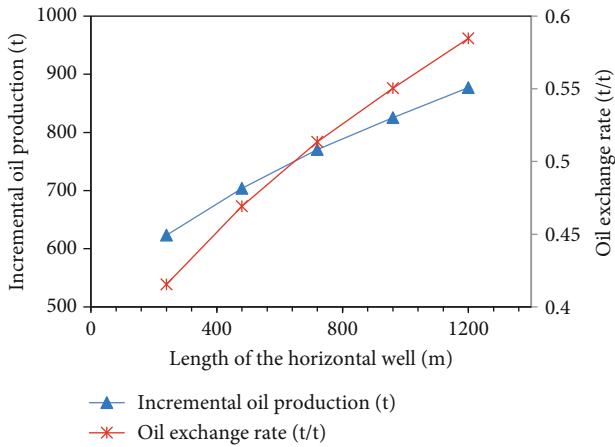


FIGURE 11: Incremental oil production and oil exchange rate through CO<sub>2</sub> huff-n-puff under different horizontal well lengths.

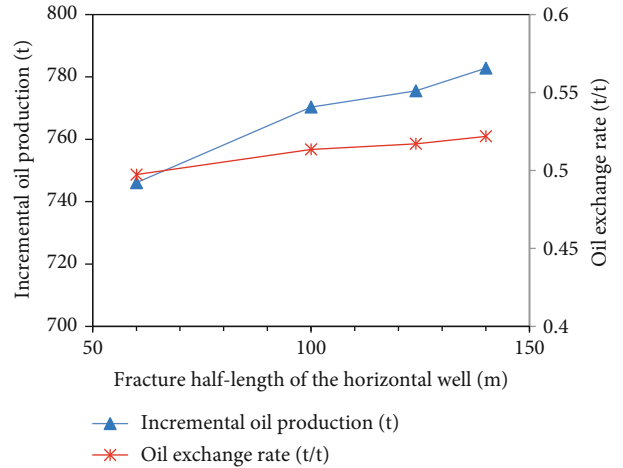


FIGURE 12: Incremental oil production and oil exchange rate through CO<sub>2</sub> huff-n-puff under different fracture half-lengths of the horizontal well.

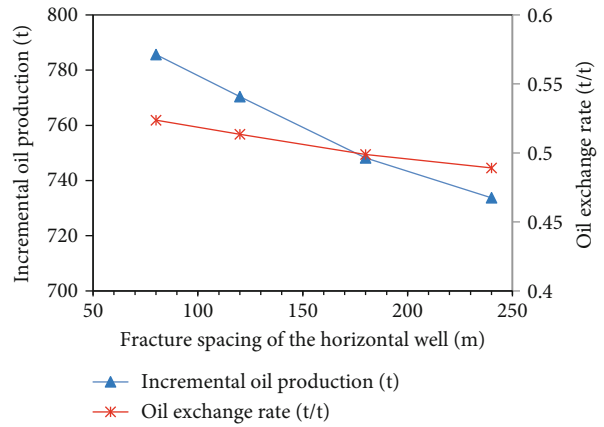


FIGURE 13: Incremental oil production and oil exchange rate through CO<sub>2</sub> huff-n-puff under different fracture spacing along the horizontal wellbore.

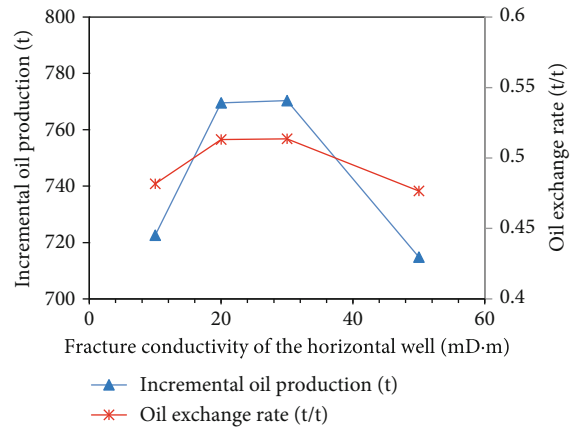


FIGURE 14: Incremental oil production and oil exchange rate through CO<sub>2</sub> huff-n-puff under different fracture conductivity.

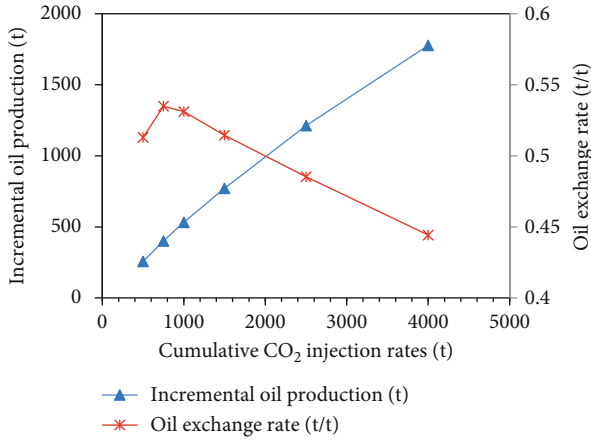


FIGURE 15: Incremental oil production and oil exchange rate through CO<sub>2</sub> huff-n-puff under different total CO<sub>2</sub> injection volumes.

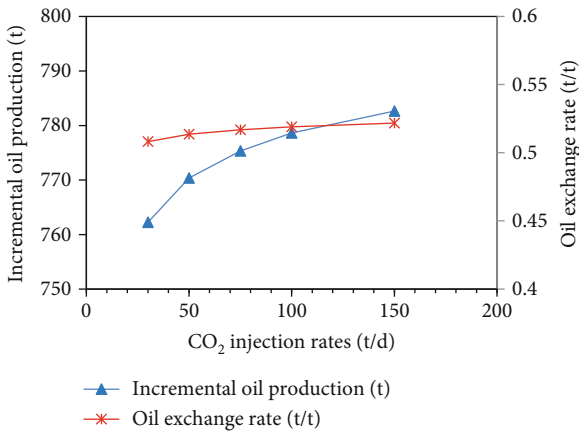


FIGURE 16: Incremental oil production and oil exchange rate through CO<sub>2</sub> huff-n-puff under different CO<sub>2</sub> injection rates.

4.5.2. *CO<sub>2</sub> Injection Rates.* The cumulative CO<sub>2</sub> injection rates are determined to be 1500 t ( $83.1 \times 10^4 \text{ m}^3$ ). The oil exchange rate and the incremental oil production show an increasing trend with higher CO<sub>2</sub> injection rates, but the trend gradually slows down as shown in Figure 16. The injection rates increase from 30 t/d to 150 t/d, and the incremental oil production increases by 20 t. Also, the oil exchange rate increases by 0.013 t/t, which has little impact on the oil production. When the injection rate is 50 t/d, the oil exchange rate can reach 0.51 and the EOR efficiency is better.

4.5.3. *Soaking Time.* Figure 17 indicates that the oil exchange rate and the incremental oil production present an increasing trend with longer soaking time, but the trend gradually slows down. The soaking time is increased from 5 d to 50 d, and the oil increase rate is increased by 40 t. In addition, the oil exchange rate is increased by 0.028 t/t, which has little impact on the oil production. When the soaking time reaches 20 days, the oil exchange rate can reach 0.51 and the EOR performance is better.

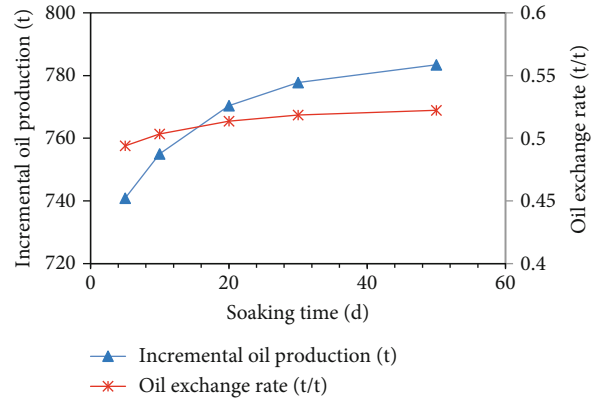


FIGURE 17: Incremental oil production and oil exchange rate through CO<sub>2</sub> huff-n-puff under different soaking times.

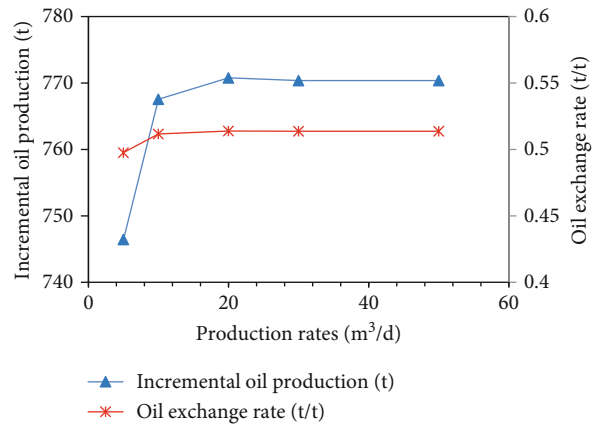


FIGURE 18: Incremental oil production and oil exchange rate through CO<sub>2</sub> huff-n-puff under different production rates.

4.5.4. *Production Rates.* Under the restriction of the minimum BHP of 11 MPa, the results are shown in Figure 18: when the production rate is 20 m<sup>3</sup>/d, the oil exchange rate and the incremental oil production reach the maximum value. The production rate increases from 5 m<sup>3</sup>/d to 50 m<sup>3</sup>/d, the oil increase rate only increases by 24 t. And the oil exchange rate increases by 0.016 t/t, so that the production rate has little influence on CO<sub>2</sub> huff-n-puff. Based on the minimum BHP, the production rate should be greater than 20 m<sup>3</sup>/d to fully release formation energy.

4.5.5. *Cycles.* Five cases are designed and the cycles change from 1 to 5 cycles, and the cumulative CO<sub>2</sub> injection rate of a single cycle is 1500 t ( $83.1 \times 10^4 \text{ m}^3$ ). The timing of CO<sub>2</sub> huff-n-puff for the first cycle is determined as the daily oil rate of depletion production is 1 m<sup>3</sup>/d, and the single cycle time is 2 years. Other control conditions are kept constant for all cases. The results are shown in Figure 19. The cumulative incremental oil production increases as the cycles increase, but the incremental oil production of the single cycle gradually decreases. The cumulative oil exchange rate was higher than 0.4 t/t in 3 cycles of CO<sub>2</sub> huff-n-puff, and the decline rate for the single cycle was less than 35%. The overall EOR performance is good.

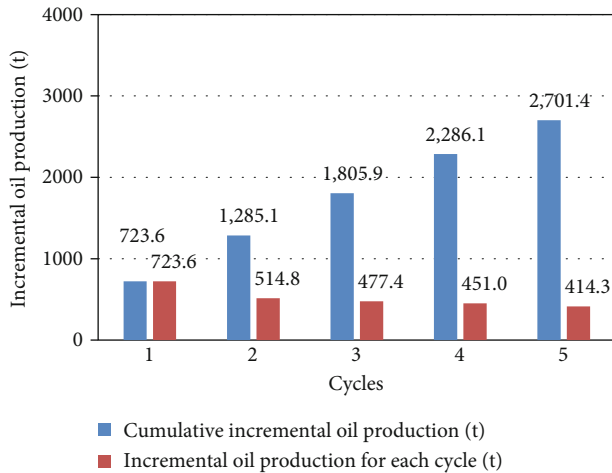


FIGURE 19: Incremental oil production through CO<sub>2</sub> huff-n-puff under different cycles.

4.6. *Sensitivity Analysis.* The purpose of sensitivity analysis is to determine the quantitative effect of different parameters on production performance. Identifying the parameters that have an important impact on CO<sub>2</sub> huff-n-puff performance in the lab scale would give a good prediction for CO<sub>2</sub>-EOR success or failure depending on reservoir properties prior to the field application. Also, it would help to optimize the operating parameters in the field scale [14, 17]. In this study, design of experiments for the factors affecting the performance of the CO<sub>2</sub>-EOR huff-n-puff process in the lab scale has been conducted. The main controlling factors affecting CO<sub>2</sub> huff-n-puff of MFHWs in tight oil reservoirs are determined. Based on reservoir parameters and choosing the oil exchange rate as the evaluation index, the dominated factors of the horizontal well and injection-production parameters were analyzed by using a range analysis method.

According to the influence of each parameter, the maximum and minimum values of the oil exchange rate are obtained, and the extreme value of the oil exchange rate of each parameter within the scope of the scheme design is obtained. The greater the variation of the oil exchange rate, the greater the influence of this parameter on CO<sub>2</sub> huff-n-puff will be. Figure 20 shows that the length of the horizontal well is the main controlling factor of the horizontal well by CO<sub>2</sub> huff-n-puff in tight oil reservoirs, followed by fracture conductivity, fracture spacing, and fracture half-length. Figure 21 shows that the cumulative CO<sub>2</sub> injection rate is the dominated factor of single-cycle injection-production parameters by CO<sub>2</sub> huff-n-puff through horizontal wells in tight oil reservoirs, followed by the soaking time, the injection rates, and the production rates.

### 5. Conclusions

In this paper, laboratory experiments and numerical simulation analysis of the reservoir are carried out to study the mechanism and performance optimization of CO<sub>2</sub> huff-n-puff for MFHWs in tight oil reservoirs to provide theoretical support for CO<sub>2</sub> huff-n-puff technology.

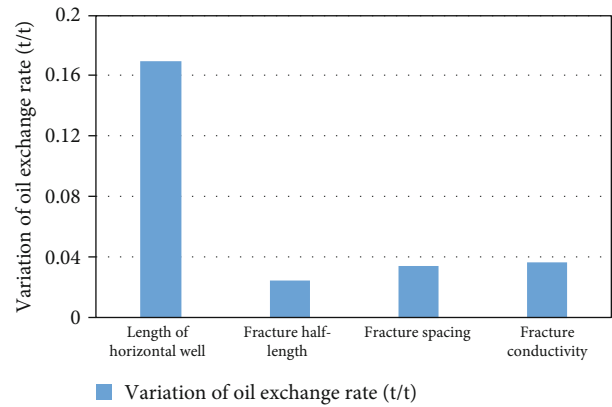


FIGURE 20: Variation distribution of the oil exchange rate with horizontal well parameters.

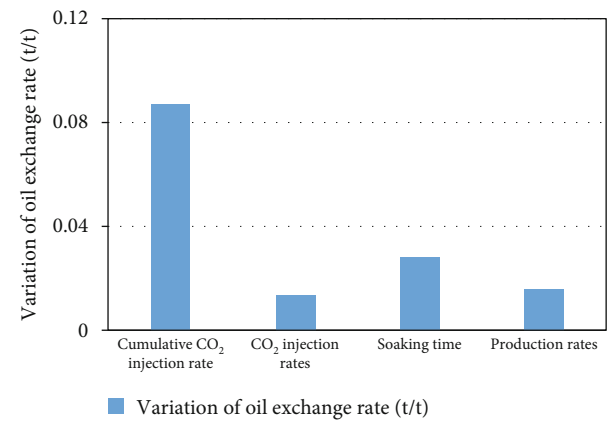


FIGURE 21: Variation distribution of the oil exchange rate of single-cycle injection-production parameters.

- (1) The PVT experiment and the slim tube experiment proved that CO<sub>2</sub> injection could effectively improve the properties of crude oil, and the CO<sub>2</sub>-crude oil system can easily achieve the miscibility condition (the MMP is 17 MPa). From the mechanism of the interaction between CO<sub>2</sub> and crude oil, the feasibility of CO<sub>2</sub> injection to improve oil recovery in this reservoir was confirmed
- (2) A single-well numerical model is established to analyze the influence of reservoir parameters, horizontal well parameters, and injection-production parameters on the CO<sub>2</sub> huff-n-puff technology. The reasonable parameters suitable for CO<sub>2</sub> huff-n-puff through MFHWs in the tight oil reservoir are obtained. The reservoir permeability is 0.1 mD to 1 mD, the reservoir thickness is 10 m to 30 m, and the reservoir porosity is 7% to 12%
- (3) Based on the reservoir parameters, the reasonable well and fracture parameters are obtained. The horizontal well length is 700 m to 1200 m, the fracture half-length is 100 m, the fracture spacing is 120 m, and the fracture conductivity is 30 mD·m. CO<sub>2</sub>



injection-production parameters are further optimized. The CO<sub>2</sub> injection volume for a single cycle is 1000 t to 2500 t, the CO<sub>2</sub> injection rate changes from 50 to 100 t/d ( $2.7 - 5.5 \times 10^4 \text{ m}^3/\text{d}$ ), and the soaking time is between 20 d and 30 d. The production rate is greater than 20 m<sup>3</sup>/d, and the two or three huff-n-puff cycles are preferred

- (4) The sensitivity analysis of influencing factors was carried out. The main controlling factors are the length of the horizontal well and the cumulative CO<sub>2</sub> injection rates

## Data Availability

Data is included in the manuscript.

## Conflicts of Interest

The authors declare that there is no conflict of interest regarding the publication of this paper.

## Acknowledgments

This work was supported by the National Science and Technology Major Projects of China (2016ZX05016), Major Special Projects of PetroChina Company Limited (2014E-3602), National Natural Science Foundation of China (51974268), and Key Project of Sichuan Province Science and Technology Department (2019YJ0423).

## References

- [1] X. Zhou, Q. Yuan, Y. Zhang, H. Wang, F. Zeng, and L. Zhang, "Performance evaluation of CO<sub>2</sub> flooding process in tight oil reservoir via experimental and numerical simulation studies," *Fuel*, vol. 236, pp. 730–746, 2019.
- [2] B. Wei, M. Zhong, K. Gao et al., "Oil recovery and compositional change of CO<sub>2</sub> huff-n-puff and continuous injection modes in a variety of dual-permeability tight matrix-fracture models," *Fuel*, vol. 276, p. 117939, 2020.
- [3] A. Abedini and F. Torabi, "Oil recovery performance of immiscible and miscible CO<sub>2</sub> huff-and-puff processes," *Energy & Fuels*, vol. 28, no. 2, pp. 774–784, 2014.
- [4] J. Qin, S. Cheng, P. Li, Y. He, X. Lu, and H. Yu, "Interference well-test model for vertical well with double-segment fracture in a multi-well system," *Journal of Petroleum Science and Engineering*, vol. 183, p. 106412, 2019.
- [5] S. S. Neshat, R. Okuno, and G. A. Pope, "Simulation of solvent treatments for fluid blockage removal in tight formations using coupled three-phase flash and capillary pressure models," *Journal of Petroleum Science and Engineering*, vol. 195, p. 107442, 2020.
- [6] H. Wang, M. N. Toksöz, and M. C. Fehler, "Laboratory and field-scale parameter optimization of CO<sub>2</sub> huff-n-puff with the staged-fracturing horizontal well in tight oil reservoirs," *Journal of Petroleum Science and Engineering*, vol. 186, 2020.
- [7] Y. He, J. Qin, S. Cheng, and J. Chen, "Estimation of fracture production and water breakthrough locations of multi-stage fractured horizontal wells combining pressure-transient analysis and electrical resistance tomography," *Journal of Petroleum Science and Engineering*, vol. 194, p. 107479, 2020.
- [8] L. SUN, C. ZOU, A. JIA et al., "Development characteristics and orientation of tight oil and gas in China," *Petroleum Exploration and Development*, vol. 46, no. 6, pp. 1073–1087, 2019.
- [9] H. U. Wenrui, Y. WEI, and J. BAO, "Development of the theory and technology for low permeability reservoirs in China," *Petroleum Exploration and Development*, vol. 45, no. 4, pp. 685–697, 2018.
- [10] Y. He, S. Cheng, Z. Sun, Z. Chai, and Z. Rui, "Improving oil recovery through fracture injection and production of multiple fractured horizontal wells," *Journal of Energy Resources Technology*, vol. 142, no. 5, 2020.
- [11] J. J. Sheng, "Critical review of field EOR projects in shale and tight reservoirs," *Journal of Petroleum Science and Engineering*, vol. 159, pp. 654–665, 2017.
- [12] K. Joslin, S. G. Ghedan, A. M. Abraham, and V. Pathak, "EOR in tight reservoirs, technical and economical feasibility," in *In: Paper SPE 185037. Presented at the SPE Unconventional Resources Conference Held in Calgary, Alberta, Canada, 2017*.
- [13] M. Ding, Y. Wang, Y. Wang, M. Gao, D. Liu, and W. Chen, "Experimental investigation of bypassed-oil recovery via CO<sub>2</sub> soaking and huff and puff injection: effects of miscibility and bypassed-oil size," *Fuel*, vol. 248, pp. 152–160, 2019.
- [14] H. U. Yongle, M. HAO, G. CHEN, R. SUN, and L. I. Shi, "Technologies and practice of CO<sub>2</sub> flooding and sequestration in China," *Petroleum Exploration and Development*, vol. 46, no. 4, pp. 753–766, 2019.
- [15] C. Song and D. Yang, "Performance Evaluation of CO<sub>2</sub> Huff-n-Puff Processes in Tight Oil Formations," in *Paper SPE 167217, Prepared for Presentation at the SPE Unconventional Resources Conference-Canada*, pp. 5–7, Calgary, Alberta, Canada, November 2013.
- [16] J. Ma, X. Wang, R. Gao et al., "Enhanced light oil recovery from tight formations through CO<sub>2</sub> huff 'n' puff processes," *Fuel*, vol. 154, pp. 35–44, 2015.
- [17] D. Alfarge, M. Wei, and B. Bai, "Data analysis for CO<sub>2</sub>-EOR in shale-oil reservoirs based on a laboratory database," *Journal of Petroleum Science and Engineering*, vol. 162, pp. 697–711, 2018.
- [18] P. Xiao, Z. Yang, X. Wang, H. Xiao, and X. Wang, "Experimental investigation on CO<sub>2</sub> injection in the Daqing extra/ultra-low permeability reservoir," *Journal of Petroleum Science and Engineering*, vol. 149, pp. 765–771, 2017.
- [19] F. Torabi, A. Q. Firouz, A. Kavousi, and K. Asghari, "Comparative evaluation of immiscible, near miscible and miscible CO<sub>2</sub> huff-n-puff to enhance oil recovery from a single matrix-fracture system (experimental and simulation studies)," *Fuel*, vol. 93, pp. 443–453, 2012.
- [20] M. O. Eshkalak, E. W. Al-Shalabi, A. Sanaei, U. Aybar, and K. Sepehrnoori, "Simulation study on the CO<sub>2</sub>-driven enhanced gas recovery with sequestration versus the refracturing treatment of horizontal wells in the U.S. unconventional shale reservoirs," *Journal of natural gas science and engineering*, vol. 21, pp. 1015–1024, 2014.
- [21] S. L. Li, Y. Tang, and C. X. Hou, "Present situation and development trend of CO<sub>2</sub> injection enhanced oil recovery technology," *Reservoir Evaluation and Development*, vol. 9, no. 3, pp. 1–8, 2019.

- [22] Z. Song, Y. Song, Y. Li, B. Bai, K. Song, and J. Hou, "A critical review of CO<sub>2</sub> enhanced oil recovery in tight oil reservoirs of North America and China," *Fuel*, vol. 276, article 118006, 2020.
- [23] S. H. Hejazi, Y. Assef, M. Tavallali, and A. Popli, "Cyclic CO<sub>2</sub>-EOR in the Bakken Formation: variable cycle sizes and coupled reservoir response effects," *Fuel*, vol. 210, pp. 758–767, 2017.
- [24] B. T. Hoffman and J. G. Evans, "Improved oil recovery IOR pilot projects in the Bakken Formation," in *In: Paper SPE 180270 Presented at the SPE Low Perm Symposium*, Denver, Colorado, USA, 2016.
- [25] J. Huang, P. Guo, and J. Zhang, "Status of CO<sub>2</sub> huff-n-puff to enhance heavy oil recovery worldwide," *J. Chengde Petroleum Coll*, vol. 10, no. 2, pp. 4–6, 2008.
- [26] R. Sun, W. Yu, F. Xu, H. Pu, and J. Miao, "Compositional simulation of CO<sub>2</sub> huff-n-puff process in middle Bakken tight oil reservoirs with hydraulic fractures," *Fuel*, vol. 236, pp. 1446–1457, 2019.
- [27] W. Yu, H. R. Lashgari, K. Wu, and K. Sepehrnoori, "CO<sub>2</sub> injection for enhanced oil recovery in Bakken tight oil reservoirs," *Fuel*, vol. 159, pp. 354–363, 2015.
- [28] P. Zuloaga, W. Yu, J. Miao, and K. Sepehrnoori, "Performance evaluation of CO<sub>2</sub> huff-n-puff and continuous CO<sub>2</sub> injection in tight oil reservoirs," *Energy*, vol. 134, pp. 181–192, 2017.
- [29] N. Alharthy, T. Teklu, H. Kazemi et al., "Enhanced oil recovery in liquid-rich shale reservoirs: laboratory to field," in *Paper SPE 175034, Presented at the SPE Annual Technical Conference and Exhibition. SPE Annual Technical Conference and Exhibition*, pp. 28–30, Houston, TX, USA, September 2015.
- [30] E. Kerr, K. K. Venepalli, K. Patel, R. Ambrose, and J. Erdle, "Use of reservoir simulation to forecast field EOR response - an Eagle Ford gas injection huff-n-puff application," in *Paper SPE 199722, Presented at the SPE Hydraulic Fracturing Technology Conference and Exhibition*, pp. 4–6, Woodlands, TX, USA, February 2020.
- [31] Y. Tang, Z. Su, J. He, and F. Yang, "Numerical simulation and optimization of enhanced oil recovery by the in situ generated CO<sub>2</sub>Huff-n-Puff process with compound surfactant," *Journal of Chemistry*, vol. 2016, 13 pages, 2016.
- [32] D. Sanchez-Rivera, K. Mohanty, and M. Balhoff, "Reservoir simulation and optimization of huff-and-puff operations in the Bakken Shale," *Fuel*, vol. 147, pp. 82–94, 2015.
- [33] R. Safi, R. K. Agarwal, and S. Banerjee, "Numerical simulation and optimization of CO<sub>2</sub> utilization for enhanced oil recovery from depleted reservoirs," *Chemical Engineering Science*, vol. 144, pp. 30–38, 2016.
- [34] C. Chen and M. Gu, "Investigation of cyclic CO<sub>2</sub> huff-and-puff recovery in shale oil reservoirs using reservoir simulation and sensitivity analysis," *Fuel*, vol. 188, pp. 102–111, 2017.

## Review Article

# Review on Phase Behavior in Tight Porous Media and Microscopic Flow Mechanism of CO<sub>2</sub> Huff-n-Puff in Tight Oil Reservoirs

Yong Tang,<sup>1</sup> Jiehong Tang,<sup>1</sup> Qi Liu,<sup>2</sup> Yong Wang ,<sup>1</sup> Zigang Zheng,<sup>3</sup> Yingjie Yuan,<sup>3</sup> and Youwei He<sup>1</sup>

<sup>1</sup>State Key Laboratory of Oil and Gas Reservoir Geology and Exploitation, Southwest Petroleum University, Chengdu, Sichuan 610500, China

<sup>2</sup>Chuanqing Drilling Engineering Co., Ltd., CNPC, Chengdu, Sichuan 610051, China

<sup>3</sup>Research Institute of Petroleum Exploration & Development, Changqing Oilfield Company, PetroChina, Xi'an, Shaanxi 710018, China

Correspondence should be addressed to Yong Wang; wangyonget@163.com

Received 21 August 2020; Revised 10 October 2020; Accepted 24 October 2020; Published 7 November 2020

Academic Editor: Jinze Xu

Copyright © 2020 Yong Tang et al. This is an open access article distributed under the Creative Commons Attribution License, which permits unrestricted use, distribution, and reproduction in any medium, provided the original work is properly cited.

The successful development of tight oil reservoirs in the U.S. shows the bright future of unconventional reservoirs. Tight oil reservoirs will be the main target of exploration and development in the future, and CO<sub>2</sub> huff-n-puff is one of the most important methods to enhance oil recovery factor of tight oil reservoirs in North America. To improve the performance of CO<sub>2</sub> huff-n-puff, injection and production parameters need to be optimized through numerical simulation. The phase behavior and microscopic flow mechanism of CO<sub>2</sub> huff-n-puff in porous media need to be further investigated. This paper presents a detailed review of phase behavior and microscopic flow mechanism in tight porous media by CO<sub>2</sub> huff-n-puff. Phase behavior in tight porous media is different from that in a PVT cylinder since the capillary pressure in tight porous media reduces the bubble point pressure and increases the miscibility pressure and critical temperature. The condensate pressure in tight porous media and nonequilibrium phase behavior need to be further investigated. The microscopic flow mechanism during CO<sub>2</sub> huff-n-puff in tight porous media is complicated, and the impact of molecular diffusion, gas-liquid interaction, and fluid-rock interaction on multiphase flow is significant especially in tight porous media. Nuclear magnetic resonance (NMR) and molecular simulation are efficient methods to describe the microscopic flow in tight oil reservoirs, while the NMR is not cost-effective and molecular simulation needs to be improved to better characterize and model the feature of porous media. The improved molecular simulation is still a feasible method to understand the microscopic flow mechanism of CO<sub>2</sub> huff-n-puff in tight oil reservoirs in the near future. The microscopic flow model in micropore network based on digital core is worth to be established, and phase behavior needs to be further incorporated into the microscopic flow model of CO<sub>2</sub> huff-n-puff in tight porous media.

## 1. Introduction

The depletion of conventional oil resources makes it hard to meet the requirement of human activity and industry, and unconventional oil reservoirs (e.g., tight oil, shale oil) have become the significant sources of energy supplement [1–5]. Tight oil reservoirs have been considered as the most promising resources among unconventional oil reservoirs. At present, the main method to exploit tight oil reservoirs is primary depletion after massive hydraulic fracturing along long horizontal wells, but the primary recovery factor is only 5%~10%

[6–10]. Successful development of tight oil reservoirs has been achieved in North America (e.g., Bakken Basin, Permian Basin, and Eagle Ford) by using CO<sub>2</sub> huff-n-puff [11–17].

CO<sub>2</sub> huff-n-puff has several advantages for improving the oil recovery of tight oil reservoirs. Firstly, compared with waterflooding, CO<sub>2</sub> molecules can enter into the micro pores more easily at the same injection pressure and CO<sub>2</sub> huff-n-puff can avoid water-sensitive effects. Secondly, low miscibility pressure of CO<sub>2</sub> in crude oil makes it easy to achieve miscible state, which reduces the viscosity of crude oil [18–20]. Thirdly, the consumption volume of CO<sub>2</sub> is relatively small, and the oil

increment is significant [21, 22]. Ma et al. [23] conducted physical simulation experiments of CO<sub>2</sub> huff-n-puff and N<sub>2</sub> huff-n-puff in tight oil core. The results showed that the oil recovery factor of through CO<sub>2</sub> huff-n-puff is about five to eight times higher than that of primary depletion, and the cumulative oil recovery factor of tight oil core through CO<sub>2</sub> huff-n-puff is higher than that through N<sub>2</sub> huff-n-puff.

CO<sub>2</sub> huff-n-puff has attracted extensive attention in recent years. On the one hand, numerical simulation has been performed to optimize injection and production parameters [24–26]. On the other hand, physical experiments have been conducted to investigate the phase behavior and microscopic flow mechanism to improve the CO<sub>2</sub> huff-n-puff performance in tight oil reservoirs [27]. The phase behavior in a PVT cylinder is different from that in porous media. Previous studies about phase behavior in tight porous media are mainly based on the principle of flash equilibrium [28]. Recently, gas breakthrough has been observed for CO<sub>2</sub> huff-n-puff in tight oil reservoirs. NMR and molecular simulation are used to investigate this. In addition, core experiments, mathematical models, etc. are used, which provide new ways for the study.

This paper firstly reviews the mechanism and dominated factors of enhancing oil recovery by CO<sub>2</sub> huff-n-puff. Then, it presents a detailed review of phase behavior and gives the achievements of microscopic flow mechanism in tight porous media by CO<sub>2</sub> huff-n-puff through different research methods.

## 2. Mechanism and Dominated Factors of Enhancing Oil Recovery by CO<sub>2</sub> Huff-n-Puff

*2.1. Mechanism of Enhancing Oil Recovery through CO<sub>2</sub> Huff-n-Puff.* Studies on the main mechanism of enhancing oil recovery through CO<sub>2</sub> huff-n-puff in tight oil reservoirs are dominated from Bakken basin in the U.S. [1, 11, 12]. CO<sub>2</sub> huff-n-puff is implemented in Bakken tight oil reservoirs after massive hydraulic fracturing. CO<sub>2</sub> transports in the fracture network firstly (see Figure 1(a)) and then infiltrates into the matrix. Meanwhile, some crude oil is pushed into the deep matrix by CO<sub>2</sub> (see Figure 1(b)). The expansion of CO<sub>2</sub> after CO<sub>2</sub> enters the matrix allows some of the crude oil in the matrix to flow into the fracture. There are also differences of gradient mass or concentration of CO<sub>2</sub> and light components in the oil and gas phase during the CO<sub>2</sub> huff and soaking stage. CO<sub>2</sub> moves from the gas phase to the oil phase, while light components move from the matrix to the fractures [29] (see Figure 2). CO<sub>2</sub> completely penetrates into the matrix and mixes with crude oil as soaking time increases. More oil flow into the fractures with the further expansion of CO<sub>2</sub>. The reinflation of CO<sub>2</sub> pushes crude oil from the matrix flowing towards the fractures with the decrease of reservoir pressure caused by oil production. The functions of CO<sub>2</sub> huff-n-puff are mainly reflected in the injection stage (pressure supplement), the soaking stage (the dissolution and diffusion), and the production stage (the dissolved gas driving) [30].

The testing analysis of crude oil from YP1-7 well in Fuyu oilfield indicated that the injected CO<sub>2</sub> changed the physical

properties of crude oil. The light components are increased after CO<sub>2</sub> huff-n-puff, while the heavy components are reduced. The viscosity of surface crude oil decreases by 50.7%, which enhances the flow ability of crude oil. The functions of CO<sub>2</sub> huff-n-puff in Fuyu tight oil reservoir are mainly reflected in the extraction on heavy components of crude oil, the viscosity reduction during miscibility, and the enhancement of the formation permeability [32].

CO<sub>2</sub> is also suggested for the exploitation of heavy oil reservoirs in EOR [33]. Jia et al. [34] points that bubbles appear and then be wrapped by resin and asphaltene, which forms the semisolid membrane. The membrane prevents bubble growing into a continuous phase, so “foamy oil” forms at this time. Viscosity of crude oil is obviously decreased, which contributes a lot to a high oil recovery factor [35].

A lot of the parameters (e.g., injection pressure, injection rate, fracture length, soaking pressure, and time of each cycle) are optimized by numerical simulations after understanding the physical mechanism of CO<sub>2</sub> huff-n-puff in tight oil reservoirs.

### *2.2. Dominated Factors for CO<sub>2</sub> Huff-n-Puff in Tight Oil Reservoirs.*

Zuloaga et al. [36] established a numerical reservoir simulation model referring to the fluid and formation data from middle Bakken formation. It was found that the incremental oil recovery factor of tight oil reservoir by CO<sub>2</sub> huff-n-puff is higher than that of CO<sub>2</sub> flooding when the permeability is lower than 0.03 mD (see Figure 3). CO<sub>2</sub> flooding is preferred when formation permeability exceeds 0.03 mD.

Sun et al. [37] simulated CO<sub>2</sub> huff-n-puff after fracturing in horizontal wells of middle Bakken oilfield by using the embedded discrete fracture model. The results suggested that CO<sub>2</sub> diffusivity had a greater influence on oil production than the number of cycles, injection time, etc. (see Figure 4). Jia et al. [1] built a CMG-GEM model based on the geological and PVT data from Bakken formation, and found that molecular diffusion plays a significant role for enhancing oil recovery factor. A maximum of 39% underestimation of oil recovery will be caused if molecular diffusion is ignored in the study.

Wang [38] pointed out that the properties of crude oil under formation condition became better, and its saturation pressure and volume coefficient are increased with the increase of CO<sub>2</sub> injection volume. The degree of reserve recovery becomes greater with the increase of the soaking pressure (Figure 5), but the CO<sub>2</sub> consumption per unit of oil production also becomes higher. The low viscosity of crude oil and the long soaking time contribute a lot to the final recovery factor of the tight oil reservoir through CO<sub>2</sub> huff-n-puff.

Yang et al. [39] simulated the CO<sub>2</sub> huff-n-puff in a tight oil reservoir by means of physical simulation experiment. The final recovery factor of CO<sub>2</sub> huff-n-puff is 12.5% higher than that of elastic production. The tight oil reservoirs in Xinjiang show medium to strong water sensitivity. To improve the tight oil recovery factor after depletion development, Ma et al. [23] carried out a physical simulation experiment of CO<sub>2</sub> huff-n-puff in the laboratory. The analyses show that more depletion energy is released by dissolved



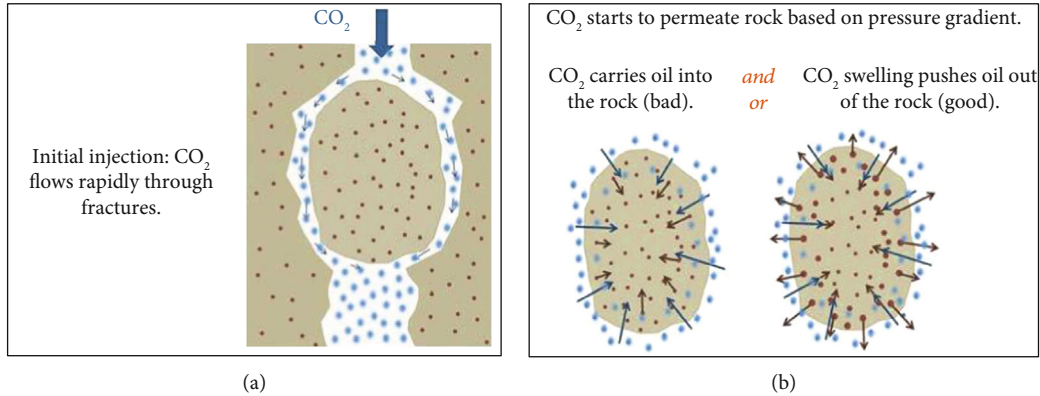


FIGURE 1: Two stages of CO<sub>2</sub> huff-n-puff process in fractured tight oil reservoir [31].

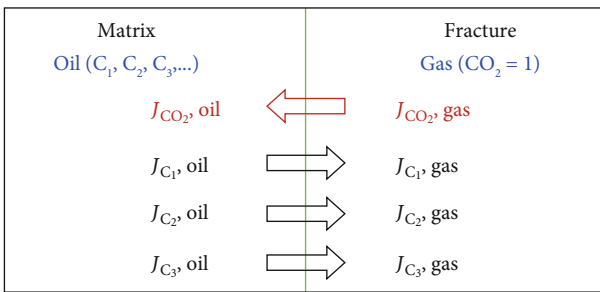


FIGURE 2: Mass transfer between oil and gas [29].

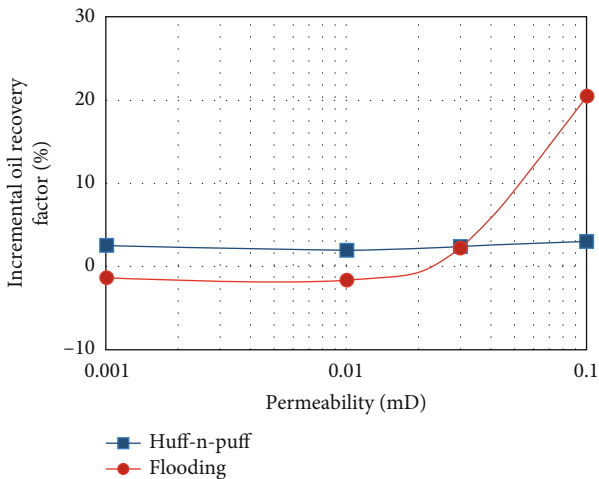


FIGURE 3: Comparison of incremental oil recovery factor between CO<sub>2</sub> flooding and CO<sub>2</sub> huff-n-puff for the range of permeability from 0.001 mD to 0.1 mD [36] (it was calculated by subtracting the oil recovery factor of base case without CO<sub>2</sub> injection).

CO<sub>2</sub> expansion with a lower the production pressure, which results in a higher oil production and a greater cumulative recovery factor. The cumulative recovery factor of CO<sub>2</sub> huff-n-puff is increased by 16%~34%, which is about five to eight times of the recovery factor by primary depletion (see Figure 6).

Liu [40] carried out laboratory experiments and field tests for Gaotaizi tight oil reservoir in Songliao Basin. The results showed that CO<sub>2</sub> huff-n-puff has good adaptability and is

an effective measure to improve the recovery factor of tight oil reservoirs. The parameters (CO<sub>2</sub> huff-n-puff time, injection rate, total injection volume, soaking time, and production flow pressure) were optimized to provide references for the production based on the evaluation of oil increment and oil exchange rate and the production dynamic analysis. In addition, parameters need to be optimized including periodic injection volume, injection pressure, and soaking pressure [29]. Ma et al. [41] found that injecting 0.1 PV CO<sub>2</sub> in the first cycle and carrying three cycles is the optimal economic scheme through the core experiment of Ordos tight oil reservoir. The scheme can improve the recovery factor up to 34.65%.

The above numerical simulations and experiments show that CO<sub>2</sub> huff-n-puff is a feasible technology to improve the recovery factor of tight oil reservoirs. Soaking time and CO<sub>2</sub> diffusivity are two dominated factors for CO<sub>2</sub> huff-n-puff in tight oil reservoirs. The phase behavior in tight porous media and microscopic flow mechanism plays an important role in updating of engineering software, so the difference of phase behavior and microscopic flow mechanism in tight porous media cannot be ignored in the numerical simulations.

### 3. Phase Behavior in Tight Porous Media

The effect of tight porous media on fluid phase behavior cannot be ignored. Recently, theoretical studies are carried out on phase behavior in tight porous media, which mainly base on the principle of flash equilibrium and consider factors such as capillary pressure, adsorption of hydrocarbons on the surface of porous media, migration of critical parameters for hydrocarbon components, and pore structure distribution of porous media [28, 42].

It is necessary to consider the wall effect of the pores, including the influence of capillary pressure and adsorption when simulating PVT experiments of shale oil. The oil recovery factor is reduced due to the adsorption of heavy oil recombination on the pore wall [43]. Lemus et al. [43] pointed that bubble point pressure will decrease because of capillary pressure. Nojabaei et al. [44] considered the effect of small pores on bubble point pressure and dew point pressure. The calculated three curves with different pore sizes indicate that the bubble point pressure decreases as the pore



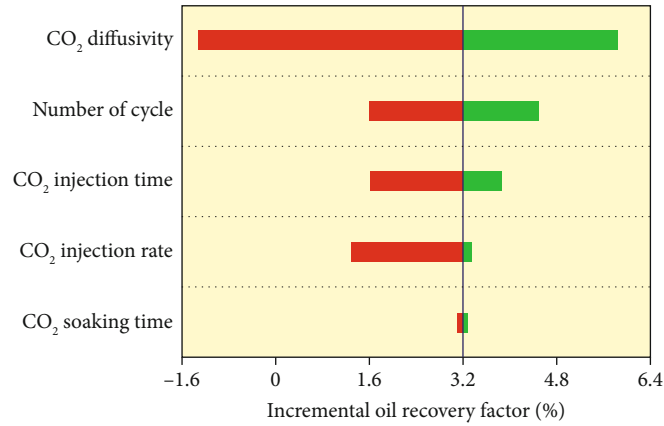


FIGURE 4: Rank of impacts of five uncertain parameters on incremental oil recovery factor [37].

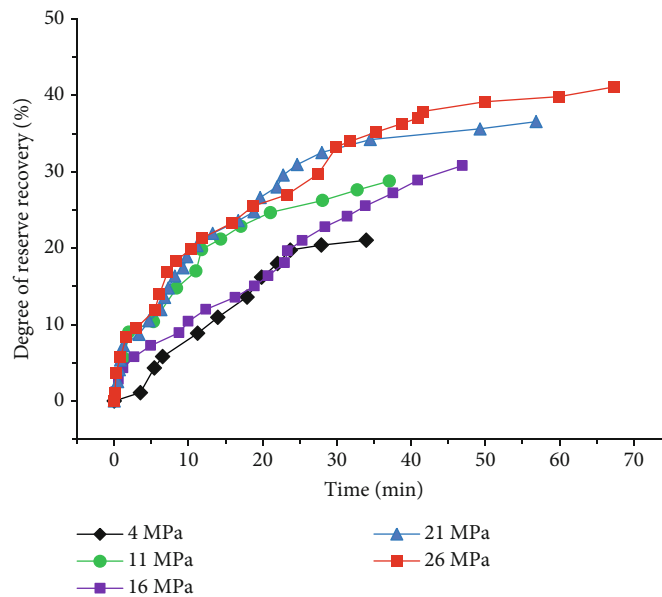


FIGURE 5: The relationship between degree of reserve recovery and time under different soaking pressure [38].

size is becoming smaller, especially at the lower temperature (see Figure 7). Besides, the dew point pressure increases if the pressure is greater than that determined at the cricondentherm, but decreases when pressure is lower than calculated at cricondentherm. Yang and Li [45] corrected the effects of molecular-wall interaction and geometric constraints on molecular-wall interaction. They carried out numerical simulation of the natural gas huff-n-puff in middle Bakken formation. The results show that the phase envelope of fluids in the reservoir tends to shrink. Under the condition of reservoir temperature, the bubble point pressure of the middle Bakken oil decreased by 17.32% considering the confinement effect. Sheng et al. [46] found that the bubble point temperature of crude oil increases with the pore diameter becoming smaller. Pang et al. [47] established a theoretical model to predict bubble point and dew point of oil in tight reservoirs. The calculation results show that the bubble point decreases as permeability becomes poor due to the increase of

capillary pressure (see Figure 8(a)). Compared with Nojabaei et al. [44], the method proposed by Pang et al. [47] is more practical because permeability is often used in petroleum industry. Besides, the dew point increases in the upper dew point interval but decreases in the lower dew point interval (see Figure 8(b)). Wu et al. [48] studied CO<sub>2</sub> injection in middle Bakken reservoir and found that bubble point pressure and minimum miscibility pressure (MMP) decreased with the increase of pore size. Zhu [49] found that the diffusion rate of oil and gas decreased while the pore size became smaller, and the inflection point pressure of displacement efficiency of n-decane was slightly larger than that of the MMP of the system in the PVT cylinder, which proved the effect of porous media on the MMP of n-decane. Yu et al. [50] studied the impact of injected gas composition on miscibility pressure, and found that the methane and nitrogen increased the miscibility pressure and delay the miscibility or near-miscibility between CO<sub>2</sub> and crude oil.

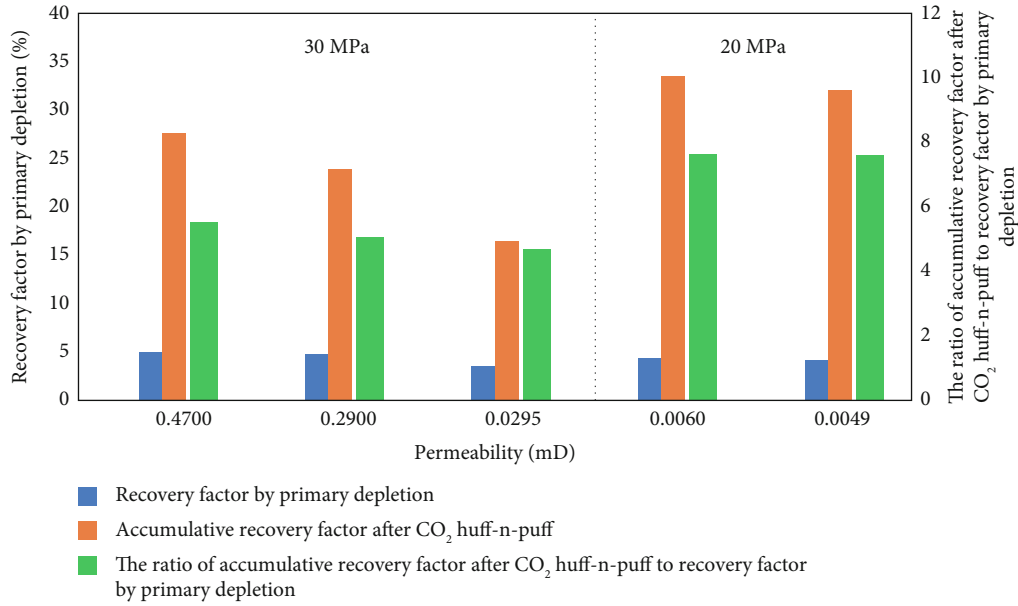


FIGURE 6: Recovery factor of cores with different matrix permeability [23].

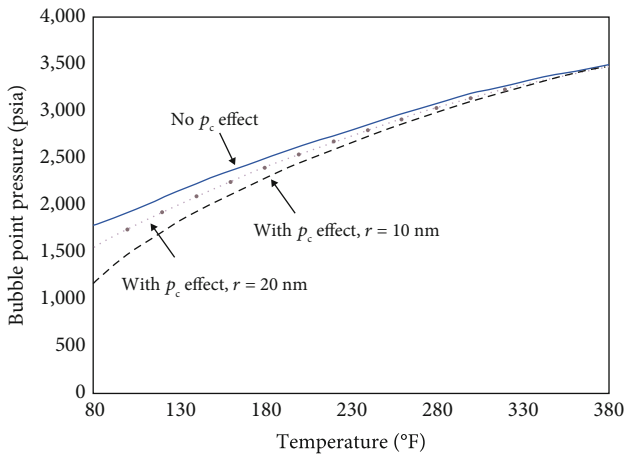


FIGURE 7: The relationship between bubble point pressure and temperature considering capillary pressure [44].

Studies have shown that the critical temperature and pore size are linearly negatively correlated. The capillary pressure reduces the bubble point pressure and the critical parameters. Jiang [28] compared the PVT experiment and the phase behavior experiment of fluid in porous medium. The bubble point pressure in porous medium was lower than that in the measured value in PVT cylinder after the crude oil was saturated with CO<sub>2</sub>, and the bubble point pressure reduction increases with the decrease of dissolved CO<sub>2</sub> and decrease of the core permeability. The results of phase behavior in tight porous media are summarized in Table 1. Generally, reduction of bubble point pressure, the bubble point temperature, and the MMP increase as permeability of porous media becomes lower.

It is difficult to observe the change of material in tight porous media directly by conventional measurement methods

so that noninterventional and visible method is introduced to measure the fluid phase behavior with the advances in experimental instruments [51]. MRI and X-ray CT are the most important noninterventional and visible methods for investigating the phase changes of oil in porous media [52]. Li et al. [51] scanned residual oil in cores after CO<sub>2</sub> immiscible flooding and miscible flooding by CT. It was obvious that residual oil saturation in cores after immiscible flooding was significantly higher than that after miscible flooding. Therefore, miscible flooding should be used to improve the recovery factor of tight oil reservoirs. There is an optimal gas injection volume, beyond which the increase of oil recovery factor is little (see Figure 9). In addition, Li et al. [51] also found that increasing CO<sub>2</sub> injection rate under miscibility condition had little influence on displacement efficiency. It indicates that when the miscibility pressure is achieved, it almost realizes a first contact miscibility with crude oil in porous media.

Although several important parameters of fluid phase behavior in tight porous media have been studied, the difference of the condensate pressure in the tight porous media from that in a PVT cylinder needs to be studied, which is significant for the development of gas-condensate reservoirs. Nonequilibrium phase behavior and the influence of capillary pressure on phase behavior need to be further investigated to obtain more reliable and accurate results.

#### 4. Microscopic Flow in Tight Oil Reservoirs

The microscopic flow of oil and injected gas in tight oil reservoirs has received much attention since the microscopic fluid flow is different from that in conventional reservoirs due to the small pore size [53–55]. Therefore, multiple experimental methods have been used to investigate the microscopic flow mechanism in tight oil reservoirs. At present, NMR experiments, molecular simulations, and other methods have been

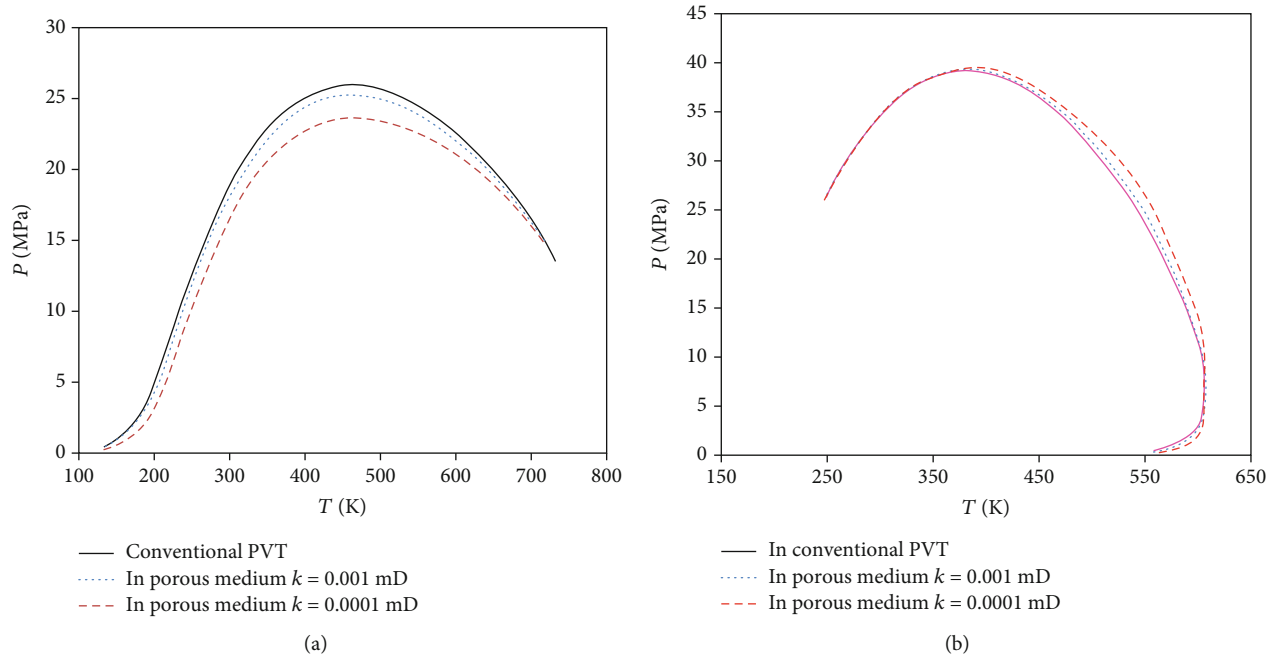


FIGURE 8: The effect of tight porous media on (a) bubble point and (b) dew point [47].

TABLE 1: Summary of the study on phase behavior in tight porous media.

Objects	Reference	Results
Wall effect	Sandoval et al. [43] Lemus et al. [43]	It is necessary to consider the wall effect while simulating PVT experiment of shale oil.
Bubble point	Jiang [28]	The pressure reduction of bubble point pressure in porous media increases as the core permeability decreases.
	Lemus et al. [43]	The bubble point pressure decreases because of the capillary pressure.
	Nojabaei et al. [44]	The bubble point pressure decreases especially at the lower temperature.
	Yang and Li [45]	The phase envelope tends to shrink. The bubble point pressure of middle Bakken oil decreases by 17.32% when the constraint effect is taken into account.
	Pang et al. [47] Wu et al. [48]	The bubble point decreases due to the capillary pressure. The bubble point pressure decreases with the increase of pore size.
Dew point	Pang et al. [47]	The dew point increases due to the capillary pressure.
	Nojabaei et al. [44]	There is either a decrease or increase for dew point pressure considering the effect of small pores.
Bubble point temperature	Sheng et al. [46]	The bubble point temperature increases as the pore diameter becomes smaller.
Minimum miscibility pressure	Wu et al. [48]	The MMP decreases with the increase of pore size. The impurity gas increases the miscibility pressure.
	Zhu [49]	
	Yu et al. [50]	
Critical temperature	Jiang [28]	The critical temperature has a linear negative correlation with the pore size.

used to analyze the microscopic flow of  $\text{CO}_2$  huff-n-puff in tight reservoirs.

**4.1. NMR Experiments.** NMR spectroscopy can be used to quantitatively analyze changes of fluid distribution, which is convenient for studying changes of oil saturation during  $\text{CO}_2$  huff-n-puff in tight oil reservoirs [56]. Ma et al. [23] ana-

lyzed eight cycles of  $\text{CO}_2$  huff-n-puff by NMR spectroscopy and found that the crude oil in large pores was produced firstly, and then oil from small pores was produced gradually with the increase of  $\text{CO}_2$  huff-n-puff cycles (see Figure 10). Therefore, the proportion of crude oil produced from the large pores decreases, while the proportion of crude oil produced from the small pores increases gradually. Wang et al.

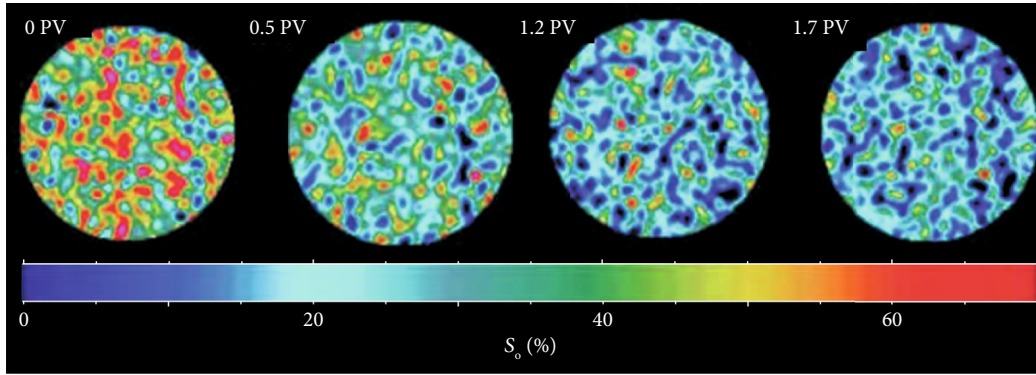


FIGURE 9: CT scanning images of residual oil at different CO<sub>2</sub> injection volumes [51].

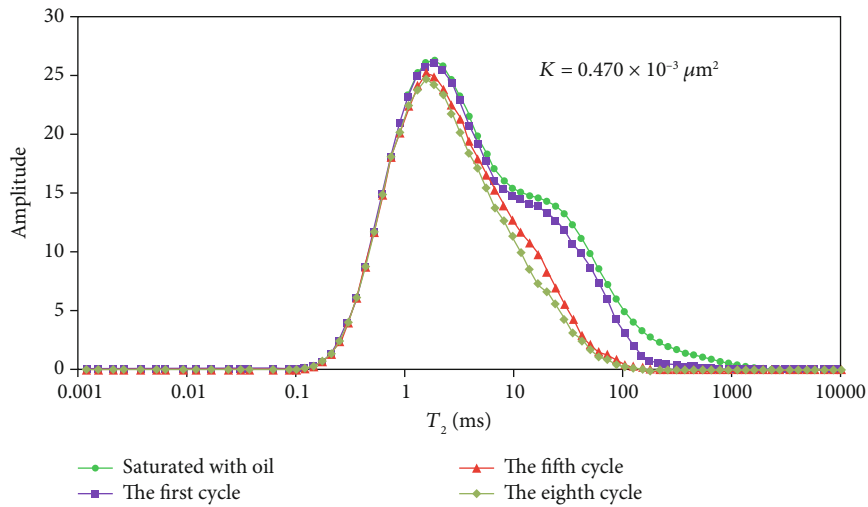


FIGURE 10: NMR spectroscopy of residual oil after different CO<sub>2</sub> huff-n-puff cycles [23].

[57] pointed out that crude oil flowed out to the core surface due to the expansion of CO<sub>2</sub> after CO<sub>2</sub> injection, which caused the relaxation time of oil less than the original 645 ms. In the first exposure experiment, the oil in each pore can be mobilized with the increase of the exposure time. More oil was produced from the macro pores (29 ms ≤ T<sub>2</sub> ≤ 645 ms) than that from the micro pores (T<sub>2</sub> ≤ 29 ms) (see Figure 11).

Chen et al. [58] performed experiment using online NMR spectrometers and concluded that residual oil in tight cores is mainly distributed in pores with pore diameters below 0.1 μm after CO<sub>2</sub> displacement. Xiao et al. [59] analyzed immiscible flooding of CO<sub>2</sub> in tight oil formation using physical simulation experiments and NMR. They pointed out that reducing asphaltene precipitation is essential to prevent core permeability reduction.

NMR experiments are applied to analyze the pore size distribution, residual oil distribution, and permeability changes. It can quickly quantify multiple indexes at the same time to better analyze the microscopic flow mechanism by NMR. However, the NMR experiment costs a lot compared with other methods. Besides, the core analyzed by NMR equipment is so small that it can only reflect microscopic flow in limited area in tight oil reservoirs. The main conclusions of

microscopic flow in tight porous media by NMR are summarized in Table 2.

**4.2. Molecular Simulation.** Traditional methods are hard to analyze adsorption and flow characteristics of tight oil reservoirs due to the limitations of large proportion nanopores in tight oil reservoirs. With the development of computer science, molecular simulation has attracted wide attention to be recognized as a feasible method to investigate microscopic flow in tight oil reservoirs [60–62]. Guo [63] used the nonequilibrium molecular dynamics to simulate the flow of alkanes in quartz pores and dolomite pores. Results show that the velocity profiles of alkanes in quartz pores and dolomite pores are parabolic, and the velocity of alkane increases with the increase of driving force or pore width. n-Pentane flows in quartz pores tends to slip, and the slip length increases with the increase of driving force, but decreases firstly and then tends to be stable with the increase of pore width (see Figure 12). However, no slip occurs in dolomite pores. The flow rate of n-pentane in two types of pores shows a nonlinear trend with the change of pressure gradient, in which convective flow rules described by Darcy’s law are not applicable.

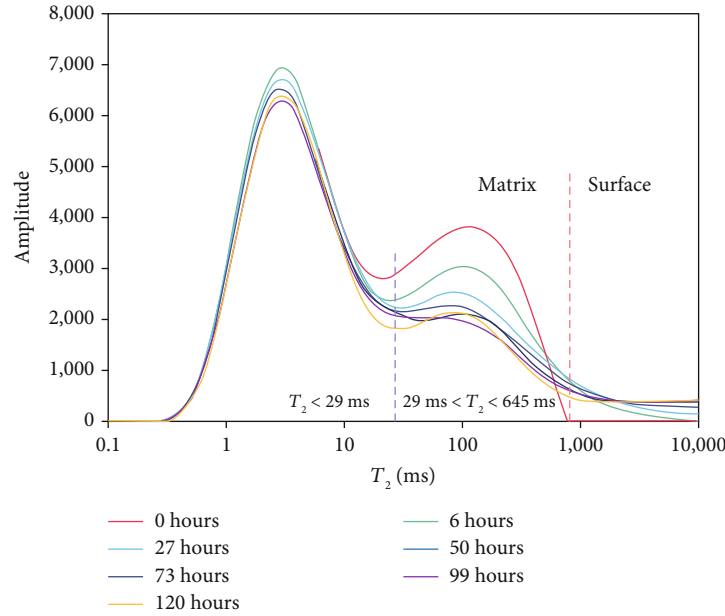


FIGURE 11: NMR  $T_2$  spectra of the first exposure experiment [57].

TABLE 2: Summary of microscopic flow mechanisms by NMR.

Research contents	Reference	Main conclusions
Oil flowing process	Ma [23]	The crude oil in the large pore is first produced, and then the crude oil in the small pore is gradually produced under the action of concentration difference and molecular diffusion.
	Wang et al. [57]	The crude oil flows out to the core surface due to the expansion of $\text{CO}_2$ . The oil in each pore can be mobilized with the increase of the exposure time in the first exposure experiment.
Residual oil distribution	Chen et al. [58]	After $\text{CO}_2$ displacement, residual oil was mainly distributed in pores with pore diameter below $0.1 \mu\text{m}$ .
Permeability	Xiao et al. [59]	Reducing the damage of asphaltene deposits to the core permeability is very important for improving oil recovery factor.

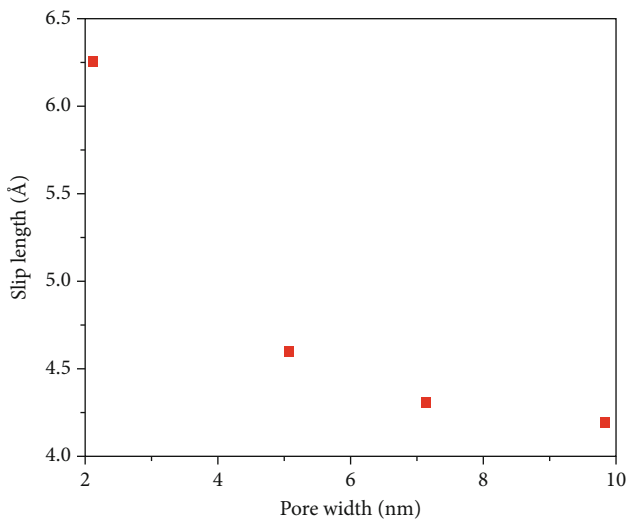


FIGURE 12: The relation between slip length and pore width of n-pentane flowing in quartz pore [63].

Slip phenomenon occurs when gas flows through porous media, especially in unconventional reservoirs [64]. Duan et al. [65] proposed an apparent permeability model to describe the gas flow in tight pores considering the boundary layer. The result shows that the velocity profile is plunger-like, and the velocity of gas molecules at the wall is consistent with that of free phase gas molecules (see Figure 13). This indicates that the slippage of gas molecules is significant at the wall. With the increase of pressure, the slippage phenomenon disappears gradually.

Zhu et al. [66] studied the  $\text{CO}_2$  huff-n-puff with Niobrara samples saturated with  $\text{C}_{10}$  and  $\text{C}_{17}$  by molecular dynamics simulation and found that  $\text{CO}_2$  molecules could replace  $\text{C}_{10}$  and  $\text{C}_{17}$  on the surface of calcite, which results in desorption and flow of hydrocarbon molecules. To analyze  $\text{CO}_2$  huff-n-puff in organic shale, Ali et al. [67] created the kerogen molecular structure and simulated  $\text{CO}_2$  huff-n-puff in shale saturated with dodecane by molecular dynamics. The results indicate that there is an optimal soaking time after which the recovery factor is not affected by soaking time anymore.



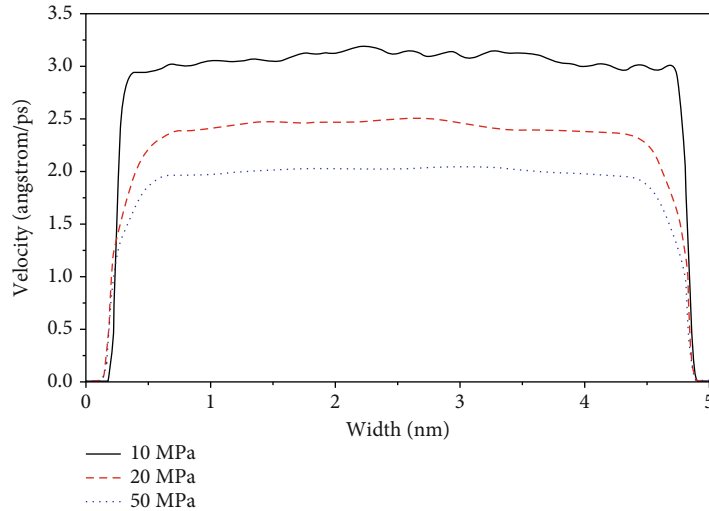


FIGURE 13: Simulation results of velocity profiles for 5 nm slit under different pressures [65].

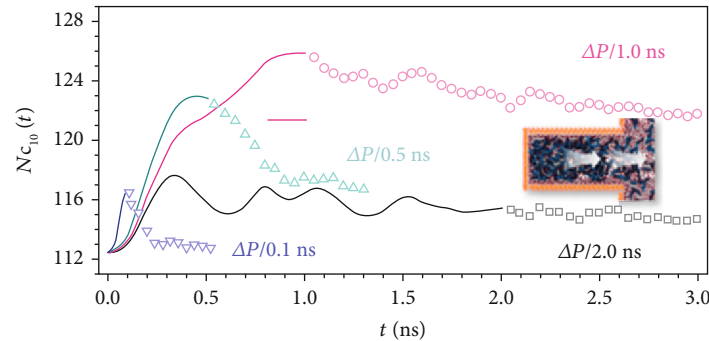


FIGURE 14: Extraction results of  $C_{10}$  molecules with different depressurization rate [68].

Additionally,  $CO_2$  is more easily adsorbed than dodecane so that dodecane is replaced by  $CO_2$ . Fang et al. [68] simulated the process of  $CO_2$  extracting hydrocarbon with reservoir depressurization by molecular dynamics. The calculation results show that the extraction amount of the alkane is different with depressurization rate changes. An appropriate depressurization rate can keep extraction at a high value (see Figure 14).

Molecular simulation can be used to analyze the flow velocity, flow rate, slip, adsorption, and extraction during  $CO_2$  huff-n-puff in tight oil reservoirs. But only small-scale molecular simulation is available due to the complicated and large-scale calculation at present. The composition of porous media and fluid simulated by molecular simulation is relatively simple compared with the real situation. Besides, pore shapes are diverse and the surface of pore is rough, which needs to be taken into account for molecular simulation [69]. Hence, the molecular simulation needs to be improved to better model microscopic flow and achieve more accurate results. The results of microscopic flow in tight porous media by molecular simulation are summarized in Table 3.

**4.3. Other Methods.** Other methods are also used to study the microscopic flow besides NMR and molecular simulation.

Zhou et al. [70] pointed out that sand filling model shows poor reference to the application in tight oil reservoirs so that the outcrop plate model was applied to discuss the influence of injection pressure on  $CO_2$  huff-n-puff. When  $CO_2$  is injected with a pressure lower than miscibility pressure,  $CO_2$  enters the matrix in a free state, causing  $CO_2$  fingering in the porous media. And  $CO_2$  is dissolved in the crude oil after soaking at a pressure higher than the miscibility pressure. Some crude oil traps the free  $CO_2$  inside the matrix. In the production stage, the free  $CO_2$  forms gas driving directly with pressure decreasing, which is beneficial to improve the EOR efficiency. Nguyen et al. [71] conducted direct visualization experiments with a microfluidic system. Results show that the efficiency of huff-n-puff depends on the solubility and miscibility of injected gas in crude oil.  $CO_2$  is more soluble in crude oil than  $N_2$ . During the production stage,  $CO_2$  can form more bubbles in the fracture network, which gradually expand with the local mass transferring between gas and liquid. With pressure reduction, bubbles displace the crude oil (see Figure 15). Alfarge et al. [72] confirmed that molecular diffusion is the main factor to control  $CO_2$  EOR in shale through comprehensive experimental investigation, field test data, and numerical simulation. Through core experiments, it is speculated that the exposure time and contact area between the injected  $CO_2$

TABLE 3: Summary of microscopic flow mechanisms by molecular simulation.

Objects	Reference	Results
Flow velocity	Guo [63]	In quartz pores and dolomite pores, the flow velocity profile of alkane is parabolic, and the flow velocity of alkane increases with the increase of driving force or pore width.
	Duan et al. [65]	The velocity profile is plunger-like, and the velocity of gas molecules at the wall is consistent with that of free gas molecules.
Slip	Guo [63]	The slip length of n-pentane flowing in quartz pores increases with the increase of driving force, and decreases firstly and then tends to be stable as the pore width increases.
	Duan et al. [65]	The slippage phenomenon disappears gradually as the pressure increases.
Flow rate	Guo [63]	The flow rate of n-pentane in pores shows a nonlinear trend with the change of pressure gradient.
Desorption	Zhu et al. [66]	CO <sub>2</sub> could replace C <sub>10</sub> and C <sub>17</sub> from the surface of calcite.
	Ali et al. [67]	Dodecane could be replaced by CO <sub>2</sub> from the pore wall.
Extraction	Fang et al. [68]	An appropriate depressurization rate can keep extraction at a high status.

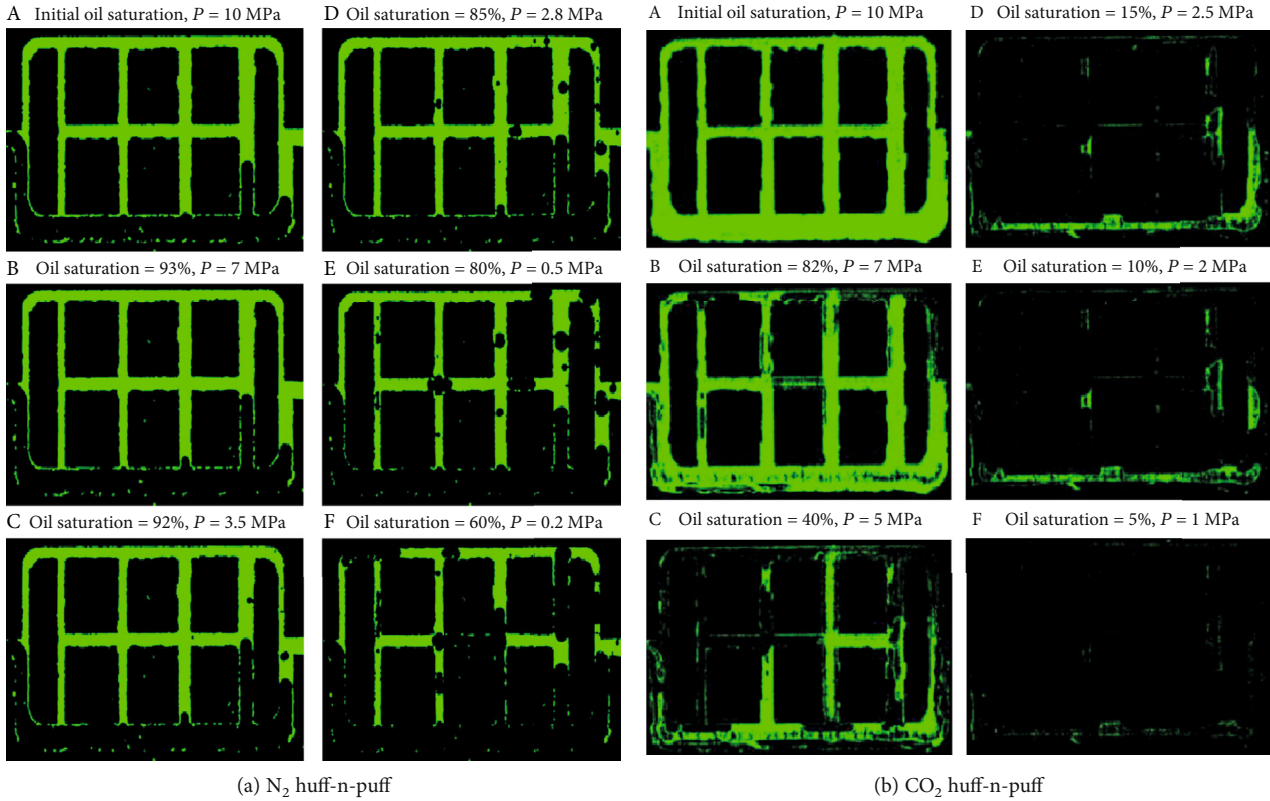


FIGURE 15: Images in visual fracture networks during depressurization [71].

and the target formation need to be significantly increased to achieve better EOR performance during the CO<sub>2</sub> huff-n-puff. Li et al. [73] studied the penetration depth of CO<sub>2</sub> huff-n-puff in tight oil reservoirs based on core experiments and numerical simulation. The results showed that the penetration depth of CO<sub>2</sub> in the first cycle was 105.6 ft and the penetration volume was approximately 36% of the reservoir volume in reservoirs where the hydraulic fracture spacing was 600 ft.

Natural fracture spacing shows the greatest impact on the penetration depth.

Most of the pre-Darcy flow models may cause errors due to the improvement of crude oil properties with CO<sub>2</sub> injection in simulation of the nonlinear flow degree. Based on the high-precision experimental data of representative cores in Fuyu reservoir, Wang et al. [74] proposed a new pre-Darcy model to characterize the influence of CO<sub>2</sub> huff-n-

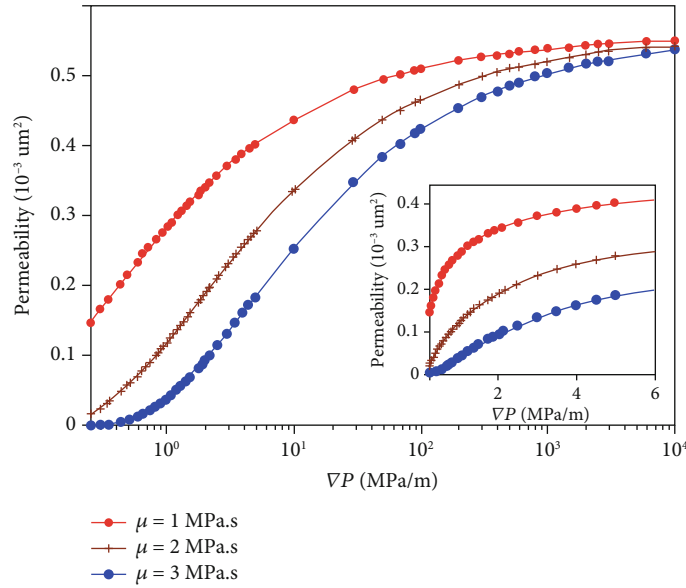


FIGURE 16: The relationship between absolute permeability and displacement pressure gradient under different fluid viscosities [75].

TABLE 4: Summary of microscopic flow mechanisms by other methods.

Methods	Reference	Main conclusions
Experiments		
Outcrop plate model experiment	Zhou et al. [70]	To inject CO <sub>2</sub> at pressure lower than miscible pressure, which is conducive to CO <sub>2</sub> fingering into the reservoir and driving out more crude oil when the well is opened.
Direct visualization experiments with a microfluidic system	Nguyen et al. [71]	The solubility of CO <sub>2</sub> is bigger than that of N <sub>2</sub> so that CO <sub>2</sub> forms more bubbles within the fracture. Bubbles gradually expand with the local mass transferring between gas and liquid and pressure reduction, and then displace the crude oil.
Core experiment	Alfarge et al. [72]	Increasing the exposure time and contact area between the injected CO <sub>2</sub> and the target formation can achieve better performance of CO <sub>2</sub> huff-n-puff.
Core experiment and numerical simulation	Li et al. [73]	Natural fracture spacing shows the greatest impact on the CO <sub>2</sub> penetration depth.
Theory		
Pre-Darcy model	Wang et al. [74]	The pre-Darcy flow models can reduce errors caused by the improvement of crude oil properties while simulating the nonlinear flow degree.
Mathematical model	Chen et al. [75]	Due to the boundary layer effect, the absolute permeability is no longer a fixed value.

puff on the description of nonlinear flow degree. The simulation results show that the proposed pre-Darcy flow model can describe the reduction of the nonlinear degree well when the properties of crude oil are improved. Chen et al. [75] established a mathematical model considering boundary layer effect based on the three-dimensional random network model. The factors affecting pore scale flows in tight formation are analyzed. The results showed that the absolute permeability is no longer a fixed value due to the boundary layer effect, but it increases as the pressure gradient increases. When the displacement pressure gradient is large enough, the permeability reaches a stable value, which is independent of the fluid viscosity (see Figure 16). Under the same pressure

gradient, the connectivity becomes greater, and absolute permeability and velocity increase as the average coordination number of the pore increases. At the same pressure gradient, the boundary layer becomes thicker as the fluid viscosity increases. Also, the effective flow space becomes smaller, and the permeability and velocity decrease.

The above experimental and theoretical researches are summarized in Table 4. Experimental researches are visualized while theoretical researches are more precise and intrinsic, which provides new ways to study the microscopic flow mechanism of CO<sub>2</sub> huff-n-puff in tight oil reservoirs.

In this section, the microscopic flow mechanism of CO<sub>2</sub> huff-n-puff in tight oil reservoirs is discussed. Various

methods are investigated and classified. NMR can quantify residual oil distribution and permeability quickly, while molecular simulation can be used to analyze the flow velocity, flow rate, and slip in tight oil reservoirs clearly. Other methods provide new visible ways and models to analyze the microscopic flow mechanism of CO<sub>2</sub> huff-n-puff in tight oil reservoirs.

The above researches are of great significance to better understand the microscopic flow mechanism of CO<sub>2</sub> huff-n-puff in tight oil reservoirs. In the near future, the improved molecular simulation is a considerable method to study the microscopic flow mechanism because the molecular-level flow mechanism can be discussed by molecular simulation while traditional methods cannot do it. The microscopic flow model in micropore network based on digital core is worth to be established, and it is important that phase behavior be taken account into the microscopic flow model of CO<sub>2</sub> huff-n-puff in tight porous media.

## 5. Conclusions

Understanding of phase behavior in tight porous media and microscopic flow mechanism is important for optimizing CO<sub>2</sub> huff-n-puff in tight oil reservoirs.

- (1) The effect of CO<sub>2</sub> huff-n-puff is mainly reflected in the injection stage (pressure supplement), the soaking stage (the dissolution and diffusion), and the production stage (the dissolved gas driving), during which the viscosity of crude oil has been decreased and the oil flows much easier. Soaking time and CO<sub>2</sub> diffusivity are two important factors for enhancing oil recovery factor through the numerical simulations of CO<sub>2</sub> huff-n-puff. The difference of phase behavior and microscopic flow mechanism in tight porous media from that in conventional reservoirs cannot be ignored in the numerical simulations
- (2) The effect of tight porous media on the phase behavior of fluid cannot be ignored since the capillary pressure in tight porous media reduces the bubble point pressure, increases the miscibility pressure and critical temperature, and shrinks the phase envelope. The difference between the condensate pressure in the tight porous media and that in a PVT cylinder needs to be discussed, which is significant for the development of gas-condensate reservoirs. Additionally, nonequilibrium phase behavior and the influence of capillary pressure on phase behavior need to be further investigated to make the results more consistent with the real situation
- (3) The microscopic flow of fluid in tight oil reservoirs is different from that in conventional reservoirs because molecular diffusion, gas-liquid interaction, and fluid-rock interaction are especially predominant in tight porous media. NMR and molecular simulation are significant methods to understand the microscopic flow in tight oil reservoirs, while NMR can quickly quantify several indexes at the same time and molec-

ular simulation can be used to analyze the molecular-level movement of gas and oil clearly. In the future, the improved molecular simulation is still a feasible method to describe and investigate the microscopic flow mechanism of CO<sub>2</sub> huff-n-puff in tight oil reservoirs. The microscopic flow model in micropore network based on digital core is worth to be established, and the phase behavior needs to be taken into account the microscopic flow model

## Conflicts of Interest

The authors declare that they have no conflict of interest.

## Acknowledgments

This work was supported by the National Natural Science Foundation of China (51974268), the Key Project of Sichuan Science and Technology Department (2019YJ0423), and the Major Special Projects of PetroChina (2014E-3602).

## References

- [1] B. Jia, J. S. Tsau, and R. Barati, "Role of molecular diffusion in heterogeneous shale reservoirs during CO<sub>2</sub> huff-n-puff," in *Proceeding of SPE Europec featured at 79th EAGE Conference and Exhibition*, Paris, France, 2017.
- [2] B. Madden and S. Vossoughi, "US shale gas and tight oil boom - the opportunities and risks for America," in *Proceeding of SPE Asia Pacific Oil and Gas Conference and Exhibition*, Jakarta, Indonesia, October 2013.
- [3] D. Du, W. Pu, J. Yang, and L. Rui, "Experimental study on EOR by CO<sub>2</sub> huff-n-puff and CO<sub>2</sub> flooding in tight conglomerate reservoirs with pore scale," *Chemical Engineering Research and Design*, vol. 156, pp. 425–432, 2020.
- [4] J. Guo, R. Xie, and L. Xiao, "Pore-fluid characterizations and microscopic mechanisms of sedimentary rocks with three-dimensional NMR: tight sandstone as an example," *Journal of Natural Gas Science and Engineering*, vol. 80, article 103392, 2020.
- [5] C. R. Clarkson and P. K. Pedersen, "Tight oil production analysis: adaptation of existing rate-transient analysis techniques," in *Proceeding of Canadian Unconventional Resources and International Petroleum Conference, SPE Paper SPE-137352-MS*, Calgary, Canada, October 2010.
- [6] X. Liu, F. An, Q. Chen, and J. Qin, "Analyses of the EOR techniques for tight oil reservoir: taking Bakken-Formation as an example," *Petroleum Geology and Oilfield Development in Daqing*, vol. 35, no. 6, pp. 164–169, 2016.
- [7] B. T. Hoffman and J. M. Rutledge, "Mechanisms for huff-n-puff cyclic gas injection into unconventional reservoirs," in *Proceeding of SPE Oklahoma City Oil and Gas Symposium, SPE Paper SPE-195223-MS*, Oklahoma City, OK, USA, April 2019.
- [8] B. Wei, M. Zhong, K. Gao et al., "Oil recovery and compositional change of CO<sub>2</sub> huff-n-puff and continuous injection modes in a variety of dual-permeability tight matrix-fracture models," *Fuel*, vol. 276, article 117939, 2020.
- [9] B. T. Hoffman and J. G. Evans, "Improved oil recovery IOR pilot projects in Bakken formation," in *Proceeding of Low Perm*



- Symposium, SPE Paper SPE-1 80270-MS*, Denver, CO, USA, May 2016.
- [10] Y. He, S. Cheng, Z. Sun, Z. Chai, and Z. Rui, "Improving oil recovery through fracture injection and production of multiple fractured horizontal wells," *Journal of Energy Resources Technology*, vol. 142, no. 5, pp. 1–19, 2020.
  - [11] D. Alarge, M. Wei, and B. Bai, "IOR methods in unconventional reservoirs of North America: comprehensive review," in *Proceeding of SPE Western Regional Meeting, SPE Paper SPE-185640-MS*, Bakersfield, CA, USA, April 2017.
  - [12] H. Madhoo, A. Acevedo, M. Koley, I. Bryant, and R. Laver, "An optimal approach to shale gas and oil exploration beyond North America," in *Proceeding of SPE/EAGE European Unconventional Resources Conference and Exhibition*, Vienna, Austria, February 2014.
  - [13] T. Phi and D. Schechter, "CO<sub>2</sub> EOR simulation in unconventional liquid reservoirs: an Eagle Ford case study," in *Proceeding of SPE Unconventional Resources Conference*, Calgary, Alberta, Canada, February 2017.
  - [14] P. Pankaj, H. Mukisa, I. Solovyeva, and H. Xue, "Enhanced oil recovery in Eagle Ford: opportunities using huff-n-puff technique in unconventional reservoirs," in *Proceeding of SPE Liquids-Rich Basins Conference - North America*, Midland, TX, USA, September 2018.
  - [15] S. Mamoudou, F. Perez, A. Tinni et al., "Evaluation of huff-n-puff in shale using experiments and molecular simulations," in *Proceeding of SPE/AAPG/SEG Unconventional Resources Technology Conference*, 2020.
  - [16] Y. He, J. Qin, S. Cheng, and J. Chen, "Estimation of fracture production and water breakthrough locations of multi-stage fractured horizontal wells combining pressure-transient analysis and electrical resistance tomography," *Journal of Petroleum Science and Engineering*, vol. 194, article 107479, 2020.
  - [17] S. A. Cox, D. Cook, K. Dunek, G. R. Daniels, C. J. Jump, and R. D. Barree, "Unconventional resource play evaluation: a look at the Bakken shale play of North Dakota," in *Proceeding of SPE Unconventional Reservoirs Conference, SPE Paper SPE-114171-MS*, Keystone, CO, USA, February 2008.
  - [18] P. Zuloaga-Molero, W. Yu, Y. Xu, K. Sepehrnoori, and B. Li, "Simulation study of CO<sub>2</sub>-EOR in tight oil reservoirs with complex fracture geometries," *Scientific Reports*, vol. 6, no. 1, pp. 33445–33455, 2016.
  - [19] J. Moore, D. Crandall, and S. Workan, "A new methodology to evaluate huff and puff effectiveness at in-situ conditions," in *Proceeding of SPE/AAPG/SEG Unconventional Resources Technology Conference*, 2020.
  - [20] Y. Tang, S. Hu, Y. He et al., "Experiment on CO<sub>2</sub>-brine-rock interaction during CO<sub>2</sub> injection and storage in gas reservoirs with aquifer," *Chemical Engineering Journal*, 2021.
  - [21] C. Song and D. Yang, "Experimental and numerical evaluation of CO<sub>2</sub> huff-n-puff processes in Bakken formation," *Fuel*, vol. 190, pp. 145–162, 2017.
  - [22] Y. Wang, J. Hou, Z. Song, D. Yuan, J. Zhang, and T. Zhao, "A case study on simulation of in-situ CO<sub>2</sub> Huff-'n'-Puff process," *SPE Reservoir Evaluation & Engineering*, vol. 21, no. 1, pp. 109–121, 2018.
  - [23] Q. Ma, S. Yang, H. Chen et al., "Effect and influencing factors of CO<sub>2</sub> huff and puff in a tight oil reservoir—taking the Lucaogou formation in the Xinjiang Jimsar sag as an example," *Petroleum Science Bulletin*, vol. 3, no. 4, pp. 434–445, 2018.
  - [24] Y. Tang, Z. Su, J. He, and F. Yang, "Numerical simulation and optimization of enhanced oil recovery by the in situ generated CO<sub>2</sub>Huff-n-Puff process with compound surfactant," *Journal of Chemistry*, vol. 2016, Article ID 6731848, 13 pages, 2016.
  - [25] C. Chen, M. T. Balhoff, and K. K. Mohanty, "Effect of reservoir heterogeneity on primary recovery and CO<sub>2</sub> huff 'n' puff recovery in shale-oil reservoirs," *SPE Reservoir Evaluation & Engineering*, vol. 17, no. 3, pp. 404–413, 2014.
  - [26] Y. Wang, J. Hou, and Y. Tang, "In-situ CO<sub>2</sub> generation huff-n-puff for enhanced oil recovery: laboratory experiments and numerical simulations," *Journal of Petroleum Science and Engineering*, vol. 145, pp. 183–193, 2016.
  - [27] A. Ellafi and H. Jabbari, "Understanding the mechanisms of huff-n-puff, CO<sub>2</sub>-EOR in liquid-rich shale plays: Bakken case study," in *Proceeding of SPE Canada Unconventional Resources Conference, SPE Paper SPE-200001-MS*, September–October 2020.
  - [28] Y. Jiang, "Experiment and characterization on phase behavior of CO<sub>2</sub> and crude oil in porous media," *Reservoir Evaluation and Development*, vol. 10, no. 3, pp. 23–27, 2020.
  - [29] W. Yu, H. Lashgari, and K. Sepehrnoori, "Simulation study of CO<sub>2</sub> huff-n-puff process in Bakken tight oil reservoirs," in *Proceeding of SPE Western North American and Rocky Mountain Joint Meeting, SPE Paper SPE-169575-MS*, Denver, CO, USA, April 2014.
  - [30] L. Li, Z. Jing, X. Zhao et al., "Understanding of CO<sub>2</sub> huff and puff effect of Chang 7 tight oil in Y oilfield," *Petrochemical Industry Application*, vol. 37, no. 1, pp. 46–48+52, 2018.
  - [31] S. B. Hawthorne, C. D. Gorecki, J. A. Sorensen, E. N. Steadman, J. A. Harju, and S. Melzer, "Hydrocarbon mobilization mechanisms from upper, middle, and lower Bakken reservoir rocks exposed to CO<sub>2</sub>," in *Proceeding of SPE Unconventional Resources Conference, SPE paper SPE-167200-MS*, Calgary, Alberta, Canada, November 2013.
  - [32] G. Hou, "Practice and understanding of the CO<sub>2</sub> huff-puff for the volume fractured horizontal well in tight oil reservoirs," *Petroleum Geology and Oilfield Development in Daqing*, vol. 37, no. 3, pp. 163–167, 2018.
  - [33] A. Bera and T. Babadagli, "Relative permeability of foamy oil for different types of dissolved gases," *SPE Reservoir Evaluation & Engineering*, vol. 19, no. 4, pp. 604–619, 2016.
  - [34] Y. Jia, L. Huang, and L. Sun, "The mechanism and simulation research of 'foamy oil' during CO<sub>2</sub> flooding," in *Proceeding of Carbon Management Technology Conference*, Houston, TX, USA, July 2017.
  - [35] C. Or, K. Sasaki, Y. Sugai, M. Makano, and M. Imai, "Swelling and viscosity reduction of heavy oil by CO<sub>2</sub>-Gas foaming in immiscible condition," *SPE Reservoir Evaluation & Engineering*, vol. 19, no. 2, pp. 294–304, 2016.
  - [36] P. Zuloaga, W. Yu, J. Miao, and K. Sepehrnoori, "Performance evaluation of CO<sub>2</sub> huff-n-puff and continuous CO<sub>2</sub> injection in tight oil reservoirs," *Energy*, vol. 134, pp. 181–192, 2017.
  - [37] R. Sun, W. Yu, F. Xu, H. Pu, and J. Miao, "Compositional simulation of CO<sub>2</sub> huff-n-puff process in middle Bakken tight oil reservoirs with hydraulic fractures," *Fuel*, vol. 236, pp. 1446–1457, 2019.
  - [38] C. Wang, *Experimental study on CO<sub>2</sub> injection in tight reservoir*, Master's Thesis, Southwest Petroleum University, 2016.
  - [39] Z. Yang, X. Liu, Z. Zhang, T. Zhou, and S. Zhao, "Physical simulation of staged-fracturing horizontal wells using CO<sub>2</sub> huff and puff in tight oil reservoirs," *Acta Petrolei Sinica*, vol. 36, no. 6, pp. 724–729, 2015.



- [40] G. Liu, "Optimization of injection and production parameters of CO<sub>2</sub> huff and puff by horizontal wells with volume fracturing in tight oil," *Petroleum Geology and Engineering*, vol. 34, no. 2, pp. 90–93, 2020.
- [41] J. Ma, X. Wang, R. Gao et al., "Enhanced light oil recovery from tight formations through CO<sub>2</sub> huff 'n' puff processes," *Fuel*, vol. 154, pp. 35–44, 2015.
- [42] Y. Tang, S. Hu, Y. Wang et al., "Phase behaviors of CO<sub>2</sub> in the whole process of injection–fracturing–flowback: a case study of well SH52 in a tight sandstone gas reservoir of the Shenmu Gas Field, Ordos Basin," *Natural Gas Industry*, vol. 39, no. 9, pp. 58–64, 2019.
- [43] D. R. S. Lemus, W. Yan, and E. H. Stenby, "Phase equilibrium in shale including porous media effects," in *Proceeding of International Petroleum Exhibition and Conference, SPE Paper SPE-197278-MS*, Abu Dhabi, UAE, November 2019.
- [44] B. Nojabaei, R. T. Johns, and L. Chu, "Effect of capillary pressure on phase behavior in tight rocks and shales," *SPE Reservoir Evaluation & Engineering*, vol. 16, no. 3, pp. 281–289, 2013.
- [45] G. Yang and X. Li, "Improved equation of state model for gas huff-n-puff EOR processes in unconventional reservoirs," in *Proceeding of SPE/AAPG/SEG Unconventional Resources Technology Conference, URTEC-2020-3179-MS*, 2020.
- [46] L. Sheng, J. L. Lutkenhaus, and H. Nasrabadi, "Experimental study of confinement effect on hydrocarbon phase behavior in nano-scale porous media using differential scanning calorimetry," in *Proceeding of SPE Annual Technical Conference and Exhibition, SPE Paper SPE-175095-MS*, Houston, TX, USA, September 2015.
- [47] J. Pang, J. Zuo, D. Zhang, and L. Du, "Effect of porous media on saturation pressures of shale gas and shale oil," in *Proceeding of SPE Canadian Unconventional Resources Conference, SPE Paper SPE-161143-MS*, Calgary, Canada, 2012.
- [48] S. Wu, Z. Li, H. K. Sarma, C. Zhang, and G. Lv, "Impact of fluid property shift and capillarity on the recovery mechanisms of CO<sub>2</sub> injection in tight oil reservoirs," *Greenhouse Gases: Science & Technology*, vol. 9, no. 5, pp. 965–978, 2019.
- [49] N. Zhu, *Research on phase behavior change and seepage characteristics of CO<sub>2</sub> and oil in porous media*, PhD Degree Thesis, Dalian University of Technology, 2013.
- [50] H. Yu, X. Lu, W. Fu et al., "Determination of minimum near miscible pressure region during CO<sub>2</sub> and associated gas injection for tight oil reservoir in Ordos Basin China," *Fuel*, vol. 263, article 116737, 2020.
- [51] N. Li, X. Tan, X. Tian, H. Wu, and X. Li, "Study on the phase behavior and displacement characteristics of CO<sub>2</sub> flooding in porous media," *Journal of Chengdu University of Technology (Science & Technology Edition)*, vol. 45, no. 4, pp. 501–504, 2018.
- [52] C. J. Werth, C. Zhang, M. L. Brusseau, M. Oostrom, and T. Baumann, "A review of non-invasive imaging methods and applications in contaminant hydrogeology research," *Journal of Contaminant Hydrogeology*, vol. 113, no. 1–4, pp. 1–24, 2010.
- [53] Z. Jin and A. Firoozabadi, "Phase behavior and flow in shale nanopores from molecular simulations," in *Proceeding of SPE Annual Technical Conference and Exhibition*, Houston, TX, USA, September 2015.
- [54] T. Wu and A. Firoozabadi, "Methane flow in shale nanopores with kerogen microstructure by molecular simulations," in *Proceeding of SPE Annual Technical Conference and Exhibition*, Dallas, TX, USA, September 2018.
- [55] Y. Tang, C. Hou, Y. He et al., "Review on pore structure characterization and microscopic flow mechanism of CO<sub>2</sub> flooding in porous media," *Energy Technology*, 2020.
- [56] D. Asthagiri, P. M. Singer, A. V. Parambathu, Z. Chen, G. J. Hirasaki, and W. G. Chapman, "Molecular dynamics simulations of NMR relaxation and diffusion of hydrocarbons," in *Proceeding of SEG/AAPG/EAGE/SPE Research and Development Petroleum Conference and Exhibition*, Abu Dhabi, UAE, 2018.
- [57] H. Wang, Z. Lun, C. Lv et al., "Nuclear-magnetic-resonance study on mechanisms of oil mobilization in tight sandstone reservoir exposed to carbon dioxide," in *Proceeding of SPE Improved Oil Recovery Conference, SPE paper SPE-179554-PA*, Tulsa, OK, USA, April 2017.
- [58] T. Chen, Z. Yang, Y. Luo et al., "Evaluation of displacement effects of different injection media in tight oil sandstone by online nuclear magnetic resonance," *Energies*, vol. 11, no. 10, pp. 2836–2852, 2018.
- [59] P. Xiao, C. Lv, R. Wang et al., "Laboratory study heterogeneity impact on microscopic residual oil distribution in tight sandstone cores during CO<sub>2</sub> immiscible flooding," *Energy Sources Part A: Recovery, Utilization & Environmental Effects*, vol. 41, no. 23, pp. 2895–2905, 2019.
- [60] J. Cao, Y. Liang, Y. Masuda et al., "Molecular simulation of methane adsorption behavior in kerogen nanopores for shale gas resource assessment," in *Proceeding of International Petroleum Technology Conference*, Beijing, China, March 2019.
- [61] D. Makimura, M. Kunieda, Y. Liang, T. Matsuoka, S. Takahashi, and H. Okabe, "Application of molecular simulations to CO<sub>2</sub>-EOR: phase-equilibria and interfacial phenomena," in *Proceeding of International Petroleum Technology Conference*, Bangkok, Thailand, November 2011.
- [62] K. Mohammad, T. B. Ali, J. R. Hansel, and M. Valera, "Enhanced oil recovery of shale oil: a molecular simulation study," in *Proceeding of SPE/AAPG/SEG Unconventional Resources Technology Conference*, Denver, TX, USA, 2019.
- [63] M. Guo, *A molecular simulation study on adsorption and flow characteristics of tight oil*, Master Degree Thesis, China University of Petroleum (East China), 2018.
- [64] N. Okamoto, Y. Liang, S. Murata, T. Matsuoka, T. Akai, and S. Takagi, "Slip velocity and permeability of gas flow in nanopores for shale gas development," in *Proceeding of SPE Asia Pacific Unconventional Resources Conference and Exhibition*, Brisbane, Australia, November 2015.
- [65] X. Duan, Z. Hu, N. Shao et al., "Establishment of a new slip permeability model of gas flow in shale nanopores based on experimental and molecular dynamics simulations studies," *Journal of Petroleum Science and Engineering*, vol. 193, article 107365, 2020.
- [66] Z. Zhu, C. Fang, R. Qiao, X. Yin, and E. Ozkan, "Experimental and molecular insights on mitigation of hydrocarbon sieving in Niobrara shale by CO<sub>2</sub> huff 'n' puff," in *Proceeding of SPE Annual Technical Conference and Exhibition, SPE Paper SPE-196136-PA*, Calgary, Alberta, Canada, September–October 2019.
- [67] A. Takbiri-Borujeni, M. Kazemi, S. Liu, and Z. Zhong, "Molecular simulation of enhanced oil recovery in shale," *Energy Procedia*, vol. 158, pp. 6067–6072, 2019.
- [68] T. Fang, Y. Zhang, Y. Yan, Z. Wang, and J. Zhang, "Molecular insight into the oil extraction and transport in CO<sub>2</sub> flooding

- with reservoir depressurization,” *International Journal of Heat and Mass Transfer*, vol. 148, article 119051, 2020.
- [69] Z. Sun, X. Li, W. Liu, T. Zhang, M. He, and H. Nasrabadi, “Molecular dynamics of methane flow behavior through realistic organic nanopores under geologic shale condition: pore size and kerogen types,” *Chemical Engineering Journal*, vol. 398, article 124341, 2020.
- [70] T. Zhou, X. Liu, Y. Wang, C. Chun, and C. Gai, “Experiments of CO<sub>2</sub> huff-n-puff process in staged fracturing horizontal wells for developing tight oil reservoirs,” *Journal of Northwest University (Science & Technology Edition)*, vol. 39, no. 2, pp. 125–131, 2017.
- [71] P. Nguyen, J. W. Carey, S. V. Hari, and P. Mark, “Effectiveness of supercritical-CO<sub>2</sub> and N<sub>2</sub> huff-and-puff methods of enhanced oil recovery in shale fracture networks using microfluidic experiments,” *Applied Energy*, vol. 230, pp. 160–174, 2018.
- [72] D. Alfarge, M. Wei, and B. Bai, “CO<sub>2</sub>-EOR mechanisms in huff-n-puff operations in shale oil reservoirs based on history matching results,” *Fuel*, vol. 226, pp. 112–120, 2018.
- [73] L. Li, Y. Du, and J. Sheng, “Investigation of gas penetration depth during gas huff-n-puff EOR process in unconventional oil reservoirs,” in *Proceeding of SPE Canada Unconventional Resources Conference, SPE Paper 189804-MS*, Calgary, Alberta, Canada, March 2018.
- [74] Q. Wang, R. Jiang, Y. Cui, and J. Yuan, “Pre-Darcy flow behavior of CO<sub>2</sub> huff-n-puff development in Fuyu tight formation: Experiment and numerical evaluation,” *Journal of Petroleum Science and Engineering*, vol. 186, article 106773, 2020.
- [75] M. Chen, L. Cheng, R. Cao, C. Lv, J. Wu, and H. Liu, “A pore network model for studying boundary layer effect on fluid flow in tight formation,” in *Proceeding of the SPE Annual Caspian Technical Conference and Exhibition*, Baku, Azerbaijan, November 2017.

## Research Article

# Sand Production Prediction Model for Tight Sandstone Oil Reservoirs

Zhan-dong Li <sup>1,2,3,4</sup>, Hong Pang <sup>3</sup>, Zhong Li <sup>5</sup>, Hai-xiang Zhang <sup>1,2,3</sup>,  
Dian-ju Wang <sup>2,3</sup> and Ji Li <sup>2,3</sup>

<sup>1</sup>Key Laboratory of Gas Hydrate Efficient Development of Heilongjiang, Daqing 163318, China

<sup>2</sup>College of Offshore Oil & Gas Engineering, Northeast Petroleum University, Heilongjiang Daqing 163318, China

<sup>3</sup>College of Offshore Oil and Gas Engineering, Northeast Petroleum University, Daqing 163318, China

<sup>4</sup>Sanya Offshore Oil & Gas Research Institute, Northeast Petroleum University, Hainan Sanya 572025, China

<sup>5</sup>CNOOC Research Institute, Beijing 100027, China

Correspondence should be addressed to Zhan-dong Li; [13644593771@163.com](mailto:13644593771@163.com)

Received 15 May 2020; Revised 18 July 2020; Accepted 30 September 2020; Published 17 October 2020

Academic Editor: Keliu Wu

Copyright © 2020 Zhan-dong Li et al. This is an open access article distributed under the Creative Commons Attribution License, which permits unrestricted use, distribution, and reproduction in any medium, provided the original work is properly cited.

Tight oil is an important unconventional resource, and sand production is an inevitable challenge during the field development. In this paper, based on data from the Daqing oilfield in Songliao Basin, the sand production of the tight sandstone oil reservoir is studied from the perspective of seepage and in situ stress distribution. Based on the combination of the formation fluid seepage law and the stress distribution around the well, a sand production prediction model is proposed to quantitatively estimate the sand production rate. The sand production prediction model is built based on the derivation of the sand production rate, which is well validated against the field data in the Daqing field with a relative error of 4.38%. The following conclusions are drawn: (1) after the critical pressure difference is exceeded, the sand production rate is smaller with a higher flowing bottom-hole pressure; (2) a smaller sand production radius makes the formation more unstable and causes a more severe sand production; and (3) various sand production rates exhibit due to different permeabilities. A larger permeability results in a higher sand production rate. The findings of this study can help for sand production prediction in the tight sandstone oil reservoir.

## 1. Introduction

Tight oil and gas is a popular energy source in the oil industry, which supports the oil and gas revolution [1]. According to statistics, the total reserves of global tight oil reservoirs are about  $9294 \times 10^8$  t, and the technically recoverable reserves are about  $460 \times 10^8$  t, among which more than 60% of the tight oil resources are mainly concentrated in 6 countries including Russia, the United States, China, Libya, Argentina, and Australia [2]. The technically recoverable amount of tight oil in the United States is about  $81.2 \times 10^8$  t, more than six times that of China. Although there are abundant resources in tight oil reservoirs, the recovery rate is generally low. In the Bakken formation in North America, for example, as one of the earliest tight reservoirs in the world, the average recovery from natural depletion in the Bakken formation is

only 5% to 10%. In 2016, the annual production of tight oil in the United States reached  $2.12 \times 10^8$  t, accounting for 52.6% of the total crude oil production in the United States. In the same year, the external oil dependence percentage in the United States dropped to about 33%.

The development of tight oil reservoirs in China started relatively late [3]. So far, a number of tight oil reserves have been discovered in Ordos, Songliao, Junggar, and Bohai bay, but they are basically in the early technical stage [4]. The supporting technologies for tight reservoir development in the United States cannot be directly applied to tight reservoir development in China due to the following reasons: most tight reservoirs in the United States are marine deposits, with high pressure, high gas-oil ratio, high oil mobility, and brittle reservoir rocks. Most of the tight reservoirs in China are continental deposits with insufficient formation energy,

low gas-oil ratio, crude oil of high viscosity, and high content of rock-plastic minerals, which negatively affect the fracturing of reservoirs. In contrast, China's tight reservoirs have a more complex geology, worse reservoir physical conditions, and more severe technical challenges. At present, China has not formed a mature development theory, experience, and equipment for the economic development of tight reservoirs, and the key technologies of tight reservoir development are still in the preparation stage before the breakthrough. China's tight oil reservoirs are still in their infancy due to the small scale, low production per well, and high development costs. In summary, the economic deviation of China's tight oil development poses a greater challenge to economic development [5].

Sand production is the inevitable problem in the development of tight oil fields. The prediction of sand production is now a popular research topic in both academia and industry. Generally, the sand production happens when the formation stress exceeds the rock strength, which is dominated by the cementation of cements, adhesion of fluids, and friction between particles[6]. The formation stress includes the structural stress, overburden stress, flow force, and production pressure difference [7]. The mechanical mechanisms of sand production include three failure types (Figure 1): (1) shear failure. The rock will exhibit the status of elastic deformation or plastic deformation while the effective stress of rock exceeds its compressive strength; (2) tensile failure. The flow channel for sand production will be generated if the stress exceeds the tensile strength; this is, the sand production will happen if the stress at the borehole is higher than the tensile strength; (3) bond failure. This mechanism is more significant in the weak cementation formation. The bond strength dominates the erosion of bare surfaces. The sand will be produced if the drag force caused by fluid flow is higher than the bond force [8]. Thus, a sand production prediction model is essential for sand control and well management [9].

The sand production is closely related with the petrophysical and fluid properties [10]. Many papers reported the sand production under the stress theory, classical sand production factors, sand production experiment, and effects of wetted fluid concentration on sand arch. Based on these studies, the main controlling factors for sand production are geology, well completion, and oil/gas production [11, 12]. The geological factors include structural stress, interparticle bonding, and fluid properties [13]. Completion factors include borehole size, well deviation, and perforation. Production factors include production pressure difference, fluid flow in the formation, water injection, formation damage, and other factors. Transport of oil in the fractured tight reservoirs can be thought of as an advective-diffusive-reactive flow process [14]. Other factors include oil viscosity and rock wettability. Under the pressure decline, the viscosity of degassed oil increases, and the wettability changes from water-wet to oil-wet. These will transform the capillary pressure from driving force to resistant force, which leads to the increase of dragging force of fluid and promotes the sand production[15]. However, previous studies are focused more on the qualitative methodology with considering very few factors. The sand production mechanism can only be deeply

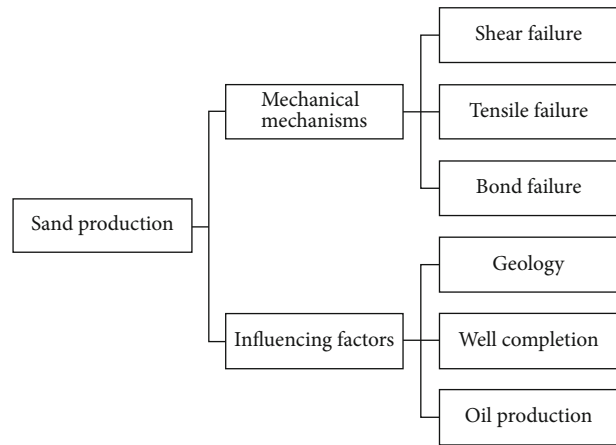


FIGURE 1: General sketch of the sand production problem.

understood by finding a clear relationship between rock properties, fluid flow, and sand production rate [16].

Few studies have been performed on sand production prediction for the tight sandstone oil reservoir [17]. In the industry, the sand production factors of the tight sandstone oil reservoir are still not clear, and factors resulting in the sand production risk are also in need to be explored [18]. Around the tight oil production wells after large-scale fracturing, rocks are cracked and destroyed under artificial action formation rock structure, so formation stress should be the main cause of sand production, and crude oil mainly flows into the bottom of the well through the fracture after fracturing. With the focus on these limitations, this study provides a sand production prediction model to dynamically assist the sand control.

Previous studies have mostly described the sand production mechanism qualitatively. In this paper, a quantitative calculation model for sand production of tight oil reservoir is obtained by combining the seepage law of tight oil with the analysis of well stress. The sand production prediction model in this study is firstly constructed by bridging the rock mechanical theory and fluid flow [19]. This model is secondly validated against the field data from the Daqing oilfield in Songliao Basin. The sand production mechanisms are thirdly discussed based on the model, which provides theoretical basis for the tight sandstone oil reservoir development [20–22].

Firstly, the seepage model of the tight sandstone oil reservoir is established to obtain the sand production within the sand production radius; then, the stress around the well is analyzed to calculate the sand production radius, and finally, the two are used to obtain the sand production from the tight sandstone oil reservoir.

## 2. Model Establishment

Due to the extremely low permeability of tight reservoirs, large-scale fracturing is generally required for production. The seepage of oil and gas in fractures follows Darcy's law, and the permeability of fractures is far greater than that of the formation matrix. Therefore, oil flow can be considered

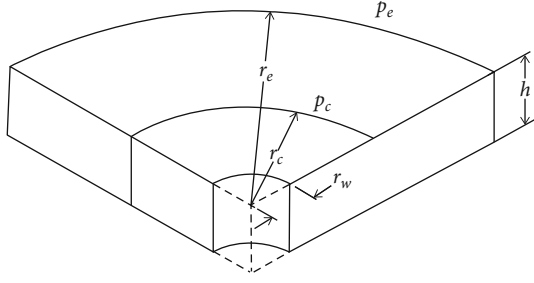


FIGURE 2: Circular finite oil reservoir model.

only through fractures during production, ignoring the formation bedrock oil production. The reservoir is assumed as a circular finite oil reservoir as shown in Figure 2. The reservoir thickness, the boundary radius, and the well radius are expressed as  $h$ ,  $r_e$ , and  $r_w$ .

The main assumptions are as follows:

- (1) Only the flow of oil and solid phases is considered
- (2) Isothermal condition
- (3) Effects of well completions on sand production are omitted

Under the plastic deformation, the relationship between the volume change and the shear velocity is as follows [23, 24]:

$$\frac{\partial v}{\partial r} + \gamma \frac{v}{r} = \Lambda \theta_\alpha \left( \frac{\partial v}{\partial r} - \frac{v}{r} \right), \quad (1)$$

$$\theta_\sigma = \text{sgn} \left( \frac{\partial v}{\partial r} - \frac{v}{r} \right). \quad (2)$$

The expansion coefficient  $\Lambda$  is related with radial stress; the flow-pattern coefficient  $\gamma$  equals to 1 in the radial flow case and 2 in the spherical flow case. By solving equation (2), the solid velocity can be obtained as follows:

$$v = \frac{C}{r^n}, \quad (3)$$

$$n = \frac{\gamma + \Lambda \theta_\alpha}{1 - \Lambda \theta_\alpha}.$$

The oil and sand production rates can be calculated as equations (4) and (5), respectively:

$$q_f = 2\pi r h w(r), \quad (4)$$

$$q_s = 2\pi r h v(r). \quad (5)$$

For the sand production formation, the velocity difference between oil and solids can be calculated as follows:

$$w - v = \frac{\beta K}{\mu} \cdot \frac{dp}{dr}, \quad (6)$$

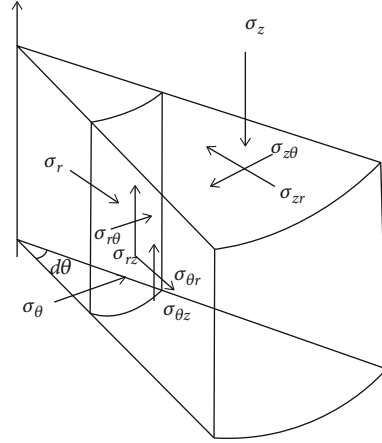


FIGURE 3: Microunit stress around the wellbore.

$$\frac{q_f}{2\pi r h} - \frac{C}{r^n} = \frac{\beta K}{\mu} \cdot \frac{dp}{dr}. \quad (7)$$

The integration procedure is as equations (8)–(10):

$$\int_{r_w}^{r_e} \frac{q_f}{2\pi r h} dr - \int_{r_w}^{r_e} \frac{C}{r^n} dr = \int_{p_w}^{p_e} \frac{\beta K}{\mu} dp, \quad (8)$$

$$\frac{q_f}{2\pi h} \ln \frac{r_e}{r_w} - \frac{C(r_c^{1-n} - r_w^{1-n})}{1-n} = \frac{\beta K(p_e - p_w)}{\mu}, \quad (9)$$

$$C = \frac{q_f/2\pi h \ln r_e/r_w - \beta K(p_e - p_w)/\mu}{(r_c^{1-n} - r_w^{1-n})/1-n}. \quad (10)$$

The sand production rate can thus be obtained as follows:

$$q_s(r_w) = \frac{[q_f \ln(r_e/r_w) - 2\pi h \beta K(p_e - p_w)/\mu](1-n)}{(r_c^{1-n}/r_w^{1-n} - 1)}. \quad (11)$$

The stress distribution around the well is studied by taking a microelement of the rock around the well, and the stress can be classified as radial stress ( $\sigma_r$ ), tangential stress ( $\sigma_\theta$ ), axial stress ( $\sigma_z$ ), and shear stress (Figure 3,  $\sigma_{\theta r}$ ,  $\sigma_{\theta z}$ , and  $\sigma_{rz}$ ).

The principal stress around the wellbore can be expressed by matrix eigenvalues [25, 26]:

$$\begin{vmatrix} \sigma_r - \sigma & \sigma_{r\theta} & \sigma_{zr} \\ \sigma_{\theta r} & \sigma_\theta - \sigma & \sigma_{\theta z} \\ \sigma_{zr} & \sigma_{\theta z} & \sigma_z - \sigma \end{vmatrix} r = 0. \quad (12)$$



TABLE 1: Petrophysical parameters of the Daqing oilfield.

Average reservoir pressure/MPa	Reservoir boundary radius/m	Well radius/m	Permeability/ $10^{-3} \mu\text{m}^2$	Depth/m	Thickness/m	Viscosity/mPa-s
28.66	186.47	0.1015	2.3	2540-2536	53.5	19.5

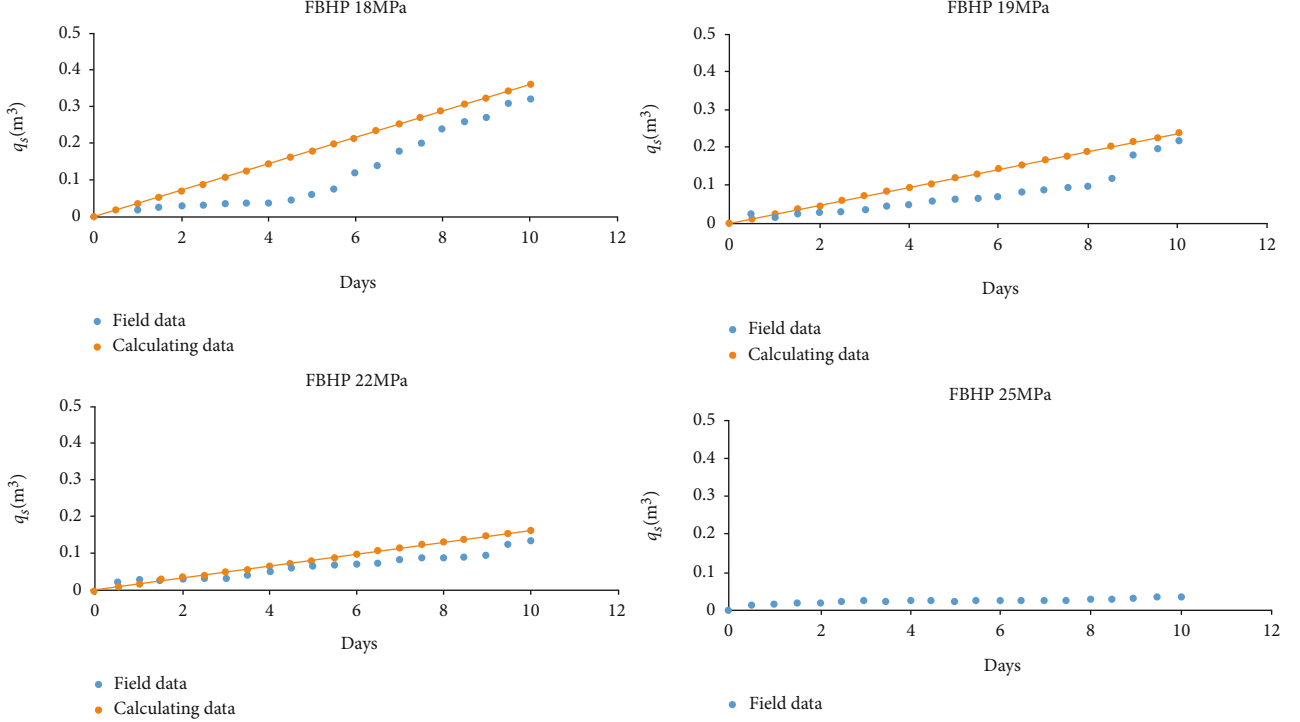


FIGURE 4: Relationship between flowing bottom-hole pressure and sand production rate.

The principle stress can be got as follows:

$$\begin{cases} \sigma'_1 = \frac{-b - 2A\sqrt{\cos(\theta/3)}}{3} \\ \sigma'_2 = \frac{[-b + (\cos(\theta/3) + \sqrt{3}\sin(\theta/3))\sqrt{A}]}{3}, \\ \sigma'_3 = \frac{[-b + (\cos(\theta/3) - \sqrt{3}\sin(\theta/3))\sqrt{A}]}{3} \end{cases} \quad (13)$$

where

$$b = -(\sigma_r + \sigma_\theta + \sigma_z), \quad (14)$$

$$c = \sigma_r\sigma_z + \sigma_\theta\sigma_z + \sigma_r\sigma_\theta - \sigma_r^2 - \sigma_\theta^2 - \sigma_z^2, \quad (15)$$

$$d = -(\sigma_r\sigma_\theta\sigma_z + 2\sigma_r\sigma_\theta\sigma_{zr} - \sigma_r\sigma_{\theta z}^2 - \sigma_\theta\sigma_{zr}^2 - \sigma_z\sigma_{r\theta}^2), \quad (16)$$

$$A = b^2 - 3c, B = bc - 9d, \quad (17)$$

$$\theta = \arccos\left(\frac{2Ab - 3B}{2A\sqrt{A}}\right). \quad (18)$$

The reservoir pressure is a function of flowing bottom-

hole pressure (FBHP) within the boundary of sand production, which can be expressed as follows:

$$p_c = p_w + \frac{p_0}{\ln(r_e/r_w)} \ln \frac{r_c}{r_w} \quad (19)$$

especially when the radius equals to  $r_c$

$$\begin{aligned} \sigma_1(p_w, r_c) - \beta_b p_p(p_w, r_c) &= 2Y \tan\left(\frac{\varphi}{2} + \frac{\pi}{4}\right) \\ &+ [\sigma_3(p_w, r_c) - \beta_b p_p(p_w, r_c)] \tan^2\left(\frac{\varphi}{2} + \frac{\pi}{4}\right). \end{aligned} \quad (20)$$

The maximum and minimum stress  $\sigma_1$  and  $\sigma_3$  can be obtained based on stress matrix:

$$\sigma_1(p_w, r_c) = \max\{\sigma'_1, \sigma'_2, \sigma'_3\}, \quad (21)$$

$$\sigma_3(p_w, r_c) = \min\{\sigma'_1, \sigma'_2, \sigma'_3\}. \quad (22)$$

Calculate the value of  $\sigma'_1, \sigma'_2$  and  $\sigma'_3$  at a certain radius, then the values of  $\sigma_1$  and  $\sigma_3$  are determined, and  $\sigma_1$  and  $\sigma_3$  are substituted into Equation (20). When Equation (20) is

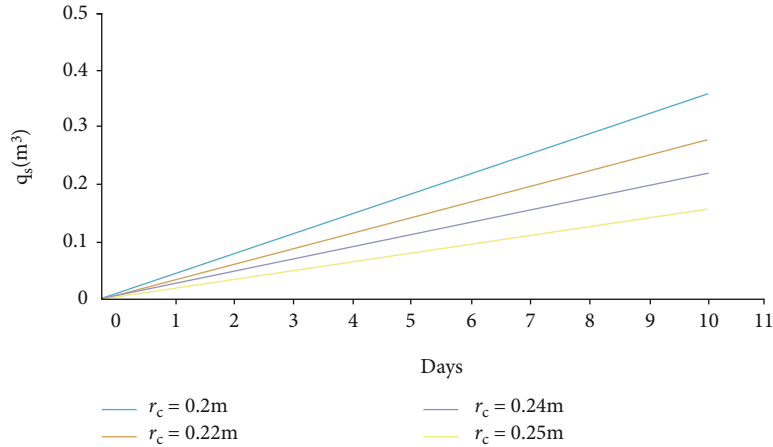


FIGURE 5: Relationship between the sand production rate and time under difference sand production radii (18 MPa).

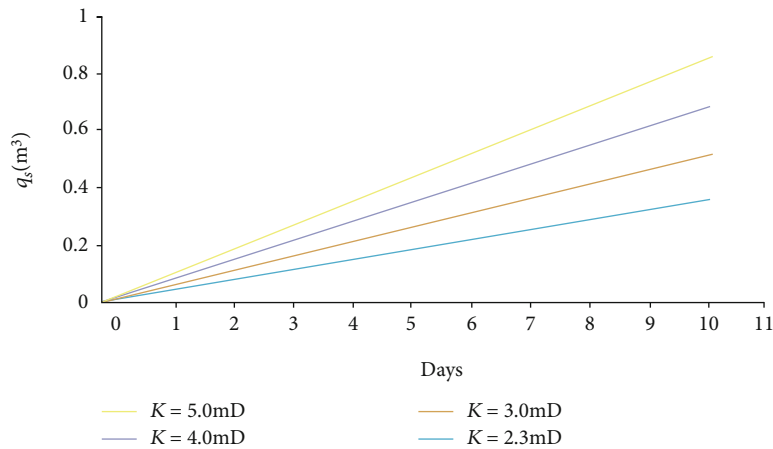


FIGURE 6: Relationship between the sand production rate and time under different permeabilities (18 MPa).

equal, the radius is determined to be the sand producing radius  $r_c$ , so the sand quantity can be calculated according to Equation (11).

### 3. Results and Discussions

In order to validate the accuracy of the proposed model, the Daqing oilfield in Songliao Basin is selected. The parameters of this tight sandstone oil reservoir are shown in Table 1. Based on these parameters, the critical FBHP of sand production is calculated and validated against real date.

Field measurement reports the critical FBHP which is 24.21 MPa, and the critical pressure difference is 4.45 MPa. This model provides an estimation of 25.27 MPa for the FBHP, which has a relative error of 4.38% compared with field data. This validation indicates the proposed model is both practical and accurate.

**3.1. Effects of Flowing Bottom-Hole Pressure on Sand Production.** The sand production rate is related with FBHP. Figure 4 shows the sand production rate under FBHP of 18 MPa, 19 MPa, 22 MPa, and 25 MPa. The solid line is the

sand production rate from the model, and the dotted points are the sand production rate from field measurement. With the time being, the FHP becomes smaller, and the sand production is easier. Specially, the sand production rate is the highest under the FBHP of 18 MPa. As the well completion factor is not considered in this model, thus the estimated critical BHP is higher than the real data. There are two types of sands during the sand production: (1) the free sands in the pores and (2) the detached sands from rock matrix. The sand production curve thus has an inflection point. With the time being, the relative difference between the model result and real data is smaller, which further shows the practical application of this model.

**3.2. Effects of Sand Production Radius on the Sand Production Rate.** The FBHP is significantly affected by sand production radius. With a larger sand production radius, the critical pressure difference will be higher. A larger sand production radius results in a lower sand production rate under a certain FBHP. Figure 5 shows the sand production rate under the FBHP of 18 MPa and sand production radii of 0.20 m, 0.22 m, 0.24 m, and 0.25 m. Overall, the possibility of sand

production is larger with the increase of producing time. While a location is closer to the borehole, the moment of force on a particle is larger, which further results in a higher sand production rate. This is because the oil production rate near the borehole is high, and the rock failure is severe, which is caused by a quick change of oil saturation and pore pressure. Compared with the near-wellbore region, the possibility of sand production in the region far away from the borehole is much lower.

**3.3. Effects of Permeability on the Sand Production Rate.** The sand production rate is also significantly affected by the permeability. Figure 6 indicates the sand production rate under the FBHP of 18 MPa and different formation permeabilities (2.3 mD, 3.0 mD, 4.0 mD, and 5.0 mD). We can see that the sand production rate is higher with a larger permeability. This is because the oil rate is higher under a larger permeability, which leads to a rapid change of pore pressure and oil saturation.

## 4. Summary and Conclusions

Although the fluid seepage and stress distribution around the well have been considered in the development of tight sandstone reservoirs, the problems encountered in actual reservoir development are more complicated. For example, the non-Darcy seepage of the formation fluid, the multimedia seepage, and the complicated stress distribution around the well, this model does not consider the above problems, there are still deficiencies, and the calculation results still have errors compared with the actual situation.

The sand production prediction model is built based on the derivation of the sand production rate, which is well validated against the field data in the Daqing field with a relative error of 4.38%. The main conclusions of this paper are as follows:

- (1) The sand production rate of the tight sandstone oil reservoir is closely related with FBHP. While the critical pressure difference is exceeded, a higher FBHP leads to a lower sand production rate
- (2) The critical FBHP is significantly affected by sand production radius. Under a certain FBHP, the sand production is more severe with a smaller sand production radius and a closer distance to borehole
- (3) Different tight sandstone oil reservoir permeabilities result in various sand production rates. A higher permeability induced a more rapid change of pore pressure and oil saturation, which further increases the possibility of sand production

## Nomenclature

### Roman Symbols

$q_f$ :	oil production rate, $m^3/d$
$K$ :	permeability, $10^{-3}\mu m^2$
$h$ :	thickness, m

$p$ :	pressure, MPa
$\mu$ :	viscosity, mPa s
$\wedge$ :	expansion coefficient
$\gamma$ :	flow-pattern coefficient
$v$ :	solid velocity, m/s
$r$ :	radial distance, m
$C$ :	integration constant, m
$n$ :	expansion index
$w$ :	oil velocity
$(dp/dr)$ :	pressure gradient coefficient
$\beta$ :	coefficient
$r_e$ :	boundary radius, m
$r_w$ :	well radius, m
$r_c$ :	sand production radius, m
$p_e$ :	reservoir pressure, MPa
$p_w$ :	FBHP, MPa.

## Data Availability

Data available upon request.

## Conflicts of Interest

We declare that we have no conflict of interest.

## Acknowledgments

The authors are grateful for CNOOC Key Research and Development Projects (CCL2019ZJFN1113), (CCL2019ZJFN1114), and (CCL2020ZJFN0314) and the Development of Natural Gas Hydrate Exploitation Mechanism and Simulation Platform (TSTAU-R2018018).

## References

- [1] US Energy Information Administration (EIA), "Outlook for shale gas and tight oil development in the US [EB/OL]," 2013, [https://www.eia.gov/pressroom/presentations/sieminski\\_05212013.pdf](https://www.eia.gov/pressroom/presentations/sieminski_05212013.pdf).
- [2] EIA, "Tight oil remains the leading source of future U. S. crude oil production [EB/OL]," 2018, <http://www.eia.gov/todayinenergy/detail.php?id=35052>.
- [3] Y. Wang, L. Liu, S. Li et al., "The forming mechanism and process of tight oil sand reservoirs: a case study of Chang 8 oil layers of the upper triassic Yanchang formation in the western Jiyuan area of the Ordos Basin, China," *Journal of Petroleum Science & Engineering*, vol. 158, pp. 29–46, 2017.
- [4] M. M. Rahman and M. K. Rahman, "A review of hydraulic fracture models and development of an improved pseudo-3d model for stimulating tight oil/gas Sand," *Energy Sources, Part A: Recovery, Utilization, and Environmental Effects*, vol. 32, no. 15, pp. 1416–1436, 2010.
- [5] X. P. Zhai, Y. S. Lou, B. S. He, and H. Ji, "Mechanical analyze of casing failure with sand production in loose sandstone reservoir," *Applied Mechanics and Materials*, vol. 217–219, pp. 2283–2286, 2012.
- [6] A. Shabdirova, N. H. Minh, and Y. Zhao, "A sand production prediction model for weak sandstone reservoir in Kazakhstan," *Journal of Rock Mechanics and Geotechnical Engineering*, vol. 11, no. 4, pp. 760–769, 2019.

- [7] H. Rahmati, M. Jafarpour, S. Azadbakht et al., "Review of sand production prediction models," *Journal of Petroleum Engineering*, vol. 2013, Article ID 864981, 16 pages, 2013.
- [8] J. Deng, L. Wang, P. Li, and W. Zhao, "The critical pressure difference prediction of sand production in deepwater sandstone gas reservoirs," *Petroleum Science and Technology*, vol. 31, no. 19, pp. 1925–1932, 2013.
- [9] A. W. Martinius, M. Fustic, D. L. Garner et al., "Reservoir characterization and multiscale heterogeneity modeling of inclined heterolithic strata for bitumen-production forecasting, McMurray formation, corner, Alberta, Canada," *Marine and Petroleum Geology*, vol. 82, pp. 336–361, 2017.
- [10] R. Gholami, B. Aadnoy, V. Rasouli, and N. Fakhari, "An analytical model to predict the volume of sand during drilling and production," *Journal of Rock Mechanics and Geotechnical Engineering*, vol. 8, no. 4, pp. 521–532, 2016.
- [11] L. Wang, Y. Tian, X. Yu et al., "Advances in improved/enhanced oil recovery technologies for tight and shale reservoirs," *Fuel*, vol. 210, pp. 425–445, 2017.
- [12] C. Dong, X. Chen, Y. Chen, R. Kang, and R. Feng, "Experimental study on mechanism and capability of sand-carrying in water-producing gas wells and its application," *Journal of China University of Petroleum*, vol. 38, no. 6, pp. 90–96, 2014.
- [13] A. Fadairo, O. Oyedele-Adeyi, A. Oladepo, and T. Ogunkunle, "Modeling the effect of entrained sand particles on pressure transverse in a flowing gas well," *World Journal of Engineering*, vol. 14, no. 5, pp. 406–413, 2017.
- [14] M. Dejam, "Advective-diffusive-reactive solute transport due to non-newtonian fluid flows in a fracture surrounded by a tight porous medium," *International Journal of Heat and Mass Transfer*, vol. 128, pp. 1307–1321, 2019.
- [15] S. F. Xue, G. S. Ma, L. G. Yu, and H. K. Ge, "Fluid-solid coupling model and its application in quantitative sand production prediction of oil and water wells," *Petroleum Exploration & Development*, vol. 34, no. 6, pp. 750–754, 2007.
- [16] E. Khamehchi and E. Reisi, "Sand production prediction using ratio of shear modulus to bulk compressibility (case study)," *Egyptian Journal of Petroleum*, vol. 24, no. 2, pp. 113–118, 2015.
- [17] M. B. Oyenehin and B. Moriwawon, "Sand production forecasts for unconsolidated gas reservoirs," *Advanced Materials Research*, vol. 62-64, pp. 466–473, 2009.
- [18] National Energy Board, *Energy briefing note, tight oil developments in the western Canadian Sedimentary Basin*, National Energy Board, Calgary, 2011.
- [19] L. Dengsheng, S. Lin, and C. Lei, "The flow research of gas-oil-sand three phase in wellbore with heavy oil reservoir," *2011 International conference of environmental science and engineering*, vol. 12, pp. 318–324, 2012.
- [20] P. G. Ranjith, M. S. A. Perera, W. K. G. Perera, B. Wu, and S. K. Choi, "Effective parameters for sand production in unconsolidated formations: an experimental study," *Journal of Petroleum Science and Engineering*, vol. 105, pp. 34–42, 2013.
- [21] M. R. Zare-Reisabadi, A. Kaffash, and S. R. Shadzadeh, "Determination of optimal well trajectory during drilling and production based on borehole stability," *International Journal of Rock Mechanics and Mining Sciences*, vol. 56, pp. 77–87, 2012.
- [22] M. Khammar and Y. Xu, "Batch solvent extraction of bitumen from oil sand. Part 2: experimental development and modeling," *Energy & Fuels*, vol. 31, no. 5, pp. 4626–4636, 2017.
- [23] S. Walspurger, G. D. Elzinga, J. W. Dijkstra, M. Sarić, and W. G. Haije, "Sorption enhanced methanation for substitute natural gas production: experimental results and thermodynamic considerations," *Chemical Engineering Journal*, vol. 242, pp. 379–386, 2014.
- [24] S. B. Grafutko and V. N. Nikolaevskii, "Problem of the sand production in a producing well," *Fluid Dynamics*, vol. 33, no. 5, pp. 745–752, 1998.
- [25] T. Xu and C. A. Tang, "Modeling of stress-induced permeability evolution and damage of rock," *Advanced Materials Research*, vol. 33-37, pp. 609–616, 2008.
- [26] D. R. Schmitt, C. A. Currie, and L. Zhang, "Crustal stress determination from boreholes and rock cores: fundamental principles," *Tectonophysics*, vol. 580, pp. 1–26, 2012.

## Research Article

# Pore-Scale Investigation on the Plugging Behavior of Submicron-Sized Microspheres for Heterogeneous Porous Media with Higher Permeability

Yafei Liu <sup>1,2</sup>, Jingwen Yang,<sup>1</sup> Tianjiang Wu,<sup>3</sup> Yanhong Zhao,<sup>4</sup> Desheng Zhou,<sup>1,2</sup> and Shun Liu<sup>1,2</sup>

<sup>1</sup>College of Petroleum Engineering, Xi'an Shiyou University, Xi'an, Shaanxi, China

<sup>2</sup>Shaanxi Key Laboratory of Advanced Stimulation Technology for Oil & Gas Reservoirs, Xi'an, Shaanxi, China

<sup>3</sup>Oil & Gas Technology Research Institute of Changqing Oil Field Company, PetroChina, Xi'an, Shaanxi, China

<sup>4</sup>Research Institute of Xi'an Changqing Chemical Group Co. Ltd., Xi'an, Shaanxi, China

Correspondence should be addressed to Yafei Liu; [yafliu@xsyu.edu.cn](mailto:yafliu@xsyu.edu.cn)

Received 12 May 2020; Revised 29 May 2020; Accepted 7 August 2020; Published 17 October 2020

Academic Editor: Andrea Brogi

Copyright © 2020 Yafei Liu et al. This is an open access article distributed under the Creative Commons Attribution License, which permits unrestricted use, distribution, and reproduction in any medium, provided the original work is properly cited.

Reservoir heterogeneity is regarded as one of the main reasons leading to low oil recovery for both conventional and unconventional reservoirs. High-permeability layers or fractures could result in ineffective water or gas injection and generate nonuniform profile. Polymer microspheres have been widely applied for the conformance control to overcome the bypass of injected fluids and improve the sweep efficiency. For the purpose of examining the plugging performance of submicron-sized microspheres in high-permeability porous media, systematic investigations were implemented incorporating macroscale blocking rate tests using core samples and pore-scale water migration analysis via nuclear magnetic resonance (NMR). Experimental results indicate that microsphere particle size dominates the plugging performance among three studied factors and core permeability has the least influence on the plugging performance. Subsequently, microsphere flooding was conducted to investigate its oil recovery capability. Different oil recovery behaviors were observed for cores with different permeability. For cores with lower permeability, oil recovery increased stepwise with microsphere injection whereas for higher permeability cores oil recovery rapidly increased and reached a plateau. This experimental work provides a better understanding on the plugging behavior of microspheres and could be employed as a reference for screening and optimizing the microsphere flooding process for profile control in heterogeneous reservoirs.

## 1. Introduction

Reservoir heterogeneity has long been a major issue that leads to unsatisfactory oil recovery efficiency and high water cut during waterflooding for both conventional and unconventional reservoirs [1–3]. Dominant flow pathways can be developed along high-permeability layers and natural or artificial fractures for tight reservoirs in which injected water or gas prefers to flow hence diminishing the sweep efficiency [3–6]. Due to the bypass of water, there still remain unswept areas in lower permeability regions with considerable oil recovery potential. In the meantime, high water production could increase the cost and energy consumption of the subse-

quent transportation and water treatment. Therefore, it is of significance to adjust waterflooding profile and improve the sweep efficiency to reduce water cut and achieve higher oil recovery efficiency.

To counter the nonuniform waterflood front, profile control technology has been developed to plug the high-permeability layers and divert the flow towards lower permeability areas [4, 7–10]. Methods like polymer flooding [11–14] and foam flooding [15–17] were considered to effectively improve the mobility ratio and sweep efficiency. However, issues like shear thinning and injectivity of polymer solution limited its performance in enhancing oil recovery [14]. Oil and water distribution becomes increasingly complex



TABLE 1: Physical properties of the cores used in the experiments.

Core no.	Permeability (mD)	Porosity (%)	Pore volume (cm <sup>3</sup> )
1	99	30.812	7.632
2	95	31.312	7.548
3	197	20.861	4.997
4	202	20.992	5.005
5	288	28.671	7.034
6	297	27.787	6.836
7	294	28.089	6.809
8	293	26.396	6.392
9	300	27.370	6.582
10	302	28.118	6.898
11	293	28.956	6.972
12	307	29.514	7.208
13	293	29.684	6.969
14	300	29.536	6.990
15	308	28.074	6.834
16	302	27.931	6.641
17	402	25.021	6.023
18	399	28.077	6.684
19	516	26.869	6.431
20	525	27.317	6.498

especially during later stage of oil field development such that polymer flooding cannot fully meet the demand for the profile control. Subsequently, polymer particles, for instance, preformed particle gels (PPGs) [18, 19], colloidal dispersed gels (CDGs) [20, 21], and polymer microspheres (PMs) [22, 23], were applied to engage in in-depth profile control owing to its small size, elastic characteristics, and the ability to penetrate into lower permeability areas. Extensive studies have been done on the fabrication and performance evaluation on these polymer particles [24]. PPGs are polymers with relatively large size and can be applied for conformance control of fractures and high-permeability layers [25]. The fabrication, mechanical properties, and plugging performance of PPGs have been extensively investigated both in lab and field [19, 26, 27]. CDGs are colloids suspended in the solution with characteristics like smaller size, lower polymer concentration, and longer formation time, yet CDGs should be carefully applied in harsh conditions [21, 28]. As the complexity of the reservoir pore throat structure raises after water injection and other flooding methods, demand has grown for polymer particles with more flexibility and stability to adjust the injection profile.

Recently, polymer microspheres with nano- to micrometer size were developed and applied for deep profile control. Features like small size, elasticity, and better deformability allow the migration of microspheres towards smaller pores and deeper formation with lower permeability. Different types of polymer microspheres with unique characteristics have been proposed in the literature and widely applied in the oil field [29–33]. The plugging performance of polymer microspheres and the aspects impacting its plugging and migration have been previously investigated [22, 23, 34, 35].

It was proposed that polymer microspheres undergo dynamic plugging in other words plugging, deformation, mobilization, and replugging thus enabling the profile control of deeper formation [30, 31, 36]. Different plugging mechanisms were also directly visualized via transparent micromodel [31] and scanning electron microscopy (SEM) [35]. Majority of the work is focused upon the migration behavior and rheological property of microspheres for deep profile control as well as the compatibility of the particle size to pore throat size. To obtain a solid understanding on the plugging performance of microspheres in a heterogeneous reservoir, systematic investigation on the parameters affecting its plugging performance in both deep formation and high-permeability zones could be essential. However, less attention was paid to the plugging capability of sub-micron-sized microspheres in higher permeability regions. The controlling factor for microsphere plugging performance remains unclear.

Therefore, in this work, submicron polymer microspheres with varying concentrations and particle sizes have been used to examine its capability to plug high-permeability porous media. To evaluate its plugging performance and investigate the plugging mechanism, a systematic investigation was implemented incorporating the effect of rock permeability, microsphere size, and concentrations on the plugging performance. Macroscale blocking rate of core samples using microspheres as well as the pore-scale inspection of water migration via NMR scanning has been integrated to obtain a better understanding of the plugging mechanism. Based upon the results obtained from this experimental work, influence of each examined parameter on the plugging performance was analyzed and the controlling factor was determined. This work also provides a reference and guidance to optimize the profile control operation in the field application via submicron polymer microspheres in heterogeneous reservoirs.

## 2. Experimental Setup

*2.1. Materials.* Artificial cores were fabricated using quartz sand and epoxy resin with designated permeability gradient distributed from 100 to 500 mD. They were utilized to examine the plugging performance of different microsphere solutions under various permeability conditions and perform coreflooding experiments to evaluate the enhanced oil recovery potential of microsphere solution. The average length and diameter of the cores are 4.9 cm and 2.5 cm, respectively. Detailed physical properties of the core samples are listed in Table 1. Distilled water and paraffin oil were used to perform the corresponding experiments.

Microspheres used in this work were acrylamide-based polymer particles fabricated via inverse emulsion polymerization. It consists of an outer hydrophilic shell, a middle hydrophobic layer, and a cationic core. Microsphere solution was prepared by diluting the polymer microsphere emulsion with distilled water. Microsphere solutions with varying concentrations (0.05, 0.1, 0.15, and 0.2 wt%) and particle sizes (50, 100, 300, and 800 nm) were used in the experiments.

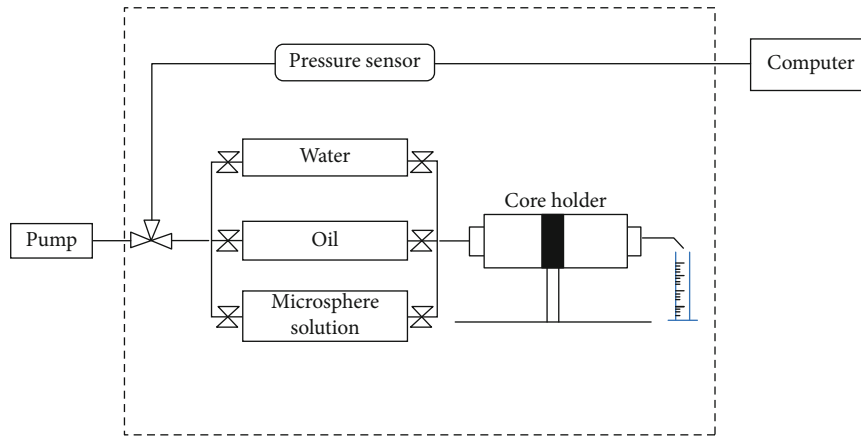


FIGURE 1: Schematic of the experimental setup.

**2.2. Experimental Procedures.** In order to evaluate the plugging performance of submicron-sized microspheres on the high-permeability regions, microsphere flooding was conducted. The core samples were vacuumed for 3 hours followed by the saturation process with distilled water for 10 hours to ensure that all cores were fully saturated. To obtain the initial distribution of the aqueous phase inside the core, NMR (MesoMR23-60H-I) tests were implemented for all the core samples. Afterwards, the core sample was then injected into the core holder. Microsphere solution was then injected into the core with an injection rate of 0.3 mL/min. Inlet pressure of the core holder was automatically monitored and recorded during the flooding process ranging from 0.01 to 0.6 MPa. Volume of the collected displaced fluids was measured to obtain the permeability of the core sample after the microsphere solution injection. The flooding process ceased as the measured pressure became stable. The second NMR test was performed for each core sample afterwards to acquire the information on the aqueous phase distribution and saturation. The whole process was repeated using microsphere solutions with varying concentrations and particle sizes inside differential permeability cores. The experimental setup was sketched in Figure 1.

The aforementioned microsphere flooding experiments were regarded as the preliminary evaluation to screen the optimal microsphere solution concentration and microsphere size and obtain its plugging mechanism. To further examine the oil displacement efficiency by the submicron microspheres, another set of experiments emulating the oil recovery process were conducted. Fresh core samples with two permeability levels were selected based upon the experimental results and evaluation. The core samples experienced the similar preparation steps involving vacuuming and establishment of initial water saturation. Subsequently, initial oil saturation was developed by oil injection at a rate of 0.3 mL/min into the core until no more water was produced. Waterflooding and microsphere flooding were conducted afterwards, respectively, at an injection rate of 0.3 mL/min until the measured pressure reached a plateau and no more oil was recovered. 10 MPa confining pressure was applied to the displacement system. Recovered oil was collected; therefore, oil recovery rate by two flooding methods was attained.

The experimental workflow for two sets of experiments was also demonstrated in Figure 2.

### 3. Results and Discussion

#### 3.1. Plugging Performance Evaluation of Microspheres

**3.1.1. Effect of Core Permeability.** Core samples with varying permeability were employed to investigate the influence of rock permeability on the plugging performance of microspheres. Two types of microsphere solutions were used for this set of experiments. Core samples used for the experiments were nos. 1, 3, 5, 17, and 19 for the 100 nm 0.1% case and nos. 2, 4, 6, 18, and 20 for the 300 nm 0.1% case, respectively. Figure 3 plots the relationship between blocking rate and core permeability. Blocking rate was calculated by the ratio of permeability reduction after the microsphere injection to the permeability of the core after water saturation, namely, higher blocking rate implies that larger portion of the pore space is plugged by the injected microspheres. Reversely, lower blocking rate suggests that injected microspheres cannot effectively block larger pores and might pass through the core instead. For the 100 nm microsphere solution with 0.1% concentration, the blocking rate fluctuates as the permeability increases yet a distinct trend was not observed and this fluctuation could be possibly due to insufficient particle size that leads to unstable plugging performance, whereas for the 300 nm microsphere solution with 0.1% concentration the blocking rate almost remains the same as the permeability increases indicating that microsphere with this particle size demonstrates more stable plugging behavior and better fits the high-permeability cores used in the experiments. In general, this result implies that rock permeability might not be the major factor affecting the plugging capability of the microspheres. When using differently sized microspheres, however, rock permeability could still make a difference in the pore scale. To understand the migration of water after microsphere injection, NMR scanning was conducted after both water saturation and microsphere injection. Pore size distribution of the artificial core samples majorly falls in the range from 0.26 to 7.65  $\mu\text{m}$ , and they were

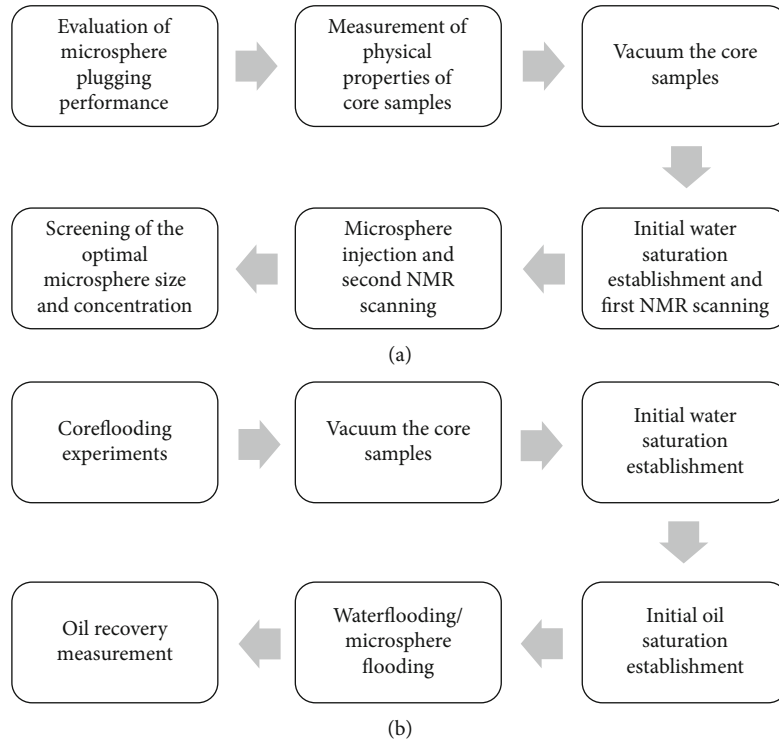


FIGURE 2: Workflow of the experimental procedures of (a) evaluation on microsphere plugging performance and (b) coreflooding experiments.

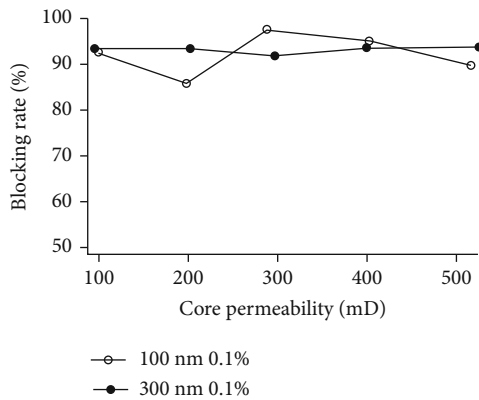


FIGURE 3: Influence of core permeability on the blocking rate of microspheres.

further categorized as small pores, medium pores, and large pores based upon the relaxation time [37].

In Figure 4, water distribution before and after microsphere injection was compared by selecting two core samples with large permeability contrast. Core no. 1 possesses smaller permeability, and NMR scanning shows the majority of the cores characterized as medium pores and large pores are scarce. Water saturation inside medium pores decreased after the microsphere injection, and this portion of water was relocated to small pores suggesting microspheres successfully plugged relatively larger pores and diverted the flow path. For the higher permeability core, majority of the pores are characterized large pores. After microsphere injection, water

inside large pores mainly migrated to medium pores and limited amount of water to small pores. Despite the fact that macroscale blocking rate does not change distinctly as rock permeability changes, rock permeability still has an impact on the pore-scale water distribution and relocation as microspheres blocked preferential flow paths.

**3.1.2. Effect of Microsphere Size and Concentration.** Permeability is the inherent property of the reservoir whereas parameters like microsphere size and concentration are convenient to adjust in the oil field. Therefore, the effect of microsphere size and its concentration was investigated to comprehend the mechanism of profile control using microspheres and optimize the formula for microsphere injection. Figure 5 shows the blocking rate of differently sized microspheres on core samples with the same permeability, and it demonstrated the relationship between blocking rate and microsphere size under two concentration levels. In this set of experiments, core samples with 300 mD permeability were selected. Core samples used for the experiments were nos. 7, 5, 6, and 8 for 0.1% concentration level and nos. 9, 10, 11, and 12 for 0.2% concentration level, respectively. In general, linear relation was not observed, and in fact, blocking rate shows nonmonotonic change as the microsphere size increases. For the lower microsphere concentration condition, 100 nm particle size showed better blocking capability possibly attributed to its compatibility with the pore throat size of the core sample. For higher microsphere concentration condition, microsphere with 300 nm size showed relatively better plugging performance. When microsphere

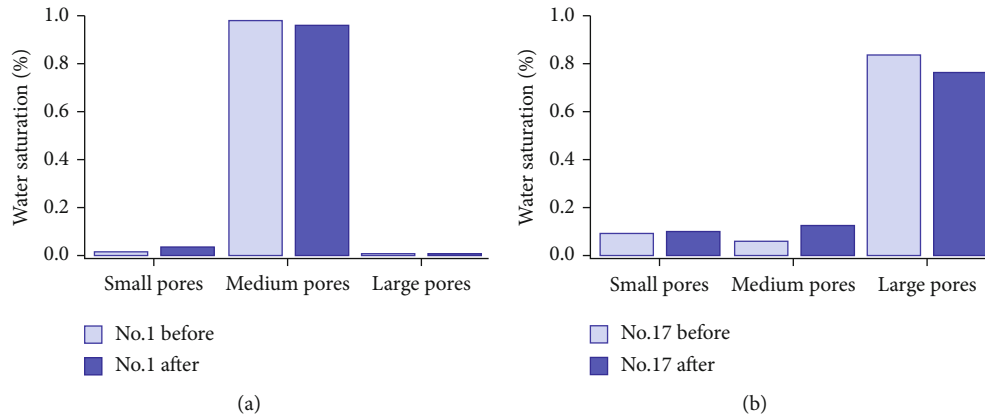


FIGURE 4: Water distribution inside the core sample with permeability of (a) 99 mD and (b) 402 mD. “Before” denotes before microsphere injection and “after” denotes after microsphere injection. Microsphere particle size is 100 nm and its concentration is 0.1%.

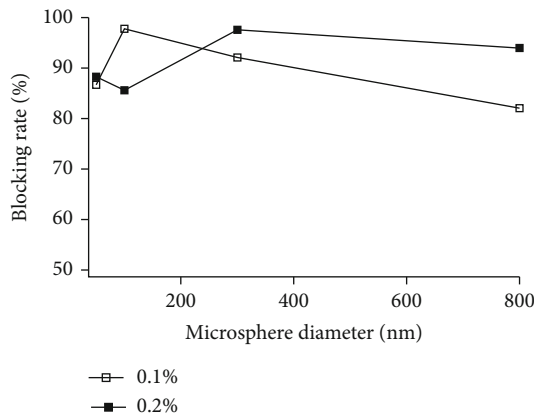


FIGURE 5: Influence of microsphere size on the blocking rate. Permeability of the cores used is 300 mD.

solution with larger particle size was used, a discrepancy in blocking rate was observed between two concentration levels. Higher microsphere concentration results in better plugging performance. To analyze the pore-scale migration of water after microsphere flooding with different particle sizes, water distribution change inside two core samples possessing the same permeability was obtained from NMR scanning with the solution concentration of 0.2%. As shown in Figure 6, for core samples with the same permeability, it is intuitive that larger microspheres could effectively block larger pores as indicated by an evident decrease in water saturation in large pores and increase in medium pores after microsphere injection shown in Figure 6(b). Little saturation change in small pores revealed that larger microsphere has a limited effect on plugging small and medium pores despite its nano-to-microscale size. Compared with Figure 6(b), Figure 6(a) shows the water saturation change after microsphere injection with smaller particle size using the same permeability core. It is not as effective as larger microspheres in terms of plugging large pores as indicated by less decrease in the water saturation inside large pores.

As for the relationship between blocking rate and microsphere concentration, Figure 7 shows that when larger microspheres were used blocking rate slightly increases as

the concentration increases yet the trend flattens out. Further increase of the concentration might not lead to distinct improvement of the blocking rate. Core samples used for the experiments were nos. 13, 5, 14, and 10 for 100 nm particle size and nos. 15, 6, 16, and 11 for 300 nm particle size, respectively. When smaller microspheres were used, block rate increases as the concentration increases. However, there is an abrupt decrease in the blocking rate at larger concentration especially at 0.2%. It was postulated that for smaller sized microspheres, blocking of larger pores relies upon the accumulation due to its insufficient size. When the concentration was increased to 0.2%, microspheres originally gathered and plugged in the pores could be squeezed out by the subsequently injected microspheres leading to a lower blocking rate, namely, higher microsphere concentration does not necessarily result in higher blocking rate and microsphere particle size should be taken into consideration as well. Presumably, for higher permeability regions, a critical concentration and microsphere size exist and beyond which the growth potential of its plugging performance can be limited. This suggests that for oil field application lower microsphere concentration solution could be more cost-effective considering the expense of the microsphere flooding and elevating microsphere concentration might not lead to considerable improvement in oil recovery. Water saturation change was also plotted in Figure 8 based upon the NMR scanning results. In general, microsphere particles are capable of blocking large pores and divert the fluid flowing towards majorly medium pores and small pores and the blocking of large pores depends upon the specific microsphere concentration and particle size. As shown in Figure 8(b), for microsphere solution with 100 nm particle size at 0.2% concentration, the migration of water was not as significant as others and this pore-scale observation coincided with the macroscale blocking rate. Interestingly, core sample no. 15 exhibits different pore size distribution than others that majority of the pore space are characterized as large pores. Microsphere particles still effectively block partial large pores resulting in the migration of water to mainly medium pores and small pores.

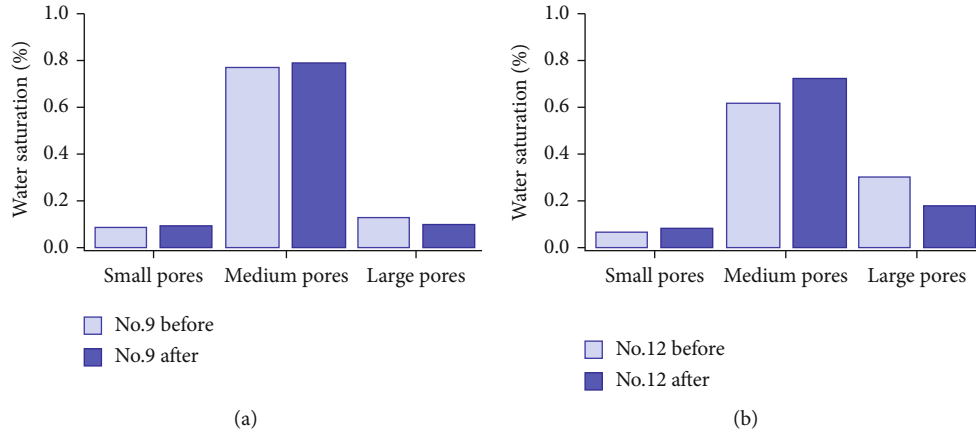


FIGURE 6: Water distribution inside the core sample of the same permeability (300 mD) after injection of microspheres with (a) 50 nm and (b) 800 nm particle size. “Before” denotes before microsphere injection and “after” denotes after microsphere injection. Microsphere concentration is 0.2%.

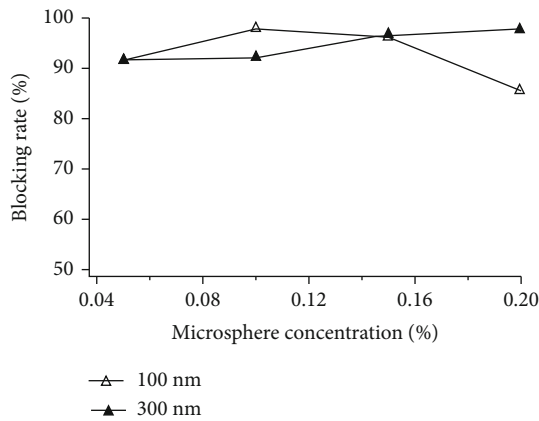


FIGURE 7: Influence of microsphere solution concentration on the blocking rate. Permeability of the cores used is 300 mD.

Overall, to determine the dominant factor impacting the blocking rate, statistical analysis was conducted. In this mixed-type orthogonal experiments, three factors were involved which are core permeability, microsphere particle size, and solution concentration. For core permeability, five factor levels were involved and they are 100, 200, 300, 400, and 500 mD, respectively. For microsphere size, four factor levels were involved and they are 50, 100, 300, and 800 nm, respectively. For microsphere solution concentration, four factor levels were involved and they are 0.05, 0.1, 0.15, and 0.2%, respectively. Based upon the analysis of the range demonstrated in Table 2, the ranking of factors that have greater impact on the blocking performance of microspheres is microsphere size, microsphere solution concentration, and core permeability successively. The corresponding microsphere size and concentration resulting in higher blocking rate were 300 nm and 0.15%, respectively. Microsphere size was considered as the dominant factor impacting the blocking rate. Therefore, based upon the experimental results, appropriate microsphere size matching with the pore size of

the rock could more effectively block the desired region. Core permeability on the other hand has the least influence on the blocking rate among the examined factors indicating submicron-sized microspheres could be applied for profile control in high-permeability regions.

**3.2. Oil Displacement Efficiency.** To further evaluate the efficiency of enhancing oil recovery by microsphere injection, waterflooding and microsphere flooding were conducted. Four cores with two permeability levels were selected. According to the previous results, microsphere with 300 nm particle size was chosen to perform the flooding experiments. Details of the experimental setup and results are displayed in Table 3. Generally, incremental oil was recovered by microsphere flooding with the average incremental rate of 9.34% under the experimental conditions yet the incremental rate depends on the microsphere solution used. The permeability of core no. 10 is three times as large as that of core no. 1; however, the incremental oil recovery rate is similar when the microsphere concentration is 0.15%. On the contrary, when the microsphere concentration decreases to 0.05%, core no. 2 with lower permeability exhibits higher incremental oil recovery rate than core no. 14. For small-sized microspheres, the blocking capability of large pores possibly depends upon the accumulation of microspheres. Optimal microsphere concentration can be conducive to plug larger pores and ultimately recovery more oil.

Oil recovery rate as a function of pore volumes of microsphere solution injected for the four core samples was plotted in Figure 9 to closely examine the blocking behavior of microspheres. First of all, for lower permeability cores (core no. 1 and no. 2), microsphere concentration has a distinct impact on the oil recovery pattern. Injection of higher concentration solution quickly improves the oil recovery rate and then gradually recovers more oil. The curve also displays step growth of the oil recovery indicating the potential migration of the microspheres into lower permeability areas that leads to the enhanced oil recovery. For core no. 2, it clearly shows a slower response to microsphere injection when the solution concentration is lower. The trend of the curve is



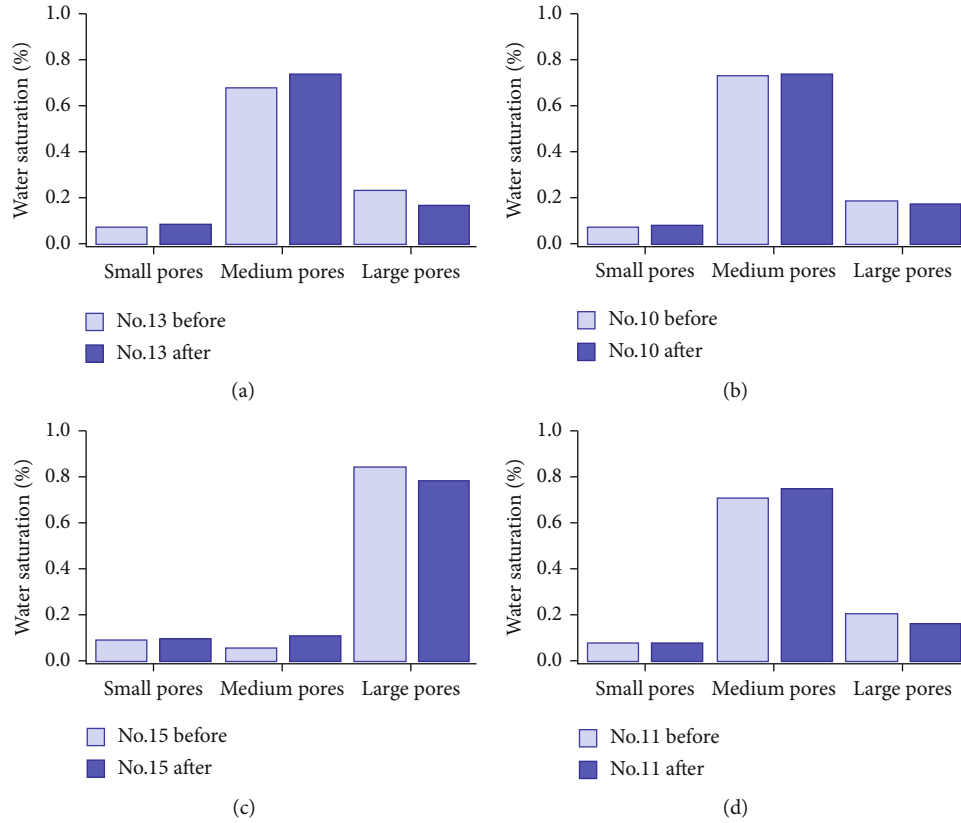


FIGURE 8: Water distribution inside the core sample of the same permeability (300 mD) using microsphere solution of (a) 100 nm 0.05%, (b) 100 nm 0.2%, (c) 300 nm 0.05%, and (d) 300 nm 0.2%. “Before” denotes before microsphere injection and “after” denotes after microsphere injection.

TABLE 2: Statistical analysis on the factors impacting the blocking rate of microspheres.

Factor level	Microsphere size (nm)	Microsphere solution conc. (%)	Permeability (mD)
1	50	0.05	100
2	100	0.1	200
3	300	0.15	300
4	800	0.20	400
5			500
Range	6.17	5.09	4.77
Order	1	2	3

similar to that of core no. 1 demonstrating a step growth characteristic yet the final recovery rate is lower which could be owing to insufficient microspheres in the core and inadequate waterflood profile control. Unlike the lower permeability scenario, when the core permeability is much higher, a rapid increase in oil recovery was observed as the microsphere solution was injected despite its concentration. Presumably, dominant seepage channels are easier to form in higher permeability media, and the gathering of microspheres could effectively divert the flow paths resulting in a significant enhancement in oil recovery. However, the curves for both core nos. 10 and 14 quickly reach a plateau indicating continuous injection of the microsphere solution could

TABLE 3: Oil recovery rate by waterflooding and microsphere solution.

Core no.	Microsphere conc. (%)	Oil recovery by waterflooding (%)	Oil recovery by microsphere (%)	Incremental oil recovery rate (%)
1	0.15	44.15	55.70	11.55
2	0.05	32.41	41.00	8.59
10	0.15	53.24	64.30	12.06
14	0.05	48.33	53.50	5.17

sabotage the original plugging by relocating and even flushing out the microspheres such that additional oil recovery was not attained. In this case, increasing solution concentration could be helpful to achieve a higher recovery rate in higher permeability porous media as indicated by comparing the curves of core no. 14 with no. 10 yet the increase might not be significant. In the field application, to plug high-permeability layers using submicron microspheres, an instant improvement could be observed yet the long-term effect of microspheres on oil recovery might not be satisfactory. To further improve the oil recovery, development plan could be adjusted and switched to higher concentration or even larger particle size based on the statistical analysis showing particle size has greater influence on the blocking rate.

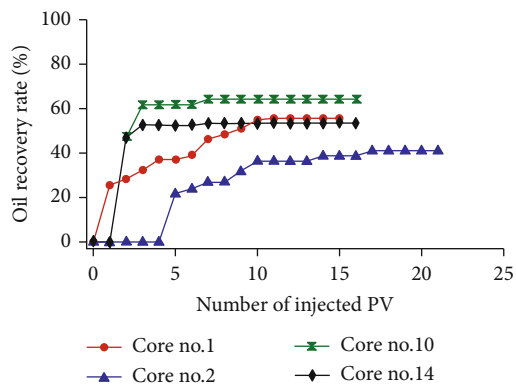


FIGURE 9: Oil recovery rate by microsphere flooding versus number of pore volumes of microsphere solution injected for four core samples.

When a step growth in oil recovery is observed after microsphere injection, increasing its concentration could more effectively enhance oil recovery. To summarize, for a fixed microsphere particle size, higher oil recovery could be achieved by increasing the solution concentration. However, to accomplish higher oil recovery for cores with larger permeability, the effectiveness of increasing solution concentration can be limited.

#### 4. Conclusions

In this work, the plugging performance of submicron microsphere solution on high-permeability porous media was investigated. Artificial core samples with designated permeability were employed to examine the plugging capability of different microsphere solutions. Experimental results indicate that microsphere size has a greater impact on the blocking rate than microsphere concentration and core permeability. Larger microsphere mainly blocks large pores whereas smaller microsphere has moderate plugging capability on large pores. The effect of microsphere concentration on the blocking rate should be combined with particle size to evaluate the plugging performance. Noteworthy, core permeability is not the dominant factor impacting the plugging performance based upon the experimental results and statistical analysis. This suggests that small-sized microspheres are capable of blocking higher permeability regions and achieve flow diversion to smaller pores. Simulated oil recovery process demonstrated that incremental oil recovery could be attained by the microsphere injection. Quicker response to the microsphere injection was observed for higher permeability cores. For cores with lower permeability, oil recovery increases stepwise as more microsphere solution is injected until a plateau is reached. When a microsphere solution with the same particle size was used, increasing the concentration could contribute to higher oil recovery yet the increment in oil recovery is associated with rock permeability. Overall, this experimental work could be beneficial for screening the polymer microsphere candidate for profile control of both conventional and unconventional reservoirs that have developed preferential flow paths or fractures to

improve the sweep efficiency and ultimately enhance oil recovery.

#### Data Availability

The data used to support the findings of this study are available from the corresponding author upon request.

#### Conflicts of Interest

The authors declare that they have no conflicts of interest.

#### Acknowledgments

This work was supported by the National Natural Science Foundation of China (Grant Nos. 51904244, 51874242, and 51934005), National Major Science and Technology Projects of China (Grant No. 2016ZX05050-009), Natural Science Basic Research Plan in Shaanxi Province of China (Program No. 2019JQ-364), and Scientific Research Program Funded by Shaanxi Provincial Education Department (Program No. 19JK0663).

#### References

- [1] M. O. Elsharafi and B. Bai, "Effect of weak preformed particle gel on unswept oil zones/areas during conformance control treatments," *Industrial and Engineering Chemistry Research*, vol. 51, no. 35, pp. 11547–11554, 2012.
- [2] P. Wei, W. Pu, L. Sun, Y. Pu, S. Wang, and Z. Fang, "Oil recovery enhancement in low permeable and severe heterogeneous oil reservoirs via gas and foam flooding," *Journal of Petroleum Science and Engineering*, vol. 163, pp. 340–348, 2018.
- [3] G. Zhao, Q. You, J. Tao et al., "Preparation and application of a novel phenolic resin dispersed particle gel for in-depth profile control in low permeability reservoirs," *Journal of Petroleum Science and Engineering*, vol. 161, pp. 703–714, 2018.
- [4] A. M. Almohsin, B. Bai, A. H. Imqam et al., *Transport of nanogel through porous media and its resistance to water flow*, 2014.
- [5] Z. Song, J. Hou, X. Liu, Q. Wei, H. Hao, and L. Zhang, "Conformance control for CO<sub>2</sub>-EOR in naturally fractured low permeability oil reservoirs," *Journal of Petroleum Science and Engineering*, vol. 166, pp. 225–234, 2018.
- [6] Y. Zhang, M. Gao, Q. You et al., "Smart mobility control agent for enhanced oil recovery during CO<sub>2</sub> flooding in ultra-low permeability reservoirs," *Fuel*, vol. 241, pp. 442–450, 2019.
- [7] S. Vossoughi, "Profile modification using in situ gelation technology—a review," *Journal of Petroleum Science and Engineering*, vol. 26, no. 1-4, pp. 199–209, 2000.
- [8] D. Caili, Y. Qing, and Z. Fulin, "In-depth profile control technologies in China—a review of the state of the art," *Petroleum Science and Technology*, vol. 28, no. 13, pp. 1307–1315, 2010.
- [9] K. S. M. El-Karsani, G. A. Al-Muntasheri, and I. A. Hussein, "Polymer systems for water shutoff and profile modification: a review over the last decade," *SPE Journal*, vol. 19, no. 1, pp. 135–149, 2014.
- [10] B. Bai, J. Zhou, and M. Yin, "A comprehensive review of polyacrylamide polymer gels for conformance control," *Petroleum Exploration and Development*, vol. 42, no. 4, pp. 525–532, 2015.

- [11] W. B. Gogarty, "Mobility control with polymer solutions," *Society of Petroleum Engineers Journal*, vol. 7, pp. 161–173, 2013.
- [12] H. L. Chang, "Polymer flooding technology yesterday, today, and tomorrow," *Journal of Petroleum Technology*, vol. 30, pp. 1–113–1–128, 2013.
- [13] D. Wang, J. Cheng, J. Wu, and G. Wang, *Experiences learned after production of more than 300 million barrels of oil by polymer flooding in Daqing Oil Field*, 2002.
- [14] K. S. Sorbie, *Polymer-improved oil recovery*, 2013.
- [15] Y. Zhang, X. Yue, J. Dong, and L. Yu, *New and effective foam flooding to recover oil in heterogeneous reservoir*, 2000.
- [16] W. Yan, C. A. Miller, and G. J. Hirasaki, "Foam sweep in fractures for enhanced oil recovery," *Colloids and Surfaces A: Physicochemical and Engineering Aspects*, vol. 282, pp. 348–359, 2006.
- [17] M. A. Fernø, J. Gauteplass, M. Pancharoen et al., "Experimental study of foam generation, sweep efficiency, and flow in a fracture network," *SPE Journal*, vol. 21, no. 4, pp. 1140–1150, 2016.
- [18] A. Goudarzi, H. Zhang, A. Varavei et al., "A laboratory and simulation study of preformed particle gels for water conformance control," *Fuel*, vol. 140, pp. 502–513, 2015.
- [19] A. Farasat, M. V. Sefti, S. Sadeghnejad, and H. R. Saghafi, "Mechanical entrapment analysis of enhanced preformed particle gels (PPGs) in mature reservoirs," *Journal of Petroleum Science and Engineering*, vol. 157, pp. 441–450, 2017.
- [20] H. L. Chang, X. Sui, L. Xiao et al., "Successful field pilot of in-depth colloidal dispersion gel (CDG) technology in Daqing Oilfield," *SPE Reservoir Evaluation & Engineering*, vol. 9, pp. 664–673, 2013.
- [21] M. Bjørsvik, H. Høiland, and A. Skauge, "Formation of colloidal dispersion gels from aqueous polyacrylamide solutions," *Colloids and Surfaces A: Physicochemical and Engineering Aspects*, vol. 317, no. 1–3, pp. 504–511, 2008.
- [22] W. Pu, S. Zhao, S. Wang, B. Wei, C. Yuan, and Y. Li, "Investigation into the migration of polymer microspheres (PMs) in porous media: implications for profile control and oil displacement," *Colloids and Surfaces A: Physicochemical and Engineering Aspects*, vol. 540, pp. 265–275, 2018.
- [23] J. Li, L. Niu, and X. Lu, "Migration characteristics and deep profile control mechanism of polymer microspheres in porous media," *Energy Sci Eng*, vol. 7, no. 5, pp. 2026–2045, 2019.
- [24] M. Abdulbaki, C. Huh, K. Sepehrnoori, M. Delshad, and A. Varavei, "A critical review on use of polymer microgels for conformance control purposes," *Journal of Petroleum Science and Engineering*, vol. 122, pp. 741–753, 2014.
- [25] A. Imqam, Z. Wang, and B. Bai, "The plugging performance of preformed particle gel to water flow through large opening void space conduits," *Journal of Petroleum Science and Engineering*, vol. 156, pp. 51–61, 2017.
- [26] M. A. Lenji, M. Haghshenasfard, M. V. Sefti, M. B. Salehi, and A. Heidari, "Experimental study of swelling and rheological behavior of preformed particle gel used in water shutoff treatment," *Journal of Petroleum Science and Engineering*, vol. 169, pp. 739–747, 2018.
- [27] H. R. Saghafi, "Retention characteristics of enhanced preformed particle gels (PPGs) in porous media: conformance control implications," *Journal of Petroleum Science and Engineering*, vol. 166, pp. 962–968, 2018.
- [28] J. C. Mack and J. E. Smith, *In-depth colloidal dispersion gels improve oil recovery efficiency*, 1994.
- [29] C. Liu, X. Liao, Y. Zhang et al., "Field application of polymer microspheres flooding: a pilot test in offshore heavy oil reservoir," *SPE Annual Technical Conference and Exhibition*, vol. 6, 2012.
- [30] Z. Hua, M. Lin, Z. Dong, M. Li, G. Zhang, and J. Yang, "Study of deep profile control and oil displacement technologies with nanoscale polymer microspheres," *Journal of Colloid and Interface Science*, vol. 424, pp. 67–74, 2014.
- [31] C. Yao, G. Lei, L. M. Cathles, and T. S. Steenhuis, "Pore-scale investigation of micron-size polyacrylamide elastic microspheres (MPEMs) transport and retention in saturated porous media," *Environmental Science & Technology*, vol. 48, no. 9, pp. 5329–5335, 2014.
- [32] X. Shi and X. Yue, "Migration and plugging mechanisms of self-aggregated microspheres as a novel profile control," *Journal of Petroleum Science and Engineering*, vol. 184, p. 106458, 2020.
- [33] J. Zhang, X. Tan, X. Zhao, Q. He, and Y. Wang, "Experimental study of small-sized polymeric microgel (SPM) in low- or median-permeability reservoirs," *Journal of Petroleum Science and Engineering*, vol. 190, p. 106829, 2020.
- [34] M. Lin, G. Zhang, Z. Hua, Q. Zhao, and F. Sun, "Conformation and plugging properties of crosslinked polymer microspheres for profile control," *Colloids and Surfaces A: Physicochemical and Engineering Aspects*, vol. 477, pp. 49–54, 2015.
- [35] S. Zhao and W. Pu, "Migration and plugging of polymer microspheres (PMs) in porous media for enhanced oil recovery\_ experimental studies and empirical correlations," *Colloids and Surfaces A: Physicochemical and Engineering Aspects*, vol. 597, p. 124774, 2020.
- [36] H. Yang, L. Hu, C. Chen et al., "Synthesis and plugging behavior of fluorescent polymer microspheres as a kind of conformance control agent in reservoirs," *RSC Advances*, vol. 8, no. 19, pp. 10478–10488, 2018.
- [37] Y. Liu, Y. Shi, L. Liu, X. Yan, D. Zhou, and S. Liu, "Determination of the pore-throat limits for water imbibition in tight sandstone reservoirs through NMR analysis," *Journal of Geophysics and Engineering*, vol. 16, no. 1, pp. 253–261, 2019.

## Research Article

# A Unified Multiple Transport Mechanism Model for Gas through Shale Pores

Fanhui Zeng<sup>1</sup>, Yu Zhang<sup>1</sup>, Jianchun Guo<sup>1</sup>, Wenxi Ren<sup>1</sup>, Tao Zhang<sup>1</sup>, Qifeng Jiang<sup>2</sup>, and Jianhua Xiang<sup>3</sup>

<sup>1</sup>State Key Laboratory of Oil and Gas Reservoir Geology and Exploitation, Southwest Petroleum University, Chengdu, China 610500

<sup>2</sup>Key Laboratory of Fluid and Power Machinery, Xihua University, Chengdu, China 610039

<sup>3</sup>Engineering Technology Research Institute, Chengdu, China 610017

Correspondence should be addressed to Fanhui Zeng; zengfanhui023024@126.com

Received 14 February 2020; Revised 17 August 2020; Accepted 19 September 2020; Published 17 October 2020

Academic Editor: Jinze Xu

Copyright © 2020 Fanhui Zeng et al. This is an open access article distributed under the Creative Commons Attribution License, which permits unrestricted use, distribution, and reproduction in any medium, provided the original work is properly cited.

Predicting apparent gas permeability (AGP) in nanopores is a major challenge for shale gas development. Considering the differences in the gas molecule-pore wall interactions in inorganic and organic nanopores, the gas transport mechanisms in shale remain unclear. In this paper, gas flow channels in shale, which are separated into inorganic pores and organic pores, are treated as nanotubes. Inorganic pores are assumed to be hydrophilic, and organic pores are assumed to be hydrophobic. In organic pores, multiple bulk free gas and surface adsorbed gas transport mechanisms are incorporated, while the bulk gas and water film are considered within inorganic pores. This paper presents a unified multiple transport mechanism model for both organic nanopores and inorganic nanopores. Unlike the earlier models, the presented models consider the absorption, stress dependence, real gas, and water storage effects on gas transport comprehensively for the entire flow regime. The results are validated with published data which is more in line with the real situation. The results show that (1) the AGP decreases gradually as the pore pressure decreases but that the decrease is sharp in small pores, (2) the AGP decreases dramatically when considering the real gas effect at 50 MPa in a 2 nm pore size, and (3) for a small pore size at the critical high-water saturation, AGP might increase suddenly as the flow regime changes from continuum flow to slip flow. The findings of this study can help for better understanding of the gas transport mechanisms for the entire flow regime in shale.

## 1. Introduction

Shale gas has become increasingly vital in supplying hydrocarbon energy due to its potential to offset conventional gas production declines. A shale gas reservoir typically has nanosized pores, which can be categorized into pores in organic matter (OM) and pores in inorganic matter (IOM) according to the mineral composition, microstructure, and wettability differences [1, 2]. The pores in OM vary in size from nanometer scale to micrometer scale, while those in IOM are on the nanometer scale [3, 4]. Generally, the bulk gas transport capacity and surface diffusion should simultaneously be considered for the coexistence of bulk gas and adsorbed gas phases in organic pores [5]. For the adsorbed gas, the adsorp-

tion flux decreases as the gas desorbs during depressurization, which increases the organic pore flow channel [6–8]. However, IOM is mainly composed of quartz and clay content, which are prone to absorb water [4, 9]. Hence, bulk gas phases and water films coexist in the pores of IOM [10].

The gas transport in shale nanopores is very different from that due to conventional macropore mechanisms because the molecular free path is comparable to the pore size [11]. The strong interfacial effects between the gas and nanotube walls increase with increasing  $K_n$ ; consequently, a continuum approach with no-slip boundary conditions is no longer valid [12].  $K_n$  is defined as the ratio of the mean free path of molecules to the flow path aperture [13] and is applied to characterize the gas flow regime as continuum



flow ( $0 < K_n < 10^{-3}$ ), slip flow ( $10^{-3} < K_n < 10^{-1}$ ), transition flow ( $10^{-1} < K_n < 10$ ), and free molecular flow ( $10 < K_n$ ) [14].

A single-nanopore gas transport mechanism investigation is the theoretical basis for AGP modeling of actual core samples, which has attracted widespread attention [15, 16]. Experimental tests and simulations have been applied to model single-nanopore gas transport capacity [14]. It is usually time-consuming and is extremely difficult to perform laboratory gas transport experiments for the nanopore range considering bulk gas, absorbed gas, real gas, and stress dependence, among other multifactor coupling effects. Second, numerical methods, such as molecular simulation via the lattice Boltzmann model (LBM), are powerful tools for studying gas transport behavior. Third, Qiu et al. [17, 18] studied the phase behavior of fluids confined in nanopores through experimental methods and found that the supercritical region of the confined fluid exists in the low pressure range. However, due to the complexity of the rough pore surface slip boundary, most LBM applications to model gas flow require considerable computational resources and time requirements, which is difficult to account for in practical engineering [4].

To overcome the inconvenience of the numerical method, two different analytical multiscale unified models are developed, coupling various flow regimes for shale gas flow through nanopores. The first method is to solve the Navier-Stokes equation directly by incorporating Maxwell's first-/second-order slip velocity slip boundary condition in the form of a rarefaction effect to cover the entire flow regime. Coupling a second-order slip velocity boundary, Beskok [19] derived a unified nanoscale pore gas transport model for all flow regimes on the basis of the Hagen-Poiseuille equation. However, Karniadakis et al. [20] noted that the unified flow model with general slip boundary conditions resulted in a significant error from that obtained through a direct simulation via the Monte Carlo method. To improve the prediction accuracy, Civan [21] introduced a rarefaction coefficient into the unified equation; this coefficient varies with  $K_n$  and can be determined by numerical or experimental data. Following this concept, several investigators [22, 23] further extended the model by incorporating shale gas transport mechanism differences in the OM and IOM. Although the prediction accuracy improved by the introduction of the rarefaction coefficient, the second-order model slip boundary condition is unable to model gas through porous media, while the first-order model is also valid in the low-moderate  $K_n$  number regime [24].

Another approach that expresses the shale gas transport capacity by different equations based on the  $K_n$  number was proposed. In this approach, the transition flow capacity is superimposed by slip flow and free molecule flow through their weighting coefficients. Adzumi [25] performed experiments on gas transport in circular capillaries, and a contribution coefficient term was applied to express the transition flow regime involvement of viscous flow and Knudsen's flow. However, these models did not provide the contribution coefficient. Javadpour [26] directly superposed the gas trans-

port capacity of slip flow and Knudsen diffusion to develop an AGP model. Furthermore, Darabi [27] introduced the fractal dimension into Knudsen diffusion to consider the pore surface roughness effect based on Javadpour's model, although both models ignored the gas transition flow regime transport capacity.

To directly overcome the limitation of flow capacity summation, several investigators introduced contribution coefficients to fuse different flow regimes. Wu et al. [28] utilized the weighting coefficient expressed by the molecular collision frequency to model gas slip flow and Knudsen diffusion transport capacity for the entire flow regime. Zeng et al. [29, 30] extended this model by directly incorporating surface effects. Chai et al. [23] integrated real gas effects, gas desorption, surface diffusion, etc., to propose a comprehensive gas transport model. However, these models consider that all the flow states coexist and ignore the gas flow state as determined by  $K_n$  [14] and the absorbed water film effect. In addition, under the high-temperature and high-pressure conditions of formations in actual gas-shale reservoirs, the assumption that gas molecules can be represented as a point is inappropriate due to the size of gas molecules compared to that of nanopores, and the real gas effect should be considered [27, 31]. In addition, Ross and Bustin [32, 33], after analyzing porosity and permeability test results, reported that shale gas sample permeability was highly stress-dependent, which further complicates shale gas transport.

Overall, the currently established models are unable to consider all the above transport mechanisms and fail to consider shale gas flow capacity differences between organic and inorganic pores. It is urgent to develop a fully coupled unified single-nanopore AGP model for shale gas, merging all the aforementioned gas transport mechanisms. This paper develops a simple but rigorous method to model the transport of shale gas through nanopores via various flow regimes. The remaining parts of this paper are organized as follows: the mathematical modeling is presented in Section 2. The model comparison and validation are presented in Section 3. The effects of the storage medium and pore size, stress dependence, real gas, surface diffusion, and water storage on the AGP are investigated in Section 4. Finally, several conclusions are provided in Section 5. Due to the complexity of considering multiphase flow, this paper does not consider the flow capacity of shale fluids in the presence of multiphase flow.

## 2. Mathematical Modeling

In the physical model, we consider bulk gas and adsorbed gas phases in organic pores and bulk gas and adsorbed water phases in inorganic pores, as shown in Figure 1.

*2.1. Bulk Gas Transport Mechanisms.*  $K_n$  is usually used to characterize shale gas flow regimes [34].

$$K_n = \frac{\lambda}{d}, \quad (1)$$



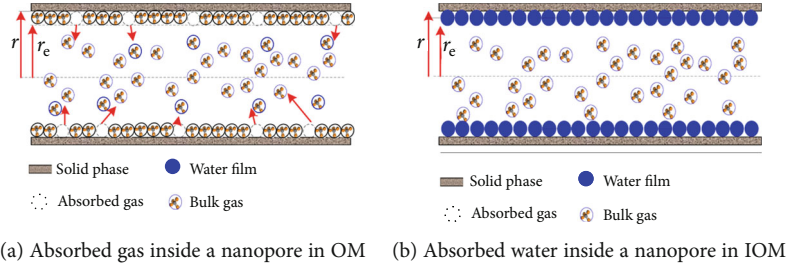


FIGURE 1: Illustration of absorbed gas/water inside shale nanopores.

Thermodynamic	Boltzmann equation				
Hydromechanic	Euler equation	Navier–Stokes equation		Burnett equation	Limit type of Boltzmann equation
Flow equation in porous media		Darcy equation	Klinkenberg equation	Bryant equation	?
		Presented equation			
$K_n$	$0 \leftarrow K_n \quad 10^{-3} \quad 10^{-1} \quad 10^0 \quad 10^1 \quad K_n \rightarrow \infty$				
Flow regimes	Continuum flow		Slip flow	Transition flow	Free molecular flow

FIGURE 2: Illustration of flow regimes and corresponding equations [14].

where  $\lambda$  is the molecular mean free path, m, and  $d$  is the effective radius of the nanopores, m.

The following equation is used to determine the mean free path:

$$\lambda(p, T) = \frac{k_B T}{\sqrt{2}\pi\delta^2 p}, \quad (2)$$

where  $k_B$  is the Boltzmann constant,  $1.3805 \times 10^{-23}$  J/K;  $T$  is the formation temperature, K;  $\delta$  is the gas molecule collision diameter, nm (the value of which is 0.42 nm for  $\text{CH}_4$ ); and  $p$  is pore pressure, MPa.

Substituting Equation (2) into Equation (1), one can obtain a more detailed expression of  $K_n$  for the gas:

$$K_n(p, T) = \frac{k_B T}{\sqrt{2}\pi\delta^2 p} \cdot \frac{1}{d}. \quad (3)$$

The gas transport mechanism is controlled by different equations for each flow regime according to  $K_n$ , as shown in Figure 2. We will derive unified multiple transport mechanism models for the entire flow regime in the following section.

**2.1.1. Continuum Flow.** The gas transport regime in pores is continuous flow when  $K_n < 10^{-3}$ . The number of collisions between the gas molecules and pore wall is assumed to be negligible, and the gas flow rate can be expressed by Hagen-Poiseuille's equation ([35]):

$$J_{\text{vicious}} = -\rho \cdot \frac{k_{\infty}}{\mu} \cdot \nabla p = -\rho \cdot \frac{r^2}{8\mu} \cdot \nabla p, \quad (4)$$

where  $J_{\text{vicious}}$  is the continuum flow volume flux,  $\text{kg}/(\text{m}^2 \cdot \text{s})$ ;  $\rho$  is the gas density,  $\text{kg}/\text{m}^3$ ;  $k_{\infty}$  is the intrinsic permeabil-

ity,  $\text{m}^2$ ;  $\mu$  is the gas viscosity, Pa·s;  $r$  is the nanopore radius, m;  $p$  is the pore pressure, Pa; and  $\nabla$  is the pressure gradient operator symbol.

**2.1.2. Slip Flow.** The gas transport regime in pores is continuous flow with a slippage effect when  $10^{-3} < K_n < 10^{-1}$ . In this regime, the gas velocity near the pore wall is no longer zero due to the slippage effect, which satisfies Klinkenberg's equation. Therefore, the AGP for slip flow can be written as [36] follows:

$$k_{\text{slip}} = k_{\infty} \cdot \left(1 + \frac{b_k}{p_{\text{aver}}}\right), \quad (5)$$

where  $k_{\text{slip}}$  is the slip flow regime AGP,  $\text{m}^2$ ;  $b_k$  is the gas slip factor, MPa; and  $p_{\text{aver}}$  is the gas phase mean pressure, MPa, which is equal to the pore pressure.

$b_k$  is defined as [27, 37]

$$b_k = \left(\frac{8\pi RT}{M}\right)^{0.5} \cdot \frac{\mu}{r} \cdot \left(\frac{2}{\alpha} - 1\right), \quad (6)$$

where  $R$  is the universal gas constant, J/(mol·K), which is 8314 J/(kmol·K);  $M$  is the molar mass, kg/mol; and  $\alpha$  is the tangential momentum accommodation coefficient (TMAC), dimensionless.

By inserting Equation (6) into Equation (5), one can obtain the AGP correction form that takes into account the slippage effect:

$$k_{\text{slip}} = k_{\infty} \cdot \left[1 + \left(\frac{8\pi RT}{M}\right)^{0.5} \cdot \frac{\mu}{p_{\text{avg}} r} \cdot \left(\frac{2}{\alpha} - 1\right)\right]. \quad (7)$$

By substituting (7) into (4), one can obtain

$$J_{\text{slip}} = -\rho \cdot \frac{k_{\text{slip}}}{\mu} \cdot \nabla p = -\rho \cdot \frac{r^2}{8\mu} \cdot \left[ 1 + \left( \frac{8\pi RT}{M} \right)^{0.5} \cdot \frac{\mu}{p_{\text{avg}} r} \cdot \left( \frac{2}{\alpha} - 1 \right) \right] \cdot \nabla p, \quad (8)$$

where  $J_{\text{slip}}$  is the volume flux for the slip regime,  $\text{kg}/(\text{m}^2 \cdot \text{s})$ .

**2.1.3. Free Molecule Flow.** The gas transport regime is free molecule flow when  $K_n > 10$ . The collision between the gas molecules and the pore walls is the most important influencing factor, and the gas transport satisfies Knudsen diffusion, which can be expressed as [38, 39]

$$J_{\text{Knudsen}} = \frac{M}{ZRT} \cdot D_k \cdot \nabla p, \quad (9)$$

where  $J_{\text{Knudsen}}$  is the volume flux for the slip regime,  $\text{kg}/(\text{m}^2 \cdot \text{s})$ ;  $D_k$  is the Knudsen diffusion constant,  $\text{m}^2/\text{s}$ ; and  $Z$  is the deviation factor.

Additionally, the Knudsen diffusion constant can be written as [14, 26]

$$D_k = \frac{2r}{3} \cdot \left( \frac{8RT}{\pi M} \right)^{0.5}. \quad (10)$$

During the gas flow in nanopores, the wall roughness has a profound effect on the Knudsen diffusion constant. The effective Knudsen diffusion constant influenced by roughness can be written as [27, 40]

$$D_{\text{eff-k}} = \left( \frac{d_m}{d} \right)^{D_f-2} \cdot D_k, \quad (11)$$

where  $D_{\text{eff-k}}$  is the effective Knudsen diffusion constant,  $\text{m}^2/\text{s}$ ;  $d_m$  is the gas molecule diameter; and  $D_f$  is the pore wall fractal dimension, dimensionless.

Substituting Equations (10) and (11) into Equation (9), the Knudsen diffusion incorporating pore wall roughness can be written as

$$J_{\text{Knudsen}} = \frac{M}{ZRT} \cdot \frac{2r}{3} \cdot \left( \frac{d_m}{d} \right)^{D_f-2} \cdot \left( \frac{8RT}{\pi M} \right)^{0.5} \cdot \nabla p. \quad (12)$$

**2.1.4. Transition Flow.** For  $10^{-1} < K_n < 10$ , the momentum transfer of molecules between the pore walls is important, and the continuous flow and Knudsen flow mechanisms coexist under such conditions [41]. It is vital to calculate the comprehensive apparent permeability through reasonable weighting coefficients of both gas transport mechanisms together. Considering gaseous mixtures flowing through capillaries simultaneously under continuum flow and Knudsen diffusion, Adzumi [42] introduced a contribution coefficient term  $\varepsilon$  to express each of the flow regimes involved in gas transport:

$$J_t = J_{\text{vicious}} + \varepsilon J_{\text{Knudsen}}, \quad (13)$$

where  $J_t$  is the volume flux,  $\text{kg}/(\text{m}^2 \cdot \text{s})$ , and  $\varepsilon$  is the contribution coefficient term, dimensionless.

Adzumi [42] noted that the value of  $\varepsilon$  varies between 0.7 and 1.0 smoothly. Unfortunately, Adzumi [42] did not explain how to obtain the specific value  $\varepsilon$  in his experiments. Based on Adzumi's research, Mohammad [43] expressed the total mass flow as a superposition of the viscous flow and free molecular flow as follows:

$$J_t = (1-\varepsilon)J_{\text{vicious}} + \varepsilon J_{\text{Knudsen}}. \quad (14)$$

To reflect the flow difference results for different regimes, the following equation is applied to provide reasonable results that vary with the Knudsen number for all the flow regimes ([43]):

$$\varepsilon = C_A \left[ 1 - \exp \left( \frac{-K_n}{K_{n\text{Viscous}}} \right) \right]^S, \quad (15)$$

where  $C_A$  and  $S$  are constants, dimensionless, which are 1;  $K_{n\text{Viscous}}$  equals  $K_n$  when the flow regime transfers from viscous to diffusion flow, which is usually set as 0.3. The simulation results show that Equation (15) fit the Monte Carlo simulation data well, which is much better than Beskok's model with the first-/second-order model slip boundary [34].

Obviously, the slip effect is not considered in Equation (14). We propose a modification of Equation (14) in this paper:

$$J_t = (1-\varepsilon)J_{\text{slip}} + \varepsilon J_{\text{Knudsen}}. \quad (16)$$

## 2.2. Absorbed Gas Transport Mechanisms

**2.2.1. Gas Desorption.** For the absorbed gas, the adsorption layer thickness decreases as the gas desorbs during depressurization, which increases the organic pore radius, as shown in Figure 1(a). The modified Langmuir adsorption isotherm equation is adopted to model this effect ([39]):

$$V = V_L \cdot \theta, \quad (17)$$

$$\theta = \frac{p/Z}{p/Z + p_L}, \quad (18)$$

where  $V$  is the adsorbed gas volume per shale unit weight under standard conditions,  $\text{m}^3/\text{kg}$ ;  $V_L$  is the Langmuir volume under standard conditions,  $\text{m}^3/\text{kg}$ ;  $\theta$  is the gas coverage under certain pressures, dimensionless; and  $p_L$  is the Langmuir pressure, Pa.

The absorbed gas in the organic matter inner wall recedes the pore flow radius as

$$r_{\text{ef-or}} = r_{\text{e-or}} - \theta \cdot d_m, \quad (19)$$

where  $r_{\text{ef-or}}$  is the effective pore flow radius considering gas desorption, m, and  $r_{\text{e-or}}$  is the original pore radius of the organic pore, m.

**2.2.2. Surface Diffusion.** Surface diffusion is a complicated process of adsorbed phase transport that can be categorized into adatom and cluster diffusion [38]. Several different mathematical models have been presented to express the surface diffusion phenomenon. In this paper, it is assumed that the adsorption and desorption processes would reach equilibrium instantly, which satisfies the Langmuir equation requirement:

$$J_{\text{surface}} = -M \cdot D_s \cdot \frac{C_s \max p_L}{(p + p_L)^2} \cdot \nabla p, \quad (20)$$

where  $D_s$  is the coefficient surface diffusion,  $\text{m}^2/\text{s}$ , and  $C_{s\max}$  is the maximum adsorption concentration,  $\text{mol}/\text{m}^3$ .

### 2.3. Multifactorial Effect Mechanisms

**2.3.1. Stress Dependence Effect.** The effective confining pressure will increase during shale gas depressurization, which will reduce the nanopore porosity and permeability. The following power law equations can be obtained ([44]):

$$k = k_0 \left( \frac{p_e}{p_0} \right)^{-s}, \quad (21)$$

$$\varphi = \varphi_0 \left( \frac{p_e}{p_0} \right)^{-q}, \quad (22)$$

where  $s$  and  $q$  are the material constants, dimensionless, which can be obtained by permeability and porosity laboratory experiments under different effective pressures;  $k$  is the permeability considering the effective stress,  $\mu\text{m}^2$ ;  $k_0$  is the permeability under the condition of atmospheric pressure,  $\mu\text{m}^2$ ;  $p_e$  is the effective stress, MPa (i.e.,  $p_c - p$ );  $p_c$  is the confining pressure, MPa;  $p_0$  is the atmospheric pressure, MPa;  $\varphi$  is the porosity under the effective stress, dimensionless; and  $\varphi_0$  is the porosity at atmospheric pressure, dimensionless.

For capillary nanotubes, the relationship between the nanopore radius and intrinsic permeability can be written as [45]

$$r = 2\sqrt{2\tau} \sqrt{\frac{k}{\varphi_0}}. \quad (23)$$

Following Equations (21)–(23), the pore effective radius considering the stress dependence effect can be written as

$$r_{\text{ef}} = r \left( \frac{p_e}{p_0} \right)^{0.5(q-s)}, \quad (24)$$

where  $r_{\text{ef}}$  is the effective flow radius considering the stress dependence effect, m.

**2.3.2. Water Storage Characteristics within Inorganic Nanopores.** The shale clay layer minerals with additional negatively charged electrostatic properties are prone to cause the water molecules to adsorb onto the inter pore surface under actual reservoir conditions. The water film formation will reduce the inorganic pore effective radius shown in Figure 1(b), and one can obtain the following water saturation equation:

$$s_w = \frac{v_w}{v_p} = \frac{\pi r_{e\text{-in}}^2 l_c - \pi r_{\text{ef-in}}^2 l_c}{\pi r_{e\text{-in}}^2 l_c} = \frac{r_{e\text{-in}}^2 - r_{\text{ef-in}}^2}{r_{e\text{-in}}^2}. \quad (25)$$

Rearranging Equation (25) gives the relationship between  $r_{\text{ef-in}}$  and  $r_{e\text{-in}}$ :

$$r_{\text{ef-in}} = r_{e\text{-in}} \sqrt{1 - s_w}, \quad (26)$$

where  $s_w$  is the shale pore water saturation, dimensionless;  $v_w$  and  $v_p$  are the bound water volume and pore volume, respectively,  $\text{m}^3$ ;  $r_{e\text{-in}}$  is the hydrodynamic radius for inorganic pores taking the stress dependence effect into account, m;  $r_{\text{ef-in}}$  is the inorganic pore effective flow radius considering the stress dependence effect and water storage characteristics, m; and  $l_c$  is the capillary length, m.

**2.3.3. Real Gas Physical Properties.** The mutual force and volume of gas molecules should be considered for evaluating shale gas reservoirs under realistic high-pressure and high-temperature conditions. The real gas effect, due to the gas compressibility factor and gas viscosity, is different from that under ideal conditions and should be considered carefully. Here, we apply pseudopressure and pseudotemperature to determine the gas compressibility factor ([39]):

$$Z = 0.702 p_r^2 e^{-2.5T_r} - 5.524 p_r e^{-2.5T_r} + 0.044 T_r^2 - 0.164 T_r + 1.15, \quad (27)$$

$$p_r = \frac{p}{p_c}, \quad (28)$$

$$T_r = \frac{T}{T_c}, \quad (29)$$

where  $p_r$  is the pseudopressure, dimensionless;  $T_r$  is the pseudotemperature, dimensionless;  $p_c$  is the critical pressure, MPa; and  $T_c$  is the critical temperature, K.

The effective viscosity for gas transport in nanopores can be presented as [46]

$$\mu_{\text{eff}} = (1 \times 10^{-7}) K_d \exp(X \rho^Y), \quad (30)$$

$$K_d = \frac{(9.379 + 0.01607M) T^{1.5}}{(209.2 + 19.26M + T)}, \quad (31)$$

$$\rho = 1.4935 \times 10^{-3} \frac{pM}{ZT}, \quad (32)$$

$$X = 3.448 + \frac{986.4}{T} + 0.01009M, \quad (33)$$

$$Y = 2.447 - 0.2224X, \quad (34)$$

where  $\mu_{\text{eff}}$  is the effective viscosity of the gas transport in nanopores, Pa·s;  $K_d$  is the intermediate variable of the viscosity calculation, dimensionless;  $\rho$  is the gas density,  $\text{kg}/\text{m}^3$ ;  $X$  is the density multiplication factor, dimensionless; and  $Y$  is the density index, dimensionless.

2.4. *The Coupling Transport Mechanism for Organic/Inorganic Nanopores.* In this section, we build unified AGP models for modeling gas transport through nanopores with various values of  $K_n$ ; these models are valid for modeling the entire flow regime and take multiple transport mechanisms into account. The presented models also consider the difference in the flow mechanism between organic and inorganic nanopores.

2.4.1. *The AGP Model for Organic Nanopores.* The total mass flux is determined by the bulk gas and adsorbed gas phases of the organic pores. The flow capacity equation can be written as follows according to the value of  $K_n$ .

- (1) *Continuum Flow* ( $K_n < 10^{-3}$ ). The bulk gas AGP is obtained through the linear superposition of the continuum flow formula and surface diffusion formula:

$$k_{app\_or1} = \frac{(r_{eff\_or} - \theta \cdot d_m)^2}{8} + M \cdot D_s \cdot \frac{C_s \max p_L}{(p + p_L)^2} \cdot \frac{\mu_{eff}}{\rho}, \quad (35)$$

where  $r_{eff\_or}$  is the effective flow radius for organic pores considering gas desorption and the stress dependence effect, m.

- (2) *Slip Flow* ( $10^{-3} < K_n < 10^{-1}$ ). The AGP of bulk gas due to the updated Kligenberg effect formula and the surface diffusion formula is obtained through their linear superposition:

$$k_{app\_or2} = \frac{(r_{eff\_or} - \theta \cdot d_m)^2}{8} \left[ 1 + \left( \frac{8\pi RT}{M} \right)^{0.5} \cdot \frac{\mu_{eff}}{p_{avg}(r_{eff\_or} - \theta \cdot d_m)} \cdot \left( \frac{2}{\alpha} - 1 \right) \right] + M \cdot D_s \cdot \frac{C_s \max p_L}{(p + p_L)^2} \cdot \frac{\mu_{eff}}{\rho}. \quad (36)$$

- (3) *Free Molecule Flow* ( $K_n > 10$ ). The bulk gas AGP due to Knudsen flow and adsorbed gas surface diffusion is given as

$$k_{app\_or3} = \frac{M}{ZRT} \cdot \frac{2(r_{eff\_or} - \theta \cdot d_m)}{3} \cdot \left( \frac{d_M}{2(r_{eff\_or} - \theta \cdot d_m)} \right)^{D_i-2} \cdot \left( \frac{8RT}{\pi M} \right)^{0.5} \cdot \frac{\mu_{eff}}{\rho} + M \cdot D_s \cdot \frac{C_s \max p_L}{(p + p_L)^2} \cdot \frac{\mu_{eff}}{\rho}. \quad (37)$$

- (4) *Transition flow* ( $10^{-1} < K_n < 10$ ). The AGP of bulk gas due to slip flow and free molecule flow, considering the surface diffusion formula, is given as

$$k_{app\_or4} = \frac{(r_{eff\_or} - \theta \cdot d_m)^2}{8} \cdot \left[ \left( \frac{8\pi RT}{M} \right)^{0.5} \cdot \frac{\mu_{eff}}{p_{avg}(r_{ep} - \theta \cdot d_m)} \cdot \left( \frac{2}{\alpha} - 1 \right) \right] \cdot (1 - \varepsilon) + \frac{2(r_{eff\_or} - \theta \cdot d_m)}{3} \cdot \left( \frac{8RT}{\pi M} \right)^{0.5} \cdot \frac{\mu_{eff}}{\rho} \cdot \varepsilon + M \cdot D_s \cdot \frac{\mu_{eff}}{\rho} \cdot \frac{C_s \max p_L}{(p + p_L)^2}. \quad (38)$$

2.4.2. *The AGP Model for Inorganic Nanopores.* The AGP for inorganic nanopores is determined by the bulk gas transport mechanisms and water film properties. Considering the stress dependence and real gas effect, the AGP for inorganic pores can be written as

- (1) *Continuum Flow* ( $K_n < 10^{-3}$ )

$$k_{app\_in1} = \frac{r_{eff\_in}^2}{8} \quad (39)$$

- (2) *Slip Flow* ( $10^{-3} < K_n < 10^{-1}$ )

$$k_{app\_in2} = \frac{r_{eff\_in}^2}{8} \left[ 1 + \left( \frac{8\pi RT}{M} \right)^{0.5} \cdot \frac{\mu_{eff}}{p_{avg} r_{eff\_in}} \cdot \left( \frac{2}{\alpha} - 1 \right) \right] \quad (40)$$

- (3) *Free Molecule Flow* ( $K_n > 10$ )

$$k_{app\_in3} = \frac{2r_{eff\_in}}{3p_{avg}} \cdot \left( \frac{d_m}{2r_{eff\_in}} \right)^{D_i-2} \cdot \frac{8RT^{0.5}}{\pi M} \cdot \frac{\mu_{eff}}{\rho} \quad (41)$$

- (4) *Transition Flow* ( $10^{-1} < K_n < 10$ )

$$k_{app\_in4} = \frac{r_{eff\_in}^2}{8} \cdot \left[ \left( \frac{8\pi RT}{M} \right)^{0.5} \cdot \frac{\mu_{eff}}{p_{avg} r_{eff\_in}} \cdot \left( \frac{2}{\alpha} - 1 \right) \right] \cdot (1 - \varepsilon) + \frac{2r_{eff\_in}}{3p_{avg}} \cdot \left( \frac{d_m}{d} \right)^{D_i-2} \cdot \left( \frac{8RT}{\pi M} \right)^{0.5} \cdot \frac{\mu_{eff}}{\rho} \cdot \varepsilon \quad (42)$$

2.5. *The AGP Model for Organic/Inorganic Nanopores.* The final AGP equations for organic and inorganic pores can be obtained through the apparent liquid phase permeability

model of organic pores and inorganic pores established in Section 2.4.

(1) *The AGP Model For Organic*

$$\left\{ \begin{array}{l} k_{app\_or1} = \frac{(r_{eff\_or} - \theta \cdot d_m)^2}{8} + M \cdot D_s \cdot \frac{C_s \max P_L}{(p + p_L)^2} \cdot \frac{\mu_{eff}}{\rho}, \quad \text{Continuum flow } (K_n < 10^{-3}), \\ k_{app\_or2} = \frac{(r_{eff\_or} - \theta \cdot d_m)^2}{8} \left[ 1 + \left( \frac{8\pi RT}{M} \right)^{0.5} \cdot \frac{\mu_{eff}}{p_{avg}(r_{eff\_or} - \theta \cdot d_m)} \times \left( \frac{2}{\alpha} - 1 \right) \right] + M \cdot D_s \cdot \frac{C_s \max P_L}{(p + p_L)^2} \cdot \frac{\mu_{eff}}{\rho}, \quad \text{Slip flow } (10^{-3} < K_n < 10^{-1}), \\ k_{app\_or3} = \frac{M}{ZRT} \cdot \frac{2(r_{eff\_or} - \theta \cdot d_m)}{3} \cdot \left( \frac{d_m}{2(r_{eff\_or} - \theta \cdot d_m)} \right)^{D_r-2} \times \left( \frac{8RT}{\pi M} \right)^{0.5} \cdot \frac{\mu_{eff}}{\rho} + M \cdot D_s \cdot \frac{C_s \max P_L}{(p + p_L)^2} \cdot \frac{\mu_{eff}}{\rho}, \quad \text{Free molecule flow } (K_n > 10), \\ k_{app\_or4} = \frac{(r_{eff\_or} - \theta \cdot d_m)^2}{8} \cdot \left[ \left( \frac{8RT}{\pi M} \right)^{0.5} \cdot \frac{\mu_{eff}}{p_{avg}(r_{ep} - \theta \cdot d_m)} \cdot \left( \frac{2}{\alpha} - 1 \right) \right] \cdot (1 - \varepsilon) + \frac{2(r_{eff\_or} - \theta \cdot d_m)}{3} \cdot \left( \frac{8RT}{\pi M} \right)^{0.5} \cdot \frac{\mu_{eff}}{\rho} \cdot \varepsilon + M \cdot D_s \cdot \frac{C_s \max P_L}{(p + p_L)^2} \cdot \frac{\mu_{eff}}{\rho}, \quad \text{Transition flow } (10^{-1} < K_n < 10) \end{array} \right. \quad (43)$$

(2) *The AGP model for Inorganic*

$$\left\{ \begin{array}{l} k_{app\_in1} = \frac{r_{eff\_in}^2}{8}, \quad \text{Continuum flow } (K_n < 10^{-3}), \\ k_{app\_in2} = \frac{r_{eff\_in}^2}{8} \left[ 1 + \left( \frac{8\pi RT}{M} \right)^{0.5} \cdot \frac{\mu_{eff}}{p_{avg} r_{eff\_in}} \cdot \left( \frac{2}{\alpha} - 1 \right) \right], \quad \text{Slip flow } (10^{-3} < K_n < 10^{-1}), \\ k_{app\_in3} = \frac{2r_{eff\_in}}{3p_{avg}} \cdot \left( \frac{d_m}{2r_{eff\_in}} \right)^{D_r-2} \cdot \left( \frac{8RT}{\pi M} \right)^{0.5} \cdot \frac{\mu_{eff}}{\rho}, \quad \text{Free molecule flow } (K_n > 10), \\ k_{app\_in4} = \frac{r_{eff\_in}^2}{8} \cdot \left[ \left( \frac{8\pi RT}{M} \right)^{0.5} \cdot \frac{\mu_{eff}}{p_{avg} r_{eff\_in}} \cdot \left( \frac{2}{\alpha} - 1 \right) \right] \cdot (1 - \varepsilon) + \frac{2r_{eff\_in}}{3p_{avg}} \cdot \left( \frac{d_m}{d} \right)^{D_r-2} \cdot \left( \frac{8RT}{\pi M} \right)^{0.5} \cdot \frac{\mu_{eff}}{\rho} \cdot \varepsilon, \quad \text{Transition flow } (10^{-1} < K_n < 10) \end{array} \right. \quad (44)$$

### 3. Model Comparison and Validation

Validation of the presented AGP models is demonstrated in this section. The coupled models established in this paper are compared with the models proposed by Xiong et al. [47], Asana et al. [48], and Song et al. [11], as shown in Table 1.

Table 1 clearly shows that the AGP models presented by Xiong et al. and Asana et al. incorporate free gas and surface diffusions to model gas transport. However, they ignore the phase behavior influence on the gas viscosity, stress dependence, desorption, and water storage effects on pore diameter. In their models, the apparent gas permeability is irrespective of  $K_n$ . Although Song et al.'s model considers the difference in the free gas and adsorbed gas transport properties between the organic and inorganic pores, it ignores the effect of nanopore diameter on water storage. The presented models are rather general, assuming that real shale is composed of both organic and inorganic matters. The presented models are capable of modeling adsorbed gas in organic nanopores and adsorbed water films in inorganic nanopores, and the stress dependence

and real gas effects are incorporated to more closely reflect the actual reservoir conditions, unlike in the previously established models.

Inputting the basic parameters listed in Table 2, the AGP for different models over the entire  $K_n$  range are calculated and shown in Figure 3.

Figure 3 illustrates the AGP of organic and inorganic pores versus pressure results from the presented model compared with those of Song et al.'s, Asana et al.'s, and Xiong et al.'s models for organic and inorganic nanopores. The presented model calculation results fit well with those of Song et al.'s, Asana et al.'s, and Xiong et al.'s models for organic and inorganic nanopores when  $K_n < 0.1$ . The presented model also fits well with Asana et al.'s model in the range of  $0.1 < K_n < 1$  for an organic nanopore, while the presented model achieves the same trend as that of Song et al.'s model for an organic nanopore when  $K_n > 0.1$ , which indicates that the presented model is valid. Notably, for values of  $K_n$  greater than 0.1, one interesting phenomenon exhibited in Figure 3(a) is that the AGP determined by Song et al.'s model shows a sudden increasing trend. The reason for this change is that Song et al.'s model is modified from Beskok-



TABLE 1: Model comparison.

Case	Apparent permeability model	Description
Xiong et al.'s model	$K_{\text{ad}} = K_a + D\mu(MC_a \max p_L / (p + p_L)) (1 - R_{\text{eff}}^2 / R_{\text{fi}}^2)$	Considers only free gas flow and surface diffusion, without considering stress dependence, real gas effects, and water storage characteristics
Asana et al.'s model	$K_{\text{gas}} = K_m + \mu D c_g + \mu D_s \left( V_{\text{sL}} \rho_{\text{grain}} B_g / \epsilon_{\text{ks}} \right) (p_L / (p + p_L))^2$	Considers only free flow and surface diffusion
Song et al.'s model	$k_{\text{app-or}} = (r_{\text{eff}}^2 / 8) \left[ 1 + (128 / 15\pi^2) \tan^{-1} (4.0 K_n^{0.4}) K_n \right] \times (1 + (4K_n / 1 + K_n)) + \mu M_g D_s C_{\text{max}} (d\theta / dp) \times [1 - (r_{\text{eff}} / r_{\text{eff-stress}})^2],$ $k_{\text{app-in}} = (r_{\text{eff}}^2 / 8) \left[ 1 + (128 / 15\pi^2) \tan^{-1} (4.0 K_n^{0.4}) K_n \right] \times (1 + (4K_n / 1 + K_n)) [1 - (r_{\text{eff}} / r_{\text{eff-stress}})^2]$	Considers only free gas flow and surface diffusion, without considering water storage characteristics
Presented models	See Section 2.5	Consider multiple transport mechanisms in organic/inorganic nanopores, stress dependence, real gas effects, adsorption/desorption, and water storage characteristics

TABLE 2: Basic simulation data.

Parameter name	Symbol	Unit	Numerical value
Gas type	$\text{CH}_4$	—	—
Ideal gas constant	$R$	J/(mol·K)	8.314
Temperature	$T$	K	412
Molecular weight	$M_{\text{gas}}$	kg/mol	$1.6 \times 10^{-2}$
Gas viscosity	$\mu$	Pa·s	$1.76 \times 10^{-5}$
Nanopore diameter	$d$	nm	0.35~1010
Rarefaction coefficient	$\alpha$	Dimensionless	0.8
Gas molecular diameter	$d_m$	m	$0.34 \times 10^{-9}$
Confining pressure	$p_{\text{con}}$	Pa	$61.8 \times 10^6$
Mean formation pressure	$p_{\text{avg}}$	Pa	$30.9 \times 10^6$
Atmospheric pressure	$p_{\text{at}}$	Pa	101300
Maximum adsorbed gas concentration	$C_{\text{smax}}$	mol/m <sup>3</sup>	24080
Langmuir pressure	$p_L$	MPa	2.38
Surface diffusion coefficient	$D_s$	m <sup>2</sup> /s	$2.73 \times 10^{-10}$
Material constant	$q$	Dimensionless	0.04
Material constant	$s$	Dimensionless	0.08
Porosity	$\varphi$	Dimensionless	0.047
Critical pressure	$p_c$	Pa	$4.834 \times 10^{-6}$
Critical temperature	$T_c$	K	150.86
Nanopore surface roughness	$D_f$	Dimensionless	2.5
Grain density	$\rho_{\text{grain}}$	Lbm/ft <sup>3</sup>	166
Langmuir volume	$V_{\text{sl}}$	scf/ton	50
Pore compressibility	$C_g$	1/psi	$3 \times 10^{-6}$
Water saturation	$s_w$	Dimensionless	0.3

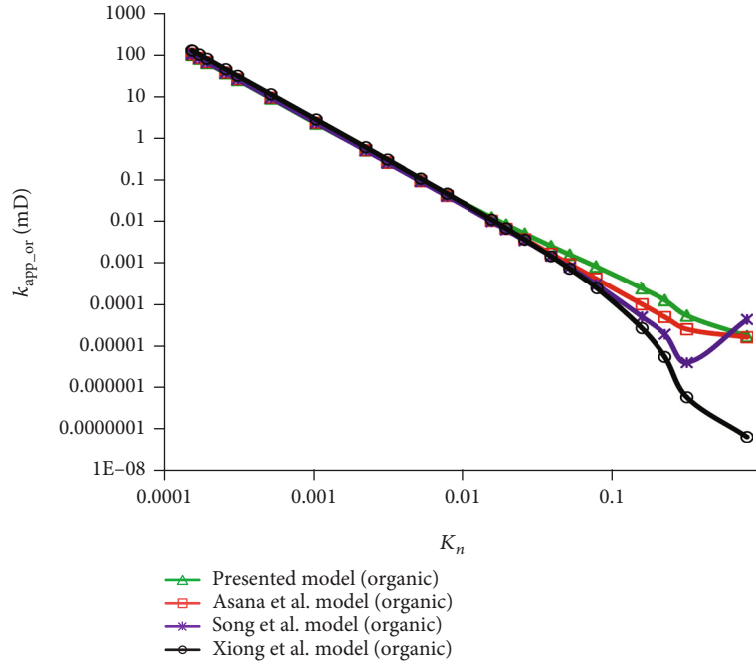
Karniadakis's model with a first-order model slip boundary condition, which incorporates a tan function, causing the AGP to fluctuate with  $K_n$ , while B-K's model with a first-order model slip boundary condition is also valid at low to moderate values of  $K_n$  [24]. In Asana et al.'s and Xiong et al.'s organic permeability models, the AGP remains constant when  $K_n > 1$  and is not related to  $K_n$ . These models neglect the phase behavior effect on gas properties, and the gas property values are treated as constants. However, in our derived model, the comprehensive effects of the flow regime, stress dependence, phase behavior, and real gas on the AGP are incorporated. Therefore, the gas viscosity and compressibility factor properties vary with pressure; these differences cause the organic AGP to decrease as  $K_n$  increases [49]. Additionally, the stress dependence, phase behavior, real gas effects, and water film effect are considered in the presented model, causing the organic nanopore AGP to be smaller than those of Asana et al.'s and Xiong et al.'s models.

#### 4. Results and Discussion

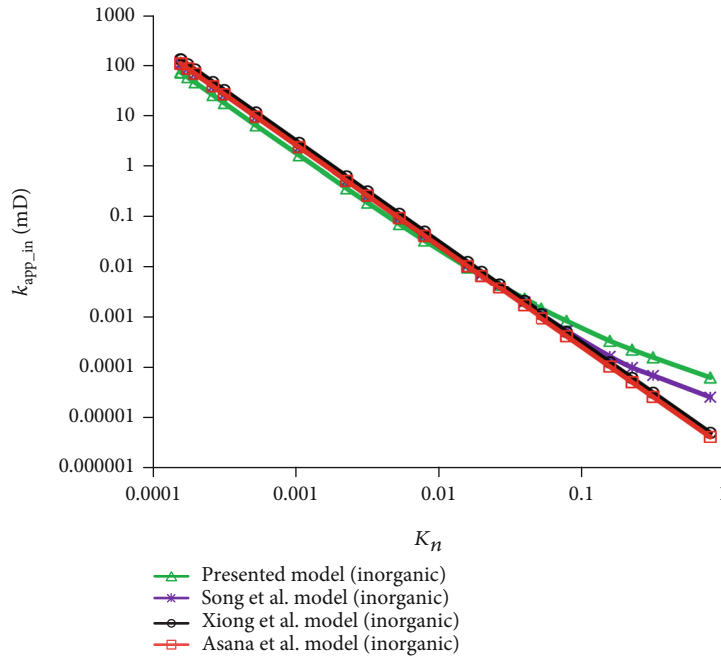
In this section, we further analyze the effects of the storage medium, stress dependence, real gas, surface diffu-

sion, and water storage on AGP. The basic parameters are listed in Table 2.

*4.1. Storage Medium and Pore Size.* Figure 4 shows that the AGP in organic/inorganic pores with sizes of 2 nm, 20 nm, and 200 nm varies from 1.0 to 50.0 MPa at a temperature of 412 K under reservoir conditions. In general, the AGP generally decreases gradually as the pore pressure decreases and decreases sharply for small pores (i.e., 2 nm and 200 nm). Taking the pore size 2 nm as an example, the AGP can reduce from 0.1197 mD to 0.0007858 mD in organic pores as the pore pressure increases from 1.0 MPa to 50 MPa. However, the AGP of the 200 nm pore remains constant with a pore pressure increase. This difference arises because in the continuum flow regime, the AGP is mainly determined by the pore size. In addition, the AGP in organic pores is usually greater than that in inorganic pores, which is attributed to the absorbed/surface diffusion in organic pores and the water film in inorganic pores. Notably, in the flow transition region, i.e., as the flow regime transitions from transition flow ( $K_n > 0.1$ ) to slip flow ( $10^{-3} < K_n < 10^{-1}$ ), the AGP in inorganic pores is greater than that in organic pores. In Figure 4, the flow transition pore pressure is 1 MPa to



(a) AGP for an organic pore versus  $K_n$



(b) AGP for an inorganic pore versus  $K_n$

FIGURE 3: Comparison of organic and inorganic matters with other models ( $p = 30.9$  MPa,  $T = 412$  K).

3 MPa for a pore size of 20 nm but 21 MPa to 25 MPa for a pore size of 2 nm.

**4.2. Stress Dependence Effect.** Figure 5 presents the conditions of considering the stress dependence effect to the AGP in organic nanopores within 2 and 20 nm pores from 1.0 to 50.0 MPa under a temperature of 412 K. The AGP decreases as the effective pressure increases, which is confirmed by the definition of effective pressure. As shown in Figure 6, the deviation in the stress dependence effect for pore sizes

of 2 nm and 20 nm, the ratio of change in the AGP to the AGP in the organic pore, varies from -20.45% to -13.69%. This result implies that the stress dependence effect has a profound effect on the AGP and cannot be neglected. Notably, the stress dependence effect usually reduces the AGP under any pressure, except at a certain pressure stage, as shown for a pore size of 2 nm between 21 MPa and 25 MPa, because the AGP increases as the pore pressure decreases, and the slip flow parameters also change with pore pressure. Assuming that the in situ stress is constant, these changes

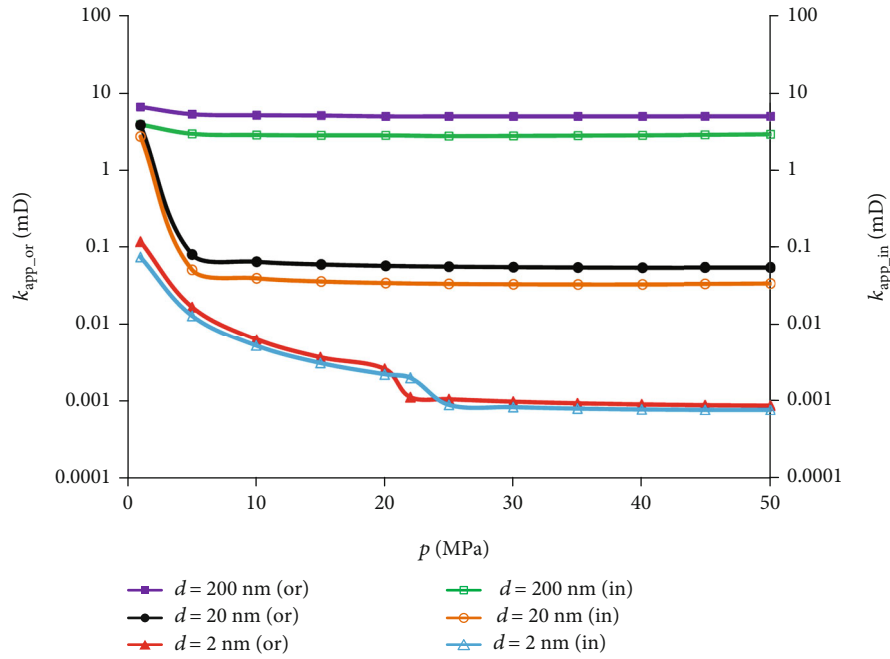


FIGURE 4: AGP comparison between organic and inorganic pores with different sizes under reservoir conditions.

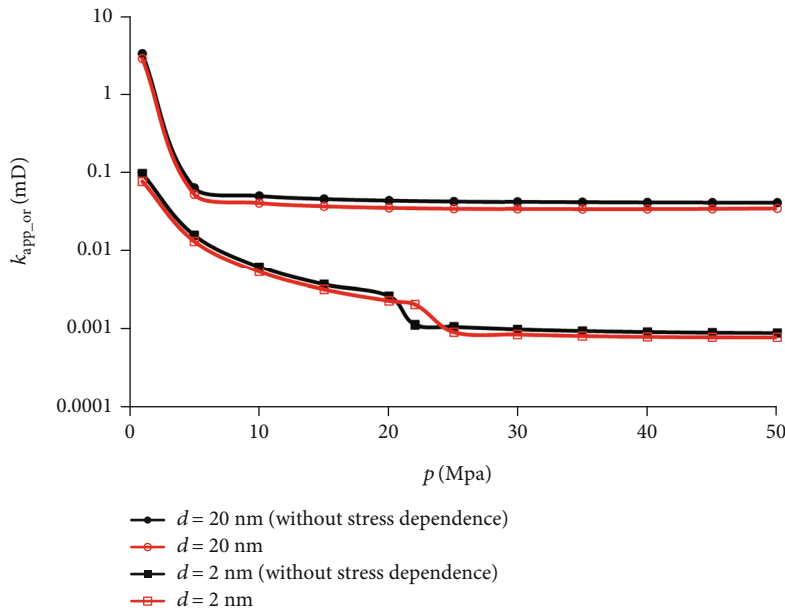


FIGURE 5: Organic pore AGP curves with and without considering the stress dependence.

have two consequences: (1) The permeability will increase with the increase in pore pressure (i.e., the effective pore pressure will decrease). (2) The slip flow will increase with increasing pore pressure, thus decreasing the AGP. Therefore, the final permeability value is determined by the interplay of the effective stress and slip flow effect.

4.3. *Real Gas Effect.* Figure 7 shows the organic pore AGP comparison between real gas and ideal gas as the pressure increases from 1 MPa to 50 MPa for pore sizes of 2 nm and 20 nm. The effect of real gas has a dramatic influence on

the organic pore AGP calculated by the ideal gas model under pressures lower than 30.0 MPa for a pore size of 20 nm and for pressures greater than 30 MPa for a pore size of 2 nm (Figure 8). This result occurs because the real gas compressibility varies with pressure and temperature, while the gas compressibility is assumed to be constant for an ideal gas [50]. Notably, the real gas effect can dramatically reduce the AGP from that calculated by the ideal gas model at 50 MPa for the 2 nm pore size because the continuum flow regime in 2 nm pores and the increased viscosity at high pressures have a profound effect on gas permeability. According to

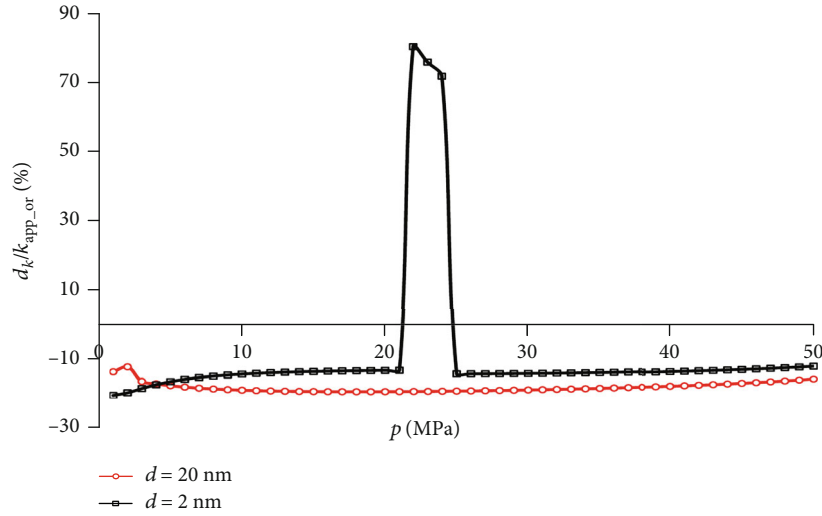


FIGURE 6: Curves of the ratio of change in the AGP to the AGP in the organic pore without considering the stress dependence.

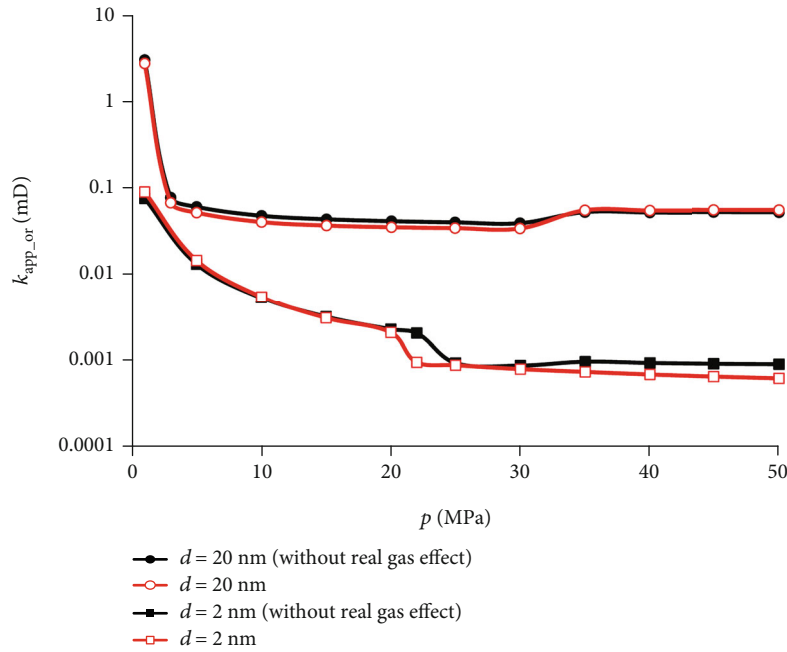


FIGURE 7: Organic pore AGP curves with and without considering the real gas effect.

Equations (29)–(36), the real gas viscosity can increase from  $1.85 \times 10^{-5}$  to  $2.62 \times 10^{-5}$  Pa·s (the relative error is 44.4%) as the pore pressure increases from 1.0 to 50 MPa at 323 K. Clearly, the real gas effect cannot be neglected.

**4.4. Surface Diffusion Effect.** Figure 9 shows the difference in the AGP in organic pores between considering surface diffusion and not considering surface diffusion at diameters of 2 nm and 20 nm as the pressure changes from 1 MPa to 50 MPa. It is obvious that the surface diffusion effect on organic pore permeability decreases as the pore pressure decreases. As shown in Figure 10, the surface effect exerts a profound influence on the organic permeability at the 2 nm pore size for the entire range of pressures, especially for low

pressures. The surface diffusion effect has little influence on the reduction in the 20 nm pore size under high pressure because the surface diffusion permeability is determined by the surface diffusion coefficient and the adsorbed gas maximum adsorption concentration to the squared pore pressure,  $C_{smax}/p^2$ . Obviously, the increase in  $C_{smax}/p$  is greater than the increase in gas maximum adsorption concentration as the pore pressure increases. In addition, the surface diffusion contribution to the organic pore permeability increases as the pore radius decreases because under the same formation pressure, the ratio of adsorbed gas area to the total pore area in a section increases as the pore size decreases. Under the condition of a pore size of 2 nm, the surface diffusion permeability deviation ranges from 74.85% to 1.67% for the pore



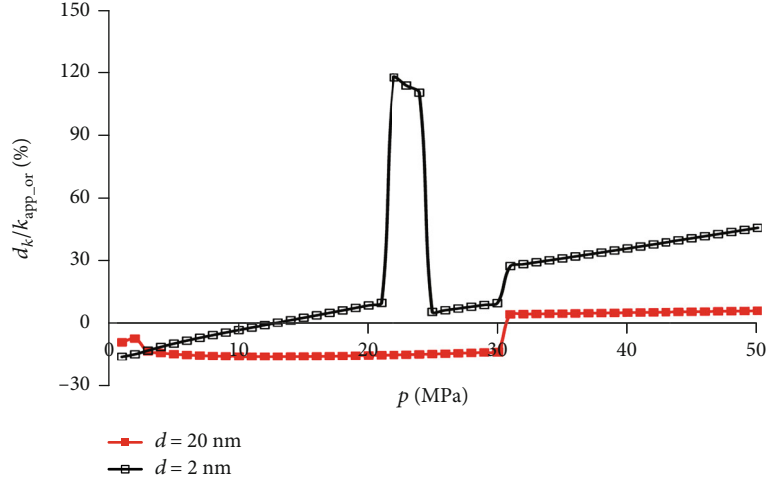


FIGURE 8: Curves of the ratio of change in the AGP to the AGP in the organic pore without considering the real gas effect.

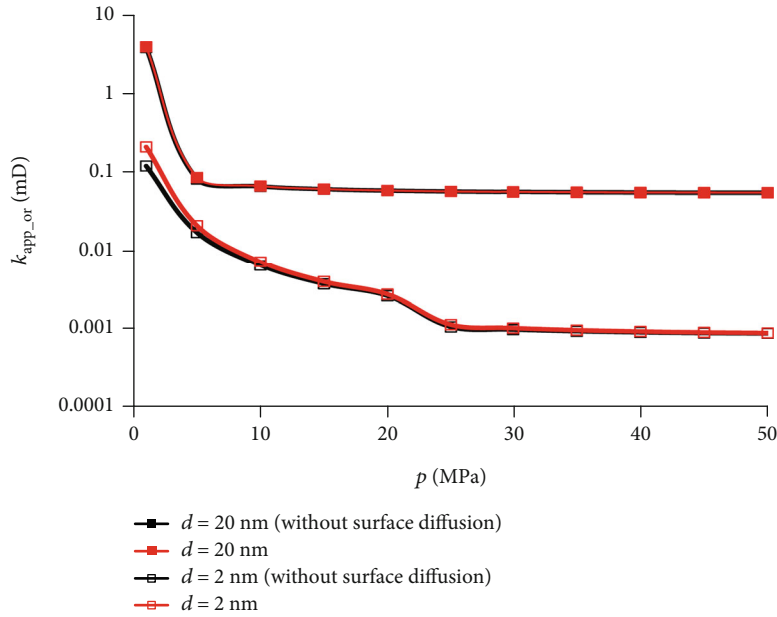


FIGURE 9: Organic pore AGP curves in with and without considering the surface diffusion effect.

pressure increase from 1 MPa to 50 MPa, revealing that surface diffusion should be considered under low pressures. When the pore pressure is greater than 10 MPa in the 20 nm pore, the surface diffusion contribution is smaller than 1.0%, which can be ignored.

**4.5. Water Storage Effect.** The gas permeability results of our models for different inorganic pore sizes with water storage are compared in Figure 11. The AGP at a low water saturation is generally larger than that at a high water saturation, which is consistent with the findings of other studies [51, 52]. In our model, according to Equation (28), the gas flow radius decreases as the water saturation increases. However, the AGP does not always decrease as the water saturation

increases for a small pore size. Figure 11 indicates a step change relationship between  $k_{app\_in}$  and  $s_w$ ; namely,  $k_{app\_in}$  first decreases with the increase in  $s_w$  at a low  $s_w$  but then increases after  $s_w$  reaches a critical value. According to Equation (26), the increase in  $s_w$  implies a decrease in the nanopore flow radius. For the gas flow regime satisfying continuum flow,  $k_{app\_in}$  decreased as water saturation increases, according to Equation (39). As  $s_w$  further increases, the effective pore size decreases and  $K_n$  increases, and the flow regime of the gas transfers from continuum flow to slip flow. The decrease in  $r_{eff\_in}$  does not imply a decrease in the gas  $k_{app}$ . Based on Equation (42), the water saturation effect on gas  $k_{app\_in}$  can be divided into two parts:  $r_{eff\_in}$  and  $b_k$ . The effective flow radius of the inorganic pore decreases,

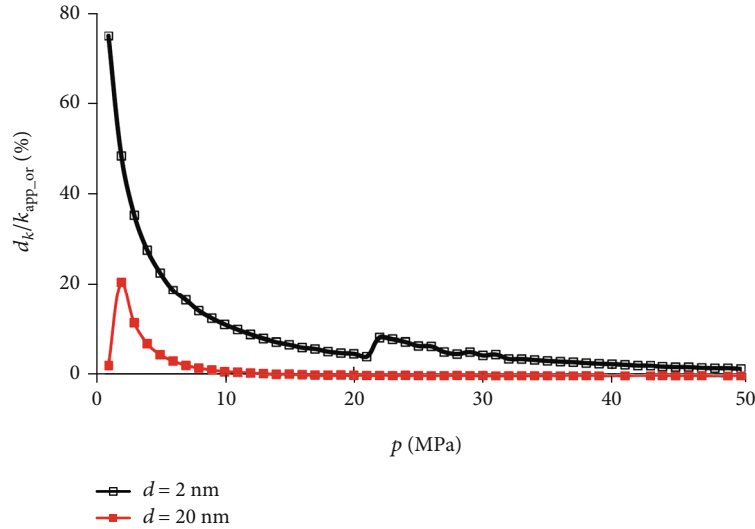


FIGURE 10: Curves of the ratio of change in the AGP to the AGP in the organic pore without considering the surface diffusion effect.

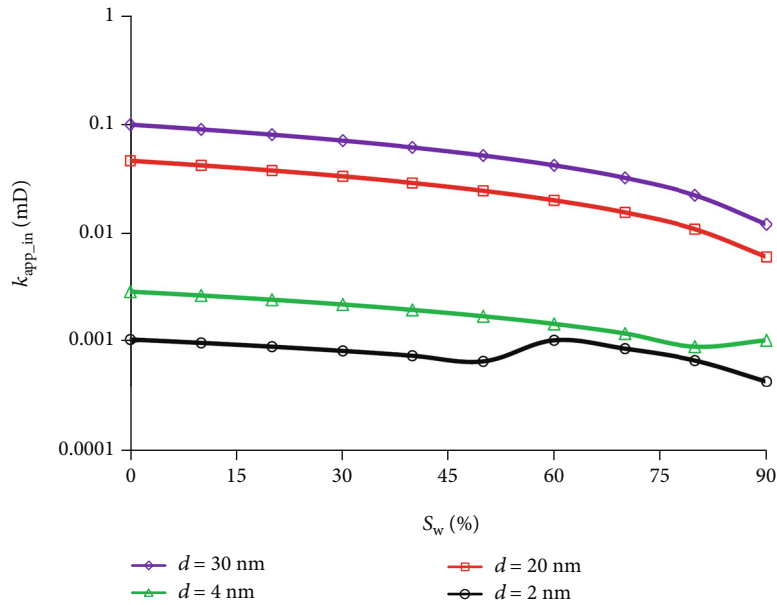


FIGURE 11: Gas permeability at different water saturations for different pore sizes.

while the gas slippage factor  $b_k$  increases under higher water saturation conditions. Whether  $k_{app,in}$  increases or decreases with  $s_w$  depends on the coupled effect of  $r_{eff,in}$  and  $b_k$ .  $k_{app,in}$  clearly exhibits a turning point as the water saturation increases to 50% for a pore size of 2 nm because the gas flow states have changed from a continuous flow regime to a slip flow regime. However,  $k_{app,in}$  exhibits no turning point with  $s_w$  for a pore size of 20 or 30 nm within the continuum flow regime for all the water saturations investigated.

## 5. Summary and Conclusions

Shale organic/inorganic pore analytical AGP models are derived in this paper. The presented AGP model results

match well with the results calculated via the models of Xiong et al., Asana et al., and Song et al. Unlike the earlier models, the presented models consider absorption, stress dependence, water storage, and real gas effects on organic/inorganic gas transport comprehensively for the entire flow regime. The results demonstrate that the AGP generally decreases gradually as the pore pressure decreases but that the decrease is sharp in small pores. Generally, the AGP usually decreases when taking the stress dependence effect into account. In real situations, the final permeability value is determined by the interplay of the effective stress and slip flow effects. Notably, the AGP decreases dramatically when considering the real gas effect at 50 MPa in a 2 nm pore size. Clearly, the surface effect exerts a profound influence on the

organic permeability of the 2 nm pore for the entire range of pressures investigated, especially at low pressures. The AGP usually decreases as the water saturation increases for high-water saturation conditions, considerably reducing the effective gas pathways. For a small pore size at the critical high-water saturation,  $k_{app}$  might increase suddenly as the flow regime changes from continuum flow to slip flow.

## Nomenclature

### Roman Alphabet

$b_k$ :	Gas slip factor (MPa)
$C_A$ :	Constants (-)
$C_{smax}$ :	Maximum adsorption concentration (mol/m <sup>3</sup> )
$d$ :	Effective radius of the nanopores (m <sup>2</sup> )
$d_m$ :	Gas molecule diameter (-)
$D_k$ :	Knudsen diffusion constant (m <sup>2</sup> /s)
$D_{eff-k}$ :	Effective Knudsen diffusion constant (m)
$D_f$ :	Pore wall fractal dimension (-)
$D_s$ :	Coefficient surface diffusion (m <sup>2</sup> /s)
$J_{viscous}$ :	The continuum flow volume flux (kg/(m <sup>2</sup> ·s))
$J_{slip}$ :	Volume flux for the slip regime (kg/(m <sup>2</sup> ·s))
$J_{Knudsen}$ :	Volume flux for the Knudsen regime (kg/(m <sup>2</sup> ·s))
$J_t$ :	Volume flux (kg/(m <sup>2</sup> ·s))
$J_{surface}$ :	Volume flux for the surface diffusion (kg/(m <sup>2</sup> ·s))
$k_B$ :	Boltzmann constant (-)
$K_n$ :	Knudsen number (-)
$k_{co}$ :	Intrinsic permeability (m <sup>2</sup> )
$K_{nViscous}$ :	$K_n$ when the flow regime transfers from viscous to diffusion flow (-)
$K_d$ :	Intermediate variable of the viscosity calculation (-)
$k_{slip}$ :	Slip flow regime AGP (m <sup>2</sup> )
$kapp_{in1}$ :	The apparent permeability of shale inorganic pores when the fluid flow pattern is continuum flow (m <sup>2</sup> )
$kapp_{in2}$ :	The apparent permeability of shale inorganic pores when the fluid flow regime is slip flow (m <sup>2</sup> )
$kapp_{in3}$ :	The apparent permeability of shale inorganic pores when the fluid flow regime is free molecule flow (m <sup>2</sup> )
$kapp_{in4}$ :	The apparent permeability of shale inorganic pores when the fluid flow regime is transition flow (m <sup>2</sup> )
$kapp_{or1}$ :	The apparent permeability of shale organic pores when the fluid flow pattern is continuum flow (m <sup>2</sup> )
$kapp_{or2}$ :	The apparent permeability of shale organic pores when the fluid flow regime is slip flow (m <sup>2</sup> )
$kapp_{or3}$ :	The apparent permeability of shale organic pores when the fluid flow regime is free molecule flow (m <sup>2</sup> )
$kapp_{or4}$ :	The apparent permeability of shale organic pores when the fluid flow regime is transition flow (m <sup>2</sup> )
$l_c$ :	Capillary length (-)
$M$ :	Molar mass (kg/mol)
$p$ :	Pore pressure (MPa)
$p_{aver}$ :	Gas phase mean pressure (MPa)
$p_L$ :	Langmuir pressure (MPa)
$p_c$ :	Confining pressure (MPa)

$p_e$ :	Effective stress (m)
$p_r$ :	Pseudopressure (-)
$q$ :	Material constants (-)
$r$ :	Nanopore radius (m)
$R$ :	Universal gas constant (J/(mol·K))
$r_{ef-or}$ :	Effective pore flow radius considering gas desorption (m)
$r_{e-or}$ :	Original pore radius of the organic pore (m)
$r_{ef}$ :	Effective flow radius considering the stress dependence effect (m)
$r_{e-in}$ :	Hydrodynamic radius for inorganic pores taking the stress dependence effect into account (m)
$r_{eff-in}$ :	Inorganic pore effective flow radius considering the stress dependence effect and water storage characteristics (m)
$r_{eff-or}$ :	Effective flow radius for organic pores considering gas desorption and the stress dependence effect (m)
$S$ :	Constants (-)
$s$ :	Material constants (-)
$S_w$ :	Shale pore water saturation, dimensionless (-)
$T$ :	Formation temperature (K)
$T_r$ :	Pseudotemperature (-)
$T_c$ :	Critical temperature (K)
$V$ :	Adsorbed gas volume per shale unit weight under standard conditions (m <sup>3</sup> /kg)
$V_L$ :	Langmuir volume under standard conditions (m <sup>3</sup> /kg)
$v_w$ :	Bound water volume (m)
$v_p$ :	Bound water pore volume (m <sup>3</sup> )
$X$ :	Density multiplication factor (-)
$Y$ :	Density index (-)
$Z$ :	Gas compressibility factor (-)

### Greek Alphabet

$\lambda$ :	Molecular mean free path (m)
$\delta$ :	Gas molecule collision diameter (m)
$\rho$ :	Gas density (kg/m <sup>3</sup> )
$\mu$ :	Gas viscosity (Pa·s)
$\mu_{eff}$ :	Effective viscosity of the gas transport in nanopores (Pa·s)
$\nabla$ :	Pressure gradient operator symbol (-)
$\alpha$ :	Tangential momentum accommodation coefficient (TMAC) (-)
$\varepsilon$ :	Contribution coefficient term (-)
$\theta$ :	Gas coverage under certain pressures (-)
$\varphi$ :	Porosity under the effective stress (-)
$\varphi_e$ :	Porosity at atmospheric pressure (-).

## Data Availability

The authors can make data available on request through a data access committee, institutional review board, or the authors themselves.

## Conflicts of Interest

The authors declare that there are no conflicts of interest in association with the reporting of the case or publication of this article.

## Acknowledgments

This work was supported by the Sichuan Science and Technology Plan Project (grant number 2020YJ013), the Natural Science Foundation of China (grant numbers 51504203, 51525404, and 51374178), and the National Key and Development Program of China (grant number 2017ZX05037-004).

## References

- [1] G. R. Chalmers, R. M. Bustin, and I. M. Power, "Characterization of gas shale pore systems by porosimetry, pycnometry, surface area, and field emission scanning electron microscopy/transmission electron microscopy image analyses: examples from the Barnett, Woodford, Haynesville, Marcellus, and Doig units," *AAPG Bulletin*, vol. 96, no. 6, pp. 1099–1119, 2012.
- [2] Z. Gao, Y. Fan, Q. Xuan, and G. Zheng, "A review of shale pore structure evolution characteristics with increasing thermal maturities," *Advances in Geo-Energy Research*, vol. 4, no. 3, pp. 247–259, 2020.
- [3] U. Kuila, D. K. McCarty, A. Derkowski, T. B. Fischer, T. Topór, and M. Prasad, "Nano-scale texture and porosity of organic matter and clay minerals in organic-rich mudrocks," *Fuel*, vol. 135, pp. 359–373, 2014.
- [4] Z. Tao, X. Li, S. Zheng et al., "An analytical model for relative permeability in water-wet nanoporous media," *Chemical Engineering Science*, vol. 174, pp. 1–12, 2017.
- [5] H. Song, M. Yu, W. Zhu et al., "Numerical investigation of gas flow rate in shale gas reservoirs with nanoporous media," *International Journal of Heat & Mass Transfer*, vol. 80, pp. 626–635, 2015.
- [6] L. He, H. Mei, X. Hu, M. Dejam, Z. Kou, and M. Zhang, "Advanced flowing material balance to determine original gas in place of shale gas considering adsorption hysteresis," *SPE Reservoir Evaluation & Engineering*, vol. 22, pp. 1–11, 2019.
- [7] M. Wei, Y. Duan, M. Dong, Q. Fang, and M. Dejam, "Transient production decline behavior analysis for a multi-fractured horizontal well with discrete fracture networks in shale gas reservoirs[J]," *Journal of Porous Media*, vol. 22, no. 3, pp. 343–361, 2019.
- [8] G. Xu, H. Yin, H. Yuan, and C. Xing, "Decline curve analysis for multiple-fractured horizontal wells in tight oil reservoirs," *Advances in Geo-Energy Research*, vol. 4, no. 3, pp. 296–304, 2020.
- [9] J. P. Korb, B. Nicot, A. Louis-Joseph, S. Bubici, and G. Ferrante, "Dynamics and wettability of oil and water in oil shales," *Journal of Physical Chemistry C*, vol. 118, pp. 23212–23218, 2015.
- [10] M. Xu and H. Dehghanpour, "Advances in understanding wettability of gas shales," *Energy & Fuels*, vol. 28, no. 7, pp. 4362–4375, 2014.
- [11] W. Song, "Apparent gas permeability in an organic-rich shale reservoir," *Fuel*, vol. 181, pp. 973–984, 2016.
- [12] F. Javadpour, D. Fisher, and M. Unsworth, "Nanoscale gas flow in shale gas sediments," *Journal of Canadian Petroleum Technology*, vol. 46, 2007.
- [13] G. A. Bird and J. Brady, *Molecular Gas Dynamics and the Direct Simulation of Gas Flows*, Vol 5, Clarendon Press Oxford, 1994.
- [14] S. Roy, R. Raju, H. F. Chuang, B. A. Cruden, and M. Meyyappan, "Modeling gas flow through microchannels and nanopores," *Journal of Applied Physics*, vol. 93, no. 8, pp. 4870–4879, 2003.
- [15] W. J. Shen, F. Q. Song, X. Hu, G. M. Zhu, and W. Y. Zhu, "Experiential study on flow characteristics of gas transport in micro- and nanoscale pores," *Scientific Reports*, vol. 9, article 10196, 2019.
- [16] J. Wang, H. Luo, H. Liu, F. Cao, Z. Li, and K. Sepehrnoori, "An integrative model to simulate gas transport and production coupled with gas adsorption, non-Darcy flow, surface diffusion, and stress dependence in organic-shale reservoirs," *SPE Journal*, vol. 22, pp. 244–264, 2019.
- [17] X. Qiu, S. P. Tan, M. Dejam, and H. Adidharma, "Isochoric measurement of the evaporation point of pure fluids in bulk and nanoporous media using differential scanning calorimetry," *Physical Chemistry Chemical Physics*, vol. 22, no. 13, pp. 7048–7057, 2020.
- [18] X. Qiu, S. P. Tan, M. Dejam, and H. Adidharma, "Experimental study on the criticality of a methane/ethane mixture confined in nanoporous media," *Langmuir*, vol. 35, no. 36, pp. 11635–11642, 2019.
- [19] G. E. K. Ali Beskok, "Report: a model for flows in channels, pipes, and ducts at micro and nano scales," *Microscale Thermophysical Engineering*, vol. 3, no. 1, pp. 43–77, 1999.
- [20] G. Karniadakis, A. Beskok, and M. Gad-El-Hak, "Micro Flows: Fundamentals and Simulation," *Applied Mechanics Reviews*, vol. 55, no. 4, p. 76, 2020.
- [21] F. Civan, "Effective correlation of apparent gas permeability in tight porous media," *Transport in Porous Media*, vol. 82, no. 2, pp. 375–384, 2010.
- [22] S. Zheng, J. Shi, K. Wu et al., "Transport capacity of gas confined in nanoporous ultra-tight gas reservoirs with real gas effect and water storage mechanisms coupling," *International Journal of Heat & Mass Transfer*, vol. 126, pp. 1007–1018, 2018.
- [23] D. Chai, G. Yang, Z. Fan, and X. Li, "Gas transport in shale matrix coupling multilayer adsorption and pore confinement effect," *Chemical Engineering Journal*, vol. 370, pp. 1534–1549, 2019.
- [24] M. R. Shahri, R. Aguilera, and A. Kantzas, "A new unified diffusion-viscous flow model based on pore level studies of tight gas formations," *SPE Journal*, vol. 18, pp. 38–49, 2012.
- [25] H. Adzumi, "Studies on the flow of gaseous mixtures through capillaries. II. The molecular flow of gaseous mixtures," *Bulletin of the Chemical Society of Japan*, vol. 12, pp. 285–291, 1937.
- [26] F. Javadpour, "Nanopores and apparent permeability of gas flow in mudrocks (shales and siltstone)," *Journal of Canadian Petroleum Technology*, vol. 48, pp. 16–21, 2013.
- [27] H. Darabi, A. Ettehad, F. Javadpour, and K. Sepehrnoori, "Gas flow in ultra-tight shale strata," *Journal of Fluid Mechanics*, vol. 710, pp. 641–658, 2012.
- [28] K. Wu, Z. Chen, and X. Li, "Real gas transport through nanopores of varying cross-section type and shape in shale gas reservoirs," *Chemical Engineering Journal*, vol. 281, pp. 813–825, 2015.
- [29] F. Zeng, F. Peng, J. Guo, Z. Rui, and J. Xiang, "Gas mass transport model for microfractures considering the dynamic variation of width in shale reservoirs," *SPE Reservoir Evaluation & Engineering*, vol. 22, no. 4, pp. 1265–1281, 2019.

- [30] F. Zeng, F. Peng, J. Guo et al., "Gas transport study in the confined microfractures of coal reservoirs," *Journal of Natural Gas Science and Engineering*, vol. 68, article 102920, 2019.
- [31] P. C. Carman, *Flow of Gases through Porous Media*, Academic Press Inc., Butterworths Scientific Publications, New York, London, 1956.
- [32] D. J. Ross and R. M. Bustin, "Characterizing the shale gas resource potential of Devonian–Mississippian strata in the Western Canada sedimentary basin: application of an integrated formation evaluation," *AAPG Bulletin*, vol. 92, no. 1, pp. 87–125, 2008.
- [33] D. J. Soeder, "Porosity and permeability of eastern Devonian gas shale," *SPE Formation Evaluation*, vol. 3, pp. 116–124, 2013.
- [34] G. Karniadakis, A. Beskok, and N. Aluru, "Microflows and Nanoflows. Fundamentals and Simulation. With a Foreword by Chih-Ming Ho," in *Interdisciplinary Applied Mathematics*, vol. 29, Springer, New York, 2005.
- [35] H. Smith, "Transport Phenomena," *Applied Mechanics Reviews*, vol. 55, no. 1, pp. R1–R4, 2003.
- [36] L. Klinkenberg, "The permeability of porous media to liquids and gases," in *Paper presented at: drilling and production practice*, American Petroleum Institute, 1941.
- [37] M. A. Jingsheng, P. J. Sanchez, W. U. Kejian, D. Gary, and Z. Jiang, "A pore network model for simulating non-ideal gas flow in micro- and nano-porous materials," *Fuel*, vol. 116, pp. 498–508, 2014.
- [38] J. G. Choi, D. D. Do, and H. D. Do, "Surface diffusion of adsorbed molecules in porous media: monolayer, multilayer, and capillary condensation regimes," *Industrial & Engineering Chemistry Research*, vol. 40, no. 19, pp. 4005–4031, 2001.
- [39] K. Wu, Z. Chen, X. Li, C. Guo, and M. Wei, "A model for multiple transport mechanisms through nanopores of shale gas reservoirs with real gas effect–adsorption–mechanic coupling," *International Journal of Heat & Mass Transfer*, vol. 93, pp. 408–426, 2016.
- [40] M. Coppens, "The effect of fractal surface roughness on diffusion and reaction in porous catalysts – from fundamentals to practical applications," *Catalysis Today*, vol. 53, no. 2, pp. 225–243, 1999.
- [41] T. Veltzke and J. Thöming, "An analytically predictive model for moderately rarefied gas flow," *Journal of Fluid Mechanics*, vol. 698, pp. 406–422, 2012.
- [42] H. Adzumi, "Studies on the flow of gaseous mixtures through capillaries. III. The flow of gaseous mixtures at medium pressures," *Bulletin of the Chemical Society of Japan*, vol. 12, pp. 292–303, 1937.
- [43] M. Rahmanian, R. Aguilera, and A. Kantzas, "A new unified diffusion–viscous-flow model based on pore-level studies of tight gas formations," *SPE Journal*, vol. 18, no. 1, pp. 37–47, 2013.
- [44] J. J. Dong, J. Hsu, W. J. Wu, T. Shimamoto, Hung, and J. Hao, "Stress-dependence of the permeability and porosity of sandstone and shale from TCDP Hole-A," *International Journal of Rock Mechanics & Mining Sciences*, vol. 47, no. 7, pp. 1141–1157, 2010.
- [45] F. Civan, C. S. Rai, and C. H. Sondergeld, "Shale-gas permeability and diffusivity inferred by improved formulation of relevant retention and transport mechanisms," *Transport in Porous Media*, vol. 86, no. 3, pp. 925–944, 2011.
- [46] H. Tran and A. Sakhaee-Pour, "Viscosity of shale gas," *Fuel*, vol. 191, pp. 87–96, 2017.
- [47] X. Xinya, D. Deepak, M. Villazon, R. F. Sigal, and F. Civan, "A fully-coupled free and adsorptive phase transport model for shale gas reservoirs including non-Darcy flow effects," in *SPE Annual Technical Conference and Exhibition*, San Antonio, Texas, USA, 2012.
- [48] W. Asana and I. Y. Akkutlu, "Permeability of organic-rich shale," *SPE Journal*, vol. 20, no. 16, pp. 1384–1496, 2015.
- [49] L. Geng, G. Li, P. Zitha, S. Tian, S. Mao, and X. Fan, "A diffusion–viscous flow model for simulating shale gas transport in nano-pores," *Fuel*, vol. 181, pp. 887–894, 2016.
- [50] K. Wu, X. Li, C. Guo, C. Wang, and Z. Chen, "A unified model for gas transfer in nanopores of shale-gas reservoirs: coupling pore diffusion and surface diffusion," *Spe Journal*, vol. 21, 2016.
- [51] R. K. Estes and P. F. Fulton, "Gas slippage and permeability measurements," *Journal of Petroleum Technology*, vol. 18, no. 10, pp. 69–73, 1956.
- [52] Q. Wu, B. Bai, Y. Ma, J. T. Ok, X. Yin, and K. Neeves, "Optic imaging of two-phase-flow behavior in 1D nanoscale channels," *SPE Journal*, vol. 19, no. 5, pp. 793–802, 2014.



## Research Article

# Numerical Simulation of the Non-Darcy Flow Based on Random Fractal Micronetwork Model for Low Permeability Sandstone Gas Reservoirs

Juhua Li  and Chen Chen

School of Petroleum Engineering, Yangtze University, Wuhan, Hubei 430100, China

Correspondence should be addressed to Juhua Li; [lucyli7509@163.com](mailto:lucyli7509@163.com)

Received 17 July 2020; Revised 24 August 2020; Accepted 21 September 2020; Published 14 October 2020

Academic Editor: Jinze Xu

Copyright © 2020 Juhua Li and Chen Chen. This is an open access article distributed under the Creative Commons Attribution License, which permits unrestricted use, distribution, and reproduction in any medium, provided the original work is properly cited.

Darcy's law is not suit for describing high velocity flow in the near wellbore region of gas reservoirs. The non-Darcy coefficient  $\beta$  of the Forchheimer's equation is a main parameter for the evaluation of seepage capacity in gas reservoirs. The paper presented a new method to calculate  $\beta$  by performing gas and con-water flow simulations with random 3D micropore network model. Firstly, a network model is established by random fractal method. Secondly, based on the network simulation method of non-Darcy flow in the literature of Thauvin and Mohanty, a modified model is developed to describe gas non-Darcy flow with irreducible water in the porous medium. The model was verified by our experimental measurements. Then, we investigated the influence of different factors on the non-Darcy coefficient, including micropore structure (pore radius and fractal dimension), irreducible water saturation ( $S_{wi}$ ), tortuosity, and other reservoir characteristics. The simulation results showed that the value of the non-Darcy coefficient decreases with the increase in all: the average pore radius, fractal dimension, irreducible water saturation, and tortuosity. The non-Darcy coefficients obtained by the fractal method of microparameters are estimated more precisely than the conventional methods. The method provides theoretical support for the productivity prediction of non-Darcy flow in gas reservoirs.

## 1. Introduction

The Darcy law describes the flow of the subsurface fluid and shows the linear relationship between the pressure gradient and the volume flow (Darcy's velocity). However, Darcy's law only applies to laminar and viscous flows. At high velocities, such as high-velocity flows near the wellbore, fluid flow behaves as an inertial flow, and Darcy's law fails to follow this high-velocity seepage law. Forchheimer proposed a classical Forchheimer equation with a non-Darcy coefficient  $\beta$  to estimate non-Darcy effects in Equation (1) and accounted for the impact of both viscous and inertial effects.

$$\frac{\Delta P}{L} = \frac{\mu}{K} U + \beta \rho U^2. \quad (1)$$

Since then, the non-Darcy coefficient  $\beta$  has attracted a lot

of research. Coefficient  $\beta$  can be obtained from analytical methods, physical experiments, and numerical simulations. Geertsma [1] conducted an experiment to establish the quantitative relationship between non-Darcy coefficient and porosity and permeability as well as influence of the immobile fluids on non-Darcy coefficients. Frederick and Graves [2] also studied experimentally the seepage process of gases in porous media considering the influence of both mobile and immobile water on nonlinear seepage of gases. Reid et al. [3] researched high-speed non-Darcy flow process of gas-water fluids in porous media and determined that the presence of irreducible and mobile water affects the gas flow in porous media, both of which reduce the gas permeability and increase the non-Darcy coefficient. However, at the same time, the effect of movable water on gas permeability and non-Darcy coefficient was found to be more significant than that of irreducible water.

Thauvin and Mohanty [4] reported the nonlinear seepage phenomena of gas by establishing the pore structure model considering the influence of pore characteristics on the non-Darcy coefficient. Firoozabadi [5], Jones [6], and others obtained the non-Darcy coefficient  $\beta$  for different rocks by physical methods. A 2D random pore network developed by Neeman et al. [7] was found that the porous medium structure has a strong effect on the flow properties. Later, Chukwudozie et al. [8] used LBM to estimate the permeability, tortuosity, and  $\beta$  factor of porous rock.

Dou [9] used analytic methods and determined that non-Darcy  $\beta$  coefficient is a function of pore size, permeability, friction coefficient, and drag coefficient. Li [10] expanded his analytical research and determined that the  $\beta$  is also dependent on the fluid density and fluid viscosity. Wang et al. [11] obtained the relationship between  $\beta$ , permeability, and porosity in high-pressure gas reservoirs by statistical analysis of data from multiple sets of rock samples under different overburden tests. Ren et al. [12] established the nonlinear seepage law affected by irreducible water in low permeability reservoirs based on the laboratory seepage experiment results.

Thus, just from the short overview of the previous literature mentioned above, one can see that a lot of theoretical and experimental work was conducted to obtain different forms of non-Darcy coefficient expression, of which the main form is the quantitative relationship between permeability, porosity, and the non-Darcy coefficient. However, due to the different methods applied as well as various porous media and fluids, the non-Darcy coefficient expressions are quite different [13–15]. There are two orders of magnitude difference in the results calculated by different expressions with the same parameters. The fundamental cause of this difference is the intrinsic complexity of micropore structure.

The goal of our work is to obtain an inner relationship of the non-Darcy flow in porous media by a random fractal pore-scale network model. We carried out some flow experiments at different pressure drops and showed the validity of the Forchheimer's equation. We vary certain pore-scale parameters, study the way it affects various flow parameters, and identify the correlation between different parameters. The mathematical characterization was carried out to confirm the essence of the nonlinear flow. This study is limited to single-phase flow in isotropic porous media.

## 2. Methodology

The section mainly presents the dynamic simulation method of non-Darcy flow using random fractal network model.

**2.1. Construction of Network Model by Random Fractal Theory.** Since the first pore network by Fatt [16], a pore numerical model is a versatile studying platform for a variety of subjects [17]. Piri and Blunt [18] developed a quasistatic random network model for researching numerous fluid configurations for two- and three-phase flow. Even since then, the complex geometry of the pore space may be reconstructed [19, 20]. Fang et al. [21] established a fundamental network model, and Mohammadi et al. [22] modified the

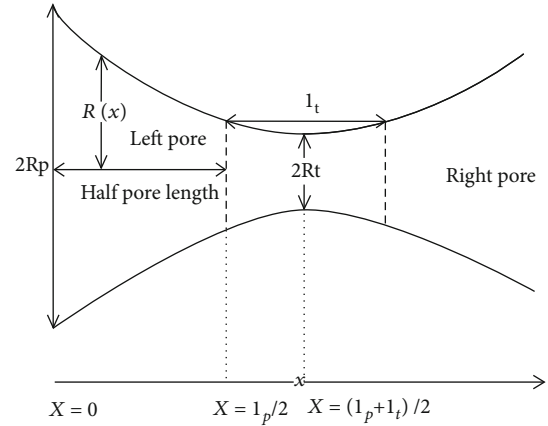


FIGURE 1: Dimension of the throat structure in the pores.

model to calculate Scri. Consequently, the construction of pore networks is extremely effective for the research of various type of flowing process in porous medium [23–25].

The pore sizes and the throats in the pore network model are also the key to be determined for researchers [26, 27]. It is difficult to describe the irregular pores in traditional geometry. Various studies have shown that the intrinsic properties of the pore meet the statistical significance of fractal distribution [28–31]. We have recently established a constructing digital core method based on fractal theory [32]. The fractal characteristics of pore size are calculated by capillary pressure curve measured from the mercury injection experiment [33]. We then developed a procedure for constructing a 3D pore-throat structure.

Our last paper [27, 32] gives the detailed derivation procedure for the fractal relationship between the pore radius ( $r$ ), fractal dimension ( $D$ ), minimum pore radius ( $r_{\min}$ ), and random number ( $\zeta$ ).

$$r = \frac{r_{\min}}{\zeta^{1/D}}. \quad (2)$$

Porous media are considered to be consisted of large amounts of pore throats which interconnect large and small pores and shrinkage intervals. These pores and pore throats can be described as “points” and “edges” in a 3D network model. The pore nodes are randomly distributed, and the pore throats are connected with a pore as the pore's coordination number which is generally between 1 and 6. Based on the node position coordinates, the pore's coordination number, and the principle that the closest pores should be priorly connected, one can first establish the main structural framework of a 3D PNM by connecting the “points” and “edges” and then obtain the geometrical parameters of pores and throats including its radius and length, shape factor, and volume to form a PNM with the topology structure and geometric characteristics of actual core pores.

**2.2. Numerical Simulation of Gas Phase Non-Darcy Flow.** The dynamic model is adopted using the Matlab program. The pore-throat structure shown in Figure 1 was used as a unit

TABLE 1: Parameters of the cores.

Sample	Dimension ( $D$ )	Fractal regime		Porosity (%)	$S_{wi}$ (%)	Permeability (mD)	$\bar{r}$ ( $\mu\text{m}$ )
		$r_{\min}$ ( $\mu\text{m}$ )	$r_{\max}$ ( $\mu\text{m}$ )				
#1	2.5942	2.613	100.75	15.9	52.32	3.1	4.369
#2	2.6465	3.835	87.45	17.6	54.64	3.2	6.351

to analyze the pressure drop caused by the fluid flowing into the pores [34]. The fluid flow corresponds to the Hagen-Poiseuille equation during the laminar flow in a porous medium. Its pressure drop is a primary mechanism to overcome the viscous drag. In our model, in addition to considering the viscous drag, the tortuosity and the pressure drop of inertial resistance caused by the gradual pore-throat radius gradient were taken into account.

Based on the pore level law presented by Thauvin and Mohanty [4], the viscous pressure drop between the centers of two adjacent pores can be described by the following equation in single-phase Darcy (slow or Stokes) flow,

$$\Delta p_v = \frac{8\mu L_t}{r_t^2} u. \quad (3)$$

In the near wellbore region, the velocity is higher, and Reynolds number increases to the order of  $Re \sim 10$  in typical gas wells. In porous media, the inertial terms become so important that it affect the additional pressure loss. It was also taken into account:

$$\Delta p_b = 0.9f\rho u^2. \quad (4)$$

The pressure drop resulting from the narrowing of the tunnel can be expressed as:

$$\Delta p_c = \left\{ 1.45 - 0.45 \left( \frac{r_t}{r_{b1}} \right)^2 - \left( \frac{r_t}{r_{b1}} \right)^4 \right\} \frac{\rho u^2}{2}. \quad (5)$$

The pressure drop caused by widening of the tunnel is expressed by the following equation:

$$\Delta p_e = \left[ 1 - \left( \frac{r_t}{r_{b2}} \right)^2 \right] \left( \frac{r_t}{r_{b2}} \right)^2 \frac{\rho u^2}{2}. \quad (6)$$

Based on the above equations, the total pressure drop across the structural unit can be obtained as:

$$\Delta p = \Delta p_v + \Delta p_b + \Delta p_c + \Delta p_e. \quad (7)$$

The pressure and velocity relationship in pore level is combined in the network model to calculate macroscopic flow parameters.

Equation (7) is shown below:

$$\Delta p = au + bu^2, \quad (8)$$

wherein  $a$  and  $b$  are shown, respectively:

$$a = \frac{8\mu L_t}{r_t^2},$$

$$b = 0.9f\rho + \left[ 1.45 - 0.45 \left( \frac{r_t}{r_{p1}} \right)^2 - \left( \frac{r_t}{r_{p1}} \right)^4 \right] \frac{\rho}{2} + \left[ 1 - \left( \frac{r_t}{r_{p2}} \right)^2 \right] \left( \frac{r_t}{r_{p2}} \right)^2 \frac{\rho}{2}. \quad (9)$$

Mass balance is applied in one of the principal directions of the pore. The relation between velocity,  $u$  in a throat, and the pressure drop between the two adjacent body centers is given by Equation (8). To solve this system of equations, we used the Newton-Raphson method. The calculations are repeated at several different pressure drops to verify the Forchheimer equation. The calculations are also repeated for pressure drops applied in each of the pore directions.

In this work, numerical simulations in pore scale are run at specified pressure gradients; meanwhile, the boundary conditions in the network consist of fixed inlet and outlet pressures.

### 3. Model Validation

We designed six groups of non-Darcy experiments for low permeability sandstone samples. To ensure that the experiments are carried out in porous media, CT scanning was used to scan the samples to avoid the existence of microfractures in the stage of preparation and the end. Finally, two real cores with #1 and #2 were selected.

*3.1. Establishment of Pore Network Model.* The original data and calculated fractal feature parameters of the rock samples in the certain gas reservoir are given in Table 1 by the capillary pressure curve Figure 2. The first step gets the information of the pore and throat size distribution using Equation (2). Through the relationship between porosity and the pore number, the porosity of rock samples #1 and #2 is 15.2% and 17.2%, respectively, so the corresponding pore numbers are 1053 and 1268. The second step is to generate a pore network model that best fits the original shape of the rock sample, the best model that accurately represents the true capillary pressure characteristics of the core sample.

The size of the random fractal micropore network established in this paper is  $3.00 \text{ mm} \times 3.00 \text{ mm} \times 3.00 \text{ mm}$ , as shown in Figure 3, in which the pore numbers are 1053 and 1268; the throat numbers are 2476 and 2982, respectively; the average coordination numbers are 4.362 and 4.614; and the tortuosities are 1.46 and 1.62. In this model, we assume

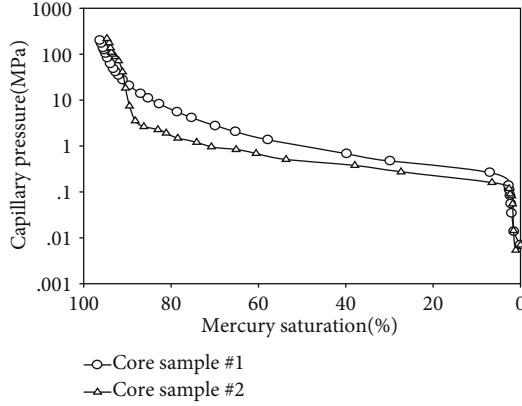


FIGURE 2: Capillary pressure curves of the two groups of rock samples.

that the shape of pore and throat is triangle, and the value ranges from 0 to 0.0418. The shape factor of pore and throat was given by the Weibull distribution.

**3.2. Simulation of the Non-Darcy Experiment.** Nitrogen and distilled water corresponded to the gas and liquid phases, respectively. The experiments were performed at room temperature. The core was placed in a holder and fixed with a pressure ring. The outlet pressure was fixed at a certain value. Inlet pressure was regulated to change the pressure gradient as needed. Gas flow was monitored and adjusted by flow meters. The experimental results are shown in Table 2.

We proved the validity of the new method by comparing it with the experiments result. The porous network in our model was filled with water and gas as well as the experiments. Water in the pores was in the film form; thus, it did not participate in the flow. The irreducible water in the network model was established according to the principle of small channel occupancy. The gas state was chosen to be constant because of the very small pressure changes under the simulated conditions. The network model had four closed sides and two open ones (the entrance and exit sides). There was no fluid flow through the four closed sides. The flow process was in quasisteady state, and the flow parameters only changed with space but not over time [35]. The model ambient conditions were room temperature. The nitrogen viscosity is 0.011 mPa·s, and the density is 150 kg/m<sup>3</sup>.

Based on the two sets of network models established earlier in the text, we simulated the single-phase nonlinear gas flow and obtained the average gas flow rate under different pressure gradients. The relationship between gas flow rate and pressure gradient was obtained. The experimental results were compared with the simulated ones (see Figure 4).

As can be seen from Figure 4, the flow rate gradually increases with the pressure gradient increase, showing a significant nonlinear relationship. The experimental results are relatively close to the simulated ones.

According to Darcy's law, the corresponding gas permeability at each flow rate can be obtained using the following

equation:

$$-\frac{dp}{dx} = \frac{\mu}{k_g} v. \quad (10)$$

As the gas velocity increases, the gas permeability calculated from the Darcy's formula decreases mainly because the gas shows nonlinear seepage flow type, and the flow resistance increases together with the flow rate. The calculated permeability was less than the intrinsic absolute permeability of the model.

According to the Forchheimer equation, the seepage velocity and pressure gradient of a fluid can be expressed as a binomial equation, in which the coefficient of the binomial first power phase is the ratio of the fluid viscosity  $\mu$  to its permeability  $k$ . The quadratic phase coefficient is the product of non-Darcy coefficient and fluid density. The quantitative relationship between the pressure gradient and the flow rate can be determined using the above equations. The pressure gradient and the flow rate are obtained from the flow simulation.

$$\frac{1}{k_g} = \frac{1}{k} + \beta \frac{\rho v}{\mu}, \quad (11)$$

where  $k_g$  is the gas permeability for different gas velocities,  $k$  is the absolute permeability of the network model,  $\beta$  is a non-Darcy coefficient,  $\rho$  is the gas density,  $\mu$  is the gas viscosity, and  $v$  is the gas flow rate. The slope of the linear relationship between  $1/k_g$  and  $\rho v/\mu$  in Cartesian coordinates is the non-Darcy coefficient  $\beta$ . It was compared with the calculated result of Geertsma formula, which is expressed as:

$$\beta = \frac{0.005}{[\varnothing^{5.5}(1 - S_{wi})^{5.5}k_g^{0.5}]}. \quad (12)$$

In the formula,  $S_{wi}$  represents the irreducible water saturation, and  $\varnothing$  represents the porosity.

The non-Darcy coefficients calculated by the network model and the experiments are shown in Table 3. However, the results of the two samples calculated by the Geertsma formula are close due to the similar values. The difference between two samples in the internal microscopic structure causes the different coefficients. The non-Darcy coefficients obtained by the fractal method of microparameters are estimated more precisely than the conventional methods. It shows that the non-Darcy flow network model is effective.

#### 4. Factors Affecting the Non-Darcy Coefficient by the Fractal Method

The non-Darcy flow model in random fractal pore network can effectively evaluate the non-Darcy flow coefficient. The internal factors affecting the non-Darcy coefficient are focused on in this section.



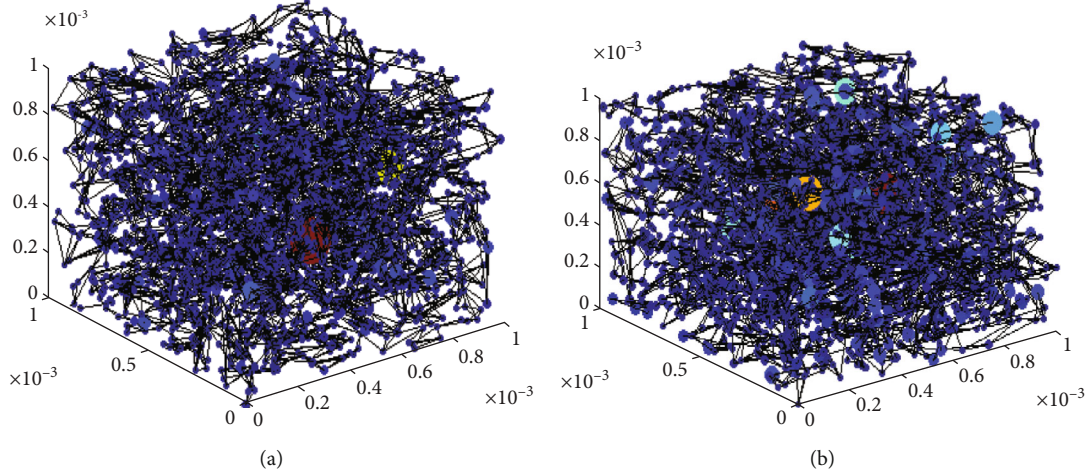


FIGURE 3: The microcosmic network models of rock sample #1 (a) and rock sample #2 (b).

TABLE 2: Gas flow velocity under different pressure gradients.

Inlet pressure (MPa)	Outlet pressure (MPa)	Pressure gradient (MPa·m <sup>-1</sup> )		Flow velocity (cm·min <sup>-1</sup> )	
		#1	#2	#1	#2
12.1	12	1.78	1.31	2.265	0.82
12.3	12	5.33	3.39	8.765	1.84
12.5	12	8.89	6.56	12.03	2.35
12.7	12	12.44	9.18	16.01	3.65
12.9	12	16.00	11.80	20.56	4.46

**4.1. The Impact of Irreducible Water Saturation.** To study the influence of irreducible water saturation, we simulated the nonlinear seepage flow under five irreducible water saturation levels ( $S_{wi} = 0, 0.1, 0.2, 0.35, \text{ and } 0.5$ ) with different fractal dimensions and obtained the non-Darcy coefficients under different conditions. Several data points from the literature [36] were added to the graph as well (see Figure 5).

Non-Darcy coefficient increased with irreducible water saturation [37–39] was mainly because the irreducible water filled the corners of the pores, only partially leaving the rest of the space for the gas. The indirectly reduced throat radius decreases the flow passage and aggravates the nonlinear flow of gas. Gas flow radius has a quantitative relationship with the gas saturation  $S_g$ . Since there are only gas and water phases in the pores,  $S_g = 1 - S_w$ . We used the power function to fit the relationship between non-Darcy coefficient and irreducible water saturation:

$$\beta = a \times (1 - S_{wi})^b, \quad (13)$$

where  $\beta$  is the non-Darcy coefficient in  $\text{m}^{-1}$ ;  $a$  and  $b$  are parameters ( $b$  is  $\sim -4.5$  according to the fitting).

**4.2. The Impact of Fractal Dimension.** To analyze the influence of fractal dimension on non-Darcy coefficients, the value of fractal dimension  $D$  was changed during the reconstruction of the rock sample data by the random fractal method. All other parameters were unchanged. Five groups

of three-dimensional network models with  $D = 2.4, D = 2.5, D = 2.6, D = 2.7, \text{ and } D = 2.8$  were established. The simulation of nonlinear gas flow in the presence of irreducible water was carried out, and the non-Darcy coefficients under different fractal dimensions are shown in Figure 6.

The fractal dimension reflects the complexity of pore radius distribution. The larger the fractal dimension, the greater the heterogeneity of pore radii and the larger the non-Darcy coefficients are. The relationship between the non-Darcy coefficient and the fractal dimension can be fitted using exponential function:

$$\beta = a \times D^b, \quad (14)$$

where  $\beta$  is the non-Darcy coefficient in  $\text{m}^{-1}$ ;  $a$  and  $b$  are the parameters (the value of  $b$  obtained from the fitting was  $\sim 4.5$ ).

**4.3. The Impact of Average Pore Size.** To analyze the effect of pore size on non-Darcy coefficients, the value of  $r_{\min}$  was changed during the reconstruction of the rock sample data by using the random fractal method. Five three-dimensional network models with average pore radii of  $r = 1, 3, 5, 7, \text{ and } 9 \mu\text{m}$  were established. The simulation of nonlinear seepage of gas under different irreducible water conditions was carried. The corresponding non-Darcy coefficients are shown in Figure 7.



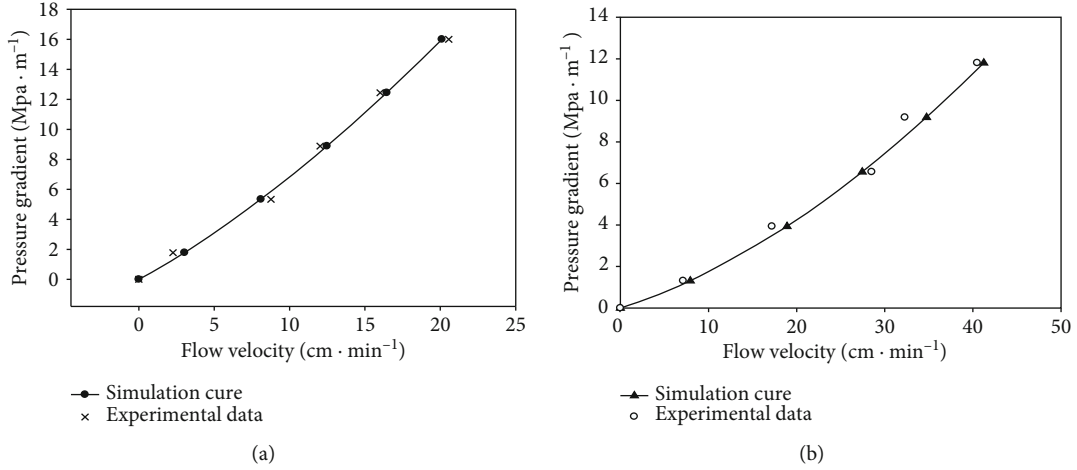


FIGURE 4: Gas velocity and pressure gradient curves of rock sample #1 (a) and rock sample #2 (b).

TABLE 3: Comparison of the  $\beta$  by the different method.

Sample number	Calculated from the experiments (m <sup>-1</sup> )	In network model	$\beta$ (m <sup>-1</sup> ) By Geertsma	In Equation (18)
#1	1.78E9	1.99E9	5.76E10	1.49E9
#2	7.21E8	6.66E8	2.08E10	3.79E8

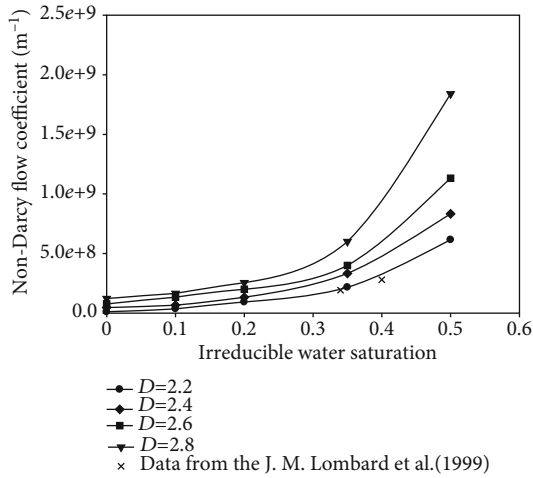


FIGURE 5: Curves of non-Darcy coefficient and irreducible water saturation at different fractal dimension.

The relationships of non-Darcy coefficient and the average pore radius are consistent under different irreducible water saturations (see Figure 7): the non-Darcy coefficient decreases with the increase of the average pore radius, which agrees with the literature data [36]. This relationship can be fitted using the following power function:

$$\beta = a \times r^b, \quad (15)$$

where  $\beta$  is non-Darcy coefficient in m<sup>-1</sup>;  $a$  and  $b$  are parameters (the value of  $b$  obtained from the fitting was  $\sim 4.5$ ).

**4.4. The Impact of Tortuosity.** To analyze the effect of tortuosity on non-Darcy coefficients, the value of tortuosity was changed, while the other parameters remained unchanged. Five sets of three-dimensional network models with tortuosity of  $\tau = 1$ ,  $\tau = 1.3$ ,  $\tau = 1.5$ ,  $\tau = 2.0$ , and  $\tau = 2.5$  were established and obtained non-Darcy coefficients are shown in Figure 8.

The relationship between the non-Darcy coefficient and the tortuosity behaves similarly, and the non-Darcy coefficient increased with the increase of the tortuosity. We fitted this relationship using the following power function:

$$\beta = a \times \tau^b, \quad (16)$$

where  $\beta$  is non-Darcy coefficient in m<sup>-1</sup>;  $a$  and  $b$  are parameters (the value of  $b$  obtained from the fitting was  $\sim 1.52$ ).

**4.5. Fractal Characterization of Non-Darcy Coefficients.** According to the analysis in the previous section, the non-Darcy coefficient can be characterized as a function of the average pore radius, fractal dimension, tortuosity, and irreducible water saturation. The mathematical characterization form is shown below.

$$\beta = \frac{\alpha D^{4.5} \tau^{1.52}}{r^{4.5} (1 - S_w)^{4.5}}, \quad (17)$$

where  $\alpha$  is the proportionality constant, and its value depends on the fluid properties (viscosity, density) as well as other parameters. Non-Darcy coefficients and their related parameters were inserted into Equation (17) to obtain  $\alpha$  for different conditions. The value of  $\alpha$  was calculated to be equal to  $3 \times 10^8$  through trial and error calculations. Therefore, the

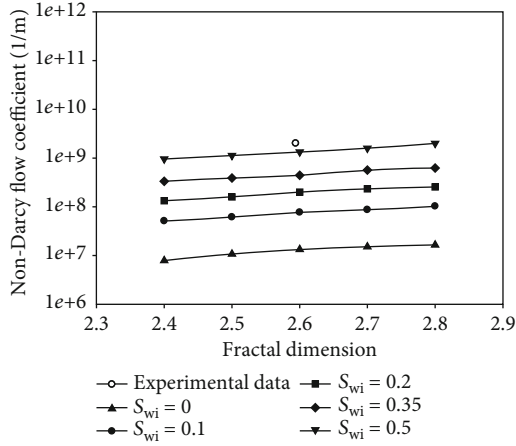


FIGURE 6: Curves of non-Darcy coefficient and fractal dimension at different irreducible water saturation.

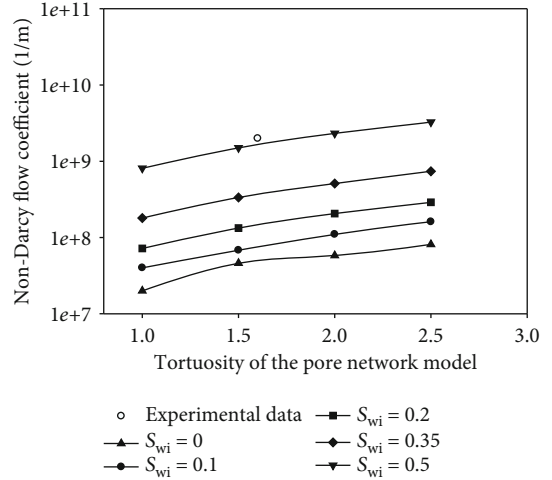


FIGURE 8: Curves of non-Darcy coefficient and tortuosity at different irreducible water saturation.

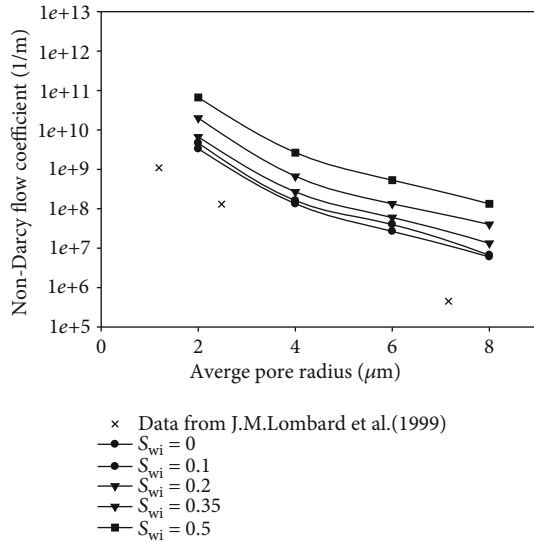


FIGURE 7: Curves of non-Darcy coefficient and average pore radius at different irreducible water saturation.

mathematical expression of non-Darcy coefficient of this model is:

$$\beta = \frac{3 \times 10^8 \times D^{4.5} \tau^{1.52}}{r^{4.5} (1 - S_w)^{4.5}} \quad (18)$$

The non-Darcy coefficient calculated by Equation (18) and the corresponding experimental results are shown in Table 3. We can see that the order of magnitude of non-Darcy coefficient calculated by the experimental data was similar to Equation (18). Equation (18) we conducted by the fractal method of microparameters reflects the influence of rock internal structure on seepage flow. It is more precise than the conventional methods that are obtained by the physical parameters of porosity and permeability. The mathematical characterization was carried out to confirm the

essence of the nonlinear flow. This study is limited to single-phase flow in isotropic porous media.

### 5. Conclusion

- (1) Fractal theory was used to analyze the microscopic pore size distribution obtained by two sets of real core mercury injection methods to determine the fractal dimensions and pore sizes. The constructed pore network models are in good agreement with real cores
- (2) The gas single-phase nonlinear seepage model was established. Besides the viscous resistance, both the tortuosity and the gradual change of the pore-throat radius can produce extraresistance. Based on the three-dimensional network model, the relation curve of flow rate and pressure gradient was obtained by the simulation of the single-phase seepage with irreducible water, and these results were compared with the non-Darcy tests. The validity of the model was confirmed by the good agreement between the obtained non-Darcy coefficient with the calculated results of non-Darcy experiments
- (3) The sensitivity analysis demonstrated that the value of the non-Darcy coefficient decreases with the increase in all parameters: the average pore radius, fractal dimension, irreducible water saturation, and tortuosity. A quantitative relationship between the non-Darcy coefficients of gas nonlinear seepage and these factors was established. We demonstrated non-Darcy flow characteristics by the fractal method

### Nomenclature

- $f$ : Fraction of the fluid from a throat that bends at the next body
- $F$ : Fraction of the pore throats closed
- $k$ : Permeability (Darcy)

$k_g$ : The gas permeability  
 $K$ : Permeability tensor (Darcy)  
 $L$ : Path length from one body center to another (cm)  
 $L_t$ : Pore-throat length (cm)  
 $\Delta p$ : Pressure drop (atm)  
 $\Delta p_b$ : Pressure drop due to bending in the path (atm)  
 $\Delta p_c$ : Pressure drop due to contraction (atm)  
 $\Delta p_e$ : Pressure drop due to expansion (atm)  
 $\Delta p_s$ : Pressure drop for Stokes' flow (atm)  
 $P$ : Pressure (atm)  
 $q$ : Flow rate ( $\text{cm}^3/\text{s}$ )  
 $r_b$ : Body radius (cm),  $r_{b1}$  is the radius of pore 1,  $r_{b2}$  is the radius of pore 2  
 $r_t$ : Throat radius (cm)  
 $r_{\min}$ : Minimum value of the radius (cm)  
 $r_{\max}$ : Maximum value of the radius (cm)  
 $r$ : The pore radius (cm)  
 $D$ : Fractal dimension  
 $\zeta$ : Random number  
 $u$ : Interstitial velocity (cm/s)  
 $v$ : Superficial velocity (cm/s)  
 $\beta$ : Non-Darcy coefficient ( $\text{cm}^{-1}$ )  
 $\mu$ : Viscosity ( $\text{g}\cdot\text{cm}^{-1}\cdot\text{s}^{-1}$ )  
 $\varphi$ : Porosity (%)  
 $\rho$ : Density ( $\text{g}\cdot\text{cm}^{-3}$ )  
 $\tau$ : Tortuosity.

## Data Availability

The data used to support the findings of this study are available from the corresponding author upon request.

## Conflicts of Interest

The authors declare that they have no conflicts of interest.

## Acknowledgments

This work is financially supported by the National Natural Science Foundation of China (No. 51504039) and Major National Science and Technology Projects of China (No. 2016ZX05060-019).

## References

- [1] J. Geertsma, "Estimating the coefficient of inertial resistance in fluid flow through porous media," *Society of Petroleum Engineers Journal*, vol. 14, no. 5, pp. 445–450, 2013.
- [2] D. C. Frederick and R. M. Graves, "New Correlations To Predict Non-Darcy Flow Coefficients at Immobile and Mobile Water Saturation," in *SPE Annual Technical Conference and Exhibition*, New Orleans, Louisiana, 1994.
- [3] R. B. Grigg and M. K. Hwang, "High velocity gas flow effects in porous gas-water system," in *SPE Gas Technology Symposium*, Calgary, Alberta, Canada, 1998.
- [4] F. Thauvin and K. K. Mohanty, "Network modeling of non-Darcy flow through porous media," *Transport in Porous Media*, vol. 31, no. 1, pp. 19–37, 1998.
- [5] A. Firoozabadi and D. L. Katz, "An analysis of high-velocity gas flow through porous media," *Journal of Petroleum Technology*, vol. 31, no. 2, pp. 211–216, 2013.
- [6] F. O. Jones and W. W. Owens, "A laboratory study of low-permeability gas sands," *Journal of Petroleum Technology*, vol. 32, no. 9, pp. 1631–1640, 2013.
- [7] H.-W. Lao, H. J. Neeman, and D. V. Papavassiliou, "A pore network model for the calculation of non-Darcy flow coefficients in fluid flow through porous media," *Chemical Engineering Communications*, vol. 191, no. 10, pp. 1285–1322, 2004.
- [8] C. P. Chukwudozie, M. Tyagi, S. O. Sears, and C. D. White, "Prediction of non-Darcy coefficients for inertial flows through the Castlegate sandstone using image-based modeling," *Transport in Porous Media*, vol. 95, no. 3, pp. 563–580, 2012.
- [9] H. Dou, "Further understanding on turbulence coefficient of high-speed non-Darcy flow of gas reservoir," *Fault Block Oil and Gas Field*, vol. 20, no. 4, pp. 465–469, 2013.
- [10] C. Li, "High rate non-Darcy flow is easier to occur in low permeability reservoirs," *Lithologic Reservoirs*, vol. 11, no. 6, pp. 111–119, 2011.
- [11] X. Wang, D. Zhang, and M. Liao, "Turbulence factor of high pressure gas reservoir in Keyi tectonic belt," *Drilling & Production Technology*, vol. 25, no. 1, pp. 44–49, 2002.
- [12] X. Ren, Q. Yan, and Q. He, "Experimental study of low permeability gas reservoir gas seepage characteristics," *Journal of Xi'an Shiyou University (Natural Science Edition)*, vol. 12, no. 3, pp. 22–25, 1997.
- [13] D. Li and T. W. Engler, "Literature review on correlations of the non-Darcy coefficient," in *SPE Permian Basin Oil and Gas Recovery Conference*, Midland, Texas, 2001.
- [14] K. Xu, X. Lei, and Q. Meng, "Study of inertial coefficient of non-Darcy seepage flow," *Chinese Journal of Rock Mechanics and Engineering*, vol. 31, no. 1, pp. 164–170, 2012.
- [15] Y. Chen and N. Dong, "A method of determining high-velocity coefficient  $\beta$  and its correlation," *Fault Block Oil and Gas Field*, vol. 5, no. 6, pp. 20–26, 1998.
- [16] I. Fatt, "The network model of porous media I. capillary pressure characteristics," *Transactions of AIME*, vol. 207, no. 1, pp. 144–181, 2013.
- [17] H. Okabe and M. J. Blunt, "Pore space reconstruction using multiple-point statistics," *Journal of Petroleum Science and Engineering*, vol. 46, no. 1-2, pp. 121–137, 2005.
- [18] M. Piri and M. J. Blunt, "Three-dimensional mixed-wet random pore-scale network modeling of two- and three-phase flow in porous media. I. Model description," *Physical Review E*, vol. 71, no. 2, article 026301, 2005.
- [19] P. A. Byrnes, R. M. Cluff, and J. C. Webb, "Analysis of critical permeability, capillary and electrical properties for Mesaverde tight gas sandstones from Western US basins: final scientific," Technical report submitted to DOE and NETL, 2009.
- [20] N. A. Idowu, "Pore-scale modeling: stochastic network generation and modeling of rate effects in water flooding," PhD thesis, Imperial College London, UK, 2009.
- [21] F. Fang, A. Firoozabadi, M. Abbaszadeh, and C. Radke, "A phenomenological modeling of critical condensate saturation," in *SPE Annual Technical Conference and Exhibition*, Denver, Colorado, 1996.
- [22] S. Mohammadi, K. S. Sorbie, and A. Danesh, "Pore-level modelling of gas-condensate flow through horizontal porous

- media,” in *SPE Annual Technical Conference and Exhibition*, New Orleans, Louisiana, 2009.
- [23] X. Zhao, Z. Yang, W. Lin et al., “Study on pore structures of tight sandstone reservoirs based on nitrogen adsorption, high-pressure mercury intrusion, and rate-controlled mercury intrusion,” *Journal of Energy Resources Technology*, vol. 141, no. 11, article 112903, 2019.
- [24] S. Zhang, X. Xian, J. Zhou et al., “Experimental study of the pore structure characterization in shale with different particle size,” *Journal of Energy Resources Technology*, vol. 140, no. 5, article 054502, 2018.
- [25] C. Lu, W. Zhao, Y. Liu, and X. Dong, “Pore-scale transport mechanisms and macroscopic displacement effects of in-situ oil-in-water emulsions in porous media,” *Journal of Energy Resources Technology*, vol. 140, no. 10, article 102904, 2018.
- [26] F. Alreshedan and A. Kantzas, “Investigation of permeability, formation factor, and porosity relationships for Mesaverde tight gas sandstones using random network models,” *Journal of Petroleum Exploration and Production Technology*, vol. 6, no. 3, pp. 545–554, 2016.
- [27] Y. Yi, J. Li, and L. Ji, “Numerical Determination of critical condensate saturation in gas condensate reservoirs,” *Journal of Energy Resources Technology*, vol. 139, no. 6, article 062801, 2017.
- [28] B. Yu and P. Cheng, “A fractal permeability model for bi-dispersed porous media,” *International Journal of Heat and Mass Transfer*, vol. 45, no. 14, pp. 2983–2993, 2002.
- [29] J. Wu and B. Yu, “A fractal resistance model for flow through porous media,” *Heat and Mass Transfer*, vol. 50, no. 19-20, pp. 3925–3932, 2007.
- [30] F. Wang, Z. Liu, L. Jiao, C. Wang, and H. Guo, “A fractal permeability model coupling boundary-layer effect for tight oil reservoirs,” *Fractals*, vol. 25, no. 5, article 1750042, 2017.
- [31] F. Wang, Z. Liu, J. Cai, and J. Gao, “A fractal model for low-velocity non-Darcy flow in tight oil reservoirs considering boundary-layer effect,” *Fractals*, vol. 26, no. 5, article 1850077, 2018.
- [32] J. Li and B. Zheng, “Digital core and pore network model reconstruction based on random fractal theory,” *International Journal of Energy and Statistics*, vol. 3, no. 1, article 1550001, 2015.
- [33] F. Wang, L. Jiao, Z. Liu, X. Tan, C. Wang, and J. Gao, “Fractal analysis of pore structures in low permeability sandstones using mercury intrusion porosimetry,” *Journal of Porous Media*, vol. 21, no. 11, pp. 1097–1119, 2018.
- [34] M. T. Balhoff and M. F. Wheeler, “A predictive pore-scale model for non-Darcy flow in porous media,” *SPE Journal*, vol. 14, no. 4, pp. 579–587, 2009.
- [35] G. Wang, X. Yang, and X. Zhang, “Numerical simulation on non-Darcy seepage of CBM by means of 3D reconstruction based on computed tomography,” *Journal of China Coal Society*, vol. 41, no. 4, pp. 931–940, 2016.
- [36] J. M. Lombard, D. Longeron, and F. Kalaydjian, “Influence of connate water and condensate saturation on inertial effects in gas-condensate fields,” in *SPE Annual Technical Conference and Exhibition*, Houston, Texas, 1999.
- [37] W. Li, X. Ma, and Y. Wang, “Effect of irreducible water saturation on deliverability of hydraulic fractured gas well taking into account non-Darcy flow,” *Oil Drilling & Production Technology*, vol. 33, no. 3, pp. 35–37, 2011.
- [38] N. Li, X. Tang, and Q. Zhang, “Experimental study on gas low-velocity non-Darcy seepage in low permeability gas reservoir,” *Natural Gas Exploration & Development*, vol. 26, no. 2, pp. 49–55, 2003.
- [39] R. D. Evans, C. S. Hudson, and J. E. Greenlee, “The effect of an immobile liquid saturation on the non-Darcy flow coefficient in porous media,” *SPE Production Engineering*, vol. 2, no. 4, pp. 331–338, 1987.

## Research Article

# Study on Propagation Behaviors of Hydraulic Fracture Network in Tight Sandstone Formation with Closed Cemented Natural Fractures

Jun Zhang <sup>1</sup>, Yu-Wei Li <sup>1</sup>, Wei Li,<sup>1</sup> Zi-Jie Chen,<sup>2</sup> Yuan Zhao,<sup>3</sup> Fa-Hao Yu,<sup>4</sup> and Yan Zheng<sup>2</sup>

<sup>1</sup>Department of Petroleum Engineering, Northeast Petroleum University, 163318 Daqing, China

<sup>2</sup>No. 5 Oil Production Plant, Dagang Oilfield Company, 301700 Tianjin, China

<sup>3</sup>China Petroleum Logging Co., LTD. Tianjin Branch, 301700 Tianjin, China

<sup>4</sup>Bohai Oilfield research institute, CNOOC Tianjin Branch Company, 300459 Tianjin, China

Correspondence should be addressed to Yu-Wei Li; [liyuweibox@126.com](mailto:liyuweibox@126.com)

Received 11 June 2020; Revised 29 July 2020; Accepted 14 August 2020; Published 11 September 2020

Academic Editor: Jinze Xu

Copyright © 2020 Jun Zhang et al. This is an open access article distributed under the Creative Commons Attribution License, which permits unrestricted use, distribution, and reproduction in any medium, provided the original work is properly cited.

Natural fractures in tight sandstone formation play a significant role in fracture network generation during hydraulic fracturing. This work presents an experimental model of tight sandstone with closed cemented preexisting fractures. The influence of closed cemented fractures' (CCF) directions on the propagation behavior of hydraulic fracture (HF) is studied based on the hydraulic fracturing experiment. A field-scaled numerical model used to simulate the propagation of HF is established based on the flow-stress-damage (FSD) coupled method. This model contains the discrete fracture network (DFN) generated by the Monte-Carlo method and is used to investigate the effects of CCFs' distribution, CCFs' strength, and in-situ stress anisotropy, injection rate, and fluid viscosity on the propagation behavior of fracture network. The results show that the distribution direction of CCFs is critical for the formation of complex HFs. When the angle between the horizontal maximum principal stress direction and the CCFs is in the range of 30° to 60°, the HF network is the most complex. There are many kinds of compound fracture propagation patterns, such as crossing, branching, and deflection. The increase of CCFs' strength is not conducive to the generation of branched and deflected fractures. When the in-situ stress difference ranges from 3 MPa to 6 MPa, the HF network's complexity and propagation range can be guaranteed simultaneously. The increase in the injection rate will promote the formation of the complex HF network. The proper increase of fracturing fluid viscosity can promote HF's propagation. However, when the viscosity is too high, the complex HFs only appear around the wellbore. The research results can provide new insights for the hydraulic fracturing optimization design of naturally fractured tight sandstone formation.

## 1. Introduction

Hydraulic fracturing is the key technology to improve the oil and gas development of the unconventional reservoir. The hydraulic fracture (HF) can effectively increase the migration channel of oil and gas and improve production and recovery [1–4]. The existence of the natural fracture (NF) system in the tight sandstone formation will change the HF's propagation path, which makes the HF generate many propagation patterns [5–8]. It is of considerable significance to understand the propagation mechanism of HF under the influence of NFs and reveal the formation condition of the complex HF

network for the optimization of hydraulic fracturing in the tight sandstone formation.

Due to the lack of accurate and effective monitoring technology, the field cannot directly observe the HF's propagation process in the underground reservoir. At present, the propagation law of HF in unconventional reservoirs is not clear. Many scholars have studied the interaction between HF and NF by laboratory-scale fracturing experiments and numerical simulation. Hou et al., Zou et al., and Xie et al. [9–12] carried out a series of triaxial hydraulic fracturing experiments with natural shale. They investigated the influence of bedding planes on the HF's propagation behavior



through acoustic emission (AE) monitoring technology. Tan et al. [13] classified the propagation pattern of HF in shale formation into four types: simple fracture, fishbone-like fracture, fishbone-like fracture with fissure opening, and multi-lateral fishbone-like fracture network. Zou et al. [14] carried out triaxial fracturing experiments on layered tight sandstone and studied the effect of natural fractures on CO<sub>2</sub> induced fracture propagation behavior. However, the fractures' distribution in the outcrop of natural rock is random, which is disadvantageous to the quantitative analysis of the fracture propagation mechanism. Therefore, some researchers tried to explore the interaction between HF and NF through the artificial fracturing specimen. In some studies, sandstone slice, gypsum slice, glass slice, or printing paper were placed in the cement mortar to simulate the NFs [15–20]. However, solid materials cannot reflect the friction effect and mechanical characteristics of closed NF. Some studies proposed to use the interface between artificial core blocks to simulate NF [21–26], but this kind of experiment model can only study the influence of a single preexisting fracture on the HF propagation path.

Due to the high cost and limited scale of laboratory experiments, many scholars have developed different numerical simulation methods to explore the HF propagation mechanism. Guo et al., Shi et al., Vahab et al., Hirmand et al., Rueda Cordero et al., Liu et al., and Zheng et al. [27–33] used the extended finite element method (XFEM) to study the propagation process of complex HF in fractured reservoirs. Wang proposed a global cohesive zone model and used it to study the formation conditions of the fracture network in fractured reservoir [34]. Zhou et al., Wang et al., Yoon et al., and Zhang et al. [35–38] used two-dimensional particle flow code (PFC2D) to simulate the effect of NF characteristics on the HF propagation behavior. Amir et al. combined the extended finite element method (XFEM) and discrete element method (DEM) to simulate the HF propagation in porous media with natural fractures [39]. Tang proposed a fully coupled flow-stress-damage (FSD) model to simulate the damage and failure process of heterogeneous materials [40]. Many studies used the FSD model to study the propagation process of HF [41–44]. Li et al. [45] used the FSD model to simulate the initiation, propagation, and associated stress evolution during the fracturing process in the glutenite formation and studied the influence of the confining stress ratio, gravel sizes, and gravel volume content on the hydraulic fracturing pattern in a conglomerate specimen. Wang et al. [46] used the FSD model to study the influence of the injection rate on the propagation behavior of HF in the formation containing a discrete fracture network (DFN). Men et al. [47] simulated the influence of bedding planes' direction and mechanical characteristics on the propagation path of HF in the shale formation. Li et al. [48] used this method to simulate the multistage hydraulic fracturing process and studied the influence of fracture spacing and stress anisotropy on the propagation and reorientation of three HF.

To explore the HF propagation behavior in tight sandstone formation containing multiple groups of CCFs, a new laboratory-scale fracturing experimental model is designed in this paper. The model not only has a closer mechanical

property to tight sandstone but also contains multiple groups of closed cemented preexisting fractures. The hydraulic fracturing experiments with this experimental model are carried out to study the influence of fracture network direction on the propagation behavior of HF. Then a large-scale numerical model used to simulate the hydraulic fracturing process in naturally fractured tight sandstone formation is established by the coupled FSD method. The discrete fracture network (DFN) generated in the model is based on the Monte-Carlo method. Through the numerical simulation, the effects of CCFs' distribution, CCFs' strength, in-situ stress anisotropy, injection rate, and fluid viscosity on the propagation behavior of the HF network are investigated.

## 2. Hydraulic Fracturing Experiment of Fractured Tight Sandstone Formation

*2.1. Preparation of Fracturing Specimen.* The research object of this paper is Quan-4 tight sandstone formation of Songliao basin in China. According to the statistics of the NFs from 16 coring wells, 58.3% of the NFs have a dip angle greater than 80° and 73% have a dip angle greater than 60°, which indicates that the fractures in this area are mainly high-angle NF. The observations and measurements of full-sized rock cores show that the NF density is 0.24–0.85 with an average of 0.58.

A new artificial experimental model is used in this study to quantitatively analyze the influence of CCF network direction on HF's propagation. Compared with the existing experimental model, the new model not only contains several groups of CCFs with different directions but also has mechanical properties closer to that of natural tight sandstone. The preparation process of this model includes two key steps:

Step (a): determination the mortar formula of artificial tight sandstone

The materials for making artificial tight sandstone specimens include natural quartz sand, clay, epoxy resin, and densifier. The screening steps of the mortar formula are shown in Figure 1. According to different formulas, the mortar is mixed and poured into the mold. The mortar specimens are solidified under the compaction pressure for 48 hours and are maintained in the incubator for 24 hours. The artificial tight sandstone specimens with the closest physical and mechanical properties to the natural tight sandstone are selected through the mechanical property test and permeability test of each group of mortar specimens.

Step (b): simulation of CCFs in the hydraulic fracturing specimen

The structure of the artificial tight sandstone fracturing specimen is shown in Figure 1. The specimen size is 300 mm × 300 mm × 300 mm. The specimen contains three layers, and each layer is 100 mm thick. L-A and L-C represent the upper and lower barriers, respectively. L-B is the hydraulic fracturing target layer, which contains closed cemented preexisting fractures in different directions. The preparation procedures are as follows: (I) the mortar is poured into the mold and solidifies under 40 MPa compaction pressure. After 48 hours, the upper barrier (L-A) is formed. (II) According to

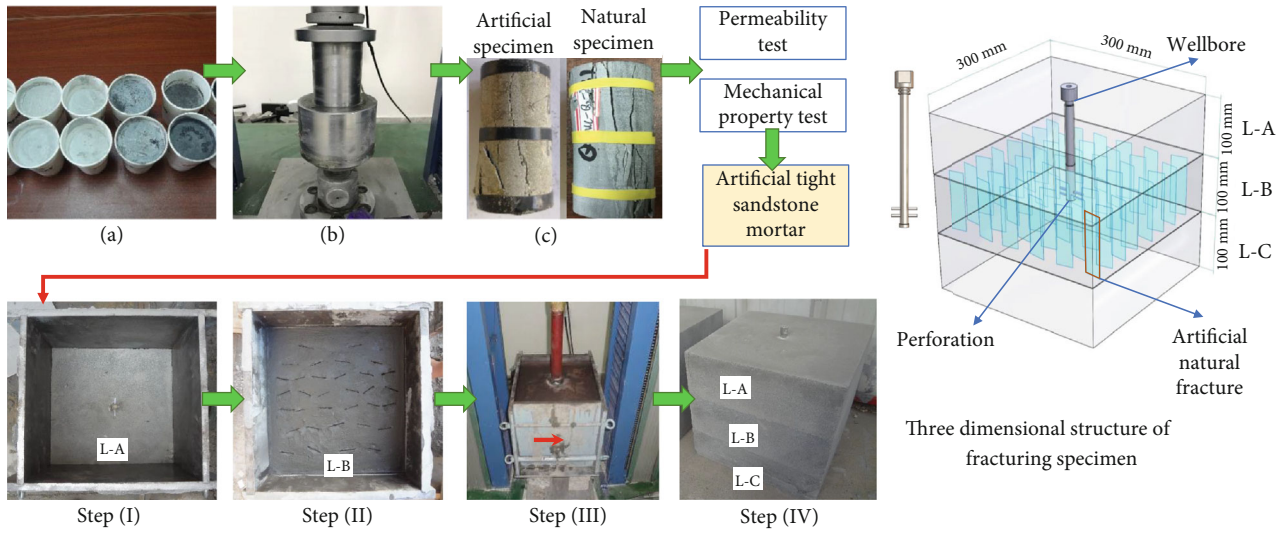


FIGURE 1: Preparation procedure of artificial tight sandstone specimens with multiple CCFs.

the formula determined in step (a), the mortar is prepared and poured into the mold which contains L-A. Then, the steel sheets (0.5 mm thick) are inserted into the mortar according to the design direction and position. (III) All steel sheets are taken out from the mortar slowly after L-B has solidified for one hour. The mold containing L-A and L-B is compacted at a pressure of 30 MPa for 48 hours. Then the preexisting fractures in L-B are closed and cemented under compaction pressure. (IV) The lower barrier is prepared according to step (I).

The angle between the CCF and the direction of horizontal maximum principal stress are defined as  $\theta$  in this paper. Considering that the natural fractures in the formation cannot be in the same direction, the angle  $\theta$  of CCFs in the three fracturing specimens are set to  $0^\circ \pm 15^\circ$ ,  $45^\circ \pm 15^\circ$ , and  $90^\circ \pm 15^\circ$ . The comparison of basic mechanical parameters of the artificial experimental model and natural tight sandstone is shown in Table 1.

**2.2. Experimental System and Procedure.** The triaxial hydraulic fracturing physical simulation experiment system of Northeast Petroleum University is used in our experiment (Figure 2). The injection rate is set to 5 ml/min, the horizontal maximum principal stress and the horizontal minimum principal stress are set to 20 MPa and 16 MPa, and the vertical stress is set to 25 MPa. Slick water mixed with red tracer is used as the fracturing fluid. The acoustic emission (AE) system is used to monitor the initiation and propagation of hydraulic fractures in the specimens during the experiment. Eight AE sensors were installed in the groove of the loading plates. The frequency-domain of the AE system was 125–750 kHz, and the gain of the channel preamplifier was 40 dB.

**2.3. Analysis of Experimental Results**

**2.3.1. Analysis of Hydraulic Fracture Geometry.** Figure 3(a) shows the HF’s propagation patterns observed at the interface between L-A and L-B. The yellow lines and red lines represent the CCFs that are not affected and communicated

by hydraulic fractures, respectively. It can be seen that the direction of CCFs has a significant impact on the propagation behavior of HF. In specimen #1 ( $\theta = 0^\circ \pm 15^\circ$ ), all the four CCFs on the HF’s propagation path are communicated by HF. Due to the small angle between the CCFs and the direction of the horizontal maximum principal stress, a simple crack with symmetrical wings is finally formed. In specimen #2 ( $\theta = 45^\circ \pm 15^\circ$ ), the HF interacts with eight CCFs and has obvious deflection behaviors. There are two possible propagation behaviors of HF after encountering CCFs: deflection along with the CCF and penetration through the CCF. In specimen #3 ( $\theta = 90^\circ \pm 15^\circ$ ), the HF penetrates the two CCFs near the wellbore with a reinitiation after a short extension distance along with the CCF. Subsequently, the HF crosses through the remaining CCFs and propagates to the direction of horizontal maximum principal stress. This shows that the geometry and propagation pattern of the HFs are the most complex when the angle between the horizontal maximum principal stress direction and CCF is between  $30^\circ$  and  $60^\circ$ .

**2.3.2. Analysis of Injection Pressure-Time Curves.** The characteristics of the injection pressure-time curve can be used to analyze the propagation behaviors of HF. As shown in Figure 4, the initiation and propagation process of HF can be divided into four stages:

Stage (I): pressurization and fracture initiation stage. The injection pressure increases sharply with the continuous injection of fracturing fluid. When the injection pressure exceeds the sum of the rock tensile strength and the horizontal minimum principal stress, the rock surrounding the wellbore breaks and the initial HF appears

Stage (II): main fracture propagation stage. The main HF propagates in the rock matrix. The injection pressure-time curve is relatively stable and has no significant fluctuation

Stage (III): fracture interaction stage. The HF interacts with the preexisting fractures significantly, which makes the injection pressure fluctuate obviously

TABLE 1: The basic mechanical parameters of the artificial experimental model and natural tight sandstone.

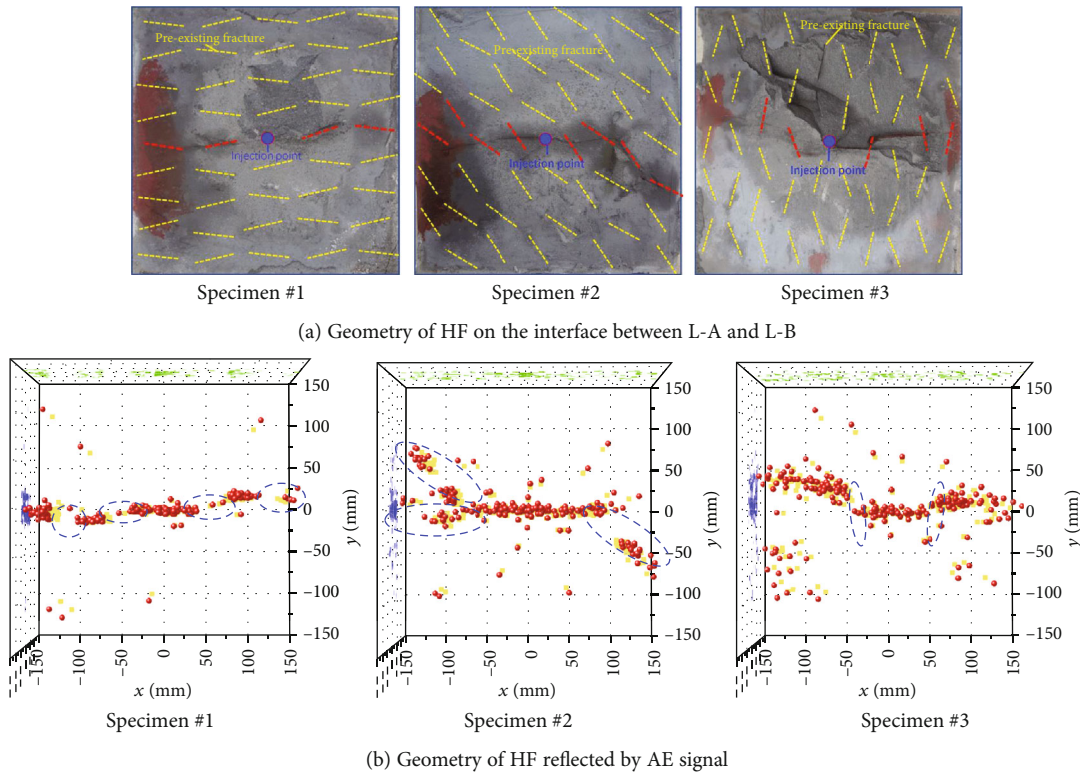
Type of specimen	Compressive strength (MPa)	Tensile strength (MPa)	Elastic modulus (GPa)	Poisson's ratio	Permeability ( $10^{-3} \mu\text{m}^2$ )	Porosity (%)
Artificial tight sandstone	61.8	6.5	24.9	0.19	0.26	11.8
Natural tight sandstone	64.3	4.5	25.6	0.168	0.493	8.54



(a) Test system

(b) AE system

FIGURE 2: Hydraulic fracturing experimental system and acoustic emission monitoring system.



(a) Geometry of HF on the interface between L-A and L-B

(b) Geometry of HF reflected by AE signal

FIGURE 3: Hydraulic fracture morphology observed in the cross-section of the fractured specimen and reflected by AE data.

Stage (IV): pump stop stage. The HF propagates to the boundary of the specimen, and the injection pressure curve declines sharply

The characteristics of the stage (I), (II), and (IV) of three specimens are similar, but stage (III) has different changes. At the stage (III) of specimen #1, the injection pressure

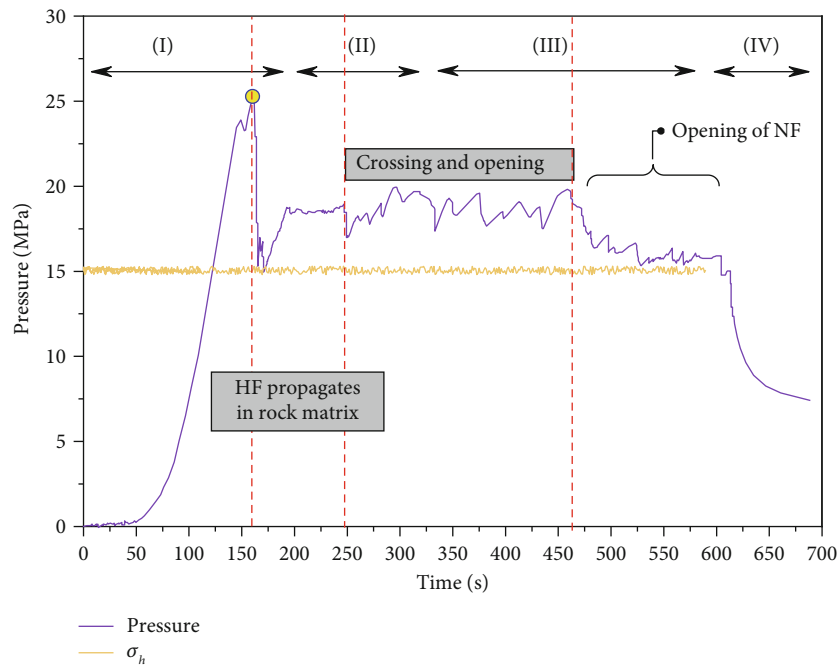
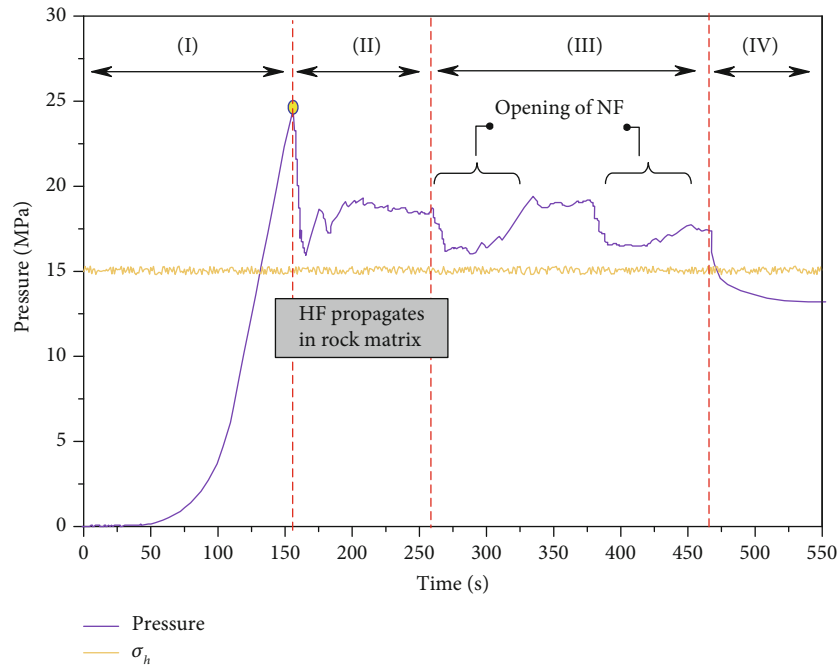
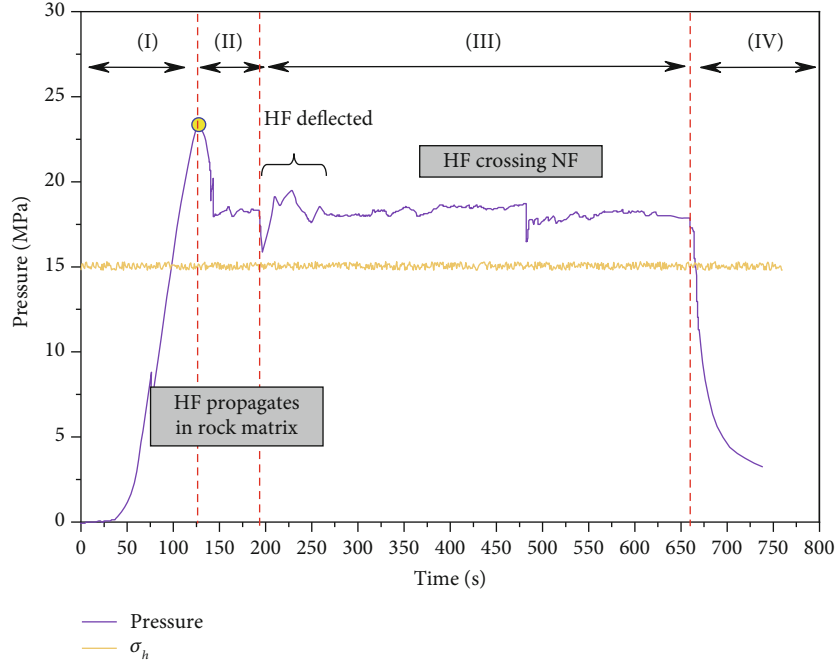


FIGURE 4: Continued.





(c) Specimen #3

FIGURE 4: The injection pressure-time curves of each specimen.

decreased twice and then increased again. When the HF intersects with the CCFs, the CCFs dilate and open, and the fracturing fluid leaks into the opened fractures, which makes the pressure drop greatly. When the opened fracture is filled with fracturing fluid, the injection pressure increases again to meet the mechanical conditions of HF propagating in the rock matrix again. At the stage (III) of specimen #2, the injection pressure curve fluctuates violently and has many peaks. At this stage, the propagation patterns of HF include deflection and penetration. Under the joint action of the reinitiation of the rock matrix and the opening of preexisting fractures, the injection pressure appears violent fluctuation. At the stage (III) of specimen #3, when the HF interacts with the first set of preexisting fractures, the injection pressure only fluctuates slightly and lasts for a short time. In the subsequent fracturing process, the change of injection pressure is small. This shows that the HF mainly propagates in the rock matrix and has no significant interaction with the CCFs.

### 3. Field-Scale Hydraulic Fracturing Numerical Simulation

Due to the limitation of the simulation scale of laboratory experiments, only three groups of hydraulic fracturing experiments are carried out to study fracture direction's influence on HF's propagation. In this paper, the influence of other key factors on the complex fracture propagation law in fractured tight sandstone formation is studied through a two-dimensional numerical model based on the FSD method.

*3.1. The Coupled Flow-Stress-Damage (FSD) Numerical Method.* The FSD model considers the coupling effects of flow, stress, and damage on the permeability changes caused by the

propagation of fractures and the evolution of rock damage. The assumptions of the model are as follows: (1) The water-rock coupling relationship is based on the Terzaghi principle, the rock seepage conforms to Darcy's law, and the rock deformation process of fluid-solid coupling conforms to the Biot consolidation theory. (2) The material of the model element is assumed to be elastic brittle material with certain residual strength. (3) The damage of the material element follows the maximum tensile strength criterion and Mohr-Coulomb failure criterion. (4) Rock is heterogeneous material, and its physical and mechanical parameters follow Weibull distribution.

The element in the FSD coupling model is defined in five states: elastic deformation, tensile failure, compression failure, tensile separation, and compression contact, as shown in Figure 5(a). The current state of each element is determined by its damage history, current stress-strain level, and material properties. Failure paths occur when elements damage, contact, and separate. When the stress state of an element satisfies any strength criterion, it begins to accumulate damage. In the elastic damage mechanics, the elastic modulus of the element decreases with the damage. Based on the assumption of strain equivalence, the elastic modulus of damage element is given by the following formula:

$$E_d = (1 - D)E_0, \quad (1)$$

where  $D$  is the damage variable.

There is only one failure mode for the elastic brittle element with residual strength. The compressive stress should be positive, and the stress-strain relationship is shown in Figure 5(b). When the minimum principal strain of the element exceeds the uniaxial tensile strain or the minimum



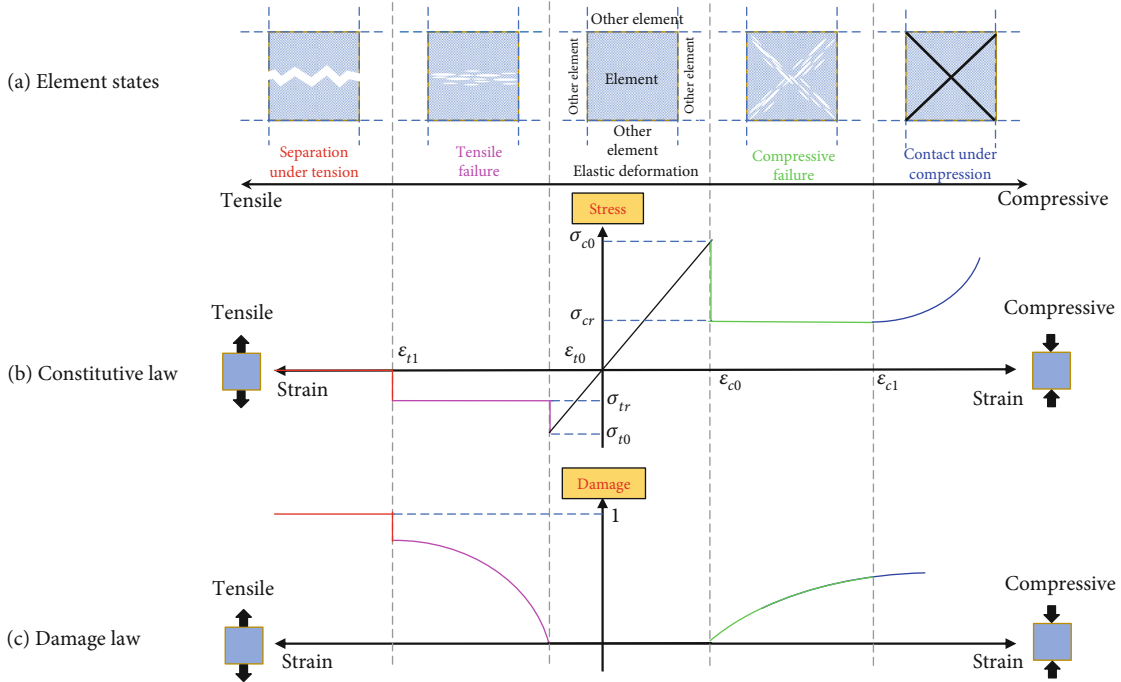


FIGURE 5: Elastic damage constitutive relation of the element under uniaxial stress.

principal stress exceeds the uniaxial tensile strength determined by the test, it is considered as the failure in the tensile mode.

$$\sigma_3 \leq \sigma_{t0}, \quad (2)$$

$$\epsilon_3 \leq \frac{\sigma_{t0}}{E}. \quad (3)$$

In the multiaxial stress state, the damage variable of the element in the tensile mode can be expressed as:

$$D = \begin{cases} 0 & \bar{\epsilon} \leq \epsilon_{t0}, \\ 1 & \epsilon_{t0} < \bar{\epsilon} \leq \epsilon_{t1}, \\ 1 & \bar{\epsilon} > \epsilon_{t1}. \end{cases} \quad (4)$$

In this case, after the element is damaged, the permeability coefficient of the element can be expressed as follows:

$$K = \begin{cases} K_0 e^{-\beta(\sigma_3 - \alpha p)} & D = 0, \\ \xi K_0 e^{-\beta(\sigma_3 - \alpha p)} & 0 < D \leq 1. \end{cases} \quad (5)$$

When the shear stress of the element satisfies the Mohr-Coulomb failure criterion, it is considered as failure in shear mode.

$$\sigma_1 - \sigma_3 \frac{1 + \sin \varphi}{1 - \sin \varphi} \geq \sigma_{c0}. \quad (6)$$

In the multiaxial stress state, the damage variable of the element in the shear mode can be expressed as:

$$D = \begin{cases} 0 & \epsilon_1 < \epsilon_{c0}, \\ 1 - \frac{\sigma_{rc}}{\epsilon_1 E_0} & \epsilon_{c0} \leq \epsilon_1. \end{cases} \quad (7)$$

In this case, after the element is damaged, the permeability coefficient of the element can be expressed as follows:

$$K = \begin{cases} K_0 e^{-\beta(\sigma_1 - \alpha p)} & D = 0, \\ \xi K_0 e^{-\beta(\sigma_1 - \alpha p)} & D > 0. \end{cases} \quad (8)$$

where  $\bar{\epsilon}$  is the equivalent principal strain of the member;  $\epsilon_{t0}$  is the elastic ultimate strain;  $\epsilon_{t1}$  is the ultimate tensile strain when the element is completely damaged;  $\xi$  is the permeability damage factor;  $\sigma_1$  and  $\sigma_3$  are the maximum and minimum effective principal stress;  $\sigma_{t0}$  and  $\sigma_{c0}$  are the tensile failure strength and compressive failure strength of the element;  $\sigma_{tr}$  is the residual tensile strength of the element;  $K$  is permeability coefficient.

Compared with other hydraulic fracturing numerical simulation models, the FSD coupling model is based on the finite element and statistical damage theory. It considers the heterogeneity of material properties and can simulate the dynamic fracturing process of the heterogeneous reservoir.

**3.2. Applicability Verification of Numerical Model.** To verify the applicability and accuracy of the numerical method, a two-dimensional numerical model of the hydraulic fracturing experiment is established. This model has a size of 400 mm  $\times$  400 mm and includes 40000 elements. The position

TABLE 2: Mechanical parameters in the numerical model.

Parameter	Rock matrix	Natural fracture
Homogeneity	3.5	2.5
Elastic modulus (GPa)	25.0	3.0
Compressive strength (MPa)	62.0	5.0
Tensile strength (MPa)	6.5	0.5
Poisson's ratio	0.2	0.25
Coefficient of residual strength	0.2	0.3
Permeability ( $10^{-3} \mu\text{m}^2$ )	0.3	3.0
Porosity (%)	0.12	0.5
Coupling coefficient	0.1	0.1

and direction of the preexisting fractures are consistent with the experiment model. The seepage boundary with a flow rate of 0 is applied around the model. The stress conditions and the rock mechanical parameters are the same as those in the experiment, as shown in Table 2.

**3.2.1. Analysis of Hydraulic Fracture Geometry.** It can be seen from Figure 6 that the fracture propagation patterns of numerical simulation are in good agreement with the experiment. The interaction stage (stage III) of the three numerical models is significantly different. The numerical model of specimen #1 finally appears a simple HF along the direction of horizontal maximum principal stress, which is consistent with the experimental results. It is worth noting that before the HF intersects with the CCF, some damage elements have appeared on the CCF. With the increase of water pressure, the HF encounters the CCF, and the number of damaged elements on the CCF increases rapidly. The HF connects the whole CCF in about 5 time steps. In the numerical model of specimen #2, the HF interacts with the first set of CCFs and appears the composed propagation pattern including penetration and deflection. After the branching fractures are formed in the numerical model, the propagation direction of some HFs changes, and the geometry of HFs becomes complex. In the numerical model of specimen #3, the HF deflects slightly at the first set of CCFs and then propagates into the rock matrix with a short deflection distance. Then, the HF penetrates through the remaining CCFs. In this process, only a few damage elements appear near the interaction point, and the CCFs remain closed.

**3.2.2. Analysis of Injection Pressure-Time Curves.** In Figure 7, the initiation pressure of specimen #1 is 23.4 MPa. The injection pressure decreases sharply and increases again at step 40 and step 70, respectively. These are the moments when the HF interacts with the CCFs. Due to the normal stress on the surface of CCF in specimen #1 is small, the connected CCFs are completely damaged. Thus, the filtration of the fracturing fluid into the preexisting fracture is significant, and the injection pressure curve is greatly reduced.

The initiation pressure of specimen #2 is 24.4 MPa. The injection pressure fluctuates sharply from step 20 to 114. During this stage, the complex branching propagation fractures appear because of many kinds of interaction patterns

between HF and CCFs. The violent interaction is accompanied by frequent filtration and pressure holding, which results in the violent fluctuation of the injection pressure curve. At step 114, the injection pressure has a sharp decline, which is the moment when the HF intersects with the second set of CCFs and deflects along with the opened fractures. After step 120, although the injection pressure fluctuates, the overall pressure is lower than that of step 20-114. During this stage, the HF not only deflects along the opened CCFs but also continue to expand in the rock matrix.

Compared with the other two groups of experiments, the initiation pressure (26.6 MPa) and propagation pressure of specimen #3 are both larger. Besides, the whole fracturing process of specimen #3 lasts a long time (276 steps), which is due to the HF mainly propagates in the rock matrix. At step 78, the injection pressure decreases slightly and rises rapidly. At this time, the HF intersects with the first set of CCFs, and the injection pressure decreases under the effect of filtration. However, due to the large normal stress on the CCFs in specimen #3, the resistance of CCF to open is large. Thus, the HF repenetrates the two CCFs after a short extension distance along with the CCF. After step 90, the injection pressure is relatively stable, which shows that HF penetrates through the remaining CCFs and propagates in the rock matrix.

**3.3. Numerical Model of Hydraulic Fracturing with Discrete Fracture Network (DFN).** To study the influence of other key factors on the propagation behavior of HFs in tight sandstone formation with CCF network, a field-scale numerical model is established based on the FSD coupling method, as shown in Figure 8. The model has a size of  $400 \text{ m} \times 600 \text{ m}$  and includes 240000 elements. A two-dimensional DFN generation program is generated based on the Monte-Carlo method. According to the fracture geometry parameters obtained from the field statistics, the DFN is inserted in the numerical model. The fracture parameters of the stochastic modeling method mainly include length, azimuth, opening, and density. This paper focuses on the influence of CCFs on HFs' propagation, so the influence of fracture opening is not considered. The width of CCFs is equivalent to the width of an element. There are two groups of CCFs in the numerical model, and the relevant parameters are in Table 3. The azimuth angle  $\theta$  is the angle between the direction of CCFs and the direction of horizontal maximum principal stress. In the DFN model, the lengths of CCFs satisfy the normal distribution, and the azimuth angles of CCFs satisfy the logarithmic normal distribution. The physical and mechanical parameters of the numerical model are shown in Table 2. In the middle of the model, there is a perforation parallel to the direction of the horizontal maximum principal stress with a length of 5 m.

## 4. Analysis of Numerical Simulation Results

**4.1. Influence of CCFs Distribution Direction.** In the numerical model, the azimuth angle ( $\theta$ ) of the two groups of natural fractures are set to  $\pm 15^\circ$ ,  $\pm 30^\circ$ ,  $\pm 45^\circ$ ,  $\pm 60^\circ$ ,  $\pm 75^\circ$ ,  $\pm 90^\circ$ , and the standard deviation is 0. The injection rate is  $10 \text{ m}^3/\text{min}$ , the

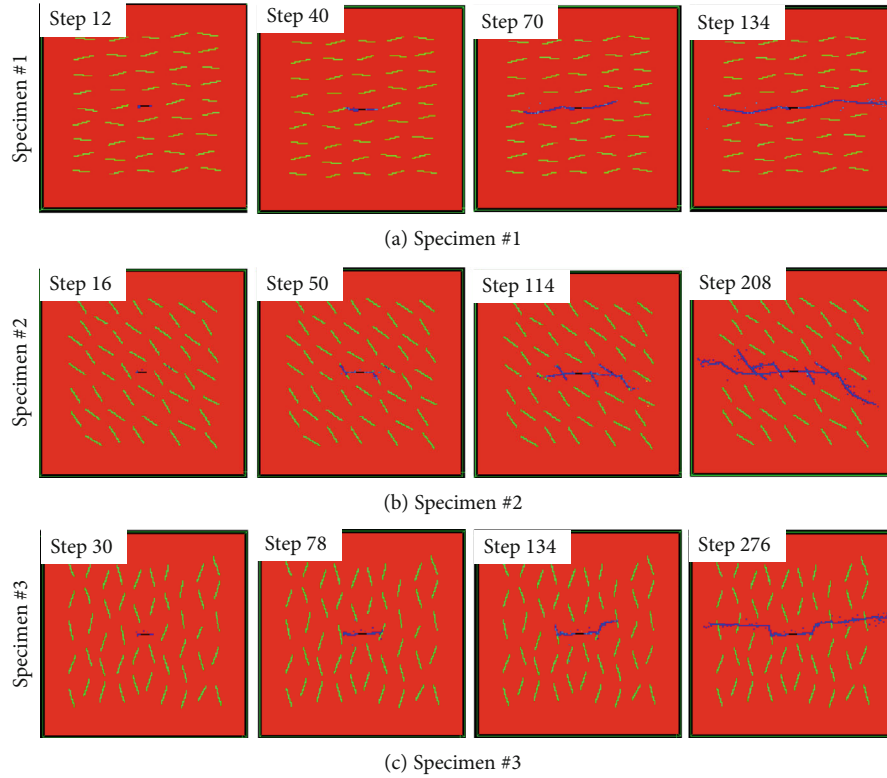


FIGURE 6: Propagation patterns of HF in different stages of each numerical model.

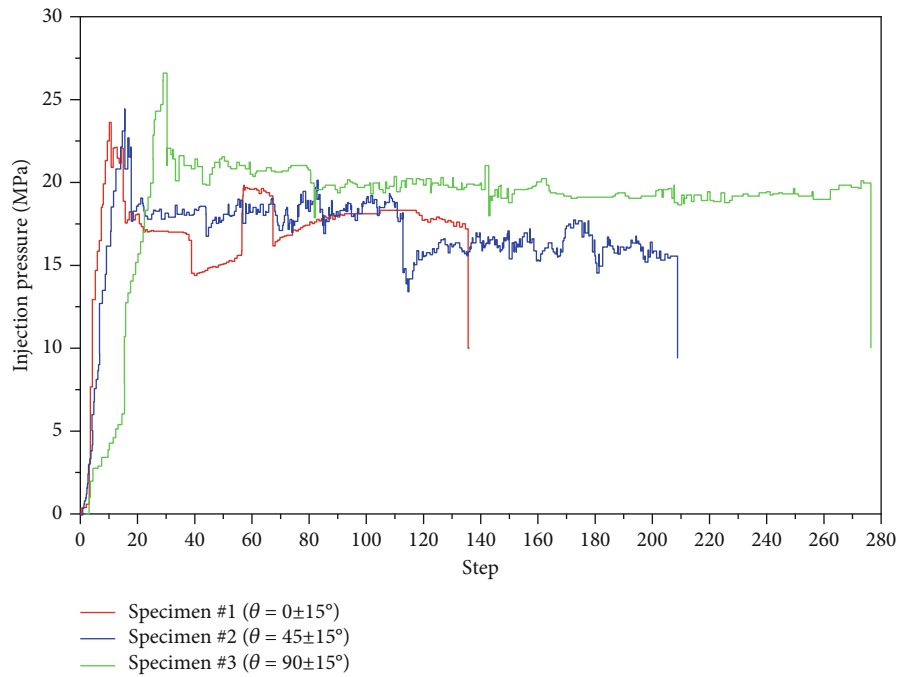


FIGURE 7: Injection pressure curves of different numerical models.

viscosity of the fracturing fluid is 60 mPa-s, and the tensile strength of CCF is set to 1 MPa. The in-situ stress is set as  $\sigma_H = 35$  MPa,  $\sigma_h = 30$  MPa. Although the numerical simulation includes six groups, we only compare the four groups with a significant difference to facilitate the analysis. These

four groups of simulation results can represent the trend of all simulation.

As shown in Figure 9, when the azimuth angle  $\theta$  is less than  $30^\circ$ , the HF mostly propagate along the CCFs with only a small deflection. When  $\theta$  is small, the normal stress acting

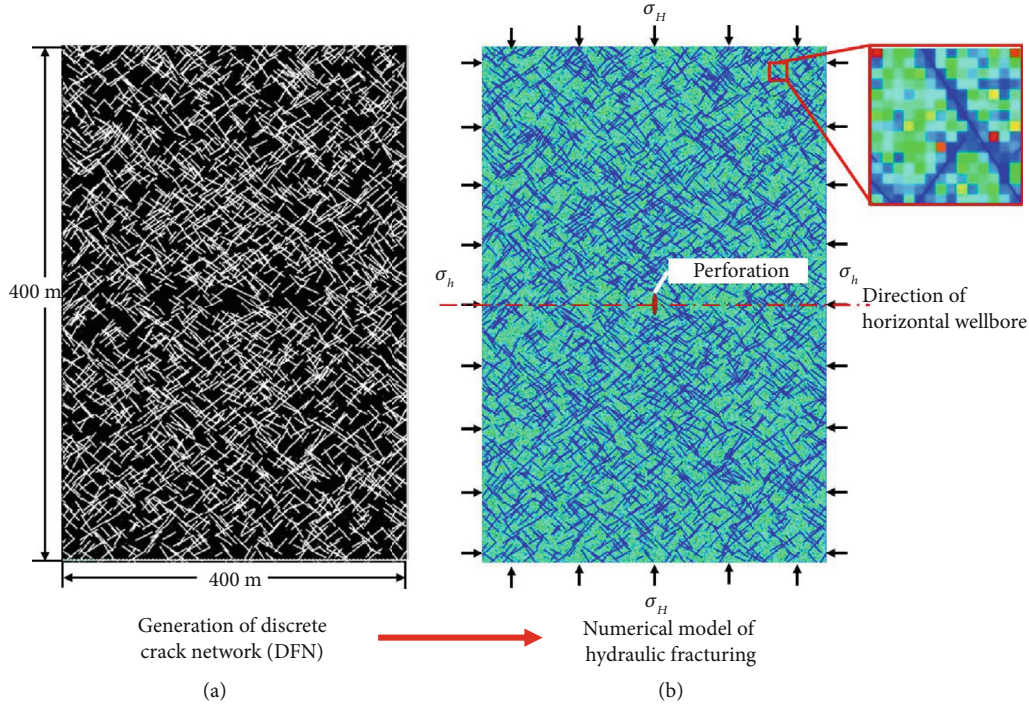


FIGURE 8: Two-dimensional numerical model of hydraulic fracturing in the fractured tight sandstone formation.

on the CCFs is small. After the HF intersects with the CCFs, the CCFs are easy to open. Under the induction of opened CCFs, the HF propagates along the direction of the fracture development direction. When the azimuth angle  $\theta$  is  $\pm 45^\circ$ , the deflection amplitude of HF is larger when it encounters the CCFs. Besides, there are some branching fractures in the HF's propagation path, and the fracture geometry after fracturing is complex. When the azimuth angle  $\theta$  is  $\pm 60^\circ$ , the HF deflect sharply along the CCFs. There are many kinds of compound fracture propagation patterns, such as penetration, branching, deflection, and offsetting. When the azimuth angle  $\theta$  is  $\pm 60^\circ$ , the fracture geometry after hydraulic fracturing is the most complex. When azimuth angle  $\theta$  is  $\pm 75^\circ$ , the deflection amplitude of the HF along the CCFs becomes smaller. The propagation pattern of HF mainly penetrates or repenetrates the CCFs after a short extension distance along the CCF accompanied by a small number of branching fractures.

Figure 10 shows the injection pressure-step curves of numerical models. The initiation pressure of HF tends to increase gradually with the increase of the azimuth angle  $\theta$ . The smaller the  $\theta$  is, the easier the HF will deflect along the CCFs, and the lower the required propagation pressure is. On the contrary, the larger the  $\theta$  is, the easier the HF will cross through the CCFs and propagate in the rock matrix.

In Figure 11, the total equivalent hydraulic fracture length (EL) and propagation area of complex fracture network (PA) increase with the increase of the azimuth angle  $\theta$  from  $15^\circ$  to  $60^\circ$ . When  $\theta$  exceeds  $60^\circ$ , the EL and PA decrease again. When  $\theta$  ranges from  $45^\circ$  to  $60^\circ$ , the normal stress acting on the CCF is small and the shear stress along the CCF is large. The CCFs have complex fracture behaviors such as dilation, opening, and shear sliding, and the HF has a variety

of propagation patterns such as penetration, deflection, and offsetting. Therefore, when  $\theta$  ranges from  $45^\circ$  to  $60^\circ$ , both the EL and PA can meet the requirements of increasing oil and gas production.

**4.2. Influence of CCFs Tensile Strength.** The establishment of DFN based on the parameters in Table 3. Under the condition that other parameters remain unchanged, the tensile strength of CCFs is set to 0.1 MPa, 0.4 MPa, 0.7 MPa, 1.0 MPa, 1.3 MPa, and 1.6 MPa, respectively.

Figure 12 shows a comparison of four representative fracture propagation patterns. The HF network's complexity after hydraulic fracturing decreases with the increase of tensile strength of CCFs from 0.1 MPa to 1.6 MPa. When the strength of CCFs is small, CCF is easier to be activated during the hydraulic fracturing process, which promotes the formation of deflecting or branching fractures. When the tensile strength of CCFs is large, the stress produced at the tip of HF is not enough to drive the activation and opening of CCFs. In this case, the possibility and distance of HF deflection are small, and the complexity of the fracture network after hydraulic fracturing is low.

In Figure 13, the tensile strength of CCFs has little effect on HF's initiation pressure when the azimuth angle of CCFs is unchanged. The initiation pressure ranges from 36.3~37.9 MPa. However, the CCFs' tensile strength has an impact on HF's propagation pressure. The propagation pressure increases with the increase of CCFs' tensile strength. In naturally fractured reservoirs, the HF's mainly deflect and propagate along the CCFs or branch at the intersection point. Thus, the greater the tensile strength of the CCFs, the greater the resistance to fracture propagation that needs to be overcome.



TABLE 3: The geometric parameters of the DFN model.

Group	Density	Length of CCF (m)			Azimuth angle (°)		
		Average value	Standard deviation	Distribution type	Average value	Standard deviation	Distribution type
# a	0.005	20	10	Normal distribution	45	7	Logarithmic normal distribution
# b	0.005	20	10		-45	7	

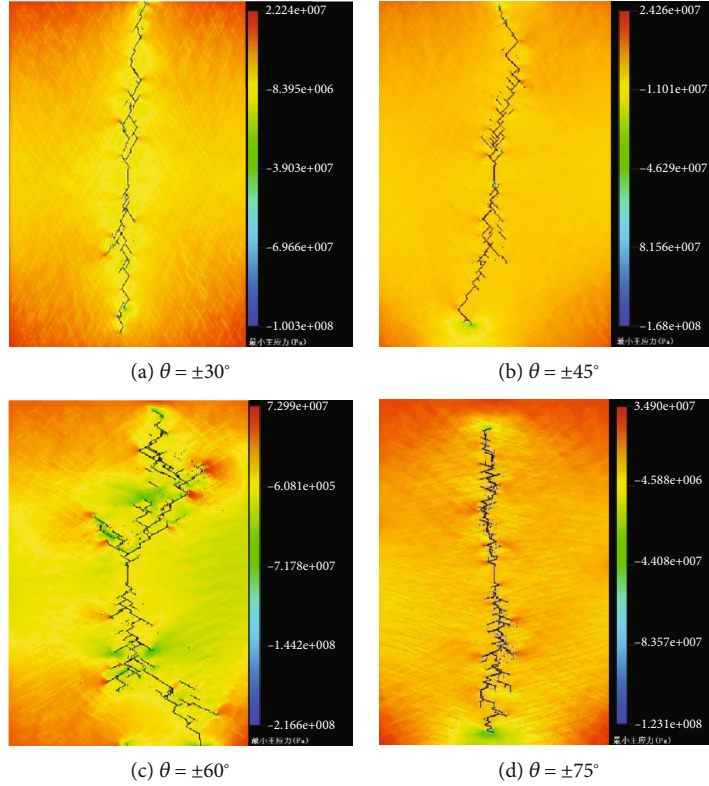


FIGURE 9: The propagation patterns of HF under different fracture distribution directions.

In Figure 14, the EL and PA have a negative correlation with the tensile strength of CCFs. Under the same stress condition, the resistance of CCFs open and shear slip decreases as the tensile strength of CCFs decreases. The smaller the tensile strength of CCFs is, the greater the activation degree of CCFs is, and HF are easier to communicate with more branching propagation fractures.

**4.3. Influence of In-Situ Stress Anisotropy.** The establishment of DFN based on the parameters in Table 3. The numerical model sets the minimum horizontal principal stress ( $\sigma_h$ ) to 30 MPa and changes the maximum horizontal principal stress ( $\sigma_H$ ) to adjust the anisotropy of in-situ stress. The horizontal in-situ stress difference of the model is as follows: 0 MPa, 1.5 MPa, 3.0 MPa, 4.5 MPa, 6.0 MPa, and 7.5 MPa. Other parameters of the numerical model remain unchanged.

Figure 15 shows a comparison of four representative fracture propagation patterns. The horizontal in-situ stress difference ( $\Delta\sigma$ ) has a significant effect on HF's propagation

patterns. When  $\Delta\sigma$  is 0 MPa, the in-situ stress has no control over the fracture propagation direction. The HF mainly propagate along the CCFs after the intersection, and the overall propagation direction of HF is consistent with the distribution direction of CCFs. At this time, although the fracture morphology is complicated, the propagation length of HF is limited. When  $\Delta\sigma$  is 1.5 MPa, the control of in-situ stress anisotropy on the propagation direction of HF increases, but most HF still propagate along the CCFs with a large deflection angle. When  $\Delta\sigma$  is between 3 MPa and 6 MPa, the HF and the CCF have obvious interaction behaviors, and the geometry of fracturing fractures is complex and the propagation length is long. When  $\Delta\sigma$  exceeds 6 MPa, in-situ stress has a strong control of fracture propagation. The deflection behavior of HF decreases while the penetration and offsetting behaviors increase. Although HF has a good propagation length, the complexity of fracture morphology decreases after hydraulic fracturing.

In Figure 16, the initiation pressure of HF has a slight increase from 37.7 MPa to 38.6 MPa with the increase of  $\Delta\sigma$ .



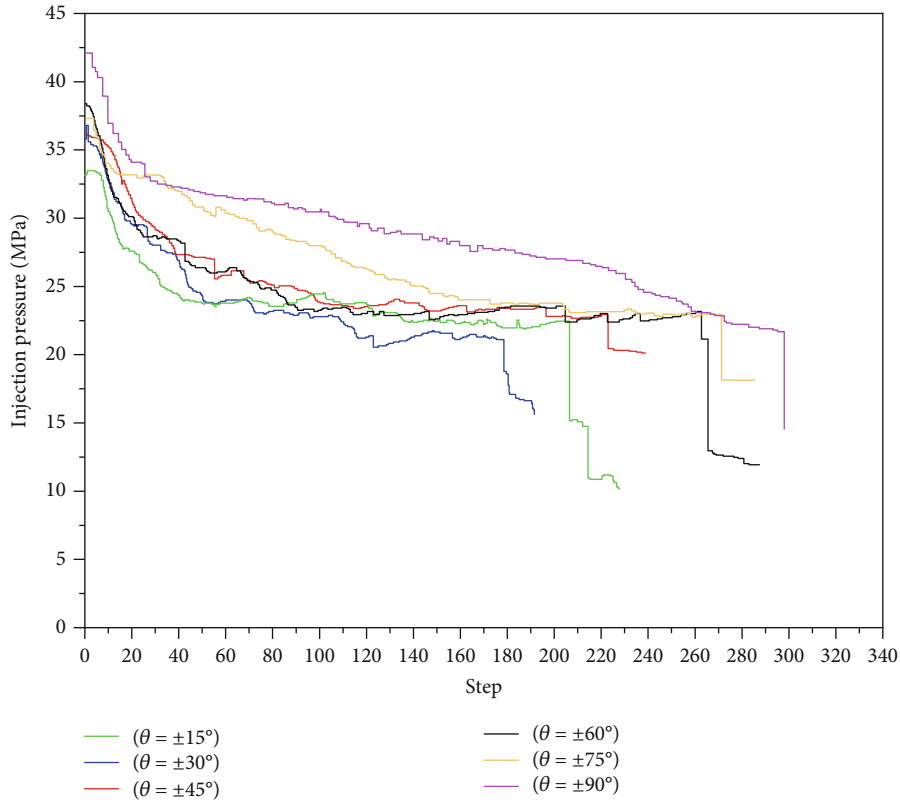


FIGURE 10: Injection pressure-step curves under different CCFs distribution direction.

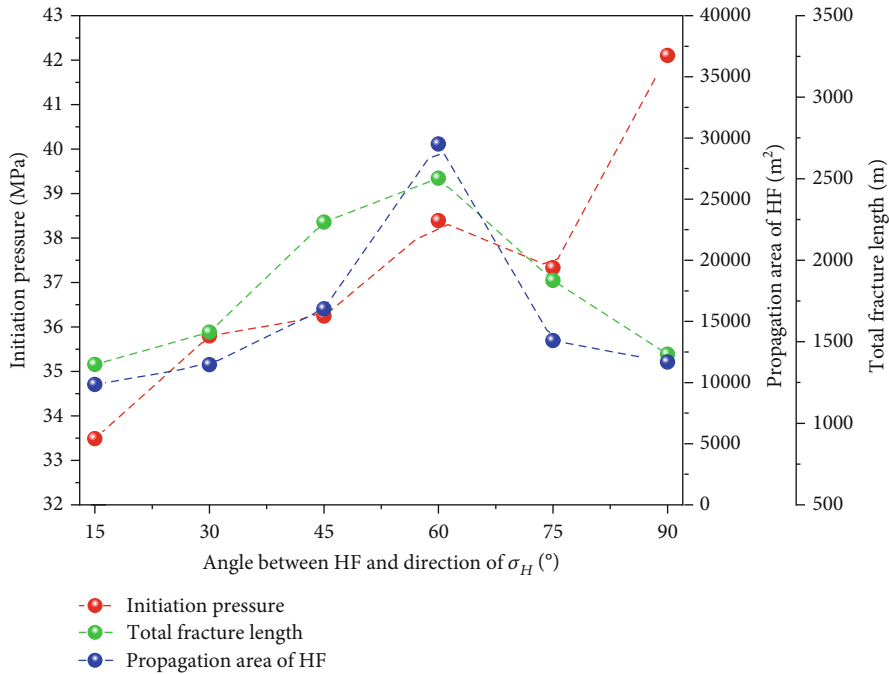


FIGURE 11: Total equivalent hydraulic fracture length and propagation area of the complex fracture network.

The initiation of HF mainly overcomes the sum of horizontal minimum principal stress and rock tensile strength. In this group of simulations,  $\sigma_h$  is a fixed value, so the variation of initiation pressure is very small. However, the propagation pres-

sure of HF increases with the increase of  $\Delta\sigma$ . The increase of  $\sigma_H$  will increase the normal stress acting on the surface of the CCF, and the resistance to be overcome when the HF propagates along CCFs will increase.

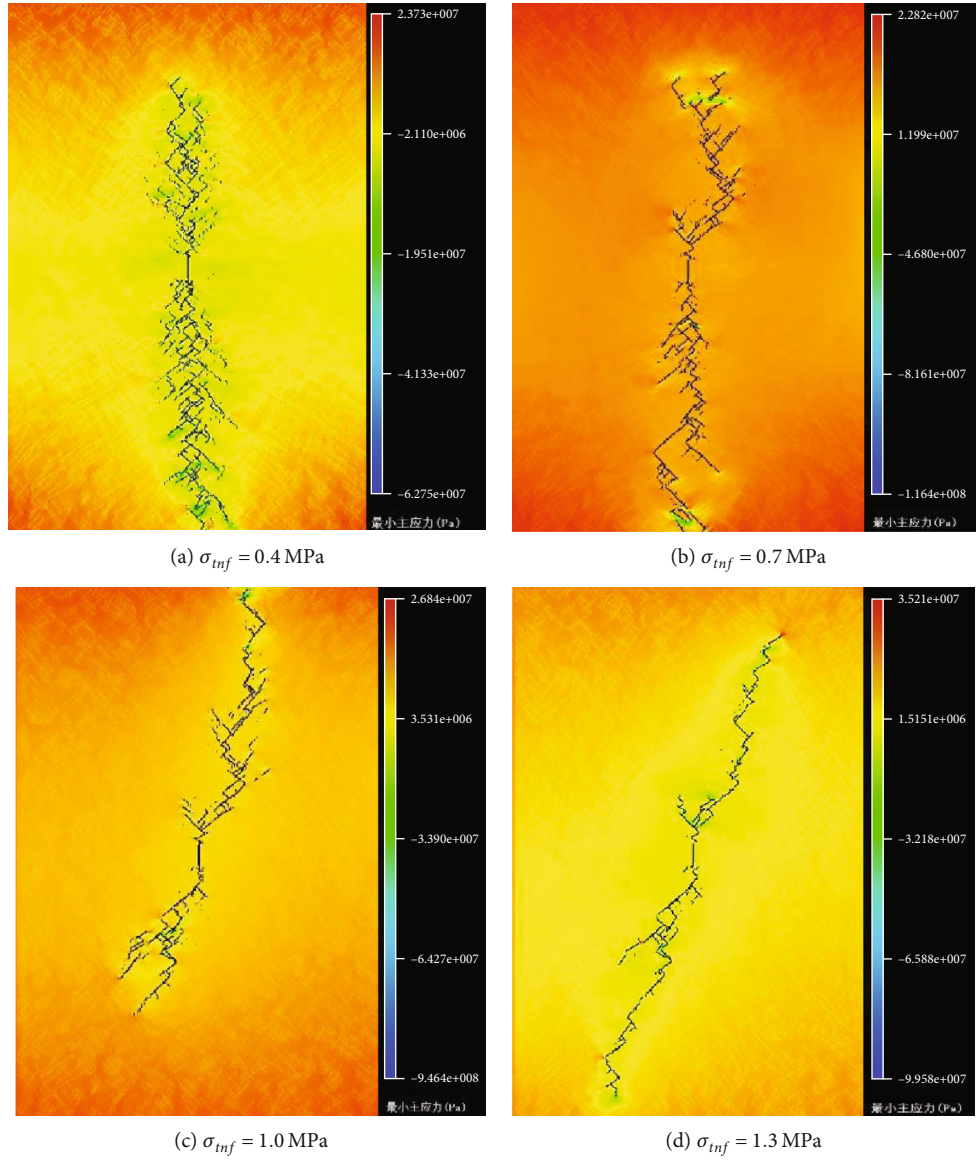


FIGURE 12: Hydraulic fracture propagation patterns under different tensile strength of CCFs.

In Figure 17, both the EL and PA increase first and then decrease as  $\Delta\sigma$  increases from 0 MPa to 7.5 MPa. The EL reaches the maximum when  $\Delta\sigma$  is 4.5 MPa, while the PA reaches the maximum when  $\Delta\sigma$  is 3 MPa. This shows that when  $\Delta\sigma$  is less than 3 MPa, the propagation of HF is dominated by the direction of CCFs, which cannot guarantee the effective propagation length. However, when  $\Delta\sigma$  exceeds 6 MPa, the propagation of HF is dominated by in-situ stress, and the degree of HF deflecting and branching is low.

**4.4. Influence of Injection Rate.** The establishment of DFN based on the parameters in Table 3. The injection rate of fracturing fluid is set to 4 m<sup>3</sup>/min, 6 m<sup>3</sup>/min, 8 m<sup>3</sup>/min, 10 m<sup>3</sup>/min, 12 m<sup>3</sup>/min, and 14 m<sup>3</sup>/min, respectively. The in-situ stress is set as  $\sigma_H = 35$  MPa,  $\sigma_h = 30$  MPa. Other parameters of the numerical model remain unchanged.

In Figure 18, when the injection rate is 4~6 m<sup>3</sup>/min, the HF interacts with CCFs and forms branching and deflecting propagation patterns, but the degree of branching and deflecting of the fracture is small. When the injection rate increases to 8 m<sup>3</sup>/min, the interaction between HFs and CCFs is strengthened, and HFs' geometry morphology is more complicated. On the whole, the hydraulic fracture network after fracturing becomes more complicated with the increase of the injection rate of fracturing fluid.

In Figure 19, the initiation pressure of HF increases from 39.7 MPa to 44.3 MPa with the increase of the injection rate. Besides, the higher the injection rate, the faster the pressure rise rate in perforation and fracture initiation rate. The HF's propagation pressure is positively correlated with the injection rate, while the hydraulic fracturing duration is negatively correlated with the injection rate.

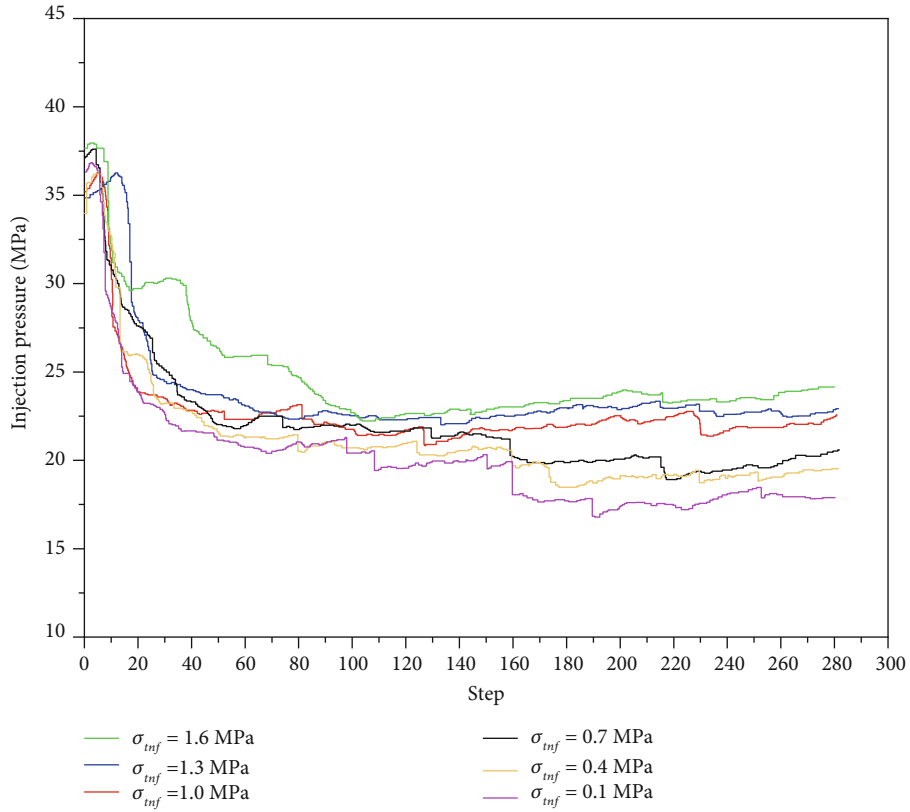


FIGURE 13: Injection pressure-step curves under different tensile strength of CCFs.

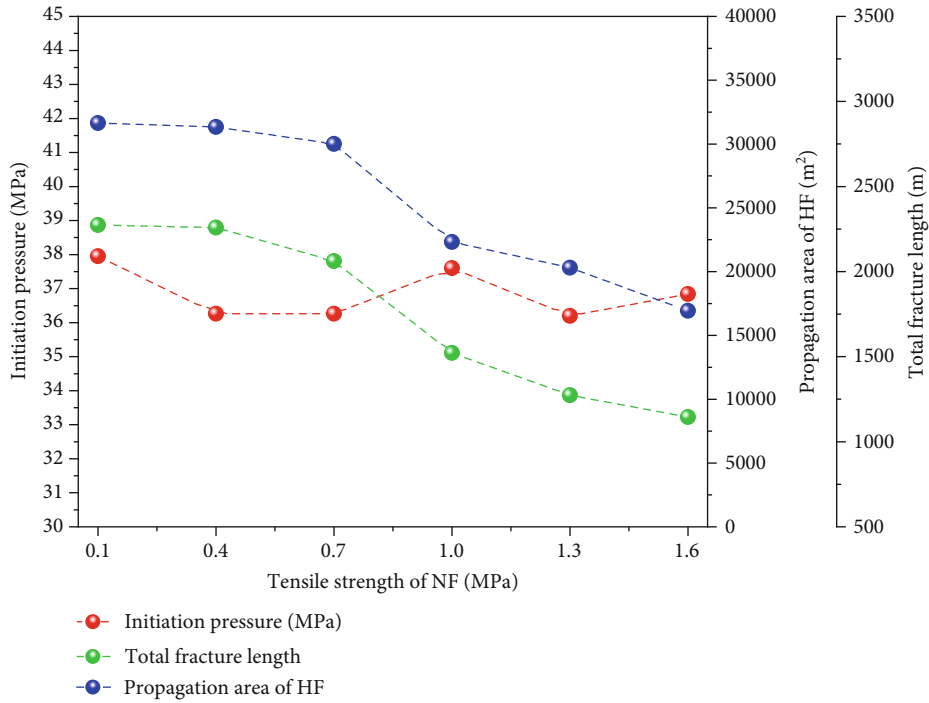


FIGURE 14: Total equivalent hydraulic fracture length and propagation area of the complex fracture network.

In Figure 20, the EL and PA gradually increase with the increase in the injection rate. However, when the injection rate is increased from 12 m<sup>3</sup>/min to 14 m<sup>3</sup>/min, the increase rate of

the EL and PA decreases. It shows that an appropriate increase in the injection rate of fracturing fluid is conducive to improving the hydraulic fracture network's complexity and sweep

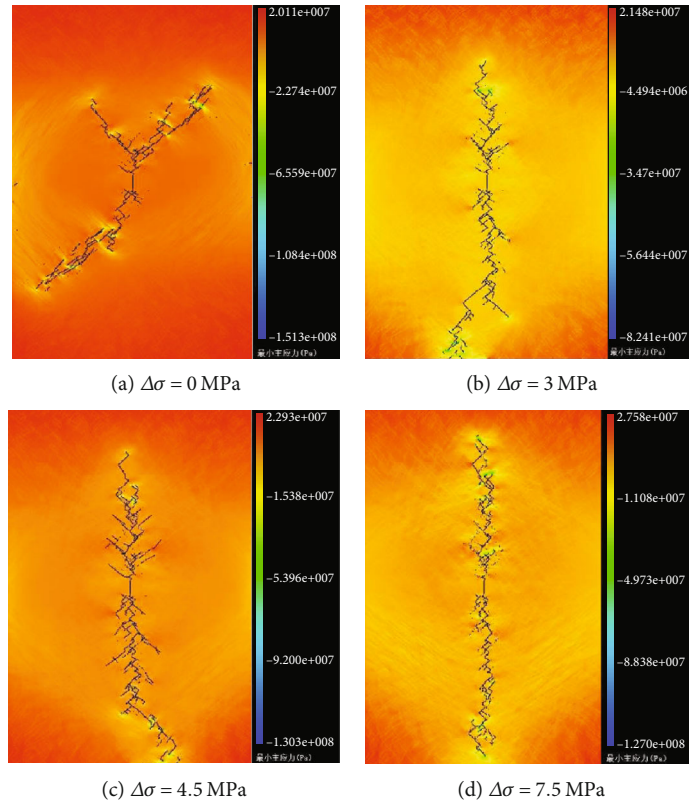


FIGURE 15: Hydraulic fracture propagation patterns under different in-situ stress anisotropy.

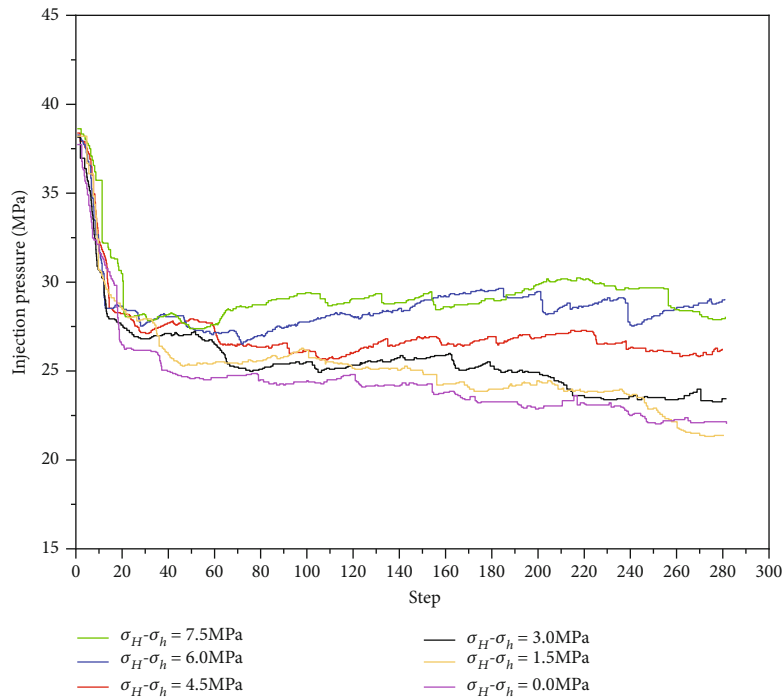


FIGURE 16: Injection pressure-step curves under different in-situ stress anisotropy.

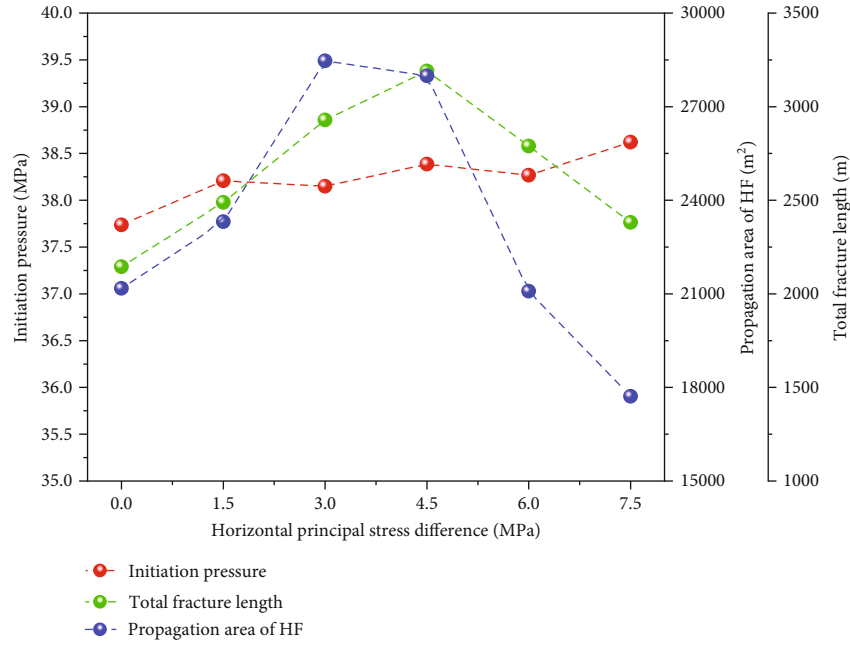


FIGURE 17: Total equivalent hydraulic fracture length and propagation area of the complex fracture network.

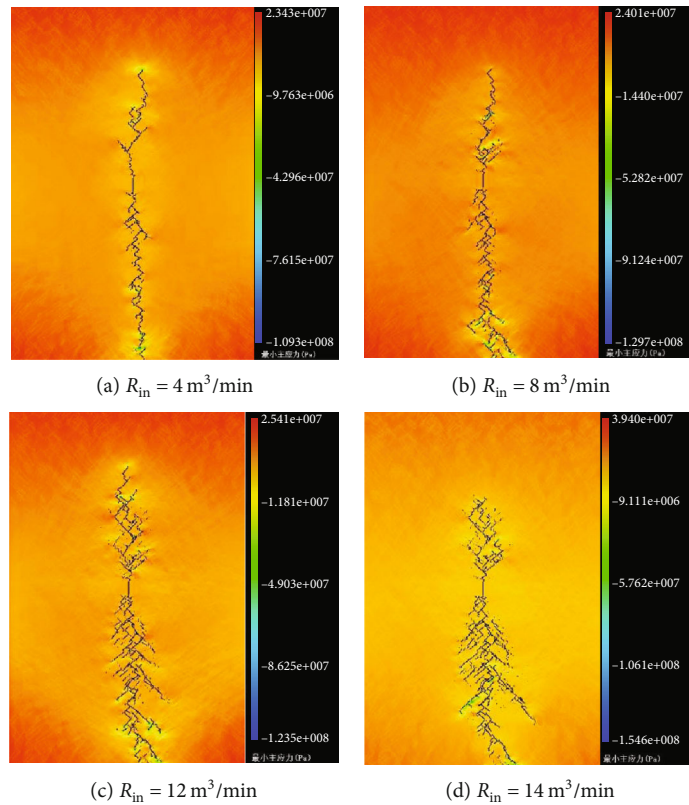


FIGURE 18: Hydraulic fracture propagation patterns under different injection rates.

area. Still, when the injection rate exceeds  $12 \text{ m}^3/\text{min}$ , the improvement degree of fracturing modification effect by the increase in the injection rate is no longer noticeable.

4.5. *Influence of Fracturing Fluid Viscosity.* The establishment of DFN based on the parameters in Table 3. The viscosity of fracturing fluid is set to 20 mPa·s, 40 mPa·s, 60 mPa·s,



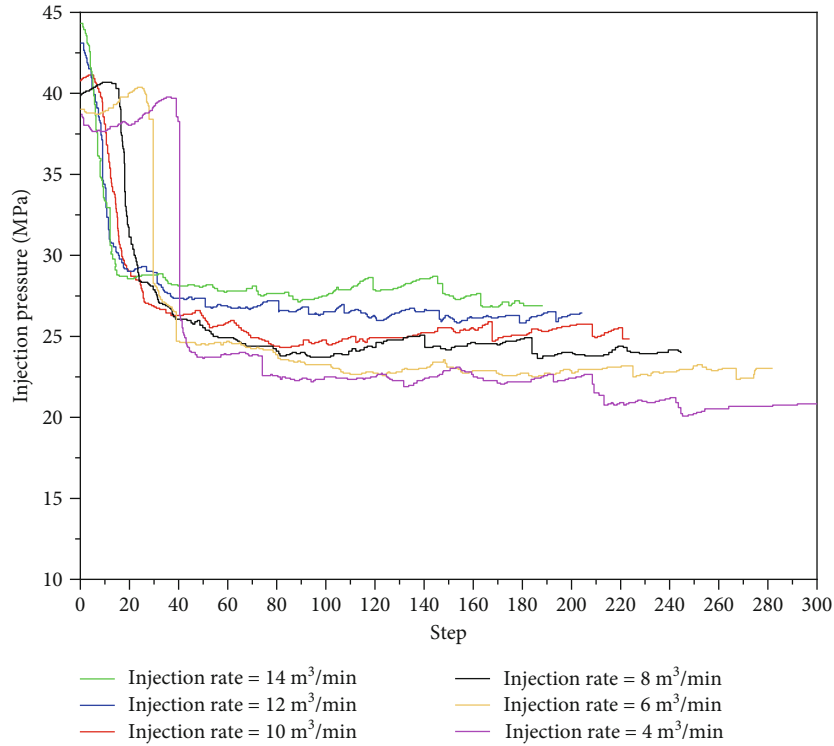


FIGURE 19: Injection pressure-step curves under different injection rate.

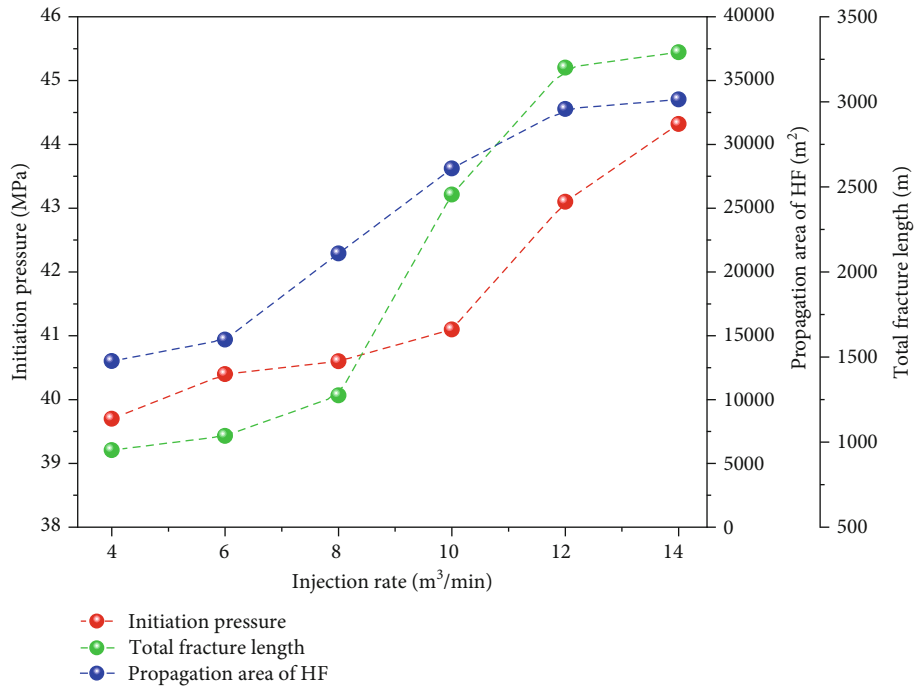


FIGURE 20: Total equivalent hydraulic fracture length and propagation area of the complex fracture network.

80 mPa-s, 100 mPa-s, 120 mPa-s, respectively. The in-situ stress is set as  $\sigma_H = 35$  MPa,  $\sigma_h = 30$  MPa. Other parameters of the numerical model remain unchanged.

In Figure 21, when the fluid viscosity is 20 mPa-s and 40 mPa-s, the HF's propagation pattern is intricate, and the crisscrossing network fractures are formed in the model.

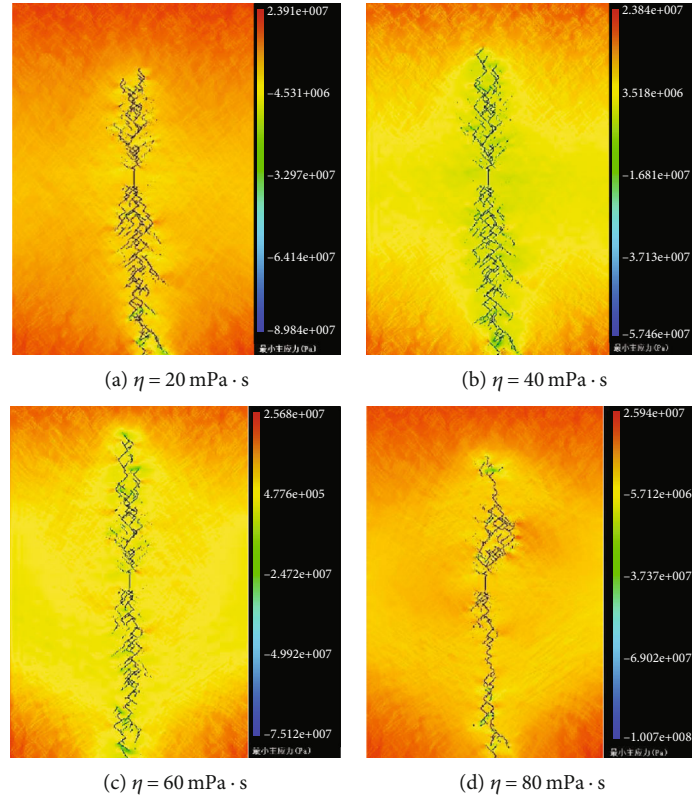


FIGURE 21: Hydraulic fracture propagation patterns under different fracturing fluid viscosity.

But when the fluid viscosity exceeds 60 mPa·s, the complexity of HFs gradually decreases with the continuous increase of fluid viscosity.

In Figure 22, the initiation pressure of HF gradually increases from 36.15 MPa to 40.05 MPa with the increase of fluid viscosity. The higher the fluid viscosity is, the faster the initiation speed of HF is. There is a good positive correlation between fracture propagation pressure and fracturing fluid viscosity. When the fracture is stably extending, the high viscosity fracturing fluid will encounter greater resistance when flowing in the fracture, and larger injection pressure is required to maintain the propagation of the HF.

In Figure 23, both the EL and PA increase when the fluid viscosity increases from 20 mPa·s to 40 mPa·s. But when the fluid viscosity exceeds 60 mPa·s, the EL and PA gradually decrease after hydraulic fracturing. This shows that in the naturally fractured tight oil reservoir, appropriately increasing viscosity can reduce the filtration loss of fracturing fluid and promote fracture propagation. However, when the viscosity is too high, the resistance of fracturing fluid in the fracture is too large, which limits the fracture propagation and eventually leads to the complex fracture network only form in a limited range around the perforation.

## 5. Conclusions

In this paper, a new laboratory fracturing experimental model is designed, which not only has mechanical properties

closer to natural tight sandstone but also contains several groups of closed cementing preexisting fractures. Based on exploring the influence of fracture network direction on hydraulic fracture propagation through hydraulic fracturing experiments, a field-scaled hydraulic fracturing numerical model of naturally fractured tight sandstone formation is established by combining FSD coupling model and Monte-Carlo simulation method. The effects of natural fracture distribution direction, natural fracture tensile strength, in-situ stress anisotropy, fracturing fluid injection rate, and fracturing fluid viscosity on the propagation of complex fracture networks are studied by this numerical model. It can be concluded as follows.

- (1) The experiment results show that when  $\theta$  is  $45^\circ \pm 15^\circ$ ; the HF has two kinds of propagation behaviors when interacting with CCFs: penetration and deflection, which leads to the most complicated HF geometry. The numerical simulation results show that when  $\theta$  ranges from  $45^\circ$  to  $60^\circ$ , the CCFs on the propagation path of HF include a variety of complex fracture behaviors such as dilation, opening, and shear sliding. This makes the HF appear in many propagation patterns such as penetration, deflection, branching, and offsetting. The numerical simulation results are in good agreement with the experimental results
- (2) The tensile strength of CCFs has a significant influence on HF's propagation patterns. As the decrease

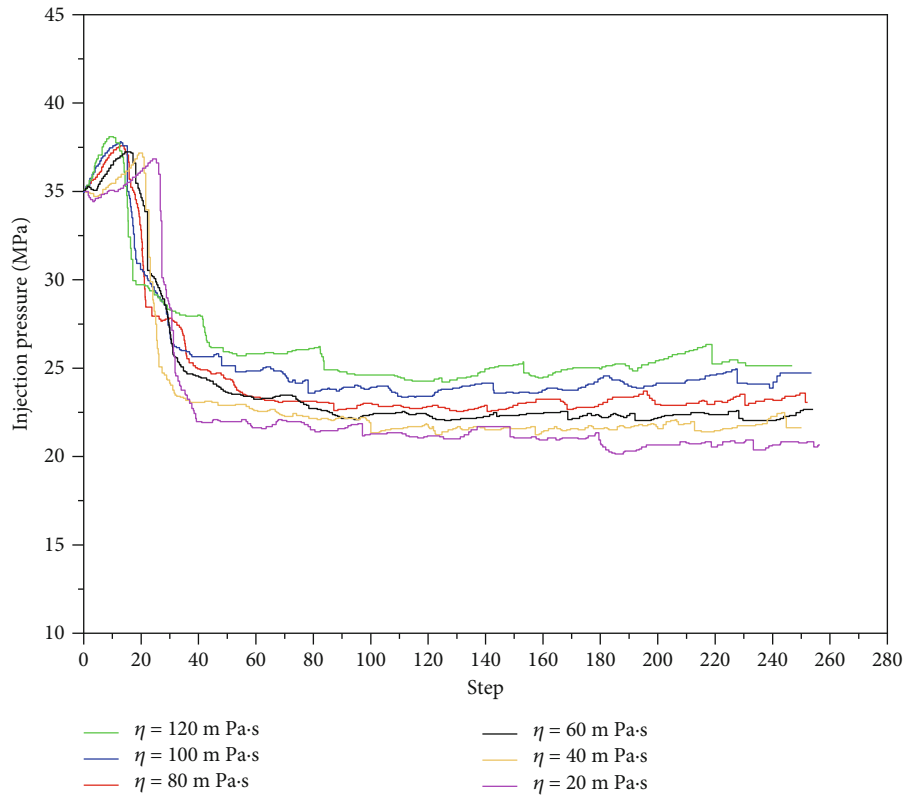


FIGURE 22: Injection pressure-step curves under different fracturing fluid viscosity.

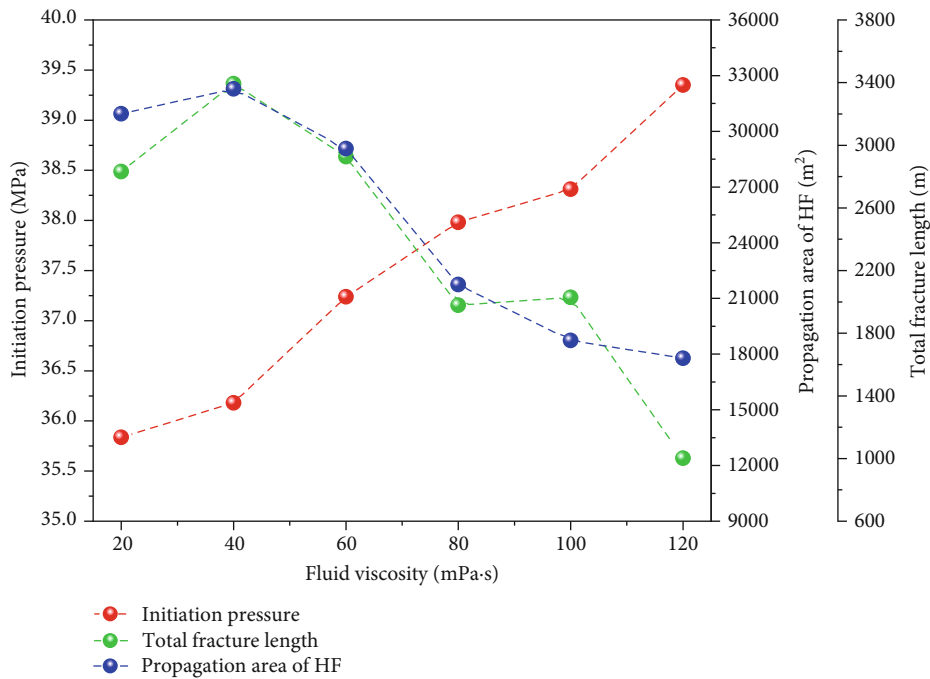


FIGURE 23: Total equivalent hydraulic fracture length and propagation area of the complex fracture network.

of CCFs' tensile strength, the number of CCFs connected by HFs increases, and the deflection amplitude of HFs increases

(3) When the horizontal in-situ stress difference is less than 3 MPa, the propagation behavior of HF is dominated by the distribution direction of CCFs, and the

effective propagation length of hydraulic fracture HF is limited. When the horizontal stress difference exceeds 6 MPa, the HF propagation is dominated by in-situ stress anisotropy, and the complexity and spread area of HFs are limited. Therefore, when the horizontal stress difference of tight sandstone formation is within the range of 3~6 MPa, the propagation length and spread area of the HF network can be guaranteed simultaneously

- (4) The increase of the injection rate of fracturing fluid is helpful to increase the complexity and spread range of HF network, but the improvement degree of fracturing modification effect by increasing the injection rate is no longer obvious when it exceeds 12 m<sup>3</sup>/min
- (5) An appropriate increase in the viscosity of fracturing fluid can reduce the filtration loss and promote the expansion of the HF. However, when the fluid viscosity is too high, the resistance of fracturing fluid in the fracture is too high, which will lead to the complex fracture network only appearing in a limited range around the perforation

## Nomenclature

HF:	Hydraulic fracture
NF:	Natural fracture
CCF:	Closed cemented fracture
FSD:	Flow-stress-damage coupling model
DFN:	Discrete fracture network
$\theta$ :	The angle between horizontal maximum principal stress and preexisting fractures
$\Delta\sigma$ :	Horizontal in-situ stress difference
EL:	Total equivalent hydraulic fracture length
PA:	Propagation area of the complex fracture network
$K$ :	Permeability coefficient
$D$ :	Damage variable
$\xi$ :	Permeability damage factor
$\varepsilon_{t0}$ :	Elastic ultimate strain
$\varepsilon_{t1}$ :	Ultimate tensile strain
$\sigma_{t0}$ :	Tensile failure strength
$\sigma_{c0}$ :	Compressive failure strength
$\sigma_{rt}$ :	Residual tensile strength of the element.

## Data Availability

The data used to support the findings of this study are available from the corresponding author upon request.

## Conflicts of Interest

The authors declared that they have no conflicts of interest to this work.

## Acknowledgments

The research was supported by the Open Project of Key Laboratory of Enhancing Oil Recovery (Northeast Petroleum University), the Ministry of Education, the research start pro-

ject of Northeast Petroleum University (NO. 1305021857), the Youth Academic Talent Training Project of Northeast Petroleum University (NO. 15041260501), and the study on near-wellbore fracture propagation of horizontal well directional fracturing in unconventional reservoirs (F2020187).

## References

- [1] Y. Li, D. Jia, Z. Rui, J. Peng, C. Fu, and J. Zhang, "Evaluation method of rock brittleness based on statistical constitutive relations for rock damage," *Journal of Petroleum Science and Engineering*, vol. 153, pp. 123–132, 2017.
- [2] G. Jiang and W. Cheng, "Hydraulic fracture deflection at bedding plane due to the non-orthogonal propagation and the dissimilar material properties," *Arabian Journal for Science and Engineering*, vol. 43, no. 11, pp. 6535–6540, 2018.
- [3] Y. Li, S. Yang, W. Zhao, W. Li, and J. Zhang, "Experimental of hydraulic fracture propagation using fixed-point multistage fracturing in a vertical well in tight sandstone reservoir," *Journal of Petroleum Science and Engineering*, vol. 171, pp. 704–713, 2018.
- [4] W. Xu, J. Zhao, S. S. Rahman, Y. Li, and Y. Yuan, "A comprehensive model of a hydraulic fracture interacting with a natural fracture: analytical and numerical solution," *Rock Mechanics and Rock Engineering*, vol. 52, no. 4, pp. 1095–1113, 2019.
- [5] D. Chuprakov, O. Melchaeva, and R. Prioul, "Injection-sensitive mechanics of hydraulic fracture interaction with discontinuities," *Rock Mechanics and Rock Engineering*, vol. 47, no. 5, pp. 1625–1640, 2014.
- [6] P. L. P. Wasantha and H. Konietzky, "Fault reactivation and reservoir modification during hydraulic stimulation of naturally-fractured reservoirs," *Journal of Natural Gas Science and Engineering*, vol. 34, pp. 908–916, 2016.
- [7] Y. Li, M. Long, L. Zuo, W. Li, and W. Zhao, "Brittleness evaluation of coal based on statistical damage and energy evolution theory," *Journal of Petroleum Science and Engineering*, vol. 172, pp. 753–763, 2019.
- [8] Y. Li, M. Long, J. Tang, C. H. Mian, and F. U. Xiaofei, "A hydraulic fracture height mathematical model considering the influence of plastic region at fracture tip," *Petroleum Exploration and Development*, vol. 47, no. 1, pp. 184–195, 2020.
- [9] B. Hou, M. Chen, W. Cheng, and C. Diao, "Investigation of hydraulic fracture networks in shale gas reservoirs with random fractures," *Arabian Journal for Science and Engineering*, vol. 41, no. 7, pp. 2681–2691, 2016.
- [10] B. Hou, R. Zhang, Y. Zeng, W. Fu, Y. Muhadasi, and M. Chen, "Analysis of hydraulic fracture initiation and propagation in deep shale formation with high horizontal stress difference," *Journal of Petroleum Science and Engineering*, vol. 170, pp. 231–243, 2018.
- [11] Z. Yushi, Z. Shicheng, Z. Tong, Z. Xiang, and G. Tiankui, "Experimental investigation into hydraulic fracture network propagation in gas shales using CT scanning technology," *Rock Mechanics and Rock Engineering*, vol. 49, no. 1, pp. 33–45, 2016.
- [12] J. Xie, W. Cheng, R. Wang, G. Jiang, D. Sun, and J. Sun, "Experiments and analysis on the influence of perforation mode on hydraulic fracture geometry in shale formation," *Journal of Petroleum Science and Engineering*, vol. 168, pp. 133–147, 2018.

- [13] P. Tan, Y. Jin, K. Han et al., "Analysis of hydraulic fracture initiation and vertical propagation behavior in laminated shale formation," *Fuel*, vol. 206, pp. 482–493, 2017.
- [14] Y. Zou, N. Li, X. Ma, S. Zhang, and S. Li, "Experimental study on the growth behavior of supercritical  $\text{CO}_2$ -induced fractures in a layered tight sandstone formation," *Journal of Natural Gas Science and Engineering*, vol. 49, pp. 145–156, 2018.
- [15] J. E. Olson, B. Bahorich, and J. Holder, "Examining hydraulic fracture: natural fracture interaction in hydrostone block experiments," in *SPE Hydraulic Fracturing Technology Conference*, The Woodlands, Texas, USA, 2012.
- [16] B. Bahorich, J. E. Olson, and J. Holder, "Examining the effect of cemented natural fractures on hydraulic fracture propagation in hydrostone block experiments," in *SPE Annual Technical Conference and Exhibition*, San Antonio, Texas, USA, 2012.
- [17] A. N. Dehghan, K. Goshtasbi, K. Ahangari, and Y. Jin, "The effect of natural fracture dip and strike on hydraulic fracture propagation," *International Journal of Rock Mechanics and Mining Sciences*, vol. 75, pp. 210–215, 2015.
- [18] W. Cheng, Y. Jin, Q. Lin et al., "Experimental investigation about influence of pre-existing fracture on hydraulic fracture propagation under tri-axial stresses," *Geotechnical and Geological Engineering*, vol. 33, no. 3, pp. 467–473, 2015.
- [19] L. Wan, M. Chen, and B. Hou, "Experimental investigation of the effect of natural fracture size on hydraulic fracture propagation in 3D," *Journal of Structural Geology*, vol. 116, pp. 1–11, 2018.
- [20] B. Zhang, J. Liu, S. G. Wang et al., "Impact of the distance between pre-existing fracture and wellbore on hydraulic fracture propagation," *Journal of Natural Gas Science and Engineering*, vol. 57, pp. 155–165, 2018.
- [21] T. Fan and G. Zhang, "Laboratory investigation of hydraulic fracture networks in formations with continuous orthogonal fractures," *Nature*, vol. 74, pp. 164–173, 2014.
- [22] Y. Wang and C. H. Li, "Investigation of the effect of cemented fractures on fracturing network propagation in model block with discrete orthogonal fractures," *Rock Mechanics and Rock Engineering*, vol. 50, no. 7, pp. 1851–1862, 2017.
- [23] E. M. Llanos, R. G. Jeffrey, R. Hillis, and X. Zhang, "Hydraulic fracture propagation through an orthogonal discontinuity: a laboratory, analytical and numerical study," *Rock Mechanics and Rock Engineering*, vol. 50, no. 8, pp. 2101–2118, 2017.
- [24] B. Huang and J. Liu, "Experimental investigation of the effect of bedding planes on hydraulic fracturing under true triaxial stress," *Rock Mechanics and Rock Engineering*, vol. 50, no. 10, pp. 2627–2643, 2017.
- [25] Z. Liu, S. Wang, H. Zhao et al., "Effect of random natural fractures on hydraulic fracture propagation geometry in fractured carbonate rocks," *Rock Mechanics and Rock Engineering*, vol. 51, no. 2, pp. 491–511, 2018.
- [26] Y. Wang, C. H. Li, Y. Z. Hu, and T. Q. Mao, "Laboratory investigation of hydraulic fracture propagation using real-time ultrasonic measurement in shale formations with random natural fractures," *Environmental Earth Sciences*, vol. 76, no. 22, article 768, 2017.
- [27] J. Guo, X. Zhao, H. Zhu, X. Zhang, and R. Pan, "Numerical simulation of interaction of hydraulic fracture and natural fracture based on the cohesive zone finite element method," *Journal of Natural Gas Science and Engineering*, vol. 25, pp. 180–188, 2015.
- [28] F. Shi, X. Wang, C. Liu, H. Liu, and H. Wu, "An XFEM-based method with reduction technique for modeling hydraulic fracture propagation in formations containing frictional natural fractures," *Engineering Fracture Mechanics*, vol. 173, pp. 64–90, 2017.
- [29] M. Vahab, A. R. Khoei, and N. Khalili, "An X-FEM technique in modeling hydro-fracture interaction with naturally-cemented faults," *Engineering Fracture Mechanics*, vol. 212, pp. 269–290, 2019.
- [30] M. R. Hirmand, M. Vahab, K. D. Papoulia, and N. Khalili, "Robust simulation of dynamic fluid-driven fracture in naturally fractured impermeable media," *Computer Methods in Applied Mechanics and Engineering*, vol. 357, article 112574, 2019.
- [31] J. A. Rueda Cordero, E. C. Mejia Sanchez, D. Roehl, and L. C. Pereira, "Hydro-mechanical modeling of hydraulic fracture propagation and its interactions with frictional natural fractures," *Computers and Geotechnics*, vol. 111, pp. 290–300, 2019.
- [32] C. Liu, J. Zhang, H. Yu, J. Chen, D. T. Lu, and H. A. Wu, "New insights of natural fractures growth and stimulation optimization based on a three-dimensional cohesive zone model," *Journal of Natural Gas Science and Engineering*, vol. 76, article 103165, 2020.
- [33] H. Zheng, C. Pu, and C. Sun, "Study on the interaction between hydraulic fracture and natural fracture based on extended finite element method," *Engineering Fracture Mechanics*, vol. 230, article 106981, 2020.
- [34] H. Y. Wang, "Hydraulic fracture propagation in naturally fractured reservoirs: complex fracture or fracture networks," *Journal of Natural Gas Science and Engineering*, vol. 68, article 102911, 2019.
- [35] J. Zhou, L. Zhang, Z. Pan, and Z. Han, "Numerical studies of interactions between hydraulic and natural fractures by smooth joint model," *Journal of Natural Gas Science and Engineering*, vol. 46, pp. 592–602, 2017.
- [36] T. Wang, W. Hu, D. Elsworth et al., "The effect of natural fractures on hydraulic fracturing propagation in coal seams," *Journal of Petroleum Science and Engineering*, vol. 150, pp. 180–190, 2017.
- [37] J. S. Yoon, A. Zang, O. Stephansson, H. Hofmann, and G. Zimmermann, "Discrete element modelling of hydraulic fracture propagation and dynamic interaction with natural fractures in hard rock," *Procedia Engineering*, vol. 191, pp. 1023–1031, 2017.
- [38] L. Zhang, J. Zhou, A. Braun, and Z. Han, "Sensitivity analysis on the interaction between hydraulic and natural fractures based on an explicitly coupled hydro-geomechanical model in PFC2D," *Journal of Petroleum Science and Engineering*, vol. 167, pp. 638–653, 2018.
- [39] G. Amir, J. Taheri-Shakib, and M. A. S. Nik, "The distinct element method (DEM) and the extended finite element method (XFEM) application for analysis of interaction between hydraulic and natural fractures," *Nature*, vol. 171, pp. 422–430, 2018.
- [40] C. Tang, "Numerical simulation of progressive rock failure and associated seismicity," *International Journal of Rock Mechanics and Mining Sciences*, vol. 34, no. 2, pp. 249–261, 1997.
- [41] Z. Zhang, X. Li, W. Yuan, J. He, G. Li, and Y. Wu, "Numerical analysis on the optimization of hydraulic fracture networks," *Energies*, vol. 8, no. 10, pp. 12061–12079, 2015.



- [42] T. Yang, H. Y. Liu, and C. A. Tang, "Scale effect in macroscopic permeability of jointed rock mass using a coupled stress–damage–flow method," *Engineering Geology*, vol. 228, pp. 121–136, 2017.
- [43] L. Bu, S. Li, S. Shi, X. Xie, L. Li, and Z. Zhou, "Numerical investigation to influence of perforation angle on hydraulic fracturing process," *Geotechnical and Geological Engineering*, vol. 37, no. 3, pp. 1125–1133, 2019.
- [44] Y. Zhao, S. Cao, D. Shang et al., "Crack propagation and crack direction changes during the hydraulic fracturing of coalbed," *Computers and Geotechnics*, vol. 111, pp. 229–242, 2019.
- [45] L. Li, Q. Meng, S. Wang, G. Li, and C. Tang, "A numerical investigation of the hydraulic fracturing behaviour of conglomerate in glutenite formation," *Acta Geotechnica*, vol. 8, no. 6, pp. 597–618, 2013.
- [46] Y. Wang, X. Li, and B. Zhang, "Numerical modeling of variable fluid injection-rate modes on fracturing network evolution in naturally fractured formations," *Energies*, vol. 9, no. 6, p. 414, 2016.
- [47] X. Men, J. Li, and Z. Han, "Fracture propagation behavior of jointed rocks in hydraulic fracturing," *Advances in Materials Science and Engineering*, vol. 2018, 12 pages, 2018.
- [48] T. Li, L. Li, C. Tang et al., "A coupled hydraulic-mechanical-damage geotechnical model for simulation of fracture propagation in geological media during hydraulic fracturing," *Journal of Petroleum Science and Engineering*, vol. 173, pp. 1390–1416, 2019.

## Research Article

# A Comprehensive Model for Estimating Stimulated Reservoir Volume Based on Flowback Data in Shale Gas Reservoirs

Qi Chen,<sup>1</sup> Shaojun Wang,<sup>2</sup> Dan Zhu,<sup>3</sup> Guoxuan Ren,<sup>4</sup> Yuan Zhang,<sup>1</sup> and Jinghong Hu<sup>1</sup> 

<sup>1</sup>Beijing Key Laboratory of Unconventional Natural Gas Geology Evaluation and Development Engineering, China University of Geosciences, Beijing 100083, China

<sup>2</sup>Research Institute of Petroleum Exploration & Development, Beijing 100083, China

<sup>3</sup>The 5th Oil Production Plant, Changqing Oilfield, Xi'an 710021, China

<sup>4</sup>Leewen-Cobra International Energy (Beijing) Technology, Co., Ltd., 100084, China

Correspondence should be addressed to Jinghong Hu; [hjhwhat@163.com](mailto:hjhwhat@163.com)

Received 12 May 2020; Revised 24 July 2020; Accepted 28 August 2020; Published 9 September 2020

Academic Editor: Jinze Xu

Copyright © 2020 Qi Chen et al. This is an open access article distributed under the Creative Commons Attribution License, which permits unrestricted use, distribution, and reproduction in any medium, provided the original work is properly cited.

Stimulated reservoir volume (SRV) which is generated by horizontal drilling with multistage hydraulic fracturing governs the production in the shale gas reservoirs. Although microseismic data has been used to estimate the SRV, it is high-priced and sometimes overestimated. Additionally, the effect of stress sensitivity on SRV is not considered in abnormal overpressure areas. Thus, the objective of this work is to characterize subsurface fracture networks with stress sensitivity of permeability through the shale gas well production data of the early flowback stage. The flowback regions are first identified with the flowback data of two shale gas wells in South China. Then, we measured the permeability stress sensitivity of the core after fracturing, coupled to the dynamic relative permeability (DRP) calculation to obtain an accurate and simple DRP curve. After that, a comprehensive model is built considering dynamic two-phase relative permeability function and stress sensitivity. Finally, we compared the calculated results with the microseismic data. The results show that the proposed model could reasonably predict the SRV using the flowback data after fracturing. Additionally, compared with the microseismic data, the stress sensitivity should be included, especially in the abnormal overpressure block. It is believed that this mathematical model is accurate and useful. The work provides an efficient approach to estimate stimulated reservoir volume in the shale gas reservoirs.

## 1. Introduction

The development of shale gas has gained increasing attention with the decline of the production from conventional reservoirs [1, 2]. Due to the ultralow permeability of shales (from  $10^{-23}$  to  $10^{-17}$  m<sup>2</sup>) [3], a combination of horizontal drilling and multistage hydraulic fracturing has been widely used to SRV, which increases effective contact significantly to improve gas production from an individual well. Therefore, characterization of the stimulated reservoir volume appears to be of vital importance to manage and predict shale reservoir performance [4, 5].

While microseismic data has been extensively used to validate the stimulated reservoir volume, the SRV obtained directly from the microseismic data is generally overestimated. For example, SRV would include large unstimulated

void regions by the convexity assumption [6–9]. Also, implementation of microseismic techniques in a field sometimes is not cost-effective, which limits a wide application in fields. Therefore, using early production data after hydraulic fracturing together with early flowback data of hydraulic fluids is fast becoming a key instrument in evaluating SRV [10–13], namely, transient analysis of flowback data.

Two-phase flow appears to be a classic and representative flow behavior during the flowback process after hydraulic fracturing [2, 14]. For example, a large number of production data obtained from wells in the Horn River shale show that two-phase flow was observed for every single well during the flowback process after hydraulic fracturing [15, 16]. Clarkson [17] and Williams-Kovacs and Clarkson [18] also discovered two-phase flow within 48 hours of well opening and production in the Barnett and Marcellus shales.

Similarly, the two-phase flow stage occurs in the Silurian Longmaxi Formation shale gas wells in South China after the well opening [19]. And an even greater advance in the research of production data patterns is that after processing the production data from shale gas wells in the Horn River Basin, Adefidipe et al. [20, 21] and Xu et al. [22, 23] divided the production data into two stages as early gas production (EGP) and late gas production (LGP) for the “V” shape of the relationship between the gas-water ratio (GWR) and the cumulative gas production. They believed that the EGP stage was special and worth studying because the LGP stage already had a matrix gas supply.

To take advantage of the two-phase flow characteristics during the early gas production (EGP) stage, research studies have endeavored to estimate the SRV by coupling rock physics with various types of reservoir models. For example, Ezulike et al. [24–26] integrated an explicitly determined dynamic relative permeability (DRP) function in linear dual-porosity models to explore the two-phase flowback data. The function extends the single-phase water flow equation to gas-water two-phase flow which was calculated using cumulative production data of water and hydrocarbon compounds. Clarkson et al. [17, 27, 28] initially used an improved method for coalbed methane (CBM) flow to analyze multiphase flows. They assumed that the flow of gas and water through the generated fracture network was similar to the simultaneous flow of gas and water during long-term production from fractured coal reservoirs. Later, they proposed a large number of two-phase flow models based on this assumption to quantitatively calculate multiframe data, including tight oil and tight gas, to help analyze the flow characteristics of shale gas wells which are analogous to analyzing two-phase (gas and water) CBM production. And in the follow-up research work [29–32], they verified the analysis results from the above methods by integrating various techniques, including a modified material balance equation (MBE) applied to before-breakthrough (BBT) (before gas breakthrough) single-phase rate-transient analysis (RTA) and after-breakthrough (ABT) (after gas breakthrough) multiphase rate-transient analysis (RTA).

While the aforementioned models provide insights in calculating SRV through multiframe data quantitatively, challenges of applying these models to the field remain because the Langmuir volume needs to be increased in the calculation process, which will lead to some extent uncertainty and inaccuracy. To overcome the complexity of applying these models in fields, Clarkson et al. [17, 28] and Fu et al. [33] established a linear matching curve relation to describe the straight line relationship between rate-normalized pressure (RNP) and material balance time (MBT). This is because fracture permeability and fracture volume can be obtained on the basis of the characteristics of the fitting curve. Also, Alkough et al. [34] modified a log-log plot of RNP and RNP derivative against MBT for both the oil and gas cases and provided a straightforward approach to calculate the key fracture parameters covering fracture permeability and fracture half-length. However, the influence of fracture compressibility during the flowback process is not taken into consideration in the models, which likely leads to estimation error of the total compressibility.

However, due to some defects in the hypothesis of DRP function, a nonlinear phenomenon occurs when the model is applied to some field cases. And the phenomenon of the nonzero intercept leads researchers to question the physical properties of these problems. It may be due to the inaccuracies caused by stress sensitivity in some areas. In particular, there is abnormal overpressure in shale gas reservoirs in southern China [35], so the influence of stress sensitivity, especially for the two-phase relative permeability, has to be taken into account [36]. Moreover, all the researchers did not make a production data verification and comparison with the microseismic data.

We thus aimed to develop a stress-dependent two-phase relative permeability, which can be used to extend the existing single-phase model. Also, we proposed a new multiphase model to estimate SRV and fracture characteristics. Moreover, to verify our model, we compared the results with the microseismic data.

In this work, we first processed the production data of shale gas wells and obtain the gas-water ratio characteristics. Then, we calculated the simple and practical two-phase dynamic relative permeability (DRP) based on the production data collected in the field belonging to shale gas wells in southern Sichuan. Subsequently, the stress-strain curves of permeability are obtained by using the laboratory experiments. Finally, the material balance equation and diffusion equation are used to process the production data to derive the model, thus calculating fracture parameters. We compared the calculation results with the microseismic data to verify the rationality and accuracy of the calculation results.

## 2. Data Preparation

*2.1. Field Data from a Typical Shale Gas Reservoir in Southern China.* In this work, we selected the flowback data from two production wells located in southern China: the shale gas formations of the Lower Silurian, a typical marine shale gas reservoir. A large number of micron-nanoscale pores are developed in the mineral grains and organic matter [37]. These pores are the main channels for shale gas storage and migration, which play an important role in improving shale gas storage performance and providing good storage space for marine shale gas accumulation and enrichment [38]. The depth of the shale gas reservoir is over 2000 m at subsurface with a formation pressure coefficient up to 2.0. The thickness of the entire shale reservoir is about 100 m with porosity ranging from 2% to 4% and matrix permeability of 0.001 mD. The production at the early stage was about  $10 \sim 20 \times 10^4 \text{ m}^3/\text{d}$  with a stable production around at  $5 \sim 8 \times 10^4 \text{ m}^3/\text{d}$ .

The east-west anticline structure belt with few faults is arranged in the left echelon row as the main geological structure of this area [39]. This drilling platform is located at the end of the anticline structure. Although two compressional-shear faults exist around the well pad, the overall upper lateral sealing performance leads to an effective accumulation and preservation of shale gas [37, 38]. Figure 1 shows the layout of the horizontal well group. Due to the low quartz content in the high-quality shale segment at the bottom of the

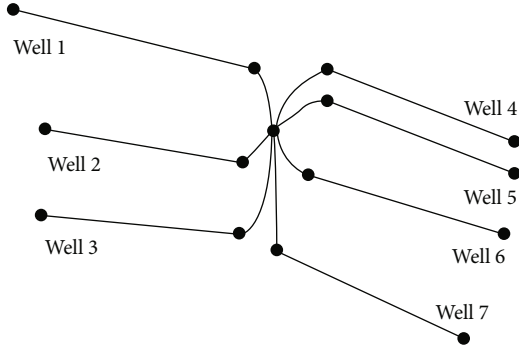


FIGURE 1: Well pad schematic. Seven MFHWs drilled in the southern Sichuan Basin.

Longmaxi Formation, natural fractures are not developed throughout the reservoir [40]. In the whole horizontal well group, Well 1, Well 4, and Well 5 are located in one formation, while Well 2, Well 3, Well 6, and Well 7 belong to another formation.

In this work, we used data from Well 3 and Well 4 to test our model for the following two reasons. Firstly, the two wells were drilled through the shale gas reservoir in different directions and are located in two different formations. Secondly, microseismic monitoring is conducted in the two wells together with a comprehensive drilling, completion data, and well test data. Figure 2 shows gas and water production rates of the two wells. The two wells both experienced gas breakthrough immediately after well opening and production, meaning that there was no single-phase flow. The difference is that Well 3 experienced a precipitous drop in production at one point (80 hrs), while Well 4 experienced a more gentle fluctuation, possibly due to different formation conditions. We are sorry that there is no further research on the causes of this phenomenon in this paper on account of insufficient high-frequency production data or complete adjacent test well data.

**2.2. Producing Gas-Water Ratios (GWR).** In order to explore the trend of GWR of production data, this section simply processes and analyzes the production data to observe whether there is an immediate gas breakthrough after the production of shale gas wells [17, 27], which means that SRV can be calculated by establishing relevant models based on production data in this area.

This is largely because the effective fracture network system is saturated with both the gas and water phases after two shut-ins. The gas source here is assumed to be from three aspects: (1) the originally existing initial gas in the active natural fracture, (2) the gas displaced by fracturing fluid under the influence of the strong countercurrent water imbibitions into the shale matrix due to the huge pressure difference during the first shut-in period, and (3) the gas accumulation that resulted from spontaneous imbibitions of fracturing fluid during the second shut-in period [41, 42].

Similarly, before establishing the model, we also need to use the gas-water yield ratio to gain the V-shaped trend. Thus, we processed the initial two-phase production data of Well 3 and Well 4 and finally obtained the trend of the gas-

water ratio (GWR). Figure 3 shows a V-shaped trend GWR over time as a feature of early two-phase flowback data. Although the inflection points in the GWR curves of the two wells occur at different times due to different formation conditions and production systems, the same V-shaped trend still appears obviously. Ghanbari et al. [15] and Abbasi [16] also found the V-shaped GWR in the wells drilled in the Horn River shales in Canada.

The gas-water ratio decreases and then increases, and we can study it from the most basic theory. Assume that the gas-water two-phase flow satisfies Darcy's law:

$$Q = -\frac{kA}{\mu} \frac{dP}{dL}, \quad (1)$$

where  $Q$  is the fluid flow rate under pressure  $P$ ,  $m^3/s$ ;  $k$  is the fluid permeability,  $\mu m^2$ ;  $A$  is the fluid flow area,  $m^2$ ;  $\mu$  is the fluid viscosity,  $mP\cdot s$ ;  $P$  is the pressure,  $MPa$ ; and  $L$  is the fluid flow length,  $m$ .

After ignoring the capillary force in the fracture network system, the gas-water ratio becomes

$$\frac{q_g}{q_w} = \frac{\mu_w}{\mu_g(P)} \frac{k_{rg}(S_g)}{k_{rw}(S_w)} \frac{\partial P_g}{\partial P_w} \approx \frac{\mu_w}{\mu_g(P)} \frac{k_{rg}(S_g)}{k_{rw}(S_w)}, \quad (2)$$

where  $q_g$  and  $q_w$  are the flow rates of the gas phase and water phase, respectively,  $m^3/d$ ;  $\mu_w$  and  $\mu_g(P)$  are the viscosity of the gas phase and water phase under  $P$  pressure, respectively,  $mP\cdot s$ ;  $k_{rg}(S_g)$  and  $k_{rw}(S_w)$  are the relative permeability of the gas phase and water phase under their respective saturation,  $\mu m^2$ ;  $S_g$  and  $S_w$  are the saturation of the gas phase and water phase, dimensionless; and  $P_g$  and  $P_w$  are the pressure of the gas phase and water phase, respectively,  $MPa$ .

After the well opening for production, the gas viscosity decreases with the decrease of pressure, while the water viscosity remains relatively unchanged. According to the change of the gas-water ratio over time, the ratio of gas-water relative permeability decreases. Therefore, on the basis of the relationship between permeability and saturation, it can be inferred that the saturation ratio has a corresponding variation trend, meaning that the initial gas saturation ( $S_{gi}$ ) is not zero, which also proves the existence of initial free gas in the fracture before well opening. When the wellbore storage effect disappears, the gas flows from the matrix to the fracture network, resulting in the replenishment of gas in the fracture system. Accordingly, the gas saturation increases, so the gas-water relative permeability increases and the gas-water ratio decreases. This is why the slope of the GWR curve drops first and then rises.

In general, the negative slope on the GWR diagnostic plot is called early gas production (EGP) and the rise of the GWR diagnostic plot is called late gas production (LGP). It is generally believed that the EGP region is the stage of wellbore storage effects and both the gas and water productions come from the effective fracture connected with the horizontal well. Also, the increase of water relative permeability is greater than the reduction of gas viscosity. The LGP phase

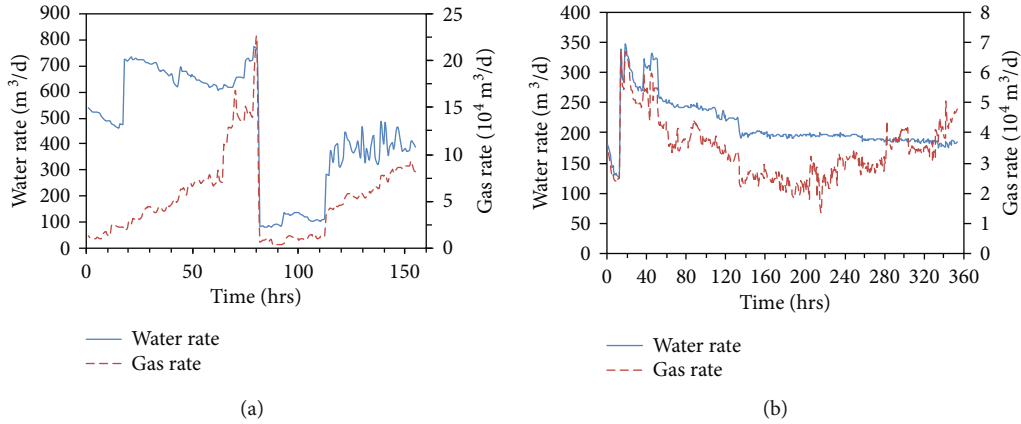


FIGURE 2: Diagnostic plots for two wells in shale gas formations belonging to southern Sichuan. (a) Production rate plot for Well 3. (b) Production rate plot for Well 4.

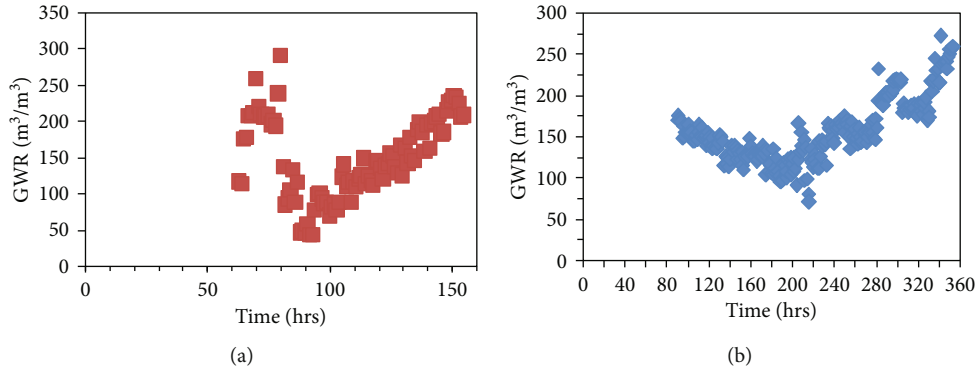


FIGURE 3: Diagnostic plots for two wells in shale gas formations belonging to southern Sichuan. (a) GWR plot for Well 3. (b) GWR plot for Well 4.

is the result of the matrix gas transfer to the fracture network after wellbore effects becoming negligible [10, 11, 17, 25–27]. According to the above analysis, we have figured out that in the EGP stage, the ground flow of flowback is only from the effective fracture system, while after the LGP stage beginning, the matrix gas initiates participation in the flow. Therefore, we will establish an analysis model for the EGP phase to calculate the SRV of shale gas wells after multistage fracturing.

### 3. Methods

**3.1. Material Balance Equation (MBE) and Diffusion Equation for the Fracture System.** In order to facilitate the establishment of the mathematical model for the EGP phase, the fracture network around the shale gas fractured well is simplified into the SRV region composed of the matrix system and fracture system. As shown in Figure 4, the effective fracture system is made up of a fracture section and a matrix section. The fracture section consists of artificial hydraulic fractures, the secondary fractures generated by fracturing, and active natural fractures. The matrix section is the shale matrix connected to the fracture section. It is worth noting that the desorption and adsorption processes were ignored in the material balance equation (MBE) [17, 43].

This model simplifies complex, active natural and secondary fractures, as well as artificial hydraulic fractures, into a simple fracture system. The length of the artificial hydraulic fracture is used as the width of the entire stimulated reservoir volume, and the length of the horizontal wellbore is used as the length. In the whole stimulated reservoir area, the height of the major fracture, including the matrix part connected to the fracture system, participates in the flow. In the equivalent fracture system, the fracture is saturated with fracturing fluid (water phase) and natural gas (gas phase). It is assumed that no matrix gas is involved in the flow during the early gas production (EGP).

It is assumed that the fracture system can be approximated as a homogeneous/closed/tank system. And the fluid flow from the fracture to the horizontal well is assumed to be linear. The mechanism driving the gas-water flow includes two aspects: (1) fracture closure and (2) expansion of the fluid (gas-water phase). Kuchuk et al. [44] also considered the assumption that fracture closure and expansion of water and free gas in the fracture system drive the accumulation of natural gas and water at the surface suggesting the occurrence of pseudo-steady-state flow in fractured reservoirs.

In general, for the purpose of facilitating the establishment and solution of the model, we made the following assumptions: (1) capillary pressure in fracture systems is



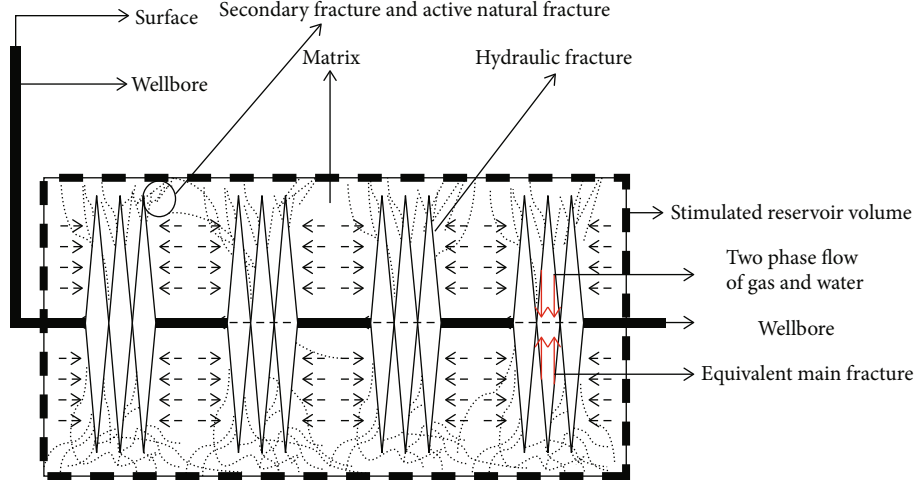


FIGURE 4: Schematic diagram of the horizontal well with multistage hydraulic fracturing for the development of material balance equation. Dashed arrows show fluid flow direction, which is sequentially from the matrix to fractures and fractures to the wellbore.

ignored; (2) the gas from the matrix is negligible in the EGP stage; (3) the fracture system is approximated as a homogeneous/closed system; (4) Darcy's law applies to fluid flow; and (5) the effective fracture system is saturated with fracturing fluid (water phase) and natural gas (gas phase) initially.

Effective compressibility terms are defined using simplified gas material balance equations (MBEs) [45–48]. In this work, the material balance equation (MBE) of the gas phase in the fracture network is simplified. The effects of gas and water (fracturing fluid) expansion and fracture closure are classified as the “effective compressibility” term given by

$$\tilde{C}_t = \left(1 - \frac{G_p}{G_{fi}}\right) \frac{B_g}{B_{gi}} S_{gi} C_g + \left(1 - \frac{W_p}{W_{fi}}\right) S_{wi} C_w + \frac{1}{V_{fi}} \frac{\partial V_f}{\partial P_f}, \quad (3)$$

where  $G_p$  and  $G_{fi}$  are the cumulative gas production and initial volume of gas in the fracture, respectively,  $m^3$ ;  $B_g$  and  $B_{gi}$  are the gas formation volume factor and gas formation volume factor at initial conditions, respectively,  $m^3/m^3$ ;  $S_{gi}$  and  $S_{wi}$  are the initial gas phase saturation and initial water phase saturation, respectively, dimensionless;  $C_g$  and  $C_w$  are the gas compressibility and water compressibility, respectively,  $Pa^{-1}$ ;  $W_p$  and  $W_{fi}$  are the cumulative water production and initial volume of water in the fracture, respectively,  $m^3$ ;  $V_f$  and  $V_{fi}$  are the volume of effective fractures and volume of effective fractures at initial conditions,  $m^3$ ; and  $P_f$  is the fracture pressure, Pa.

$\tilde{C}_t$  is analogous to the total compressibility term proposed for conventional multiphase well testing. This is represented as a function of measurable flowback parameters, including cumulative gas production and cumulative water production. Each term in its expression outlines different driving mechanisms in the fracture system: (1) expansion of the gas phase, (2) expansion of liquid phase, and (3) fracture closure. Among them,  $(1/V_{fi})(\partial V_f/\partial P_f)$  is similar to the formation compressibility coefficient in traditional conventional mate-

rial balance analysis [49]. When dealing with fractures, it refers to the inverse of the fracture stiffness determined by the elastic or strain energy required to keep the hydraulic fracture open [50].

Ignoring the gas flow rate from the matrix system to the fracture, the gas phase material balance equation is

$$0 - q_g \rho_g^0 = \frac{\partial}{\partial t} \left[ (V_g(t)) \rho_g^R \right], \quad (4)$$

where  $\rho_g^0$  and  $\rho_g^R$  are the density of gas at surface conditions and reservoir conditions, respectively,  $kg/m^3$ ; and  $V_g(t)$  is the volume of gas in the fracture system at any time,  $m^3$ .

According to the relationship between gas volume  $V_g$ , fracture volume  $V_f$ , and water volume  $V_w$  in the fracture system, the definition of gas compressibility is obtained as

$$-q_g B_g = V_g c_g \frac{\partial P_f}{\partial t} - \frac{\partial V_w}{\partial t} + \frac{\partial V_f}{\partial t}, \quad (5)$$

where  $V_f$ ,  $V_g$ , and  $V_w$  are the fracture volume, gas volume, and water volume in the fracture system, respectively,  $m^3$ .

By substituting the gas production  $G_p$  and water production  $W_p$ , then using the chain rule, the total volume of fractures is derived:

$$-\frac{1}{V_{fi}} (q_g B_g + q_w B_w) = \frac{(G_{fi} - G_p) B_g c_g}{G_{fi} B_{gi} / S_{gi}} \frac{\partial P_f}{\partial t} + \frac{(W_{fi} - W_p) B_w c_w}{W_{fi} B_{wi} / S_{wi}} \frac{\partial P_f}{\partial t} + \frac{1}{V_{fi}} \frac{\partial V_f}{\partial P_f} \frac{\partial P_f}{\partial t}, \quad (6)$$

where  $B_w$  is the water formation volume factor at initial conditions,  $m^3/m^3$ .

In the early gas production (EGP), it is assumed that  $B_w \approx B_{wi}$ , the final material balance equation, can be obtained

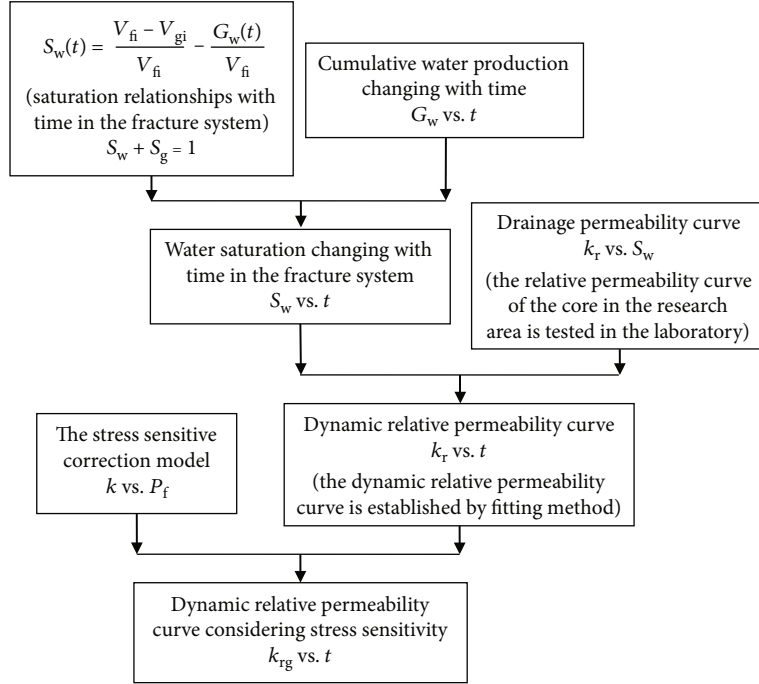


FIGURE 5: Procedure to estimate the dynamic relative permeability (DRP) curve considering stress sensitivity.

by defining a compressibility term and the total fluid flow rate by simplifying the above equation is

$$\frac{\partial P_f}{\partial t} = -\frac{q_t}{\tilde{C}_t V_{fi}}, \quad (7)$$

where  $q_t = q_g B_g + q_w B$  is total producing rate,  $m^3/d$ .

Given that single-phase, steady-state flow can be described using the continuity equation and Darcy's law, the single-phase gas diffusion equation in the fracture system is given by Zhang and Winter [51]:

$$\nabla \left[ \frac{P_f}{\mu_g Z} \nabla P_f \right] = \frac{\phi_f P_f}{K_f Z} \tilde{C}_t \frac{\partial P_f}{\partial t}, \quad (8)$$

where  $Z$  is the gas compressibility factor, dimensionless;  $\phi_f$  is the porosity for the fracture system, dimensionless; and  $\nabla$  is the gradient operator.

Define the pseudopressure and pseudotime functions [46, 52] as

$$\psi(P_f) = \int_0^{P_f} \frac{2P_f}{\mu_g Z} \partial P_f, \quad (9)$$

$$t_a = \int_0^t \frac{k_g(t)}{\mu_g \tilde{C}_t} \partial t, \quad (10)$$

where  $k_g(t)$  is the relative permeability of the gas at a given time,  $\mu m^2$ ; and  $\tilde{C}_t$  is the total effective compressibility,  $Pa^{-1}$ .

Then, the governing equation of single-phase gas flow in the fracture system is

$$\frac{\partial^2 \psi(P_f)}{\partial y^2} = \frac{\phi_f}{K_f} \frac{\partial \psi}{\partial t_a}. \quad (11)$$

**3.2. Coupling Stress Sensitivity with Dynamic Relative Permeability Function.** In Equation (10),  $k_g(t)$  is the variable function of single-phase gas with time. By introducing the dynamic relative permeability (DRP) function  $k_{rg}(t)$ , the diffusion equation of single-phase gas is transformed into the diffusion equation of the two-phase system [53].

The method in this paper is similar to that in Ezulike and Dehghanpour's study [53], but due to the geological conditions of formations belonging to southern Sichuan being different from those of North America, the dynamic relative permeability (DRP) function of the gas phase is obtained by using the method of fitting field data. In the previous study, we have assumed that the fracture system is saturated with gas and water. The relationship between cumulative gas and water production and time can be reported through field data. Therefore, the gas-water saturation in the fracture system can be established as a function of gas-water production with time. Given the characteristics of abnormal overpressure in this area, the stress sensitivity in this area cannot be ignored [36, 54, 55]. Therefore, the stress-sensitive model was considered in the dynamic relative permeability function. The specific process is shown in Figure 5.

In Figure 6, the relative permeability of the cores after fracturing in the research area is tested through laboratory experiments. The curve of pressure change with time during the flowback period is shown in Figure 7. Stress-strain

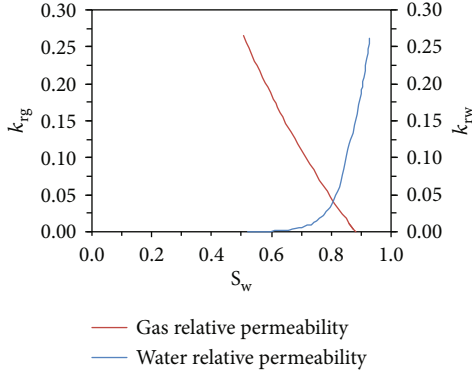


FIGURE 6: Gas-water relative permeability curve of the cores from Well 3 and Well 4.

experiments were performed to describe the curves between dimensionless permeability and effective stress by stabilizing the confining pressure and reducing the internal pressure. This is more in line with the actual formation flowback pressure changes. The early flowback stage of shale gas wells after well opening is significantly short; therefore, it can be assumed that the formation pressure has not changed much, but the inner pressure begins to decrease after the fluid flows out of the cores.

Take the stress sensitivity experiments of cores belonging to the stimulated area of Well 3 as an example. Both the matrix and the fractures are most likely contained in these cores. We had required as many experiments as possible to obtain the stress-sensitive test data in the stimulated region after fracturing as accurately as possible. However, subject to the insufficient samples or the different distances of samples from the horizontal well, these data maybe cannot represent the whole area in fact but still have considerable reference and research value.

The specific experimental procedures are as follows: (1) the initial confining pressure was set as the original formation pressure which is 38 MPa, and the internal pressure was 23 MPa; (2) the confining pressure was increased to 58 MPa slowly which is the formation pressure before well opening for flowback, and the internal pressure was increased to 43 MPa at the same time to keep the effective stress constant; and (3) the internal pressure was reduced to different pressure points to increase the effective stress, and the gas permeability of the sample was measured after each pressure point was stabilized.

Dimensionless permeability is defined as

$$\frac{K}{K_0} = ae^{-b(p_i - p_f)}, \quad (12)$$

where  $K$  is the relative permeability of the gas at a given time,  $\mu\text{m}^2$ ;  $K_0$  is the initial gas relative permeability,  $\mu\text{m}^2$ ; and  $a$  and  $b$  are stress sensitivity coefficients by experiments, dimensionless.

The experimental results are reported in Figure 8. According to the calculation method in Figure 5, the results in Figure 9 were finally obtained. Then, according to the fitting curve, the function of gas-phase relative permeability changing with time is

$$k_{rg}(t) = \alpha t - \beta. \quad (13)$$

Since the above equation is obtained based on flowback data and core experiment relative permeability,  $\alpha$  and  $\beta$  are called the flowback data coefficient and flowback data intercept, respectively, which are determined by the data fitting curve.

**3.3. Two-Phase Flowback Model for Early Gas Production (EGP).** By substituting Equation (13) into Equation (10), the governing equation of single-phase gas flow in the fracture system is changed into the two-phase flow model. This means that when gas-water two-phase flow occurs in the fracture system, the new real pseudotime function is transformed into

$$t_a = \int_0^t \frac{k_{rg}(t)}{\mu_g \tilde{C}_t} dt. \quad (14)$$

In order to establish the relationship between pseudo-pressure function and pseudotime function, we make the following transformation:

$$\frac{\partial \psi}{\partial t_a} = \frac{\partial P_f}{\partial t} \times \frac{\partial \psi}{\partial P_f} \times \frac{\partial t}{\partial t_a}. \quad (15)$$

And  $\partial P_f / \partial t$  is derived by the final material balance equation (Equation (7)); in a similar way, we can gain  $\partial \psi / \partial P_f$  and  $\partial t / \partial t_a$  by the defined pseudopressure (Equation (9)) and new pseudotime equation (Equation (14)), respectively. Finally, Equation (15) becomes

$$\frac{\partial \psi}{\partial t_a} = -\frac{2}{V_{fi}} \frac{q_t}{k_{rg}(t)} \frac{P_f}{Z}. \quad (16)$$

Define the equivalent gas rate as [48]

$$q_g^* = \frac{1}{k_{rg}(t)} [q_g B_{gi} + q_w B_w]. \quad (17)$$

Substituting  $P_f / Z$  in Equation (16) using the real gas law, then combine it with the equivalent gas rate (Equation (17)):

$$\frac{\partial \psi}{\partial t_a} = \left[ -\frac{2}{V_{fi}} \frac{P_i}{Z_i} \right] q_g^*. \quad (18)$$

By substituting  $\partial \psi / \partial t_a$  (Equation (18)) in Equation (11), we can establish the two-phase diffusion equation:

$$\frac{\partial^2 \psi(P_f)}{\partial y^2} = \frac{\phi_f}{K_f} \left[ -\frac{2}{V_{fi}} \frac{P_i}{Z_i} \right] q_g^*. \quad (19)$$

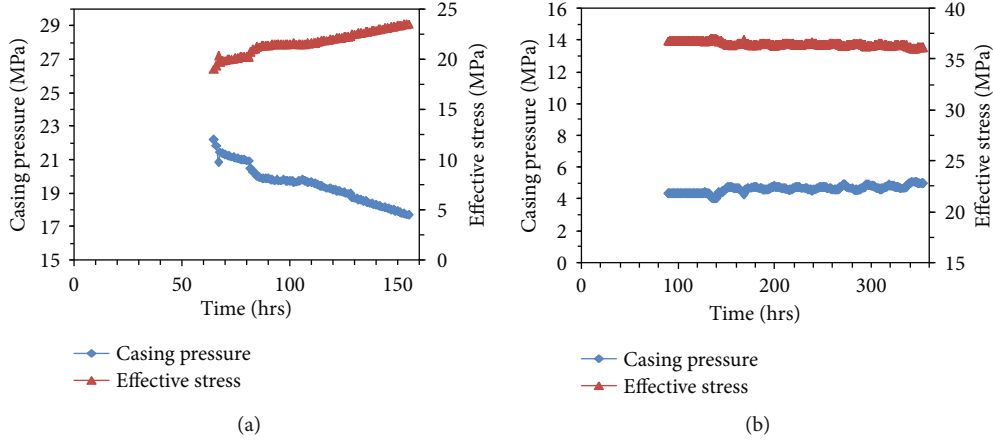


FIGURE 7: Casing pressure and effective stress changed with time for two wells in shale gas formations belonging to southern Sichuan. (a) Well 3 and (b) Well 4.

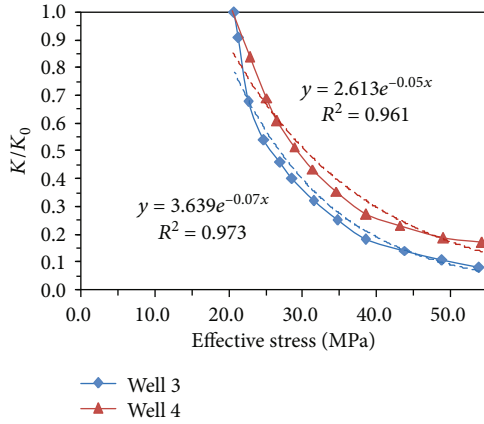


FIGURE 8: Stress-strain experiment results of Well 3 and Well 4.

Then, the following inner and outer boundary conditions can be solved:  $y = Y_e$ ,  $\partial\psi(P_f)/\partial y = 0$ , and  $y = 0$ ,  $\psi(P_f) = \psi(P_{wf})$ .

Define the fracture storage coefficient as

$$C_{st} = \frac{V_{fi}Z_i}{2P_i}. \quad (20)$$

Then, the following relationship is gained:

$$\frac{\psi(\bar{P}_f) - \psi(P_{wf})}{q_g^*} = \frac{\phi_f}{K_f} \frac{1}{C_{st}} \left[ \frac{Y_e^2}{3} \right]. \quad (21)$$

Substitute Equation (20) into Equation (18) and integrate to obtain

$$t_a = C_{st} \frac{\psi(P_i) - \psi(\bar{P}_f)}{q_g^*}. \quad (22)$$

By combining Equation (22) with Equation (15), we can

modify the final two-phase flow model of the early gas production stage as follows:

$$\left[ \frac{\psi(P_i) - \psi(P_{wf})}{q_g^*} \right] = \left[ \frac{1}{C_{st}} \right] t_a + \frac{\phi_f}{K_f} \left[ \frac{1}{C_{st}} \right] \left[ \frac{Y_e^2}{3} \right]. \quad (23)$$

Theoretically, a plot of the rate-normalized pseudopressure (RNP) vs. the pseudotime should yield a straight line relationship. With the pseudotime function as an independent variable and the left side of the equation as a dependent variable, the slope and intercept can be obtained according to the fitting curve, and the relationship between the equivalent fracture porosity/half-length of the effective fracture system and effective fracture system permeability can be described as follows:

$$C_{st} = \frac{1}{\text{slope}} = \frac{V_{fi}Z_i}{2P_i}, \quad (24)$$

$$Y_D = \frac{y\text{-axis intercept}}{\text{slope}} = \frac{\phi_f}{K_f} \left[ \frac{Y_e^2}{3} \right]. \quad (25)$$

**3.4. Analysis Procedure.** We propose the following analysis procedure:

- (1) Obtain and process water and gas flowback data to explore a V-shaped gas-water ratio trend (see Figures 2 and 3 and Equation (2))
- (2) The early flowback period (EGP) is distinguished from the late flowback period (LGP) according to the V-shaped trend of the GWR curve (see Figure 3)
- (3) Conduct a simpler fracture network system model for the EGP (see Figure 4)
- (4) Calculate effective compressibility by Equation (3) to deduce the two-phase material balance equation (MBE) (Equation (7)) for the fracture system

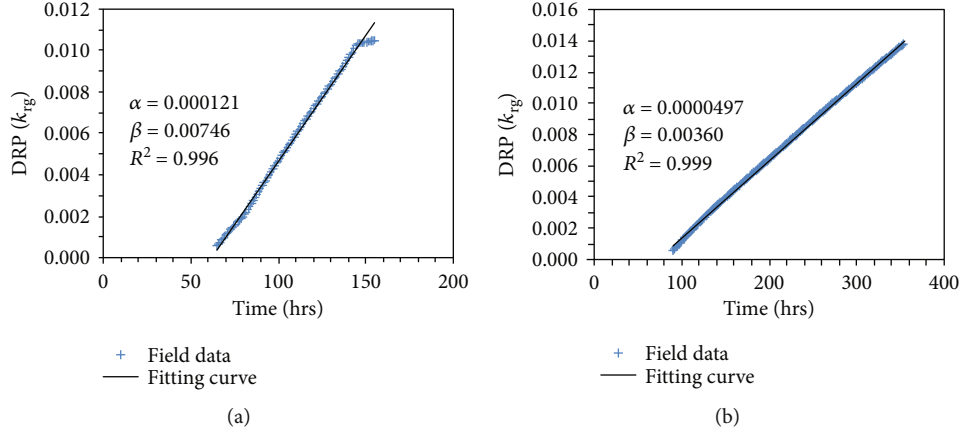


FIGURE 9: Dynamic relative permeability function over time considering stress sensitivity for two wells in shale gas formations belonging to southern Sichuan. (a) DRP fitting curve for Well 3. (b) DRP fitting curve for Well 4.

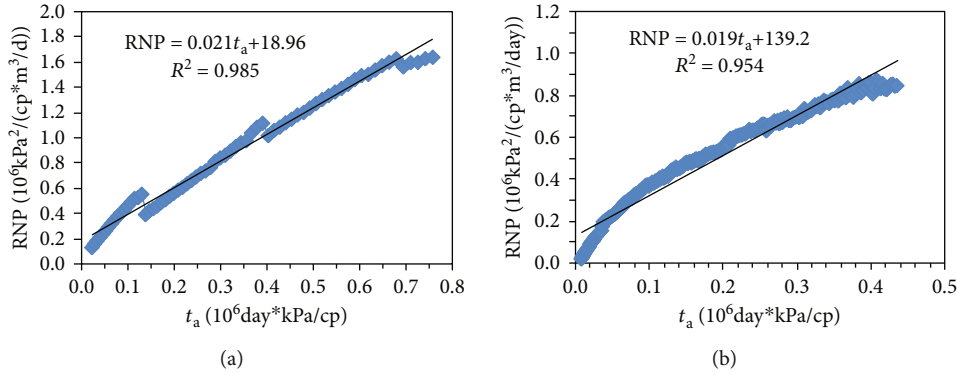


FIGURE 10: Analysis of EGP data of two wells belonging to southern Sichuan: rate-normalized pressure change with pseudotime. (a) Well 3 and (b) Well 4.

- (5) Define the pseudopressure and pseudotime functions (Equations (9) and (10)) to deduce the gas diffusion equation (Equation (11)) of the fracture system
- (6) Plot the gas-water relative permeability curve (see Figure 5) and the curves of dimensionless permeability with effective stress (see Figure 8) by experiments
- (7) Calculate gas DRP coupling stress sensitivity (see Figure 9) following the steps by Figure 6 to transform the gas diffusion equation (Equation (11)) into the two-phase diffusion equation (Equation (19))
- (8) Modify the final two-phase flow mode (Equation (23)) by combining Equation (22) with Equation (15)
- (9) Plot rate-normalized pressure change with pseudotime (see Figure 10)
- (10) Calculate SRV by Equation (24) and effective fracture system permeability by Equation (25)
- (11) Verify the analytical model against microseismic data (see Figure 11)

The flowback data we need to obtain include production rates and pressure and cumulative production data profiles. Then, we got a V-shaped trend in the gas-water ratio curve by processing the flowback data. Thus, an analytical model was established for the EGP stage. Finally, the calculated results were compared with the microseismic data to validate the mathematical results.

#### 4. Results and Discussions

**4.1. Stimulated Reservoir Volume.** We apply the analytical model presented above to analyze the flowback data of Well 3 and Well 4. However, there are several issues that need to be addressed and discussed:

- (1) It is difficult to gain an appropriate initial gas saturation of the fracture system from actual field data. Unlike conventional numerical simulation, this parameter is unknown in actual field data. After the



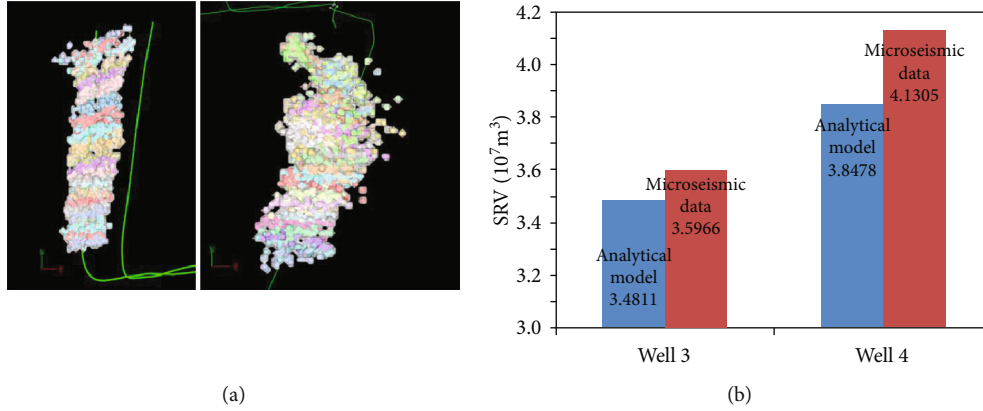


FIGURE 11: (a) Renderings of microseismic detection technology for Well 3 and Well 4. (b) Comparison between the analytical model and the microseismic data.

fracturing operation is completed, the effective fracture system connecting the wellbore is filled with fracturing fluid approximately. Thus, after the well is opened for flowback operation and before production, the volume of the recovered fracturing fluid under the ground is filled with gas renewedly. Therefore, in this paper, we take a reasonable value which is the recovery percentage of the total injection amount of fracturing fluid as the initial fracture system gas saturation in calculation. According to Xu's paper [48], there is a little significant difference between the actual value of initial gas saturation and the recovery percentage. However, this was still not rigorous enough. Then, other possible values are substituted into the calculation by us to get the new SRV. The results showed that the impact of this value on SRV estimation was not obvious within the error range, and the difference was less than 1% compared with the microseismic data

Due to that, fracturing fluid may leak off into the existing inactive natural fractures and into the matrix during injection; the fluid flowback percentage decreases, but the initial gas saturation in the fracture system increases. Hence, when a significant portion of the injected fluid volume does not contribute to create fracture volume, this value of the initial gas saturation for calculation is actually low. One direction of future work is to consider using the results to iteratively optimize the initial gas saturation value.

- (2) The value of the fracture closure term in the total compressibility cannot be accurately expressed. Fortunately, it is found that this value has no obvious influence on the results in the calculation process. Since this value refers to the inverse of fracture stiffness when dealing with fractures, it is considered to give a reasonable value in the subsequent work from the perspective of rock fracture mechanics

The final model calculation results are shown in Figure 10. Since microseismic detection technology was used to estimate the final hydraulic fracture stimulated effect in the

two wells. We compared the calculated results with the microseismic data and finally found that the difference between the calculated results of the analytical model and the microseismic data was minor, as shown in Figure 11. This reason is that quantities of fractures that do not connect effectively with fracture systems are counted in the final result when microseismic detection techniques are used. Those "dead" fractures skew the microseismic results.

*4.2. Effective Fracture System Permeability of Stimulated Reservoir.* As shown in Table 1, after obtaining the slope of rate-normalized pressure change with pseudotime (see Figure 10), SRV was gained by Equation (17). On the basis of the average length of hydraulic fractures provided by the microseismic data of the drilling platform where Well 3 and Well 4 are located and the average porosity of the cores after fracturing obtained through experiments, the permeability of the effective fracture system in the stimulated region is calculated by using Equation (18). The results are shown in Table 1, where the absolute deviation refers to the difference between the SRV calculated by the analytical model and estimated by the microseismic data, and the relative deviation refers to the ratio of the absolute deviation to the SRV estimated by microseismic data. Numerical errors in porosity of the effective fracture system are responsible for the error of permeability.

If the SRV estimated by microseismic data is taken as a reference for comparison, the specific calculation process is as follows:

$$d_A = V_A - V_M, \quad (26)$$

$$d_R = \frac{(V_A - V_M)}{V_M}, \quad (27)$$

where  $d_A$  and  $d_R$  are the absolute deviation and the relative deviation between the SRV calculated by the analytical model and estimated by the microseismic data, respectively,  $\text{m}^3$ ; and  $V_A$  and  $V_M$  are the SRV calculated by the analytical model and the SRV estimated by the microseismic data,  $\text{m}^3$ .

TABLE 1: Different results of the analytical model and microseismic data.

Parameter name	Well 3	Well 4
SRV calculated by the analytical model	$3.4811 \times 10^7 \text{ m}^3$	$3.8478 \times 10^7 \text{ m}^3$
SRV estimated by the microseismic data	$3.5966 \times 10^7 \text{ m}^3$	$4.1305 \times 10^7 \text{ m}^3$
The absolute deviation	$1.1150 \times 10^6 \text{ m}^3$	$2.8270 \times 10^6 \text{ m}^3$
The relative deviation	3.2%	6.8%
Effective fracture system permeability	0.301 mD	0.244 mD
Average half-length of hydraulic fractures	320 m	285 m
Effective fracture system porosity	15.5%	13.8%

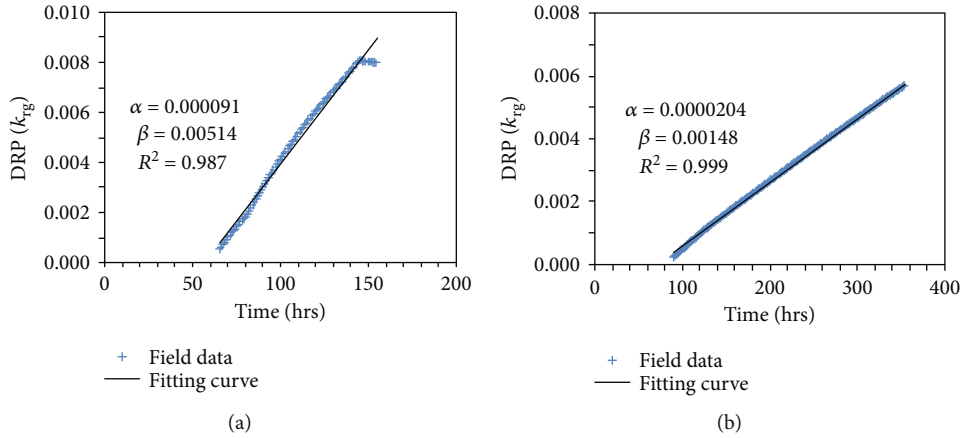


FIGURE 12: Dynamic relative permeability function over time without stress sensitivity for two wells belonging to southern Sichuan. (a) DRP for Well 3. (b) DRP for Well 4.

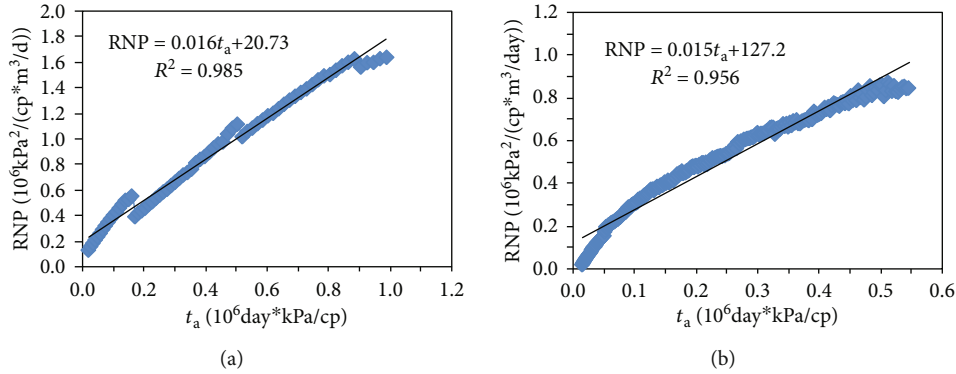


FIGURE 13: Analysis without considering stress sensitivity of EGP data of two wells in shale gas belonging to southern Sichuan: rate-normalized pressure change with pseudotime. (a) Well 3 and (b) Well 4.

4.3. Analytical Model without Considering Stress Sensitivity. If the stress sensitivity effect is not considered in the process of the DRP calculation, the deviation of the DRP curve will occur, as shown in Figure 12. And the curve with a large error was substituted into the step shown in Section 3.4 to get the result in Figure 13. As a result, both the slope and the intercept of the RNP curve had changed. We obtained the new slope and intercept of the curve and calculated a new SRV according to Equations (17) and (18). Then, the calculation results and corresponding deviations as shown in Figure 14 were obtained.

It can be seen that the relative deviation calculated without considering the stress sensitivity effect is greater than that calculated with considering the stress sensitivity effect. Moreover, because the real SRV has been overestimated by the microseismic data, the calculation results of the model without considering the stress sensitivity effect are higher than those of the microseismic data, which further indicates that the calculation results without considering the stress sensitivity effect in the high-pressure area will have a large error, which cannot be ignored. We also calculated the permeability of the effective fracture system, and the effective permeability

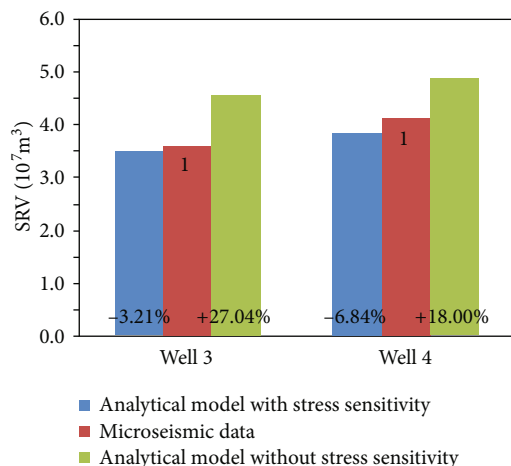


FIGURE 14: Comparison between the analytical model with or without considering stress sensitivity and the microseismic data.

of Well 3 and Well 4 was 0.432 mD and 0.283 mD, respectively. It can be seen that the calculation results are 43.50% and 15.75% more than those considering the stress sensitivity effect.

## 5. Conclusions

In this paper, a comprehensive model is developed to predict SRV in the shale gas reservoirs using the flowback data after fracturing. The stress sensitivity is included as well. The results of SRV are compared with the microseismic data. The following conclusions can be drawn:

- (1) The flowback data show that the gas-water ratio is V-shaped, i.e., the early descending stage and the late ascending stage in this field, which can be used to estimate the volume of the effective fracture system
- (2) The stress sensitivity is a key factor affecting the permeability of the effective fracture system as well as the SRV in the shale gas reservoirs. Once it is neglected, the estimation will be overestimated
- (3) Stress sensitivity is taken into account to forecast SRV in this typical block. Results show that the relative deviation of stimulated reservoir volume calculated by this proposed model and the microseismic data is less than 10%, indicating that this method could provide reasonable prediction

## Data Availability

The test data used to support the findings of this study are included within the article. Readers can obtain data supporting the research results from the test data table in the paper.

## Conflicts of Interest

The authors declare that there is no conflict of interest regarding the publication of this paper.

## Acknowledgments

This research was funded by the National Science and Technology Major Project of China (2017ZX05009-005), Fundamental Research Funds for the Central Universities (2652018209), and National Natural Science Foundation of China (51804282).

## References

- [1] G. Wang, A. Jia, Y. Wei, and C. Xiao, "Transient pressure analysis for multifractured horizontal well with the use of multi-linear flow model in shale gas reservoir," *Geofluids*, vol. 2020, Article ID 8348205, 20 pages, 2020.
- [2] W. Zhou, R. Banerjee, B. D. Poe, J. Spath, and M. Thambayagam, "Semianalytical production simulation of complex hydraulic-fracture networks," *SPE Journal*, vol. 19, no. 1, pp. 6–18, 2014.
- [3] C. E. Neuzil, "How permeable are clays and shales?," *Water Resources Research*, vol. 30, no. 2, pp. 145–150, 1994.
- [4] R. S. Jones Jr., B. Pownall, and J. Franke, "Estimating reservoir pressure from early flowback data," in *Unconventional Resources Technology Conference*, pp. 25–27, Denver, Colorado, August 2014.
- [5] B. Zanganeh, M. Soroush, J. D. Williams-Kovacs, and C. R. Clarkson, "Parameters affecting load recovery and oil breakthrough time after hydraulic fracturing in tight oil wells," in *SPE/CSUR Unconventional Resources Conference*, pp. 20–22, Calgary, Alberta, October 2015.
- [6] A. Mohammadnejad, R. F. Shelley, L. V. Lehman, K. Shah, D. Gusain, and M. T. Conway, "Development of the brittle shale fracture network model," in *SPE Hydraulic Fracturing Technology Conference*, pp. 4–6, The Woodlands, Texas, USA, February 2013.
- [7] J. Xu, C. Guo, W. Teng, M. Wei, and R. Jiang, "Production performance analysis of tight oil/gas reservoirs considering stimulated reservoir volume using elliptical flow," *Journal of Natural Gas Science and Engineering*, vol. 26, pp. 827–839, 2015.
- [8] M. Wu, M. Ding, J. Yao, S. Xu, L. Li, and X. Li, "Pressure transient analysis of multiple fractured horizontal well in composite shale gas reservoirs by boundary element method," *Journal of Petroleum Science and Engineering*, vol. 162, pp. 84–101, 2018.
- [9] Z. Chen, X. Liao, X. Zhao, W. Yu, and K. Sepehrnoori, "A workflow based on a semianalytical model to estimate the properties of stimulated reservoir volume of tight-oil wells," *Journal of Petroleum Science and Engineering*, vol. 178, pp. 892–903, 2019.
- [10] D. Ilk, D. M. Anderson, G. W. J. Stotts, L. Mattar, and T. A. Blasingame, "Production-data analysis, pitfalls, diagnostics," *SPE Reservoir Evaluation & Engineering*, vol. 13, no. 3, pp. 538–552, 2013.
- [11] D. Ilk, S. M. Currie, D. Symmons, J. A. Rushing, N. J. Broussard, and T. A. Blasingame, "A comprehensive workflow for early analysis and interpretation of flowback data from wells in tight gas/shale reservoir systems," in *SPE Annual Technical Conference and Exhibition*, pp. 19–22, Florence, Italy, September 2010.
- [12] M. A. Abbasi, H. Dehghanpour, and R. V. Hawkes, "Flowback analysis for fracture characterization," in *SPE Canadian*

- Unconventional Resources Conference*, Calgary, Alberta, November 2012.
- [13] M. A. Abbasi, D. O. Ezulike, H. Dehghanpour, and R. V. Hawkes, "A comparative study of flowback rate and pressure transient behavior in multifractured horizontal wells completed in tight gas and oil reservoirs," *Journal of Natural Gas Science and Engineering*, vol. 17, no. 2, pp. 82–93, 2014.
- [14] Y. Zhang and C. Ehlig-Economides, "Accounting for remaining injected fracturing fluid in shale gas wells," in *SPE/AAPG/SEG Unconventional Resources Technology Conference*, pp. 25–27, Denver, Colorado, USA, August 2014.
- [15] E. Ghanbari, D. Bearinger, M. A. Abbasi, and H. Dehghanpour, "Flowback volumetric and chemical analysis for evaluating load recovery and its impact on early-time production," in *SPE Unconventional Resources Conference Canada*, pp. 5–7, Calgary, Alberta, Canada, November 2013.
- [16] M. A. Abbasi, *A comparative study of flowback rate and pressure transient behavior in multi-fractured horizontal wells*, [Ph.D. thesis], University of Alberta, Edmonton, Alberta, Canada, 2013.
- [17] C. R. Clarkson, "Modeling two-phase flowback of multifractured horizontal wells completed in shale," in *SPE Canadian Unconventional Resources Conference*, Calgary, Alberta, Canada, November 2012.
- [18] J. D. Williams-Kovacs and C. R. Clarkson, "Modeling of two-phase flowback from multi-fractured horizontal tight gas wells stimulated with nitrogen energized frac fluid," in *SPE Unconventional Resource Conference Canada*, Calgary, Alberta, November 2013.
- [19] Z. Tao, L. Xiangfang, Y. Lifeng, L. Jing, W. Yonghui, and F. Dong, "Effects of shut-in timing on flowback rate and productivity of shale gas wells," *Natural Gas Industry*, vol. 37, no. 8, pp. 48–60, 2017.
- [20] O. A. Adefidipe, Y. Xu, H. Dehghanpour, and C. J. Virues, "Immediate gas production from shale gas wells: a two-phase flowback model," in *SPE Unconventional Resources Conference-USA*, The Woodlands, Texas, April 2014.
- [21] O. A. Adefidipe, Y. Xu, H. Dehghanpour, and C. J. Virues, "Estimating effective fracture volume from early-time production data: a material balance approach," in *SPE/CSUR Unconventional Resources Conference-Canada*, Calgary, Alberta, October 2014.
- [22] Y. Xu, O. A. Adefidipe, and H. Dehghanpour, "Volumetric analysis of two-phase flowback data for fracture characterization," in *SPE Western Regional Meeting*, Garden Grove, California, April 2015.
- [23] Y. Xu, Y. Fu, D. O. Ezulike, H. Dehghanpour, and C. J. Virues, "Modeling two-phase flowback data using an open tank model," in *SPE/CSUR Unconventional Resources Conference*, Calgary, Alberta, October 2015.
- [24] D. O. Ezulike, H. Dehghanpour, and R. V. Hawkes, "Understanding flowback as a transient two-phase displacement process: an extension of the linear dual-porosity model," in *CPR Unconventional Resources Conference-Canada*, Calgary, Alberta, November 2013.
- [25] D. O. Ezulike and H. Dehghanpour, "A workflow for flowback data analysis—creating value out of chaos," in *2014 Unconventional Resources Technology Conference*, Denver, Colorado, August 2014.
- [26] D. O. Ezulike, H. Dehghanpour, and C. J. Virues, "A flowback-guided approach for production data analysis on tight reservoirs," in *2014 SPE/CSUR Unconventional Resources Conference-Canada*, Calgary, Alberta, October 2014.
- [27] C. R. Clarkson and J. D. Williams-Kovacs, "A new method for modeling multi-phase flowback of multi-fractures horizontal tight oil wells to determine hydraulic fracture properties," in *SPE Annual Technical Conference and Exhibition*, New Orleans, Louisiana, October 2013.
- [28] C. R. Clarkson, F. Qanbari, and J. D. Williams-Kovacs, "Innovative use of rate-transient analysis methods to obtain hydraulic-fracture properties for low-permeability reservoirs exhibiting multiphase flow," *Leading Edge*, vol. 33, no. 10, pp. 1108–1122, 2014.
- [29] J. D. Williams-Kovacs and C. R. Clarkson, "Stochastic modeling of multi-phase flowback from multi-fractured horizontal tight oil wells," in *SPE Unconventional Resource Conference-Canada*, Calgary, Alberta, November 2013.
- [30] J. D. Williams-Kovacs and C. R. Clarkson, "Stochastic modeling of two-phase flowback of multi-fractured horizontal wells to estimate hydraulic fracture properties and forecast production," in *SPE Unconventional Resource Conference USA*, The Woodlands, Texas, April 2013.
- [31] J. D. Williams-Kovacs and C. R. Clarkson, "A modified approach for modeling two-phase flowback from multi-fractured horizontal shale gas wells," in *Unconventional Resources Technology Conference*, San Antonio, Texas, July 2015.
- [32] J. D. Williams-Kovacs and C. R. Clarkson, "A modified approach for modeling two-phase flowback from multi-fractured horizontal shale gas wells," *Journal of Natural Gas Science and Engineering*, vol. 30, pp. 127–147, 2016.
- [33] Y. Fu, D. O. Ezulike, and H. Dehghanpour, "Estimating effective fracture pore-volume from early single-phase flowback data and relating it to fracture design parameters," in *SPE/CSUR Unconventional Resources Conference*, Calgary, Alberta, October 2015.
- [34] A. B. Alkough, S. McKetta, and R. A. Wattenbarger, "Estimation of effective-fracture volume using water-flowback and production data for shale-gas wells," *Journal of Canadian Petroleum Technology*, vol. 53, no. 5, pp. 293–303, 2014.
- [35] X. Wang, Y. Zhu, and C. Fu, "Experimental investigation of the stress-dependent permeability in the Longmaxi Formation shale," *Journal of Petroleum Science and Engineering*, vol. 175, pp. 932–947, 2019.
- [36] X. Yan, J. Sun, and D. Liu, "Numerical simulation of shale gas multiscale seepage mechanism-coupled stress sensitivity," *Journal of Chemistry*, vol. 2019, Article ID 7387234, 13 pages, 2019.
- [37] W. Liu, J. Liu, M. Cai, C. Luo, X. Shi, and J. Zhang, "Pore evolution characteristic of shale in the Longmaxi Formation, Sichuan Basin," *Petroleum Research*, vol. 2, no. 4, pp. 291–300, 2017.
- [38] S. Chen, Y. Zhu, S. Chen, Y. Han, and C. Fu, "Hydrocarbon generation and shale gas accumulation in the Longmaxi Formation, Southern Sichuan Basin, China," *Marine and Petroleum Geology*, vol. 86, pp. 248–258, 2017.
- [39] C. Wang, B. Zhang, Y. Lu et al., "Lithofacies distribution characteristics and its controlling factors of shale in Wufeng Formation-Member 1 of Longmaxi Formation in the Jiaoshiba area," *Petroleum Research*, vol. 3, no. 4, pp. 306–319, 2018.
- [40] T. Dong, S. He, M. Chen et al., "Quartz types and origins in the paleozoic Wufeng-Longmaxi Formations, Eastern Sichuan

- Basin, China: implications for porosity preservation in shale reservoirs,” *Marine and Petroleum Geology*, vol. 106, pp. 62–73, 2019.
- [41] Y. Cheng, “Impact of water dynamics in fractures on the performance of hydraulically fractured wells in gas-shale reservoirs,” *Journal of Canadian Petroleum Technology*, vol. 51, no. 2, pp. 143–151, 2013.
- [42] J. Zhang, A. Kamenov, A. D. Hill, and D. Zhu, “Laboratory measurement of hydraulic-fracture conductivities in the Barnett shale,” *SPE Production & Operations*, vol. 29, no. 3, pp. 216–227, 2014.
- [43] L. Fan, J. W. Thompson, and J. R. Robinson, “Understanding gas production mechanism and effectiveness of well stimulated in the Haynesville shale through reservoir simulation,” in *SPE Unconventional Resources & International Petroleum Conference*, Calgary, Alberta, October 2010.
- [44] F. J. Kuchuk, D. Biryukov, and T. Fitzpatrick, “Rate transient and decline curve analyses for continuously (dual-porosity) and discretely naturally fractured reservoirs,” in *SPE Annual Technical Conference and Exhibition*, Amsterdam, Netherlands, October 2014.
- [45] N. M. A. Rahman, L. Kok, and K. Zaoral, “A new method for computing pseudo-time for real gas flow using the material balance equation,” *Journal of Canadian Petroleum Technology*, vol. 45, no. 10, pp. 36–44, 2006.
- [46] S. Moghadam, O. Jeje, and L. Mattar, “Advanced gas material balance in simplified format,” *Journal of Canadian Petroleum Technology*, vol. 50, no. 1, pp. 90–98, 2013.
- [47] V. K. Singh, “Overview of material balance equation (MBE) in shale gas & non-conventional reservoir,” in *SPE Middle East Oil and Gas Show and Conference*, Manama, Bahrain, March 2013.
- [48] Y. Xu, O. A. Adefidipe, and H. Dehghanpour, “A flowing material balance equation for two-phase flowback analysis,” *Journal of Petroleum Science & Engineering*, vol. 142, pp. 170–185, 2016.
- [49] J. C. Martin, “Simplified equations of flow in gas drive reservoirs and the theoretical foundation of multiphase pressure build up analyses,” *Transactions of the AIME*, vol. 216, no. 1, pp. 321–323, 2013.
- [50] D. P. Craig, *Analytical modeling of a fracture-injection/fall-off sequence and the development of a refracture candidate diagnostic test*, [Ph.D. thesis], Texas A&M University, College Station, Texas, 2006.
- [51] D. Zhang and C. Winter, “Moment-equation approach to single phase fluid flow in heterogeneous reservoirs,” *SPE Journal*, vol. 4, no. 2, pp. 118–127, 1999.
- [52] S. H. Tabatabaie, L. Mattar, and M. Pooladi-Darvish, “Pseudo-time calculation in low permeability gas reservoirs,” in *SPE Unconventional Resources Conference Canada*, Calgary, Alberta, Canada, November 2013.
- [53] D. O. Ezulike and H. Dehghanpour, “Modelling flowback as a transient two-phase depletion process,” *Journal of Natural Gas Science and Engineering*, vol. 19, pp. 258–278, 2014.
- [54] Y. Zhao, Z. Wang, X. Qin, J. Li, and H. Yang, “Stress-dependent permeability of coal fracture networks: a numerical study with lattice Boltzmann method,” *Journal of Petroleum Science and Engineering*, vol. 173, pp. 1053–1064, 2019.
- [55] Z. Ru, K. An, and J. Hu, “The impact of sulfur precipitation in developing a sour gas reservoir with pressure-sensitive effects,” *Advances in Geo-Energy Research*, vol. 3, no. 3, pp. 268–276, 2019.



## Research Article

# The Role of Microfabric and Laminae on Pore Structure and Gas Transport Pathways of Marine Shales from Sichuan Basin, China

Yi Shu,<sup>1</sup> Shang Xu ,<sup>1</sup> Feng Yang ,<sup>1</sup> Zhiguo Shu,<sup>2</sup> Pan Peng,<sup>3</sup> Senxin Huang,<sup>1</sup> and He Zhen<sup>1</sup>

<sup>1</sup>Key Laboratory of Tectonics and Petroleum Resources (China University of Geosciences), Ministry of Education, Wuhan 430074, China

<sup>2</sup>Research Institute of Petroleum Exploration and Development, SINOPEC Jiangnan Oilfield Company, Wuhan 430223, China

<sup>3</sup>Shenzhen Branch, CNOOC China Limited, Shenzhen 518000, China

Correspondence should be addressed to Shang Xu; xushang0222@163.com and Feng Yang; fengyang@cug.edu.cn

Received 13 April 2020; Revised 12 June 2020; Accepted 20 June 2020; Published 21 July 2020

Academic Editor: Keliu Wu

Copyright © 2020 Yi Shu et al. This is an open access article distributed under the Creative Commons Attribution License, which permits unrestricted use, distribution, and reproduction in any medium, provided the original work is properly cited.

This study investigated the effects of microfabric and laminae on the pore structure and gas transport pathways of the Silurian Longmaxi shales from Sichuan Basin. 23 shale samples with varied lithofacies were comprehensively investigated by mineralogy, organic geochemistry, pycnometry, and low-pressure nitrogen adsorption analysis. The fabric and laminae of these samples were identified using petrographic microscope and scanning electron microscopy. Permeabilities were measured using the nonsteady-state method on both perpendicular and parallel to bedding shales. The effective pore diameter controlling gas transport was estimated from gas slippage factors obtained in permeability measurements. These values were also compared to those calculated using the Winland equation. Siliceous shales studied are faintly laminated to nonlaminated and have larger porosity and specific surface area. Argillaceous/siliceous mixed shales are well laminated, whereas argillaceous shales contain many oriented clay flakes along the lamination. Both porosity and surface area are positively correlated with TOC content. Unlike most conventional reservoirs, there is a negative correlation between porosity and permeability values of the samples studied. Permeabilities parallel to bedding, ranging from 0.4 to 76.6  $\mu\text{D}$ , are in control of the oriented clay flakes and silty microlaminae. Permeability anisotropy values of the shales vary between 1.3 and 49.8. Samples rich in oriented clay flakes and microlaminated fabric have relatively larger permeability and permeability anisotropy values. The effective transport pore diameters derived from gas slippage measurements are slightly lower than those calculated from the Winland equation. However, both methods have shown that the effective transport pore diameters of argillaceous shales (averaging 552 nm) are significantly higher than siliceous shales (averaging 198 nm), which underlines the control of microfabric, rather than porosity, on gas transport pathways of the shales studied.

## 1. Introduction

Shale systems have received increased research activities since hydrocarbons have been commercially extracted from unconventional reservoirs. Shale reservoirs consist of various fine-grained sedimentary rocks that mainly include mudrocks, shales, and siltstones [1–3]. Due to the large variability in lithology and involvement of organic matter, reservoir characteristics of shales are very complex. To characterize the complex pore structure, innovative approaches are implemented to obtain information about the nanometer- to micrometer-sized pore systems of shales

[4–8]. A variety of organic matter-hosted and inorganic matter-related pores with pore size ranging from micropore (<2 nm, IUPAC classification) to mesopore (2–50 nm, IUPAC classification) to macropore (>50 nm, IUPAC classification) have been reported in shales [9–11]. Pore structure characteristics (morphology, porosity, pore size distribution, and specific surface area) of shales are found to be associated with rock composition, total organic carbon (TOC) content, maturity, and other geological factors [12–16].

Permeability is one of the most important petrophysical parameters for reservoir evaluation and hydrocarbon production [17, 18]. Since shale reservoirs commonly have

permeabilities down to micro- to nano-Darcy range, steady and nonsteady-state flow tests are employed to determine the permeability values of shales [19]. Permeabilities are affected by many geological factors, including fabric, lithology, mineralogy, pore size distribution (PSD), and microfractures. Studies on high-maturity Horn River shales have shown that the matrix permeabilities were largely related to the connectivity between macropores and micropores [20]. Permeability values of coarser grained sandstones are commonly higher than those of finer grained mudstones by several orders of magnitude [21]. Permeabilities are further affected by diagenetic process. Mechanical compaction and mineral cementation can significantly decrease pore space and fluid transport pathways of rocks. Clay minerals are reported to cement with the framework minerals and thus decrease permeability of Eagle Ford shales [22]. It should be noted that most of the samples in these studies are low-maturity or organic-lean, and most porosity is associated with the interparticle pores of inorganic matter. Recently, advanced scanning electron microscopy has documented diverse pores in shale systems [6, 16]. However, there are relatively few detailed studies to relate pore structure to the transport properties of shales. Especially, organic matter- (OM-) hosted pores are critical for gas adsorption in many overmature marine shales [23–25], but the role of OM-hosted pores on fluid storage and transport needs more study in detail. Furthermore, permeability can be estimated from more easily determined petrophysical properties, such as mean pore diameter and pore throat size distribution [26, 27]. However, many pore space analysis methods are conducted at atmospheric pressure. It would be much more meaningful to apply these pore structure parameters in the estimations of permeability under in situ conditions [19, 28]. What is more, the effective pore diameter for gas transport can be further derived from gas slippage in gas permeability measurements [29]. These link a direct relationship between pore structure and gas transport.

Concerns about the economic potential of shale systems have led to many studies about reservoir properties of shales [12, 30, 31]. Significant progresses have been achieved in basin structure, sedimentology environment, organic geochemistry, and petrophysical features of shales [17, 32–36]. Shales are commonly composed of fine-grained minerals intercalated with coarser-grained quartz and carbonate microlaminae. High-frequency laminations and strong heterogeneities probably lead to different permeability values and significant permeability anisotropy even on the same formation [37, 38]. Gas transport in shales is controlled not only by geometry (pore size distribution) but also topology of pores (connectivity, preferential pathways, etc.) [39]. Although some studies have documented the heterogeneities and the pore systems associated with facies in gas shales [30, 40, 41], the effects of microfabric and laminae on gas flow are not yet described in detail.

We report on a suite of shale samples that represent various properties from the Jiaoshiba area, Sichuan Basin, China. This study examines the role of microfabric and laminae on pore space and transport properties of shales. With a combination of imaging observation (petrographic

microscope and scanning electron microscope) and fluid invasion measurements (helium expansion porosimetry, low-pressure  $N_2$  adsorption-desorption, and pulse-decay  $N_2$  tests), petrophysical properties of Longmaxi shales are comprehensively characterized. Pore structures of various shales are qualitatively described. The effects of minerals and microfabric on porosity, PSD, and pore structure of shales are discussed. Furthermore, both the Winland equation and gas permeability measurements are applied to calculate the effective pore diameter. Hereby, controls of microfabric and laminae on gas transport on shales are assessed.

## 2. Geological Background

Jiaoshiba shale gas field, the first commercially developed shale reservoirs in China, is located in the Fuling District, Chongqing Municipality, in the eastern Sichuan Basin (Figure 1). Gas production in the Jiaoshiba shale reservoir is reported to be up to  $50 \times 10^4 \text{ m}^3/\text{day}$  per well [42]. The Jiaoshiba structure is a wide and gentle anticline, constrained by two sets of northeast-trending faults [43–45]. As a part of Sichuan Basin, the Jiaoshiba structure was subjected to multistage tectonic movements during the formation of Yangtze platform [43, 46]. In Late Ordovician–Early Silurian time, the Sichuan Basin transformed from a passive continental margin basin to a foreland basin. Because of the uplift in the southern, central, and eastern boundaries, the Sichuan Basin formed a shelf structure of being open on the northern side. Correspondingly, the sedimentary environment was undercompensated and anoxic in the study area [47–49]. There were two global transgressions at the end of Ordovician period and the beginning of Silurian period [50, 51], which caused the deposition of Ordovician Wufeng–Silurian Longmaxi ( $O_3w-S_1l$ ) shale system. After that, the sea level gradually declined. A mass of terrigenous detrital materials were involved in the middle and late deposition of  $S_1l$  Formation [49].

From the lower to upper sections of  $O_3w-S_1l$  shales, the sedimentary facies transformed gradually from deep-water shelf to shallow-water shelf [52]. The  $O_3w-S_1l$  shales can be approximately divided into three members based on lithological features. The lower member of the Longmaxi shales (including the  $O_3w$  formation), deposited in a deep-water shelf sedimentary environment, is dominated by dark gray and black siliceous shales. A lot of benthic algae, radiolarian, graptolite, and radiolarian fossils are documented in the lower section of Longmaxi shales previously [52], which provide organic matter for siliceous shales [16]. At the same time, the sedimentary environment was anoxic and euxinic when siliceous shales were deposited, which is beneficial to the preservation of organic matter in siliceous shales [47]. The middle part of Longmaxi Formation is basin-slope facies. Compared to the early deposition of Longmaxi shales, the supply of terrigenous clasts at the middle Longmaxi Formation was significantly increased [46, 52]. Consequently, lithological features of the shales gradually converted from siliceous into silt-bearing shales. Silty laminae are developed well in the middle part of Longmaxi shales. The upper section was formed in shallow-water shelf environments [48]. Shales

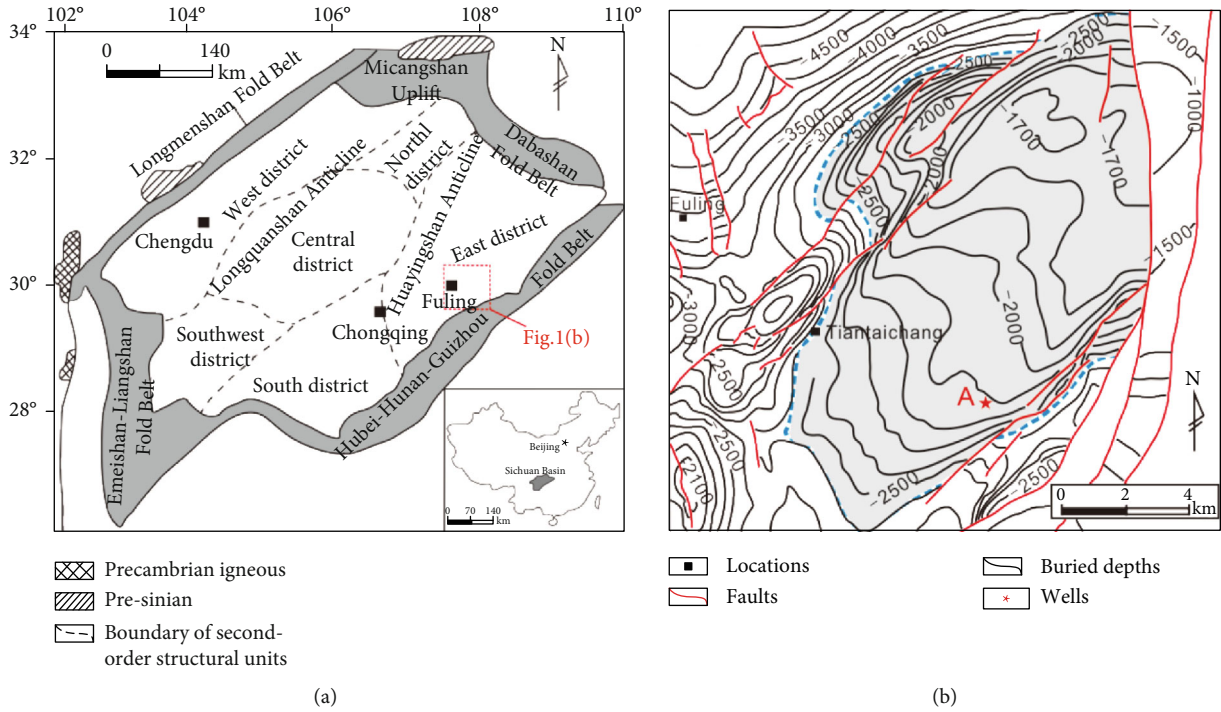


FIGURE 1: Geological structure of the Sichuan Basin (modified after [44]). (a) Location of the study area in Sichuan Basin. (b) Tectonic map of the Jiaoshiba area, the top buried depth map of Longmaxi formation, and sampled shale gas well A.

TABLE 1: Lithofacies, TOC, and mineralogy compositions of the Longmaxi shale samples. TOC and mineral content are presented in weight percent (wt %).

Sample	Depth (m)	Lithofacies	TOC	Quartz	Total feldspar	Carbonates	Pyrite	Total clays	I/S	Illite	Chlorite
JYA-1	2527.8	CM	0.5	33.3	8.6	0.0	1.8	56.3	19.7	11.3	25.3
JYA-2	2531.1	CM	0.3	31.1	6.2	0.0	0.0	62.7	18.8	17.6	26.3
JYA-3	2537.1	CM	0.6	30.5	7.0	2.2	1.5	58.8	21.2	16.5	21.2
JYA-4	2540.5	CM	1.0	32.2	8.1	2.2	1.9	55.6	20.0	16.7	18.9
JYA-5	2543.1	CM	1.4	34.7	4.2	5.0	3.3	52.8	15.8	15.8	21.1
JYA-6	2549.2	M	2.3	32.3	6.0	10.9	3.9	46.9	19.2	10.8	16.9
JYA-7	2551.2	CM	1.5	33.1	3.7	3.7	1.7	57.8	16.8	17.9	23.1
JYA-8	2553.1	CM	1.7	35.3	5.7	2.3	1.5	55.2	17.7	16.6	21.0
JYA-9	2563.1	M	1.4	37.4	8.2	10.0	3.0	41.4	17.4	14.9	9.1
JYA-10	2563.4	M	2.0	38.1	7.6	9.1	4.0	41.2	14.4	14.4	12.4
JYA-11	2569.3	M	1.4	35.9	9.7	11.7	1.9	40.8	16.7	11.4	12.6
JYA-12	2579.4	M	2.3	37.2	6.2	5.9	2.2	48.5	17.5	15.5	15.5
JYA-13	2582.0	S	2.5	38.4	9.3	11.9	5.5	34.9	12.2	16.1	6.6
JYA-14	2585.4	S	3.1	40.6	7.6	9.8	5.1	36.9	19.2	11.4	6.3
JYA-15	2587.2	S	3.0	44.7	7.2	6.8	4.1	37.2	18.2	14.1	4.8
JYA-16	2593.0	M	1.4	30.6	7.5	36.6	3.4	21.9	10.7	7.0	4.2
JYA-17	2594.0	S	2.6	41.3	7.0	13.9	4.0	33.8	15.6	11.8	6.4
JYA-18	2597.3	S	3.0	47.1	7.2	12.6	6.6	26.5	13.0	10.3	3.2
JYA-19	2600.1	S	3.0	45.2	7.9	14.5	4.0	28.4	13.6	11.1	3.7
JYA-20	2603.3	S	3.0	38.5	12.9	19.4	4.9	24.3	10.5	11.2	2.7
JYA-21	2606.2	S	4.0	53.2	10.5	7.3	3.8	25.2	13.6	8.8	2.8
JYA-22	2612.2	S	4.4	49.3	8.10	6.3	4.3	32.0	16.3	14.1	1.6
JYA-23	2615.3	S	5.3	58.4	3.50	8.1	5.5	24.5	13.2	8.3	2.9

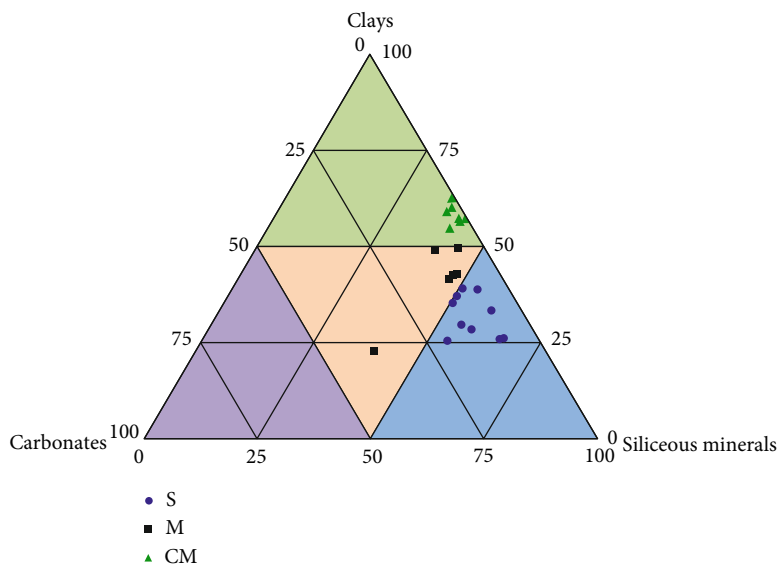


FIGURE 2: Ternary diagram of the mineralogy of the Silurian shale samples. Shale samples were classified into three groups: siliceous shale lithofacies (S), argillaceous/siliceous/calcareous mixed shale lithofacies (M), and silica-rich argillaceous shale lithofacies (CM).

in the upper section are dominated by light gray mudstones and siltstones [52]. The variability of lithology from the lower to the upper member of the Longmaxi shales in Jiaoshiba area offers a suitable case for assessing the relationship between shale lithofacies and reservoir characteristics. The Longmaxi Formation in the Jiaoshiba area varies in thickness from 60 to 150 m. Longmaxi shales with the vitrinite reflectance equivalent values being higher than 2.0% are highly overmatured [25, 47].

### 3. Experimental Section

**3.1. Sample Preparation.** Marine shale samples were collected from the lower to upper section of Longmaxi Formation. Twenty-three samples with depth ranging from 2527.8 to 2615.3 m were obtained from a shale gas well drilled in the Jiaoshiba shale gas field (Table 1). Samples were selected to cover the variability of total organic carbon (TOC), inorganic minerals composition, and shale lithofacies. 21 cylindrical plugs with 25–40 mm in length and 25.4 mm (1 inch) in diameter were drilled parallel to the bedding, and 8 plugs were drilled perpendicular to bedding. Cylindrical plugs were dried in a vacuum oven (105°C) for at least 12 h before porosity and permeability measurements. Petrologic and scanning electron microscope analyses were carried out on subsamples (fragments). Mineralogical components, TOC content, and low-pressure nitrogen adsorption-desorption analyses were performed on dry particles (0.15 mm particle size).

**3.2. Imaging Methods.** Petrologic observations were conducted on polished thin sections to analyze the rock fabric, texture, microorganism, and mineralogy. Polished thin sections with thickness between 0.02 and 0.06 mm were prepared and photographed using a Leica DMRX microscope.

Visual pore structure was observed on a Zeiss Merlin Compact field emission-scanning electron microscope (FE-

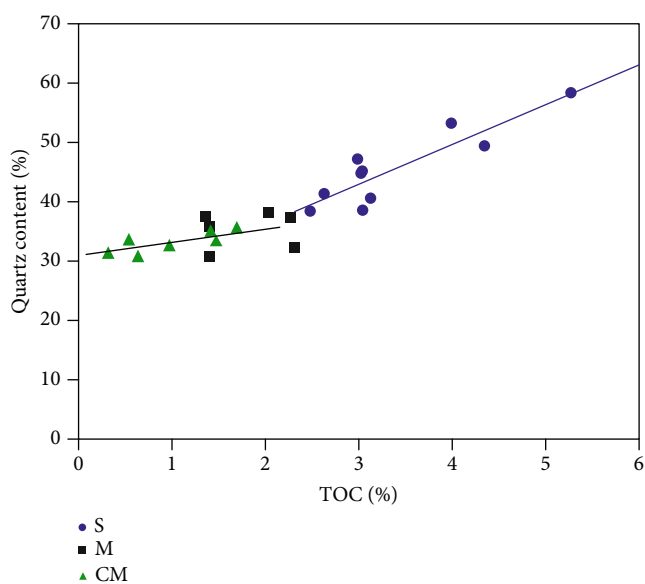


FIGURE 3: Relationship between TOC content and quartz content of shale samples. There is obviously a stronger positive relationship between TOC content and quartz content in organic-rich siliceous shale lithofacies (S) samples.

SEM). This apparatus is equipped with backscattered electron (BSE) and secondary electron (SE) detectors and achieves the highest pixel resolution of about 0.8 nm at 15 kV operating voltage. Shale samples were ion polished and coated with gold before the visual observations.

**3.3. Low-Pressure Low-Temperature Nitrogen (N<sub>2</sub>) Adsorption.** Low-pressure N<sub>2</sub> adsorption-desorption experiments at -196°C (77 K) were performed to obtain information about the specific surface area, pore size distribution (PSD), and pore volume. Powder shales were first degassed



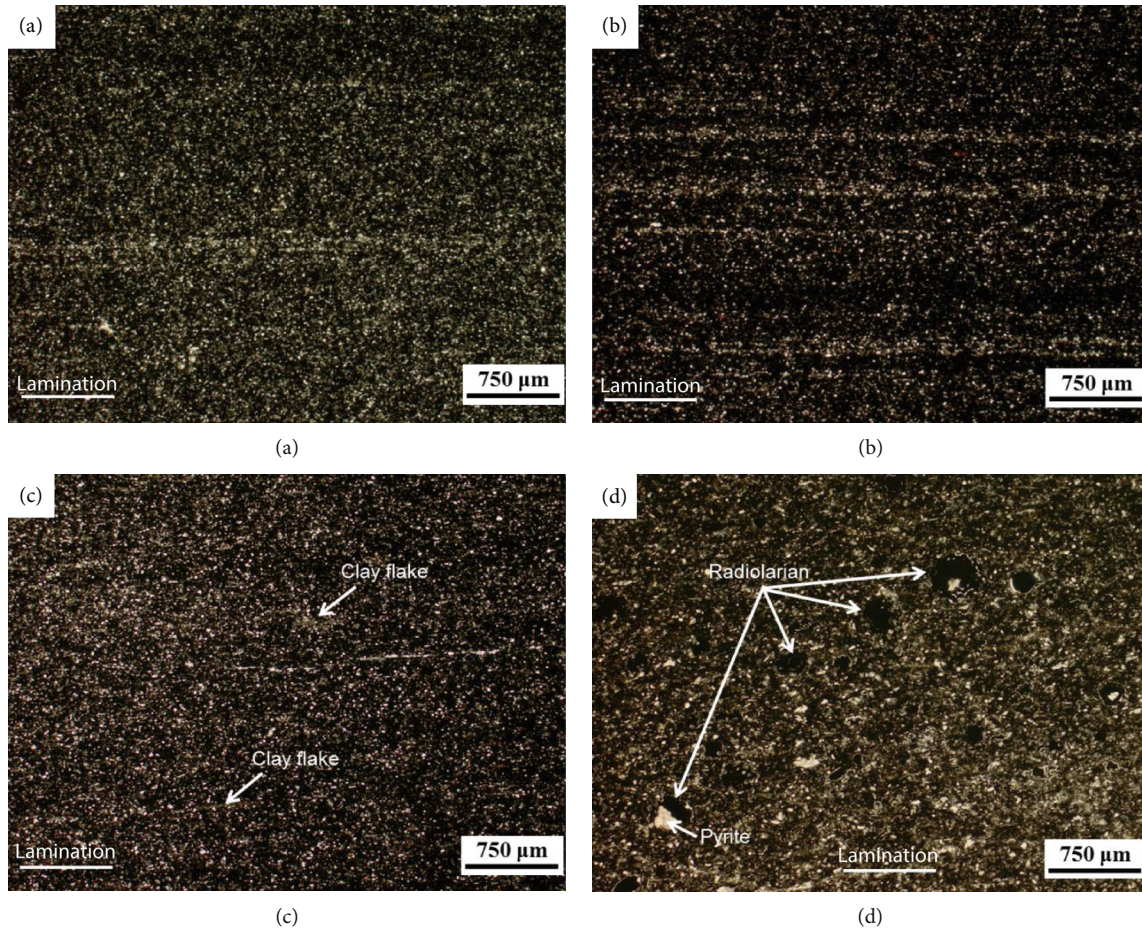


FIGURE 4: Transmitted light thin section images of siliceous shale lithofacies (S). (a) Faint laminae of silty quartz. JYA-17,  $K_h = 24.4 \mu\text{D}$ , 2594.03 m. (b) Slight laminae of silty quartz. Mixed organic matter and clays (black) distributed between the laminae. JYA-18,  $K_h = 14.95 \mu\text{D}$ , permeability anisotropy ( $\beta$ ) = 9.3, 2597.3 m. (c) No obvious lamina is observed. Miniature lenticular clay flakes distributed along the lamination. JYA-22,  $K_h = 0.4 \mu\text{D}$ , permeability anisotropy ( $\beta$ ) = 1.3, 2612.2 m. (d) Nonlaminated siliceous shale. Abundant radiolarians are observed. Some radiolarians are replaced by pyrite. JYA-23, 2615.29 m.

overnight at 105°C in a vacuum chamber.  $\text{N}_2$  adsorption and desorption isotherms were obtained by collecting adsorption data on degassed samples at a pressure up to 730 mm Hg. The nitrogen adsorption data were interpreted to obtain specific surface area and PSD according to Brunauer-Emmett-Teller (BET) and Barrett-Joyner-Halenda (BJH) theories [53].

**3.4. Helium Pycnometry and Gas Permeability.** Helium pycnometry was applied on dried cylindrical plugs to determine the skeletal density ( $\rho_{\text{skeletal}}$ ). The bulk density ( $\rho_{\text{bulk}}$ ) of these plugs was measured from the geometric dimensioning of cylindrical plugs using a caliper and the weight of samples. Then, porosity values ( $\phi$ ) under unconfined conditions were determined from the bulk density and skeletal density values according to  $\phi = 1 - \rho_{\text{bulk}}/\rho_{\text{skeletal}}$ .

Gas permeability coefficients were measured on dried cylindrical samples using  $\text{N}_2$  as measuring gas at room temperature. Sample plugs were placed in a customer-designed pulse-decay permeameter (PDP-200, Core Lab) at a selected confining pressure of 2000 PSI. Small pressure pulses of about 0.5–1.0 MPa were introduced to the upstream reservoir, and the pressures of the upstream and downstream reservoirs

were monitored with high-precision pressure transducers. Different average pore pressures are obtained via introducing several small-pressure pulses. The nonsteady-state nitrogen permeability at different pore pressures was determined using a linear regression performed on the pressure time data according to the fundamental flow equations [37]. The measured nitrogen permeability was corrected using the Klinkenberg method based on the permeability values at different pore pressures [29].

## 4. Results

**4.1. Mineralogy and TOC Content.** Mineralogy compositions of the studied Longmaxi samples are illustrated in Figure 2. The Jiaoshiba shale samples mainly consist of quartz (30.5–58.4%) and clay minerals (21.9–62.7%) with a minor amount of plagioclase (3.5–9.9%), dolomite (0–32.2%), calcite (0–8.4%), pyrite (0–6.6%), and potassium feldspar (0–3.0%). These agree with the results of other studies, showing that quartz and clays are the most common minerals in the Jiaoshiba shales [47]. In general, quartz content in our samples decreases from the bottom to top Longmaxi Formation



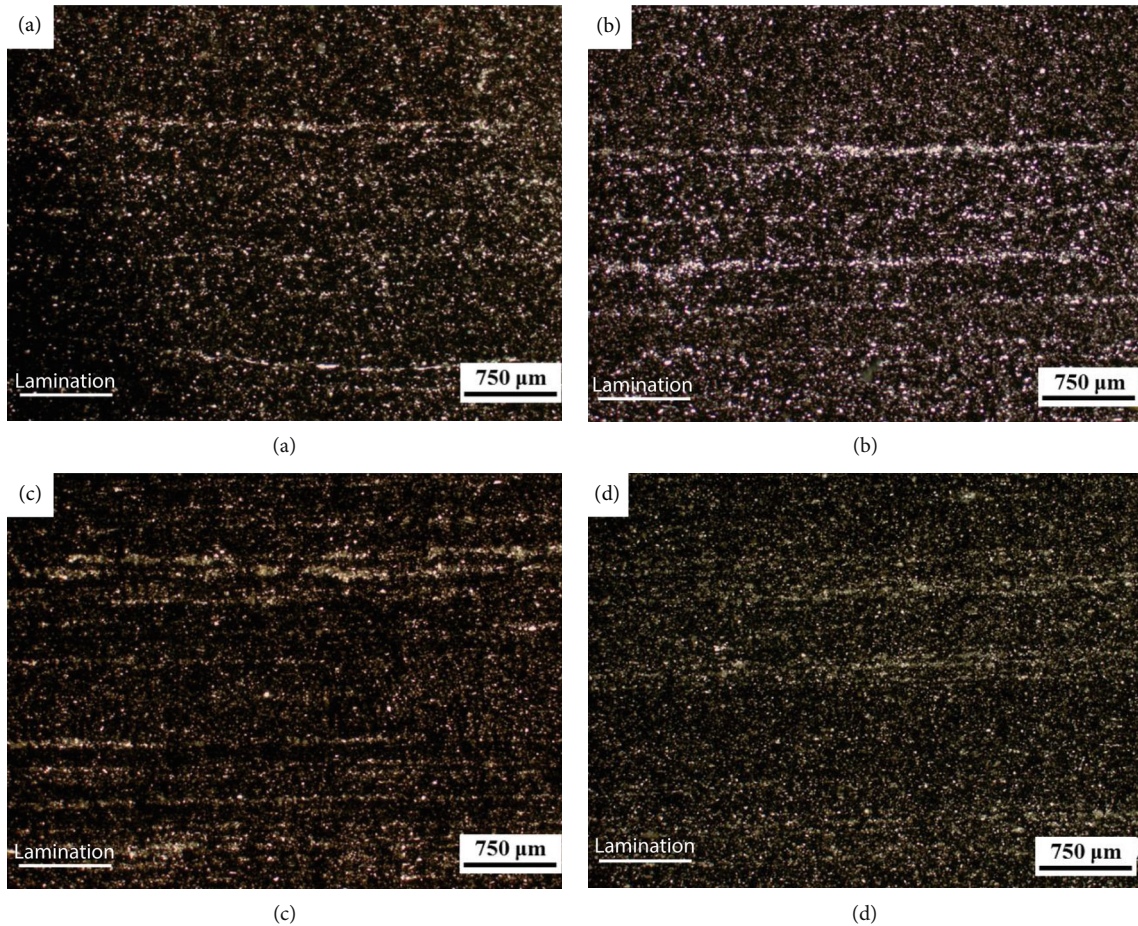


FIGURE 5: Transmitted light thin section images of argillaceous/siliceous mixed shale lithofacies (M). (a) Laminae of silty quartz. JYA-6,  $K_h = 25.9 \mu\text{D}$ , permeability anisotropy ( $\beta$ ) = 2.9, 2549.19 m. (b) Laminae of silty quartz. JYA-10,  $K_h = 68.2 \mu\text{D}$ , permeability anisotropy ( $\beta$ ) = 8.9, 2563.4 m. (c) Well-laminated fabric. Mixed organic matter and clays distributed between the laminae. JYA-11,  $K_h = 14.2 \mu\text{D}$ , 2569.28 m. (d) Slight laminae of silty quartz. JYA-16,  $K_h = 11.3 \mu\text{D}$ , 2593.02 m.

whereas clay minerals present a reverse trend (Table 1). TOC content in our data set ranges from 0.3 to 5.3 wt.% with a mean value of 2.2 wt.% (Table 1). TOC content is relatively higher in the lower member of Longmaxi Formation. There is a positive correlation between quartz and TOC content (Figure 3). The positive correlation is due to that the quartz in the lower part of Longmaxi Formation is mainly of biogenic origin [20].

**4.2. Types of Shales.** Lithofacies record geological information about the rock types, texture, bedding, mineral compositions, grain size distribution, and sorting and roundness characteristics [40, 41]. Initially, lithofacies were mainly applied to analyze the mineralogy and petrology of conventional reservoirs [54]. Since the shale gas development is active, lithofacies were introduced to unconventional reservoirs [24, 41]. Shale lithofacies comprehensively describe reservoir characteristics and quality [41]. Based on the mineralogy composition, shales can be divided into siliceous shales (siliceous minerals content > 50%), argillaceous/siliceous mixed shales (siliceous, carbonate, and clay minerals content is less than 50%, respectively), and argillaceous shales (total clays content > 50%) (Figure 2 and Table 1).

**4.2.1. Siliceous Shales.** Siliceous shales (S) are mainly found in the lower member of Longmaxi Formation (Table 1). Siliceous shale samples are rich in quartz and relatively low in clay minerals. In siliceous shales, the content of siliceous minerals ranges from 50.3% to 66.2% with a mean value of 56.5%. The total clay mineral content ranges from 25.6% to 38.9% with an average of 31.9%. Illite-smectite (I/S) mixed clay minerals represent the major components of clay minerals (range from 10.5% to 19.2% with an average of 14.5%), followed by illite (range from 8.3% to 16.1% with an average of 11.7%) and chlorite (averages 4.1%). Siliceous shale samples are commonly rich in pyrite. Pyrite in siliceous shales exhibits an average of 4.8% (ranges from 3.8% to 6.6%).

Thin sections of siliceous shales show that the fabric of siliceous shales ranges from faintly laminated to nonlaminated with increasing depth (Figure 4). Abundant radiolarians are observed in siliceous shales (Figure 4(d)). Some radiolarians are replaced by pyrite. Most of the quartz particles in siliceous shales are silt-sized scale. Clays are dyed by organic matter and scattered in the minerals. Only minor lenticular clay flakes are observed along the lamination (Figure 4(c)). Siliceous shales are TOC-rich. Siliceous shales have TOC content ranging from 2.5% to 5.3% (average 3.4%).



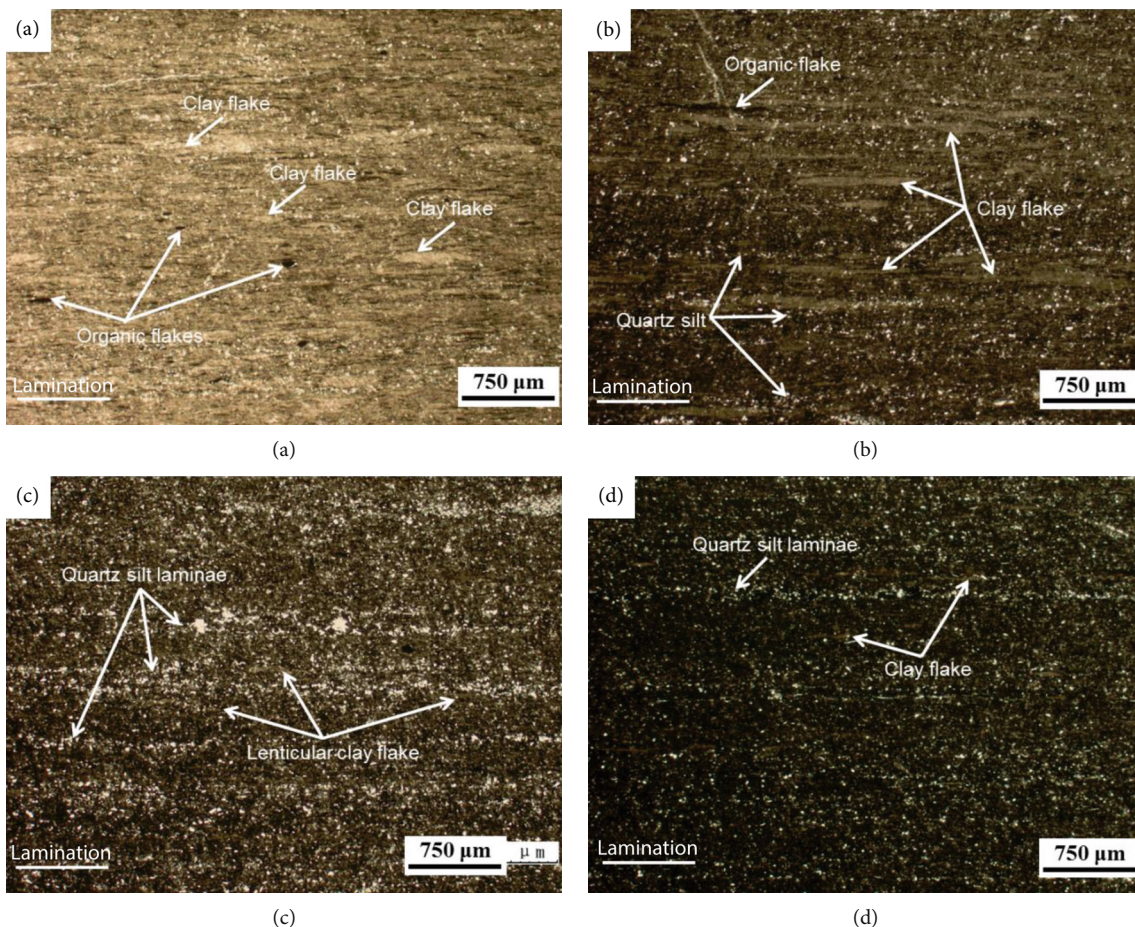


FIGURE 6: Transmitted light thin section images of silica-rich argillaceous shale lithofacies (CM). (a) Long striped clay flakes distributed along the lamination. Minor organic flakes are intermittent along the lamination. No obvious laminae of silty quartz are observed. JYA-2,  $K_h = 76.6 \mu\text{D}$ , permeability anisotropy ( $\beta$ ) = 13.4, 2531.09 m. (b) Long striped and lenticular clay flakes distributed along the lamination. Organic flake along the lamination is observed. Clay flakes are dyed by organic matters. Minor laminae of silty quartz are intermittently along the lamination. JYA-3,  $K_h = 64.7 \mu\text{D}$ , permeability anisotropy ( $\beta$ ) = 49.8, 2537.09 m. (c) Intermittent laminae of silty quartz. Miniature lenticular clay flakes are along the lamination. JYA-4,  $K_h = 2.0 \mu\text{D}$ , 2540.47 m. (d) Slight laminae of silty quartz. Miniature lenticular clay flakes are along the lamination. JYA-8,  $K_h = 7.8 \mu\text{D}$ , permeability anisotropy ( $\beta$ ) = 10.6, 2553.09 m.

**4.2.2. Argillaceous/Siliceous Mixed Shales.** Argillaceous/siliceous mixed shales (M) are mainly distributed in the middle section of Longmaxi Formation (Table 1). This kind of shales is characterized by the moderate siliceous and clay mineral contents. In this kind of shale lithofacies, siliceous mineral content is between 39.4% and 47.6% (averages 44.1%), while total clay mineral content varies between 22.7% and 50.0% (averages 41.4%). Mass contents of I/S mixed clay minerals (averages 16.0%), illite (averages 12.3%), and chlorite (averages 11.8%) are comparable in mixed shales.

The argillaceous/siliceous mixed shales (M) are well laminated (Figure 5). The laminae mainly consist of silty quartz. The width of laminae ranges from 0.01 to 0.40 mm. Clays in argillaceous/siliceous mixed shales are commonly dyed by organic matter. TOC content of the mixed Longmaxi shales is between 1.4% and 2.3% with a mean value of 1.8%.

**4.2.3. Argillaceous Shales.** The argillaceous shales (CM) are the predominant lithofacies in the upper section of Longmaxi Formation (Table 1). This kind of shales is characterized by

the highest content of total clays and the lowest content of quarts. The total clay mineral content in CM shales studied varies from 54.6% to 62.7% (averages 58.0%), whereas the siliceous mineral content ranges between 37.3% and 42.7% (averages 39.8%). Chlorite is the highest content of clay minerals in CM shales. Chlorite exhibits a mean of 22.4% (ranges from 18.9% to 26.3%), and I/S mixed clay minerals average 18.6% (ranges from 15.8% to 21.2%). Slight of pyrite is found in CM shales (averages 1.6%).

Thin sections of CM shales show nonlaminae to intermittent laminae (Figure 6). In argillaceous shales, many long striped and large lenticular clay flakes are oriented along the lamination. Minor organic flakes are also found in CM shales (Figure 6(a)). Quartz is either scattered in the minerals (Figures 6(a) and 6(b)) or exhibits intermittent laminae (Figures 6(c) and 6(d)). TOC content of CM shales is really low and ranges from 0.3% to 1.7% (averages 1.0%).

**4.3. Visual Pore Structure.** FE-SEM imaging experiments were conducted on selected Longmaxi shales representing

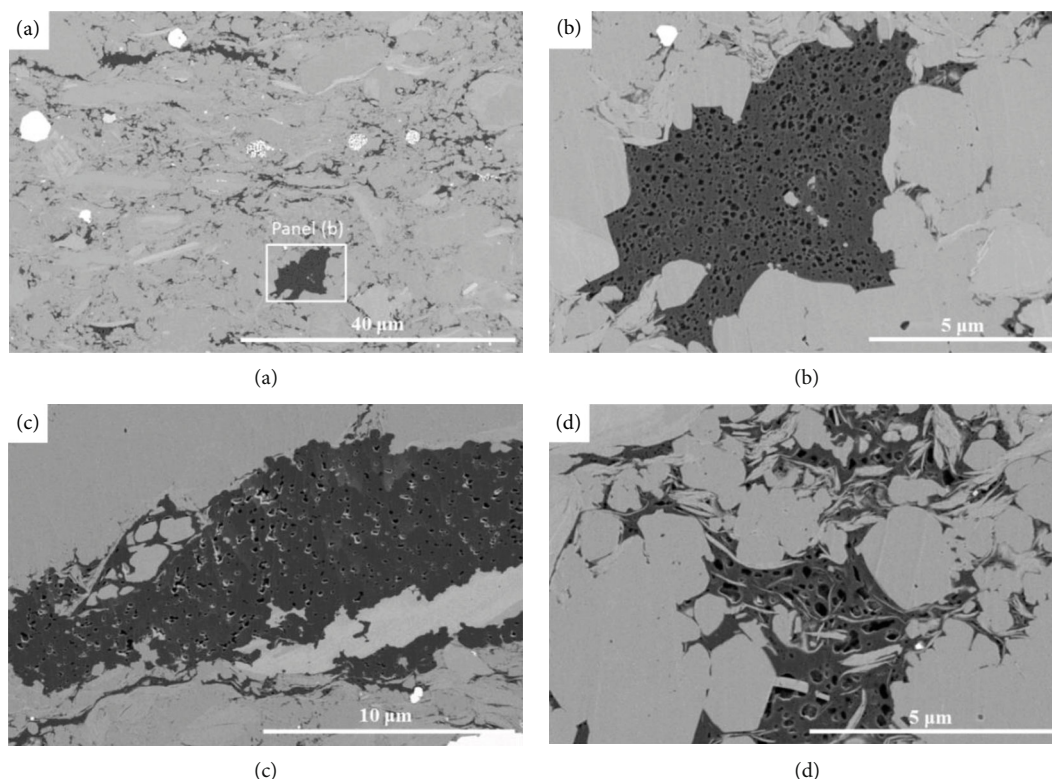


FIGURE 7: FE-SEM images of siliceous shales (S). (a) Back-scattered electron of siliceous shale lithofacies. (b) Ellipsoid pores in spongy organic matter particles. (c) Abundant pores in spongy organic matter particles. (d) Abundant mesomacropores in organic matter particles.

different kinds of shale lithofacies. Many organic matter (OM) particles in siliceous shales are spongy (Figure 7). The diameter of OM particles varies from several to dozens of micrometers (Figures 7(b) and 7(c)). Among them, abundant OM-hosted pores with a diameter of several to hundreds of nanometers are developed. The OM-hosted pores are commonly ellipsoid (Figures 7(c) and 7(d)). A certain amount of irregularly polygonal pores can also be observed in siliceous shales (Figure 7(d)).

In mixed shales (M), OM particles are dispersed and commonly captured in the pore spaces among rigid framework minerals (Figure 8). A handful of OM-hosted pores can be found in these residual organic matters (Figures 8(c) and 8(d)). OM particles with large volume occur in argillaceous/siliceous mixed shales, but pores are less developed in these bulky OM particles (Figure 8(b)). Apparently, these bulky OM particles are difficult to be thermally decomposed or migrated. Dissolution pores are commonly found in argillaceous/siliceous mixed shales (Figures 8(c) and 8(d)). These dissolution pores appear to be so scattered that they are probably less connected. Dissolution-related pores/rims develop among the boundaries of feldspar grains (Figure 8(c)).

When it comes to CM shales, the amount of silty with large particles becomes less than that in mixed shales (M). Clay minerals are really common in the field of vision (Figure 9). Most clay flakes are oriented along the lamination (Figure 9(a)). There are many intraparticle pores in clay flakes, and these pores can be enhanced by bending/splitting related to compaction (Figure 9(c)). A spot of organic matter

is captured in the corners of framework minerals (Figure 9(c)). However, these residual organic matters are either nonporous or less porous. Kerogen-clay aggregates are commonly observed and parallel with lamination (Figure 9(d)). However, many pore spaces in kerogen-clay aggregates are unobservable due to strong postcompaction. Large OM particles with smooth surface can be observed occasionally, but OM pores are unobservable in these OM particles under the resolution of FE-SEM (Figure 9(b)).

**4.4. Porosity, Pore Size Distribution, and Pore Structure Parameters.** Porosity of the Longmaxi shales studied ranges from 1.5% to 7.1% and averages 3.7% (Table 2). The porosity values of shale samples are associated with shale lithofacies. Siliceous shales generally show higher porosity values than other shales (Figure 3). Porosity of siliceous shales is between 3.4% and 7.1% with an average of 4.9%. Porosity of mixed shales ranges between 1.9% and 3.3% (averages 2.4%), whereas the porosity of argillaceous shales ranges from 1.5% to 4.3% (averages 3.1%). Positive relationships exist among TOC content, siliceous mineral content, and porosity values of the Longmaxi shales studied (Figure 10).

Low-pressure  $N_2$  adsorption-desorption isotherms for the Longmaxi Formation samples are shown in Figure 11. Samples rich in organic matter generally adsorb the high amount of nitrogen. What is more, siliceous shale samples obviously adsorb a higher amount of  $N_2$  than other samples (Figure 11(a)). All these Longmaxi shales exhibit hysteresis loops, formed by the divergence between adsorption and



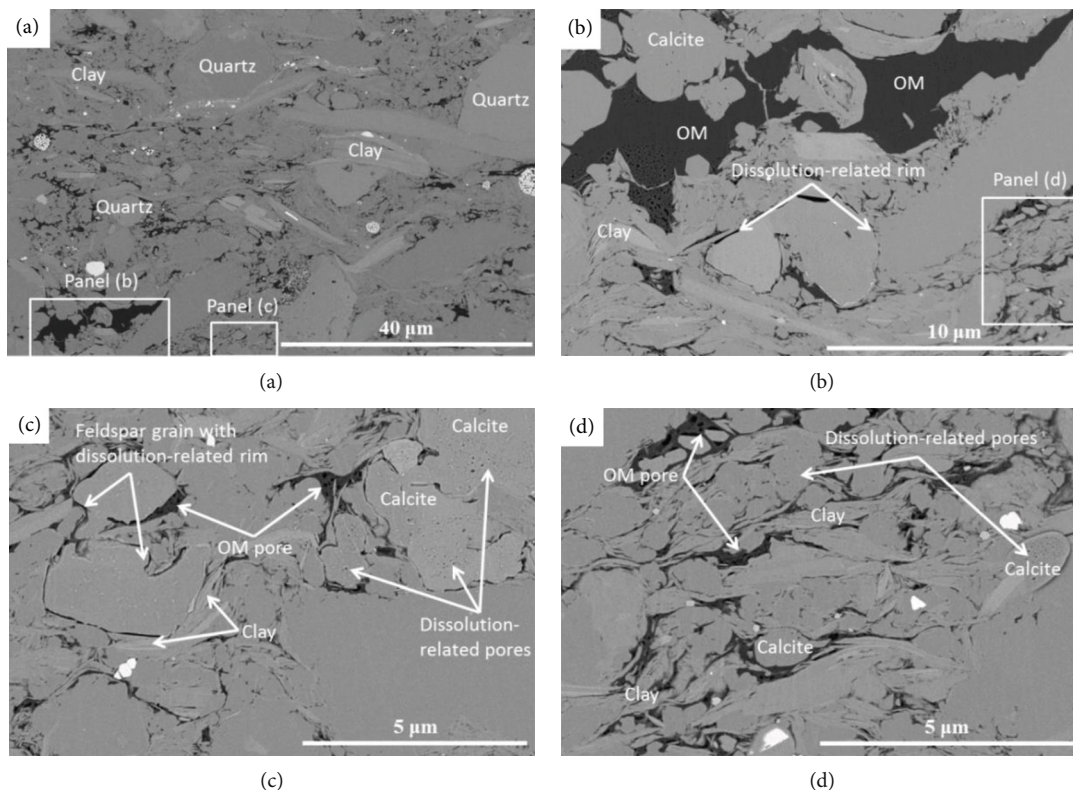


FIGURE 8: FE-SEM images of argillaceous/siliceous mixed shales (M). (a) Back-scattered electron of argillaceous/siliceous mixed shale lithofacies. There are many silt-sized quartz particles in argillaceous/siliceous mixed shale sample. (b) Large OM particles in argillaceous/siliceous mixed shale, but pores are less developed. (c) Dissolution-related rims in the boundary of feldspar. Dissolution-related pores in calcite are less connected. (d) OM-hosted pores in the residual OM particles.

desorption branches. It is interesting to observe that the areas of hysteresis loops on siliceous shales (S) are generally higher than that of mixed (M) and argillaceous shales (CM). According to the physical adsorption theory, the shape of hysteresis loop is associated with the complexity of pore structure [53]. Large hysteresis loops qualitatively indicate that pores of the materials are mainly ink-bottle-shaped or amorphous. The pore structure of siliceous shales are much more complicated than other samples, which are probably related with the high TOC content of siliceous shales [16].

The adsorption branches of nitrogen adsorption isotherms were used to calculate the PSD. All the samples exhibit broad PSDs ranging from micropores to mesopores and macropores (Figure 11). PSD of these Longmaxi shales are dominantly bimodal. There is one maximum in the microporous ranges of PSDs. The other maximum is in the 2–3 nm on the PSDs. Comparing the peaks of different shales, it is found that the first peak in the micropore range of siliceous shales (S) is obviously higher than others, whereas the second peak of mixed (M) and argillaceous shales (CM) is slightly higher than siliceous shales (S).

Pore structure parameters measured by  $N_2$  adsorption on the Longmaxi shales are summarized in Table 2. BET-specific surface areas of the Longmaxi shales vary from 9.7 to 26.9  $m^2/g$ , with a mean value 17.0  $m^2/g$ . The total pore volumes vary from 0.011 to 0.033  $cm^3/g$ . Both specific surface areas (SSA) and pore volumes of siliceous Longmaxi shales

are higher than those of mixed (M) and argillaceous (CM) Longmaxi shales. The total pore volume of S, M, and CM shales averages as 0.023, 0.017, 0.015  $cm^3/g$ , respectively. TOC content shows obviously positive linear relationships with both the BET SSA and pore volume (Figures 12(a) and 12(b)), indicating that the pore structure of organic-rich marine shales is controlled by organic matter. The intercept of these linear fitting is approximately 9  $m^2/g$  and 0.01  $cm^3/g$  (Figures 12(a) and 12(b)), which is related to the inorganic matter. A moderate positive correlation exists between siliceous mineral content and pore structure parameters (Figures 12(c) and 12(d)). Negative relationship exists between clay mineral content and pore structure parameters of the Longmaxi shales (Figures 12(e) and 12(f)).

**4.5. Permeability and Permeability Anisotropy.** Gas permeability values of overall 29 core plugs were determined. Among them, twenty-one samples were drilled parallel to bedding and eight plugs were perpendicular to bedding. Parallel to bedding, the Klinkenberg-corrected nitrogen permeability (intrinsic permeability) values measured using the pulse-decay permeameter on the confining pressure of 2000 psi ranging from 0.4 to 76.6  $\mu D$  ( $10^{-18} m^2$ ) (Table 2). The Klinkenberg-corrected permeability values measured parallel to bedding ( $K_h$ ) of siliceous shales are generally lower than those of other shales. The average  $K_h$  of the Longmaxi shales studied decrease in a descending order: argillaceous

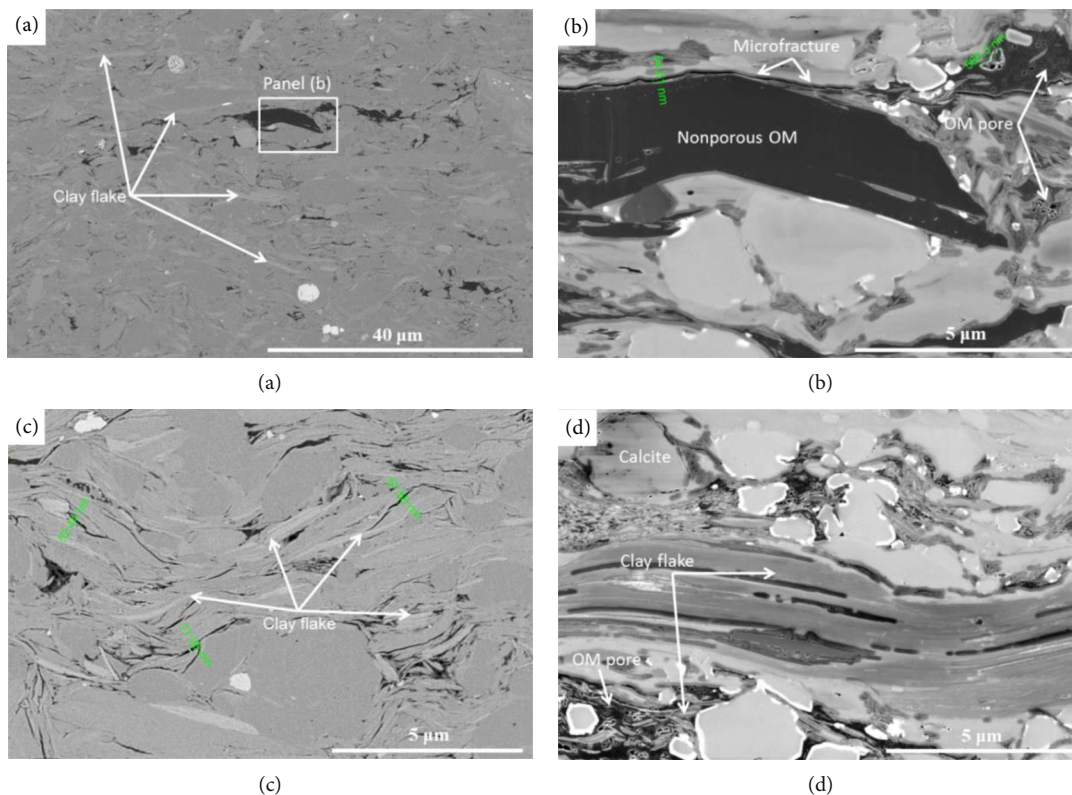


FIGURE 9: FE-SEM images of silica-rich argillaceous shales (CM). (a) Back-scattered electron of silica-rich argillaceous shales. Abundant clay flakes are commonly oriented along the lamination. (b) Nonporous organic matter particles in silica-rich argillaceous shale. There is microfracture between organic matter particle and framework minerals. (c) Intraparticle pores are observed in clay flakes. (d) Pores in oriented kerogen-clay aggregates.

shales ( $37.6 \mu\text{D}$ ) > mixed shales ( $24.4 \mu\text{D}$ ) > siliceous shales ( $8.2 \mu\text{D}$ ). The permeability measured perpendicular to bedding ( $K_v$ ) of these samples ranges between 0.3 to  $8.9 \mu\text{D}$ . Permeability anisotropy values show large variations and range from 1.3 to 49.8. The permeability anisotropy is related to the fabrics and mineralogy of the samples (Figures 4, 5, and 6). The  $K_h$  of argillaceous shales are generally more than one order of magnitude higher than that measured perpendicular to bedding (Table 2). Furthermore, samples rich in laminated fabric always show high permeability anisotropy (Figure 4).

Gas slippage factors for nitrogen on these shales range from 0.04 to 0.88 MPa. Gas slippage factors of siliceous shales are larger than argillaceous shales. The slippage factors of siliceous minerals range from 0.14 to 0.26 MPa, while those of argillaceous shales are between 0.07 to 0.14 MPa.

## 5. Discussion

**5.1. The Effect of Minerals and Microfabric on Pore Structure.** Mineralogical controls on pore spaces have been extensively investigated on both marine and lacustrine shales [12, 16]. Generally, there is a positive correlation between porosity and TOC content of many mature and overmature shale systems [16]. Similarly, porosity of the Longmaxi shales in our data set is positively related to TOC content. The average porosity related to inorganic matter is estimated as 1.7%

according to the interception of the linear relationship (Figure 10(a)). The positive correlation between TOC content and porosity of Longmaxi shales studied underlines the key role of organic matter on pore spaces of overmatured marine shales. With increasing TOC content, peaks in the microporous range in PSD of Longmaxi shales are higher (Figure 11(b)). TOC content also shows an obviously positive relationship with BET SSA of Longmaxi shales studied (Figure 12(a)).

Further investigations reveal that porosity of shale samples is associated with the types of shales. Porosity of siliceous shales (averages 4.9%) is commonly larger than mixed shales (averages 2.4%) and argillaceous shales (averages 3.1%) (Table 2). High porosity values of siliceous shales (S) are ascribed to high TOC content (Figure 7). However, inorganic matter contributes a lot to the pore space of mixed shales (M) and argillaceous shales (CM). For argillaceous/siliceous mixed shales, dissolution-related porosity is commonly observed in feldspars and carbonates. Dissolution-related pores occur as intraparticle pores in feldspars and carbonate grains or interparticle pores at the rims of carbonates (Figure 8). This kind of pore mainly forms by the dissolution of organic acidic during the process of hydrocarbon generation [15, 16]. Moreover, silty quartz and carbonates occur in laminae as clasts (Figure 5) and serve as rigid skeleton to support matrix. Interparticle pores exist between soft organic matter and rigid clasts (Figure 8). These kinds



TABLE 2: Pore structure, porosity, permeability, and permeability anisotropy ( $\beta$ ) of the shale samples.

Sample	Lithofacies	Porosity (%)	BET SSA (m <sup>2</sup> /g)	Pore volume (mL/g)	Pore diameter <sup>a</sup> (nm)	$K_h$ ( $\mu$ D)	$K_v$ ( $\mu$ D)	Permeability anisotropy ( $\beta$ )	Slippage factor (MPa)	Transport pore diameter <sup>b</sup> (nm)	$2r_{p35}$ <sup>c</sup> (nm)
JYA-1	CM	2.1	10.1	0.0115	4.5	22.13	—	—	0.05	569	686
JYA-2	CM	1.5	9.7	0.0114	4.7	76.64	5.70	13.4	0.04	787	1386
JYA-3	CM	2.0	12.7	0.0133	4.2	64.70	1.30	49.8	0.04	826	1133
JYA-4	CM	4.2	14.0	0.0151	4.3	2.04	—	—	0.14	218	172
JYA-5	CM	4.3	14.1	0.0161	4.5	52.10	—	—	0.05	589	732
JYA-6	M	2.1	18.5	0.0190	4.1	25.92	8.90	2.9	0.12	269	740
JYA-7	CM	4.3	16.4	0.0178	4.3	—	—	—	—	—	—
JYA-8	CM	3.5	17.4	0.0186	4.3	7.76	0.73	10.6	0.10	322	342
JYA-9	M	3.3	14.5	0.0169	4.6	1.17	—	—	0.39	80	150
JYA-10	M	1.9	15.0	0.0171	4.5	68.20	7.63	8.9	0.03	983	1186
JYA-11	M	3.0	11.9	0.0150	5.0	14.22	—	—	0.13	246	481
JYA-12	M	2.4	18.7	0.0213	4.5	25.35	—	—	0.07	463	690
JYA-13	S	4.3	18.9	0.0211	4.5	7.53	—	—	0.16	256	307
JYA-14	S	5.0	20.6	0.0223	4.3	7.01	—	—	0.26	158	276
JYA-15	S	5.4	21.2	0.0244	4.6	10.96	—	—	0.14	305	326
JYA-16	M	1.9	10.8	0.0117	4.3	11.25	—	—	0.10	315	532
JYA-17	S	3.9	16.1	0.0196	4.9	24.41	—	—	0.14	294	545
JYA-18	S	3.4	18.4	0.0218	4.7	14.95	1.60	9.3	0.14	290	466
JYA-19	S	4.0	18.7	0.0210	4.5	1.09	—	—	0.37	111	133
JYA-20	S	4.4	18.7	0.0196	4.2	4.77	1.38	3.5	0.25	169	248
JYA-21	S	7.1	21.5	0.0229	4.3	2.33	—	—	0.34	120	145
JYA-22	S	5.8	26.8	0.0334	5.0	0.40	0.30	1.3	0.51	81	71
JYA-23	S	5.9	26.9	0.0254	3.7	—	—	—	—	—	—

<sup>a</sup>The average pore diameter was determined by low-pressure N<sub>2</sub> adsorption analysis. <sup>b</sup>The transport pore diameter was derived from gas slippage measurement on parallel to bedding samples. <sup>c</sup>The dominant pore-throat aperture ( $r_{p35}$ ) was estimated using the Winland equation [59].

of interparticle pores occur as preferable transport pathways for bitumen and gas.

Argillaceous shales have specific microfibrils. In argillaceous shales, clay minerals are deformed (Figure 9(c)). Intraparticle pores are situated along cleavage planes of clay flakes and enhanced by bending/splitting related to compaction. Interparticle pores also exist between soft clay flakes and rigid clasts (Figure 9(c)). The inorganic-porosity seems to be reflected in the PSD. The peaks in 2–3 nm range of mixed (M) and argillaceous shales (CM) are higher than those of siliceous shales (Figures 11(b), 11(d), and 11(f)), which is likely contributed by clay minerals [55].

Linear combination is a useful tool to quantitatively assess the petrophysical properties of rocks [12, 25]. Total porosity of shales can be viewed as the sum of porosity values related to OM, framework minerals, and total clay minerals:

$$\phi = \rho_{\text{bulk}} \cdot [w_{\text{OM}} \cdot \bar{v}_{\text{OM}} + w_{\text{Framework}} \cdot \bar{v}_{\text{Framework}} + w_{\text{Clay}} \cdot \bar{v}_{\text{Clay}}] \quad (1)$$

Here,  $w_{\text{OM}}$ ,  $w_{\text{Framework}}$ , and  $w_{\text{Clay}}$  are the mass fractions of OM, framework minerals (quartz, carbonates, pyrite, etc.), and total clays, respectively;  $\bar{v}_{\text{OM}}$ ,  $\bar{v}_{\text{Framework}}$ , and  $\bar{v}_{\text{Clay}}$

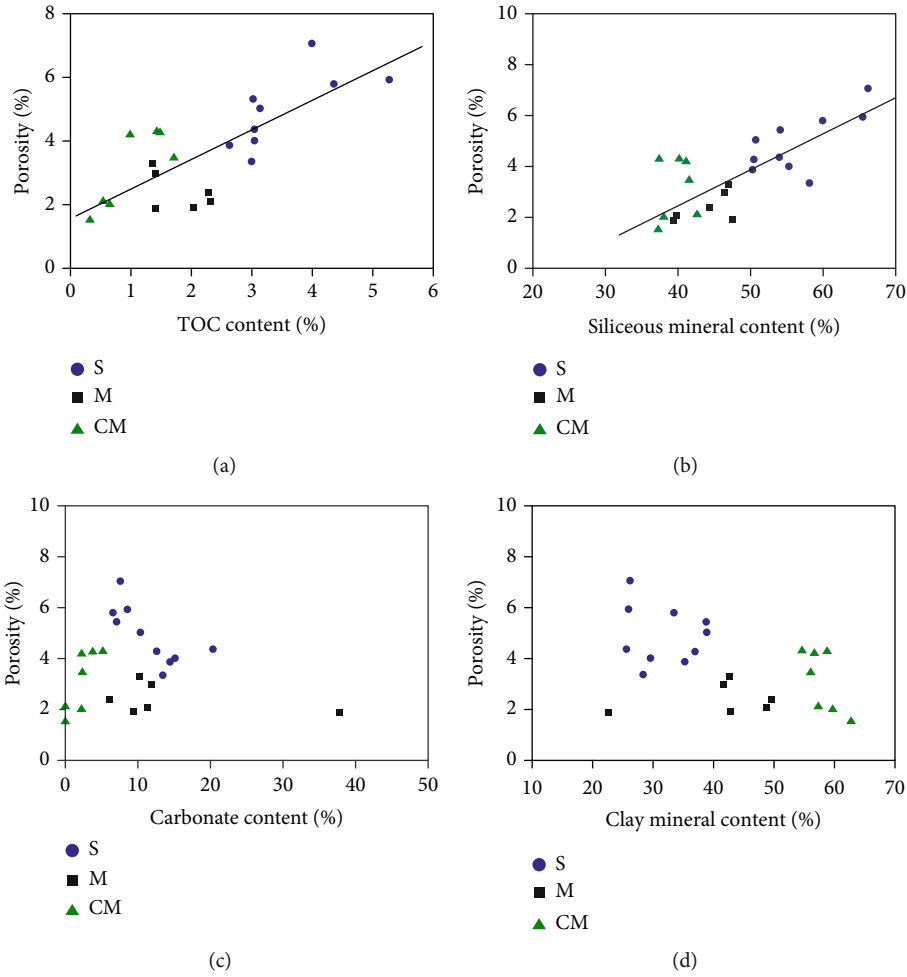


FIGURE 10: Relationship between porosity and (a) TOC content, (b) siliceous minerals content, (c) carbonate content, and (d) clay minerals content of shale samples.

( $\text{cm}^3/\text{g}$ ) are the pore volume of organic matter, framework minerals, and total clays, normalized to the mass of rock, respectively.

The bulk density ( $\rho_{\text{bulk}}$ ) and porosity ( $\phi$ ) values can be determined from helium pycnometry measurements, while the mass fractions of individual mineral components can be obtained from XRD analysis. Thus, there are three unknown parameters (specific pore volumes  $\bar{v}_{\text{OM}}$ ,  $\bar{v}_{\text{Framework}}$ , and  $\bar{v}_{\text{Clay}}$ ) in the physical model, which can be simultaneously solved using a multielement nonlinear regression on a suit of shale samples. The fitted  $\bar{v}_{\text{OM}}$ ,  $\bar{v}_{\text{Framework}}$ , and  $\bar{v}_{\text{Clay}}$  of the Longmaxi shales is  $0.4534 \text{ cm}^3/\text{g}$ ,  $0.0002 \text{ cm}^3/\text{g}$ , and  $0.0124 \text{ cm}^3/\text{g}$ , respectively. Consequently, the organic matter-hosted pores account for 79% of the total porosity while clay minerals pores account for 20% of total porosity in siliceous shales (Figure 13). In mixed shales, organic matter-hosted pores account for 62% while the pore spaces associated with clay minerals account for 38% of the total porosity. Argillaceous shales are dominant by pores associated with clay minerals. In argillaceous shales, clay minerals account for 62% of the total porosity while the OM-hosted pores account for 37%. It should be noted that the linear combination method pro-

vides fast and semiquantitative characterization of pore spaces. The effects of mineralogy on porosity and pore space of rocks are much more complicated and associated to the interaction between organic and inorganic matters. The contribution of organic matter to porosity of argillaceous shales is probably an optimistic value since it is difficult to find lots of OM-hosted pores in argillaceous shales (Figure 9).

**5.2. The Effect of Microfabric and Laminae on Permeability and Permeability Anisotropy.** Shale permeability is related to many geological controls: including fabric, texture, lithology, porosity, and pore size distribution [20, 38]. Geological controls on permeable property of tight shales are always rock specific. In Devonian gas shales from the Horn River and Liard Basins of Canada, high matrix permeability shales were found to contain connected transport pathways between macropores and micropores [20]. Gas shales containing balanced ratio of micro-, meso- and macropores have higher matrix permeability values. Yang and Aplin [21] analyzed the effect of lithology on permeability of deeply buried mudstones and found that coarser-grained mudstones always have higher permeability values than finer-grained

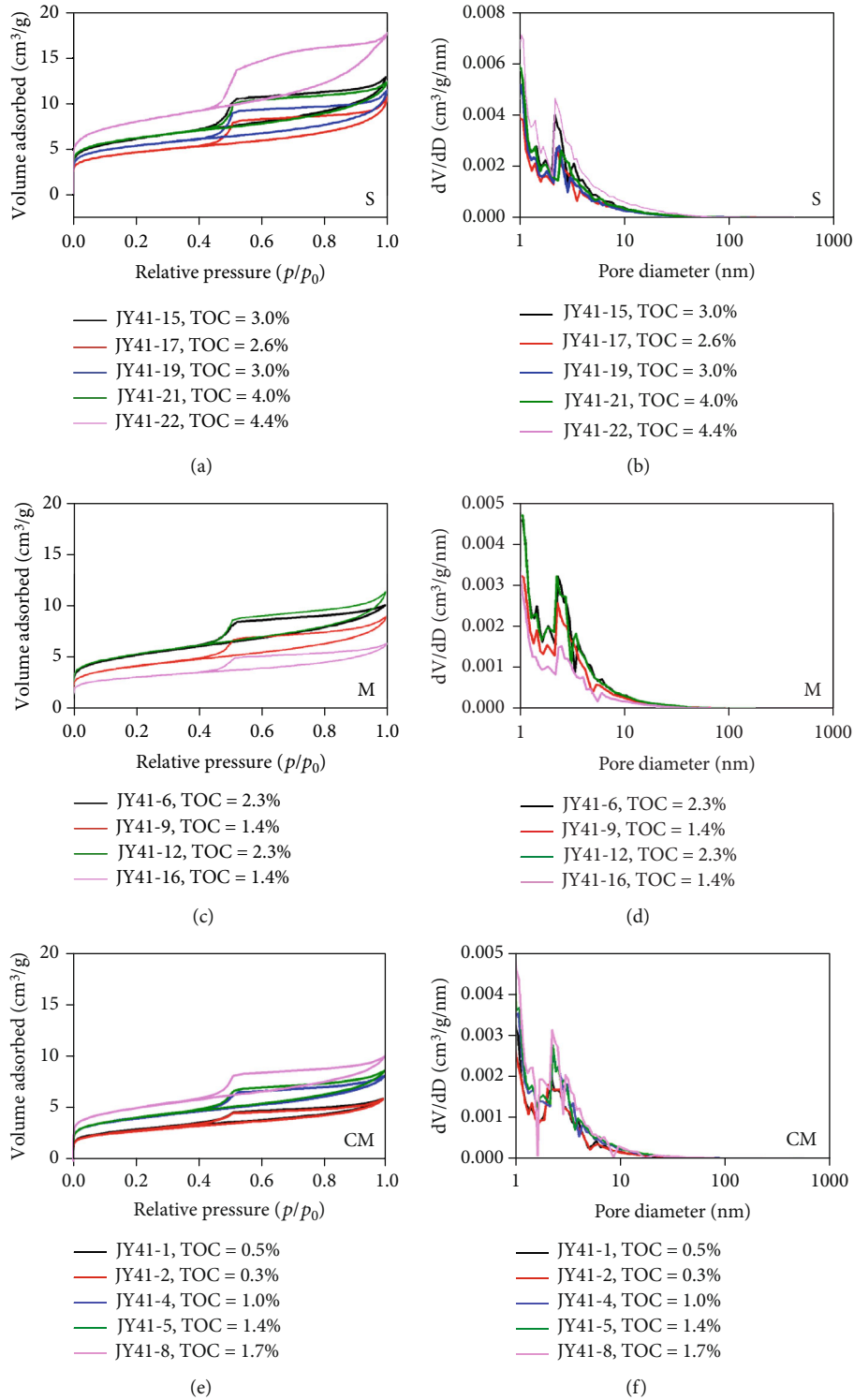


FIGURE 11: Low-pressure nitrogen adsorption isotherms and of pore size distributions of shale samples. (a, b) Siliceous shale lithofacies (S); (c, d) argillaceous/siliceous/calcareous mixed shale lithofacies (M); (e, f) silica-rich argillaceous shale lithofacies (CM).

mudstones. However, permeable property of Longmaxi shales in our data set is mainly associated with the fabric and laminae instead of pore-size distributions. Though the porosity of mixed shales (M) and argillaceous shales (CM) is lower than that of siliceous shales (S), the average  $K_h$  values

of argillaceous shales ( $37.6 \mu D$ ) and mixed shales ( $24.4 \mu D$ ) are obviously larger than those of siliceous shales ( $8.2 \mu D$ ). The reason for that is that the clay flakes and the microlaminae of clasts oriented to the lamination/bedding noticeably influence the permeabilities ( $K_h$ ) of these Longmaxi shales

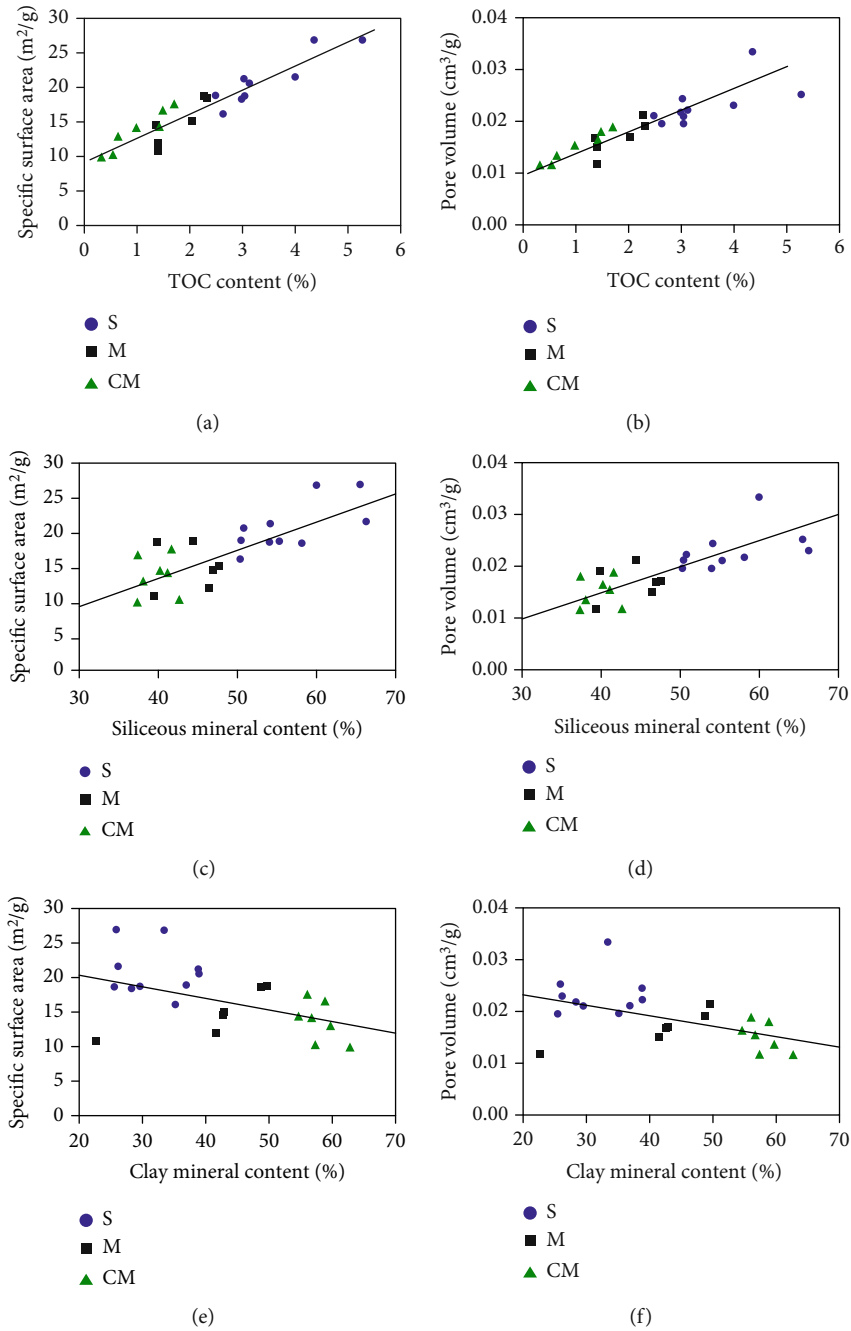


FIGURE 12: The relationship between (a) TOC content and specific surface area, (b) TOC content and total pore volume, (c) siliceous mineral content and specific surface area, (d) siliceous mineral content and pore volume, (e) clay mineral content and specific surface area, and (f) clay mineral content and pore volume of shale samples.

studied (Figures 5 and 6). Intraparticle pores of oriented clay minerals and interparticle pores between rigid clast particles and soft minerals (clay minerals or OM) are commonly distributed along the lamination/bedding of argillaceous shales and mixed shales (Figures 8 and 9). Though the inorganic matter-related porosity is less than OM-hosted porosity, the intraparticle pores in clay minerals and interparticle pores between organic and inorganic minerals play a significant role (preferable pathways) in fluid transport processes. These can be illustrated by the residual bitumen (migrabitumen)

captured in these pore spaces among grains (Figures 8(c) and 8(d) and Figure 9(c)). Conversely, siliceous shales at the bottom of Longmaxi Formation are mainly formed in euxinic sediment environment [48, 49]. Siliceous shales in Longmaxi Formation are obviously less in laminae compared to mixed and argillaceous shales (Figure 4). In siliceous shales, a lot of spongy organic matter are distributed without any preferred direction in the vision of SEM (Figure 7). What is more, permeabilities ( $K_h$ ) of siliceous shales with faint laminae (JYA-17, JYA-18) are also higher than nonlaminated

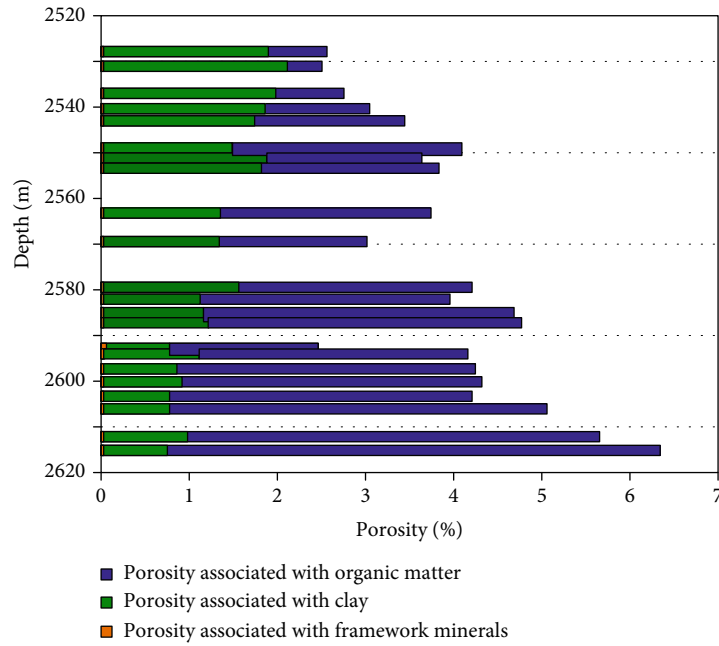


FIGURE 13: The semiquantitative estimation of porosity related to mineralogy using the linear combination approach.

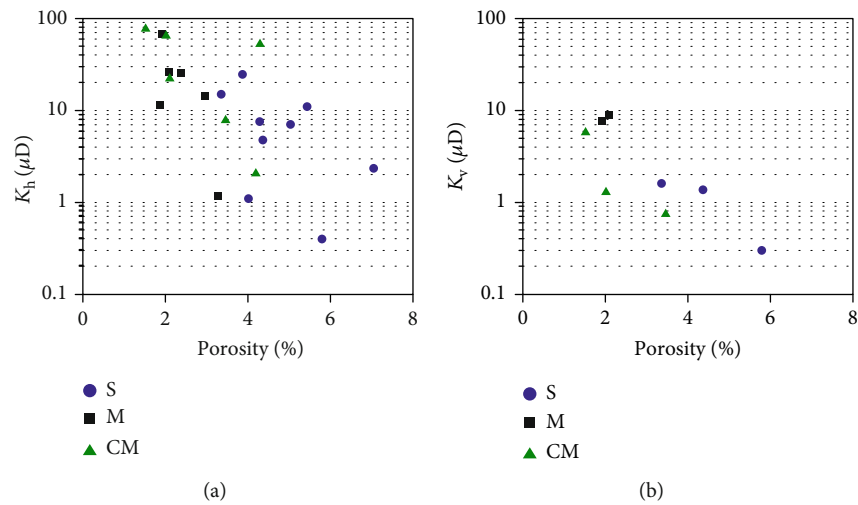


FIGURE 14: Effect of lithology on the relationship between permeability and porosity. (a) The permeability ( $K_h$ ) was measured parallel to bedding. (b) The permeability ( $K_v$ ) was measured perpendicular to bedding.

siliceous shales (JYA-22, Figure 4). In a word, TOC content does influence the porosity of these Longmaxi shales but is not the critical factor on permeability.

The porosity-permeability relationships of shales have been assessed in previous investigations. Some investigators reported a power law relationship between porosity and permeability [21]. In this study, there is a weak negative relationship between porosity and permeability coefficients (Figure 14). The fabric and texture highly influence the relationships between porosity and permeability. Though the porosity of siliceous shales is larger than other shales, permeability values of this kind of shales are actually lower. The intraparticle pores of oriented clay minerals and interparticle pores between organic and inorganic matters (microlaminae

of clasts) develop in M and CM shales (Figures 5 and 6), which contribute to both  $K_h$  and  $K_v$ .

Permeability anisotropy (the ratio of horizontal permeability  $K_h$  to vertical permeability  $K_v$ ) has been reported on shale systems [37, 56]. Permeability anisotropy of Longmaxi shales in this study varies from 1.3 to 49.8 (confining pressure of 2000 psi), which is comparable to other shales [37]. Permeability anisotropy is related to the pores with oriented alignment, permeable layers, and preferable migration pathway of shales. In this study, permeability anisotropy of argillaceous shales is higher than that of siliceous shales (Figure 15). The permeability anisotropy values of three siliceous shale samples are less than ten, whereas  $K_h$  of argillaceous shales are generally higher than  $K_v$  more than one order of



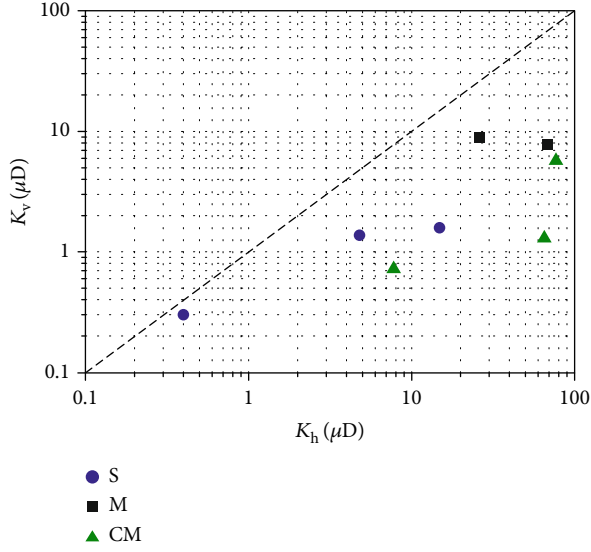


FIGURE 15: Klinkenberg-corrected permeability coefficients measured parallel ( $K_h$ ) and perpendicular ( $K_v$ ) to bedding.

magnitude. This is probably related to the microfabric of the shales. Abundant clay flakes are oriented to the lamination in argillaceous shales (Figures 6(a) and 6(c)), whereas quartz in siliceous shales is randomly orientated and clays are scattered (Figures 4(a) and 4(d)). Furthermore, samples rich in laminated fabric (sample) always show high permeability anisotropy (Figure 4(b) and Figure 5(b)).

**5.3. Effective Transport Pore Diameter of Shales.** The effective transport pore diameter can be derived from gas slippage factors during permeability measurements [19, 57]. By assuming cylindrical pores, the effective transport pore diameter is a function of gas slippage factors using the theory of Klinkenberg [29]:

$$d = \frac{8c\lambda P_m}{b} \quad (2)$$

where  $d$  (m) is effective pore diameter for gas transport;  $c \approx 1$  is the Adzumi constant,  $\lambda$  (m) is the gas mean free path,  $P_m$  (Pa) is mean pore pressure, and  $b$  (Pa) is the gas slippage factor.

Combined with the slippage factors, the effective transport pore diameter for gas transport in the shales parallel to the bedding ranges from 80 to 983 nm at the experimental confining pressure. These values are much higher than the average pore diameters derived from low-pressure  $N_2$  adsorption analysis (Table 2). The pore diameter obtained from low-pressure  $N_2$  adsorption analysis is a representation of pore structure of shale matrix, while the pulse-decay permeability is directional and strongly influenced by the occurrence of preferential pathways (laminae or microfractures). The effective transport pore diameter of siliceous shales ranges between 81 and 305 nm (averaging 191 nm), while the effective transport pore diameter of argillaceous shales ranges from 218 to 826 nm (averaging 552 nm). There is a

negative correlation between TOC content and effective transport pore diameters of the shales studied (Figure 16(a)), while a positive correlation exists between clay mineral content and effective transport pore diameters of shale samples (Figure 16(b)). This further implies that there are developed preferred transport paths in argillaceous shales. Through comparison with the visual pore structure characteristics, it is thought that the intraparticle pores between the oriented minerals are the preferential transport pathways.

The Winland equation, originally developed from mercury intrusion capillary pressure (MICP) measurements of conventional reservoir rocks, was recently used to identify the flow unit and estimate the dominant pore throat diameters for fluid flow in shales [58]. Though the Winland equation is an empirical method based on MICP data, it provides visual information about the pore diameter and permeability. The Winland equation describing the rock permeability (mD), porosity (decimal), and  $r_{p35}$  (dominant pore-throat aperture,  $\mu\text{m}$ ) can be written as [58, 59]

$$r_{p35} = 2.665 \left[ \frac{k}{100\phi} \right]^{0.45} \quad (3)$$

Using the permeability and porosity values, the dominant pore throat diameter ( $2r_{p35}$ ) for fluid transport estimated from the Winland method ranges from 71 to 1386 nm (Table 2). These values are slightly larger than those estimated from gas slippage measurements, which is probably related to the difference of tortuosity in shales and the conventional reservoir rocks. However, both these two methods show that the effective transport pore diameters of siliceous shales are commonly lower than those of argillaceous shales (Figure 17). The dominated pore-throat diameter of siliceous shales lies between 50 and 300 nm, while that of argillaceous shales is between 100 and 1000 nm. These values underline the controls of microfabric and texture on transport pathways of Longmaxi shales.

## 6. Conclusions

Comprehensive investigations on reservoir characteristic of Longmaxi shales from a shale gas well in the Jiaoshiha area, Sichuan Basin, were conducted. Special attentions were focused on the effects of microfabric and laminae on pore structure and gas transport pathways of shales. The following conclusions can be drawn:

- (1) In general, there are three different kinds of lithofacies in the Longmaxi Formation: faintly laminated to nonlaminated siliceous shales (S), laminated mixed shales (M), and argillaceous shales (CM) with oriented clay flakes. Porosity of these Longmaxi shales studied is positively correlated with TOC content and ranges from 1.5 to 7.1%. Organic matter approximately contributes 79% to the pore spaces of siliceous shale samples, whereas interparticle pores related to inorganic matter contribute 63% to the pore spaces of argillaceous shale samples

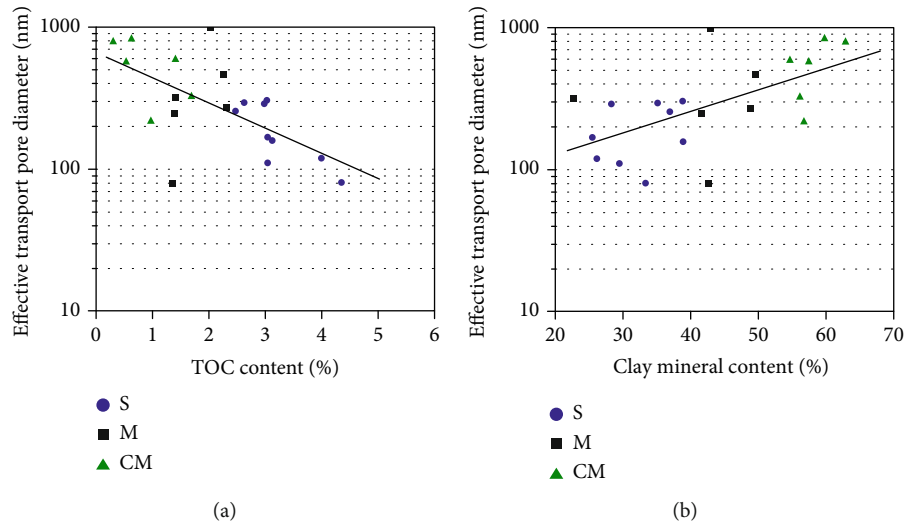


FIGURE 16: The relationship between (a) TOC content, (b) clay mineral content, and transport pore diameter of shale samples.

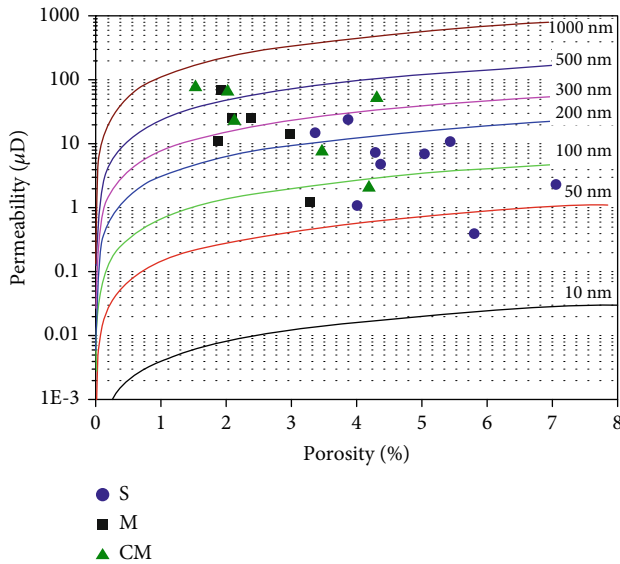


FIGURE 17: The crossplot of Klinkenberg-corrected permeability versus porosity along with the lines based on the Winland equation [59] for different values of  $r_{p35}$ .

- (2) The intrinsic permeability of Longmaxi shales parallel to bedding ( $K_h$ ) ranges between 0.4 and 76.6  $\mu\text{D}$ . The average parallel to bedding permeability values decreases in a descending order: CM shales (averaging 37.6  $\mu\text{D}$ ) > M shales (averaging 24.4  $\mu\text{D}$ ) > S shales (averaging 8.2  $\mu\text{D}$ ). Permeability anisotropy of shales varies from 1.3 to 49.8
- (3) Permeability of these shales mainly depends on the rock microfabric, other than TOC content and porosity. There is a negative correlation between permeability values and porosities of the samples studied. Samples with well-developed laminae and oriented clay flakes show higher permeability and permeability anisotropy

- (4) The effective transport pore diameter was estimated using two different methods: gas slippage measurements and the Winland equation. The effective transport pore diameters of argillaceous shales (averaging 552 nm) are commonly larger than those of siliceous shales (averaging 198 nm), which is related to the preferential transport pathways of laminated fabric and intraparticle pores of oriented clay minerals

### Data Availability

Data will be made available upon request.

### Conflicts of Interest

The authors declare that they have no conflicts of interest.

### Acknowledgments

The authors would like to acknowledge the financial support of the National Natural Science Foundation of China (Grant Nos. 41690134, 41821002, 51604249, and 41702155), the Programme of Introducing Talents of Discipline to Universities (No. B14031), and the Open Research Fund of Teaching Laboratory, China University of Geosciences (Wuhan) (No. SKJ2018019).

### References

- [1] J. B. Curtis, "Fractured shale-gas systems," *AAPG Bulletin*, vol. 86, pp. 1921–1938, 2002.
- [2] R. Rezaee, *Fundamentals of Gas Shale Reservoirs*, Published by John Wiley & Sons, Hoboken, New Jersey, USA, 2015.
- [3] D. A. V. Stow and D. J. W. Piper, "Deep-water fine-grained sediments: facies models," *Geological Society, London, Special Publications*, vol. 15, no. 1, pp. 611–646, 1984.
- [4] C. R. Clarkson, N. Solano, R. M. Bustin et al., "Pore structure characterization of North American shale gas reservoirs using USANS/SANS, gas adsorption, and mercury intrusion," *Fuel*, vol. 103, pp. 606–616, 2013.

- [5] X. Dong, H. Liu, J. Hou, K. Wu, and Z. Chen, "Phase equilibria of confined fluids in nanopores of tight and shale rocks considering the effect of capillary pressure and adsorption film," *Industrial and Engineering Chemistry Research*, vol. 55, no. 3, pp. 798–811, 2016.
- [6] R. G. Loucks, R. M. Reed, S. C. Ruppel, and D. M. Jarvie, "Morphology, genesis, and distribution of nanometer-scale pores in siliceous mudstones of the Mississippian Barnett Shale," *Journal of Sedimentary Research*, vol. 79, no. 12, pp. 848–861, 2009.
- [7] R. G. Loucks, R. M. Reed, S. C. Ruppel, and U. Hammes, "Spectrum of pore types and networks in mudrocks and a descriptive classification for matrix-related mudrock pores," *AAPG Bulletin*, vol. 96, no. 6, pp. 1071–1098, 2012.
- [8] C. Lyu, Z. Ning, Q. Wang, and M. Chen, "Application of NMRT2 to pore size distribution and movable fluid distribution in tight sandstones," *Energy & Fuels*, vol. 32, no. 2, pp. 1395–1405, 2018.
- [9] R. Holmes, H. Aljamaan, V. Vishal, J. Wilcox, and A. R. Kovscek, "Idealized shale sorption isotherm measurements to determine pore capacity, pore size distribution, and surface area," *Energy & Fuels*, vol. 33, no. 2, pp. 665–676, 2019.
- [10] M. Mastalerz, A. Schimmelmann, A. Drobniak, and Y. Chen, "Porosity of Devonian and Mississippian New Albany shale across a maturation gradient: insights from organic petrology, gas adsorption, and mercury intrusion," *AAPG Bulletin*, vol. 97, no. 10, pp. 1621–1643, 2013.
- [11] R. M. Slatt and N. R. O'Brien, "Pore types in the Barnett and Woodford gas shales: contribution to understanding gas storage and migration pathways in fine-grained rocks," *AAPG Bulletin*, vol. 95, no. 12, pp. 2017–2030, 2011.
- [12] L. Chen, Z. Jiang, K. Liu, J. Tan, F. Gao, and P. Wang, "Pore structure characterization for organic-rich Lower Silurian shale in the Upper Yangtze Platform, South China: a possible mechanism for pore development," *Journal of Natural Gas Science and Engineering*, vol. 46, pp. 1–15, 2017.
- [13] J. Li, K. Wu, Z. Chen et al., "Effects of energetic heterogeneity on gas adsorption and gas storage in geologic shale systems," *Applied Energy*, vol. 251, p. 113368, 2019.
- [14] K. L. Milliken, M. Rudnicki, D. N. Awwiller, and T. Zhang, "Organic matter-hosted pore system, Marcellus formation (Devonian), Pennsylvania," *AAPG Bulletin*, vol. 97, no. 2, pp. 177–200, 2013.
- [15] Q. R. Passey, K. Bohacs, W. L. Esch, R. Klimentidis, and S. Sinha, "From oil-prone source rock to gas-producing shale reservoir-geologic and petrophysical characterization of unconventional shale gas reservoirs," in *International Oil and Gas Conference and Exhibition in China*, Beijing, China, 2010.
- [16] F. Yang, Z. Ning, Q. Wang, R. Zhang, and B. M. Krooss, "Pore structure characteristics of lower Silurian shales in the southern Sichuan Basin, China: Insights to pore development and gas storage mechanism," *International Journal of Coal Geology*, vol. 156, pp. 12–24, 2016.
- [17] K. Wu, Z. Chen, X. Li, C. Guo, and M. Wei, "A model for multiple transport mechanisms through nanopores of shale gas reservoirs with real gas effect-adsorption-mechanic coupling," *Heat and Mass Transfer*, vol. 93, pp. 408–426, 2016.
- [18] K. Wu, Z. Chen, X. Li et al., "Flow behavior of gas confined in nanoporous shale at high pressure: real gas effect," *Fuel*, vol. 205, pp. 173–183, 2017.
- [19] R. Fink, B. M. Krooss, and A. Amann-Hildenbrand, "Stress-dependence of porosity and permeability of the Upper Jurassic Bossier shale: an experimental study," *Geological Society London Special Publications*, vol. 454, no. 1, pp. 107–130, 2017.
- [20] G. R. L. Chalmers, D. J. K. Ross, and R. M. Bustin, "Geological controls on matrix permeability of Devonian gas shales in the Horn River and Liard basins, northeastern British Columbia, Canada," *International Journal of Coal Geology*, vol. 103, pp. 120–131, 2012.
- [21] Y. Yang and A. C. Aplin, "Permeability and petrophysical properties of 30 natural mudstones," *Journal of Geophysical Research*, vol. 112, no. B3, 2007.
- [22] M. Pommer and K. Milliken, "Pore types and pore-size distributions across thermal maturity, Eagle Ford Formation, southern Texas," *AAPG Bulletin*, vol. 99, no. 9, pp. 1713–1744, 2015.
- [23] P. Psarras, R. Holmes, V. Vishal, and J. Wilcox, "Methane and CO<sub>2</sub> adsorption capacities of kerogen in the eagle ford shale from molecular simulation," *Accounts of Chemical Research*, vol. 50, no. 8, pp. 1818–1828, 2017.
- [24] X. Tang, Z. Jiang, H. Huang et al., "Lithofacies characteristics and its effect on gas storage of the Silurian Longmaxi marine shale in the southeast Sichuan Basin, China," *Journal of Natural Gas Science and Engineering*, vol. 28, pp. 338–346, 2016.
- [25] F. Yang, Z. Ning, R. Zhang, H. Zhao, and B. M. Krooss, "Investigations on the methane sorption capacity of marine shales from Sichuan Basin, China," *International Journal of Coal Geology*, vol. 146, pp. 104–117, 2015.
- [26] H. Qinhong, Y. Zhang, X. Meng, L. Zheng, Z. Xie, and L. Maowen, "Characterization of micro-nano pore networks in shale oil reservoirs of Paleogene Shahejie Formation in Dongying Sag of Bohai Bay Basin, East China," *Petroleum Exploration and Development*, vol. 44, no. 5, pp. 720–730, 2017.
- [27] F. Rashid, P. W. J. Glover, P. Lorinczi, D. Hussein, R. Collier, and J. Lawrence, "Permeability prediction in tight carbonate rocks using capillary pressure measurements," *Marine and Petroleum Geology*, vol. 68, pp. 536–550, 2015.
- [28] Z. Gao and Q. Hu, "Estimating permeability using median pore-throat radius obtained from mercury intrusion porosimetry," *Journal of Geophysics and Engineering*, vol. 10, no. 2, article 025014, 2013.
- [29] L. J. Klinkenberg, *The permeability of porous media to liquids and gases*, American Petroleum Institute, New York, New York, 1941.
- [30] D. M. Jarvie, R. J. Hill, T. E. Ruble, and R. M. Pollastro, "Unconventional shale-gas systems: the Mississippian Barnett shale of north-central Texas as one model for thermogenic shale-gas assessment," *AAPG Bulletin*, vol. 91, no. 4, pp. 475–499, 2007.
- [31] J. Tan, B. Horsfield, R. Fink et al., "Shale gas potential of the major marine shale formations in the Upper Yangtze Platform, South China, part III: mineralogical, lithofacial, petrophysical, and rock mechanical properties," *Energy & Fuels*, vol. 28, no. 4, pp. 2322–2342, 2014.
- [32] B. Bruns, R. Littke, M. Gasparik, J.-D. van Wees, and S. Nelskamp, "Thermal evolution and shale gas potential estimation of the Wealden and Posidonia Shale in NW-Germany and the Netherlands: a 3D basin modelling study," *Basin Research*, vol. 28, no. 1, pp. 2–33, 2016.
- [33] R. Littke, J. L. Urai, A. K. Uffmann, and F. Risvanis, "Reflectance of dispersed vitrinite in Palaeozoic rocks with and without cleavage: implications for burial and thermal history modeling in the Devonian of Rursee area, northern Rhenish

- Massif, Germany,” *International Journal of Coal Geology*, vol. 89, pp. 41–50, 2012.
- [34] A. T. Stock, R. Littke, J. Schwarzbauer, B. Horsfield, and C. Hartkopf-Fröder, “Organic geochemistry and petrology of Posidonia Shale (Lower Toarcian, Western Europe) - The evolution from immature oil-prone to overmature dry gas-producing kerogen,” *International Journal of Coal Geology*, vol. 176–177, pp. 36–48, 2017.
- [35] K. Wu, X. Li, C. Wang, W. Yu, and Z. Chen, “Model for surface diffusion of adsorbed gas in nanopores of shale gas reservoirs,” *Industrial and Engineering Chemistry Research*, vol. 54, no. 12, pp. 3225–3236, 2015.
- [36] H. Zhao, Z. Ning, T. Zhao, R. Zhang, and Q. Wang, “Effects of mineralogy on petrophysical properties and permeability estimation of the Upper Triassic Yanchang tight oil sandstones in Ordos Basin, Northern China,” *Fuel*, vol. 186, pp. 328–338, 2016.
- [37] A. Ghanizadeh, A. Amann-Hildenbrand, M. Gasparik, Y. Gensterblum, B. M. Krooss, and R. Littke, “Experimental study of fluid transport processes in the matrix system of the European organic-rich shales: II. Posidonia Shale (Lower Toarcian, northern Germany),” *International Journal of Coal Geology*, vol. 123, pp. 20–33, 2014.
- [38] A. Ghanizadeh, C. R. Clarkson, S. Aquino, O. H. Ardakani, and H. Sanei, “Petrophysical and geomechanical characteristics of Canadian tight oil and liquid-rich gas reservoirs: I. pore network and permeability characterization,” *Fuel*, vol. 153, pp. 664–681, 2015.
- [39] Q. Hu, R. P. Ewing, and H. D. Rowe, “Low nanopore connectivity limits gas production in Barnett formation,” *Journal of Geophysical Research: Solid Earth*, vol. 120, no. 12, pp. 8073–8087, 2015.
- [40] J. J. Hickey and B. Henk, “Lithofacies summary of the Mississippian Barnett shale, mitchell 2 T.P. Sims well, Wise County, Texas,” *AAPG Bulletin*, vol. 91, no. 4, pp. 437–443, 2007.
- [41] R. G. Loucks and S. C. Ruppel, “Mississippian Barnett Shale: lithofacies and depositional setting of a deep-water shale-gas succession in the Fort Worth Basin, Texas,” *AAPG Bulletin*, vol. 91, no. 4, pp. 579–601, 2007.
- [42] J. Dai, C. Zou, S. Liao et al., “Geochemistry of the extremely high thermal maturity Longmaxi shale gas, southern Sichuan Basin,” *Organic Geochemistry*, vol. 74, pp. 3–12, 2014.
- [43] T. Guo, “Evaluation of highly thermally mature shale-gas reservoirs in complex structural parts of the Sichuan Basin,” *Journal of Earth Science*, vol. 24, no. 6, pp. 863–873, 2013.
- [44] F. Hao, T. Guo, Y. Zhu, X. Cai, H. Zou, and P. Li, “Evidence for multiple stages of oil cracking and thermochemical sulfate reduction in the Puguang gas field, Sichuan Basin, China,” *AAPG Bulletin*, vol. 92, no. 5, pp. 611–637, 2008.
- [45] F. Hao, H. Zou, and Y. Lu, “Mechanisms of shale gas storage: implications for shale gas exploration in China,” *AAPG Bulletin*, vol. 97, no. 8, pp. 1325–1346, 2013.
- [46] L. Chen, Z. Jiang, K. Liu et al., “Effect of lithofacies on gas storage capacity of marine and continental shales in the Sichuan Basin, China,” *Journal of Natural Gas Science and Engineering*, vol. 36, pp. 773–785, 2016.
- [47] T. Guo and H. Zhang, “Formation and enrichment mode of Jiaoshiba shale gas field, Sichuan Basin,” *Petroleum Exploration and Development*, vol. 41, no. 1, pp. 31–40, 2014.
- [48] X. Guo, D. Hu, Y. Li, Z. Wei, X. Wei, and Z. Liu, “Geological factors controlling shale gas enrichment and high production in Fuling shale gas field,” *Petroleum Exploration and Development*, vol. 44, no. 4, pp. 513–523, 2017.
- [49] Y. F. Li, D. Y. Shao, H. G. Lv, Y. Zhang, X. L. Zhang, and T. W. Zhang, “A relationship between elemental geochemical characteristics and organic matter enrichment in the marine shale of Wufeng Formation-Longmaxi Formation Sichuan Basin,” *Acta Petrolei Sinica*, vol. 36, pp. 1470–1483, 2015.
- [50] C. L. Mu, K. K. Zhou, W. Liang, and X. Y. Ge, “Early Paleozoic sedimentary environment of hydrocarbon source rocks in the Middle-Upper Yangtze Region and petroleum and gas exploration,” *Acta Geologica Sinica*, vol. 85, no. 4, pp. 526–532, 2011.
- [51] L. Zhang, B. Li, S. Jiang et al., “Heterogeneity characterization of the lower Silurian Longmaxi marine shale in the Pengshui area, South China,” *International Journal of Coal Geology*, vol. 195, pp. 250–266, 2018.
- [52] Z. F. Wang, Y. F. Zhang, X. L. Liang et al., “Characteristics of shale lithofacies formed under different hydrodynamic conditions in the Wufeng-Longmaxi Formation, Sichuan Basin,” *Acta Petrolei Sinica*, vol. 35, no. 4, pp. 623–632, 2014.
- [53] S. J. Gregg and K. S. W. Sing, *Adsorption, surface area and porosity*, Academic Press, New York, 2nd edition, 1982.
- [54] W. C. Krumbein, “Lithofacies maps and regional sedimentary-stratigraphic analysis,” *AAPG Bulletin*, vol. 32, no. 10, pp. 1909–1923, 1948.
- [55] U. Kuila, D. K. McCarty, A. Derkowski, T. B. Fischer, T. Topór, and M. Prasad, “Nanoscale texture and porosity of organic matter and clay minerals in organic-rich mudrocks,” *Fuel*, vol. 135, pp. 359–373, 2014.
- [56] A. R. Bhandari, P. B. Flemings, P. J. Polito, M. B. Cronin, and S. L. Bryant, “Anisotropy and stress dependence of permeability in the Barnett shale,” *Transport in Porous Media*, vol. 108, no. 2, pp. 393–411, 2015.
- [57] G. Gaus, A. Amann-Hildenbrand, B. M. Krooss, and R. Fink, “Gas permeability tests on core plugs from unconventional reservoir rocks under controlled stress: a comparison of different transient methods,” *Journal of Natural Gas Science and Engineering*, vol. 65, pp. 224–236, 2019.
- [58] C. R. Clarkson, J. L. Jensen, P. K. Pedersen, and M. Freeman, “Innovative methods for flow-unit and pore-structure analyses in a tight siltstone and shale gas reservoir,” *AAPG Bulletin*, vol. 96, no. 2, pp. 355–374, 2012.
- [59] R. Aguilera, “Incorporating capillary pressure, pore aperture radii, height above free water table, and Winland  $r_{35}$  values on Picket plots,” *AAPG Bulletin*, vol. 86, pp. 605–624, 2002.